NASA Conference Publication 2229

Twelfth Space Simulation Conference

"Shuttle Plus One - A New View of Space"

JUN 1982
RECEIVED

(NASA-CP-2229) TWELFTH SPACE SIMULATION CONFERENCE: SHUTTLE PLUS ONE. A NEW VIEW OF SPACE (NASA) 339 p HC A15/MF A01 CSCL 22B
N82-25291
THRU
N82-25311
Unclas
G3/18 21935

Proceedings held at
Pasadena, California on
May 17 to 19 1982

NASA

PRECEDING PAGE BLANK NOT FILMED

FOREWORD

The Institute of Environmental Sciences twelfth Space Simulation Conference "Shuttle Plus One - A New View of Space" provided participants a forum to acquire and exchange information on the state-of-the-art in space simulation test technology, thermal simulation and protection, contamination, and dynamics testing and assessment. These technologies have played in important role in the successful development of the Space Transportation System. This year's program, held in Pasadena, California, offered a wide spectrum of useful data in these disciplines.

The Goddard Space Flight Center of the National Aeronautics and Space Administration welcomes this opportunity to act in concert with the Jet Propulsion Laboratory, the American Institute of Aeronautics and Astronautics, the American Society for Testing and Materials, and the host society, the Institute of Environmental Sciences, in publishing these NASA Conference Proceedings for international distribution.

Norman L. Martin, Chief
Engineering Services Division
Goddard Space Flight Center

PRECEDING PAGE BLANK NOT FILMED

PREFACE

The Twelfth Space Simulation Conference, held at the Pasadena Hilton Hotel, Pasadena, CA, and hosted by the Jet Propulsion Laboratory, May 17 to 19, 1982, was sponsored jointly by the Institute of Environmental Sciences (IES) and supported by the American Institute of Aeronautics and Astronautics (AIAA) and the American Society for Testing and Materials (ASTM). The conference is further supported by the National Aeronautics and Space Administration (NASA) by their publication of these proceedings.

The Twelfth Space Simulation Conference presented a wide variety of papers dealing with the current state of space simulation. A panel discussion of Shuttle results was held and should form the basis for future simulation studies and testing. It is hoped that the papers presented at this conference and the resulting discussions will indeed carry out the conference theme of forming - a new view of space.

The conference committee is pleased that the Jet Propulsion Laboratory offered to host this conference. JPL has supported this conference over the years with papers, personnel, attendees and speakers and we thank the Laboratory again for hosting the conference and providing a fine tour of Laboratory facilities.

This document is a product of the efforts of many individuals. It represents the work of the authors, the various conference committees, the staff of IEC and others. I would like to take this opportunity to publicly thank a few of those whose efforts have made this conference possible. Thanks go to John W. Harrell, Technical Program Chairman, JPL; R. L. Daniel, Arrangements Chairman, JPL; R. T. (Tom) Hollingsworth, Publications Chairman, NASA Goddard Space Flight Center, for their invaluable contribution. In addition, we all wish to thank Betty L. Peterson, Executive Director, IES; and Janet A. Ehmann, Assistant to the Director, IES, for handling all the details which permit a smooth running conference. Finally, our thanks to John D. Campbell, IES Meeting Manager, for being the continuing driving force behind this conference.

It is my hope that this conference has been an enjoyable, informative and valuable experience for all who attended both in the technical sessions and in the informal discussions between colleagues working in the field.

Sincerely,

George F. Wright, Jr.
General Chairman

12th SPACE SIMULATION CONFERENCE

Pasadena Hilton Hotel - Pasadena, California

May 17 - 19, 1982

Host Society: **Institute of Environmental Sciences**

Supported by: **Jet Propulsion Laboratory, National Aeronautics and Space Administration, American Institute of Aeronautics and Astronautics, and American Society for Testing and Materials**

MEETING MANAGEMENT COMMITTEE

General Chairman: **George F. Wright, Jr.**, Sandia National Laboratories

Technical Program Chairman: **John W. Harrell**, Jet Propulsion Laboratory

Facilities Chairman: **Robert Daniel**, Jet Propulsion Laboratory

IES Meeting Manager: **John D. Campbell**, Perkin-Elmer Corporation

Publication Chairman: **Russell T. Hollingsworth**, NASA Goddard Space Flight Center

Publications Editor: **Janet Ehmann**, Institute of Environmental Sciences

Executive Director: **Betty Peterson**, Institute of Environmental Sciences

TECHNICAL PROGRAM COMMITTEE

Emile S. J. Wang, McDonnell Douglas Corporation

Albert R. Lunde, The Boeing Company

Eugene N. Borson, The Aerospace Corporation

Raymond Kruger, NASA Goddard Space Flight Center

David G. Billingsley, Johnson Space Center

Ernest Oddo, McDonnell Douglas Astronautics

Robert Parrish, Martin Marietta Corporation

JOINT POLICY COMMITTEE

IES - **John D. Campbell**, Perkin-Elmer Corporation
George Frankel, Grumman Aerospace

ASTM - **Eugene N. Borson**, The Aerospace Corporation
Charles H. Duncan, NASA Goddard Space Flight Center

AIAA - **David G. Billingsley**, Johnson Space Center
Albert R. Lunde, The Boeing Company

TABLE OF CONTENTS

Page

SESSION I: SHUTTLE RESULTS PANEL DISCUSSION (No printed text) 1
Moderator: David G. Billingsley, Johnson Space Center
Panel Members: Herbert E. Smith, Jr., Johnson Space Center;
Norman H. Chaffee, Johnson Space Center
Dr. John Peller, Rockwell International

SESSION II: THERMAL SIMULATION AND PROTECTION 3
Session Organizers: Robert Parrish, Martin Marietta Aerospace
George Mikk, Perkin-Elmer Corporation

PRECISE THERMAL CONTROL DEMONSTRATION ON SIMULATED HARDWARE 5
R. Bettini and R. Wegrich, Perkin-Elmer Corporation

SPACECRAFT THERMAL BALANCE TESTING USING INFRARED SOURCES 7
G. Tan and J. Walker, European Space Agency, ESTEC

IMPROVED MLI APPLICATION APPROACH 33
George Mikk, Perkin-Elmer Corporation

TRANSIT THERMAL CONTROL DESIGN FOR GALILEO ENTRY PROBE FOR PLANET JUPITER 35
G. Haverly and W. Pitts, General Electric Company

SESSION III: THERMAL SIMULATION AND PROTECTION 53
Session Organizers: Robert Parrish, Martin Marietta Aerospace
George Mikk, Perkin-Elmer Corporation

A SURVEY OF METHODS FOR MEASURING THERMALLY INDUCED DISTORTIONS OF TEST ARTICLES UNDERGOING SOLAR THERMAL VACUUM TEST 55
R. D. Rempt, Martin Marietta Aerospace

OPTICAL CHARACTERIZATION OF SOLAR CONCENTRATOR FACETS USING THE SOLAR BEAM OF THE JPL 25 FT. SPACE SIMULATOR 63
M. Argoud and E. Dennison, Jet Propulsion Laboratory

SIMPLIFIED MLI PUMPDOWN CALCULATION APPROACH 83
R. G. Bettini, Perkin-Elmer Corporation

SESSION IV: SPACE SIMULATION TEST TECHNOLOGY 85
Session Organizers: Albert R. Lunde, Boeing Aerospace
S. Liu, TRW Space Systems

NUCLEAR HARDENING TESTING OF LARGE SCALE SATELLITES 87
N. K. Shirk, J. Sargent, and T. Wilks, General Electric Company

Page

A CRYOPUMP FOR LARGE PULSES OF HYDROGEN 89
B. C. Moore, R. G. Camarillo, and J. T. Morrow, McDonnell Douglas

EDUCATION AND TRAINING OF PERSONNEL IN SPACE SIMULATION 113
R. D. Rempt, Martin Marietta Aerospace

SESSION V: SPACE SIMULATION TEST TECHNOLOGY 119
Session Organizers: Albert R. Lunde, Boeing Aerospace
S. Liu, TRW Space Systems

A MICROPROCESSOR-BASED, MULTI-ZONE THERMAL CONTROLLER 121
W. F. Petrie, Perkin-Elmer Corporation

A REAL-TIME DYNAMIC SPACECRAFT SIMULATOR FOR THE LANDSAT-D MISSION 123
A. R. Coffin, General Electric Space System Division

ENVIRONMENTAL TEST FACILITIES USED IN EUROPE FOR ESA SATELLITE PROGRAMS 141
P. Brinkman, European Space Agency, ESTEC

SESSION VI: DYNAMICS, TESTING AND ASSESSMENT 169
Session Organizers: Ernest T. Oddo, McDonnell Douglas Astronautics Company
R. A. Colonna, NASA Johnson Space Center

CORRELATION OF MODEL AND FULL SCALE ACOUSTICAL NOISE GENERATED DURING STS LAUNCH 171
R. Trudell, McDonnell Douglas Astronautics Company

"DATE" – THE SHUTTLE PAYLOAD ENVIRONMENTAL MEASUREMENT PROGRAM 173
Edward Kirchman and W. F. Bangs, NASA Goddard Space Flight Center

DYNAMICS ENVIRONMENT FOR SPACE SHUTTLE PAYLOADS 175
D. L. Kern and M. R. O'Connell, Jet Propulsion Laboratory

ENVIRONMENTAL NOISE ASSESSMENT STS-I COLUMBIA LAUNCH AT KENNEDY SPACE CENTER 193
George Putnicki, University of Texas/Dallas

OUTGASSING: ITS EFFECT ON SPACECRAFT VIBRATION DAMPING MATERIALS 209
M. L. Drake, M. F. Kleusener, and W. R. Goddard,
University of Dayton Research Institute

ERRORS ASSOCIATED WITH SHUTTLE ACOUSTICAL DATA REDUCTION TECHNIQUES 235
Carol Tanner, The Aerospace Corporation

Page

SESSION VII: REMOTE SENSING 237
Session Organizers: Emile S. J. Wang, McDonnell Douglas Corporation
Richard Hartenbaum, RCA Corporation

THUNDERSTORM OVERFLIGHT PROGRAM 239
O. H. Vaughan, Jr., NASA Marshall Space Flight Center

DESIGN AND DEVELOPMENT OF ERBE DATA MANAGEMENT SYSTEM 241
J. F. Kibler, NASA Langley Research Center

PROVIDING RADIO FREQUENCY SPACE LINKS BETWEEN EARTH STATION AND SATELLITE FOR MEASURING SATELLITE ELECTRICAL PERFORMANCE WITHIN SIMULATED SPACE ENVIRONMENTS 257
K. R. Rauhala, General Electric Company

REMOTE SENSING OF TORNADIC STORMS FROM SPACE 259
R. H. Hung and R. E. Smith, University of Alabama/Huntsville

MEASUREMENTS BY THE PLASMA DIAGNOSTICS PACKAGE ON STS-3 271
Dr. Stanley D. Shawhan and Dr. G. Murphy, University of Iowa

SESSION VIII: CONTAMINATION 279
Session Organizers: Raymond Kruger, NASA Goddard Space Flight Center
Eugene Borson, The Aerospace Corporation

SPACE SHUTTLE PRELIMINARY CONTAMINATION ASSESSMENT FROM STS-1 AND STS-2 281
L. J. Leger, S. Jacobs, and H. K. Ehlers, NASA Johnson Space Center

A FACILITY FOR THE SIMULATION OF LOW ORBIT ATMOSPHERIC OXYGEN BOMBARDMENT 303
G. S. Arnold, R. R. Herm, and D. R. Peplinski, The Aerospace Corporation

AUTOMATING A RESIDUAL GAS ANALYZER 305
W. Petrie and A. Westfall, Perkin-Elmer Corporation

SESSION IX: CONTAMINATION 307
Session Organizers: Raymond Kruger, NASA Goddard Space Flight Center
Eugene Borson, The Aerospace Corporation

THE EXPERIMENTAL DETERMINATION OF THE EXTENT OF OUTGASSING FROM THE EUROPEAN EXPERIMENTS FOR SPACELAB 309
M. Debeir, European Space Agency

CONTAMINANT CHARACTERIZATION OF FIVE SATELLITE MATERIALS 311
Dr. J. A. Muscari, Martin Marietta Corporation

IUS MATERIALS OUTGASSING CONDENSATION EFFECTS ON SENSITIVE SPACECRAFT SURFACES 327
C. R. Mullen, Boeing Aerospace Company

SESSION 1

SHUTTLE RESULTS PANEL DISCUSSION
(No printed text)

Moderator: David G. Billingsley, Johnson Space Center

Panel Members:

Herbert E. Smith, Jr., Johnson Space Center

Norman H. Chaffee, Johnson Space Center

Dr. John Peller, Rockwell International

PRECEDING PAGE BLANK NOT FILMED

SESSION II

THERMAL SIMULATION AND PROTECTION

Session Organizers: Robert Parrish, Martin Marietta Aerospace

George Mikk, Perkin-Elmer Corporation

PRECEDING PAGE BLANK NOT FILMED

PRECISE THERMAL CONTROL DEMONSTRATION ON SIMULATED SPACE HARDWARE

R. Bettini and R. Wegrich

Perkin-Elmer Corporation
Danbury, Connecticut 06810

ABSTRACT

Numerous space applications require precise thermal control on functional hardware to maintain critical dimensions and minimize changes in these dimensions in operational environmenta. An example of this kind of structure is the Space Telescope's main ring assembly, which holds the primary mirror, the secondary mirror truss assembly, and the instrument support structure. A simulated portion of the main ring was fabricated and tested to determine whether thermal stability could be maintained in a complex structural assembly. The test confirmed the effectiveness of the highly insulated, non-critical reference surface approach.

N82 25292

PRECEDING PAGE BLANK NOT FILMED

SPACECRAFT THERMAL BALANCE TESTING USING INFRARED SOURCES

G.B.T. Tan

J.B. Walker

European Space Research and Technology Centre
ESTEC Noordwijk, Holland.

ABSTRACT

A thermal balance test (controlled flux intensity) on a simple black dummy spacecraft using IR lamps has been performed and evaluated, the latter being aimed specifically at Thermal Mathematical Model (TMM) verification. For reference purposes the model has also been subjected to a solar simulation test (SST). The results show that the temperature distributions measured during IR testing for two different model attitudes under steady state conditions are reproducible with a TMM. The TMM test data correlation is not as accurate for IRT as for SST. Using the standard deviation of the temperature difference distribution -that is analysis minus test- the SST data correlation is better by a factor of 1.8 - 2.5. The lower figure applies to the measured and the higher to the computer-generated IR flux intensity distribution. Techniques of lamp power control are presented. A continuing work programme is described which is aimed at quantifying the differences between solar simulation and infrared techniques for a model representing the thermal radiating surfaces of a large communications spacecraft.

INTRODUCTION

BACKGROUND

The solar simulator used in classical spacecraft thermal balance tests is a complex and expensive item (Ref. 1). When considering the thermal balance testing of large Ariane or STS-launched spacecraft available solar simulation facilities are inadequate. There are facilities in Europe, large enough in all respects except the size of solar simulator beam, (Fig. 1). It is apparent that means of reproducing the effect of the energy input from the sun to the spacecraft on test other than the conventional solar simulator merit consideration, both from the point of view of containing capital expenditure and as a means of circumventing the logistic and scheduling problems associated with solar-simulation-testing a European spacecraft outside Europe. The provision of heat sources local to the spacecraft inside the vacuum chamber offers an economic and potentially acceptable technical solution to the problem. Tungsten filament quartz lamps have long been used in thermal test work.

Their use on the Apollo Telescope Mount tests in 1971 is extensively described in Ref. 2. One commercially available type* fitted with a vacuum-environment-compatible reflector was chosen for the work of the present paper. An arrangement of such lamps provides an overlapping mosaic of beams at a spacecraft surface.
Combining this with accurate control of electrical power dissipated at each lamp was expected to produce a flexible and well described intensity distribution. Moreover, this energy could be presented in a reasonably solar-like spectrum, resulting in absorbed fluxes which are well defined and close to orbit conditions. This would allow the imposition of important spacecraft gradients in order to demonstrate adequately the thermal subsystem performance. The type of lamp chosen has performance characteristics such that in providing one solar constant at a surface, approximately 9 lamps per sq. metre are required. Considerations in arriving at this figure are;

- o Lamp to specimen distance giving low blockage to the [illegible] sink.
- o Intensity dispersion at the specimen surface
- o Nominal operating power level enabling accurate lamp control at a preferred wavelength of the emitted energy.

SOURCE WORK

The use of IR lamps has been fairly extensively reported, for example in Refs. 2 to 6. Very little information about the characteristics of particular lamp types is available. Some warnings about gravity vector effects on the tungsten filament have been issued for longer lamps of the same general type as the 5 inch chosen for the work. Knowledge of the lamp/reflector characteristic flux intensity distribution is fundamental to the success of the test method. A small test programme was therefore carried out with the object of establishing:

- The characteristic output curve
- Power variation effects
- Gravity vector variation effects
- Scatter due to lamp/reflector manufacturing and set up variations

Varying lamp power in the planned working range of 20% to 85% resulted in negligible differences in intensity distribution. Gravity-vector, manufacturing and set-up variations accounted for characteristic distribution changes as high as ± 14%. Other results of the test work are presented in Fig. 2. Armed with the characteristic distribution of the lamp, it should be possible, by developing computer software, to determine the intensity distribution on a complex spacecraft geometry from arrays of lamps quickly and economically. Optimum lamp arrangements with known intensity distributions could then be produced with minimal changes in the actual physical test set-up.

---

* RI Controls Type 5236-5, 500W at 120V.

This approach would minimise expensive spacecraft test set-up time.

MODEL TESTS

A simple dummy spacecraft, the socalled "Ideal Model" (IM), used in an earlier development programme was refurbished and made available for a series of tests aimed at assessing the method. It was installed in the ESTEC solar simulation facility and tested using first the Xenon arc solar simulator and then infra-red lamps. This was done for two solar aspect angles, named Attitude I and Attitude IV. These two were selected from a total of six angles studied and which were considered suitable both analytically and from the point of view of complexity of IR lamp set-up.

MODEL DESCRIPTION

The IM is shown in Fig. 3. The core of the test item is a cube of edge 0.40 m. On top of this cube is a pyramid 0.28 m high, with the upper cube surface as a base plate. There is a circular hole cut in the lower cube surface, through which the thermocouple wires are guided. The four remaining cube surfaces serve as base plates for four prisms, two of triangular cross-section and two of trapezoidal cross-section. The prisms with similar cross-sections are adjacent to each other. The height of the triangles and trapeziums is 0.20 m. The plates are made of 0.3 mm thick copper and conductively de-coupled using small nylon washers.

All IM face plates are coated at both sides with Glassofix black paint. The solar absorptivity and hemispherical emissivity are, respectively, α_s= 0.976 and ε_h= 0.85.
The IR absorptivity could not be measured for the appropriate wavelength (> 2.5μm). Based on available data for similar total absorbers in the range 0.3 - 10 μm, it seems an acceptable first approximation to set α_{ir} equal to α_s. For the IR lamps at half rated voltage, which is the minimum voltage applied during test, 98.5% of the total energy falls below 10 μm.

The thermocouple wire test cable was thermally protected with a number of layers of 3 mil aluminised Mylar. The optical properties were α_s= 0.17, ε_h=0.57 for the Mylar side and α_s= 0.16, ε_h= 0.05 for the aluminised side

TEST ARRANGEMENT

Model and lamp support

The IM for both types of test was suspended on stainless steel cables with a Teflon insulation spacer between the end cable attachment and the IM bracket support ring. Fine adjustment was provided to allow the model to be levelled at the desired height. An arrangement of 10 mm diameter, black painted, stainless-steel tubing and clamping brackets provided a supporting structure for the IR lamps. The brackets were designed to facilitate adjustment and rearrangement of the lamps. The final connection between lamp reflector and tubular structure was in the form

of a clamp enabling 45° of angular adjustment. All the components in the system were designed with a view to their re-use in IR lamp arrays. The tubular structure also provided support for the liquid-nitrogen-cooled shrouds ('baffles') which were positioned local to the IM and used to shield surfaces not to be exposed, to the IR lamps. The IR test arrangements are shown in Figs. 4 and 5.

Baffles

Baffles, actively cooled by liquid nitrogen, were used to shield model surfaces which would not be solar exposed in an orbit case, from IR lamp radiation. Fig. 3 depicts a typical case, the Attitude I situation of the IM tests. In certain cases this problem can be overcome by accepting the "inadvertent" heat input, measuring it, and introducing this into the TMM. Both the baffle and the measurement approach were used during the IM tests.

Attitude I - The pyramid irradiating lamps were baffled such that spillover could not irradiate the IM top surfaces. Surfaces 25 and 26 were irradiated and surfaces 9, 13, 23, and 18, Fig. 6, were baffled.

The lamps irradiating the trapezoidal faces were baffled such that spill-over could not radiate to the triangular prism faces. Surfaces 15 and 22 were irradiated and surfaces 7 and 12 were baffled.

Attitude IV - The lamps irradiating the pyramid were baffled such that spill-over could not irradiate the model's top surface. Surfaces 27 and 28 were irradiated and surfaces 9, 13, 18 and 23 were baffled. Spill-over from lamps intended to irradiate surfaces 16 and 21 was measured at surfaces 7 and 12 and introduced into the TMM. In this case the flux level was low, averaging 150 Wm^{-2} normal to the surface. This approach was adopted in order to assess the technique as an alternative to the more complex LN_2-cooled baffle method.

Power Control

Accurate control of the power source was achieved by using a power supply specially matched to the lamp sources. The significant features of the equipment are:

- o 1% control accuracy over the power dissipated at the source.
- o Computer monitoring and command capability.
- o Low noise and smooth control.

Each power supply channel is capable of 1000 W output at 120 V DC. The voltage level was chosen to allow lamp operation in the pressure range 760 - 10^{-6} torr and beyond without coronae problems. The power level allowed two lamps to be used in parallel per channel when testing very large regular surfaces, such as is necessary when thermal-cycling solar

cell arrays.
A smoothed DC supply was chosen to achieve minimum electromagnetic interference, allowing working spacecraft prototypes and flight models to be tested. In the present work the power supplies were used in conjunction with single lamps to give the best control over the mosaic flux pattern.

TEST PHASES

Similar procedures were used for all tests and followed normal thermal-balance-tests routine, namely;

- Pump down of facility
- Cool shrouds to LN_2 temperature whilst maintaining a spacecraft temperature of about 20°C during this transient phase.
- Achievement of steady state conditions with facility at 10^{-5} torr, shroud at 100°K and desired solar (or IR) input to the spacecraft.
- Eclipse phase when input to spacecraft is turned off for a period of 1 hour.
- Return to solar (or IR) input case, steady state.
- Return facility to ambient conditions, ending the test phase.

TEST EVALUATION

When assessing the test evaluation it should be realised that the thermal behaviour of the IM deviates considerably from that of an actual spacecraft (S/C). The IM is not insulated, the face plates are coupled by radiation only, and no internal heat is generated; consequently there is an extreme temperature difference between the front and back sides (ΔT=180°C).
Furthermore, the temperature of the IM is exceptionally sensitive to the optical properties of the black coating. Small variations in α/ϵ have a significant effect on the temperature of heat exposed surfaces. Finally, the hardware used does not conform with the high quality standards of S/C thermal hardware. These factors influenced the test data correlation perhaps more than desirable, but since they were applicable to both types of tests, it was possible to compare the results.A first effort to correlate test temperatures with a simple TMM of one node per surface (30 nodes), was abandoned because the gradients were too large in most of the surfaces, and no acceptable correlation could be achieved. A comprehensive TMM was then produced and a satisfactory correlation achieved for the SST test phases in spite of the deficiencies in the thermal behaviour of the test specimen referred to above. Introducing the IRT environment, leaving the basic model parameters untouched, gave a poorer correlation. This is attributed to the unknowns in the applied flux and optical properties.
The test evaluation has been performed for the two SST IM attitudes I and IV, the corresponding IRT phases and two IRT phases with reduced levels totalling four test phases per attitude. In addition, the evaluation involved two ways of generating the flux used in the TMM; by actual measurement and by computer.

THERMAL MATHEMATICAL MODEL

Nodal distribution and thermocouple (TC) outputs

136 TCs are installed on the IM, of which 128 are correlated to nodes. Fig. 6 shows the complete layout of the IM nodal distribution. The rectangular surfaces and the trapezia are divided into 3 x 3 nodes. The triangles of the pyramid are divided into 2 nodes and of the prisms into 3 nodes. The split bottom plate of the internal cube is divided into 2 x 3 nodes. The total number of nodes is 202. The TMM node numbers are obtained by concatenation of surface number and surface-element number. For the sake of simplicity the temperatures of the underlined nodes are directly compared to the corresponding TC output. It has been accepted that this induces an error in the correlation; this is quantified later. The centre node of each face plate is provided with two TCs at the periphery. In these cases the TC outputs have been averaged to derive the comparable nodal test temperatures (nodes 75, 85, 115, 125, 155, 165, 175, 205, 215, 225). The hole in plate 6, between nodes 65 and 62, is for the test cable. The test cable (not shown in the diagram) has been approximated by a rectangular cylinder 1 m high and 0.08 m in diameter. For SST the cold boundary ("space") is set to -190°C corresponding to the measured average test-chamber shroud temperature. For IRT the boundary temperature is set to -160°C, a temperature composed of the measured average baffle temperature and a 10% estimated shroud-blockage effect due to lamps and "hot" lamp mounting structures.

Fluxes

SST - An important aspect of the exercise is evaluation of the thermal fluxes on the different surfaces. An arbitrary solar constant is defined. To achieve comparable temperature levels for SST and IRT, a flux level of 1500 Wm^{-2} in the test plane has been used for SST, this to allow for the effects of the cosine power distribution and the flux decrease with the second power of the distance to the source*. For the two test phases defined, the absorbed power for different surfaces has been calculated taking shadowing into account. Due to the high absorption, multiple reflections are neglected ($\alpha_s = 0.976$).

IRT - The IRT flux distribution was not chosen to duplicate the SST flux distribution, particularly since this is a divergent beam, but to create a flux distribution corresponding to a collimated beam with a flux intensity of one solar constant. To obtain more information on the IM response, two additional test phases were carried out for each attitude with reduced intensity (1300 Wm^{-2} and 1200 Wm^{-2}) This is a useful feature of the method, easy to implement by ratioing down the voltage.

The direct IR fluxes were obtained in two ways:

- The absolute flux levels were measured with fixed black-plate sensors and the relative flux distribution was measured in air before the test with a hand-held device. It is assumed that the relative flux distribution does not change in the vacuum chamber.

---

*Typical characteristics for ESTEC HBF-3 solar simulator

o The IR lamp characteristics, measured during the single lamp evaluation tests, were stored in the computer. A newly developed computer programme was used to calculate the flux distribution, using lamp voltage, location and model geometry.

ANALYSIS RESULTS

To assess the merits of IRT compared with TMM correlation, SST data correlation has been used as a reference. After achieving satisfactory SST-TMM correlations for both attitudes, the IRT environment has been introduced into the TMM. In practice, this means that the flux intensity distribution and the cold boundary temperature are altered for each case, all other parameters such as internal interchange factors, linear conductors, and emissivity, being kept constant. This analysis only assesses steady-state test phases, transient analysis remaining a subject for future studies.

Figs. 7 and 8 characterise the temperature distributions across the IM for the two test attitudes during SST and IRT. Each figure depicts the measured and calculated temperatures identified by "m" or "c" of one or more series of nodes. The hatched areas indicate the "sun"-exposed nodes.

Fig. 7 gives the temperature distribution across the external surface in a plane perpendicular to the IM main axis and through the centre of each plane. The temperature extremes occur in this plane.

Fig. 8 gives the temperature distribution of the cube and pyramid. In view of the thermocouple locations, the nodes of the cube are chosen diagonally on each surface to present as many data points as possible.

Fig. 9 gives the temperature distributions of the top and bottom plates of the adjacent prisms.
To highlight the deviations between test and analysis more clearly, the temperature difference distribution (TDD) is presented on a larger scale for the same series of nodes in figs. 10 - 12, the temperature difference ΔT being defined as: T(analysis) - T(test). It is assumed that the TDD is Gaussian. The overall quality of TMM test correlation can be quantified from the standard deviation and the bias (mean value).

These parameters and the positive and negative extreme temperature deviations are summarised in table 1 for all test phases. The corresponding histograms are given in fig. 13.

DISCUSSION OF RESULTS

Solar simulation test

Since the SST evaluation was the reference for IRT, the main error

sources are identified together with the corresponding estimated delta temperature of the IM surfaces most affected. Errors not related to solar beam sources are also applicable for the IRT evaluation.

Front-to-back gradient - The temperature gradient between the front and back-sides is larger for the TMM than during the test. The deviations are of the same magnitude for both attitudes; ΔT is negative for the exposed surface and positive for the surfaces facing the chamber wall. This is attributed to the assumption that the faceplates are conductively decoupled together with the neglected backscatter from the chamber walls. The backscatter is in the order of 7.5 Wm^{-2} in the test plane. Considering the temperature level of the cold side ($T_{sst\ i}$ = -60°C, $T_{sst\ iv}$ = -80°C), this causes a temperature increase of 5°C. In addition, to this the emissivity of the black coating tends to decrease with temperature, causing an increasing α/ε ratio, thereby increasing sensitivity to backscatter.

Fluxes of directly exposed areas - The temperature deviation at the exposed surfaces for SST is within the achievable accuracy. The accuracy for the calculated direct flux on each surface is ± 5%, being estimated as ± 5%. As the flux applied during test is known within 3%, the resulting tolerance for ΔT is ± 7°C for the hot side and ± 4°C for the cold side. The sensitivity at the exposed side is about twice that at the cold nonexposed side. The tolerance band for internal surfaces (cube) lies in between these figures. An additional uncertainty, the corresponding temperature deviation of which is difficult to estimate, is caused by some deficiencies in the hardware, which was not of the high quality standard of a real S/C. To prevent heat being trapped inside the IM, the gaps between the face plates were taped off with black painted Kapton tape. This process inadvertently bent the plates, so that surfaces that should have been shaded were exposed to stray light. The tape also touched parts of the internal cube which were supposed to be conductively isolated, resulting in the cube receiving direct heat inputs. An exact calculation of the fluxes absorbed by the various nodes due to these deficiencies is not possible. A heat absorbed allowance has been made at the nodes based upon estimated gap areas, local flux and absorptivity.

It is assumed that these edge effects are very similar for the different attitudes and test methods and this approach has therefore been applied consistently to the different test phases and to both test methods. For reasons of objective comparison, the flux distribution for SST or IRT was not varied within its tolerance band. Doubtless a much better correlation would have been possible if this had been done.

Mismatch between TC location and node centre - The mismatches between thermocouple locations and node centres are most significant for those surfaces that are exposed to large gradients, such as the cube and the top and bottom surfaces of the prisms. For the corner nodes of the cube face plates, for example (nodes 11, 13, 17, 19, etc.), a correction of 2° - 3°C is estimated by linear interpolation. The correction is negative if the node temperature is less than the centre node and positive if it is greater. For the bottom plates of cube and prisms, a simple

interpolation does not seem realistic. Corrections of 4° - 6°C are estimated in these cases.

Reflections from the cable loom - Additionally, in the case of the bottom plates of the cube and prisms (surfaces 6, 10, 14, 19 and 24), solar reflections from the cable loom magnify the deviation. This is a specific problem for SST. The cable insulation geometry is not well defined. The approximation in the TMM by a rectangular cylinder does not reproduce the correct test flux pattern. It will be seen later that the IRT correlation for these surfaces produces somewhat better results than the SST.

IRT at 1400 Wm^{-2} level

As expected, the correlation achieved between the TMM and test data is best for Attitude-IV, as can be seen from Figs. 10 to 12. The Attitude-I test contained too many inaccuracies arising from lack of experience of the test method, a situation exacerbated by the short period of availability of the test facility for the test programme.
TMM_c shows better correlation for Attitude-I than Attitude-IV, suggesting that the approach is less responsive to learning-curve improvements. For Attitude-IV there is a significant difference between TMM_c and TMM_m correlation. In general, a better correlation is to be expected with the flux measured at the spot than with a computer-generated flux, for the simple reason that the data fed into the computer are based on one lamp in a fixed position. The flux is a function of the lamp position with respect to gravity and it has been shown during individual lamp tests that this, together with variations due to manufacturing tolerances, is not negligible.
It is clear from Table I that the TMM correlates better with SST data than IRT data by a factor 2, and that the TMM_m again correlates better than TMM_c for Attitude-IV. In Attitude-I, the difference in correlation is not significant.

Front-to-back gradient - Referring to Figs. 10 to 12, the TDD pattern for the c-case for both attitudes is very similar to that of SST and looks more consistent. That of the m-case shows errors of a more random nature. The SST backscatter is not present, but spillover to other surfaces due to not accurately baffling off is causing a reduction in temperature gradients.

Fluxes and spillover - The TDD curves show clearly the difficulty of estimating the flux distribution and the spillover to surfaces supposed not to be exposed. Surfaces 18 and 23 for Attitude-IV are good examples. These are the top surfaces of the trapezium-based prisms and are supposed to be shaded off by LN_2-cooled baffles. The test configuration did not allow accurate adjustment of the baffles (which might not be the case for a larger test item). An over-baffling of these surfaces would have been beneficial for the correlation. At the given temperature level a gap of 1 to 2 cm would allow sufficient spillover to increase the temperature of surface 18 by 5-10°C. Surface 23 shows a larger deviation, which can only be partially explained by spillover; here the assumed edge effect, mentioned earlier maybe more severe due to the lamp position. Spillover

was specifically accepted and measured prior to testing on surfaces 7 and 12 in Attitude-IV and introduced into the TMM.

Cable loom - The bottom plates correlate better than in the case of the SST because there were no cable reflections due to the IR lamp geometry. This is an example of one of the positive features of IR testing.

IR lamp-induced gradients - The thin IM face plates have the advantage that the IRT induced gradients are made visible. Fig. 14 shows the test data giving TDD for the TC outputs of the corresponding exposed surfaces for SST and IRT for Attitudes I and IV. The node in the centre of the surface, is taken as a reference. The gradients are significant, emphasising that conduction through a surface and the homogeneity of the flux must be carefully considered when using IRT.

Blockage factor - The blockage effect of the lamps and lamp structure from the cold shroud is a rather complicated issue. Each node has its own thermal environment depending on the build of the supporting structure and the lamp configuration. Modelling of such details would have to be very comprehensive to achieve acceptable accuracy. The most significant effect is that of the baffle temperature. The blockage by structure and lamps is estimated at 10% and these have been combined by setting an effective shroud temperature of -160°C. It is realised that this approach is rather coarse and will have local effects on the temperature distribution. An effort to calculate the effective radiative coupling to the chamber shrouds by using the cool down curve was not successful due to lack of data.

IRT phases with reduced power levels (1300 Wm^{-2} and 1200 Wm^{-2})

Attitudes I and IV were exposed to power levels of 1300 Wm^{-2} and 1200 Wm^{-2} by ratioing down the voltage applied to the lamps. These test phases were introduced to show the feasibility of extrapolating to other flux levels. In the TMM for both m and c the flux at each node was ratioed down to the required levels, and as expected the TMM correlation was somewhat improved. The TDD remained the same to within ± 1°C, for each attitude. The remarkable equivalence of TMM IRT data correlation confirmed that at least between 1400 Wm^{-2} and 1200 Wm^{-2} the shift in the frequency distribution of the lamps for black paint is negligible. It therefore suffices to show only the frequency distributions for the 1400 Wm^{-2} Flux case.

SUMMARY OF PROBLEM AREAS

(i) The accurate determination of flux intensity

The test analysis confirmed the findings of earlier lamp evaluation work and showed that the IR lamp characteristics cannot be described sufficiently accurately for computer flux generation alone to be used for intensity distribution

purposes. Measurement of the actual flux from a particular IR lamp array is necessary. In these tests the use of a greater number of calibrated flux sensors would have increased confidence in the flux distribution.

(ii) The control and intensity measurement of the spillover

For TMM verification low intensity spillover is not necessarily a problem, as long as it is known and measured.

(iii) Flux homogeneity

The temperature ripple induced by the nonhomogeneity of the IR flux has an effect on temperature tolerances and consequently on the thermal environment at unit level and unit operational temperature limits. The measured maximum temperature gradient for the 0.3 mm copper plate of the IM was 12°C (see Fig. 14). This was significantly improved as experience was gained in the technique; in the later case the gradient was at worst 4°C. (see Fig. 14 Attitude IV). The impact of this on the test method is a likely requirement for there to be more thermocouples than for a typical spacecraft SST.

(iv) Extrapolation temperatures

Changing the flux intensity level shows that within the chosen intensity band of 1400--1200 Wm^{-2}, for the black painted IM, temperature extrapolation is permissible.

WORKING METHODS

For the IR method of thermal balance testing to be successful, more than for SST, close cooperation between the analyst and the tester is essential. With IR techniques the possibility for error is greater than with solar simulation where years of experience have resulted in the development of accepted and well known methods. The use of baffles, the measurement of flux distribution and spillover are typically areas where the analyst must have a clear view of the tester's work. Similarly, the tester must have the flexibility to propose arrays of lamps and baffles and areas of spillover which will result in an optimum test configuration. The thermal balance test thus becomes more a question of designing an experiment that will prove the TMM than a reproduction of the spacecraft working environment.

CURRENT PROGRAMME OF WORK

With a view to tackling the problem areas not yet addressed, or not addressed sufficiently, by the above work a continuing programme is planned.
This consists of absorptivity measurements for typical spacecraft surfaces in the IR lamp flux regime and comparison with solar energy response and a series of tests to be made on a more complex spacecraft

model. This model is intended to be similar thermally to the radiating surfaces of a large telecommunications spacecraft. The model, named NOSAT, consists of a simple insulated box, one face of which has areas of second surface mirrors (SSM), areas of high insulation and discontinuities and protrusions typical of the real spacecraft radiator. Dummy internal dissipating sources are thermally connected to this face. The opposite box face is a simple SSM radiator without protrusions and discontinuities, but with internal dissipators attached. A shadow-casting dummy antenna is fitted to the model.
Using this model in conjunction with the absorptivity measurements referred to above, solar-simulation and infrared tests will be carried out. A thermal mathematical model of some 120 nodes is in preparation and the intention is to compare correlations in a similar way to the work reported in this paper. It is hoped that good correlation in the IR case can be achieved for this model and that the correlation will be more close to that for solar simulation than was the case with the small black model.

ACRONYMS, ABBREVIATIONS, MNEMONICS AND SYMBOLS

TMM : Thermal Mathematical Model
SST : Solar Simulation Test
IRT : Infra-red Test
α_s : Solar Absorptivity
ε_h : Hemispherical emissivity
IM : Ideal Model
m : Used as index to refer to the measured flux
c : Used as index to refer to the computer generated (calculated) flux
K : Degrees Kelvin
C : Degrees centigrade.
TDD : Temperature Difference Distribution
TC : Thermocouple
S/C : Spacecraft
SSM : Second surface mirrors

REFERENCES

1) Walker J.B.; Development of Infrared Techniques for Testing Spacecraft p 47 ESA Bulletin, 25, February 1981.
2) Bachtel FD. and Loose J.D.; Design and Control of an Orbital Heating Simulator 6th AIAA Thermophysics Conference April 1971.
3) Anderson J.W., et.al, Preliminary design of Heat Flux Simulation for Apollo Telescope Mount, Lockheed Report LMSC/687335, May 1969.
4) Williams F.U.; Analysis of Radiative Sources with Both Specular and Diffuse Characteristics in the visible and Infrared Spectrum. NASA SP-379, 1975.
5) Sousek D.; Orbital Simulation of the Titan III Transtage Spacecraft Institute of Environmental Sciences 1966 Annual Technical Meeting Proceedings.
6) Nuss H.E.; Thermal vacuum testing of solar panels by solar simulation and infra-red simulation. Proceedings Institute of Environmental Sciences, 25th Technical annual meeting, Seattle 1979, p 188.

ORIGINAL PAGE IS
OF POOR QUALITY

ATTITUDE I							
Test Methods	SST	IRT					
Flux [Wm^{-2}]		MEASURED			CALCULATED		
	1500 **	1400	1300	1200	1400	1300	1200
Temperature [°C]							
Bias	- 1.1	- 3.9	- 3.8	- 3.7	2.2	2.2	2.2
Stand.dev.	4.4	8.0	7.6	7.4	7.7	7.4	7.2
Extremes min.	-12.4	-21.0	-20.3	-19.8	-19.2	-19.8	-18.7
" max.	9.6	23.6	23.0	22.0	24.7	24.0	23.0
Sample size *	128	124	125	125	124	125	125
ATTITUDE IV							
Temperature [°C]							
Bias	- 1.5	- 0.8	- 0.8	- 0.9	0.05	0.05	0.03
Stand.dev.	4.1	7.0	6.9	6.8	10.5	10.2	10.0
Extremes min.	- 9.6	-25.1	-24.9	-24.8	-20.2	-20.0	-20.1
" max.	8.2	16.0	15.6	15.3	31.3	30.5	29.5
Sample size *	128	126	126	126	126	126	126

* Excludes failed Thermocouples
** Test plane

Table 1. - Statistics summary Table of the temperature difference distribution for all test phases

ORIGINAL PAGE IS
OF POOR QUALITY

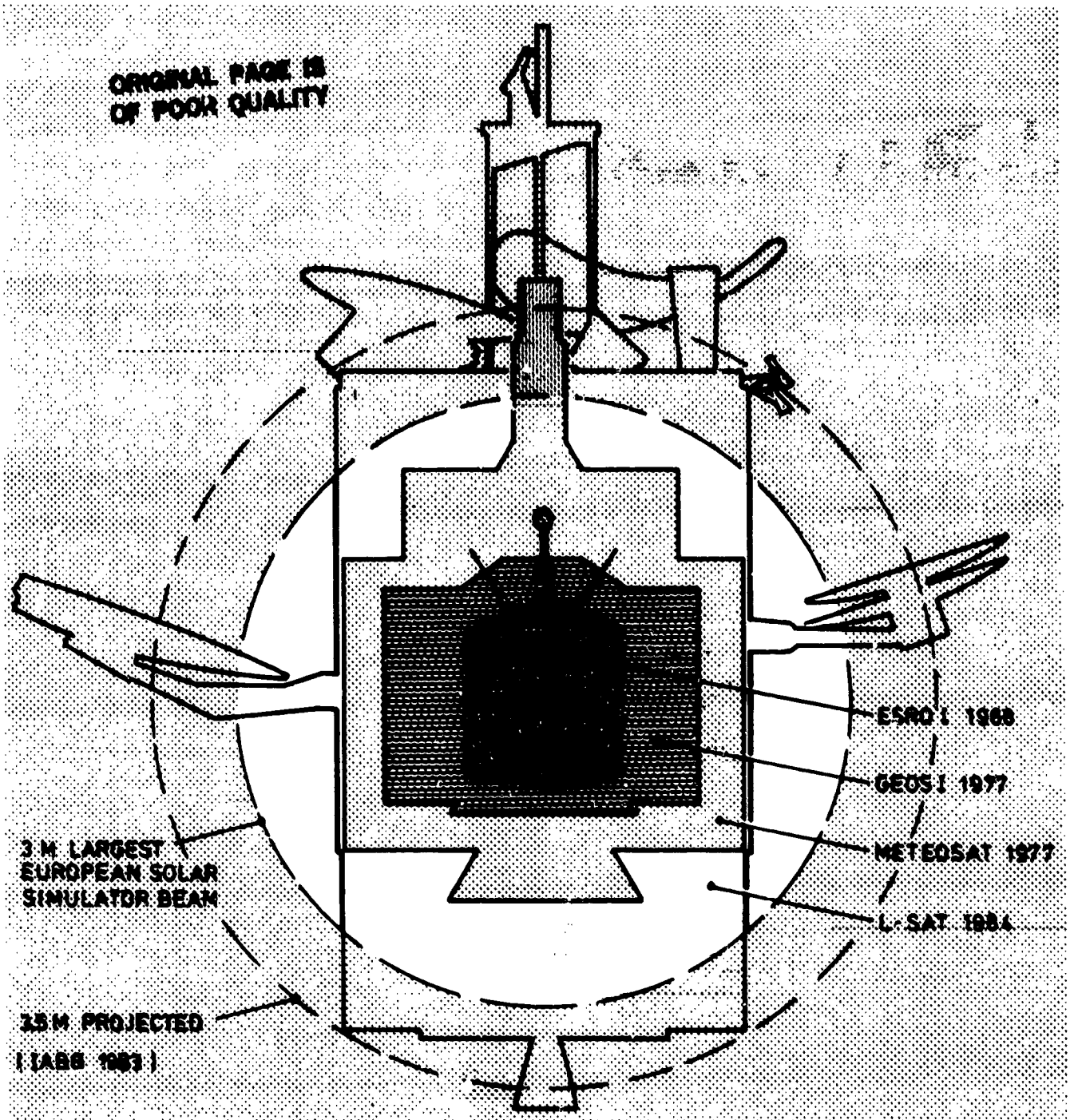

FIG.1 THE INCREASING SIZE OF ESA SPACECRAFT OVER THE YEARS

ORIGINAL PAGE IS
OF POOR QUALITY

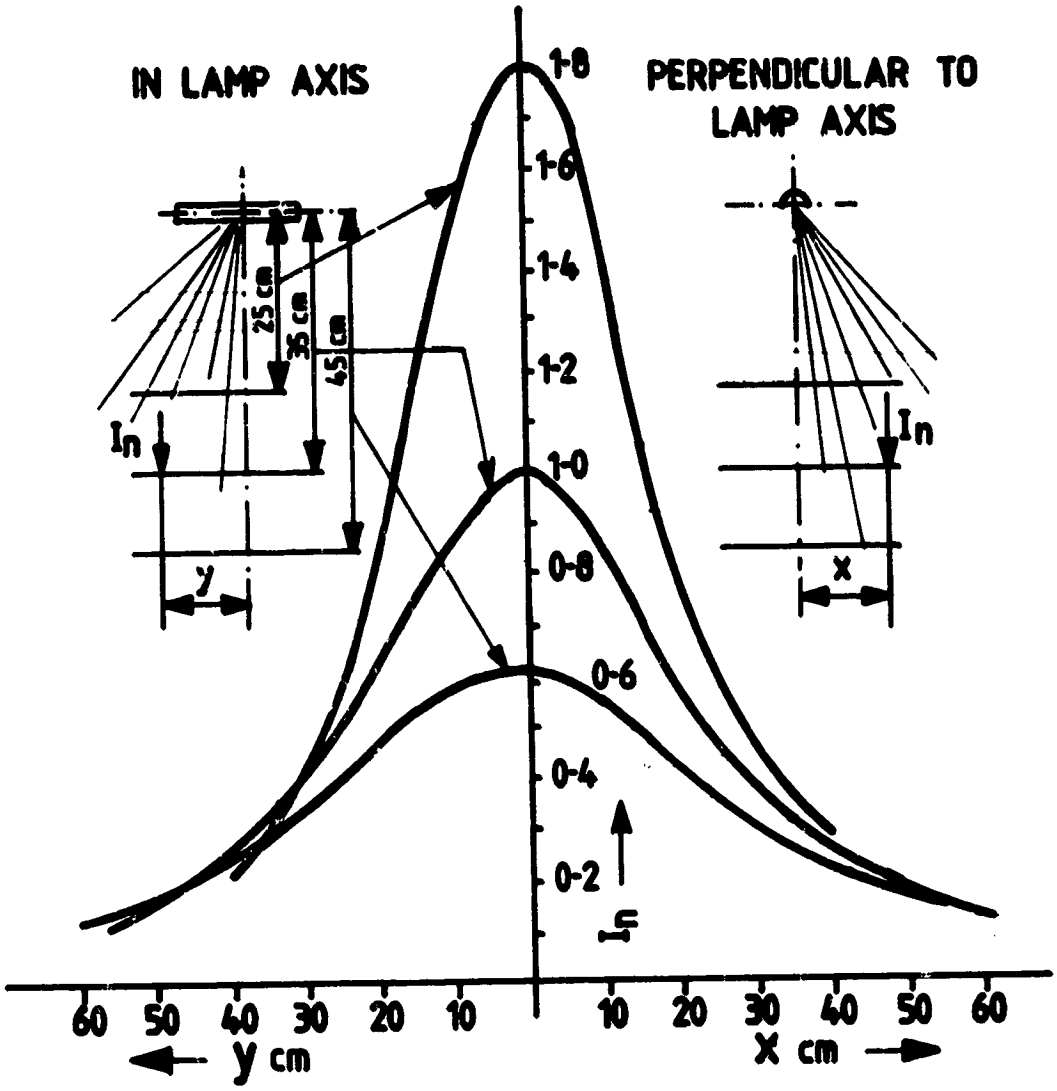

I_n RELATIVE NORMAL INTENSITY AT 3 LAMP HEIGHTS

FIG. 2

ORIGINAL PAGE IS
OF POOR QUALITY

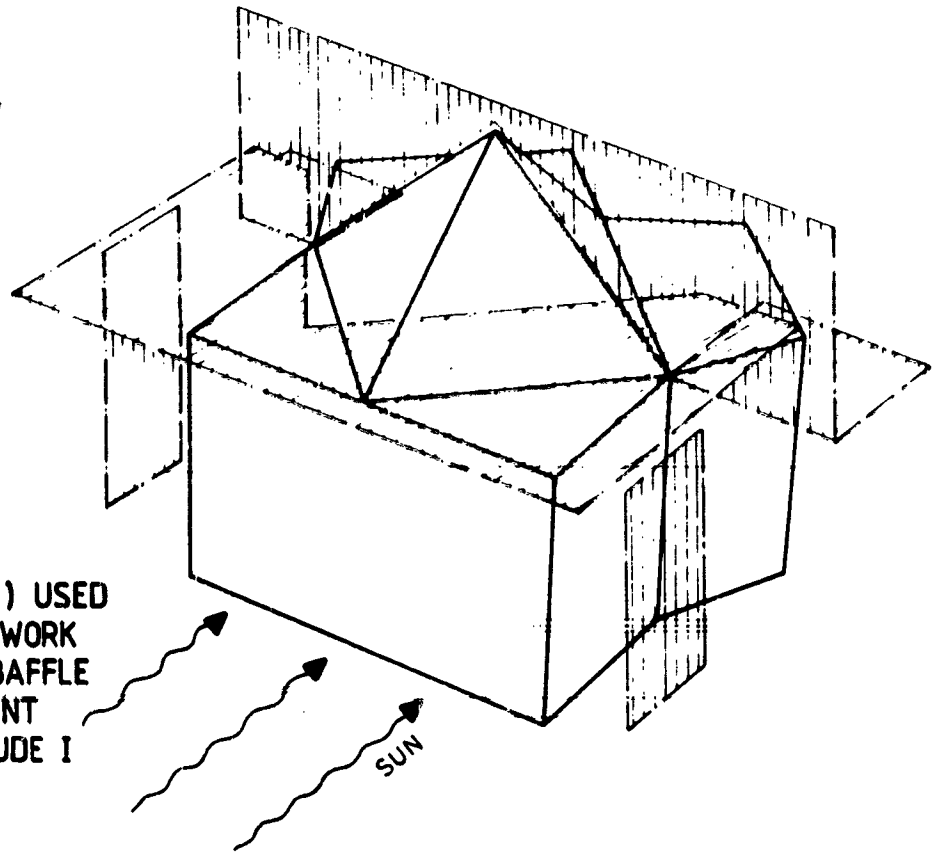

FIG. 3. MODEL (1M) USED FOR TEST WORK SHOWING BAFFLE ARRANGEMENT FOR ATTITUDE I

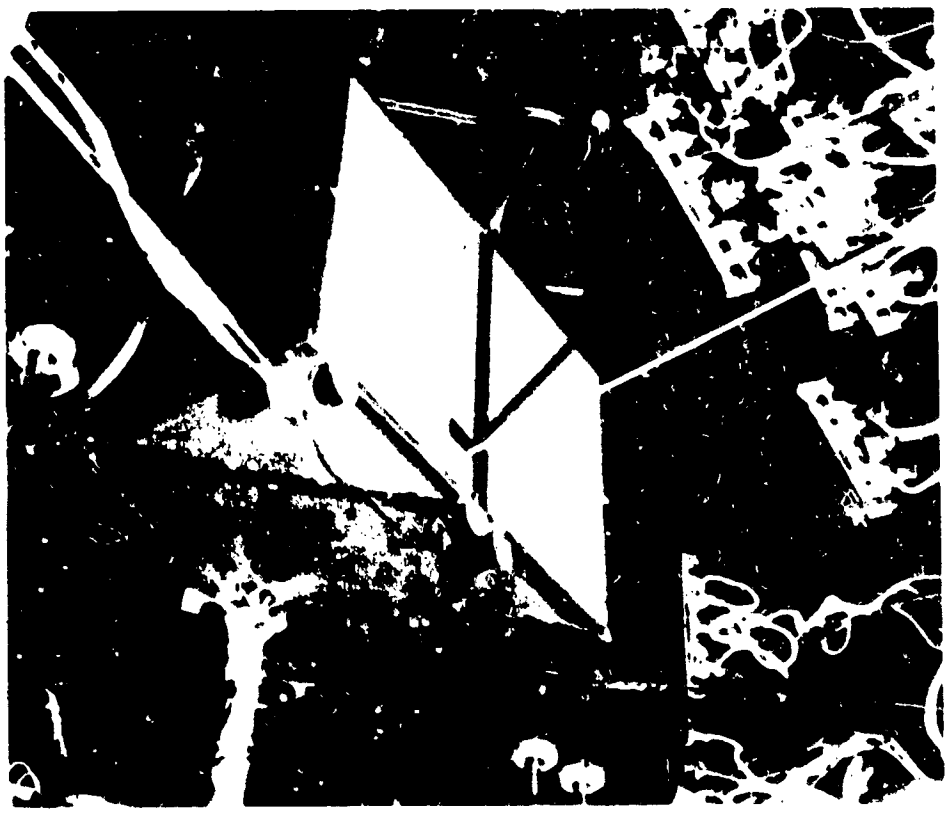

FIG. 4 TEST ARRANGEMENT FOR ATTITUDE I

ORIGINAL PAGE IS
OF POOR QUALITY

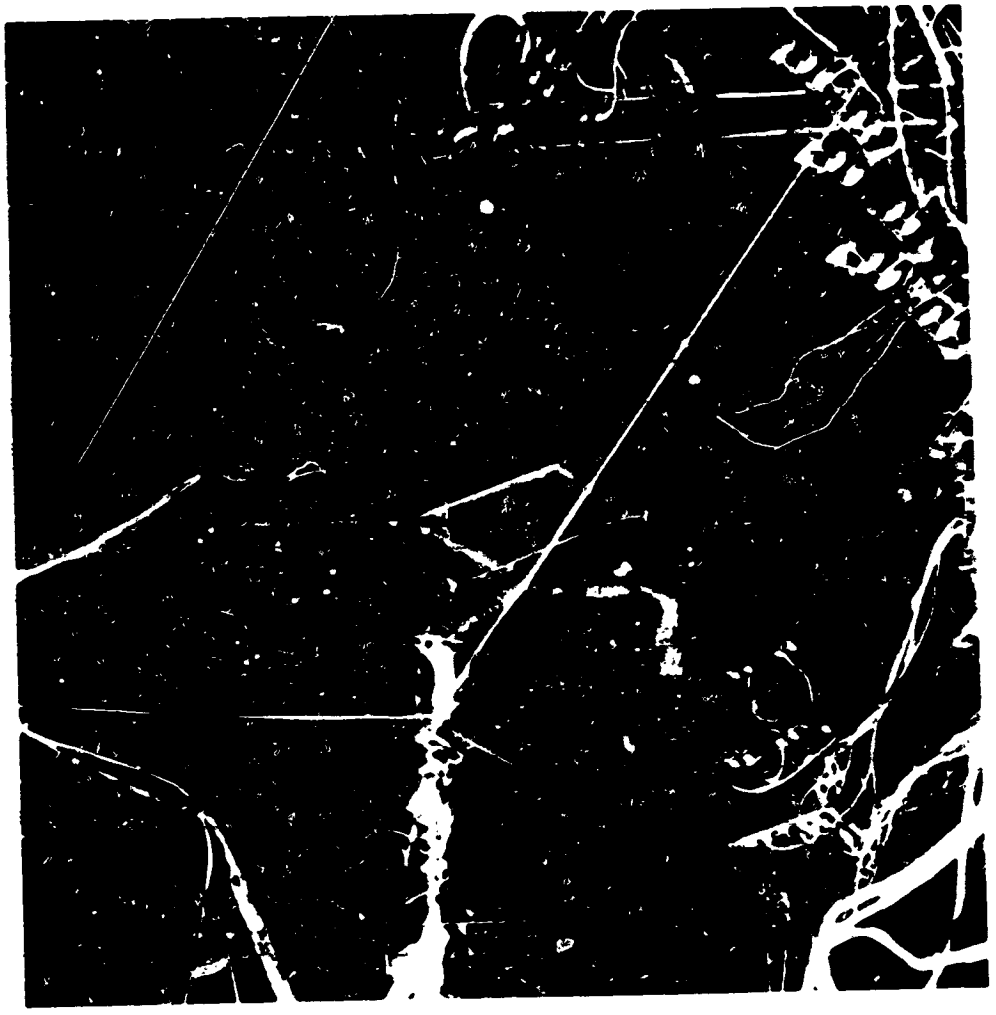

FIG. 5 TEST ARRANGEMENT FOR ATTITUDE IV

ORIGINAL PAGE IS
OF POOR QUALITY

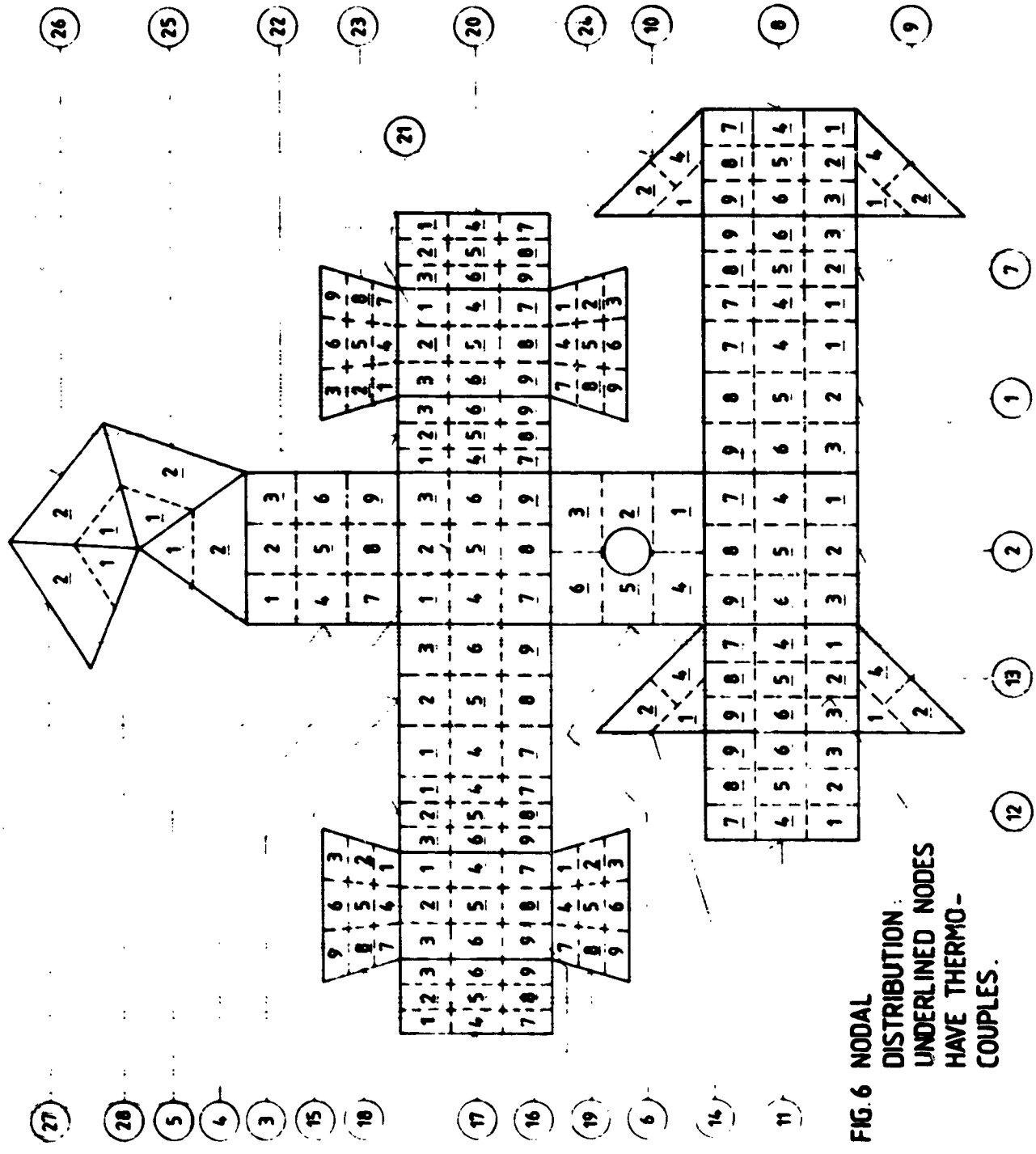

FIG.6 NODAL DISTRIBUTION. UNDERLINED NODES HAVE THERMO-COUPLES.

ORIGINAL PAGE IS
OF POOR QUALITY

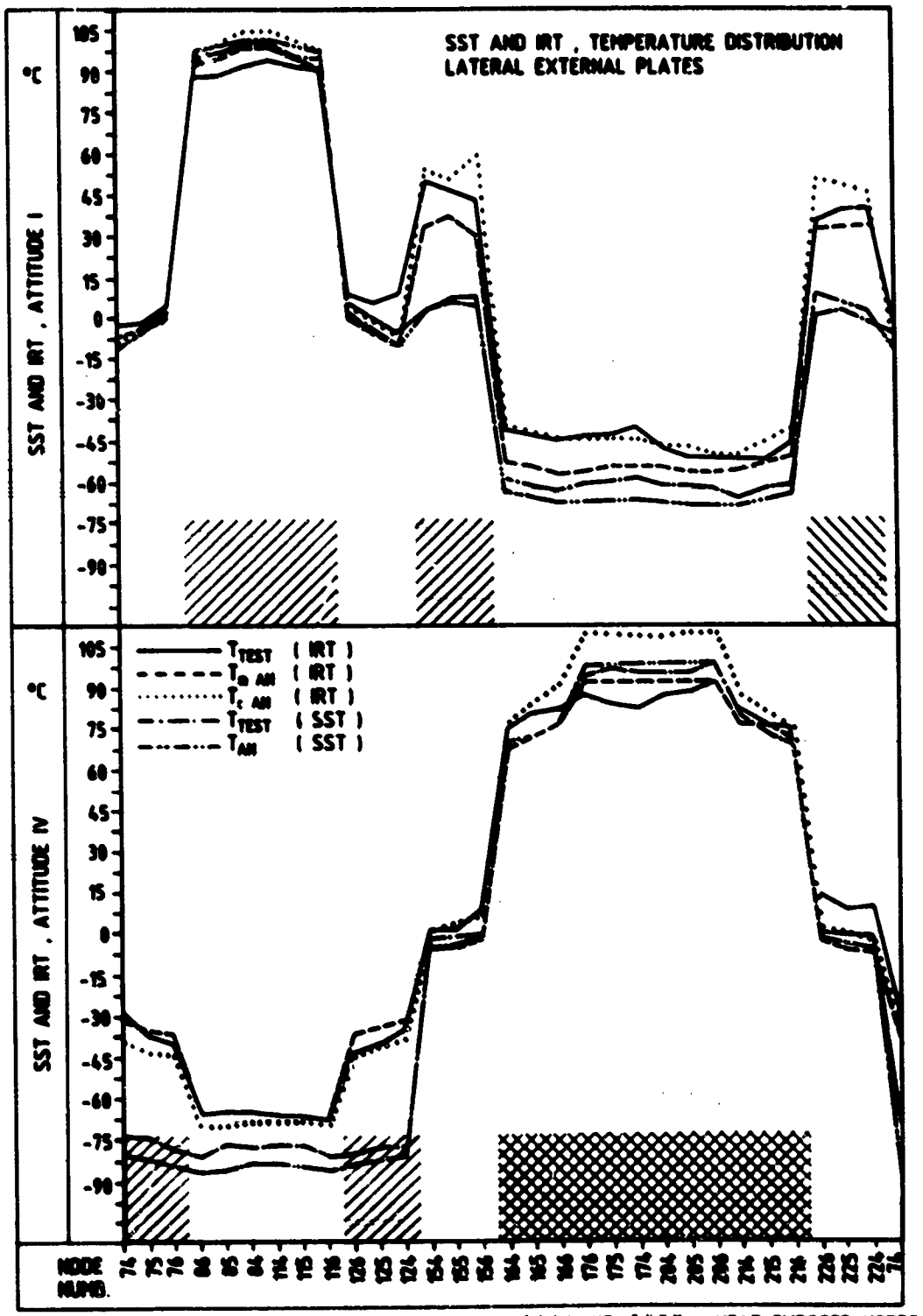

NOTE: //////, AND XXXXX = HEAT EXPOSED NODES

FIG. 7

ORIGINAL PAGE IS
OF POOR QUALITY

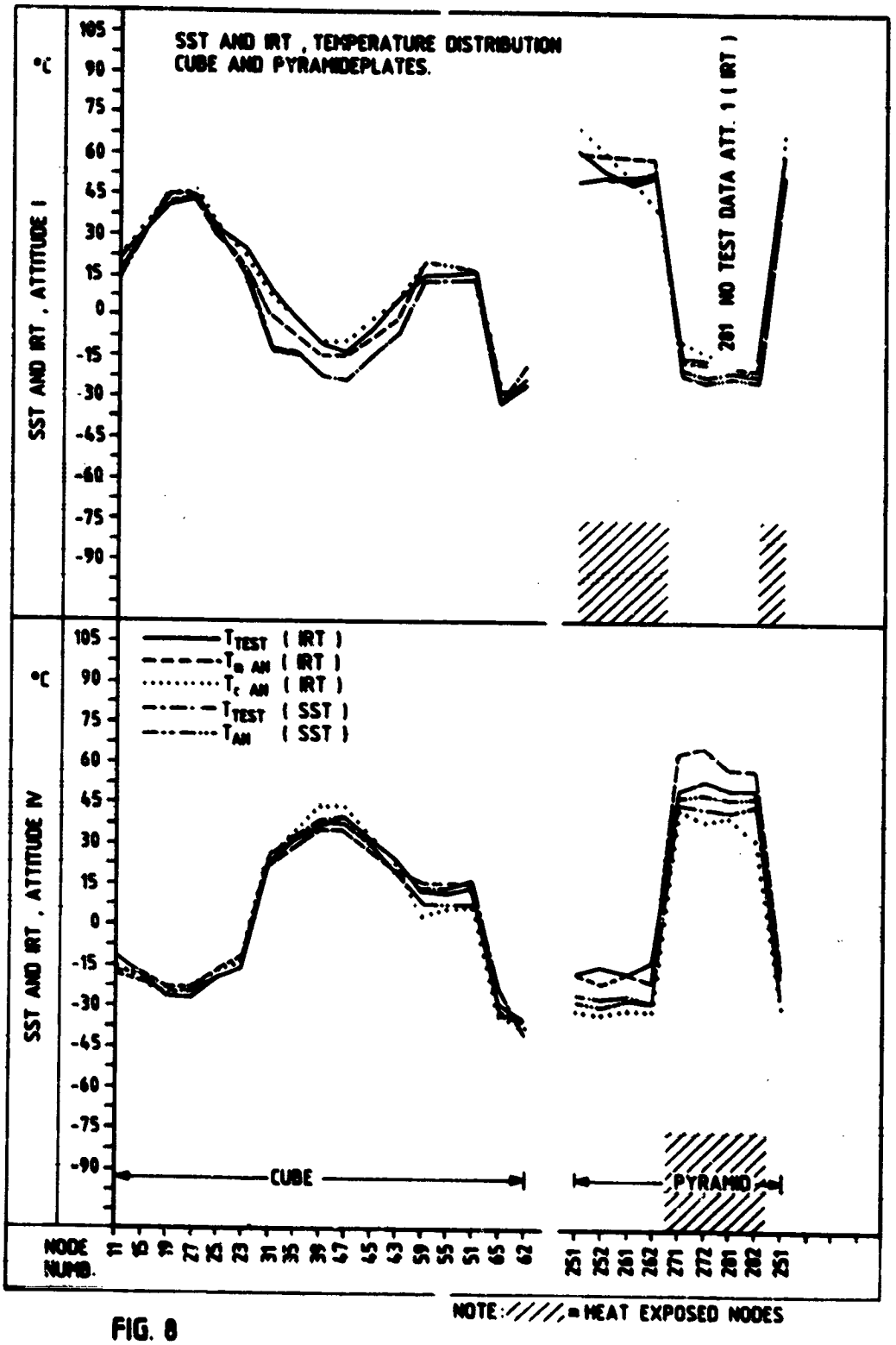

FIG. 8

ORIGINAL PAGE IS
OF POOR QUALITY

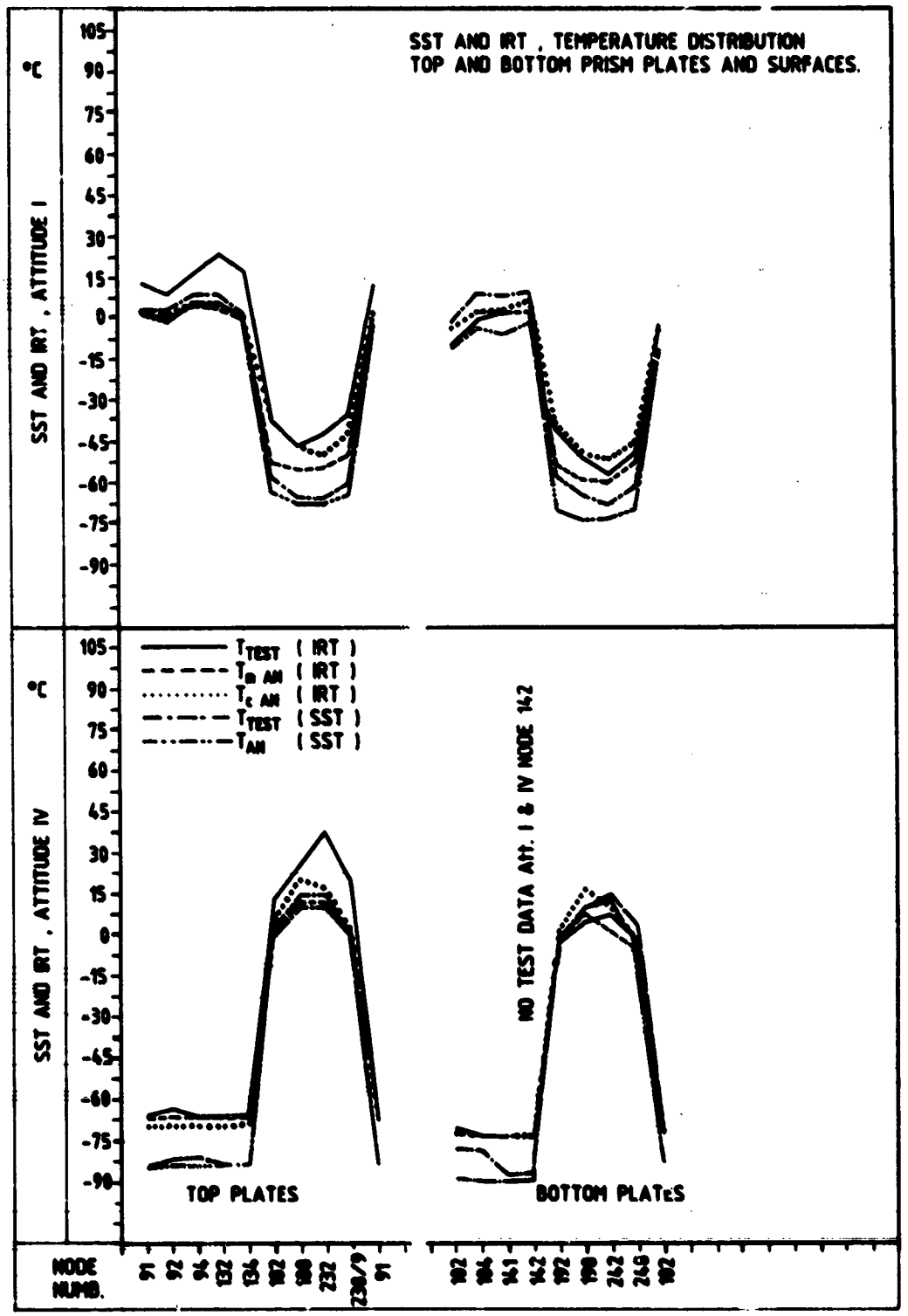

FIG. 9

SST AND IRT , TEMPERATURE DIFFERENCE DISTRIBUTION
LATERAL EXTERNAL PLATES

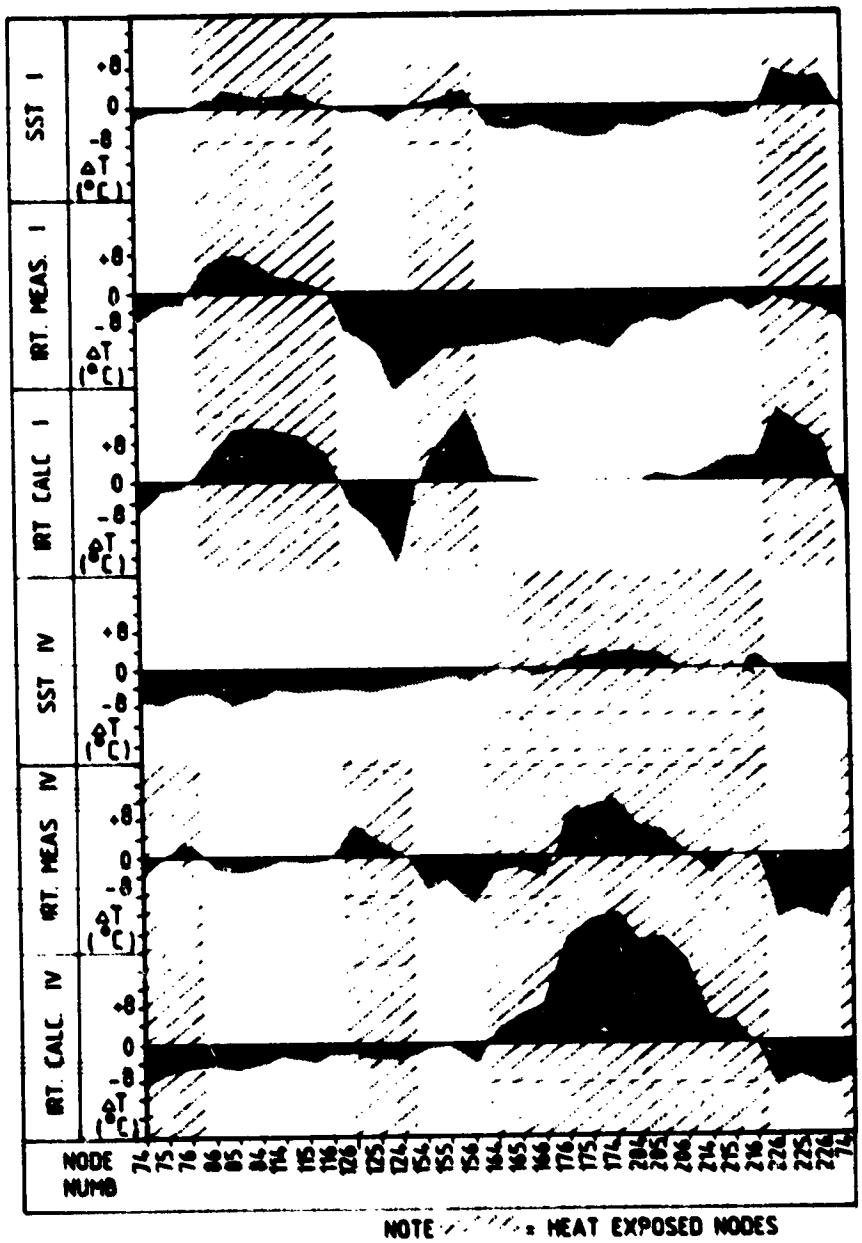

NOTE : = HEAT EXPOSED NODES

$\Delta T = T_{AM.} - T_{TEST}$

FIG. 10

SST AND IRT , TEMPERATURE DIFFERENCE DISTRIBUTION
CUBE AND PYRAMID PLATES

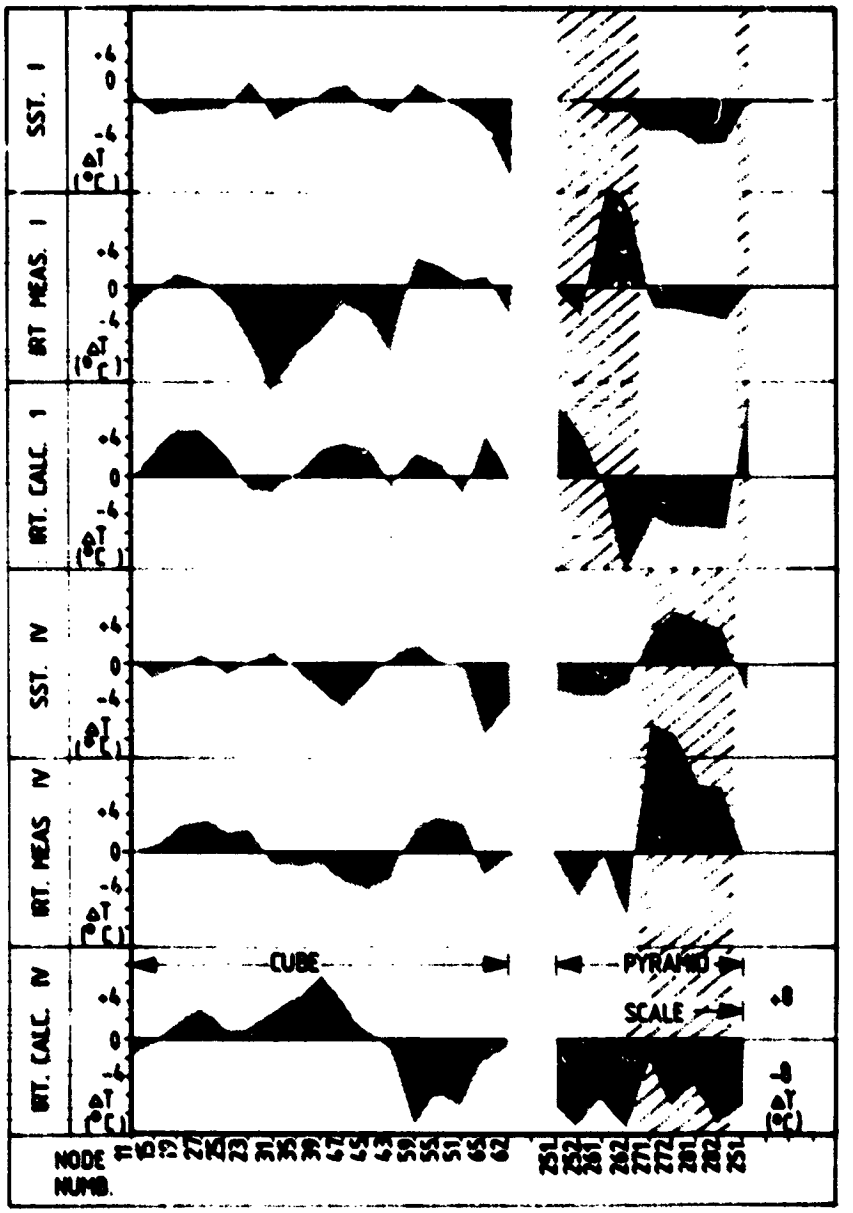

NOTE: ////// = HEAT EXPOSED NODES

$\Delta T = T_{AN} - T_{TEST}$

FIG. 11

ORIGINAL PAGE IS
OF POOR QUALITY

SST AND IRT TEMPERATURE DIFFERENCE DISTRIBUTION
TOP AND BOTTOM PRISM PLATES

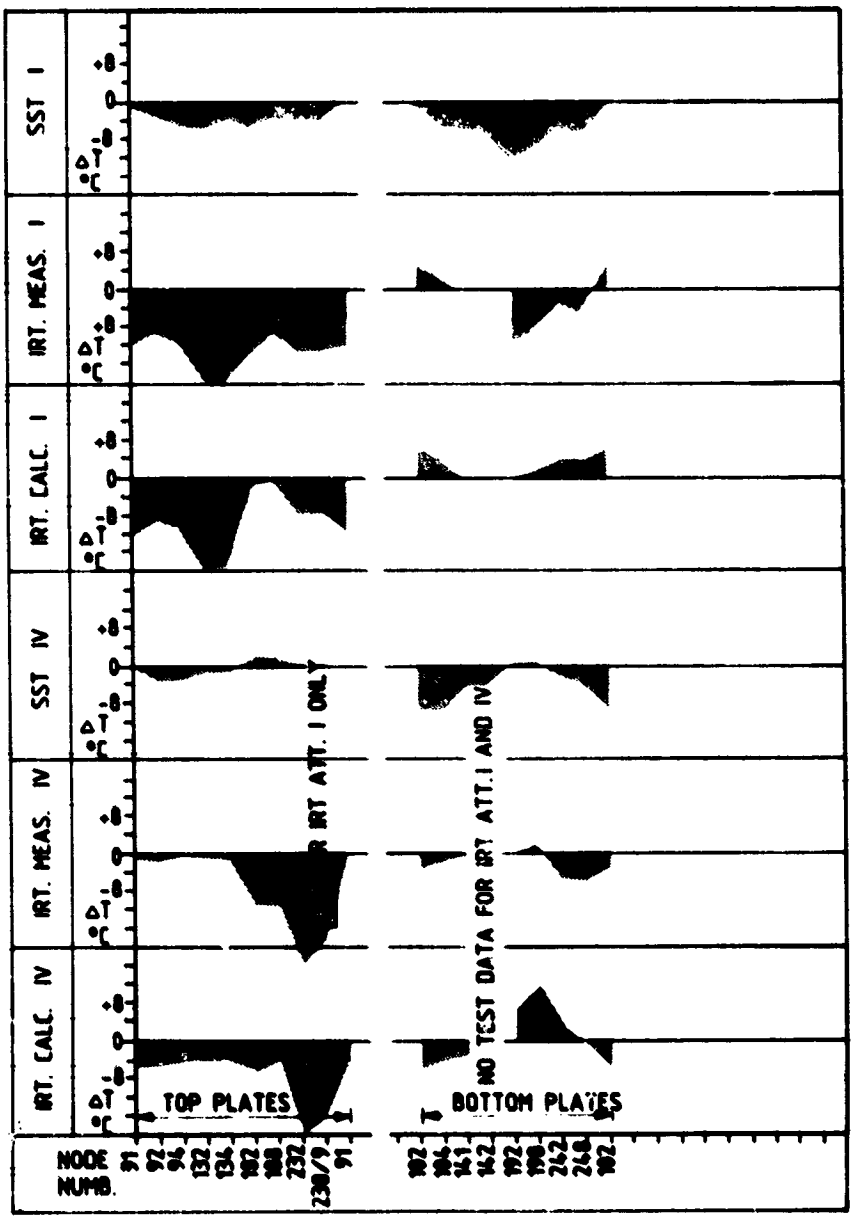

FIG. 12

$\Delta T = T_{AN.} - T_{TEST}$

ORIGINAL PAGE IS
OF POOR QUALITY

FIG. 13 HISTOGRAMS OF TEMPERATURE DIFFERENCE DISTRIBUTION

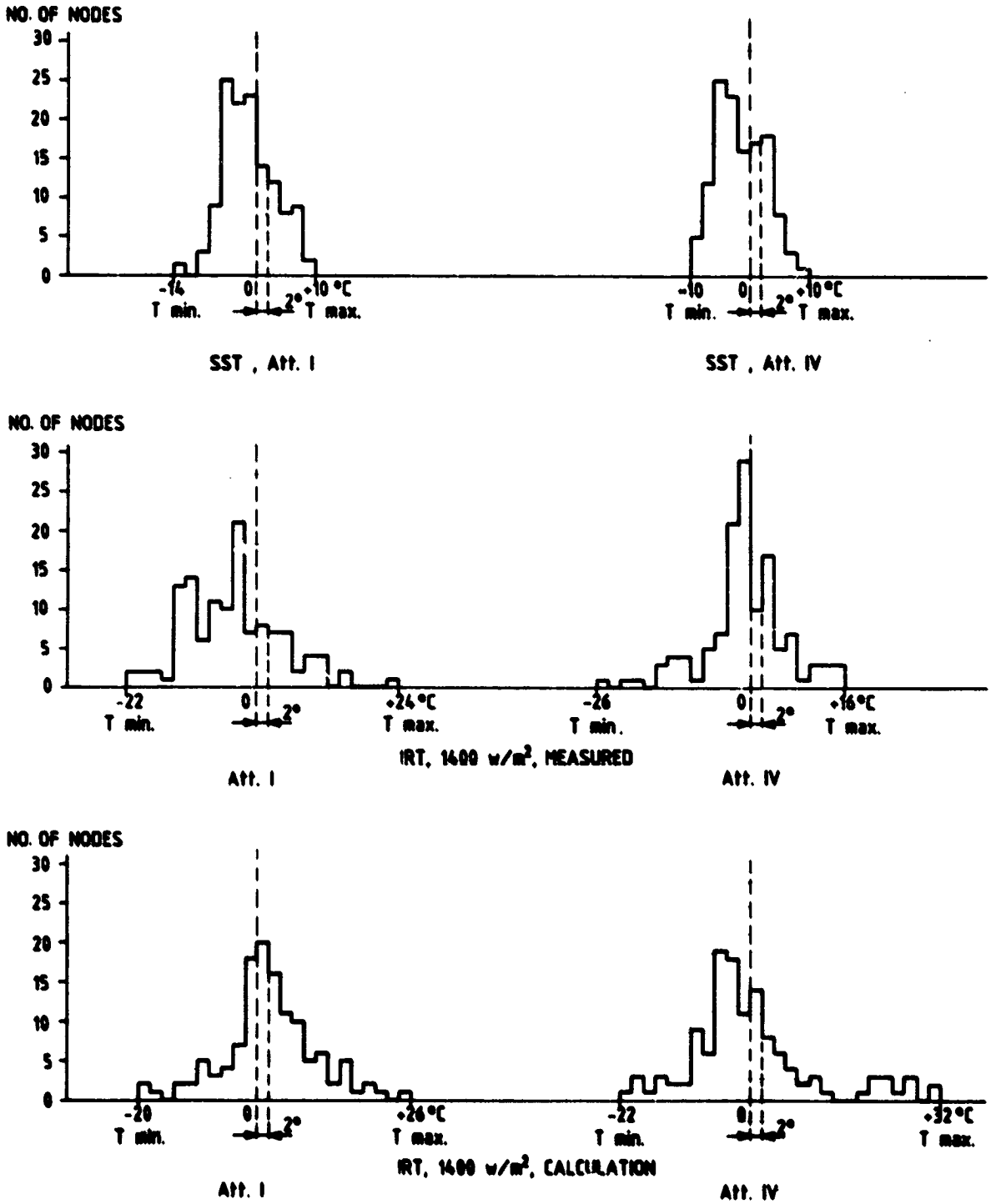

ORIGINAL PAGE IS
OF POOR QUALITY

IRT, INDUCED GRADIENTS IN HEAT - EXPOSED PLATES

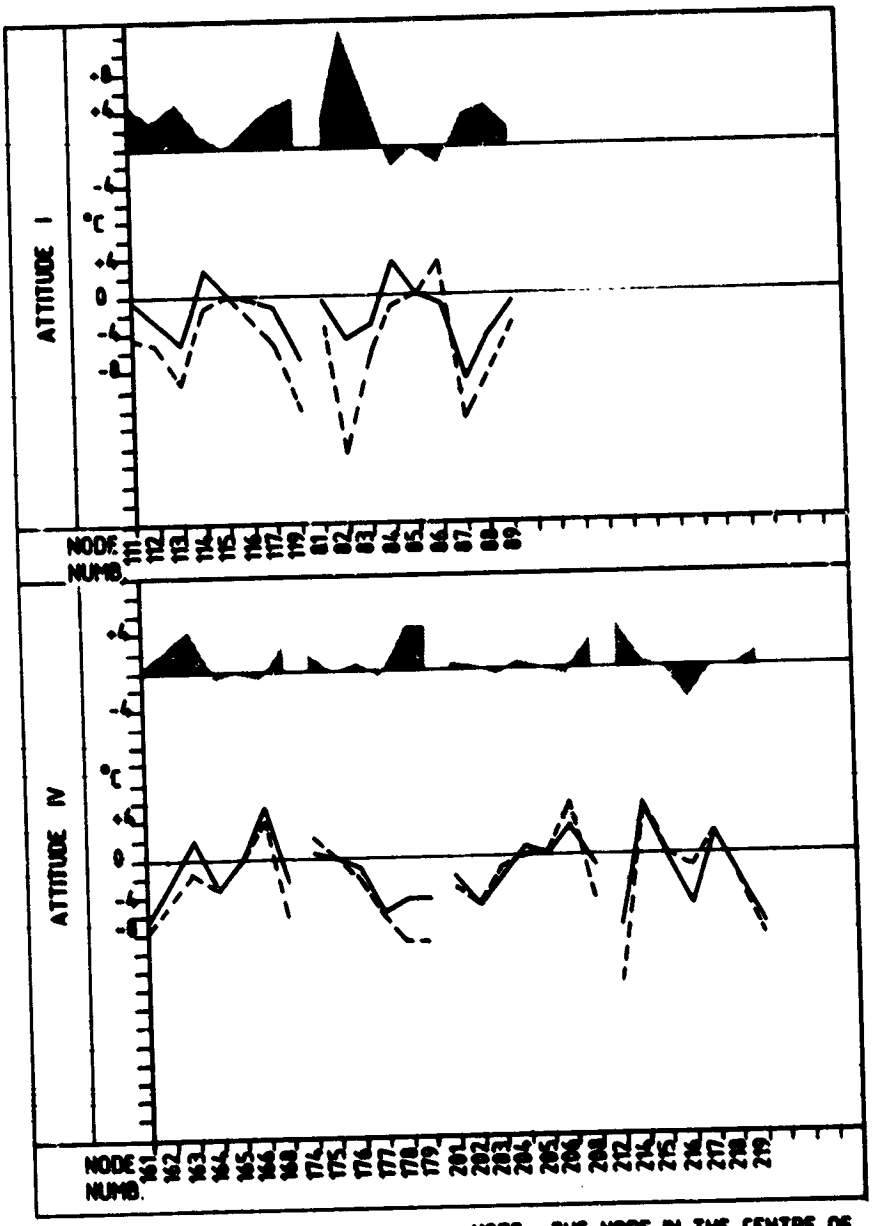

FIG. 14

NOTE · THE NODE IN THE CENTRE OF EACH PLATE IS TAKEN AS REFERENCE AND ACTUAL TEST TEMPERATURES ARE USED.

SHADED AREAS ARE $\Delta\Delta T = \Delta T_{SST} - \Delta T_{IRT}$.

ΔT_{IRT}

ΔT_{SST}

N82 25293

IMPROVED MULTILAYER INSULATION APPLICATIONS

George Mikk
The Optical Technology Division of The Perkin-Elmer Corporation

ABSTRACT

Multilayer insulation blankets are used for the attenuation of radiant heat transfer. Typically, blanket effectiveness is degraded by heat leaks in the joints between adjacent blankets and by heat leaks caused by the blanket fastener system. This paper describes an approach to blanket design based upon modular sub-blankets with distributed seams and upon an associated fastener system that practically eliminates the through-the-blanket conductive path. Test results are discussed providing confirmation of the approach.

TYPICAL BLANKETS AND INSTALLATION PERFORMANCE CONSIDERATIONS

Multilayer, reflective shield, insulation blankets are used to attenuate radiant heat transfer between heat sinks and sources. In normal applications, a predetermined number of reflective, parallel and practically noncontacting radiation shields are assembled into a "blanket", and the number of shields used is dictated by the degree of attenuation required.

The reflective layers, generally, are thin layers of plastic film (Mylar, Kapton, etc.) which are aluminized on either one, or both sides, depending on the intended method of maintaining physical layer separation in service. Singly aluminized layers are typically 0.00025 inch in thickness, usually Mylar, and are mechanically crinkled with a random pattern. When these layers are assembled into a blanket, the through-the-blanket conduction is minimized by the relatively small number of naturally occurring contact points between the layers, resulting in a very long conduction path through the blanket. The blanket is assembled with care to assure that the coated side of the reflective layer faces the uncoated side of the adjacent reflective layer to further minimize both through-the-layer and along-the-layer conductive heat flow. This type of blanket design is effective and is normally used in areas not subject to physical space limitations which would prevent the normal separation of the layers under orbital operational conditions.

In assemblies where the blanket installation envelopes are such as to preclude the "fluffy" installation approach described above, a plastic membrane, aluminized on both sides, is used as the reflective element of the blanket. Typically, the membrane is 0.00017 inch thick. In this approach, the radiant shields are kept separated by an interspace net, similar to a bridal veil. The net serves as a physical barrier preventing layer contact. The through-the-blanket conduction is controlled by definition of the net mesh, material, geometry and construction; in practice, it can provide a performance level similar to the crinkled approach, even under slight com-

pression which may result during installation in limited space areas. The disadvantage of this approach is that it is more difficult to work with because of the thinner reflective membranes and the presence of the spacer net.

In either approach, the loose blanket layers are assembled into a blanket by fasteners: stapling; plastic snap-button types; or a piece of plastic monofilament provided with button-type devices at each end. In the finished form, the blanket thus has a "quilted" appearance. Generally, the blanket edges are either sewn, taped or left as is, depending on the type of joint to the adjacent blankets, to complete the assembly. It should be noted here that any local disturbance of the blanket, which either pinches the layers together or shorts through them, becomes a significant heat leak on the scale of heat control addressed, particularly when blankets of typical performance goals of effective emittance, $\varepsilon^* \leq 0.01$ are considered.

Due to the complex geometric nature of the spacecraft, various blanket shapes are required for a typical installation. The blanket-to-blanket interface becomes very important here because of the conflicting requirements of high blanket performance, limited spacecraft power, spacecraft function, manufacturability, installability, cost, schedule, etc. As a result, blanket-to-blanket interfaces include butt joints, overlap joints, fold-over joints and individually-interleaved joints. The butt joint is the least desirable from a performance point of view since, in a typical joint, there is only a single layer of attenuation for the length of the joint, i.e., that of the tape holding the butt joint together. It is generally used where space allocations do not permit an overlap or other type of joints; it is relatively simple to implement, although blanket dimensional tolerances are important.

The overlap joint is exactly that: the interfacing blankets overlap by a predetermined distance and the blanket is twice as thick in the joint area. Although it is a simple joint to implement, it still carries a performance penalty due to heat leaks emanating laterally through the gap between the overlapping blankets. Even if it is taped, it will behave similarly to the butt joint, although not as severely.

To overcome the continuing performance problem with the overlap joint, a fold-over joint is frequently used. In this installation, the adjacent blanket joint portions are placed adjacent to each other, taped together, and then folded over to create a flat, interlocked roll, which is then folded down and taped to one of the base blankets. The foldover serves to significantly diminish the radiant energy leak characteristic of the simple overlap. While this is quite effective, the joint requires more space and is difficult to implement in areas of complex geometry.

The ultimate in performance of blanket joints is an interleaved joint. The reflective layers of the adjacent blankets are interleaved, thus approaching the performance conditions of an unbroken blanket. This application technique is usually limited to very performance critical assemblies or systems. It is quite costly to implement because extensive labor is required to interleave the layers during installation.

A further degradation source in blanket installation is the type of fasteners used to hold the blanket in place on the object being insulated. For example, let us take a fastener that is typically a plastic post, which penetrates the blanket and is fastened to the substrate. It is fitted with a plastic disk at the other end to keep the blanket in place. This device can be a relatively significant cause of heat loss in some critical installations because the retaining disk is a radiating pin coupled directly to the substrate with good conductive path. Each application varies and must be evaluated on the specific design utilized, such as fastener size, the coating used, the number used per unit area, source and sink temperatures, and other similar considerations to determine the impact on the overall blanket performance.

It should be noted here that it is not the purpose of this paper to generate and present parametric data on general blanket system configurations; such data is widely available in the existing body of literature on this subject. The foregoing general discussion was provided to serve as the introduction to improvements in multilayer insulation (MLI) applications that are described in the following sections of this paper.

MOTIVATION AND OBJECTIVES FOR BLANKET IMPROVEMENT

The thermal control system for the Optical Telescope Assembly, the major element of the Space Telescope, makes extensive use of multilayer thermal insulation in order to meet its design performance goals. These goals are characterized by the need to maintain the telescope's structure temperature stability within fractions of degrees while operating with stringent power allocations, derived from the capacity of the Space Telescope's solar panels. Meeting these requirements dictated the use of blankets with an installed performance level of 0.01 for the blanket effective emittance, ε^*. Additionally, available space and weight considerations made it imperative that the number of blanket layers, i.e., weight, be minimized.

A review of literature and experience from various sources seemed to indicate that to obtain an installed effective emittance of 0.01, a total of 20 layers would be required as a mimimum. It should be noted that the theoretical performance, ε^*, of a 20 layer blanket is 0.002. This indicates quite a discrepancy between design theory and the actual results in real installations.

An evaluation was conducted to identify the possible sources of the differences. The areas identified as potential contributors to blanket design performance degradation are listed below in their order of importance.

- Joints and seams
- Blanket fasteners
  - Blanket
  - Blanket to substrate
- Layer contact conduction
- Residual gas conduction

Joints and seams were determined to be the major potential contributors to degradation, accounting for an estimated degradation of nearly 60% over the performance of the basic blanket. The assumed configuration of fasteners was estimated at approximately 10% in contrast.

The layer contact conduction, based on using a spacer net, was determined to be a relatively low value, and a decision was made to optimize it by increasing the net mesh to a maximum practical size while minimizing the thread size. It was felt that the next contribution can be calculated and will be relatively constant once defined by design.

With regard to residual gas conduction, this was determined by calculation and experiment to be a relatively short-term phenomenon as far as blanket performance degradation was concerned. The details of this evaluation are presented in reference 1.

Therefore, the improvement effort was concentrated on the following design, fabrication and installation items:

- Effective elimination of the major performance degradation factors:
  - Seam/joints effects
  - Fasteners effects
- Simplification of design, fabrication and installation process to assure consistent, repeatable performance in the as-installed system.
  - Eliminate the need for tight dimensional tolerances.
  - Simplify/eliminate blanket fabrication jigs, fixtures and hardware models.
  - Eliminate the need for prior location of blanket fasteners to the hardware and develop automatic methods for locating and fastening blanket fasteners on the hardware.
  - Reduce the skill level required to fabricate and install the blankets.

RESULTS OF EVALUATION EFFORTS

As a result of the integrated evaluation of the above improvement areas and associated analysis, design and experimental efforts, an improved method for designing and applying multilayer blankets appears to have been achieved. Experimental data at this moment is not extensive (some are reported in reference 2), but it appears to fully confirm the approach that has been developed.

The blanket configuration shown schematically in figure 1 is based on the use of sub-blankets nominally consisting of four radiation shields, fastened together at the edges by tape and by attachment of the blanket fasteners over the expanse of the blanket.

The blanket system consists of a predetermined number of sub-blankets installed over each other so as to distribute (off-set) the joints in each sub-blanket from those of others in the blanket system. Minimum offsets are

typically greater than 2 inches and are optimized in the installation for maximum practical relative spacing in the blanket system.

Each individual sub-blanket may be joined to its associated mates, either by a butt or overlap joint; the integrated blanket system is relatively insensitive to individual sub-blanket joints.

This approach is equally applicable to simple or complex surfaces. The effect of this blanket design and installation process is that any break in a single sub-blanket in the system is backed by other unbroken sub-blankets, thus insuring, as a minimum, the performance of the unbroken sub-blankets in the joint location. Due to the number of layers and sub-blankets used, the practical consequence is that there are negligible seam/joint heat loss effects in the blanket assembly, i.e., the assembly very closely approximates a seamless blanket.

The placement of the joints in the blanket system is not critical, thereby permitting relaxation of dimensional controls normally exercised during manufacture and installation. This provides both installation and manufacturing flexibility, resulting in considerable cost and time savings over more traditional approaches.

The use of the sub-blanket approach also simplifies the solution of the blanket fastener heat leak problem, since it provides the means to effectively eliminate the through-the-blanket heat leaks due either to the blanket fasteners or the blanket-to-substrate fasteners. In this approach, the fastener assembly is composed of two parts which can be mated and demated by mechanical means, for example, hook and pile. During fabrication, one-half of the fastener assembly is permanently mounted to the blanket. The mating part is then mated to the secured half. The mating part is provided with a protected adhesive surface which is uncovered prior to the installation of the sub-blanket to the next sub-blanket or to the substrate, as appropriate. The relative location of the fasteners is thus determined automatically during the initial sub-blanket installation sequences.

Since the fasteners are located during the blanket assembly and installation process, the need for specific dimensional control is eliminated, along with manufacturing tooling, jigs and closely dimensioned drawings.

TEST PROGRAM

Two significant experiments were conducted during this effort. The first was an experiment to verify the validity of the "staggered" joint/sub-blanket system approach, and the second was an experiment to determine the performance characteristics of a "flightlike" blanket system as described in this paper when applied to a simulated, complex representation of real spacecraft hardware.

In the first experiment, a prototype part, a relatively complex graphite/epoxy structural member, was prepared with heaters, instrumented

and insulated with a system of five two-layer sub-blankets with staggered seams. No intersub-blanket fasteners were used because the objective was to assess the success of the seam elimination, a major source of blanket performance degradation, by itself. The test article was suspended in a vacuum chamber outfitted with LN_2 background shrouds.

Two types of tests were performed to determine the blanket average ϵ^* as follows:

- o <u>Transient Test</u> - The test article was stabilized at a nominal average temperature of 70°F with cold shrouds. Test article heaters were then shut off and the temperature decay recorded. The ϵ^* was calculated from the rate of change of the test article temperature.

- o <u>Steady State Test</u> - The test article temperature was maintained at a constant temperature when operating in a cold shroud environment. The ϵ^* was calculated from the measured heater power.

The results were as follows:

ϵ^* Predicted	ϵ^* Transient Test	ϵ^* Steady State Test
0.004	0.004	0.004

As can be seen, the measured performance was surprisingly good and provided the motivation to proceed to a complete blanket simulation. In the second experiment, a segment of the telecope support ring was built to simulate the thermal performance characteristics of the structure. This is one of the more couplex areas on which to install blankets due to a large number of attaching structural members. This simulated structural part was insulated with a blanket system made up of three four-layer sub-blankets equipped with the fastener system as described earlier. Both transient and steady state tests were conducted. Performance measurements indicate a system performance of ϵ^* in the ranged of 0.006 to 0.010, compared to a predicted performance of $\epsilon^* = 0.006$. The details of this experiment, its related analysis and results are discussed in detail in reference 2. It is significant to consider these results in the light of general experience which indicates a need of 20 layers, installed by experts, to assure the achievement of a performance level of $\epsilon^* \leq 0.01$. The blankets in this experiment were fabricated and installed by untrained personnel on a very complex test article, consisting of 12 layers and achieved a performance level very close to predicted values.

CONCLUSION

The blanket system presented in this paper permits insulation of complex space hardware in a simple, cost-effective, manner while at the same time achieving performance levels for installed blankets very close to analytically-predicted values. The application of these techniques should be of considerable importance in improving the cost-effectiveness for thermal control systems in future spacecraft.

REFERENCES

1. Bettini, R.G.: "Simplified MLI Pumpdown Calculation Approach". Presented at the AIAA/IES/ASTM/NASA 12th Space Simulation Conference at Pasadena, California; May 17-19, 1982.

2. "Wegrich, R. and Bettini, R.C.: "Precise Thermal Control Demonstration on Simulated Space Hardware". Presented at the AIAA/IES/ASTM/NASA 12th Space Simulation Conference at Pasadena, California; May 17-19, 1982.

ORIGINAL PAGE IS
OF POOR QUALITY

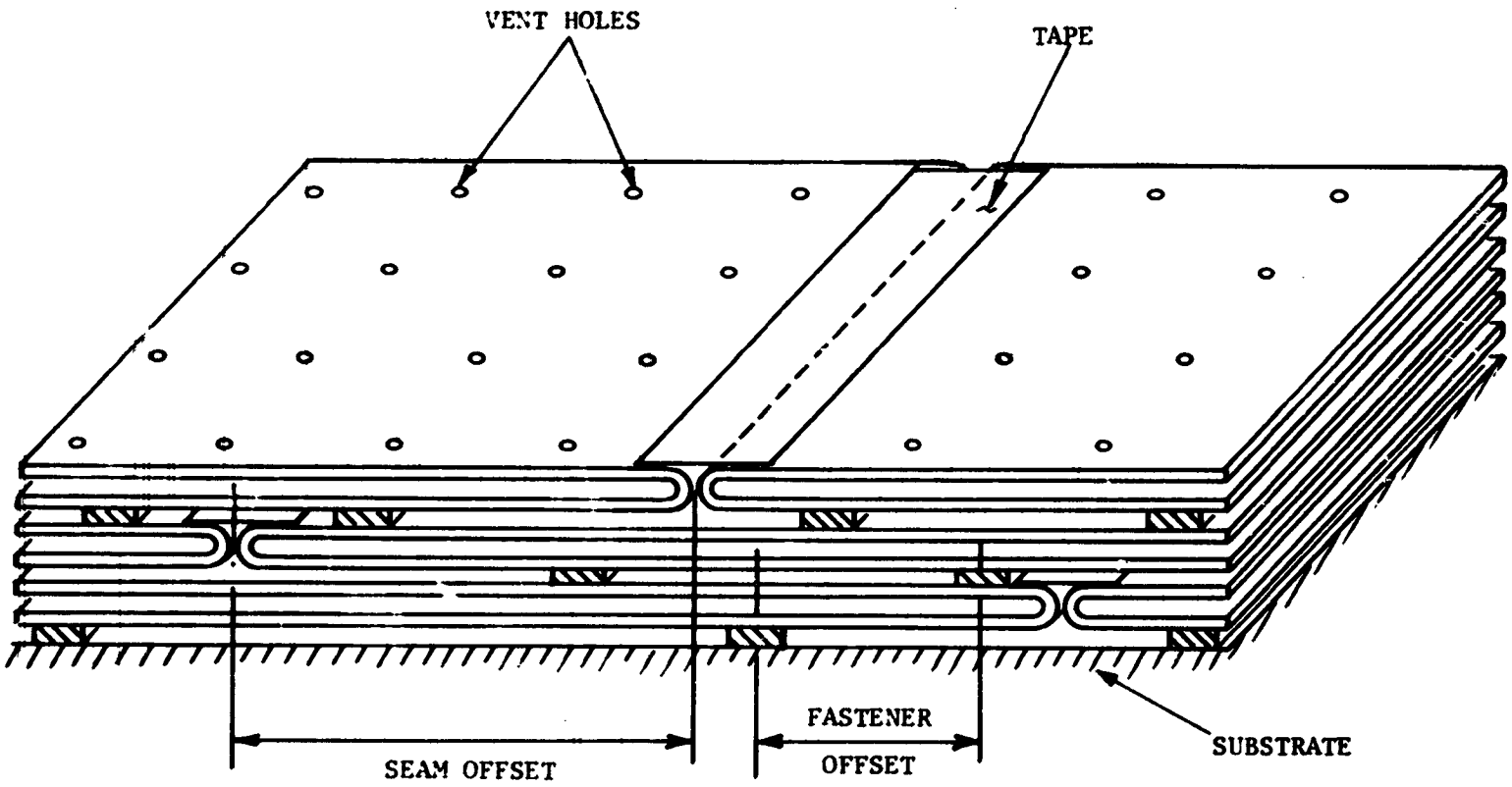

Figure 1. Schematic of Blanket Installation

N82 25294

ORIGINAL PAGE IS
OF POOR QUALITY

TRANSIT THERMAL CONTROL DESIGN FOR GALILEO ENTRY PROBE FOR PLANET JUPITER

George C. Haverly
Galileo Probe Thermal Design Engineer
Re-Entry Systems Division, General Electric Company

Senior Engineer, Environmental Control Sub-Systems Engineering
Space Systems Division, General Electric Company

William Pitts
Research Scientist, Ames Research Center
National Aeronautics and Space Administration

ABSTRACT

A totally passive design has been completed for the thermal control of the Galileo entry probe during its transit to the planet Jupiter. The design utilizes radio-isotope heater units, multilayer insulation blankets and a thermal radiator, in conjunction with a design conductance support structure to achieve both the required storage and critical initial planet atmosphere entry temperatures. The probe transit thermal design has been completed and verified based on thermal vacuum testing of a prototype probe thermal test model.

INTRODUCTION

The Galileo Probe is being prepared for exploration of the atmosphere of the planet Jupiter in an extension of the earlier Pioneer Probes which successfully sampled the atmosphere of the planet Venus. The environments for the Galileo Probe present unusual and challenging thermal design requirements. The planet Jupiter's size, distance from both the sun and earth, and potential range in atmosphere composition and density profiles are primary contributors to the uniqueness of these thermal requirements.

This paper summarizes the design, development, and test verification for the probe design for thermal control of the probe during its transit from earth and up to its initial entry into the Jupiter atmosphere.

The probe is designed for attachment to the Galileo Orbiter. The Orbiter/Probe Assembly is to be carried by the Shuttle in a launch from Cape Kennedy to a parking orbit about the earth. The combined Orbiter/Probe Assembly is to then be put into a transfer orbit for the planet Jupiter. The nominal time for this joined assembly transit phase is approximately 730 days from its separation from the Shuttle until it is at a proper location and trajectory relative to Jupiter.

PRECEDING PAGE BLANK NOT FILMED

The normal attitude and orientation of the Galileo Orbiter and Probe, during its transit from earth to Jovian capture, is such that the Orbiter completely shades the Probe from solar insolation. There are intermittent periods, during this transit phase, when the Orbiter/Probe attitude is changed to permit interrogation by earth control stations. Direct solar heating of the Probe forebody section may occur during these brief periods, dependent upon the transit trajectory and earth/sun relative positions. The maximum time during which direct solar heating of the probe can occur during these periods has been limited by system considerations to four (4) hours.

The Probe will then be separated from the Orbiter for its continued approach to the planet. This separation will occur 75 ± 25 days before the Probe will begin its entry into the planet's atmosphere. The primary (and coldest) thermal design transit environment for the Probe is this nominal 75 day period. The solar insolation, at this location in our solar system, of approximately 5 watts/ft^2, is insufficient and too trajectory-constraining to effect solar heating for Probe thermal control.

PROBE TRANSIT THERMAL DESIGN REQUIREMENTS

Pre-Separation Phase

A design probe interior average temperature range was selected for the nominal 720 days of transit (i.e. while joined to the Orbiter) based on the storage/life characteristics of the lithium oxygen entry battery cells and the experiment, telemetry and control components storage temperature requirements. The design range considers the above maximum of four (4) hours duration, during which the Orbiter attitude can be such that the sun may illuminate portions of the Probe or adjacent Orbiter surfaces. The Probe design temperature range and Orbiter: Probe thermal interface conditions are summarized in Table 1.

Up to five (5) watts of electrical power can be provided to the Probe from the Orbiter during this first transit phase. However, the Orbiter power requirements are such that a goal for the Probe design was to accomplish its thermal control without use of this power.

Post-Separation Phase

The primary Probe design environment is that encountered during the 50 to 100 days following the Probe's separation from the Orbiter, as the Probe approaches the Jupiter planet. The design objective is for the Probe's interior average temperature to equilibrate to 0°C $^{+10°C}_{-5°C}$ following its separation from the Orbiter. This minimum temperature is that which the lithium oxygen battery cells are sufficiently warm to provide the electrical energy as required for experiment, telemetry and control upon planet atmosphere entry. The maximum temperature was selected so that maximum experiment operation time will be realized during the Probe's descent into the planet's atmosphere. This operational time period will be limited to that time at which the equipment ceases operation due to the excessive descent environment-induced temperatures.

PROBE THERMAL DESIGN PHILOSOPHY

Preliminary studies indicated that post-separation transit thermal control of the Probe by either controlled electrical heating or utilization of an enhanced thermal capacitance was spacecraft weight prohibitive.

The basic one-watt, U238, Radio-isotope Heating Units (RHUs) used so successfully for local appendage heating for the JPL Voyager Spacecraft and earlier military applications offered a promising low-weight thermal energy source. The design problem in the utilization of the RHUs for Probe transit thermal control is the accommodation of the RHU's continuous thermal dissipations during all phases of pre-launch, launch, and transit, and the resulting Probe temperatures.

A Probe thermal design evolved from considerations of the various Probe thermal environments which incorporates the direct exposure of a specific area of the Probe heat shield nose as a space thermal radiator. This direct exposure of the Probe nose increases the required number of RHU watts at significant associative costs. However, the objective of this direct exposure is to provide a design bias on the heat loss "paths" and the resulting Probe thermal equilibration temperatures for each launch and transit phase.

The other basic elements of the Probe transit thermal design are a multiple layer insulation (MLI) blanket set, a three-element Probe: Orbiter support adapter set having a design thermal radiative/conductive characteristic and three Probe: support adapter thermal insulators. The basic Probe transit thermal control configuration is shown in Figure 1.

The Probe design thus contains no active elements to trim or modulate either the effects of the RHU thermal output or the heat loss from the Probe exterior during this design post-separation planet approach period. The Probe interior temperature distribution realized during this period will be primarily determined by the insulation blanket's performance (e.g., effective emissivity) and the thermal energy radiated directly from Probe exposed surfaces (including the separation support interface surfaces). As indicated previously, the equilibrated temperatures of the individual Probe components attained during this phase will be their "start-up" temperatures at the beginning of entry into the Jovian atmosphere, and will constrain the experiment's operational period

Similarly, the Probe's pre-separation transit interior temperature is dependent upon achieving a sensitive design balance between the continuous thermal dissipation of the radio-isotope heater units (RHUs), the heat loss thru the Probe support structure, the insulation blankets, from the exposed heatshield nose area, and thru radiation to the adjacent Orbiter surfaces.

PROBE TRANSIT THERMAL CONTROL ELEMENTS

Radio-Isotope Heating Units (RHUs)

The RHUs are the only source of thermal energy for the Probe during its post-separation transit phase. The RHU design is a weight-reduced version of the earlier Pioneer RHU. Each RHU contains the precise quantity of U238 isotope to release 1.0 watts of energy at three (3) year's following fabrication. The design half-life for this isotope is 86 years. Each RHU consists of multiple metal cylindrical enclosures of the U238, which contain, absorb, and limit the isotope gamma and neutron radiation. The outermost metal cylinder is, in turn, enclosed in a machined graphite cylinder with the resulting outside nominal dimensions of 2.5 cm. O.D. x 3.1 cm. in length. The nominal weight for each RHU is 38 gm.

The RHUs are attached to the interior surface of the Probe forebody and aft cover heat shield aluminum liners as shown in Figure 1. The number used and location of the RHUs were analytically determined based on MLI blanket, nose radiator and temperature gradient considerations.

MLI Blanket Set

The primary component in the Probe assembly which will determine the RHU thermal dissipation requirement is the multiple layer insulation (MLI) blanket set. This blanket set will restrict the heat loss from the relatively large Probe forward and aft exterior surfaces (approximately 3.5 m^2). There is an extensive history in the design and utilization of MLI insulation for nearly every satellite and space vehicle system. The Galileo MLI blanket's application requirement is unique, with regards to this experience, in that it is essential that their thermal insulation performance be precisely known and maintained. If the blanket's heat loss is greater than the design range during the Probe's planet approach, then the equilibrated Probe's interior temperature will be colder than the design limit for activation of the Probe payload and power assemblies. Conversely, if the blankets provide greater insulation than their design range, then the temperatures of the Probe's payload and power assemblies will be higher than the design limit. Both science payload and power system mission performance will be significantly affected by storage and activation temperatures in excess of +20°C.

The MLI blankets have been configured such that joints, penetrations, fasteners, electrostatic (ESD) grounding and installation effects will be minimum in their effect on Probe heat loss while in transit environments. Thermal vacuum testing and blanket manufacturing control are essential to the Probe thermal design. The Probe is expected to encounter charged particle fields, as it approaches Jupiter, of approximately 40 times greater than those encountered by geosynchronous satellites orbiting the earth. Particular care has been given to providing electrical grounding of all of the Probe exterior elements. A black, electrically-conductive coated, vacuum deposited aluminum, Kapton outer layer was used as the outer layer for all of the MLI blanket areas which could experience solar heating. All surfaces of the blankets and tapes were provided a ground path to the electrically-conductive, phenolic carbon, forward heat shield.

Probe Space Thermal Radiator

The design objective of the direct exposed Probe thermal radiator is to bias the heat leak from the Probe such that it is predominantly via the Probe forebody surface. This bias thus minimizes the thermal differences between the post-separation environment effects and pre-separation thermal effects of the Orbiter upon the Probe aft surfaces and support interface. The second design objective of the nose radiator is to desensitize the Probe's thermal balance equilibration temperature to the MLI blanket set's thermal performance. The accompanying Figure 2 summarizes, schematically, the design Probe thermal balance distribution goals for both the Probe's pre-separation and post-separation thermal environments.

It was recognized early in the Probe transit thermal design concept effort that there should be some means of realistically accomplishing a trim on the thermal balance of the final Probe flight assembly in view of:

1. MLI blanket set installation effects on realized blanket performance.

2. Differences in thermal performance between development and flight MLI blanket set thermal performances.

3. Substantial efforts involved in the Probe heat shield disassembly required to add or remove internally-mounted RHUs to achieve design equilibration temperatures.

A "trimable" thermal radiator design evolved which employed use of a stable, low emissivity tape, in conjunction with the inherent high emissivity of the Probe forebody phenolic graphite forebody heat shield. The design involved space exposure of a specific area of the forebody nose phenolic carbon surface and a proportioned area of exposed adjacent low emissivity (ϵ_H) tape-covered forebody. All other significant surface areas of the post-separation Probe are enclosed by the MLI blanket set.

A vacuum-deposited gold coated Kapton tape, with a silicone adhesive was selected for the low ϵ_H radiator tape. Thermal balance adjustment of the Probe flight set can then be effected by removal (or addition) of the taped areas of the exposed forebody to compensate for the realized final assembly MLI blanket set performance.

Probe Support Attachments

The Probe nominal design temperature during its early transit phase (i.e. while joined with the Orbiter) is -10°C, which is 10°C less than its nominal design temperature following separation from the Orbiter. The thermally conductive coupling of the Probe thru its supports with the Orbiter offered a means of compensation for the effects of the thermal radiative presence of the orbiter relative to the Probe aft

surfaces. This compensation is possible since the Probe support, Orbiter mounting interface temperature is lower than the Probe design internal temperature.

A Probe support thermal design was accomplished that provides a net conductive heat transfer thru the three support assemblies to the Orbiter to compensate for the radiative presence of the Orbiter. The design includes a carbon phenolic conical insulator between the local Probe mating surfaces and the three support assemblies. This design also depends upon a low thermal conductance and a low emissivity of the three support assemblies. The low thermal conductance is achieved by the use of titanium alloy 6AL-4V and minimum strut cross-sections. Low emissivity of the surfaces of the three support assemblies is obtained by covering them with the same gold-coated Kapton tape used for achieving low ϵ_h on the selected areas of the Probe forebody space thermal radiator.

Electrical Heaters

The Probe transit thermal control design was accomplished in time-parallel, both with the JPL Orbiter design effort and several planet-entry Probe trade considerations which presented potential design/support interface uncertainties. Three 1.66W thermostatically-controlled electrical heaters were incorporated into the Probe design to prevent excessively low interior temperatures during the pre-separation transit phase in the event that the Orbiter: support adapter's interface temperature evolved to $< -150°C$, or increased Probe weight necessitated larger support assembly cross-sections and/or materials with increased Probe support net conductive heat loss.

The design objective has continued to be for a totally passive pre-separation transit Probe thermal control (i.e. no electrical heating).

DESIGN TRADES

An analytical model was constructed of the Probe to simulate, thermally, its response and equilibration to the various mission thermal environments. The basic model was configured to represent the Probe in its primary design post-separation mission phase. The model, as constructed, consisted of 104-nodes and simulated a 1/6 section of the Probe, reflecting its symmetry and the need for prediction accuracy of local temperatures with consideration of computer trade costs. This model was used to assess the sensitivity of the post-separation Probe configuration to the number of RHUs, MLI blanket set thermal performance, space radiator area exposure and radiator tape effective emissivity.

A second analytical model was constructed by the addition of nodes to thermally simulate the Probe and support adaptor's effects on the Probe responses and equilibration to the pre-separation transit environment, in combination with the Orbiter thermal interfaces.

This pre-separation Probe model continued the symmetrical representation of 1/6 of the Probe and included conductance to the adjacent support adapter and simulation of the adjacent Orbiter thermal radiative presence. The resulting model consisted of 136-nodes and also included simulation of the three previously identified thermostatically-controlled electrical heaters.

The post-separation and pre-separation Probe thermal models were exercised to predict equilibrated temperatures for various combinations of MLI effective thermal performance, number of RHUs, total radiator exposed area, radiator tape effective emissivity, and tape coverage. Figures 3 and 4 show the results from several of these trades. A specific Probe design was selected, based on these trades, as the design having the minimum sensitivity to the probable range in design parameters.

The final selected Probe design thermal parameters are summarized in Table 2. These Probe thermal models were also modified to permit evaluation of both thermal response and equilibrated Probe temperatures to specific storage and Shuttle Bay thermal environments.

PROBE THERMAL BALANCE TESTS

The passive thermal design of the Probe and its critical post-separation equilibration temperature made thermal vacuum testing an essential part of the thermal design development. Such testing in the post-separation configuration was necessary to provide an assessment of:

1. The MLI blanket set thermal performance.
2. The nose radiator thermal performance.
3. The equilibration temperature and Probe interior temperature gradients with the selected 31 RHU complement.
4. A calibration of the effect of RHU dissipation on Probe equilibration temperature.
5. A calibration of the effect of radiator gold tape coverage on Probe equilibration temperature.

Similarly, thermal balance test in the pre-separation Probe configuration was necessary to provide an assessment of:

1. The adequacy of the thermal conductance designed support adaptors to compensate for the effect of the Orbiter's thermal presence upon the Probe's equilibration temperature.
2. The effects of Orbiter: adaptor interface and Orbiter thermal sink temperatures upon the Probe equilibration temperature.

3. An assessment of the electrical heater power requirements.

4. The equilibration temperature and Probe interior temperature gradients with the selected 31 RHU complement.

The Probe structural test model, with an experiment package in place, was fitted with 44 simulated (electrically-heated) 1-watt RHUs. The design gold tape radiator pattern was applied to its forward heat shield nose, leaving the selected surface exposure of 660 cm^2 of phenolic graphite. A design 3-element, MLI blanket set was installed and the Probe assembly was properly completed for thermal vacuum testing in its post-separation configuration. The assembly was then installed in a liquid nitrogen-cooled vacuum test chamber. The Probe assembly was brought to temperature equilibration at two RHU complement dissipation levels (33 and 39W). The corresponding Probe internal average equilibration temperatures were -21.5 and -12.3°C. The Probe was then modified by adding an additional 465 cm^2 of gold tape to the nose radiator and again exposed, with 39 watts of dissipation, to the liquid nitrogen vacuum simulated post-separation environment. The resulting equilibration Probe average internal temperature was +.8°C. The accompanying Figures 5 and 6 summarize these test results.

The Probe and test facility were then modified to provide simulation of the effects of a range of Orbiter: support adapter and Orbiter radiative thermal sink temperatures upon the Probe. This pre-separation Probe configuration (with the "added taped" radiator) was brought to temperature equilibration with 39 RHU watts, for the design Orbiter adaptor interface and sink temperatures of -150°C, 0°, and +31°C. Figure 7 summarizes the resulting equilibration Probe average internal temperatures.

The electrical heaters were energized during the final stages of the pre-separation Probe's equilibration to the design -150°C Orbiter interface conditions. All three of the independently-controlling thermostats turned "off" their corresponding heaters at this condition.

CONCLUSIONS

The passive transit thermal design for the Probe is validated for both the post-separation and pre-separation design conditions.

Both the MLI blanket and the thermal radiator's performance were somewhat less than initially expected but are within the design adjustment capability. This reduced performance results primarily from two design development decisions:

1. The initial MLI blanket design involved enclosure of all of the Probe aft surfaces, as well as a part of the forward heat shield surface, with a single MLI element. This design was changed to two individual MLI elements covering these Probe surfaces to simplify the blanket configuration and

Probe: blanket assembly procedures. This design change resulted in approximately a 300% increase in the blanket set joint length and a reduced set thermal performance.

2. A somewhat similar design change involved the installation of the radiator gold tape as butting strip segments rather than overlapping segments. This decision resulted in an approximate 20 mil. average gap exposure of the carbon phenolic heat shield between each segment. This exposure resulted in an approximate 30% increase in the effective emissivity of the taped radiator area.

Evaluation of the test results indicates that the realized thermal performance parameters for the individual MLI blanket elements and the radiator were as follows:

- Aft MLI element effective emissivity (ϵ_{eff}) ~ .021.
- Transition MLI element ϵ_{eff} ~ .04.
- Forward MLI element ϵ_{eff} ~ .024.

  Overall (area average) MLI set ϵ_{eff} ~ .026.
- Area Average gold taped radiator section ϵ_H ~ .075.
- Bare phenolic carbon ϵ_H ~ .89.

The Probe pre-separation electrical heaters and thermostats are not needed and may be removed from the flight Probe hardware.

TABLE 1

PROBE TRANSIT THERMAL DESIGN REQUIREMENTS AND INTERFACE CONDITIONS

DESIGN PROBE INTERNAL TEMPERATURES	DESIGN TEMP.	RANGE TOLERANCE
EARLY TRANSIT PHASE (W/SUN)	-10°C	+30°C -10°
TRANSIT (W/O SUN)	-10°C	+20° -10°
POST SEPARATION (JOVIAN ATMOSPHERE ENTRY)	0°C	+10°C - 5°C
ORBITER/ADAPTOR THERMAL INTERFACE	**W/SUN**	**W/O SUN**
MOUNTING TEMPERATURE	-50°C	-150°C
EFFECTIVE RADIATION SINK (FOR ADAPTOR AND AFT COVER)	-50°C	-150°C

ELECTRICAL

HEATING ($\leq$5 WATTS) AVAILABLE FROM ORBITER DURING EARLY TRANSIT PHASE.

TABLE 2

SELECTED PROBE TRANSIT THERMAL CONTROL DESIGN CHARACTERISTICS

- o 3 Element MLI Blanket
  - 2-Mil. VDA Kapton inner and outer layers.
  - 11 layers Dacron Mesh, alternated with 10 layers .25 Mil. VDA Mylar
  - Pre-Separation, space-exposed blanket areas had Sheldahl conductive (Carbon Polyester) covering.
  - All Kapton and Mylar layers were electrostatically grounded to local conductive heat shield.
- o Design Exposure of 5444 cm^2 of Forebody Nose as Thermal Radiator
  - Coverage of 4784 cm^2 of this exposed Forebody with gold-coated 2-Mil. Kapton tape.
- o Nominal Complement of 31 1-watt RHUs, with Mounting Brackets for additional 13 RHUs
  - Nominal RHU distribution consisting of:
    - 6, located on Aft Heat Shield Liner
    - 7, located on Forward Heat Shield Frustrum Liner
    - 18, located on Forward Payload Support Ring
- o Conical Carbon Phenolic Insulator (.2" thick) between Probe and 3 Support Adaptor Mounting Surfaces
- o Thermal Conductance Designated Titanium (6 AL-4V) Support Adaptors (3), with Low ϵ_H Gold Taped Surfaces
- o Thermostatically-controlled 1.66W Electrical Heaters (3) Bonded to Probe Internal Longerons

FIGURE 1

GALILEO PROBE TRANSIT THERMAL CONTROL DESIGN

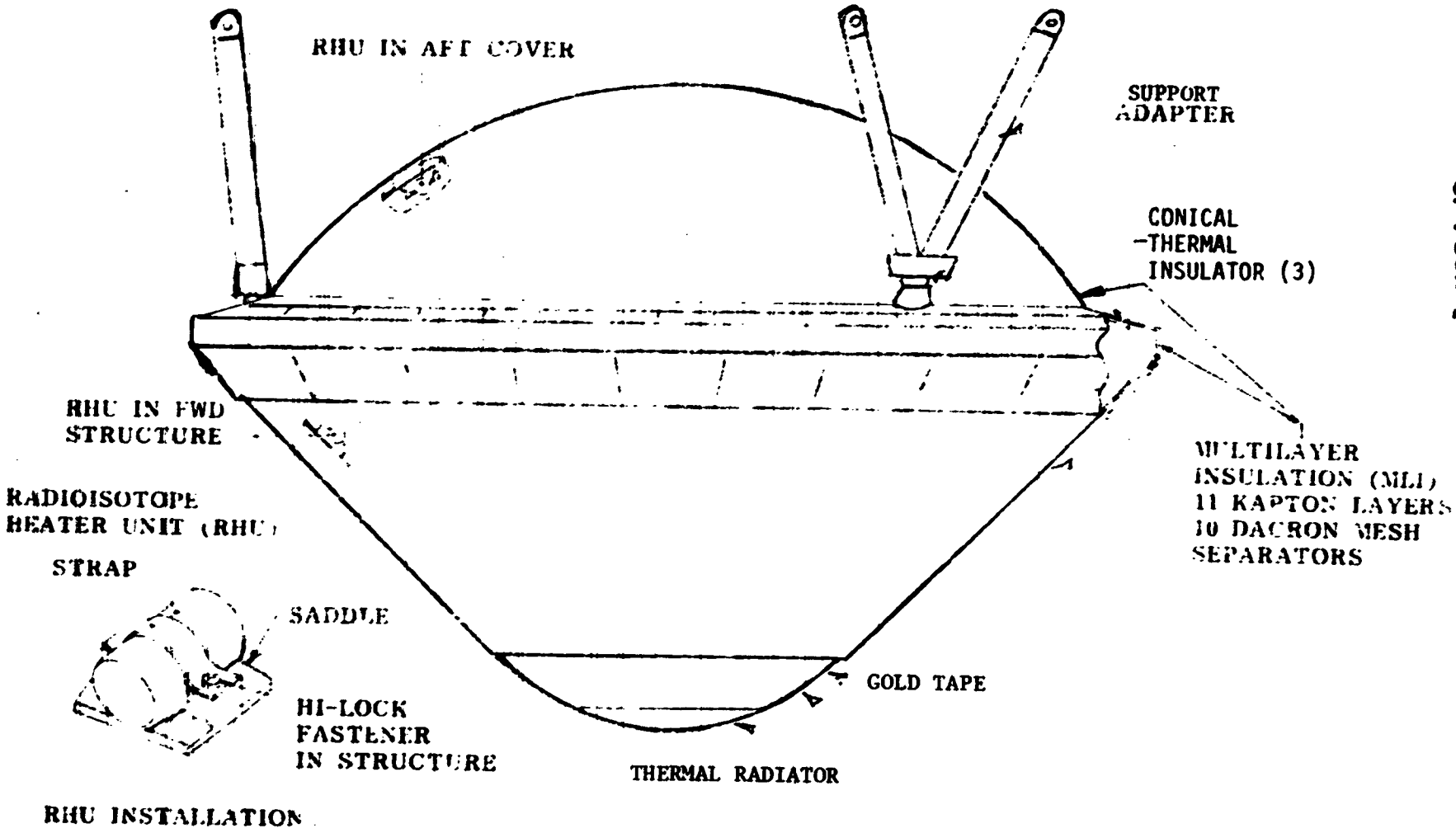

ORIGINAL PAGE IS OF POOR QUALITY

FIGURE 2

PROBE TRANSIT THERMAL BALANCE

POST-SEPARATION PHASE

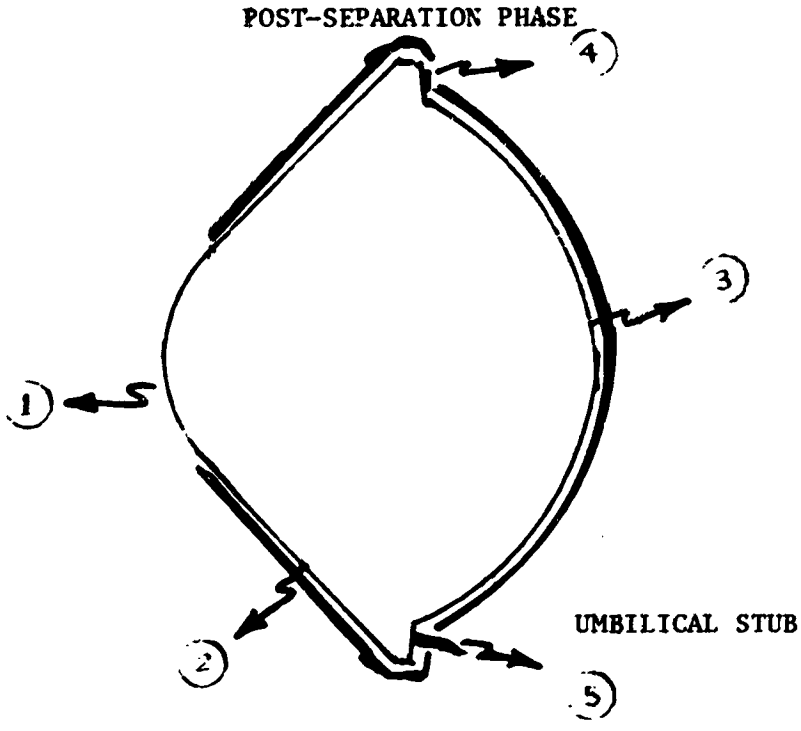

THERMAL LOSS		PREDICTED	TEST
Nose Radiator	1	56%	37%
Forward MLI	2		17%
Transition MLI	3	43%	19%
AFT MLI			
Support Surface	4	< 1%	< 8%
Umbilical Stub	5	< 1%	-

PRE-SEPARATION PHASE

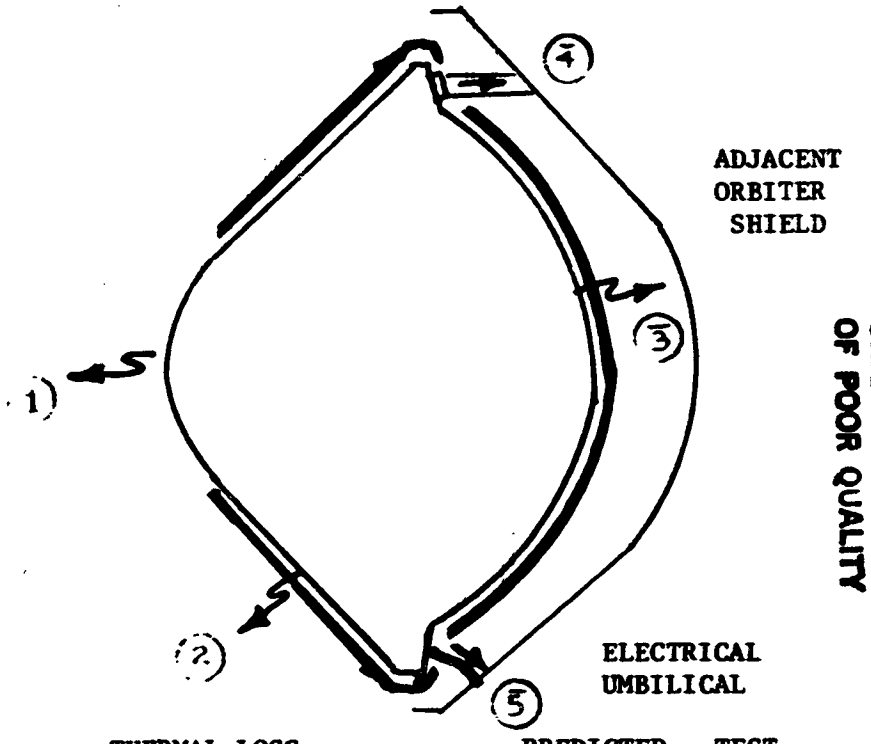

THERMAL LOSS		PREDICTED	TEST
Nose Radiator	1	44%	39%
Forward MLI	2		18%
Transition MLI	3	30.5%	19%
AFT MLI			20%
Support Adaptor	4	25.5%	< 7%
Electrical Umbilical	5	< 1%	

ORIGINAL PAGE IS
OF POOR QUALITY

ORIGINAL PAGE IS
OF POOR QUALITY

FIGURE 3

RADIATOR AND MLI BLANKET PERFORMANCE
EFFECTS ON PROBE POST-SEPARATION TEMPERATURE

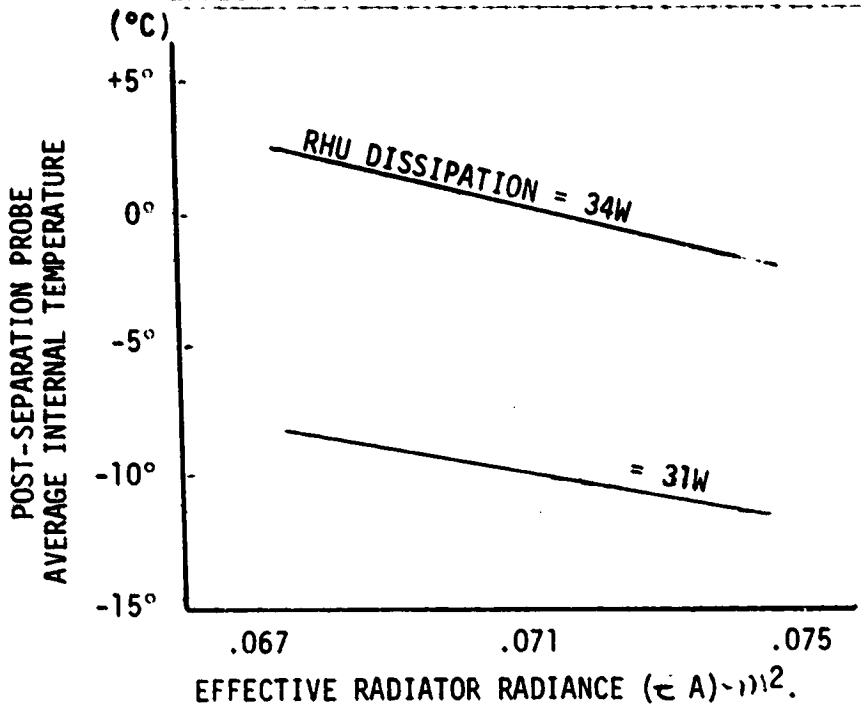

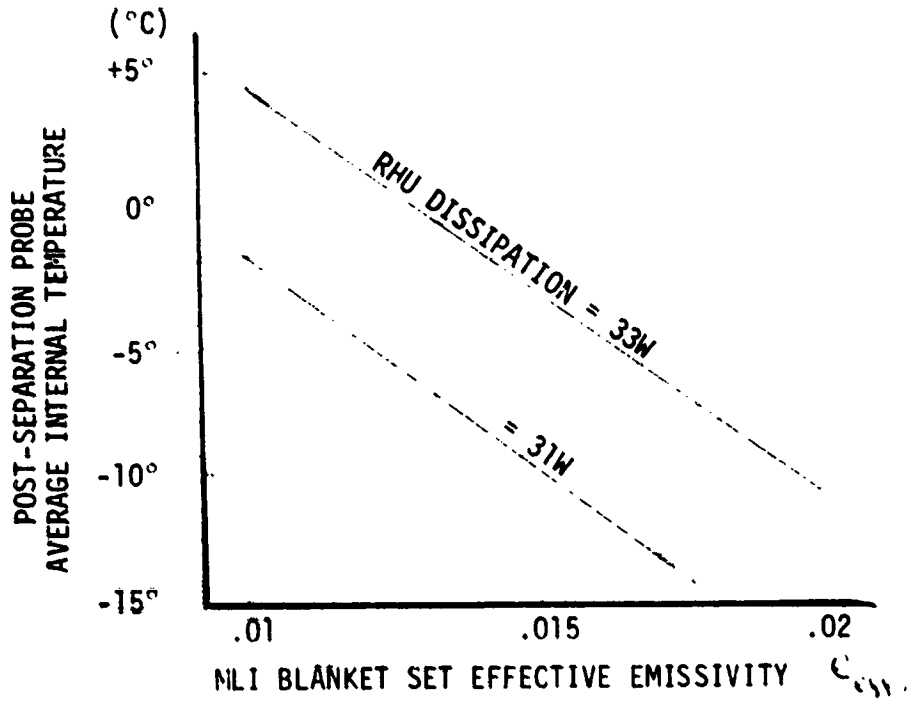

ORIGINAL PAGE IS
OF POOR QUALITY

FIGURE 4
SUPPORT INTERFACE AND MLI BLANKET
EFFECTS ON PROBE PRE-SEPARATION TEMPERATURE

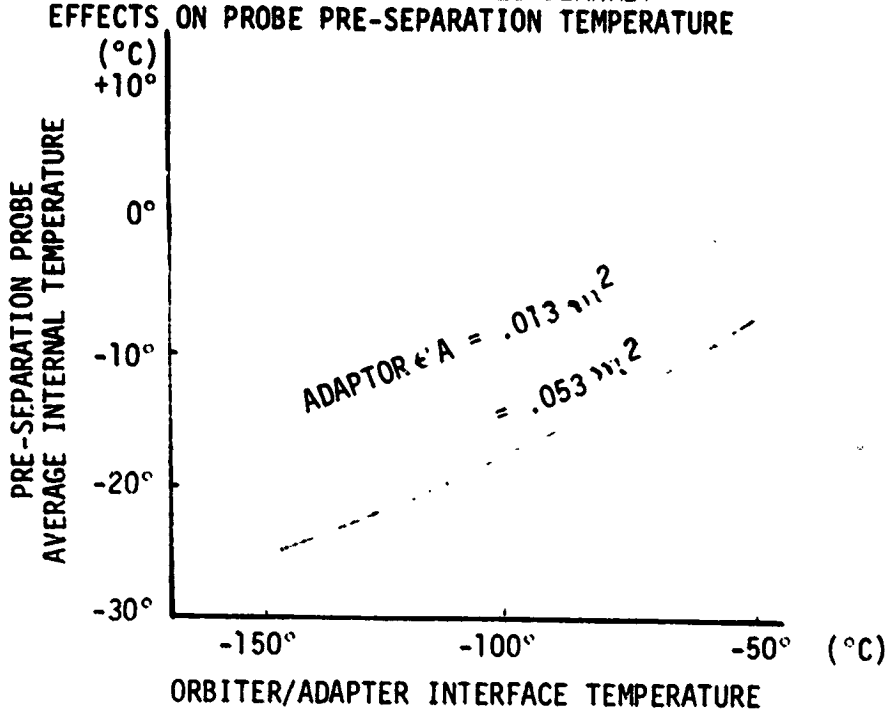

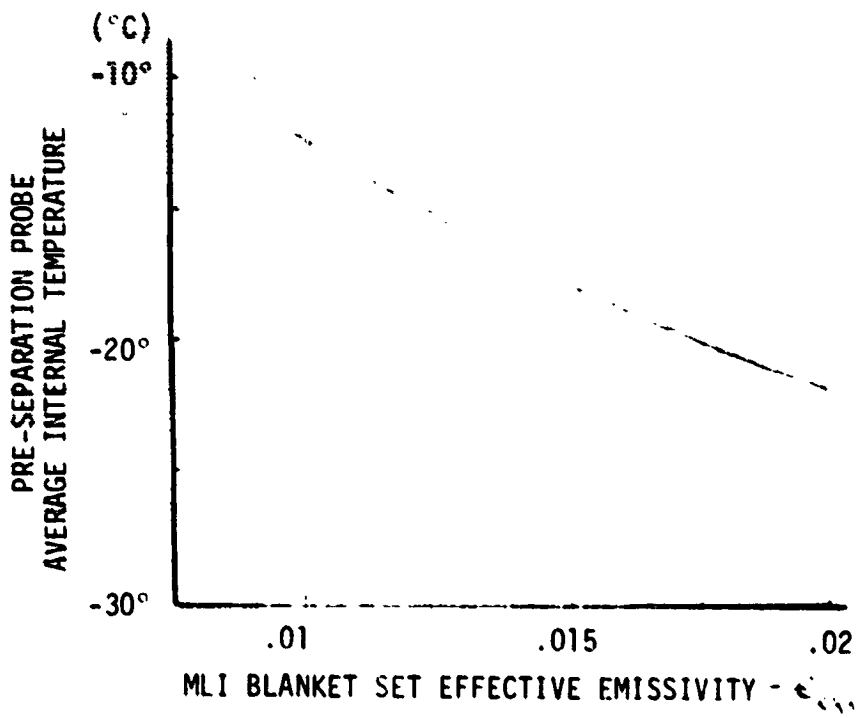

ORIGINAL PAGE IS
OF POOR QUALITY

FIGURE 5
POST-SEPARATION TEST EFFECTS OF RHU DISSIPATION
AND RADIATOR TAPE COVERAGE ON AVERAGE PROBE TEMPERATURE

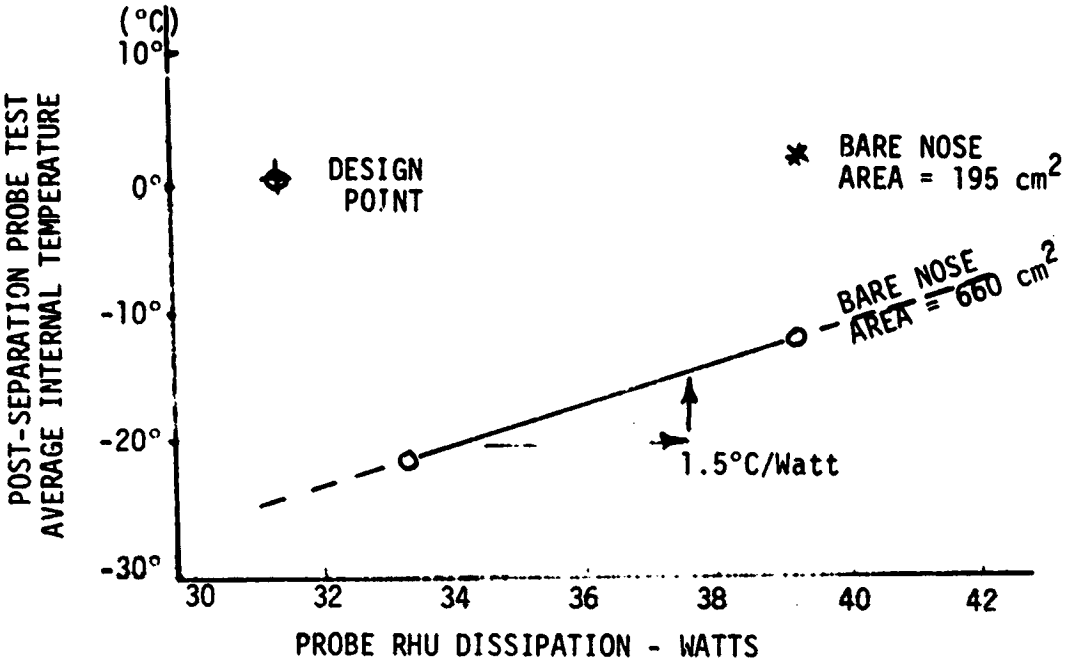

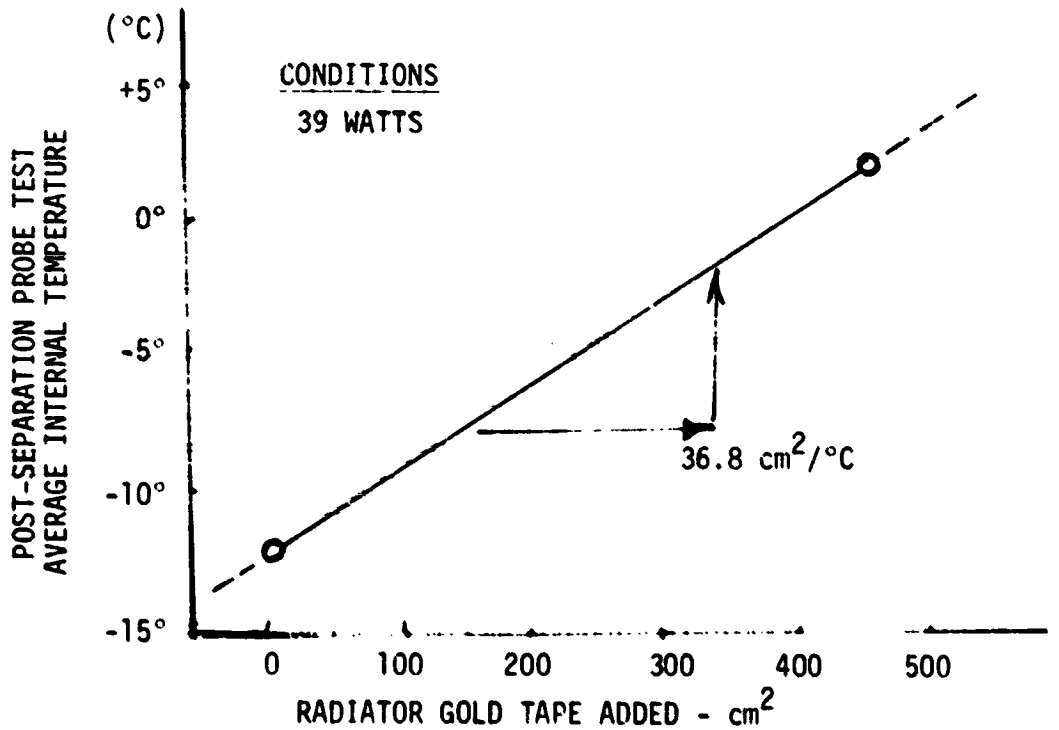

FIGURE 6
POST-SEPARATION PROBE EQUILIBRATION TEMPERATURES
(39 WATTS & 195 cm^2 BARE NOSE)

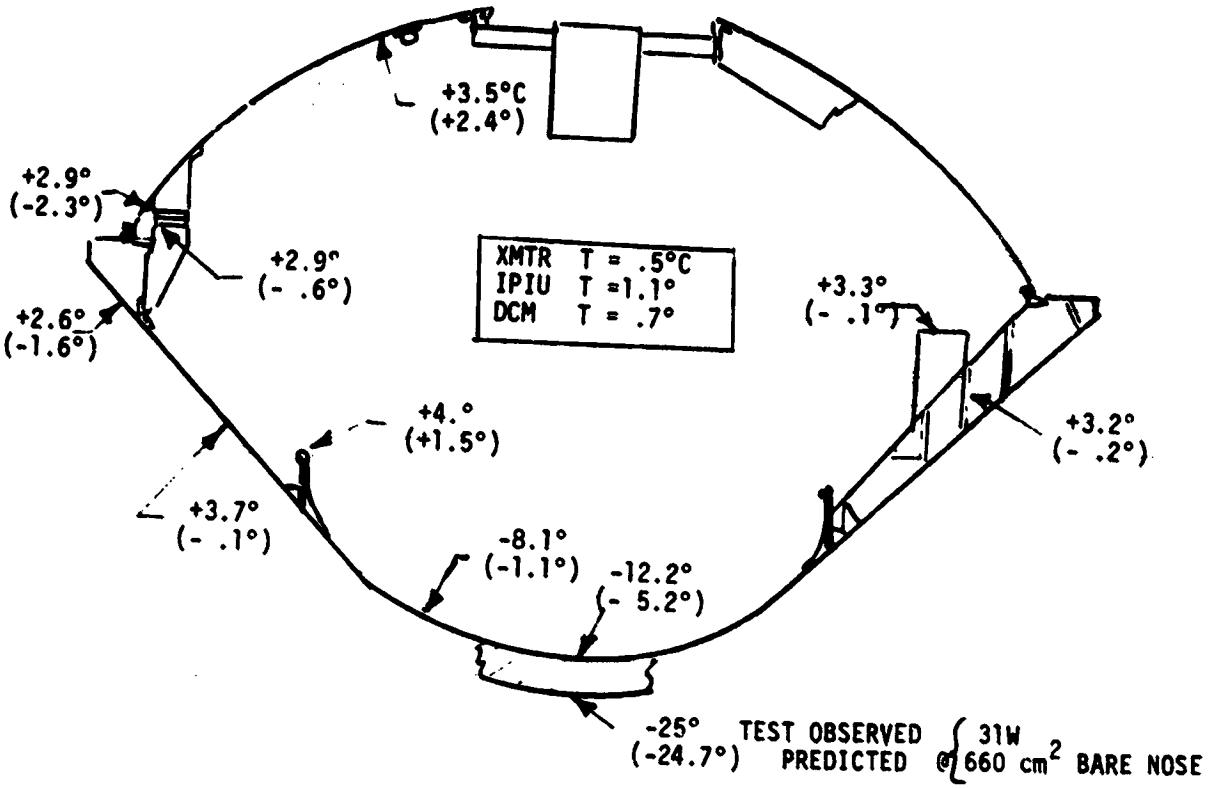

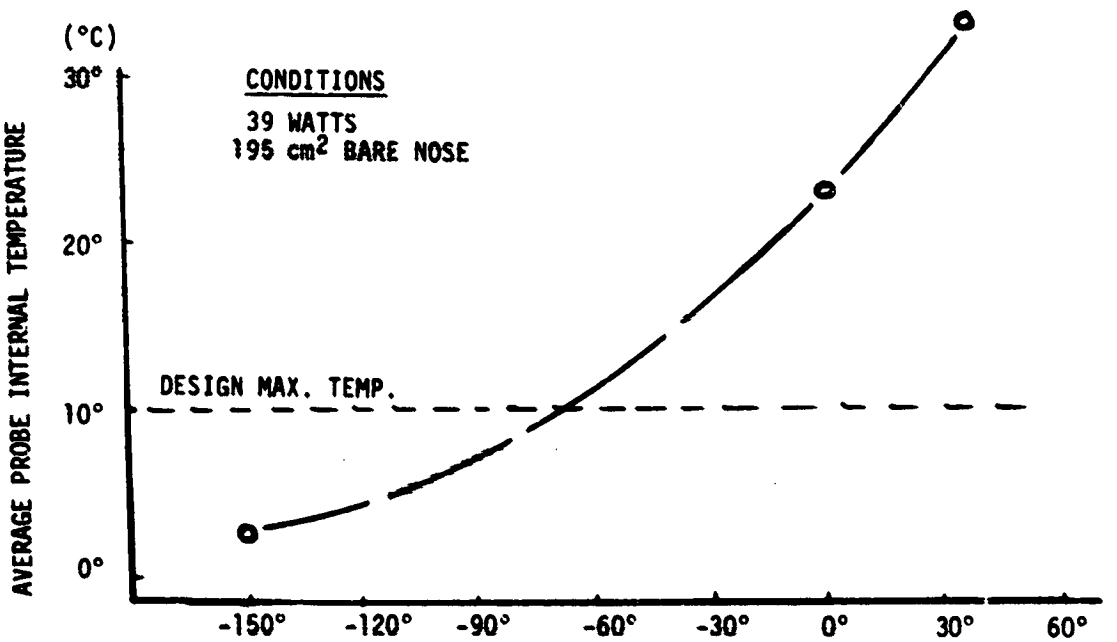

FIGURE 7
PRE-SEPARATION PROBE AFT SINK AND ADAPTOR
MOUNTING INTERFACE TEMPERATURE - °C

PRECEDING PAGE BLANK NOT FILMED

SESSION III

THERMAL SIMULATION AND PROTECTION

Session Organizers: Robert Parrish, Martin Marietta Aerospace

George Mikk, Perkin-Elmer Corporation

PRECEDING PAGE BLANK NOT FILMED

N82 25295

A SURVEY OF METHODS FOR MEASURING THERMALLY INDUCED DISTORTIONS OF TEST ARTICLES UNDERGOING SOLAR THERMAL VACUUM TEST

R. D. Rempt
Martin Marietta, Denver, Colorado

ABSTRACT

Recent trends in space vehicle test requirements have called for precise knowledge of small thermally induced distortions experienced either by various points on the vehicles or by deviations of surfaces from a known shape during solar thermal vacuum test. Various methods of gathering such information during test are presented in this paper. State-of-the-art application of both photographic and real time observation are discussed. The relative merits of each of the methods are compared and evaluated in their applications to different types of test articles and situations. Magnitudes of thermally induced distortions which may be expected to be routinely measurable by the various methods are presented and compared.

INTRODUCTION

In order to select the best methods of precisely measuring thermally induced distortions in test articles for various configurations and conditions, a survey of the current state-of-the-art was made. The survey includes investigation of the applicability of all reasonable methods of performing the measurements. Each method is discussed, and its applicability evaluated with respect to measurement type, test article type and environment, along with the resolution which can be ascribed to the particular instruments. A matrix summarizing the applicable channels of each method is presented as a conclusion.

PHOTOGRAMMETRY

In the last decade and a half, nontopographic photogrammetry has been developed to routinely record and measure small distortions. Cameras suitable for operation inside of thermal vacuum chambers have been developed and used with a good degree of success. Owing to the capability of precisely locating a point on a developed plate with a comparator, accuracies of one part in sixty thousand of the largest diameter of the test article are routinely achievable. These, of course, are relative measurements. If absolute measurements are required, a suitable gauge bar is necessary which must be placed properly within the field of view of the cameras, and which will not change appreciably over the temperature range of the test.

The most important immediate application of photogrammetry to thermal vacuum testing is where knowledge of an entire surface is of interest. A photograph records the position of all points on the surface instantaneously whether the surface is in thermal equilibrium or not. No other methods can

record the changing of a flexible surface, but only the initial and final positions when thermal equilibrium is established. Also, any line of sight application will only give information concerning a few points rather than the whole surface at once. It is often of interest to know how much a surface such as an antenna mesh deviates from a known preset configuration such as a paraboloid of revolution. Photogrammetry provides this knowledge accurately and routinely. Also, a permanent record is taken which may be recalled later for additional analysis without having to rerun an expensive test.

The photogrammetric process depends on affixing of a large number of adhesive targets to the surface of the test article. Test articles which cannot tolerate such targets or are not capable of being distinctly targetted in some other way, are generally not measurable by photogrammetric means. Presently, NASA is investigating the possibility of mensurating the thermo-reflective tiles on the STS orbiter for distortion after each flight by photogrammetric means.

The greatest drawback of this process is that the data are not available in real time. After the plates are developed, several days are required to measure and reduce the data. This process must be performed by highly trained and experienced personnel, and therefore photogrammetric capabilities are most easily acquired through a subcontractor. If many tests are to be made, development of the capability in-house may be cost effective, but due to the experience required on the learning curve, such development will not come quickly.

DIRECT LINE-OF-SIGHT METHODS

For purposes of this discussion, these types of measuring techniques will be confined to direct optical line of sight established by instrumentation sighting through a window in the thermal vacuum chamber. The requirement of a window adds expense for optical flatness as well as for the thickness required for vacuum safety. All instruments employing optical line of sight detect movement perpendicular to the line of sight. This requires that no surfaces which bend or otherwise redirect the line of sight be used unless their movement is independently monitored. Since the instrumentation required to monitor the beam bending apparatus is equivalent to the instrumentation making the measurements of interest, it is hardly advantageous to bend the beam unless geometry requires it. Hence, the term "direct line of sight". This is demonstrated in figure one.

The great advantage of direct line of sight (DLOS) is that initial coarse alignment may be achieved quite easily by personnel outside the vacuum chamber. There are two requirements to ensure meaningful DLOS performance. The first is that all instrumentation must be mounted on stable fixtures which are not disturbed by the movement of personnel and equipment outside the chamber. The second is that the test article has distinctly identifiable and precisely locatable "targets".

For measurements where orientational changes only are of interest, theodolites may be used. Good instruments have resolutions 1×10^{-5} rad for the manual types and 3×10^{-5} rad for the electronic digital types.

The measurements are made by sighting on a suitable optical target or auto-collimating with the theodolite on an optical mirror. One optical target or one mirror is necessary per rotational axis of interest.

For measurements of translation of distinct points in three-dimensional space, there are several ways of obtaining the information. A jig transit square mounted on a tooling bar with an optical micrometer may be travelled parallel to the absolute measurement of interest. Two instruments mounted on mutually perpendicular tooling bars would be required for measurement in the plane perpendicular to the DLOS. A third instrument could be sighted perpendicular to the DLOS of the first two to recover information from the remaining axis. Such a setup would require at least two vacuum windows mounted in planes at right angles. Since tooling bars are so large and massive, continuous checks are necessary to confirm that the bars themselves are not moving with respect to the vacuum chamber. Resolution of a good optical micrometer is 5×10^{-6} M.

If sufficient field of view is available through windows, measurements may be made by triangulation with theodolites. Manual theodolites may be used, but the calculations required with their use are cumbersome. Digital theodolite systems have the advantage of computer interface which facilitates computation of positions of points in space once calibration is set. If a temperature independent gauge bar is not available, a normal gauge bar may be placed outside the chamber for purposes of calibration with no loss of accuracy. An important advantage of the digital theodolite is that angles are "read" automatically and the values transferred to the computer, relieving the operator of reading a vernier, thus greatly decreasing his eye fatigue.

An interesting application of theodolites may be made when the angular measurements of interest are quite small. In such a case, a lens system may be mounted on the telescope of the theodolite to convert it to a remote "microscope". In this instance, care must be taken to affix fine enough marks or scratches on the test article.

The two draw backs of all DLOS applications are optical vacuum windows which are quite expensive, and training of operating personnel.

An application of theodolites to perform stereotriangulation mensuration of a test article is shown in figure two.

LASER INTERFEROMETRY

In contrast to DLOS instruments, laser interferometers are capable of measuring CHANGE IN OPTICAL PATH LENGTH, which is parallel to the optical path. Since the capability of counting interference fringes is the fundamental principal of detection, resolutions of fractions of optical wavelengths are possible. Typical resolutions of $\lambda/8$ are routinely achievable. This translates into about 8×10^{-8} M for a Helium-Neon laser, which is the most commonly used for applications of this type. Since change in optical path is simply twice the actual "distortion" along that path, real time readout of actual distortion values is possible. In most cases, dynamic

thermal distortions may be continuously monitored in real time, since interferometers may be rigged to count fringes equivalent to a distortion rate of several meters per minute.

Although it is not quite a "drawback", a complication of laser interferometry is that a separate beam must be used to detect change in path for each path of interest. If rotation is of interest, since it takes place in a plane, at least two beams are required for measurement about only one axis. Also, since change along the entire path is detected, if the beam must be "bent", the movement of the beam bending apparatus must be monitored by an additional beam and subtracted out in order to make the measurement of interest meaningful. Figure three shows a typical laser setup to measure the distortion of a rectangular parallelapiped. All beams may be brought in through the same window, (allowing measurement of "hidden" points), or through different windows. If a multichannel interferometer is used, all measurements may be simultaneously monitored in real time. The best way to take advantage of all data is to interface with a computer and reconstruct the motion of the test article as a whole from the path length changes detected by the interferometers.

The expense of the laser head or heads and the interferometers with their associated electronic counting equipment and computers are the only drawback to their wholesale application for distortion measurements. If the interferometers are designed properly, the vacuum windows may be of only average optical quality without affecting performance appreciably. The magnitudes of the distortions, however, must be kept quite small, < 1 cm to prevent the beams from being "lost" from the aperture of the retroreflectors. It would be impractical to attempt to mensurate a large number of points to "cover" a whole surface due to the amount of beams required along with the sophisticated monitoring equipment for each. These methods are best applicable therefore to structural assemblies such as trusses rather than to surfaces. Flexible members cannot be measured by laser interferometers since the retroflectors must be rigidly mounted.

CONCLUSION

Table one shows the various types of instruments and their respective applicability for various types of measurements, test articles, and test environments. In each case, the minimum number of instruments or laser beams necessary to make the measurement is stated. Greater redundancy can, in general, increase the accuracy of any particular measurement. This may be achieved by increasing the number of instruments, provided each is aligned along an additional line of sight or optical path. Additional cameras will also increase the photogrammetric accuracy with the same proviso.

METHOD & INSTRUMENTATION	REAL TIME	ENTIRE SURFACE	LENGTH ABSOLUTE	LENGTH RELATIVE	TRIANGLE ON OR APPOINTING 3 MEMBERS OR DIMENSIONS	4 LENGTH CHANGE FOR LARGE APPLICATIONS	5 DIMENSIONS	ROTATION 2 AXES	3 AXES	SMALL ARTICLES REQUIRING MICROSCOPE	LARGE DISTORTION CAPABILITY FOR CHANGE	FLEXIBLE	ARTICLE MUST BE TARGETED	STATIC	DYNAMIC	HIDDEN POINTS	WINDOWS REQUIRED	ARTICLE REMOVABLE FOR COARSE ALIGNMENT	RESOLUTION
PHOTOGRAMMETRY WITH AT LEAST 3 CAMERAS		X	X	X	X	X	X	X	X	X		X	X	X	X	X			1/100,000 OF LARGEST ARTICLE DIMENSION
1 AS TRANSIT SQUARE	X		X	X	X							X	X	X	X			X	X	5×10⁻⁵ M PER DIMENSION
2 AS TRANSIT SQUARES	X		X	X	X	X						X	X	X	X			V	X	5×10⁻⁵ M PER DIMENSION
3 AS TRANSIT SQUARES AND SPIRIT LEVEL	X		X	X	X	X	X					X	X	X	X			X	X	5×10⁻⁵ M PER DIMENSION
1 MANUAL THEODOLITE	X				X			IF ORIENTED PROPERLY		X	X	X	X	X				X	X	10⁻⁵ RAD PER MEASUREMENT
2 MANUAL THEODOLITES	X		X	X	X	X	X	X	ORIENTED PROPERLY	X	X	X	X	X				X	X	10⁻⁵ RAD PER MEASUREMENT
3 MANUAL THEODOLITES	X		X	X	X	X	X	X	X	ORIENTED PROPERLY	X	X	X	X	X			X	X	10⁻⁵ RAD PER MEASUREMENT
1 DIGITAL THEODOLITE	X				X			ORIENTED PROPERLY			X	X	X	X	X			X	X	10⁻⁵ RAD PER MEASUREMENT
2 DIGITAL THEODOLITES	X	POSSIBLY IF TARGETS WELL PLACED	X	X	X	X	X	X	ORIENTED PROPERLY		X	X	X	X	X			X	X	10⁻⁵ RAD PER MEASUREMENT
3 DIGITAL THEODOLITES	X	POSSIBLY IF TARGETS WELL PLACED	X	X	X	X	X	X	X	ORIENTED PROPERLY	X	X	X	X	X			X	X	10⁻⁵ RAD PER MEASUREMENT
1 BEAM	X				X										X	X	X	X	NECESSARY	1/0 PER PATH
2 BEAMS	X				X	X		X							X	X	X	X	NECESSARY	1/0 PER PATH
3 BEAMS	X				X	X	X	X	X	ORIENTED PROPERLY					X	X	X	X	NECESSARY	1/0 PER PATH
4 BEAMS	X				X	X	X	X	X	ORIENTED PROPERLY					X	X	X	X	NECESSARY	1/0 PER PATH

* FOR LARGER APPLICATION AT LEAST ONE EXTRA BEAM IS REQUIRED FOR EACH DEGREE OF EACH BEAM PLACED TO THE RETROREFLECTOR

TABLE I

APPLICABILITY CHARTS OF THE MEASUREMENT METHODS WITH THEIR RESPECTIVE INSTRUMENTATION CONFIGURATIONS FOR VARIOUS TEST SITUATIONS

ORIGINAL PAGE IS OF POOR QUALITY

ORIGINAL PAGE IS
OF POOR QUALITY

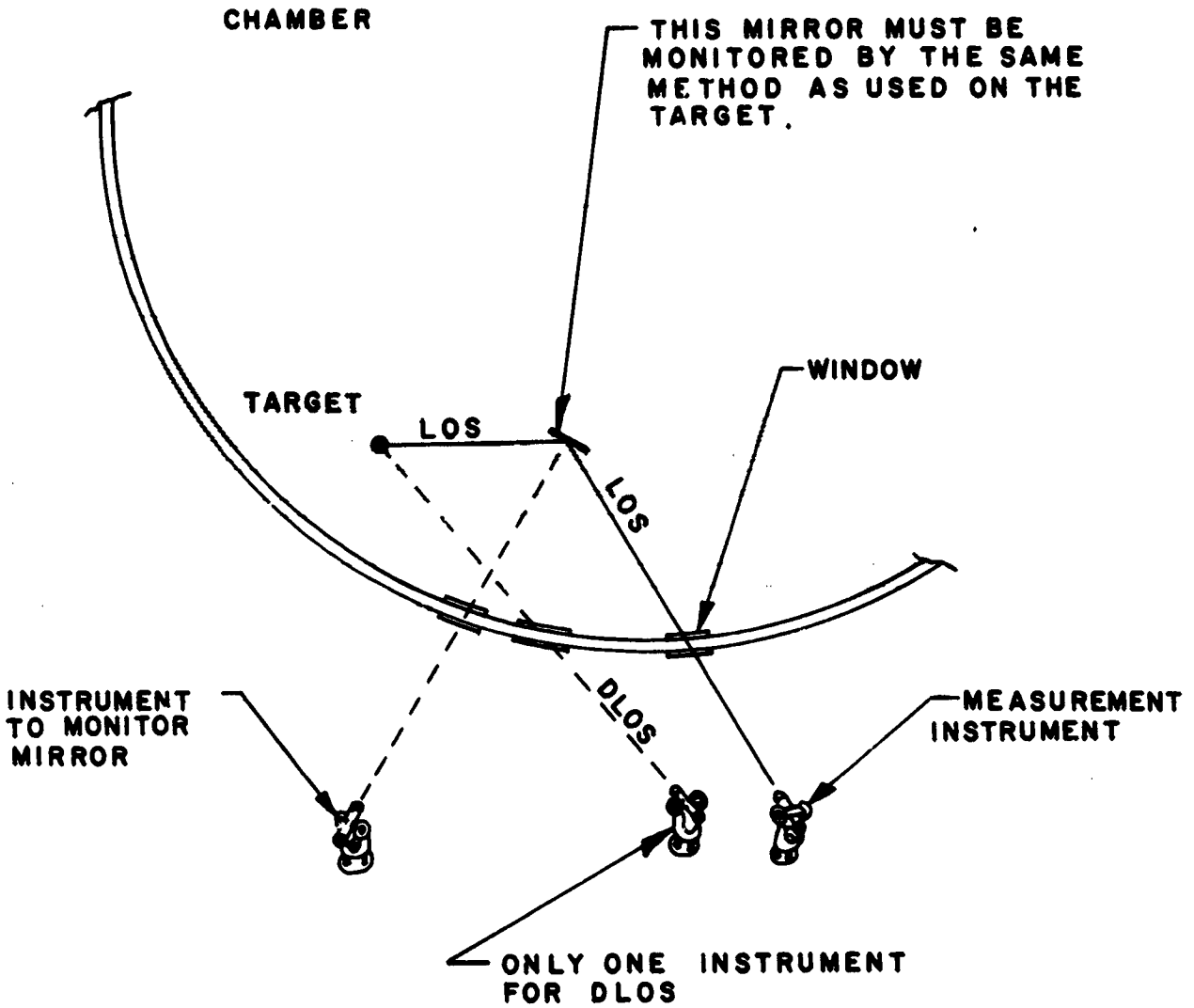

THE DLOS ELIMINATES EXTRA MONITORING, AND SHOULD BE USED UNLESS GEOMETRY PROHIBITS.

FIG. 1 DLOS CONCEPT

ORIGINAL PAGE IS
OF POOR QUALITY

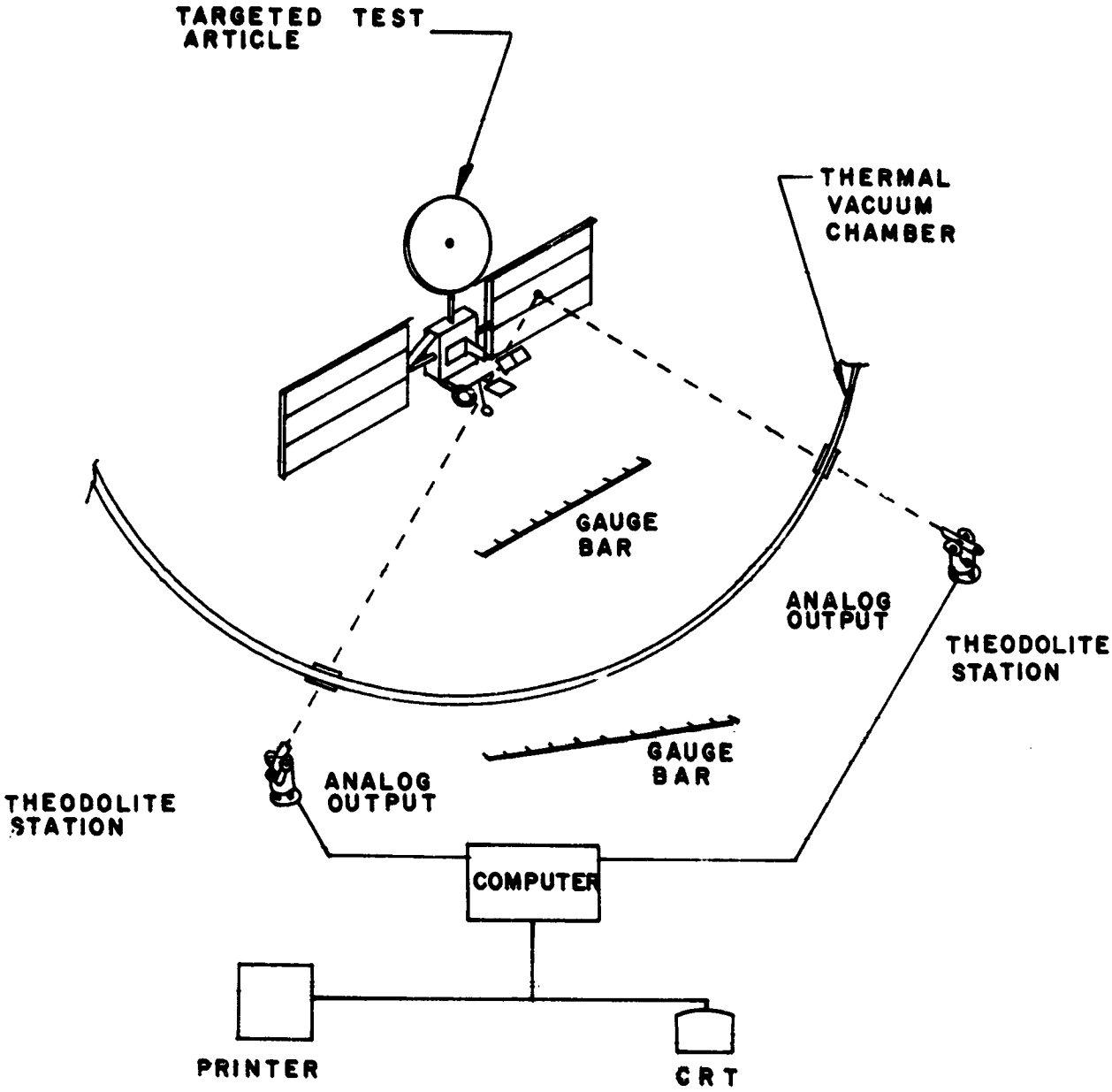

FIG. 2

TYPICAL STEREOTRIANGULATION SETUP WITH THEODOLITES. COMPUTER SHOWN FOR DIGITAL ELECTRONIC THEODOLITES. GAUGE BAR MAY BE PLACED EITHER INSIDE OR OUTSIDE OF CHAMBER.

ORIGINAL PAGE IS
OF POOR QUALITY

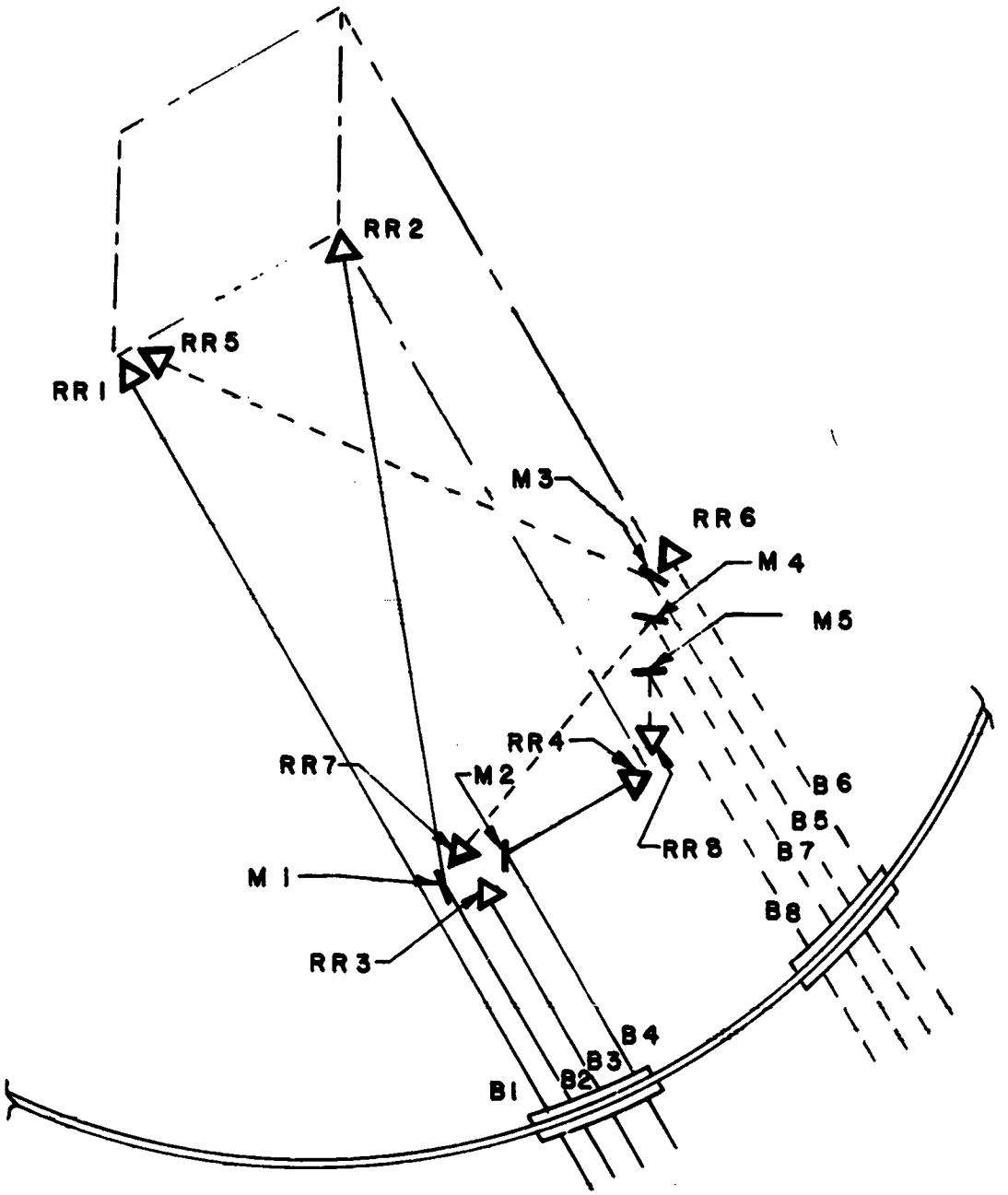

FIG. 3 TYPICAL SETUP FOR LASER INTERFEROMETRIC MENSURATION OF ONE FACE OF A RECTANGULAR PARALLELAPIPED. MINIMUM INSTRUMENTATION IS 4 SEPARATE INTERFEROMETER BEAMS, (B1-B4), 4 RETROREFLECTORS, (RR1-RR4) AND TWO MIRRORS (M1, M2). THIS SETUP MENSURATES MOTION IN THE PLANE OF THE FACE ONLY. FOR MOTION PERPENDICULAR TO THE FACE, ADDITIONAL BEAMS B5-B8 WITH THEIR RESPECTIVE MIRRORS AND RETROREFLECTORS ARE NEEDED. THESE BEAMS ALSO MENSURATE THE LOWER "END" FACE OF THE ARTICLE.

N82 25296

OPTICAL CHARACTERIZATION OF SOLAR CONCENTRATOR MIRRORS USING THE SOLAR BEAM OF THE JPL 25-FOOT SPACE SIMULATOR*

Maurice J. Argoud and Edwin W. Dennison
Jet Propulsion Laboratory
California Institute of Technology
Pasadena, California, 91109

ABSTRACT

The JPL 25-Foot Space Simulator with its 5.8-m (19-ft) diameter simulated solar beam provides an excellent facility for measuring the optical characteristics of parabolic solar concentrator panels and gores.

The virtual source position and size were determined by using a single lamp of the 37 xenon 30-kW source array with only the center lens in the 19-channel optical mixer. This data was used to define the optical test geometry, and it allowed accurate measurement of focal length and surface deviations of the mirror under test. A flux distribution of a typical solar concentrator placed directly on the solar beam gives measurements of performance at the focal point of the parabolic surface.

INTRODUCTION

The availability of the JPL 25-foot Space Simulator, with its 5.8-m simulated solar light beam, provides an excellent facility for measuring the optical characteristics of parabolic solar concentrator panels and gores.

The JPL 25-foot Space Simulator (Figure 1(a) and (b)) was constructed for the purpose of testing spacecraft in an environment which simulates launch and interplanetary space flight. The basic chamber is 7.61 m (25 ft) in diameter and 25.9 m (85 ft) high. Environmental parameters involve pressure, temperature, vibration, and solar illumination. The solar illumination system consists of thirty-seven 30-kW xenon arc lamps focused through a 19-element mixing lens onto a 7.01-m (276-in) diameter mirror that produces a beam of

*The research described in this paper was carried out by the Jet Propulsion Laboratory, California Institute of Technology for the U.S. Department of Energy through an agreement with the National Aeronautics and Space Administration.

light 5.8 m (19 ft) in diameter. For the solar panel tests, one arc lamp and the center transfer lens were used. The chamber was operated at normal room temperature. Figure 2 shows a panel mounted in the chamber. Figure 3 is a view of the same panel mounted in the chamber and an image at the focal plane.

MEASUREMENT PROCEDURE

JPL has been most fortunate to have the 25-foot Space Simulator available for evaluating solar concentrator panels. It is recognized that this facility's availability is limited. However, the techniques used in our analysis and the problems of illumination characterization, test geometry, and image measurement are common to all parabolic and refracting solar concentrators.

A key factor in developing cost-effective solar concentrators is the relationship between cost, as determined by design and manufacturing procedures, and performance requirements (e.g., receiver aperture size and flux distribution). To establish this relationship, it is essential that adequate techniques be found to evaluate the optical performance of concentrator optical elements. It is important to measure the optical characteristics in order to evaluate the panel and to predict the energy flux distribution of an assembled solar concentrator. This prediction can be verified by field measurements and used to evaluate the performance of a candidate thermal receiver.

Spherical optical elements such as the panels used on the JPL Test Bed Concentrators** can be evaluated directly by measuring the image formed from a point source of light and an image plane located at the center of curvature of the panel. Parabolic or refracting optical elements are most easily analyzed by the use of a collimated beam of light. Other complex illumination techniques have been considered but have not been found practical for measurement of solar concentrator panels.

The most basic characteristic of an optical element is the intensity distribution in an image formed from a point source of light (point spread function). The point spread function can be used with the concentrator focal length, the anticipated structural deflections, the specular reflectance, the solar image intensity distribution, and other factors to determine the predicted concentrator flux distribution. The point spread function must be measured to an accuracy which is consistent with the total concentrator requirements. For example, there is no value in measuring the point spread function to less than 1 mrad when the sun has a radius of 5 mrad.

Direct measurements of the solar image are possible, but they generally required large mobile structures and the availability of good sky conditions. Direct measurements can obscure design or manufacturing defects.

**Constructed by E-Systems Inc. and located at the JPL Parabolic Dish Test Site Edwards Air Force Base, California.

SIMULATOR OPTICAL BEAM CHARACTERIZATION

Under operating conditions, the optical beam was characterized in terms of a virtual source. The source distance was determined by using a 1.89-m (74.5-in) x 0.80-m (31.5-in) rectangular frame with 1.6-mm (1/16 in) diameter holes. The frame was first placed on the floor and the hole centers marked on a large piece of paper. Next, the frame was raised to approximately 3.1 m (122 in) above the floor and then leveled and oriented with two plumb bobs as shown in Figure 4. The centers of holes as projected on the floor by the illuminating beam were then marked. The distance from the virtual source above the floor is given by

$$D = \frac{H}{1-M_1/M_2} \tag{1}$$

where D is the vertical height of the virtual source,

H is the upper position height of the frame,
M_1 is the frame hole separation, and
M_2 is the projected hole separation.

The position on the chamber floor of the vertical projection of the virtual source was determined from the intersection of the lines drawn through the corresponding upper and lower hole marks. The angular size of the virtual source was measured with a lens having a 1.52-m (60-in) focal length. The final results gave a virtual source size of 0.9 mrad at a distance of 410 m (1345 ft) above the chamber floor centered over a point 58 cm (23 in) east and 25 cm (10 in) north of the chamber center. The practical results of this characterization are that the source can be assumed to be a point source for slope errors greater than 1 mrad. The finite virtual source distance above the chamber floor requires a small modification of the test geometry.

GEOMETRIC LAYOUT

Testing parabolic mirrors in the 25-foot Space Simulator is a cumbersome problem because an assembled parabolic solar concentrator panel has three degrees of freedom for positioning with respect to the image measurement (focal) plane. Typically these are the axial distance of one panel edge to the focal plane and the inner and outer radial distance from the optical axis. Unless these degrees of freedom are reduced, the point spread function must be determined as a function of three independent parameters.

The procedure can be accomplished efficiently if the panel designer has established and specified the focal length and the relationship between the mounting datum points and the reflecting surface. In addition, the panel must have the design radial distance to the inner edge. These data are the minimum required for accurate panel characterization; the lack of these data will generally result in large uncertainties in the measurements and data interpretation.

The first step in inplementing the panel test geometry is to establish a reference plane which contains the optical axis, the virtual source (on the optical axis), and the centerline of the panel under test. For our tests, we used a plumb line and a theodolite which were adjusted to be co-planer with the virtual source. This reference plane is shown in Figure 5. Dimensions D, H_1, CH, V_2, V_0, V_1, and V_2 are measured. H_1 is calculated, and the panel positioned as indicated. V_0 and V_1 may be adjusted for image alignment. The remaining dimensions are calculated.

The image intensity distribution should be measured in the design focal plane. Measurements may also be made in two other focal planes; that which has the smallest image and that which has its image closest to the optical axis. For images with centroids not in the optical axis, the predicted concentrator flux distribution must be based on both the point spread function and the radial distance of the image centroid from the optical axis.

For adjustable panels, one degree of freedom can be removed by measuring the chord distance between the inner and outer panel center points. The second degree of freedom can be removed by locating the inner edge center point at the specified radial distance from the optical axis. This leaves the difference between the inner and outer edge center points in the axial direction ($Z_0 - Z_1$) and the focal length as dependent parameters. The panel should be rotated around the inner/outer edge centerline to locate the image on the optical axis. If the outer edge of the panel is adjusted as specified and the image is on the optical axis at the design focal plane, the image intensity distribution can be measured in this plane and the point spread function determined. If the image is not at the optical axis intersection of the focal plane, then either the focal plane or the outer panel edge can be adjusted. A further possibility is to adjust the focal plane and the outer edge of the panel to give the best image.

For all of these adjustments, the inner edge of the panel must remain at the design point, and the panel must be rotated to pace the image on the optical axis. The best configuration can be selected on the basis of the receiver aperture plane adjustment range, and the concentrator flux distribution requirements. In all cases, the test results will give a focal distance, the panel mounting requirements, and the point spread function.

MEASUREMENT PROCEDURES

Four different image measurement techniques have been used to quantitatively interpret the images. The first three techniques are used to derive numerical data for quantitatively representing the point spread function. A fourth technique is a powerful diagnostic tool for determining the characteristics and source of surface irregularities. For all image measurements, the image is measured in a plane which is orthogonal to the optical axis.

Using the first technique, a white screen is placed in the focal plane, and the image is photographed with a sheet film camera. Part of the film is left unexposed to permit a sensitometric calibration. The film is scanned in the JPL imaging processing laboratory, and the intensity distribution of the image is determined. An image center is selected, and the total intensity within a series of circular zones is computed. This technique has the advantage of giving extremely high spacial resolution, but it is subject to the photometric limitations of the photographic process.

With the second technique, the intensity distribution data are obtained by using a silicon diode which is mechanically scanned over the image (Figure 6). These data are then numerically integrated to give the total intensity within circular zones. This technique gives accurate intensity data, but it is limited in spacial resolution.

The third approach uses a lens located near the focal plane to form an image of the aperture panel under test onto a white screen in an enclosure. A photocell measures the total light in the panel aperture image. A series of successively larger aperture or circular masks is placed over the image and the total intensity within a circular zone is measured directly. This technique gives accurate intensity information but no data about the form of the image. This approach has been used very successfully for characterizing the test bed concentrator (TBC) spherical facets, but has not as yet been used in the space simulator. This approach may prove to be very effective in controlling the quality of large volume manufacturing of solar concentrator panels.

To diagnose solar panels imperfections, the image of the panel aperture is formed by a lens near a focal plane onto a screen and is photographed (Figures 7 and 8). The image can be covered by circular apertures, disks, or annular slots. The photographs show the amount of image error resulting from each area of the panel. For example, if a disk of 2-mrad diameter is placed in the image plane over the image center, the photograph will show which parts of the panel have errors greater than plus or minus 1 mrad. Most of the panels which have been analyzed to date indicate that the image errors are the result of large-scale irregularities in the panel generating tools.

Figure 9 shows typical photographs made with this technique. These photographs are for three different panels. The top row of photographs are the focal plane images, and the remaining photographs are the aperture images. The first is with no focal plane aperture and the remaining aperture images are made with successively larger annular slots centered on the focal plane image. The bottom row of photographs were made with a panel which has a separation between the reflecting glass surface and the cellular glass substrate. Figure 10 shows typical results on a reflector panel using various apertures at the focal plane.

DATA ANALYSIS

The objective of the data analysis program is to apply an alogrithm which will give a mathematical representation of the measured data. The parameters of this representation should give both a direct measure of the image quality and provide a basis for predicting the flux distribution of the concentrator. For our initial approach to this problem, we have chosen to represent the data by an intercept factor curve. This curve gives the fraction of the total energy included within a circular aperture.

The equation which gives a satisfactory representation of the intercept factor curves is of the form

$$\Phi = 1 - (1-A) \quad \mathrm{EXP}\left[\frac{-r^2}{2\sigma_0^2}\right] - A \quad \mathrm{EXP}\left[\frac{-r^2}{2\sigma_I^2}\right]$$

where Φ is the intercept factor,

r is the aperture receiver radius,

σ_0 is the outer standard elevation,

σ_I is the inner standard deviation, and

A is the amplitude of the inner component.

This equation assumes the image intensity distribution is represented by the sum of two Gaussian distributions. The procedure for determining the parameters, σ_0, σ_I, and A is based on first fitting the outer points to a Gaussian curve and second fitting a second Gaussian curve to the difference between the inner measured points and the calculated values of the outer curve. For comparison, a single Gaussian curve was also used to fit the measured data. In all cases, the parameters were determined using linear regression analysis.

Table 1 shows the derived parameters for a single and double Gaussian fit of the data taken with both silvered glass on cellular glass and reflecting film on molded plastic panels. Figure 11 shows the plots of these data.

The purpose of this data analysis procedure, as stated above, was to find a convenient mathematical representation of the data. The execellent fit of the data to the double Gaussian curve suggests that most of the panel errors may arise from two distinct souces and that these errors are random in character. The sources of these errors have not been determined. These data have been used to estimate the performance of concentrators using these panels.

TABLE 1. CURVE FIT DERIVED PARAMETERS

Reflector Type	Gaussian Fit			
	Single	Double		
	σ	σ_0	σ_1	A
Glass	1.7 cm (0.67 in)	1.9 cm (0.75 in)	0.86 cm (0.34 in)	0.49
Plastic	6.6 cm (2.60 in)	8.6 cm (3.40 in)	3.38 (1.33)	0.77

CONCLUSION

Optical testing of parabolic reflecting panels is a key part of developing cost-effective solar concentrators and the JPL 25-foot Space Simulator is an excellent facility for this task. The illuminating beam was characterized in terms of virtual source distance, angular size, and vertical projection point on the chamber floor, and the illuminating beam does not have a significant effect on slope error measurement greater than 1 mrad. A procedure for positioning the panel and focal measurement plane was developed and used for image measurement. The data were reduced to a table of total intensity and measured intercept factor as a function of radial distance from the image center. Fitting these data to a Gaussian curve by means of a least-squares linear regression appears to be satisfactory. This mathematical representation was used to calculate the expected performance of a parabolic dish concentrator.

The test facility is also ideal for testing large concentrator panels because it provides a high quality collimated beam of light for measuring the optical characteristics of parabolic solar concentrator panels and gores.

ORIGINAL PAGE
BLACK AND WHITE PHOTOGRAPH

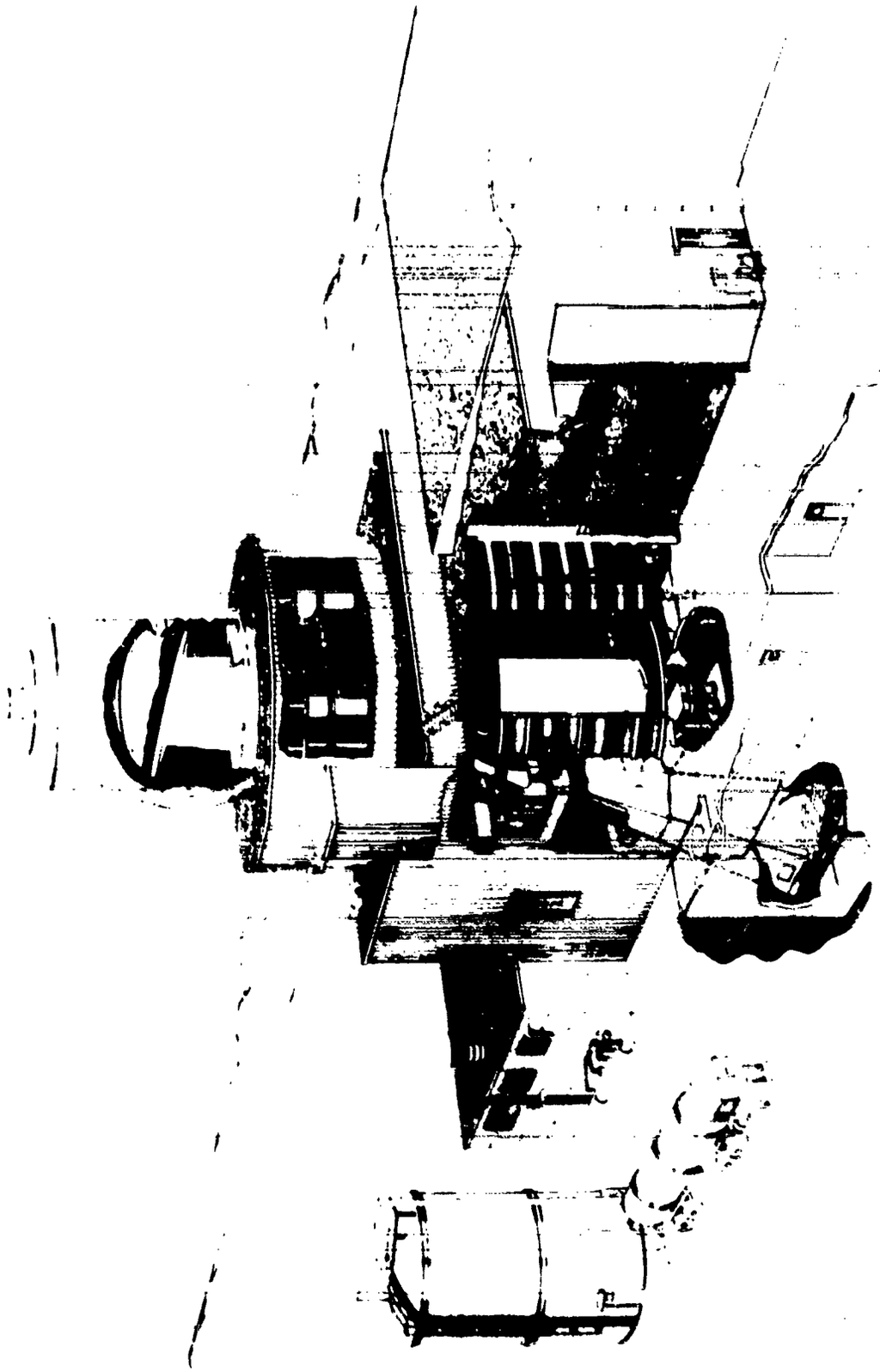

Figure 1(a). 25-foot Space Simulator Facility

ORIGINAL PAGE IS
OF POOR QUALITY

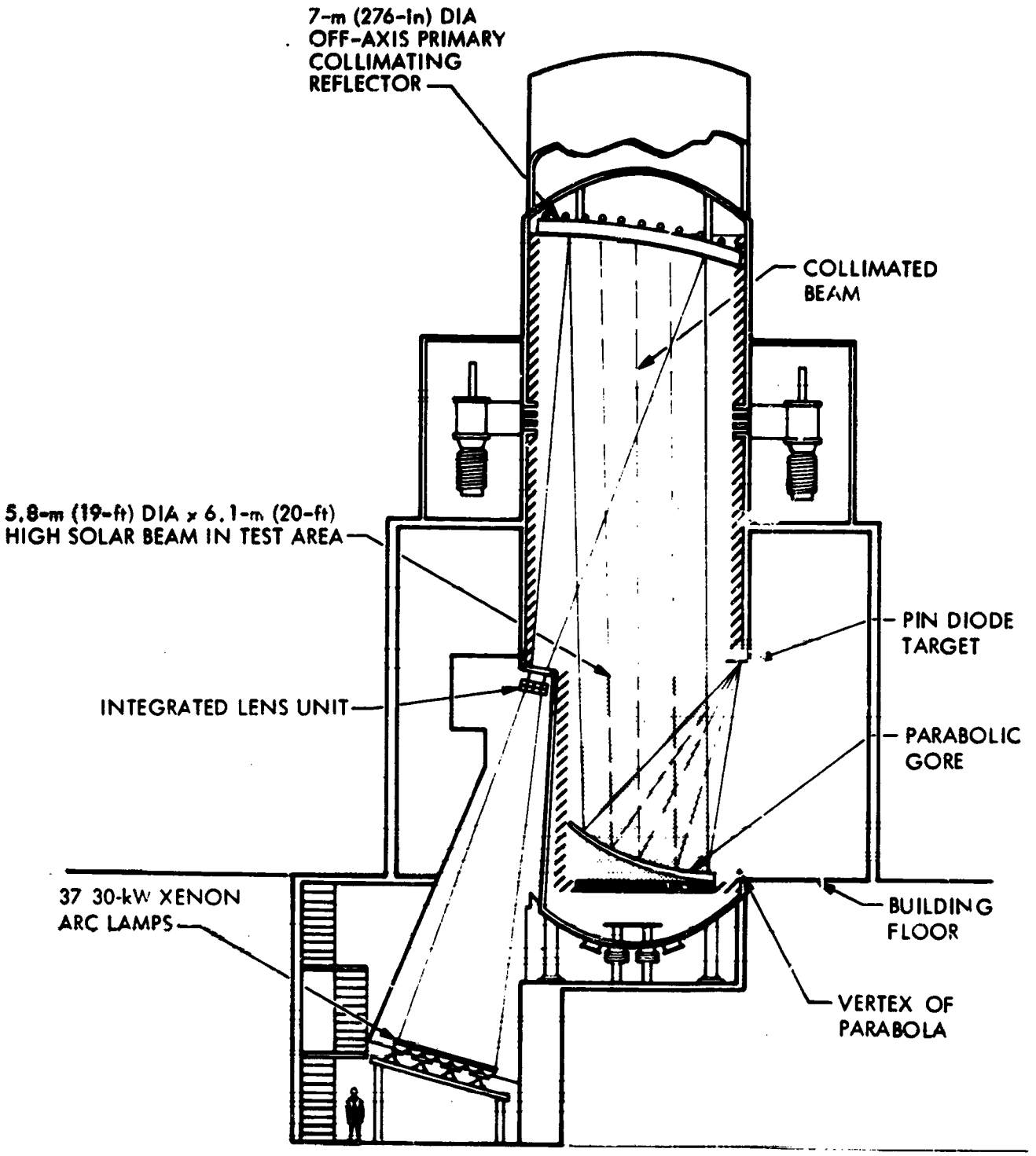

Figure 1(b). Cutaway View of Simulator Facility Showing Parabolic Mirror

ORIGINAL PAGE
BLACK AND WHITE PHOTOGRAPH

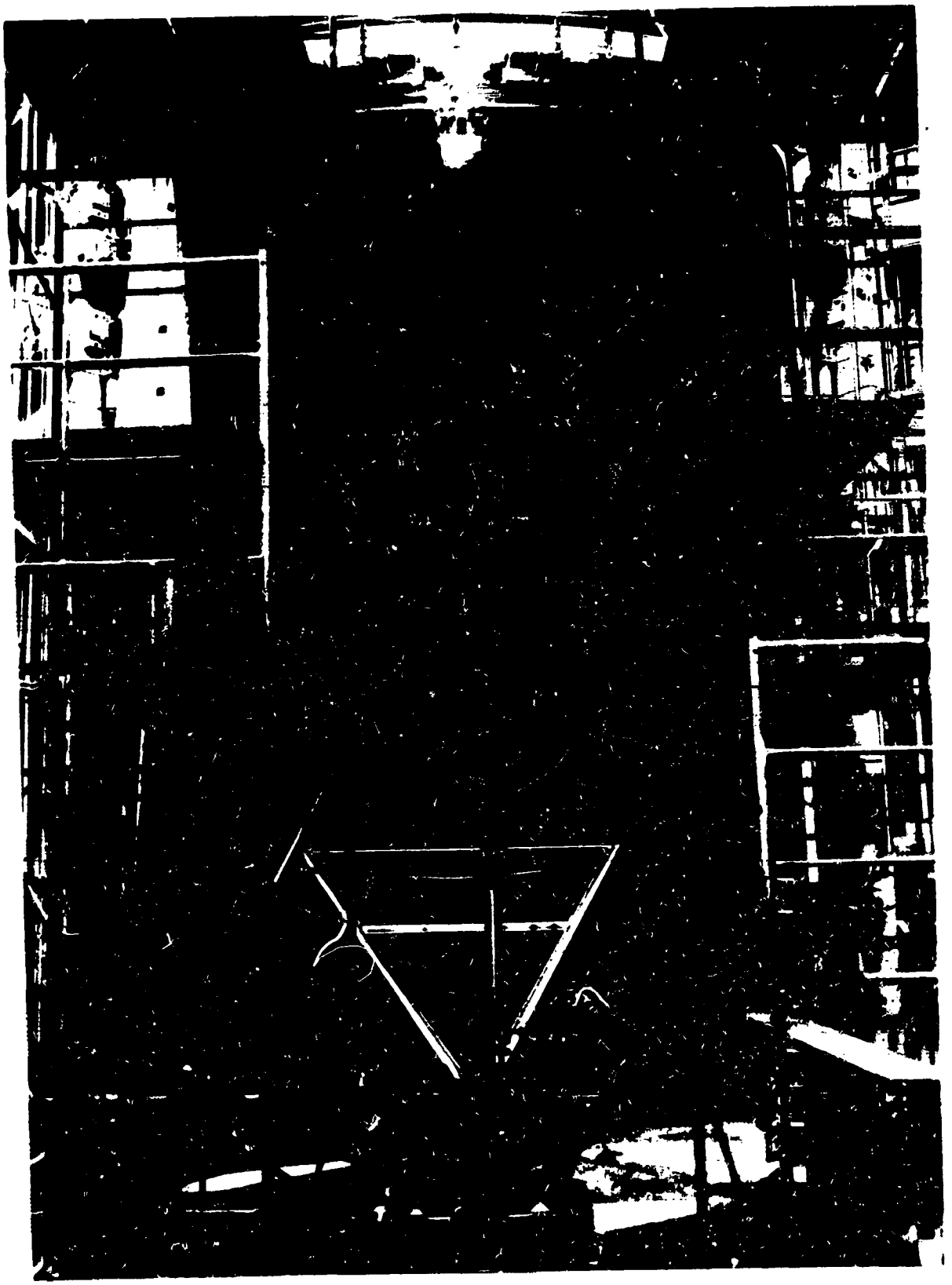

Figure 2. Simulator with a "Fiberglass Balsa Sandwich" Concentrator Panel

ORIGINAL PAGE IS
OF POOR QUALITY

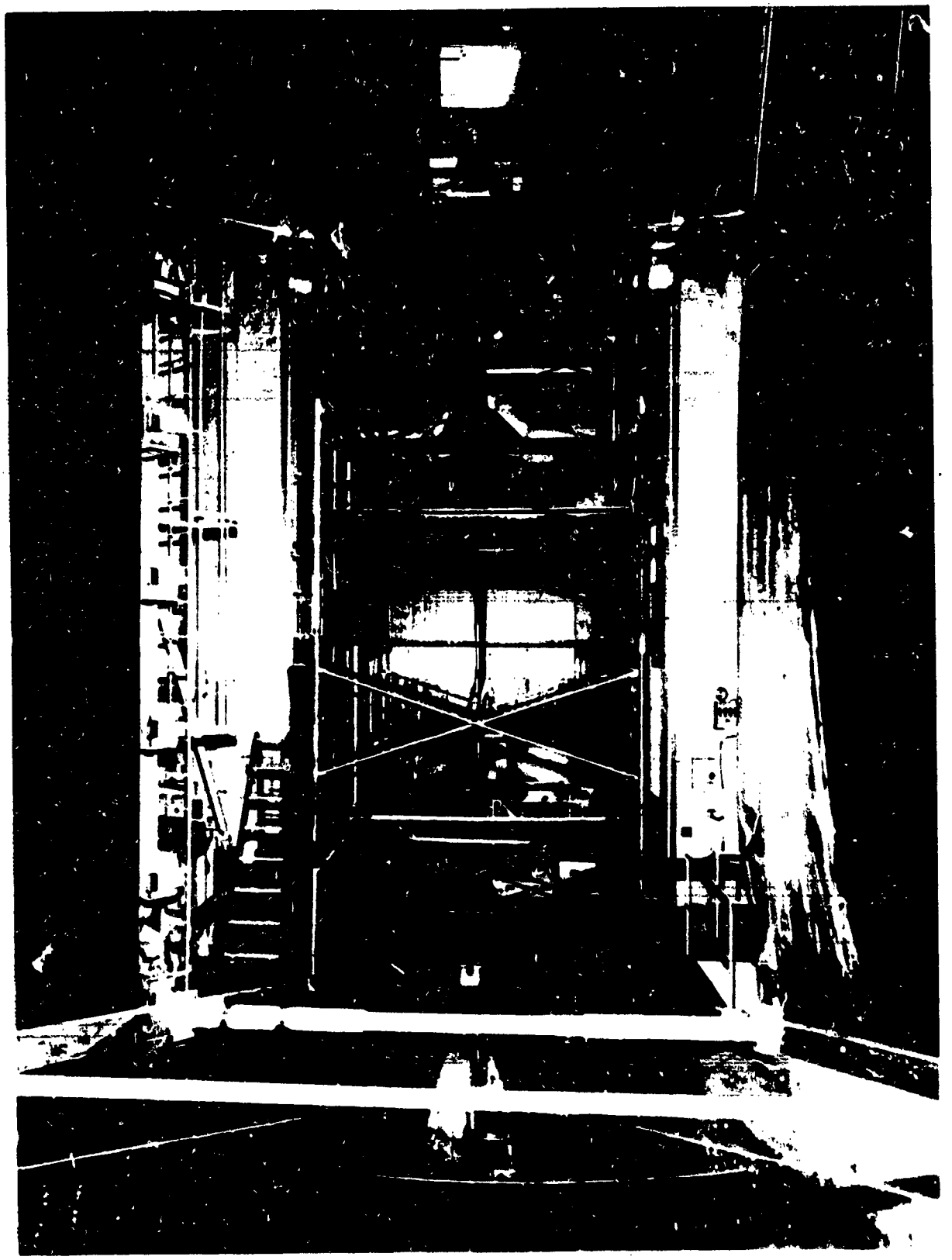

Figure 3. View of Panel Mounted in the Chamber (Bottom) and on Image at the Focal Plane (Top)

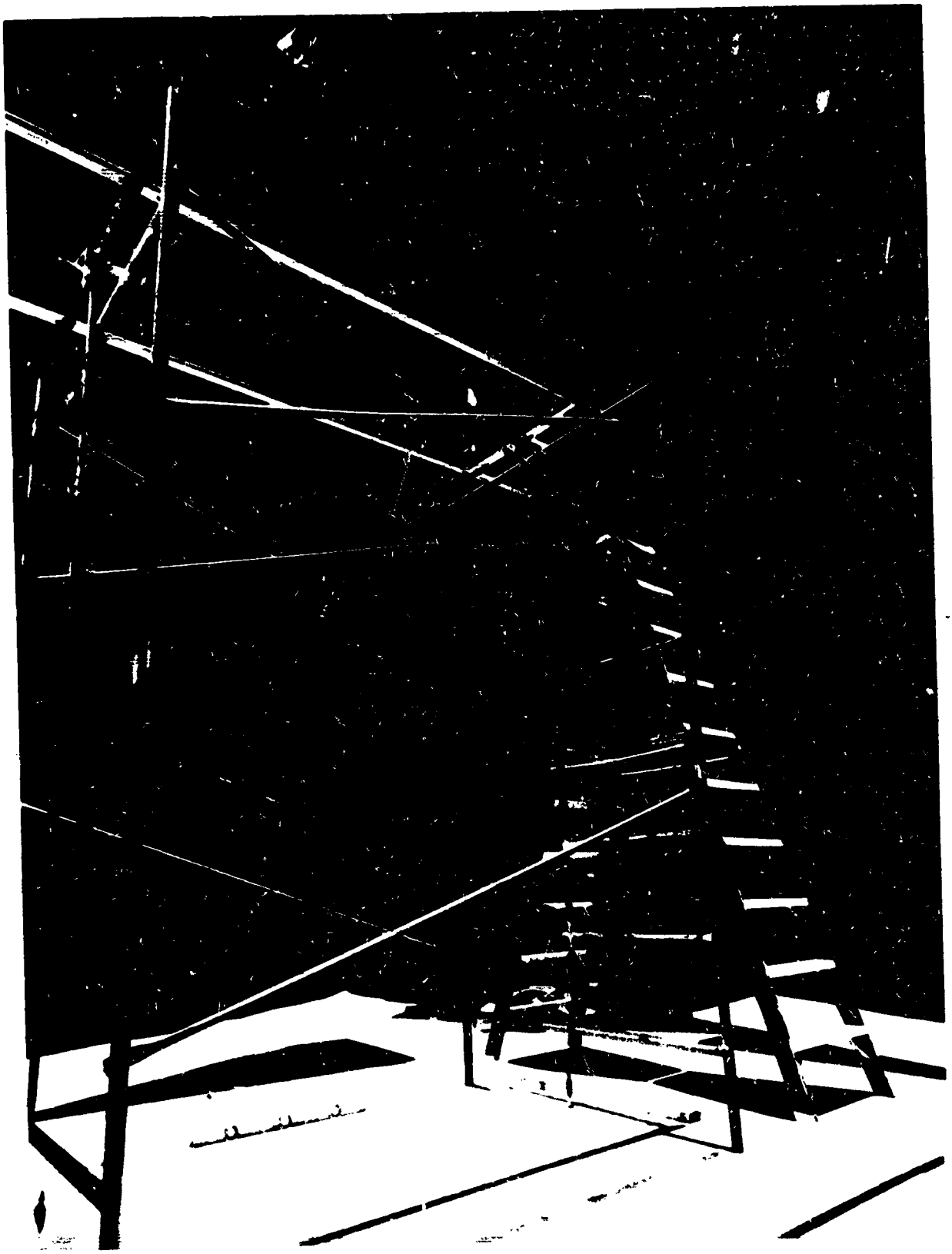

Figure 4. Test Configuration Beam Characterization (Frame in Upper Position)

ORIGINAL PAGE IS
OF POOR QUALITY

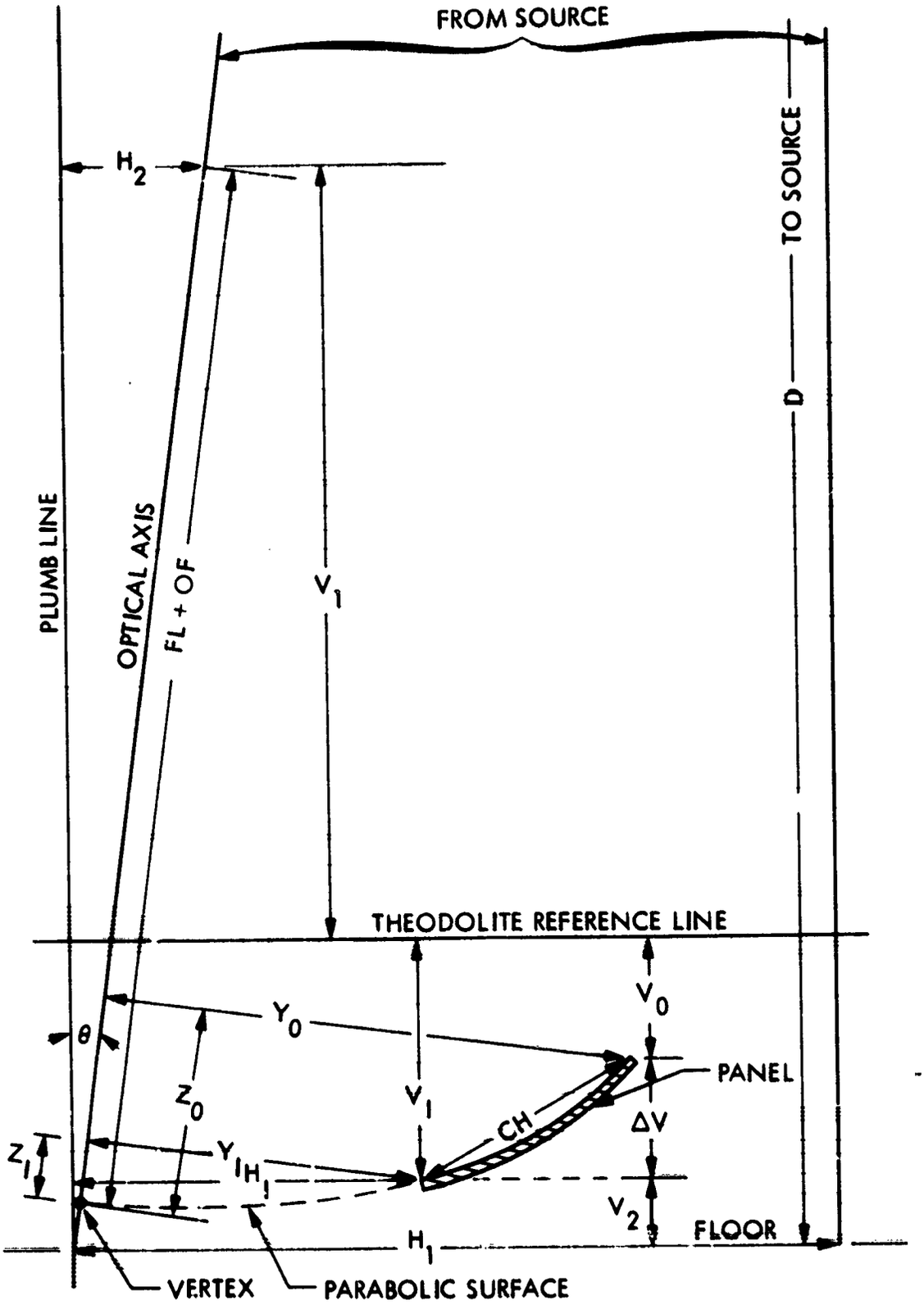

Figure 5. 25-foot Space Simulator Geometric Layout

ORIGINAL PAGE
BLACK AND WHITE PHOTOGRAPH

Figure 6. Scanning Intensity Distribution of Image in a Target With a Silicon Diode

ORIGINAL PAGE
BLACK AND WHITE PHOTOGRAPH

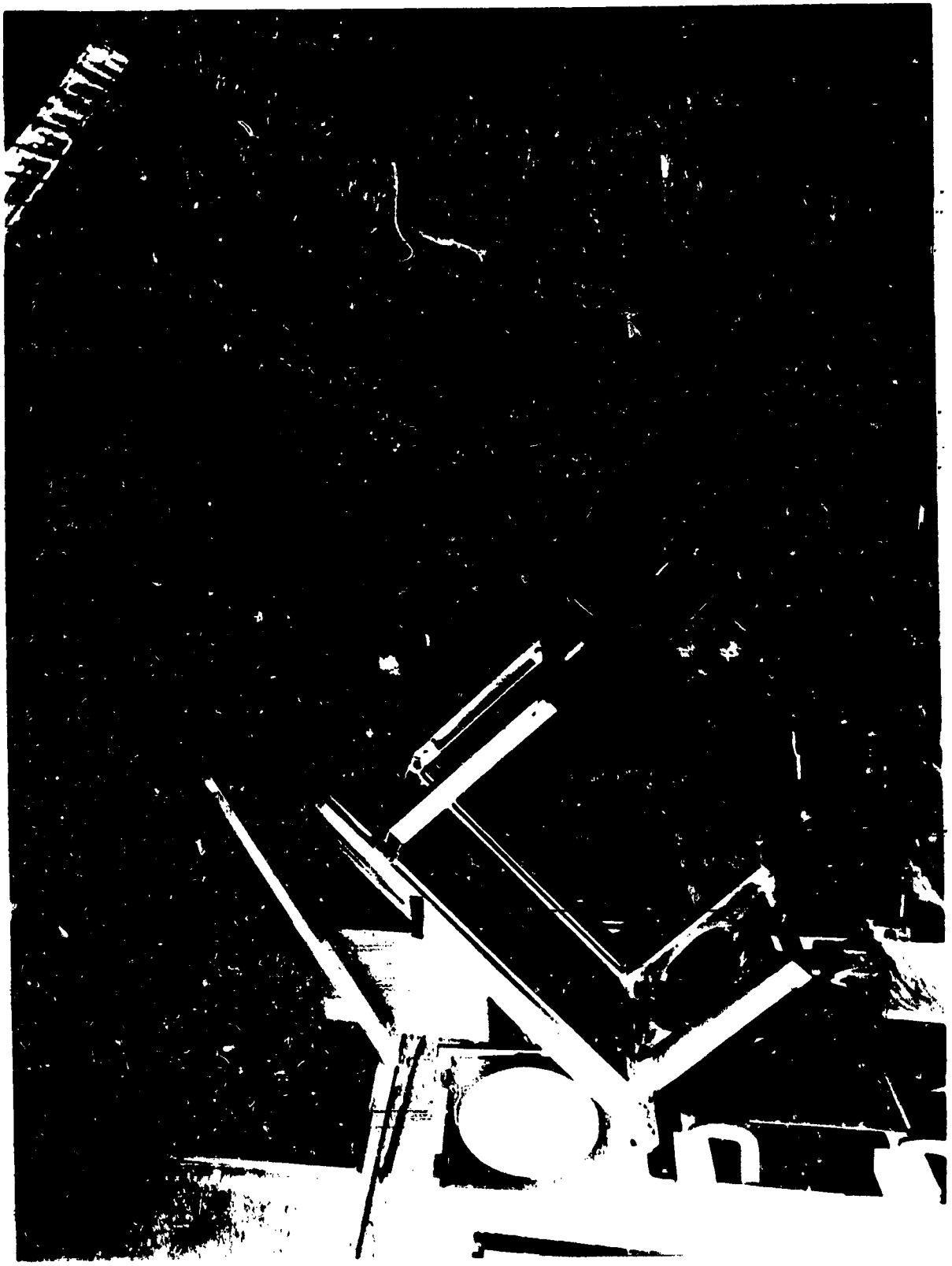

Figure 7. Panel Error Diagnostic Configuration with Annulus at Focal Plane

ORIGINAL PAGE
BLACK AND WHITE PHOTOGRAPH

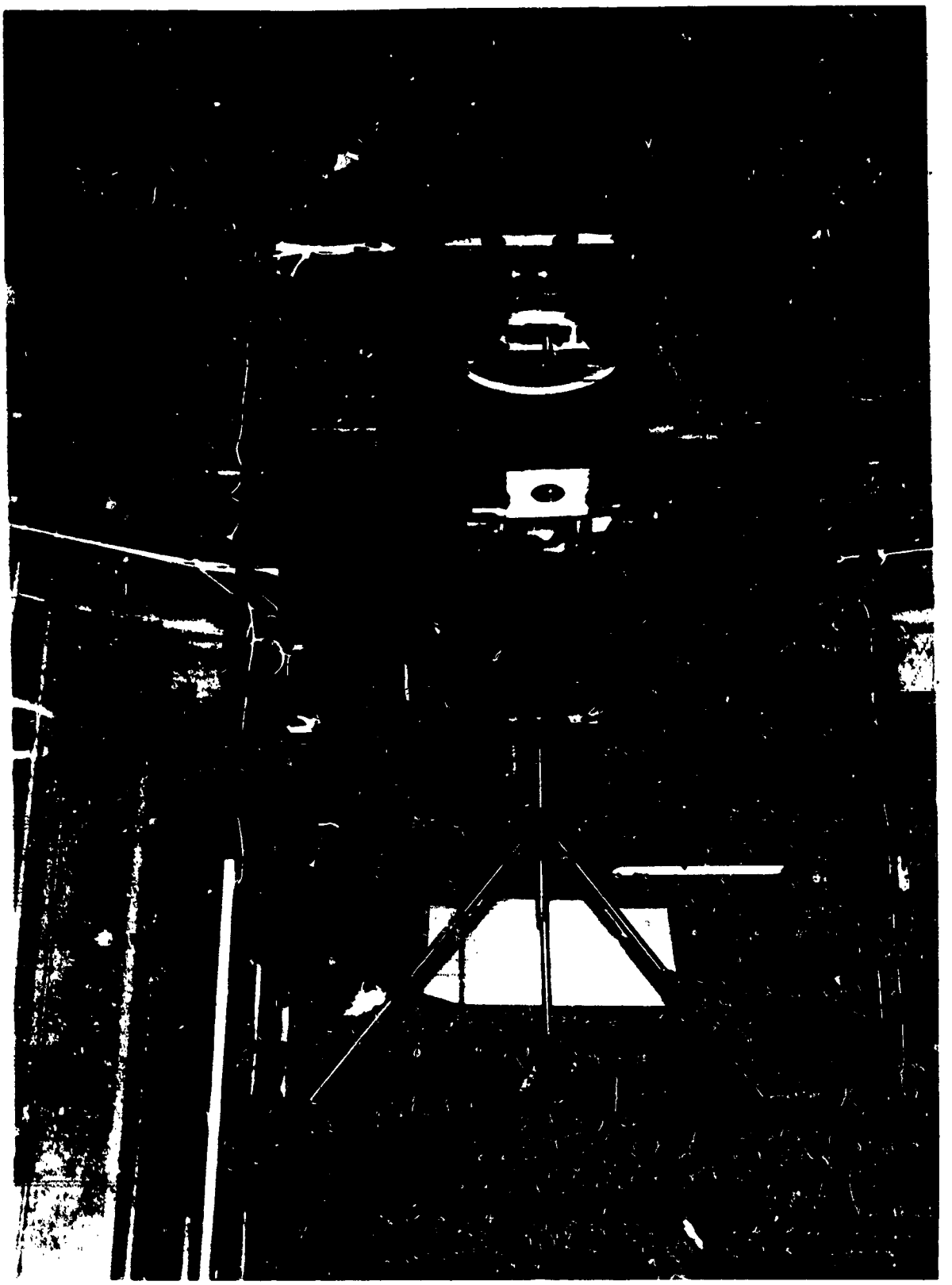

Figure 8. Panel Error Diagnostic Configuration with Focal Plane Aperture

ORIGINAL PAGE
BLACK AND WHITE PHOTOGRAPH

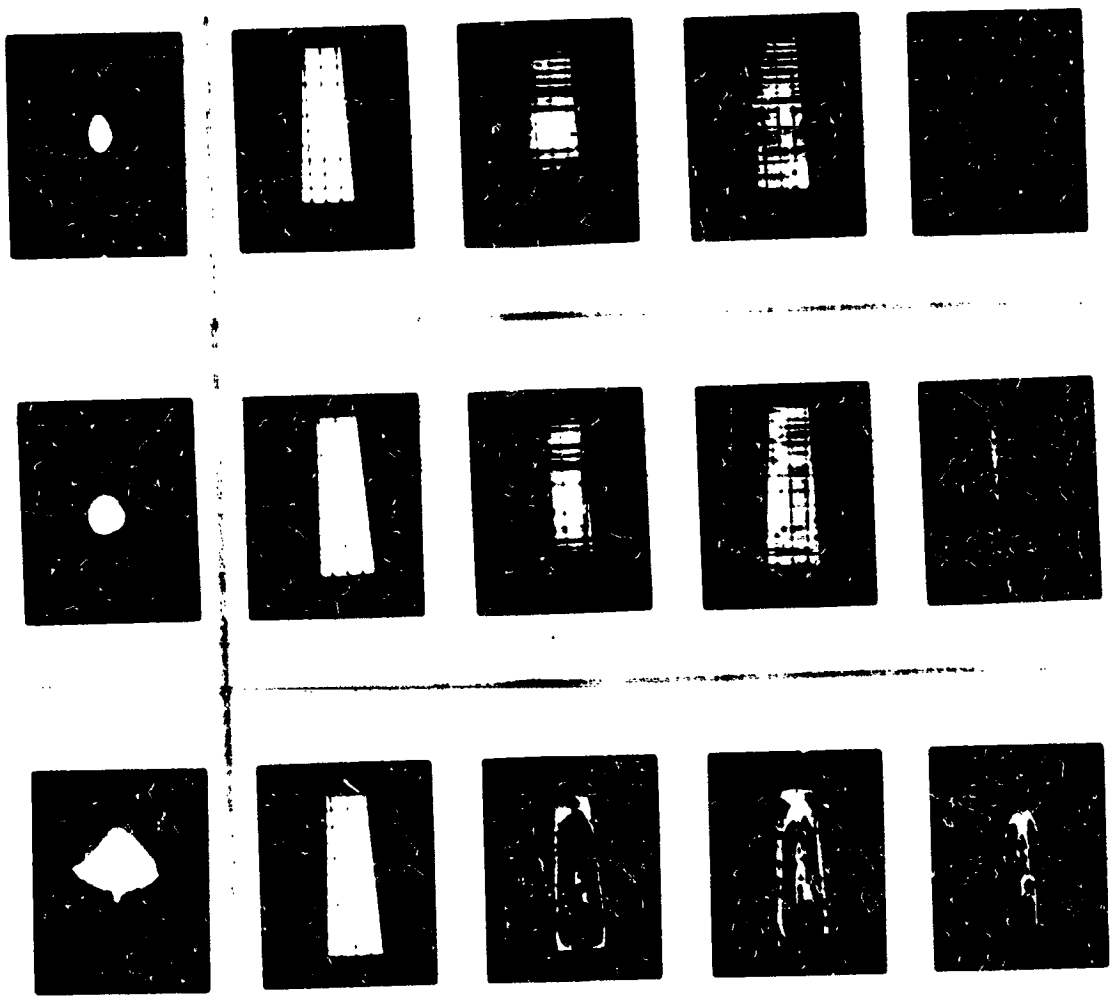

Figure 9. Typical Panel Error Diagnostic Photographs Using Annulus for Apertures

ORIGINAL PAGE
BLACK AND WHITE PHOTOGRAPH

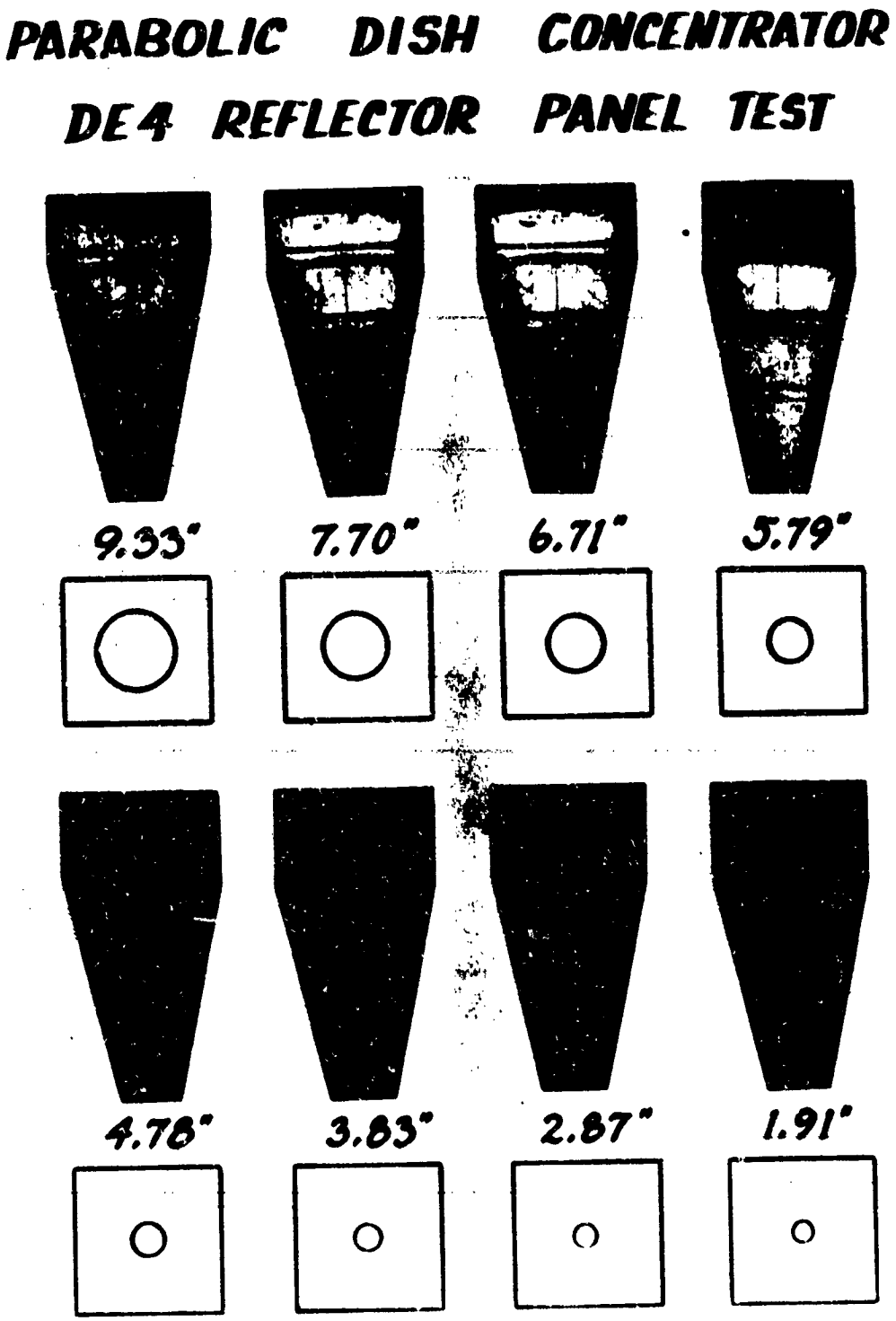

Figure 10. Typical Panel Error Diagnostic Photographs Using Apertures Only

ORIGINAL PAGE IS
OF POOR QUALITY

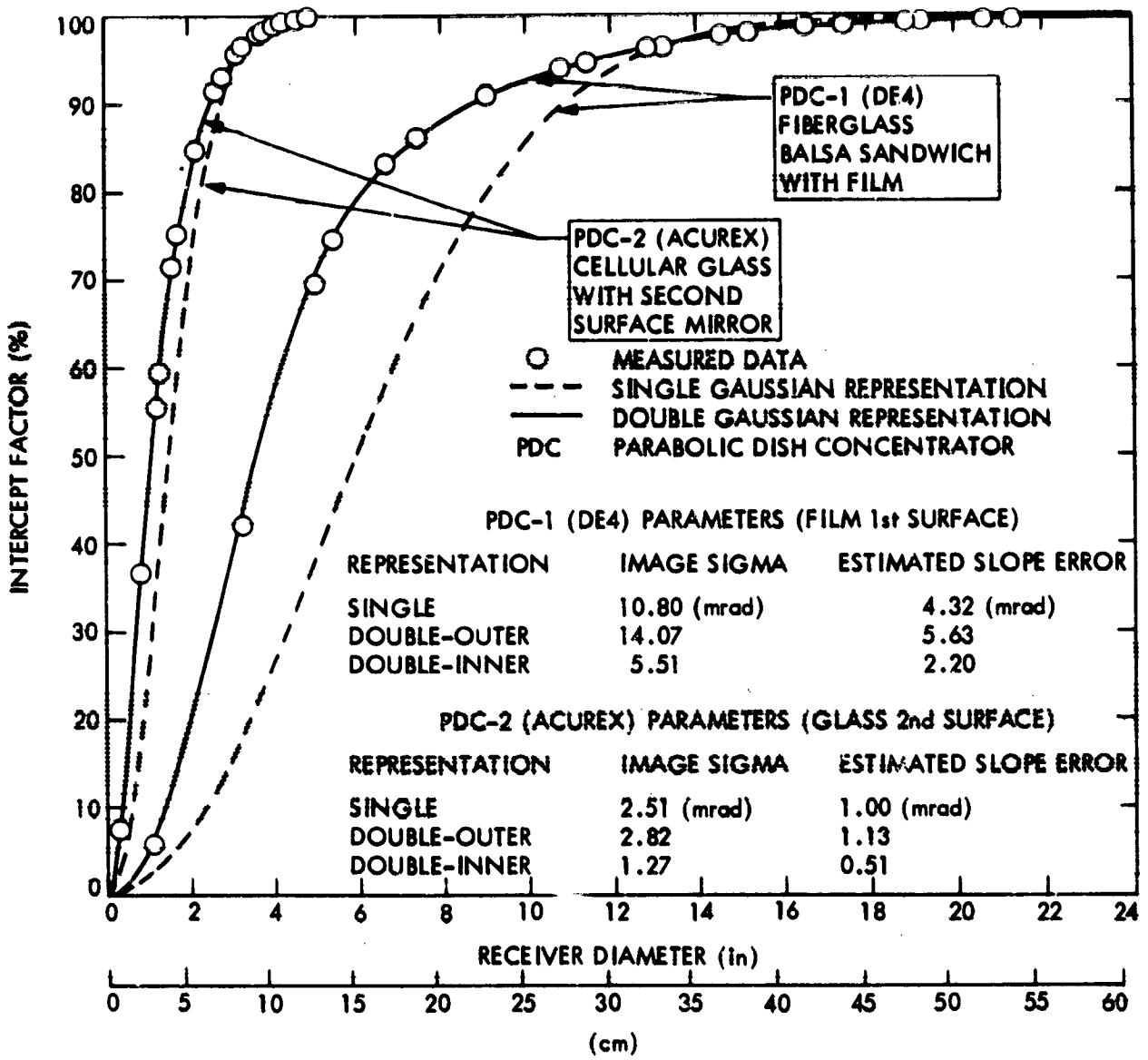

Figure 11. Measured and Calculated Intercept Factor Data

PRECEDING PAGE BLANK NOT FILMED

SIMPLIFIED MLI PUMPDOWN CALCULATION APPROACH

R. G. Bettini

The Perkin-Elmer Corporation
Danbury, Connecticut 06810

ABSTRACT

During launch, or simulated launch, of space vehicles such as NASA's Space Telescope, pressure within Multilayer Blanket (MLI) must decay from atmospheric to minimum effective operational (10^{-5} torr) levels rapidly, to prevent excessive cooling of insulated hardware during venting time. This evacuation rate is a function of ambient pressure decay rate, number of shields, enclosed volume, venting area, initial temperature, trapped gas, and outgassing rate. A simplified computer simulation that estimates blanket internal pressure during an isentropic evacuation as a function of the above variables is presented. Analytical predictions are compared to test data from various sources to confirm the reasonableness of this approach.

PRECEDING PAGE BLANK NOT FILMED

SESSION IV

SPACE SIMULATION TEST TECHNOLOGY

Session Organizers: Albert R. Lunde, Boeing Aerospace

S. Liu, TRW Space Systems

NUCLEAR HARDENING TESTING OF LARGE SCALE SATELLITES

John Sargent, Neil K. Shirk, and Tom Wilks

General Electric Company
Philadelphia, Pennsylvania 19101

ABSTRACT

The DSCS III Satellite is a third generation satellite designed to provide communications for the Department of Defense. It is a synchronous three axis stabilized satellite containing six wide band SHF communications channels and a single channel transponder which communicates with all UHF equipped force elements (planes, ships, etc.). It has a design life of 10 years. This paper will describe the approaches and instrumentation necessary to test the DSCS III Satellite named "STARSAT" for the purpose of evaluating the effects on Nuclear radiation on various subsystems. It was integrated into the "HURON KING" underground Nuclear Test sponsored by the Department of Defense.

The experiment configuration was composed of a nuclear device buried 1000 feet underground, a vertical line of sight (VLOS) pipe to the surface, a scatterer, and a vacuum tank which held the satellite. The 250 ton steel tank provided a vacuum of 2×10^{-4} torr.

The satellite was monitored at the time of the detonation by 440 oscilloscopes, 92 direct record and 248 FM tape channels.

Instrumentation of the satellite for the purpose of monitoring effects during the Nuclear Event included Pin voltages, core currents, pin currents, shield currents, B Dot Sensors, I Dot Sensors, etc.

PRECEDING PAGE BLANK NOT FILMED

N82 25297

CRYOPUMP FOR LARGE PULSES OF HYDROGEN*

B. C. Moore, R. G. Camarillo, and J. T. Morrow
McDonnell Douglas Astronautics Company

INTRODUCTION

A test involving a flow of hot hydrazine decomposition products at a rate of 13.6 g/s (0.03 lb/s) established the requirement to maintain pressure in the McDonnell Douglas Astronautics Company (MDAC) 11.9-m-(39 ft) diameter space chamber below 200 μm. The flow, 2/3 hydrogen and 1/3 nitrogen by volume, continued for several periods ranging from 3 to 15 min. The pressure requirement was necessary to minimize thermal effects of the gas on the test vehicle but was well beyond the capability of the existing facility pumps. Various methods of obtaining additional temporary pump capacity were considered (see Table I). From these, the slugged-charcoal approach was selected as the quickest and least expensive method to implement.

CRYOPUMP — PRELIMINARY DESIGN

GENERAL CONCEPT

The operational concept of the cryopump is based on heat transfer from the gas exhaust to a bed of charcoal mixed with lead wool. The hot gas exhaust is partially cooled by LN_2 surfaces to some unknown temperature. The gas falls on the 20 K charcoal and is sorbed, giving up both thermal energy and the heat of adsorption.

Because this heat warms the charcoal, a mass of lead wool is needed to limit the rise in temperature. The hydrogen gas itself carries the heat from the charcoal to the lead.

CHARCOAL QUANTITY REQUIRED

The volume of hydrogen sorbed by charcoal before the equilibrium pressure reaches 200 μm varies sharply with the charcoal temperature (References 1 and 2), as shown in Figure 1. Also shown is a design point; 453 kg (1000 lb) of charcoal would sorb the hydrogen in a 5-min run, assuming 12.5 cm^3 hydrogen [standard temperature and pressure (STP)] per gram of charcoal and provided the temperature remains under 65 K. (This calculation is idealized; it assumes the charcoal has the same temperature throughout the bed and ignores the nitrogen component of the gas.)

*Part of this work was funded by the US Army, Ballistic Missile Defense System Command, Huntsville.

MASS OF LEAD REQUIRED

The energy required to raise the temperature of lead from 20 K, the temperature of the facility cryopump, to 50 K, which is well within the maximum allowable temperature, is 2.53 J/g. (To raise the temperature to 60 K requires 3.58 J/g.) (Reference 3.)

The heat of adsorption of hydrogen on charcoal varies with the quantity previously adsorbed. At 20 cm^3 STP, the heat of adsorption is estimated at 2000 cal/mol, while at 200 cm^3 STP it drops to 1000 cal/mol (Reference 1). It continues to drop toward the heat of liquefaction (271 cal/mol) with increasing amounts. The 5-min hydrazine run would generate, initially:

$$0.85 \frac{\text{mol}}{\text{s}} \times 300 \text{ s} \times \frac{2000 \text{ cal}}{\text{mol}} \times 4.19 \frac{\text{J}}{\text{cal}} = 2.14 \times 10^6 \text{ J}$$

This heat would raise 907 kg (2000 lb) of lead from 20 K to 50 K.

This estimate can be refined to allow for the continued flow of heat to the refrigerator, for nitrogen condensation, and for cooling the gas. A lead mass of 907 kg (2000 lb) was used in the test setup.

HEAT TRANSFER - CHARCOAL TO LEAD

The ton of lead is made up of 1609 km (1000 mi) of strands, 0.025 cm (0.01 in.) in diameter. Its surface area is 1300 m^2 (14,000 ft^2), a square 36.6 m (120 ft) on a side. Even with molecular flow conditions, the hydrogen gas should hold the charcoal within 1 K of the surrounding lead wool. Details are given in the Appendix.

TEST OF SMALL SECTION OF CRYOPUMP

A model test was conducted on a section that was 2.18% of the cryopump area but of full thickness. The test section was 99 cm (39 in.) by 29 cm (11.6 in.), as shown in Figures 2, 3, and 4. It was filled with 7 kg (15.5 lb) of charcoal and 14 kg (31 lb) of lead wool (all as bought, without preconditioning). A flow tube was calibrated for 1 cfm flow of room temperature hydrogen-nitrogen gas mixture (2 parts H_2 to 1 part N_2). With this flow, the pressure rise would be 0.71 of the full-scale test.

The cryopump was cooled to 48 K (top), 22 K (center), and 19 K (bottom). Gas pulses were admitted, and the resulting pressure transients were recorded as shown in Figures 5 through 8. As shown, the speed of the pump decayed steadily with time as the charcoal warmed up.

From this test it was concluded that:

1. Pressures in the full-scale test would be less than 200 μm for a 3-min flow.

2. More than one 3-min flow test could be run before warmup and purging of the cryopump.

3. Vacuum bake of the charcoal was not required.

4. Lengthy cooldown of the cryopump could be expected.

FULL-SCALE CRYOPUMP AND OPERATIONS

The cryopump was built as shown in Figures 9 through 11. It is approximately 3.7 m (12 ft) by 3.7 m (12 ft) by 15 cm (6 in.) deep. Cooling tubes were soldered to a copper base, spaced 30 cm (12 in.) apart, and vertical copper fins were placed every 30 cm (12 in.) to speed the cooldown. The pump was filled with 453 kg (1000 lb) of charcoal (4 x 5 mesh at $1.75/lb) mixed with 907 kg (2000 lb) of lead wool ($0.75/lb). The mix was then compressed to a depth of 7.6 cm (3 in.). The top and sides of the bed were shielded with aluminized mylar to help cooldown. The bottom was shielded by a liquid-nitrogen-cooled panel 5.8 m (19 ft) in diameter. The charcoal and lead wool were mixed together and placed in the bed as received, with no cleaning or bakeout treatment.

Temperature histories of the bed are shown in Figures 12 through 15. The bottom of the bed was below 20 K at the start of all tests. The center and top of the bed were considerably warmer but continued to cool throughout the test period.

Pressure during all tests stayed below 200 μm as shown in Table II. A typical pressure transient is shown in Figure 16.

Cryopump performance improved steadily throughout the test period; both temperature and pressure peaks became smaller. This improvement is consistent with both a continued slow reduction in bed temperature and with a reduction in the heat of adsorption as hydrogen is sorbed.

SUMMARY

The slugged-charcoal approach to supplementing the cryopump capacity was a successful method of maintaining pressure in the MDAC space chamber below 200 μm during hydrazine tests of 3- to 12-min duration. Vacuum bake preconditioning of the charcoal and surrounding lead wool was not required, and nine tests were completed without any warmup and purge cycle. Cryopump performance improved steadily: pressures and temperatures in the later tests were lower.

Although temperatures in the cryopump bed were not uniform (varying from 20 K at the cooled surfaces to 65 K at the top center of the bed), they never exceeded 65 K. Cooldown times were lengthy, but these could be reduced by the use of additional fins.

REFERENCES

1. Stern, S. A.; Mullhaupt, J. T.; Hemstreet, R. A.; and DiPaolo, F. S.: J. Vac. Sci. Tech., 2, 165, 1965.

2. Scott, R. B.: Cryogenic Engineering, Van Nostrand, NY, 1959, Figure 6.9.

3. Corruccini, R. J. and Gniewek, J. J.: NBS Monograph 21, 1960.

4. Dushman, S. and Lafferty, J. M.: Scientific Foundations of Vacuum Technique, Wiley, 1962.

Appendix

HEAT TRANSFER BETWEEN CHARCOAL AND LEAD WOOL

What ΔT exists between charcoal and lead at a heat load of 8540 W? (Assuming all H_2 and 1/5 of N_2 condenses)

- Assume 10-μm pressure
- Assume molecular flow (ΔT for viscous flow is smaller)

$$E = \alpha \Lambda P_\mu \left(\frac{273.2}{T_i}\right)^{\frac{1}{2}} \cdot (T_s - T_i) \quad \text{(Reference 4)}$$

where:

$E = W/cm^2$

α = accommodation coefficient

= 0.3 assumed vs 0.35 for polished surface
0.5 - 0.7 for black surface

P_μ = Pressure = 10 μm

T_s = Surface temperature = 20 K

T = Gas temperature = 21 K

$\Lambda = 60.72 \times 10^{-6}$ for H_2

$E = 6.73 \times 10^{-4}$ W/cm^2, at 1 K ΔT

Lead Area:

Lead wool strands = 0.24 mm to 0.25 mm (0.0095 to 0.01 in.) dia (measured)

$\rho = 11.34$ g/cm^3

Wire length = 1.66×10^8 cm

Wire area = 1.3×10^7 cm^2

$E \times A = 6.73 \times 10^{-4} \times 1.3 \times 10^7 = \underline{8700}$ W

$\therefore \Delta T < 1$ K

Table I. METHODS TO PUMP HYDRAZINE EXHAUST

Method	Features
Blowers	Large machines, expensive, and long delay
Steam ejectors (6-stage)	Large machines, expensive, and long delay
N_2 ejector (multistage)	Large machine, requires development
Liquid helium	Costly use of cryogen
Remove diffusion pump baffles	Increases pump speed but still required blowers
Titanium sublimation	Need to deposit 72.6 kg (160 lb) in 5 min
Zr-Al getter strips	18 km (60,000 ft) of getter strip required
Charcoal at 20 K	Need 8-kW refrigerator vs 1.5-kW available
Slugged charcoal	453 kg (1000 lb) of charcoal, kept cold by 907 kg (2000 lb) of lead wool
Molecular sieve in place of charcoal	Charcoal has greater speed and higher equilibrium capacity

Table II. CRYOPUMP PERFORMANCE

	Startup--single pulse				Continuation--intermittent pulses				
Test	Time s	g/s (lb/s)	kg (lb)	Chamber pressure μm	Time s	g/s (lb/s)	kg (lb)	Duty cycle %	Chamber pressure μm
1	45.75* + 50.25	13.52 (0.0298)	1.296 (2.857)	196	123.0	7.03 (0.0155)	0.866 (1.910)	52.0	-
2	51.5	13.47 (0.0297)	0.693 (1.527)	150	90.5	3.08 (0.0068)	0.278 (0.613)	22.3	52
3	25.5	15.65 (0.0345)	0.174 (0.383)	132	92.5	1.68 (0.00371)	0.156 (0.343)	10.3	17
4	110.75	11.34 (0.025)	1.257 (2.772)	160	127.5	7.12 (0.0157)	0.907 (2.000)	62.8	126
5	45.5	15.83 (0.0349)	0.720 (1.587)	150	92.25	3.27 (0.0072)	0.299 (0.660)	20.2	24
6	62.75	13.56 (0.0299)	0.852 (1.879)	138	589.0	4.63 (0.0102)	2.73 (6.010)	34.0	160
7	9.75** + 15.5	15.83 (0.0349)	0.400 (0.881)	116	80.5	1.65 (0.00363)	0.132 (0.292)	10.1	16
8	75.0	11.43 (0.0252)	0.856 (1.887)	120	159.0	4.72 (0.0104)	0.753 (1.661)	41.6	76
9	27.25	13.61 (0.0300)	0.385 (0.848)	108	94.0	1.54 (0.0034)	0.145 (0.319)	11.0	24

*Warmup interrupted for 17.5 s.
**Warmup interrupted for 9.75 s.

Total exhaust weight: 12.895 kg (28.429 lb).

Total hydrogen sorbed = 1.61 kg (3.55 lb) = 806 mol = 1.81×10^7 cm^3 (STP), less fraction pumped away by diffusion pump.

Cumulative hydrogen loading of charcoal = 19.9 cm^3 (STP) of hydrogen/gram charcoal.

ORIGINAL PAGE IS OF POOR QUALITY

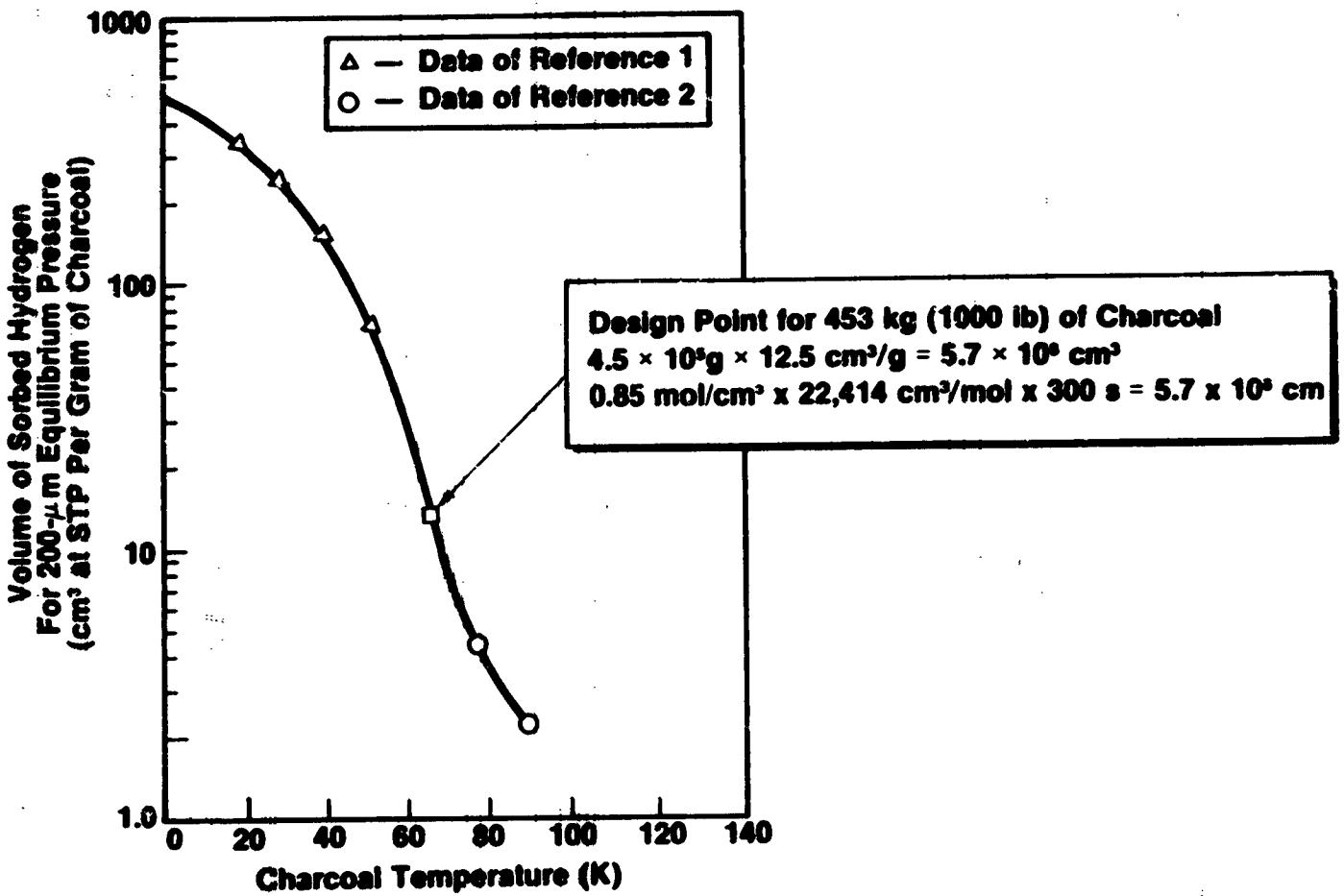

Figure 1. Hydrogen Capacity of Charcoal Versus Temperature For Equilibrium Pressure of 200 μm

ORIGINAL PAGE IS
OF POOR QUALITY

ORIGINAL PAGE IS
OF POOR QUALITY

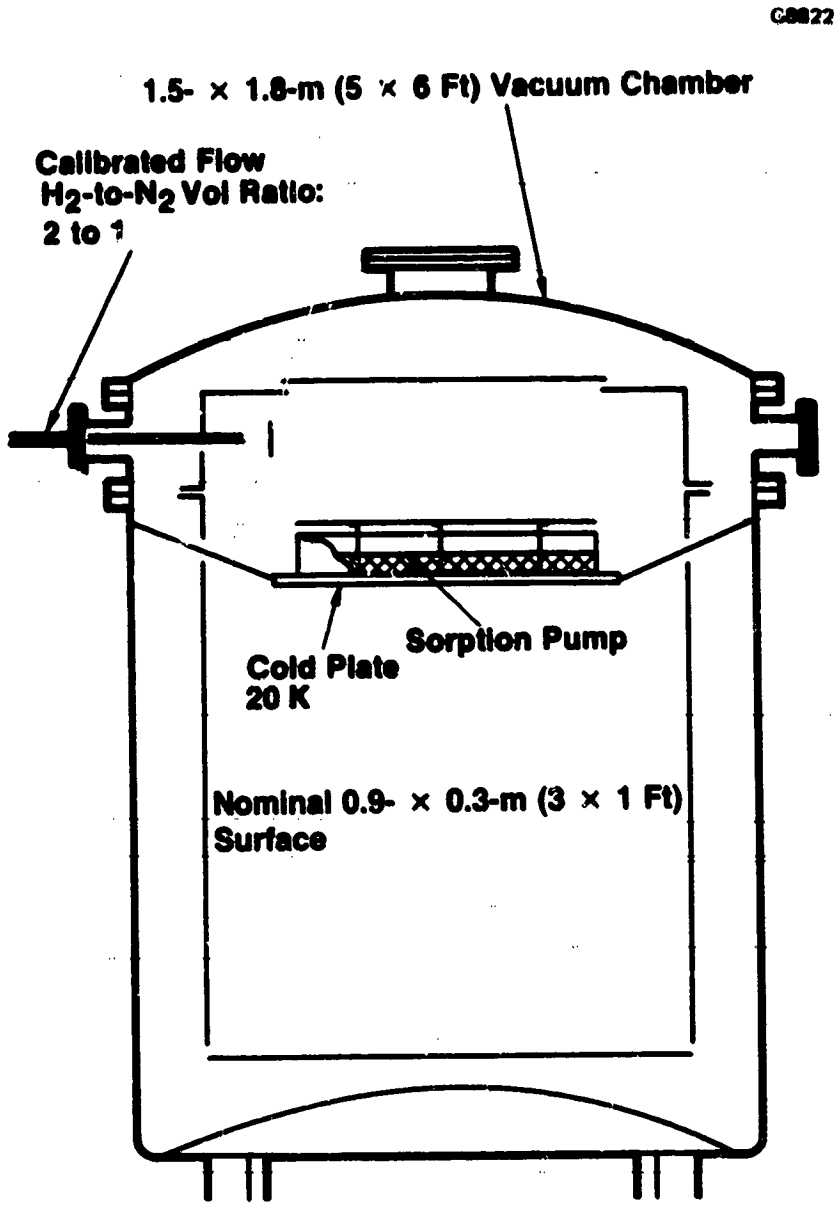

Figure 2. Cryopump Section

ORIGINAL PAGE
BLACK AND WHITE PHOTOGRAPH

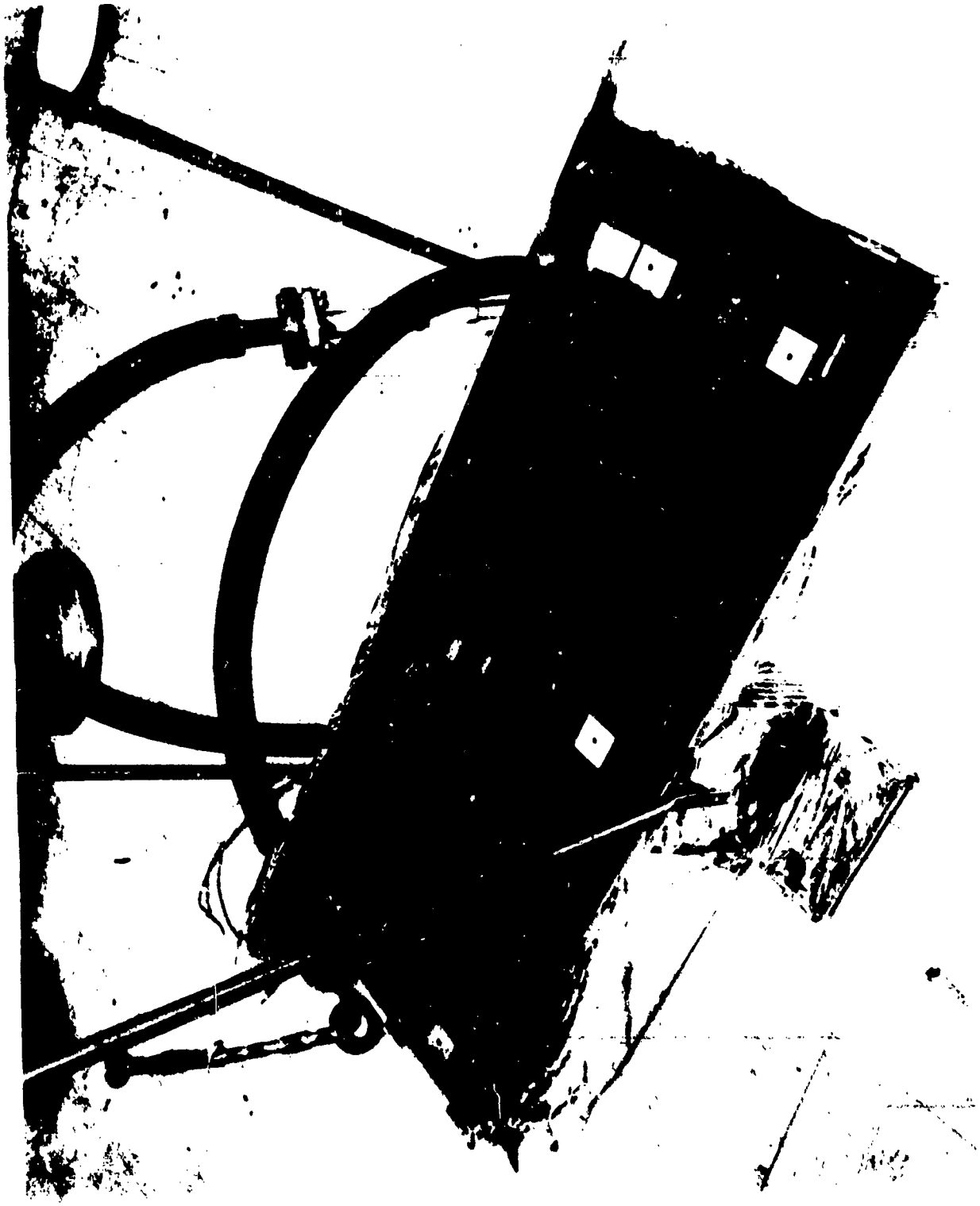

Figure 3. Cryopump Section

ORIGINAL PAGE
BLACK AND WHITE PHOTOGRAPH

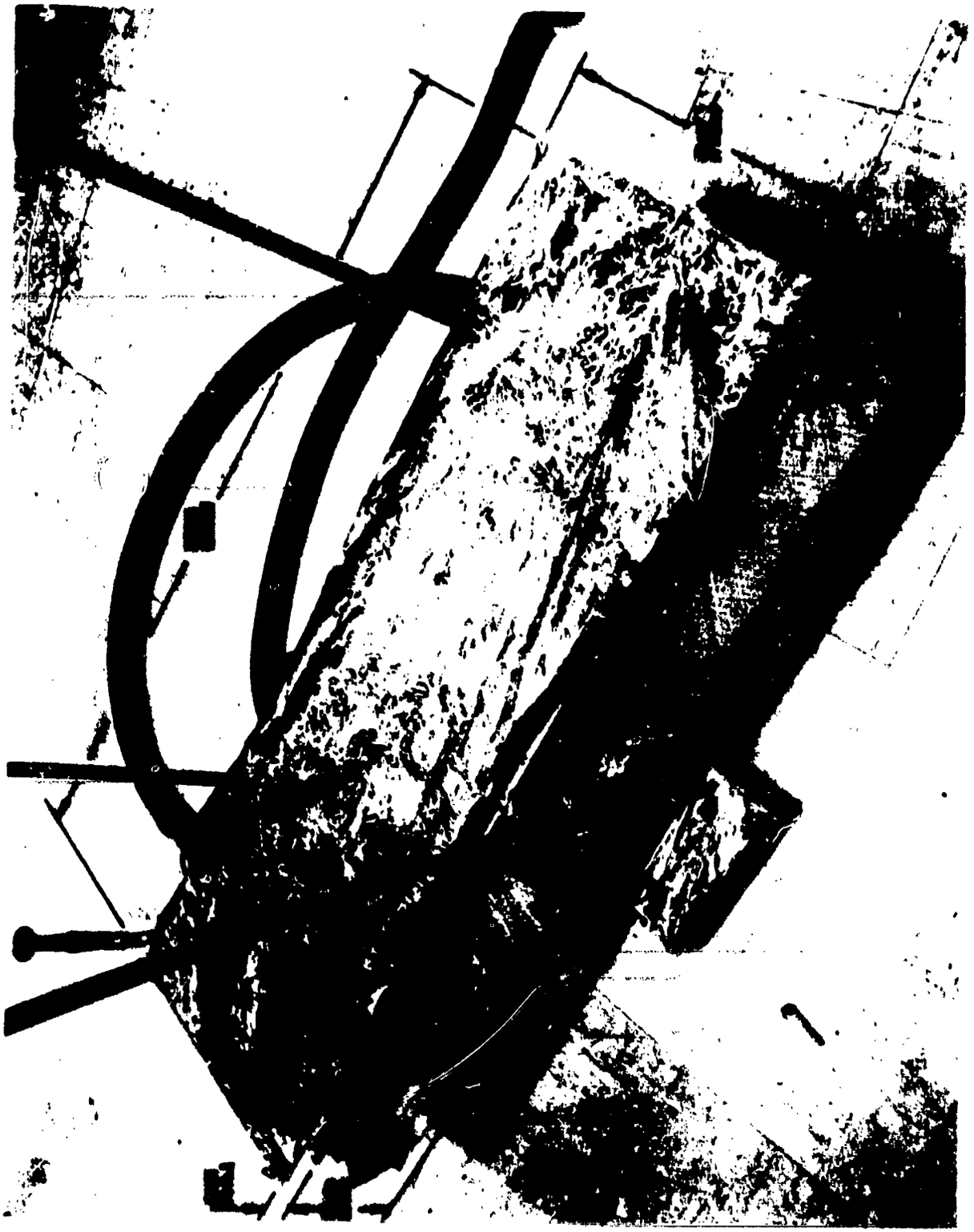

Figure 4. Cryopump Section — Lid Installed

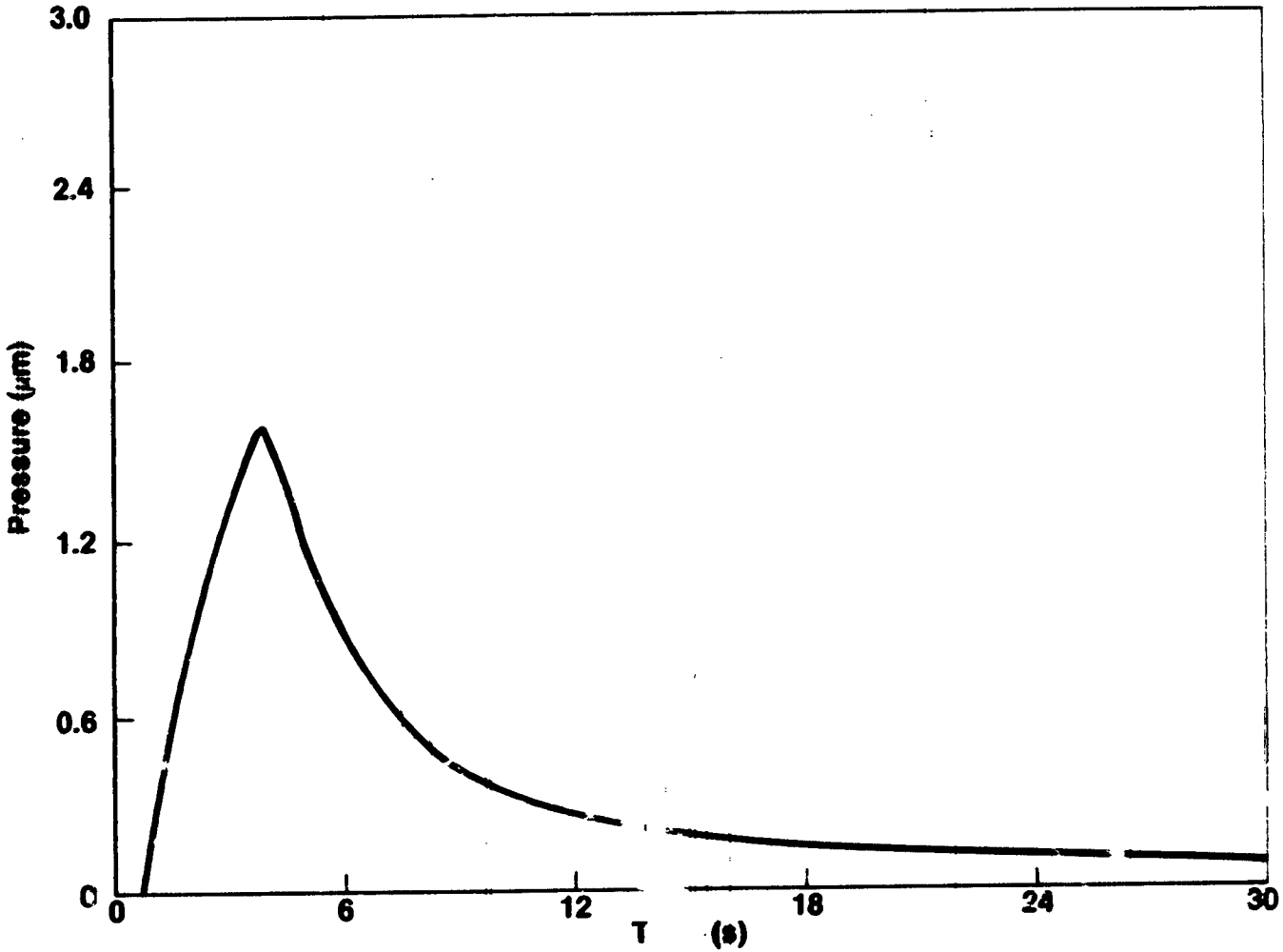

Figure 5. Section Resp...se to 3.5-s Gas Pulse

ORIGINAL PAGE IS
OF POOR QUALITY

ORIGINAL PAGE IS
OF POOR QUALITY

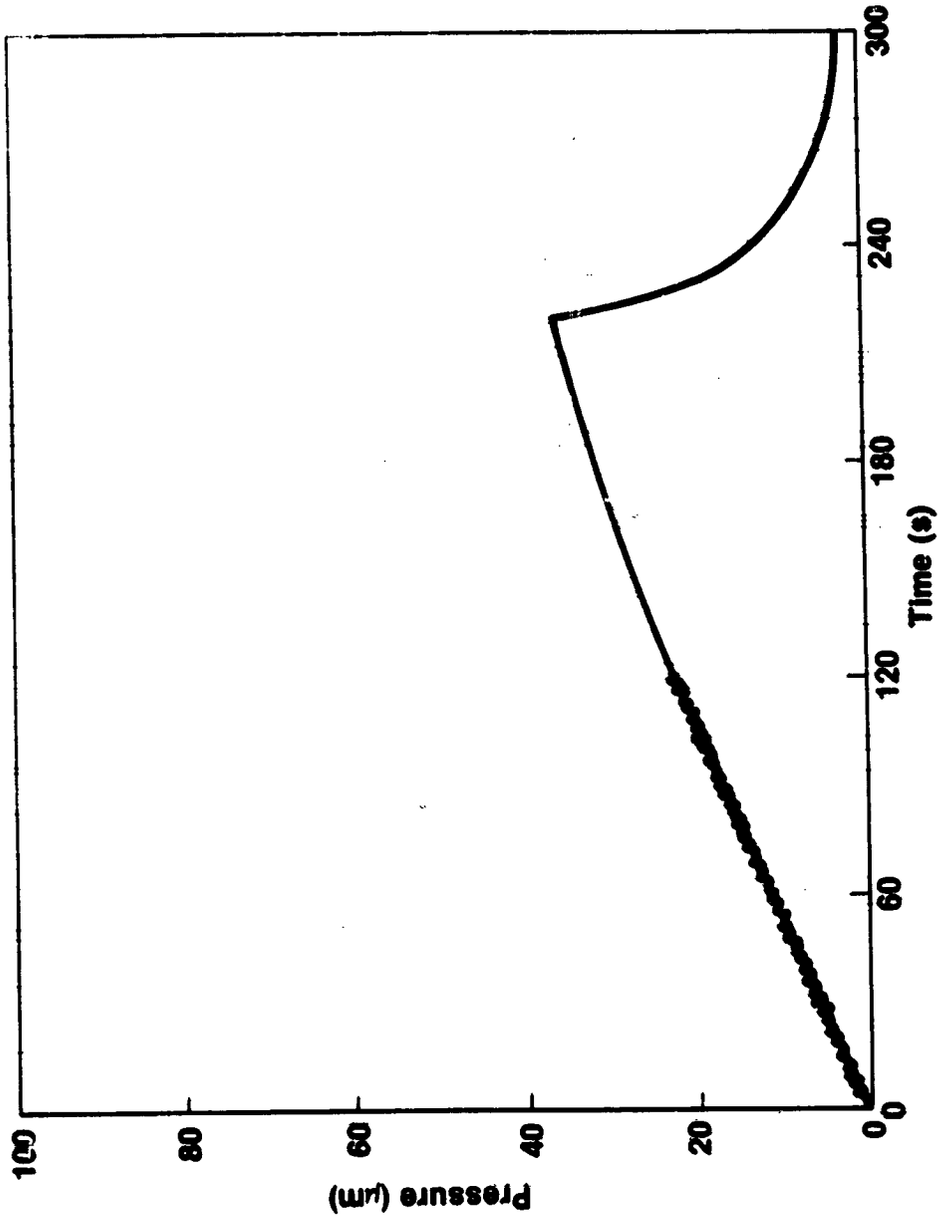

Figure 6. Section Response to 3.5-Min Gas Pulse

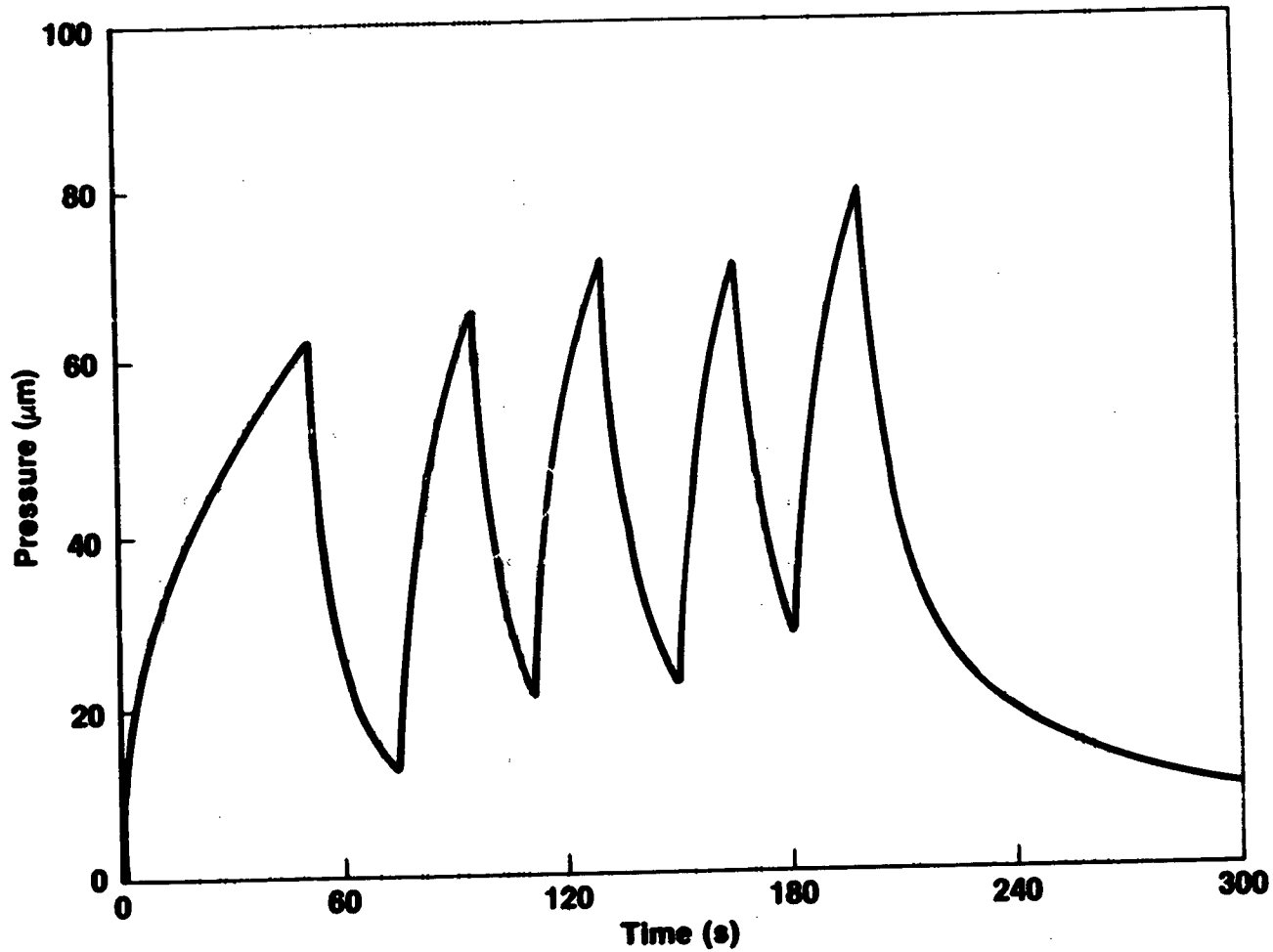

Figure 7. Section Response to Cyclic 3.5-Min Gas Flow

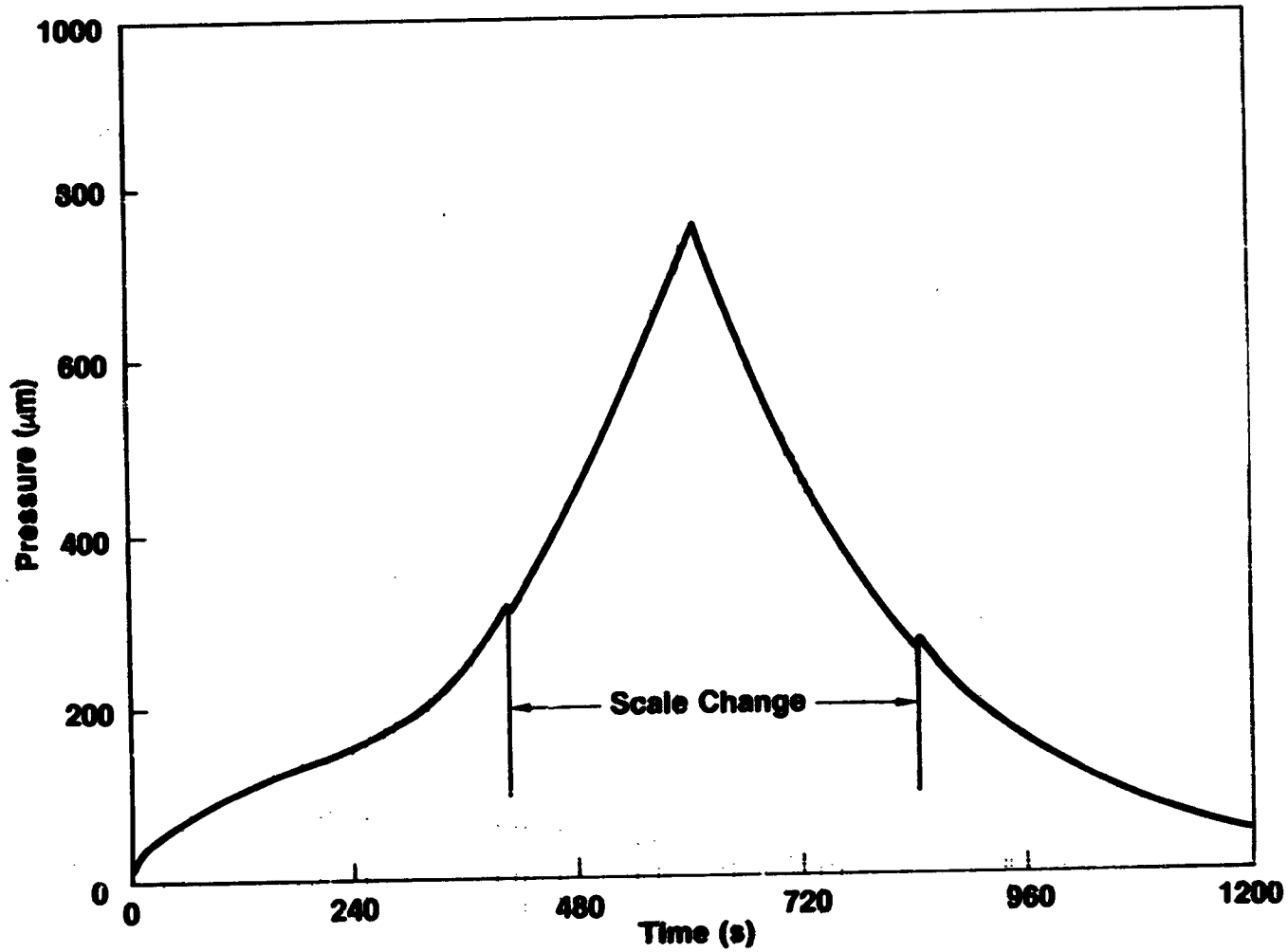

Figure 8. Section Response to 10-Min Gas Flow

ORIGINAL PAGE IS
OF POOR QUALITY

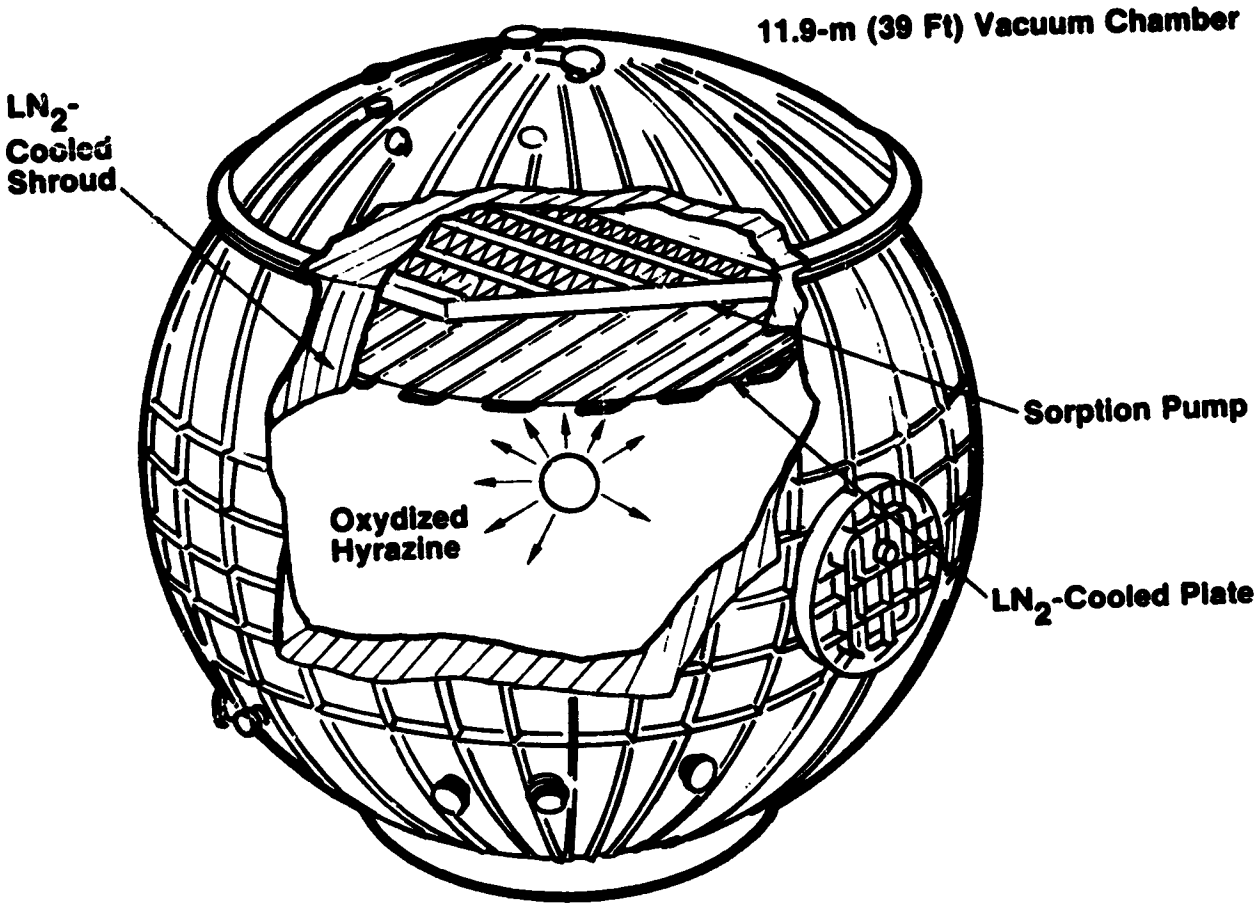

Figure 9. Full-Scale Cryopump

ORIGINAL PAGE
BLACK AND WHITE PHOTOGRAPH

Figure 10. Cryopump Fabrication

ORIGINAL PAGE
BLACK AND WHITE PHOTOGRAPH

Figure 11. Cryopump Installed

ORIGINAL PAGE IS
OF POOR QUALITY

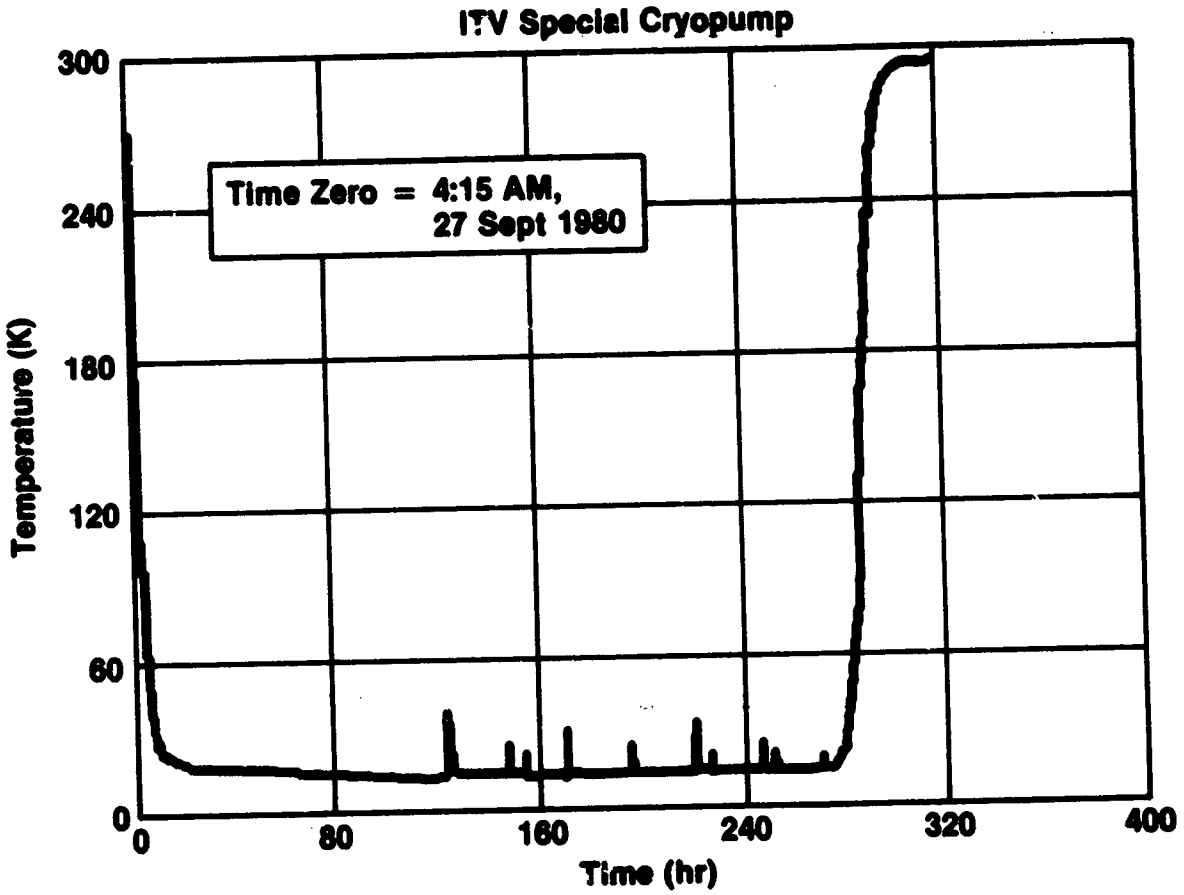

Figure 12. Temperature History, Bottom of Bed

ORIGINAL PAGE IS
OF POOR QUALITY

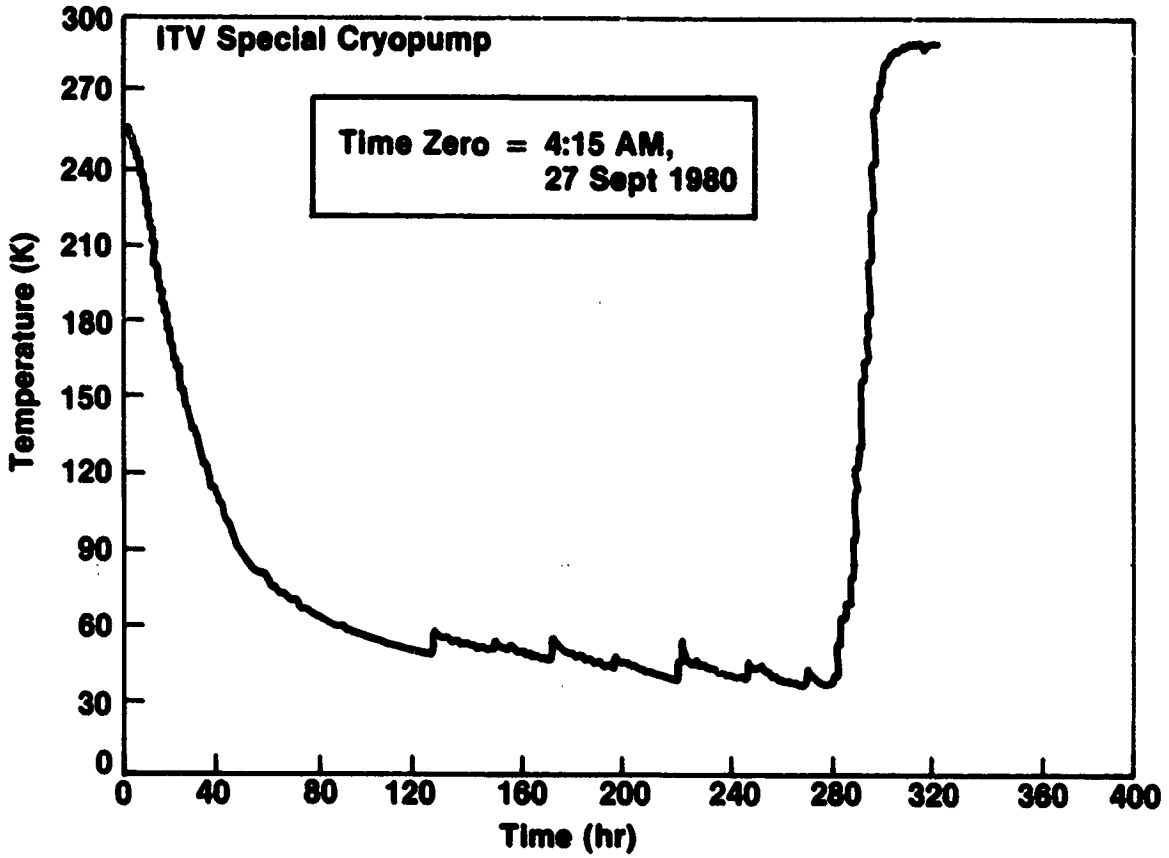

Figure 13. Cryopump Temperature History, Center of Bed

ORIGINAL PAGE IS
OF POOR QUALITY

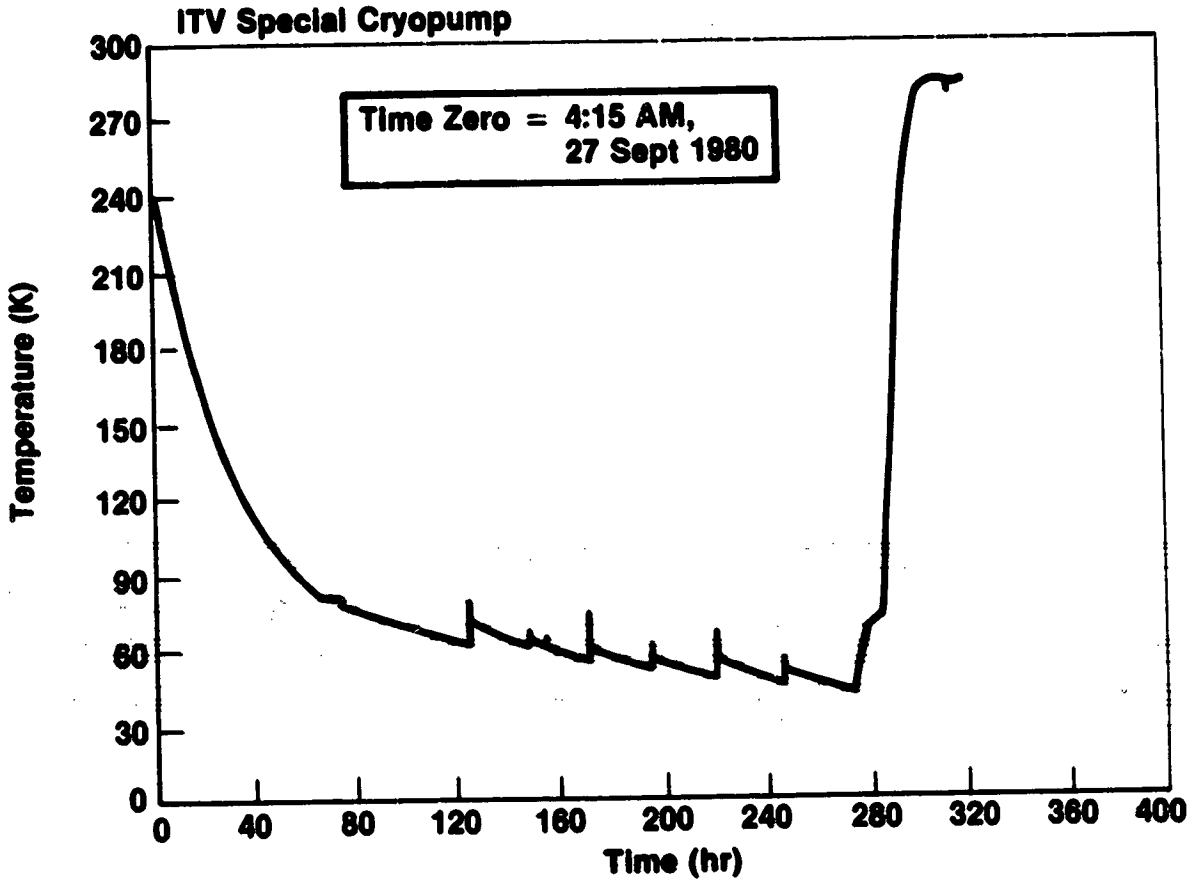

Figure 14. Cryopump Temperature History, Top of Bed

ORIGINAL PAGE IS
OF POOR QUALITY

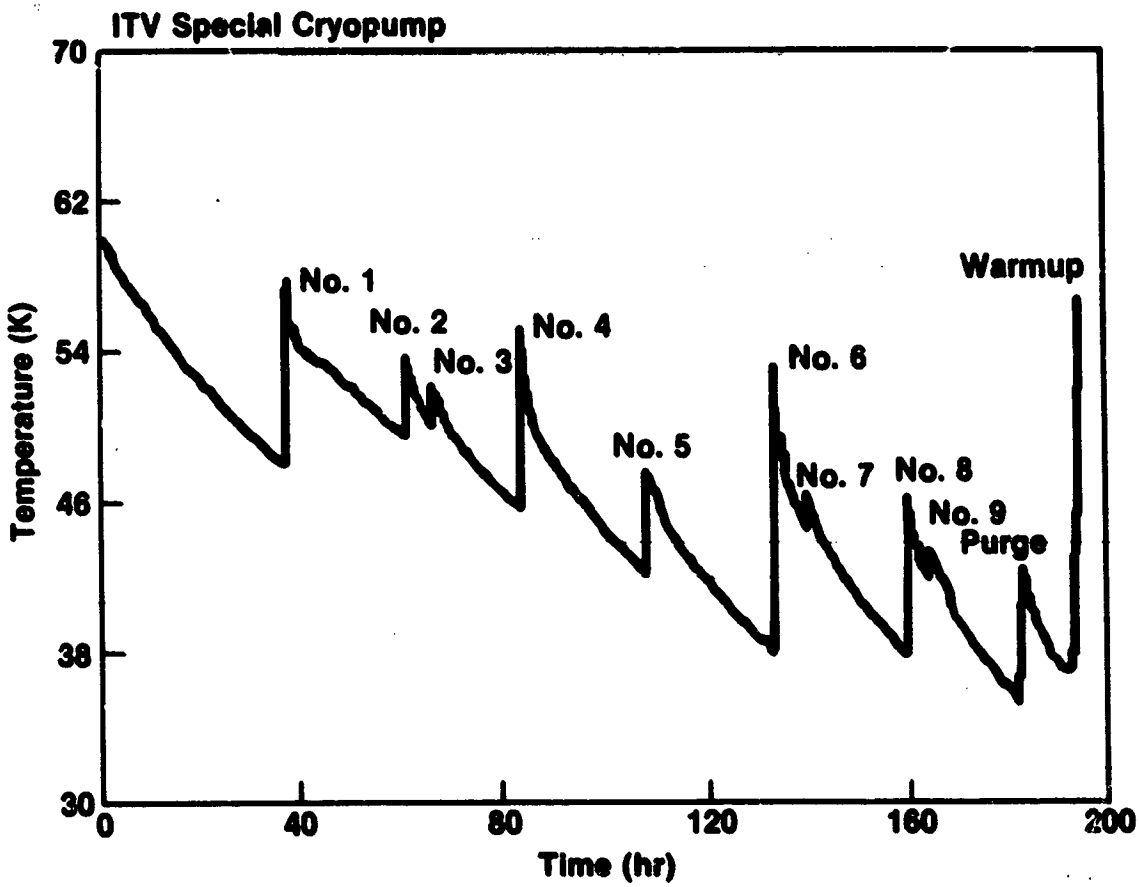

Figure 15. Cryopump Temperature History, Center of Bed (Expanded Scales)

ORIGINAL PAGE IS
OF POOR QUALITY

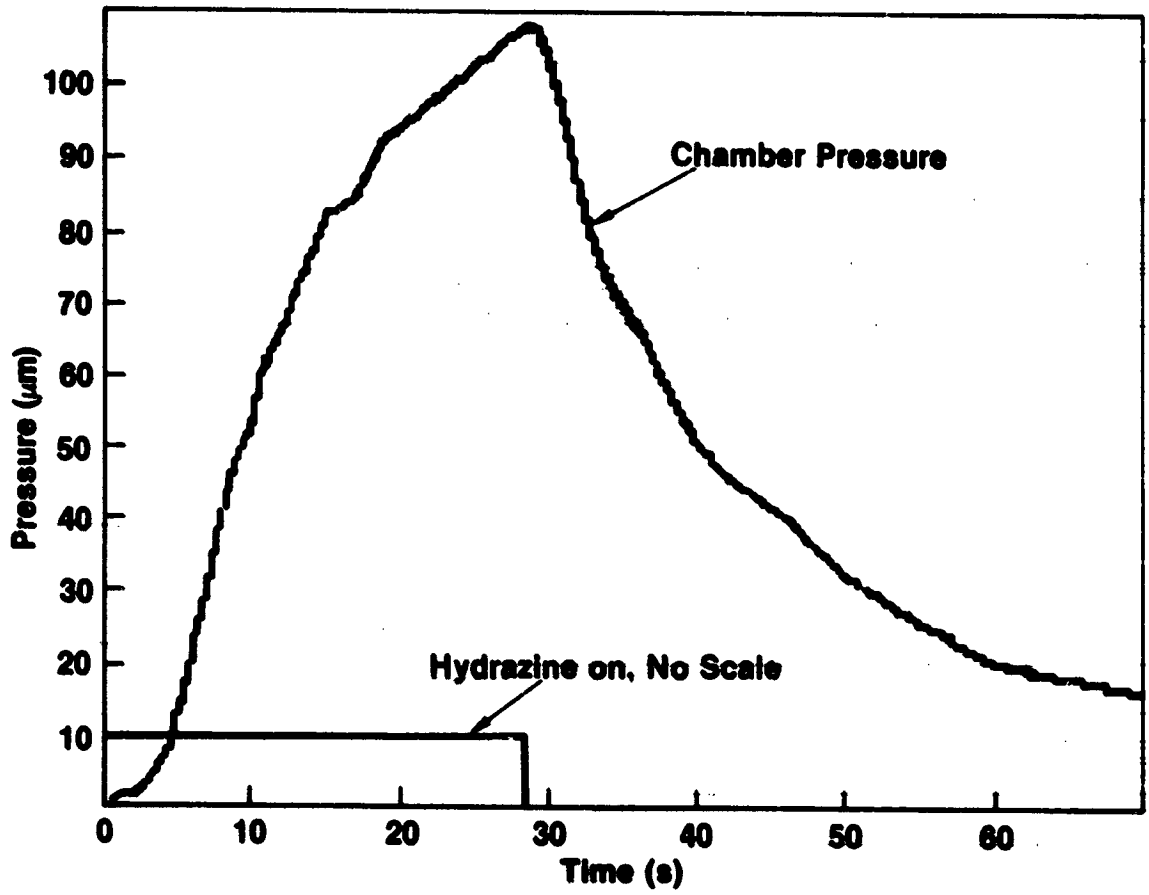

Figure 16. Pressure Transient, Test No.9

N82 25298

PRECEDING PAGE BLANK NOT FILMED

EDUCATION AND TRAINING OF PERSONNEL IN SPACE SIMULATION

R. D. Rempt
Martin Marietta
Denver, Colorado

ABSTRACT

The unique requirements demanded in necessary academic disciplines and practical experience for personnel in space simulation, force most facilities to develop some sort of training program for their personnel. This paper reports on the training program and procedures developed and implemented at the space simulation laboratory at Martin Marietta Aerospace in Denver. The training of technicians and professionals as well as preparation for instructors is covered. Training manuals and their compilation are reported as applicable to the specific needs of the laboratory. The development of a space simulation course as part of the Martin Marietta Continuing Education Night School approaching space simulation from an academic viewpoint is presented. Finally, public relations tours of the facility as an informational/educational tool are discussed.

INTRODUCTION

A paper concerning a topic such as personnel training at a specific facility is probably best approached from a rather narrative posture. For this reason, there will be some departure from the use of the passive voice as is the norm for technical papers. The development of the various phases of the training program at SSL will be presented more or less historically.

SPACE SIMULATION AT MARTIN MARIETTA

The space simulation facility at Martin Marietta is a service laboratory whose purpose is to provide space environments for testing of various in-house programs, and for outside uses as well. For this reason, the operation of equipment and the interface between laboratory personnel and the "customers" (whether in-house or not) have become the two most important areas of performance for personnel.

The laboratory conducts many tests every year for a multitude of different types and sizes of programs. Often there are several tests running simultaneously with several more being planned or designed, including required fabrication for fixturing and support hardware underway in the laboratory shop. To further intensify the situation, most tests run around the clock and require attention of personnel. Tests of classified programs require that laboratory personnel possess the necessary security clearances to support the test. All of these factors, coupled with the unique areas of academic

expertise called for by space simulation, require care and dedication in the training program.

Functionally, the laboratory is divided into three groups. These are the test operations group, the test programs group, and the laboratory engineering group. The engineering group essentially functions in a supporting capacity to the other two and as a result, the training program is not applicable to this group to the same degree as to the other two, which have much more direct interaction with the program personnel before and during each test.

TEST OPERATIONS GROUP

This group is primarily responsible for operating the environmental equipment in the laboratory. It is the group which is almost continually required to work in shifts around the clock, and to keep program personnel informed of test status. Most of the twelve to fifteen people in this group are technicians with either a two-year associate degree or less in formal education. The training needs of the personnel in this group are in operation and maintenance of specific laboratory hardware, as well as in understanding HOW the equipment works.

TEST PROGRAMS GROUP

This group is responsible for interfacing with program personnel from the start to the finish of each test. They must understand the program objectives and requirements, and how the laboratory capabilities may be of service in meeting them in a cost effective way. They are mostly engineers with college degrees. Their needs in training are to be able to explain to the programs our capabilities and the alternative methods of producing the environments called for by the various program tests. Fundamental vacuum theory and procedure, as well as basic heat transfer concepts and knowledge of the electromagnetic spectrum in the space environment, are specific areas with which they must be familiar. Some updating on certain aspects of instrumentation and recording devices is also necessary for their interface with test programs who usually know what they want, but are not always sure of how to go about getting it, and most always are not aware of the difficulties imposed by hostile environments such as hard vacuum. Understanding and ability to EXPLAIN such things are most essential for personnel in this group.

TRAINING PROGRAM DEVELOPMENT

The training program for personnel at the space simulation facility has been developed essentially out of need. As it became increasingly clear what was needed, short courses, manuals, and academic courses were developed to augment the on-the-job training that personnel were receiving.

When I came onboard, the director of the laboratory wanted to acquaint me with the entire facility as well as develop a training course and manual for the technicians in the lab. He felt that the most efficient way to do both was to ask me to prepare the course. I then acquainted myself with the equipment in the laboratory by studying operating procedures and instruction

manuals and put together a short course for the technicians. A training manual was written from which the course was taught. The manual was arranged in a modular fashion, which allowed the application and/or operation of specific subject areas immediately after the discussion of each. There was first a discussion of a topic such as vacuum technology, followed by an immediate application such as how to operate the smaller chambers. Next came a discussion of basic solar simulation, followed by the operation of the immediate chamber with its associated solar simulators. Finally, there was a discussion of basic cryopumping followed by the operation of the large space chamber. In each case, the subject area was followed by a detailed description of a specific piece of laboratory hardware to which the subject area directly applied, as well as a discussion of the actual operating procedure.

Incorporated in the course was also a review of applicable arithmetic for the benefit of shop personnel. This included addition and subtraction of signed numbers, simple temperature conversion formulas, and most important, proficiency working with powers of ten notation.

The course was given over a two-week period for an hour per day. The shift work of the personnel required some advanced planning to allow them all to attend, and sometimes there had to be two sessions due to the demands of the test programs during those two weeks.

My approach in teaching the course was to encourage all questions from the technicians. This was somewhat of a risk owing to the diversity of formal training represented. But after the first two sessions, they saw that any question which is asked sincerely was neither wrong nor stupid, and they started to open up and "fire away".

Training for the test programs personnel came about in a different way. Martin Marietta has a night school program the size of a small college, with between three and four thousand registrants. I was asked if I thought there was a course I might like to teach. After giving it some thought, I felt that a space simulation course approached from an academic standpoint might have some appeal. I did not try to recruit personnel from the laboratory, and the first semester only one person from the lab took the course. The second semester, all of the test programs group except one were waiting to take the course. They wanted to upgrade their ability to interface with the various programs concerning space simulation. Since vacuum technology and solar simulation are normally not taught at the universities, the course provided them with those needed academic disciplines.

As presented, this course covered the space environment, vacuum technology, solar simulation, test philosophy and the space chamber at Martin Marietta. A thermal vacuum test of a major program was covered, with the thermal data compared to the flight data received on mission. All in all, the course was fairly successful as demonstrated by the enthusiasm of the students at the end of the semester. The course was concluded with a tour of the space simulation laboratory conducted by myself. To me, it was most gratifying to observe the interest in the course demonstrated by the test programs group as well as employees from other areas at Martin Marietta.

Text materials for the course included many different "handouts", as well as several chapters of "Handbook of Solar Simulation for Thermal Vacuum Testing", which was compiled through the IES and distributed compliments of Spectrolab, Inc. There were several handouts from current journals demonstrating one or another aspect being covered in the course.

Assignments were given, and questions were encouraged. Where helpful, basic physics was quickly reviewed. Two exams were given in which the performance of the students was on the whole, acceptable. There was a good amount of interaction between myself and the students. Some use was made of visual aids, and some hardware was passed around in class for students to inspect more closely.

RESULTS

For myself, as the instructor and developer of the training program, there were two important factors. First was the situation which more or less forced me to acquaint myself with the lab, its equipment, and its capabilities well enough to explain it to others. I am convinced that a person understands something when they can explain it to others. This necessarily affects the ability of engineers in the test programs group to effectively interface with the various program personnel.

The second factor was more in the category of conclusions drawn about human nature especially as it applies to teaching and/or training, and the "learning curve". These will be mentioned in the next section.

The recent expansion of Martin Marietta resulted in several new personnel in the space simulation lab As they heard from the older employees about the training course, they began requesting that it be taught again. This reflects both the positive response of those that took the course as well as the recognized need for training in the newer employees. An expression for more training is a healthy attitude from personnel.

The training course paved the way to foster meaningful interaction between myself and most of the personnel in the lab. They started to come to my office with questions about their work. In a certain sense, they saw me as a resource from which they could benefit.

A natural byproduct of developing the training course was the capability to give tours of the facility. The space simulation laboratory with its large space chamber is a prime "attraction" for dignitaries and executive type visitors and customers. Giving these tours provides opportunity to continually "polish" both understanding and more important, the presentation. A good presentation during a tour, whether it be 15 minutes or two hours, gives a professional impression of the whole facility. This is often very important when those being given the tours are prospective customers.

CONCLUSIONS

There are a number of interesting and important things I have learned as a result of my training efforts in space simulation. The first is that

personnel in general want training more than their supervisors would think. This is especially true for those at the lower levels. After some time spent on the job with "hands on" training, they are helped by and have a naturally increasing interest in learning the application of their efforts. If this interest is not responded to by their supervisors, something is lost that is very difficult to regain.

The second is that any responsible attempt to train personnel is better than no attempt. Those doing training will most certainly learn in the process and see how to better their course content, presentation, and interaction with their students. Providing for the learning of employees gives rise to a certain amount of grace on the part of the employees towards their instructors. If no such provision is made, employees tend to be less understanding with their supervisors and an adversarial type of relationship has a much higher probability of evolving.

Finally, when management provides training opportunity, the personnel feel like something is being done <u>for</u> them rather than only that something is being expected from them. This leads to an appreciative attitude as well as a solicitation of further training. When management takes the initiative to train, the embarrassment often experienced by personnel in requesting training is avoided.

PRECEDING PAGE BLANK NOT FILMED

SESSION V

SPACE SIMULATION TEST TECHNOLOGY

Session Organizers: Albert R. Lunde, Boeing Aerospace

S. Liu, TRW Space Systems

PRECEDING PAGE BLANK NOT FILMED

A MICROPROCESSOR-BASED, MULTI-ZONE THERMAL CONTROLLER

W. F. Petrie

Perkin-Elmer Corporation
Danbury, Connecticut 06810

ABSTRACT

Many Thermal/Vacuum tests require multi-zoned thermal control using electric heaters. Usually this control is provided by individual controllers for each thermal zone. Even with highly simplified, "on-off" controllers, this can still be costly when many control zones are required. Moreover, use of this type of controller will often require a sacrifice of some accuracy in control. A system that can provide highly accurate thermal control for a large number of zones with a relatively simple, inexpensive controller has been developed based on microprocessor control. As temperature data for the individual zones are provided, the microprocessor program solves the control algorithm for each zone, and a data "word" is formed consisting of one data bit for each zone. Once the "word" is formed, the microprocessor loads it bit by bit into an output shift register. When the shift register is loaded, the data word is shifted into latches that turn the power of individual zones "on" or "off" depending on whether the latched control bit for the zone is a "1" or "0" respectively. In a specific test application, 32 individually controlled thermal zones were provided. Despite the "on-off" nature of the control technique, temperature control to better than ±1/4°F was achieved. Variations in the basic concept can improve control accuracy and simplify control operations for the test operator.

N82 25299

PRECEDING PAGE BLANK NOT FILMED

A REAL-TIME DYNAMIC SPACECRAFT SIMULATOR FOR THE LANDSAT-D MISSION [1]

Allen R. Coffin
Manager, Landsat Ground Segment Integration and Test
General Electric, Space Systems Division

ABSTRACT

A REAL-TIME DYNAMIC SPACECRAFT SIMULATOR FOR THE LANDSAT-D MISSION

The Landsat-D spacecraft, scheduled for launch in July 1982, is the first of the next generation of satellite technology for remote sensing of earth resources. A real-time dynamic simulator for this spacecraft has been developed and has played an integral role in the development and validation of both the ground control system and of the on-board flight software.

The simulator utilized an electronic replica of the spacecraft on-board computer and data handling hardware interfaced to a VAX 11/780 computer and simulation software.

Key features of the simulator design are a modular software architecture tailored to the VAX/VMS real-time capabilities, a microprocessor controlled interface between the VAX and the flight hardware replica, complete simulation of the spacecraft and NASA network communication links, and a flexible and powerful scenario structuring and operator control capability.

The design goals and trade-offs, software, and hardware design are summarized. The application of the simulator to the validation of both the ground systems and on-board software is reviewed in detail.

[1] This work was performed under NASA/GSFC contract No. NAS52300.

INTRODUCTION

The Landsat-D mission, scheduled for first launch in July 1982, will be a major step in the orderly development and application of remotely sensed data from space to the management of the earth's resources. It will provide enhanced remote sensing capabilities relative to earlier Landsat missions through inproved sensors, wider acquisition of global data, and more rapid processing of the data for users.

The Landsat-D observatory will operate from a circular sun-synchronous orbit, imaging the same swath of the earth surface each 16 days. Image data is transmitted in real-time at KU-band via the Tracking and Data Relay Satellite (TDRS) to its ground terminal at White Sands, New Mexico where it is recorded and then relayed via a domestic communications satellite (DOMSAT) to the Goddard Space Flight Center (GSFC) in Maryland for processing. (Figure 1)

Image data will also be transmitted directly to foreign or domestic ground stations at X-band in addition to or in lieu of transmissions via TDRS. A separate S-band direct link compatible with the Landsat 1,2 and 3 is also provided to transmit MSS data to those stations only equipped for receiving at S-band. Normal spacecraft telemetry and command communications are via TDRSS at S-band; Additional telemetry and command capability is provided through the NASA-GSTDN stations.

Initial tracking data for Landsat-D will be obtained via TDRS and the GSTDN stations. Ephemeris determination required by the spacecraft for attitude control and the ground segment for both mission planning and image correction processing are computed at the Goddard Space Flight Center. However, the Landsat-D spacecraft will be equipped with a Global Positioning System (GPS) receiver/processor which, after checkout and calibration, will provide a second source of spacecraft ephemerides.

The major components of the Landsat-D Flight Segment (Figure 2) are the NASA Multimission Modular Spacecraft (MMS), the Multispectral Scanner (MSS), and Thematic Mapper remote sensing instruments, the Wideband instrument data communications subsystem, and the Global Positioning System (GPS).

The major elements of the Landsat-D Ground Segment (Figures 3 and 4) are the Control and Simulation Facility (CSF), Mission Management Facility (MMF), Image Generation Facility (IGF) and Landsat Assessment System (LAS). The Control and Simulation Facility will provide daily planning and control in support of spacecraft health, safety, and instrument operation. As its name inplies it also houses the spacecraft simulation capability which is the subject of this paper. The Mission Management Facility supports the planning and management of image data acquisition and processing in response to the needs of the Landsat user community. The Image Generation Facility supports the ingest and processing of raw imagery data from both the MSS and Thematic Mapper instruments. It produces radiometrically and geodetically corrected imagery products. The Landsat Assessment System is an R&D facility consisting of image processing hardware and software to serve as a resource for investigation and development of new earth resources management techniques using data from the Thematic Mapper sensor.

A major component of the Control and Simulation Facility (CSF) is the Test and Simulation Subsystem (TSIM). This hardware/software subsystem is designed to provide a real-time dynamic spacecraft simulation capability for the Landsat-D mission. It is intended to support development and pre-launch validation of the ground segment, operator training and evaluation, and to provide a capability to validate both on-board computer software updates and CSF software updates before implementation in the actual spacecraft. Subsequent paragraphs will review the design of the major hardware and software components comprising the TSIM, and the major functional capabilities of the system. Finally, the application of TSIM to the development and verification of the Landsat-D system to date and plans for its operational applications will be reviewed.

LANDSAT-D TEST AND SIMULATION SUBSYSTEM

The TSIM Landsat-D dynamic spacecraft simulator is implemented as an integral part of the CSF (Figure 5) whose primary functions are the daily planning, command, control, and evaluation of the Landsat-D spacecraft. To accomplish these functions the CSF consists of three identically configured DEC VAX 11/780 computer systems each having 2.5 Mbytes of memory and three 176 Mbyte disk storage devices. CSF software, including

TSIM, consists of over 120,000 lines of executable code executing under the VAX/VMS real-time operating system. All CSF special-purpose hardware, including the TSIM support hardware, is either replicated redundantly on all 3 systems or fully switchable to the desired system (Figure 6).

The three CSF computers are interconnected with their counterparts and the MMF computer system by the DECNET inter-computer network software. The CSF implementation also utilizes the International Data Base Systems Inc. "SEED" DBMS to support the storage and retrieval of critical mission support and planning data.

The heart of the TSIM spacecraft simulation is an hardware replica of the MMS Command Data Handling Subsystem (CDHS). The TSIM hardware includes a replica of the NSSC-1 on-board computer, standard interface and control hardware, and remote interface logic. This hardware is interfaced to the TSIM host VAX 11/780 computer via a custom designed microprocessor controlled TSIM/VAX interface unit (VIU), (Figure 7). The TSIM hardware interfaces to either of the three VAX 11/780 computers via 5 DMA data paths which are supported by a manually switchable UNIBUS interface (DR11B/DT07) combination. The CDHS hardware replicates all spacecraft on-board data acquisition, processing, (including execution of the actual on board computer software), generation and distribution functions in exact real-time. The VIU interfaces these functions to the software simulation functions in the VAX 11/780 computer. As shown, (Figure 8) TSIM aslo utilizes the same NASCOM interface hardware used by CSF to communicate with the spacecraft via the NASA Communication Network (NASCOM) to support data flow between the simulation and the command and control elements of CSF. The TSIM simulation software in the VAX 11/780 consists of the following major real-time functional elements:

* simulation control and operator interface
* interface unit (VIU) synchronization
* telemetry/dump data handler
* uplink command handler
* network communications interface
* spacecraft subsystem and environment simulation
* history generation

The following paragraphs summarize the flow of data and the functions performed by the major hardware and software elements within the TSIM real-time simulation.

The internal control timing of the CDHS hardware provides the synchronization for all critical TSIM functions. Once each 128 milliseconds, the VIU collects and transfers a buffer containing all spacecraft subsystem commands dispatched within the CDHS during the previous interval. The receipt of this transfer (Path 1) within the VAX 11/780 activates the interface unit synchronization module.

The synchronization module buffers the data transfers for two intervals and transfers the commands to the spacecraft subsystem simulation (SCSS) module once every 256 milliseconds. The SCSS module is the heart of the dynamic simulation and performs spacecraft command translation, spacecraft subsystem and environment modelling and translation of analog and digital data into CDHS format each 256 millisecond simulation cycle. The module faithfully simulates the orbital environment and attitude control dynamics of the spacecraft. All major spacecraft subsystem functions, commands, and telemetry points are modelled including the:

* attitude control subsystem
* solar array and TDRS antenna drives
* power subsystem
* thermal subsystem
* narrow-band tape recorders
* GPS
* instrument payloads
* safehold control mode
* propulsion module

The resulting spacecraft data, having been converted to CDHS format, is transferred back to the CDHS via the interface hardware (Path 2) every 256 milliseconds. The interface hardware buffers this data and controls access by both the on-board computer and CDHS telemetry formatter to the data. The CDHS telemetry formatter is synchronized to the internal 128 millisecond cycle and accesses data from both the on-board computer (OBC) memory and the interface unit to create the continous spacecraft telemetry stream at 1 kbps or 8 kbps, as commanded. High data rate OBC memory dump data is generated on command at 32 kbps by similar hardware within the CDHS.

These two data streams are buffered in the VIU interface hardware and transferred in real-time (Paths 3 and 4) to the VAX 11/780 where the telemetry/dump data handling software captures this data. The data is packaged into NASCOM formatted blocks by the network interface software and metered out with the appropriate protocol and data rate via the NASCOM interface (NIF) hardware to be routed to the CSF real-time processing functions. CSF generated ground commands are also received by the NIF hardware and deblocked by the network interface software command handler, which transfers the command data via the VIU interface hardware (Path 5) to the CDHS hardware. This completes the closed-loop flow of data between CSF ground support functions, simulation software, and the CDHS hardware replica. All data transfers are synchronized to ensure proper data access and data generation access by the CDHS of data flowing to and from the simulation software.

The definition, initiation, control and display of simulations is the function of the simulation control module. It provides the capability to define simulation scenarios using a powerful scenario definition language which provides the ability to define initial conditions and to specify real-time event sequences including time-tagged and conditional executions. All simulation data is accessed via a global data structure, access to which can be made from the controller to set or display the value of any variable. The scenario definition language includes the capability to define macro-like sub-scenarios to facilitate the creation of very complex scenarios. Operator control of the simulation via the console keyboard is allowed at all times. A single display format provides a header with simulation time displayed, a scrolled window of current scenario commands as they are executed, and a window for display of selected simulation variables. A command entry line and message area appear at the bottom of the screen. In addition to real-time simulations synchronized to the CDHS hardware, step-mode and faster than real-time software-only simulation capability is supported. An history generation function captures all operator and scenario commands and optionally generates "snapshots" of selected areas of the global data structure for post-scenario evaluation.

All of the functional software modules discussed are implemented as independent processes under control of the VAX/VMS real-time operating system. The system design and implementation exploits the very powerful and flexible features of this operating system to control real-time processing priorities, inter-process communication, and process synchronization.

Much of the functionality traditionally found in the executive control software of the typical real-time simulator is, in TSIM, performed by VMS operating system support services.

TSIM APPLICATIONS

The TSIM subsystem hardware and software were deliberately developed and integrated as part of a phased test program with basic TSIM capabilities demonstrated relatively early in the CSF development cycle. Thus, TSIM was available relatively early in the program as a realistic test data generator to support the development and testing of real-time telemetry and dump data acquisition and processing software. The decommutation, calibration, and detail processing of spacecraft telemetry in CSF is controlled by real-time data tables which are themselves generated from telemetry description data stored in the CSF data base management system. TSIM also has access to this data base and generates its own real-time tables from the same data base. This provides the capability to reflect changes in analog telemetry function calibration data consistently in both the simulation and processing software. TSIM was also designed to the greatest extent possible, to model key spacecraft subsystems using redefinable constants, alignment values and related parameters. The ability to control any element of the global data structure has been a vital tool for developing baseline test scenarios which have supported verification of the complex telemetry, limit, alarm, and event processing logic within CSF by carefully controlling the profiles of predefined analog and digital telemetry functions within a test scenario.

Similarly, TSIM has supported preliminary verification of the CSF spacecraft command generation and verification software. It has also proved useful as a generator of synthetic ephemeris data for use in testing elements of the Image Generation Facility.

Perhaps the most interesting application of TSIM to the Landsat-D development has been its use in the OBC flight software validation effort. The design of the spacecraft dynamics models within TSIM had as a goal to produce adequate fidelity to support validation of post-lauch flight software modifications prior to their use in the actual spacecraft. During reviews of early test results of the spacecraft subsystem modeling software it was recognized that elements of the TSIM software could be very effectively utilized in the validation of critical elements of

the OBC flight software, namely the attitude control, ephemeris processing, and spacecraft control processors. The flight software test facility already included a VAX 11/780, CDHS replica and interface unit (VIU) identical to those contained in the CSF hardware. A non-real-time on-board computer emulator was also a key part of the existing flight software test facility. A custom software interface was implemented allowing the TSIM spacecraft simulation software to execute in non-real-time against FORTRAN engineering models of the basic spacecraft control algorithms. The results of these tests were compared with engineering tests of the same control algorithms against engineering models of the spacecraft dynamic components. These results were used to validate, correct, and tune the TSIM dynamic models. These same tests were then repeated using the OBC emulator executing the prototype flight software against the TSIM dynamic models. Finally the same software was tested in real-time operation against the TSIM models using the flight software facility's VAX 11/780 CDHS and interface hardware. This sequence of testing has provided a high degree of confidence in the validity of the spacecraft control laws, as implemented in the flight software, and the correctness of the TSIM models with respect to the design of the actual spacecraft. Moreover, the utility of the TSIM subsystem to support post-launch flight software maintenance was clearly demonstrated.

TSIM is just now beginning to be used to support realistic real-time operational scenarios within the CSF. Its capability to support end-to-end data flows and line tests for both system tests and operations has been demonstrated. Currently, integration and test resources are developing TSIM scenarios to support demonstrations of full-up CSF real-time spacecraft command and control as part of the Ground Segment acceptance testing. These scenarios will be enhanced and updated to support operational readiness testing and on-going training of the maintenance and operations staff.

SUMMARY

The TSIM subsystem has played a key role in the development and verification of both the ground and flight segments of the Landsat-D mission. The combination of hardware emulation of all critical on-board data handling and computation with a flexible and dynamically accurate software simulator provide a power capability for pre-launch testing and post-launch maintenance and operations.

REFERENCES

1. LANDSAT-D THE NEXT GENERATION SYSTEM
   T.C. Aepli, W. Wolfe General Electric Company
   Western Electric Show and Convention Sept 18-20, 1979

An Introduction to the Major Elements of the LANDSAT-D System

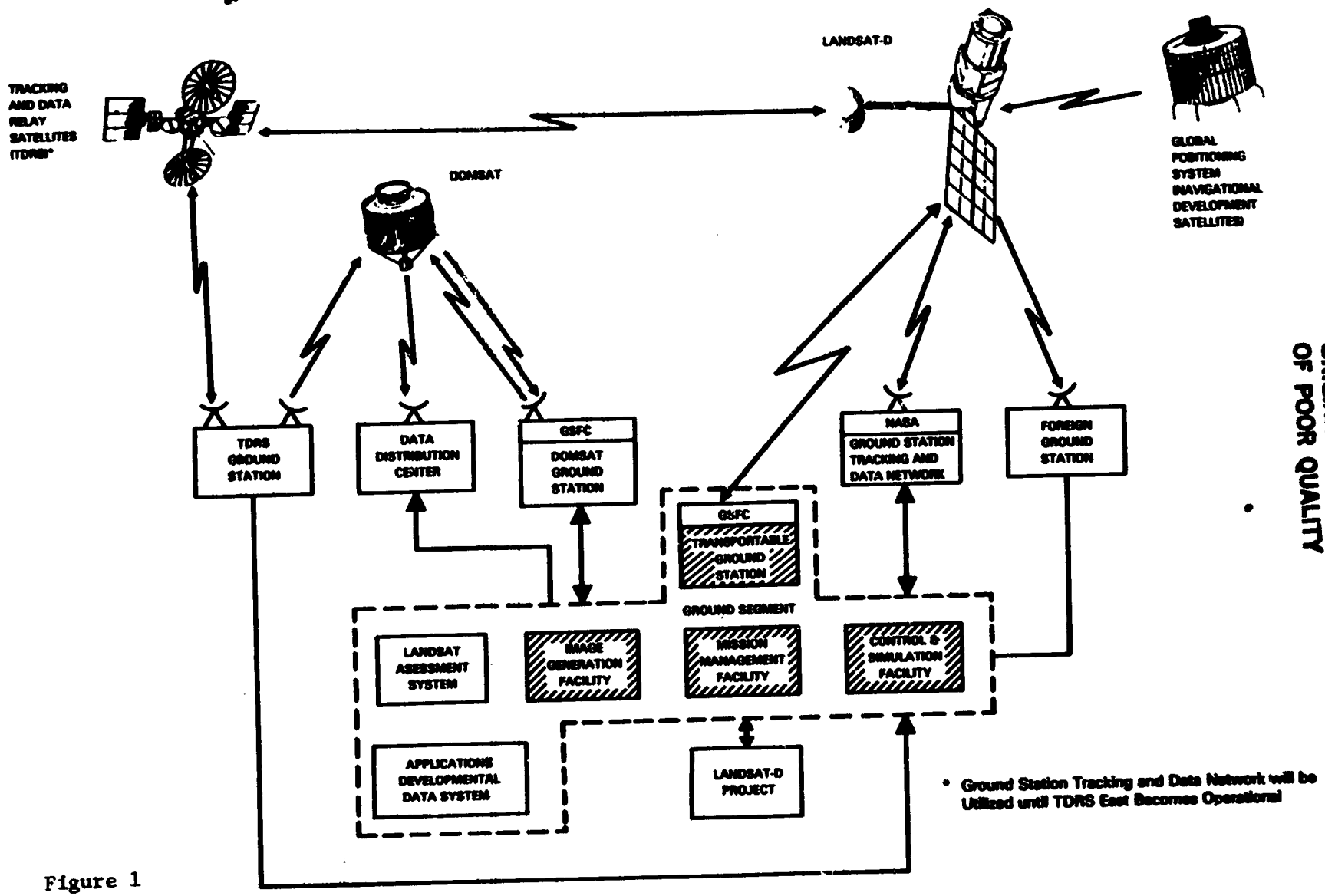

Figure 1

ORIGINAL PAGE IS OF POOR QUALITY

LANDSAT D FLIGHT SEGMENT

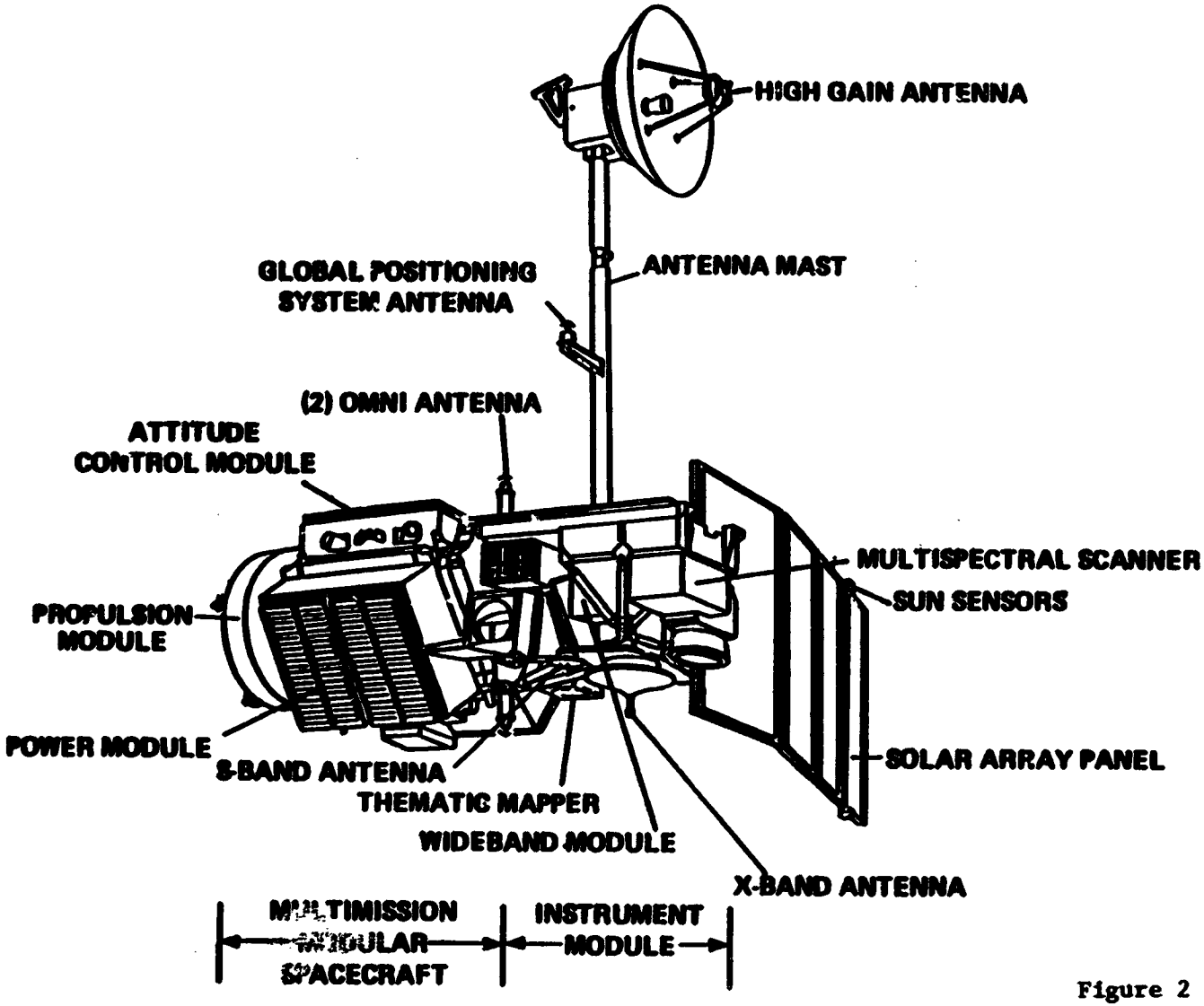

Figure 2

ORIGINAL PAGE IS OF POOR QUALITY

ORIGINAL PAGE IS
OF POOR QUALITY

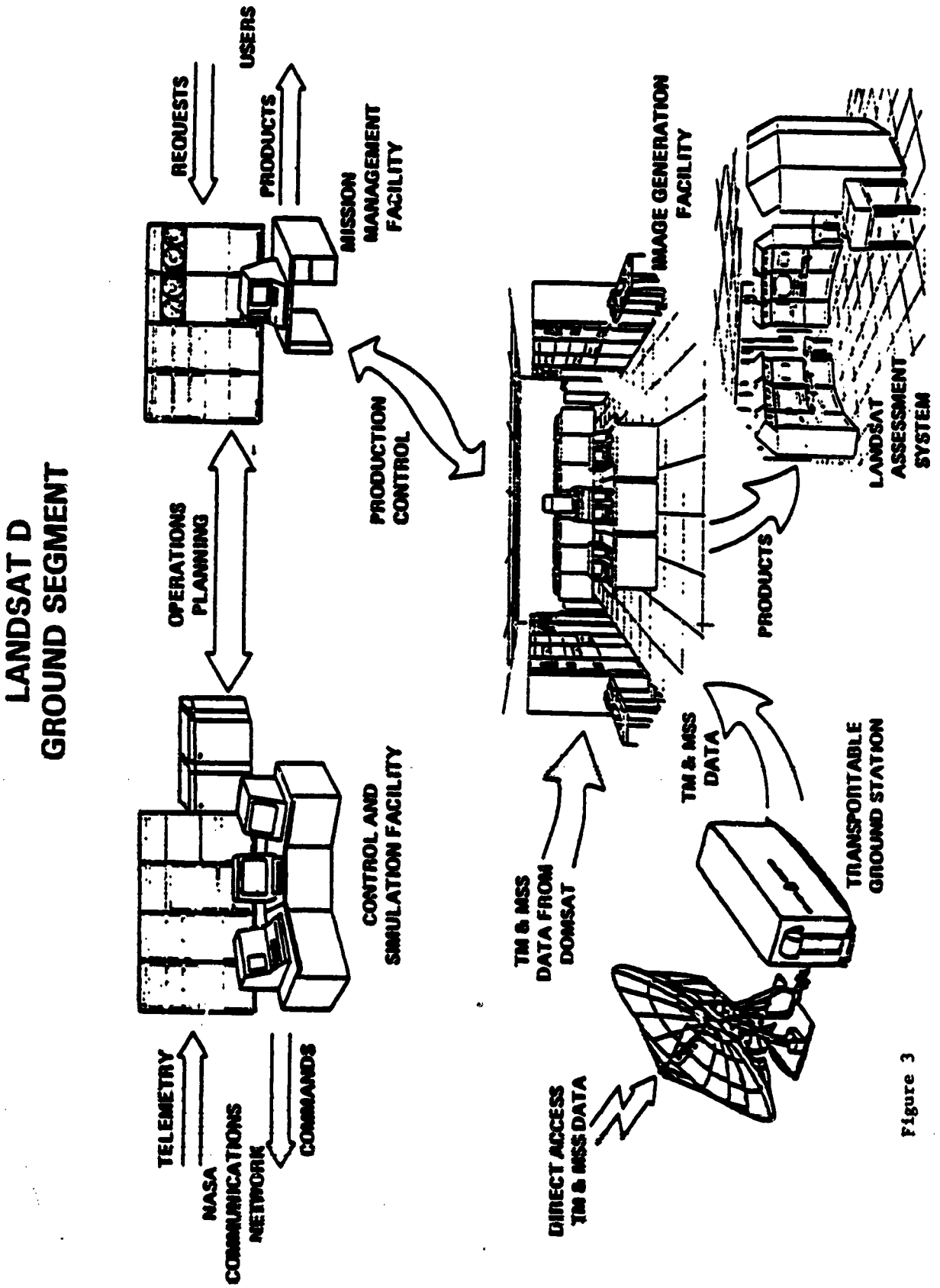

Figure 3

LANDSAT-D GROUND SEGMENT

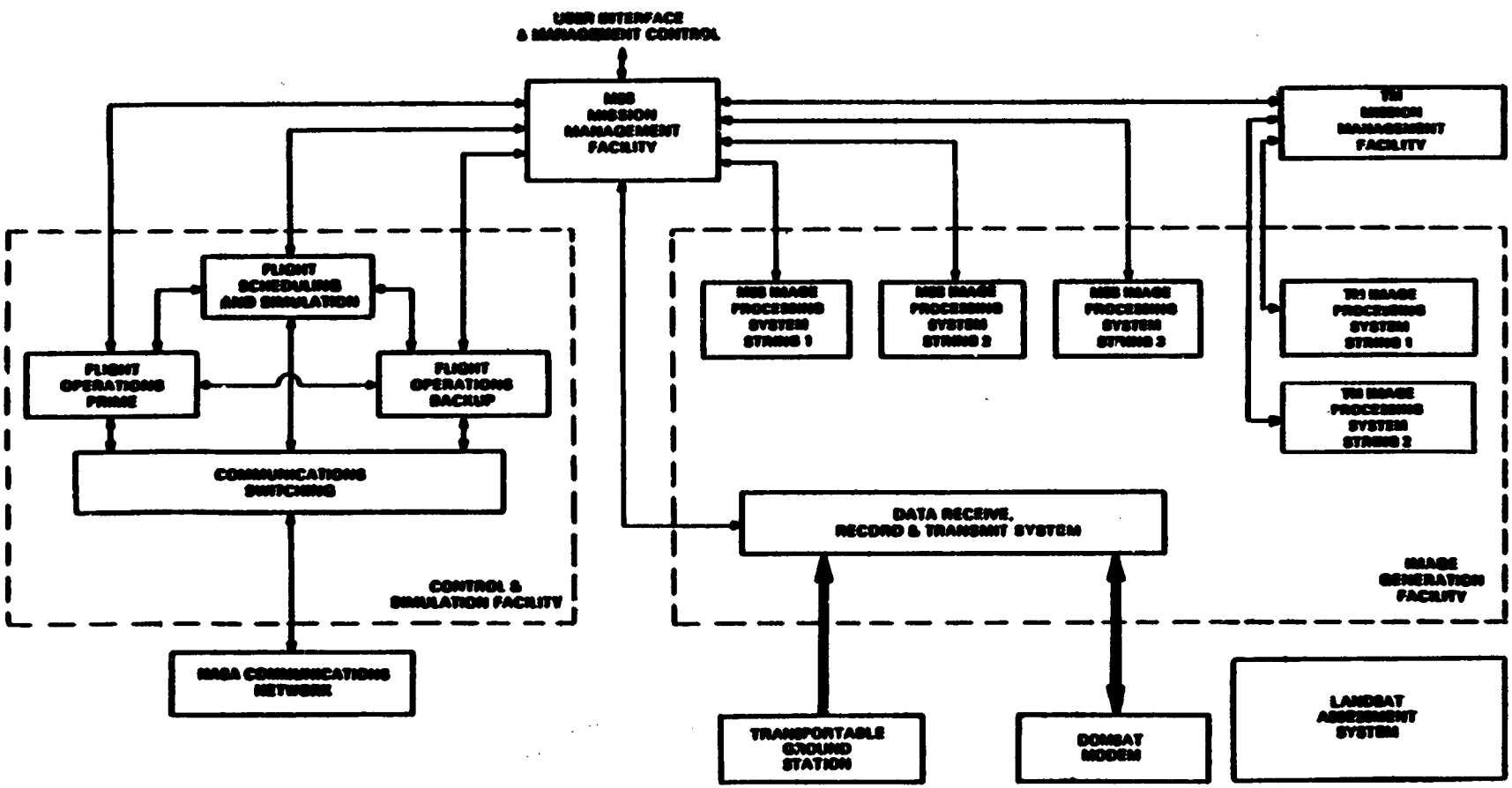

Figure 4

ORIGINAL PAGE IS
OF POOR QUALITY

CONTROL AND SIMULATION FACILITY

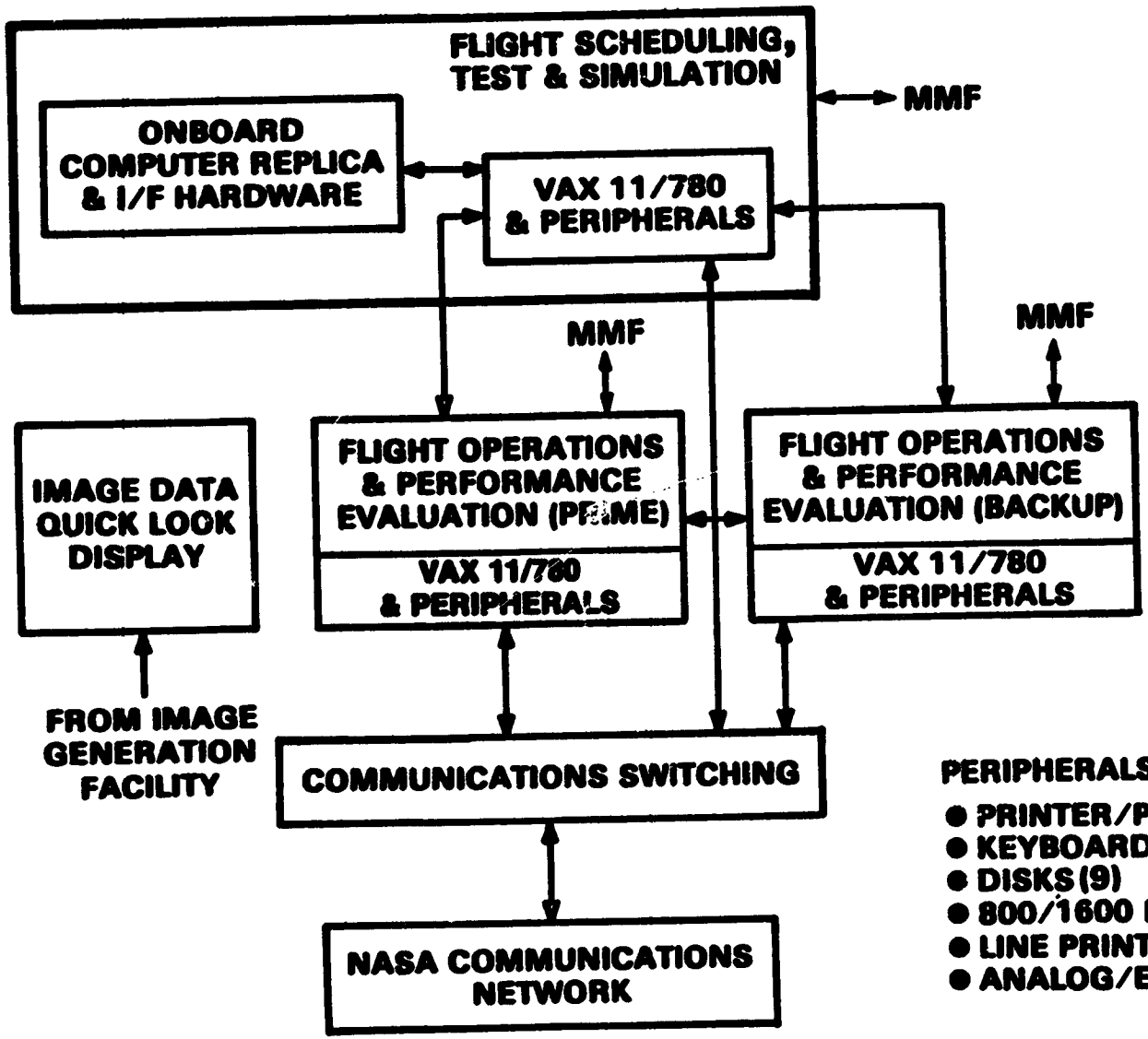

PERIPHERALS INCLUDE

- PRINTER/PLOTTERS (3)
- KEYBOARD/CRT'S (10)
- DISKS (9)
- 800/1600 BPI TAPE UNITS (9)
- LINE PRINTERS (3)
- ANALOG/EVENT RECORDERS (3)

Figure 5

ORIGINAL PAGE IS OF POOR QUALITY

CSF HARDWARE OVERVIEW

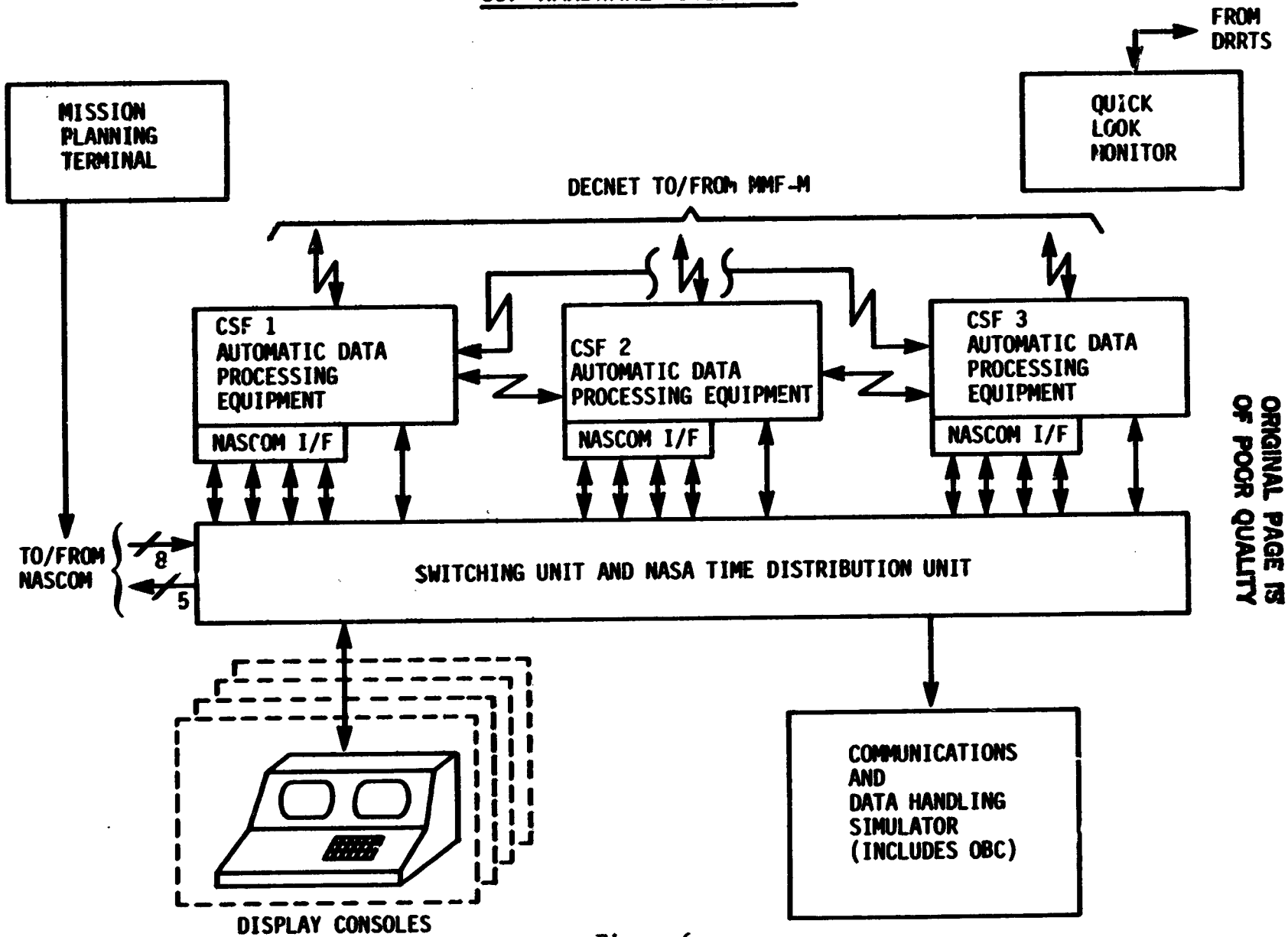

Figure 6

ORIGINAL PAGE IS OF POOR QUALITY

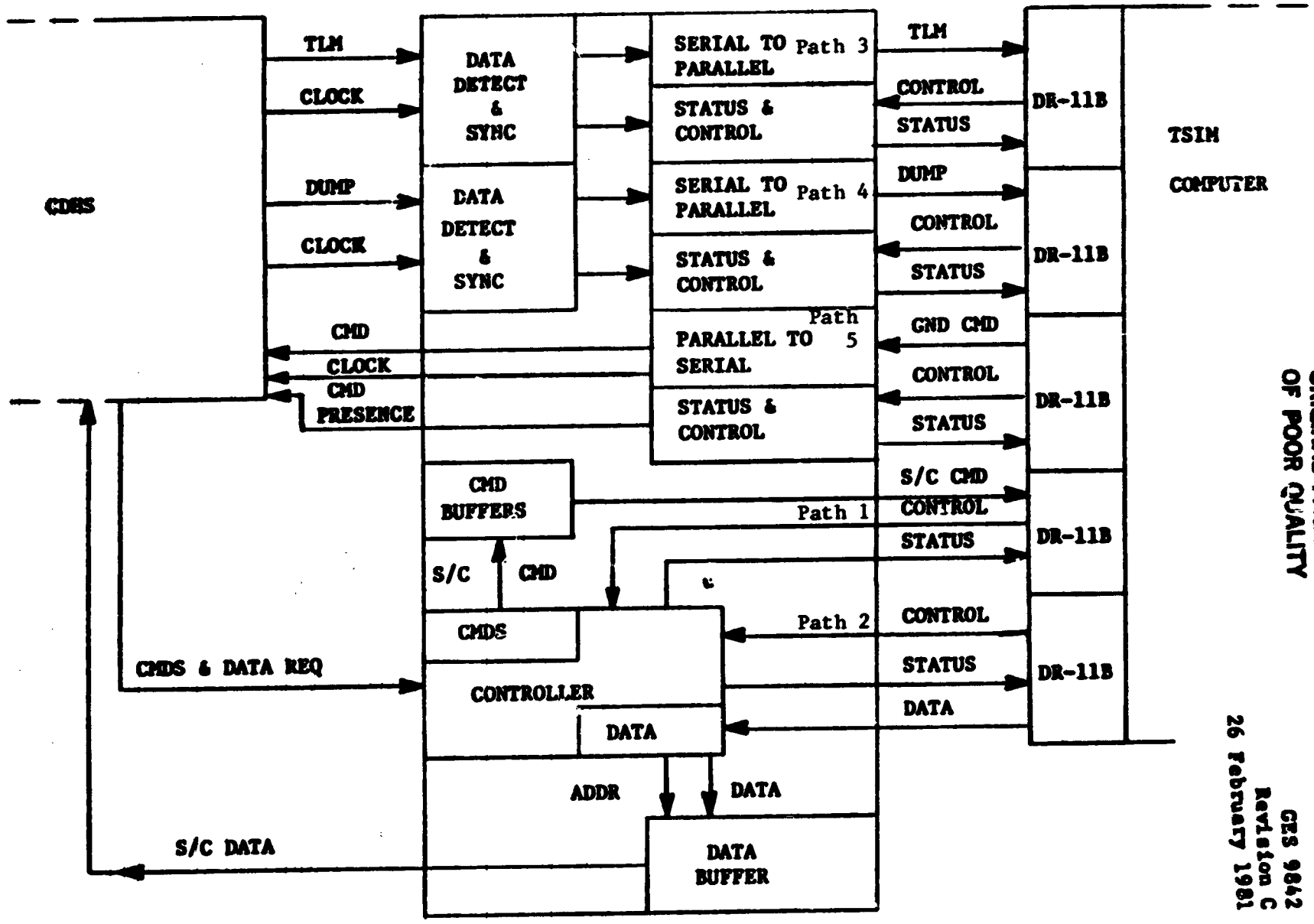

Figure 7 TSIM Interface Unit Block Diagram

ORIGINAL PAGE IS
OF POOR QUALITY

ORIGINAL PAGE IS
OF POOR QUALITY

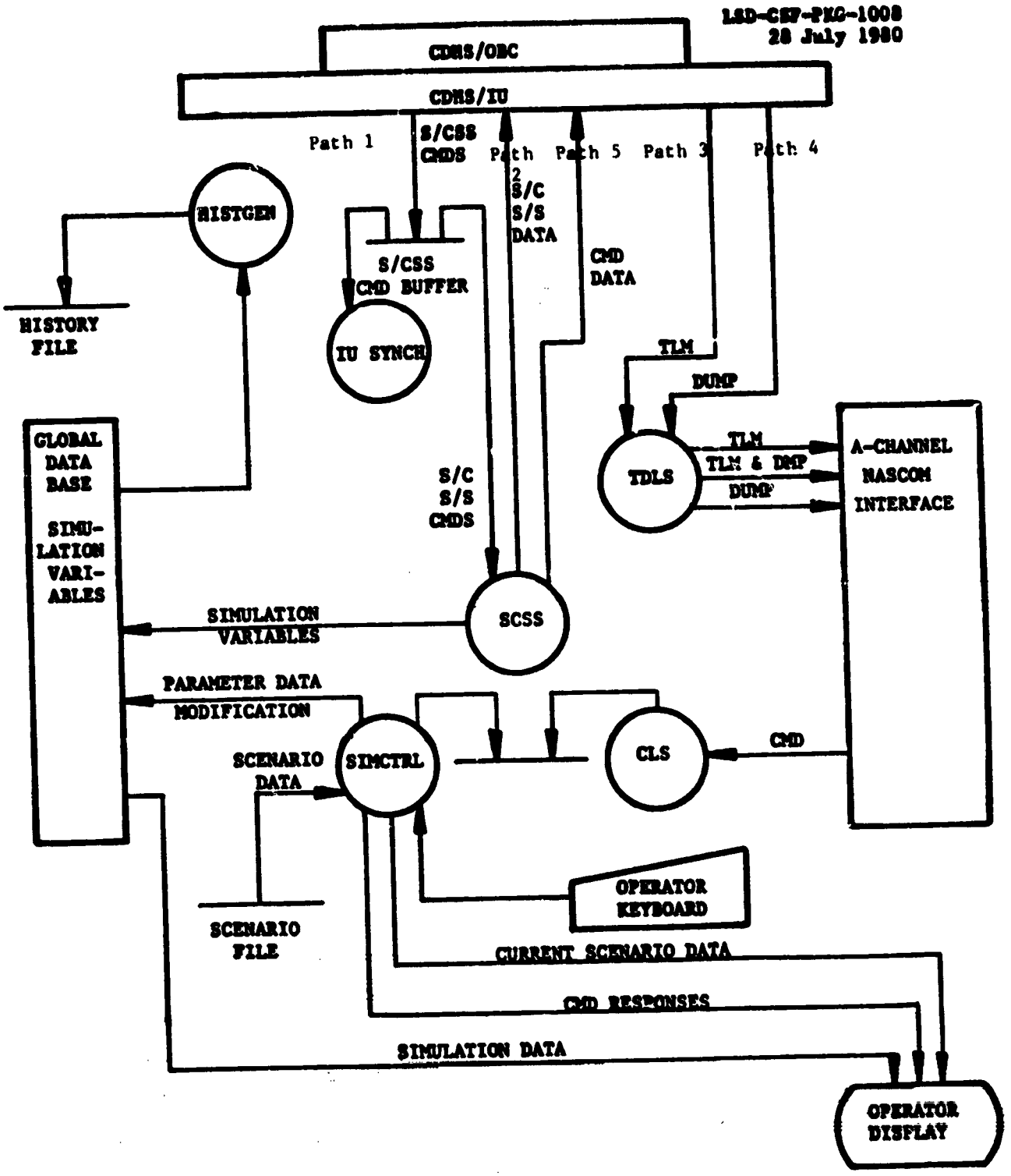

Figure 8 RTSIM Functional Data Flow

PRECEDING PAGE BLANK NOT FILMED

N82 25300

ENVIRONMENTAL TEST FACILITIES USED IN EUROPE FOR ESA SATELLITE PROGRAMMES

Peter W. Brinkmann

European Space Research and Technology Centre ESA/ESTEC
Noordwijk, The Netherlands

ABSTRACT

The paper outlines the structure of the European Space Agency and its largest establishment, ESTEC. In particular it summarises ESTEC's responsibility for allocation and coordination of European environmental test facilities.
The paper describes the major test facilities used for ESA programmes and highlights facility characteristics and special test methods applied for programmes of the Agency.

INTRODUCTION

ESA-EUROPEAN SPACE AGENCY

The purpose of the European Space Agency (ESA), as described in its Convention, is to provide for and promote, for exclusively peaceful purposes, cooperation among European states in space research and technology, and their space applications, with a view to their being used for scientific purposes and for space applications systems. To fulfil its mission the Agency :

a) elaborates and implements a long term space policy, recommends space objectives to its Member States, concerts the policies of the Member States with respect to other national and international organisations and institutions;
b) elaborates and implements activities and programmes in the space field;
c) coordinates the European space programme and national programmes, integrating the latter progressively and as completely as possible into the European space programme, in particular as regards the development of applications satellites;
d) elaborates and implements the industrial policy appropriate to its programme, and recommends a coherent industrial policy to the Member States.

The ten founder members of ESA are Belgium, Denmark, France, Germany, Italy, the Netherlands, Spain, Sweden, Switzerland and the United Kingdom. Ireland, although not a member of the previous space organisations, also signed the ESA Convention in December 1975 and thus is now a full member of the Agency. Three other states are closely associated with the Agency: Austria is an associate member, with the status defined in the Convention; Canada has an agreement for close cooperation; Norway has

observer status but negotiations are under way for this state to acquire associate membership.

The Agency's policy making body is the ESA Council, composed of representatives of the Member States. The Council takes decisions on the policy to be followed by the Agency, and on scientific, technical, administrative and financial matters. The chief executive and legal representative of the Agency is the Director General, who is appointed by the Council. He is assisted by six directors who are responsible for the following directorates: Administration, Applications Programmes, Spacecraft Operations, Scientific Programmes, Space Transportation Systems, and the Technical Directorate.
The ESA organigramme is shown in fig. 1.

ESA ESTABLISHMENTS

ESA's total staff amounts to about 1400 persons, drawn from the Member States and located at the Headquarters and the various establishments.

- The ESA Headquarters is situated in Paris.
- ESOC (European Space Operations Centre) is located at Darmstadt in Germany. It is in charge of all satellite operations and of the corresponding ground facilities and communications networks. The ESOC controlled network includes a central control centre in Darmstadt and telemetry, tracking and control facilities at Michelstadt (Germany), Redu (Belgium), Villafranca (Spain), Kourou (French Guiana) and Carnarvon (Australia). In addition to these sites, the Agency uses the following ground stations: Malindi (Kenya), Fucino (Italy), Kiruna (Sweden) and Maspalomas (Canary Islands/Spain).
- ESRIN (previously European Space Research Institute) is located in Frascati, near Rome, Italy. Two programmes are on site: IRS (Information Retrieval Service), responsible for the operation of the most powerful automated documentation retrieval system in Europe, with a file of more than 18 million bibliographic references; and Earthnet, which collects, preprocesses and distributes images and data from remote-sensing satellites.
- Several technical teams are located in national establishments for the conduct of specific programmes. The Agency also has a liaison office in Washington.
- ESTEC (European Space Research and Technology Centre) is ESA's largest establishment located at Noordwijk in the Netherlands (approx. 35 km from Amsterdam) and has a staff of approx. 1200 (ESA staff and contractors). Most of the project teams and the Technical Directorate are located at ESTEC. The five departments of the Technical Directorate (TD) at ESTEC support the ESA Programme Directorates in studies, design and development of satellites in cooperation with industry and the scientific community. The Technical Directorate is also responsible for applied research in space technology, for standardisation of hardware and software, and for maintenance and extension of competence and capability with respect to technical facilities, mathematical/computer support and product assurance activities. Fig. 2 shows the organigramme of TD. Within the "Assurance, Testing and Mathematical" Department the "Test Services"

Division is in particular responsible for :

- project support for environmental testing;
- study of new facilities and test methods;
- management, operation and maintenance of the ESA environmental facilities;
- engineering facilities;
- management of the laboratory equipment pool;
- coordination of major test facilities in Member States for ESA-programmes.

Fig. 3 shows the ESTEC site.

EUROPEAN TEST FACILITIES

FACILITY COORDINATION

The European Space Agency has developed and maintains major environmental test facilities which are at the disposal of industry, scientific institutes and projects to support Agency programmes as well as space programmes of ESA Member States. Similarly some Member States have established national test centres to support their national programmes.

Therefore European industry and scientific institutes did not have to procure those environmental test facilities, which would not only have required extensive investments but also significant costs for operation and maintenance. In order to avoid duplication of facilities and subsequent underutilisation of facilities in Europe, The Technical Directorate (TD) became responsible for the coordinated use of ESA and major national installations. ESA identified a number of national facilities in Belgium, France and Germany, which were complementary to those of the Agency and indispensable for the execution of the Agency's programme. These together with the ESA facilities form a "facility pool" under the name CETeF (Coordinated European Test Facilities). TD is responsible for the coordination of tests performed in CETeF for all ESA programmes. This includes central planning and liaison between users of facilities (project groups and/or contractors and facility owners). ESA shares a portion of the fixed costs of national CETeF and therefore enjoys a certain priority for the use by its own programmes.

ENVIRONMENTAL TEST FACILITIES

Vibration facilities

The test centres at ESTEC, IABG and CNES are each equipped with one electrodynamic vibrator of the 140 to 170 KN class. (Smaller shakers are available in addition). Solid state amplifiers and digital control and data handling systems have been implemented during the last few years, which has increased reliability and safety on one side and which has improved the flexibility and speed of operations and test evaluation on the other side. The main facility parameters are summarised in table 1.

ESTEC is at present procuring a new 140 KN long-stroke vibrator. Pending approval, a second vibrator of the same type will be installed in the near future. This will enable the implementation of a twin-shaker arrangement allowing tests on specimen with high masses or large dimensions to become compatible with requirements for ARIANE and SHUTTLE payloads.
Fig. 4 shows the present ESTEC vibrator during acceptance tests of the Infrared Astronomy Satellite (IRAS).

Physical-properties-machines and dynamic test facilities

The three environmental test centres are equipped with a set of machines that make it possible to determine the physical properties of specimens; the set includes spin-machines and dynamic balancing machines. The machines at ESTEC can be operated in the 10 meter dynamic test chamber (DTC) under vacuum at pressure levels of about 1 Torr (133 Pa).
Table 1 lists the main existing facilities and characteristics.

EMC and magnetic facilities

a) ESTEC has two well-equipped EMC facilities, which are characterised in table 3. The EMC facilities of national centres do not form part of the CETeF, since there are several facilities in European industry, and this limits the demand for Agency-supplied facilities in this area.

b) The CETeF facility-pool maintains one magnetic test facility at IABG (Germany) which was originally set-up for the German-US cooperative programme "HELIOS".
The facility consists of a large precision coil system with the corresponding power supplies and precise measuring instruments, and a second coil system for magnetisation and demagnetisation. Typical tasks are :

- Measuring the magnetic cleanliness of test objects;
- magnetising and demagnetising test objects to determine permanent, remanent and induced magnetic fields;
- measuring dipole/multipole field distribution surrounding test objects;
- measuring eddy current fields;
- attitude control testing of magnetically stabilised spacecraft;
- calibration magnetometers.

The main element of the facility, which has been constructed from non-magnetic materials exclusively, is a 3-axis square coil system with 4 coils per axis of 15 x 15 m. The free access area is 4 m x 4 m. Fig. 5 shows a sketch of this unique European facility. The earth's field can be compensated within a spherical volume of 3 m with a resolution of 0.1 nT and a homogeneity of $<$ 1 nT. DC field vectors can be established in the range from 0 to 75 000 nT in each axis with an accuracy of approx. 5×10^{-5} respective 0.1 nT.

The magnetisation/demagnetisation system uses square Helmholtz coils (3.7 x 3.7 m) mobile on tracks and provides a homogeneity of $<$ 30%

in a spherical volume of 3 m. The field amplitudes can be varied from 0 to 5 mT within a frequency range of 0.1 to 3 Hz. Fig. 6 shows the GEOS satellite during magnetic tests at IABG.

ESTEC has developed and implemented methods to achieve far-field predictions from near field measurements. Therefore even large satellites w.r.t. the facility dimensions can be tested. (Ref. 1).

Solar simulation facilities -At present the CETeF contain 3 solar simulation facilities of different characteristics. The main parameters are summarised in table 2. The facilities are evacuated with oil-free high-vacuum pumping systems and meet extreme cleanliness requirements. All three facilities are equipped with 2-axis gimbal systems allowing continuous spin motion and attitude motions of ± 180°. Data transmission between satellite and external test equipment (C/O and data handling) is facilitated by specially designed slipring systems. This includes the capacity to transfer several hundred thermocouple data (Copper-Constantan). Refs. 2 and 3 provide details in this respect. The specific characteristics are as follows :

- ESTEC heat balance facility "HBF-3". This facility is equipped with a divergent solar simulator providing a hexagonal beam with an interior hexagon diameter of 2.6 m. Fig. 7 shows the basic layout of this facility. The solar simulator provides a radiation pattern, which is highly symmetric on the one hand, and which has a continuous slope of intensity from the beam-center towards the beam edges on the other hand. It has also been verified that the intensity pattern is preserved in different planes (normal to the beam-axis) within the test volume. These conditions were utilised when establishing a model of the beam characteristics, which enables fairly easy and accurate predictions to be made of incident or absorbed fluxes on satellite surfaces, (Ref. 4). Fig. 8 shows the main beam parameters and fig. 9 presents the relative intensity distribution at the reference plane. The differences between measured and modelled data are very small ($<$ 1%). Fig. 10 shows the Spacelab airlock in "HBF-3" during qualification tests at ESTEC in 1981.
  The "HBF-3" has been equipped with a photogrammetry system, which allows contact-free deformation measurements of specimen during solar simulation or thermal vacuum testing. (This system is under commissioning at present. Expected accuracies $<$ 0.3 mm).

- IABG "3mWSA". This solar simulation facility provides a collimated horizontal beam with a diameter of 2.4 m. With the aim of test cost reductions ESTEC has developped in cooperation with IABG a special test rig for this facility, which permits the simultaneous testing of up to 3 solar panels with dimensions of 1.3 x 1.7 m each in the test facility with a beam diameter of only 2.4 m. In this way the test costs for the ECS/MARECS (ESA Telecommunications Programmes) solar array thermal cycling tests were cut down by 60%. The test set-up and the results are indicated in figs. 11 and 12. (Ref.5)

The "3m-WSA" solar simulation facility will be replaced in the near future by a 6.5 m chamber with a 3.5 m diameter parallel solar beam. The chamber will be denominated "WSA/TVA". It can be used for solar simulation tests as well as for temperature-vacuum-cycling tests.

o CNES "SIMLES". SIMLES is at present the largest solar simulation facility in Europe. It is equipped with a 3 m collimated sun with horizontal beam. Fig. 13 outlines size and shape of this chamber, which has been used for tests on all ESA telecommunication programmes so far. These tests included the simulation of electrostatic discharges on a full scale model of METEOSAT-1 after anomalies of on-board electronics had occurred in orbit.

Large vacuum facility -ESTEC has a large vacuum facility of 10 m diameter and 14 m height, which was originally set-up to perform dynamic tests, such as deployments, balancing, spin tests, etc. at pressure levels of about 1 Torr. It is known as "DTC" (Dynamic Test Chamber). Fig. 14 shows the layout of this facility. During the past years this chamber has been converted into a test facility, which can serve various test purposes utilising the following features:

- A mechanical reference structure insulated from chamber and building motions with mechanical noise of $< 10^{-3}$g serves as a platform for the specimen;
- an oil free high vacuum system (Turbomolecular pumps and LHe-pumps) with high pumping speed (240 000 l/sec) provides a working pressure of $< 10^{-6}$ Torr;
- an LN_2-supply is available to feed test specific shroud systems. (The chamber is not yet permanently equipped with a shroud);
- 6 GN_2 loops can supply 6 independant shroud elements at different temperatures each in the temperature range from -60°C to +60°C;
- a large infrared test rig is available to perform temperature cycling tests on solar arrays. The test rig as shown in fig. 15 is designed to perform a test on the two wings of an INTELSAT-V solar array simultaneously. Fig. 16 shows the preparation of a test on the INTELSAT-V F9 solar array. (Details will be reported in ref. 6).

Two of the more spectacular tests, which were performed in the DTC, were the separation test of the ARIANE nose-cone and the thermal balance test of the Faint Object Camera (F.O.C.), which is an instrument of the Space-Telescope. During the latter test the Space-Telescope environment was simulated by independantly controlled shroud sections. High temperature stability (0.1 degr./12h) and low temperature gradients ($< \pm$ 1.5 degr) were achieved across the 6 sections. The size of each section was 4 m x 1.5 m.

Optical calibration facility. The Institute of Astrophysics at Liège (IAL) has gained large experience in the field of optical calibration and has built special vacuum facilities which have become part of the Agency supported facilities. Among others the facilities were used for the

calibration of the METEOSAT IR-Telescope. Presently, the facilities are required for the Space Telescope/FOC (Faint Object Camera) programme and for support of studies which are performed by ESTEC to promote the application of infrared technology for thermal-vacuum testing (Ref. 7).

Acoustic facility. One test facility for system level tests has been sufficient for European programmes due to the short duration of acoustic tests. This facility is located at IABG. It has a volume of 725 m^3 and can provide a noise level of 152 dB. The lay-out is shown in fig. 17. The French national centre CNES is considering the procurement of a larger facility of 1400 m^3, which will be compatible with future ARIANE 4 payloads.

FUTURE DEVELOPMENTS

The present European facilities are to a large extent capable of performing tests on satellites upto about 1000 kg. Extension and also new facilities will become necessary to cover the requirements of future ARIANE 3 and 4 and also SHUTTLE payloads. With respect to thermal tests ESTEC is in the process of developing and processing hardware and software to implement infrared test methods for the implementation of tests in existing facilities. ESTEC has also proposed the procurement of a large solar simulator with a beam diameter of about 6 m. However, a decision had not yet been taken when this paper was submitted. The implementation of the so called "Multi-Shaker-Systems" with electrodynamic vibrators is envisaged in the near future, and studies for the use of hydraulic shakers are being caried out at present for multi-degree-of-freedom excitation. The advantage of those systems will be high force capabilities, however, the frequency range will be limited to about 200 Hz. Test preparation and satellite integration areas will have to be extended for future programmes also taking into consideration associated electrical and mechanical ground support equipment.

While planning further facility developments and implementation of even larger facilities it is also required to develop test and verification methods utilising existing hardware. Also satellite design will have to take facility limitations into account to a larger extent than previously.

REFERENCES

1. K. Mehlem, Multiple Magnetic Dipole Modeling and Field Prediction of Satellites. IEEE Transaction on Magnetics, Vol. MAG-14, no.5, Sept. 1978.

2. J.B. Walker, The Spacecraft Motion System for ESTEC Heat-Balance Facility HBF-3, ESRO TN-118.

3. L. Simons, A. Voordijk, J.B. Walker, A variable Temperature Reference Junction for Thermocouples Developed for the Measurements of Spacecraft Temperatures during Thermal Vacuum Tests, ESRO TN-111.

4. P.W. Brinkmann, Methods of Determining Intensity Levels at Points or Areas within the Test Volumne of the Divergent Solar Simulator of the HBF-3 at ESTEC, ESRO TN-119.

5. P.W. Brinkmann, J. Reimann, Efficient Thermal Cycling of Solar Panels in Solar Simulation Facilities with a Multi-Panel Test Rig, ESA-SP-147, June 1980.

6. P. Bonnot, P.W. Brinkmann, Large Infrared Test Rig for Vacuum Temperature Cycling Tests in the ESTEC DTC. Paper in preparation for 3rd European Symposium on Photovoltaic Generators in Space. (May 1982).

7. G.B.T. Tan, J.B. Walker, Spacecraft Thermal Balance Testing Using Infrared Sources. 12th AIAA Space Simulation Conference NASA CP-, 19 (Paper of this compilation).

Table 1. Mechanical Tests

EUROPEAN COORDINATED ENVIRONMENTAL TEST FACILITIES (CETeF) - ABSTRACT-

Status: January 1982

TYPE OF TEST	MACHINE SPECIFIC	GENERAL CHARACTERISTICS					LOCATION
		Shaker Force	Amplifier	Control Modes	Sliptable	Data Handling	
Vibration	Electrodynamic Shaker	140 KN	192 kva	sinus random	yes	108 channels	ESTEC
		70 KN		" "	yes	108 channels	ESTEC
		170 KN	150 kva	" "	yes	84 channels	CNES
		160 KN	196 kva	" "	yes	72 channels	IABG
Physical Measurements		ADMISSIBLE LOAD					
	Center of Gravity	3 facilities mass	from 2 kg to 2000 kg				ESTEC
		1 facility	up to 1130 kg				CNES
		1 facility	up to 600 kg				IABG
	Moment of Inertia	3 facilities mass	from 2 kg to 2000 kg				ESTEC
		1 facility	up to 1000 kg				CNES
		1 facility	up to 2000 kg				IABG
	Dynamic Balance		up to 1000 kg (upgrading envisaged)				ESTEC
			up to 2000 kg				CNES
			up to 600 kg				IABG
	Spin		up to 1400 kg (upgrading envisaged)				ESTEC
			up to 1500 kg				CNES
			up to 750 kg				IABG
Acoustic	Reverberant Chamber	volume 725 m^3	noise level 152 dB		data handling		IABG
Dynamic Tests (deployment etc.)	Vacuum Vessel DTC (see also table 2)	volume ø 10 m, height 14 m, pressure 1 torr for mechanical tests; can accomodate MOI and dynamic balance machines for high accuracy measurements; spin table interface available in DTC.					ESTEC

NOTE: up to date information and full details of above facilities are available on request in TEST SERVICES DIVISION / ESTEC

ORIGINAL PAGE IS OF POOR QUALITY

Table 2. Thermal Tests EUROPEAN COORDINATED ENVIRONMENTAL TEST FACILITIES (CETeF) - ABSTRACT -

Status: January 1982

TYPE OF TEST	MACHINE SPECIFIC	GENERAL CHARACTERISTICS						LOCATION
		Int.dimensions	Vacuum/ torr	Temp.	Sun Simulator	Spin Attitude Control	Data Handl. Temp.	
Solar Simulation	HBF3	Ø 3m x 4m high	5.10^{-7}	LN2	Ø 2.6m divergent	700 kg	284 cha	ESTEC
	SIMLES	Ø 6m x 7m high	5.10^{-7}	LN2	Ø 3m parallel	1500 kg	317 cha	CNES
	3m-WSA 1)	Ø 3m x 5.5m long	1.10^{-6}	LN2	Ø 2.4m parallel	1000 kg	280 cha	IABG
Thermal Vacuum		Int.dimensions	Vacuum/Torr	Temperature				
	VTCA	Ø 1.5m x 2.5m high	$<1.10^{-5}$	150° k to 400° k				ESTEC
	Corona	Ø 1.5m x 2.5m high	$<1.10^{-4}$ (22 sec)	-				ESTEC
	VTC 0.6	$0.6\ m^3$	$<1.10^{-5}$	123° k to 423° k				ESTEC
	VTC 0.4 (3)	$0.4\ m^3$	$<1.10^{-5}$	123° k to 423° k				ESTEC
	Ultra high vac	$0.5\ m^3$	$<1.10^{-10}$	up to 523° k				ESTEC
	Ultra high vac	$0.3\ m^3$	$<1.10^{-10}$	up to 523° k				ESTEC
Special Application (IR-Tests etc.)	Vacuum Chamber DTC	Ø 10m x 14m high	$<1.10^{-6}$	I.R. radiation sources and shrouds tailored to test requirements Large I.R./LN2-test-rig for T/V-tests on 2 flat panels/ arrays with dim. upto max. 6 x 2.5m each.				ESTEC

1) This facility is being replaced by a 6.8m chamber with a 3.5m Solar Simulator

NOTE: up to date information and full details of above facilities are available on request in TEST SERVICES DIVISION / ESTEC

ORIGINAL PAGE IS OF POOR QUALITY

Table 3. Other Facilities EUROPEAN COORDINATED ENVIRONMENTAL TEST FACILITIES (CETeF) - ABSTRACT -

Status: January 1982

TYPE OF TEST	MACHINE SPECIFIC	GENERAL CHARACTERISTICS	LOCATION
Magnetic	Magnetic Facility	magnetic properties - AC field <0.1 gamma RMS magnetic simulation - zero field: Resolution <0.1 nT DC field : sphere Ø 3 m; homogeneity <1 nT AC field : 0 Hz to 20 KHz - 0 to 10000 nT x Hz	IABG
EMC	EMC-Ternois	int.volume: 6m x 5.5m x 5.25m high-frequency up to 18 GHz	ESTEC
	EMC-Belling & Lee	int.volume: 4.7m x 3.7m x 4m high-frequency up to 12.4 GHz	ESTEC
Optical calibration under thermal vacuum	Large Chamber	int.volume Ø 1.80m; vacuum 1.10^{-6}/Torr; temp. -70° + 50°C optical bench 0.80m x 4m inside the chamber	IAL
	Small Chamber	int.volume Ø 1.00m; vacuum 1.10^{-5}/Torr; temp. -70° + 50°C	IAL
Alignment	Modular Alignment Equipment	2 laser autocollimators 1 reference mirror Ø 1m mounted onto a moving frame 2 alignment tables with attached optics (beam splitters and mirrors) span: 3m x 1,1m number of alignment units: variable (maximum available 20) reading accuracy: with occular -5" in a field of view of 10' 8" " " " " " " 1° on TV screen -2" " " " " " " 10' 8" " " " " " " 1°	ESTEC

NOTE: up to date information and full details of above facilities are available on request in TEST SERVICES DIVISION / ESTEC

ORIGINAL PAGE IS OF POOR QUALITY

ORIGINAL PAGE IS
OF POOR QUALITY

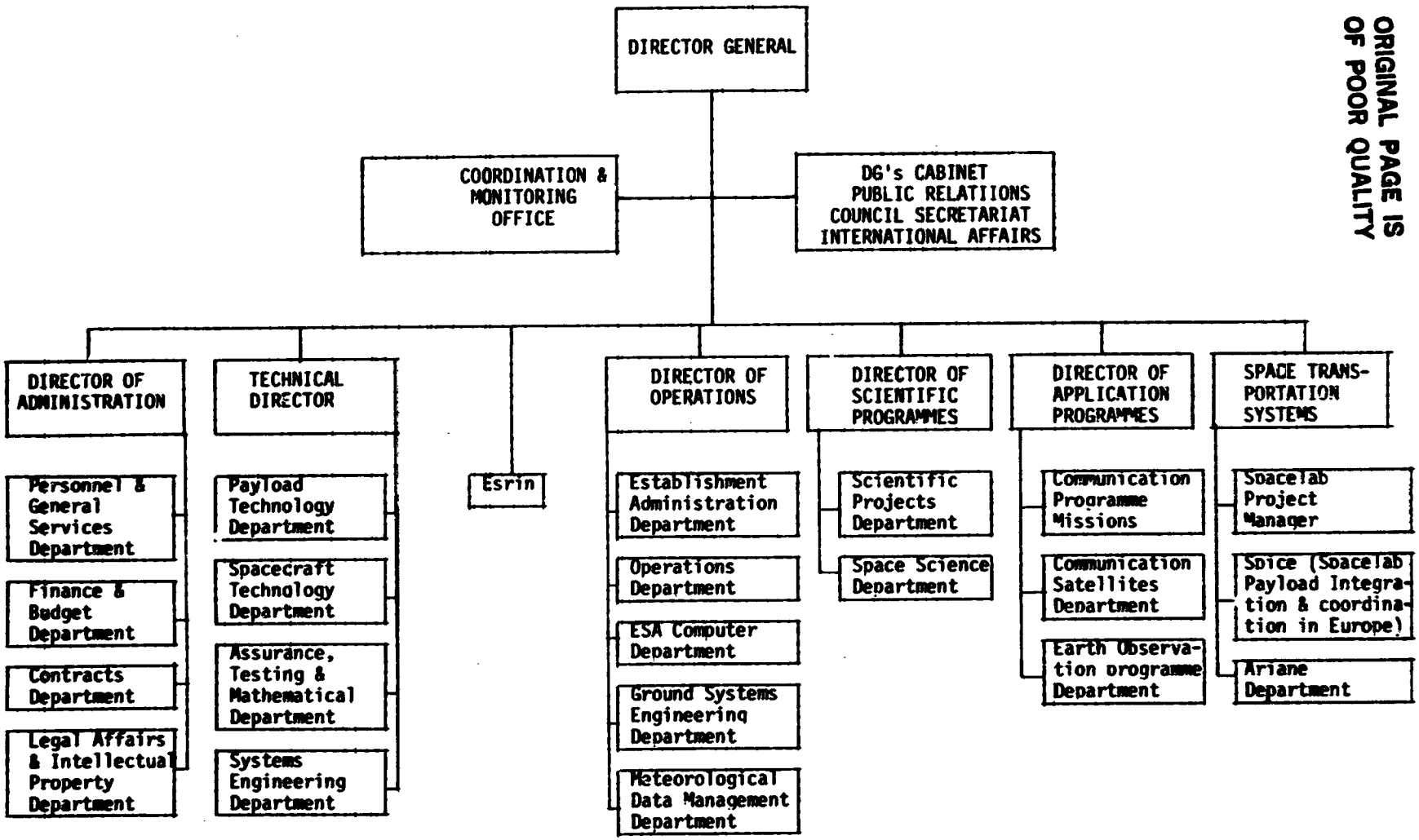

Fig. 1 ESA-Organigramme

(Nov. '81)

ORIGINAL PAGE IS
OF POOR QUALITY

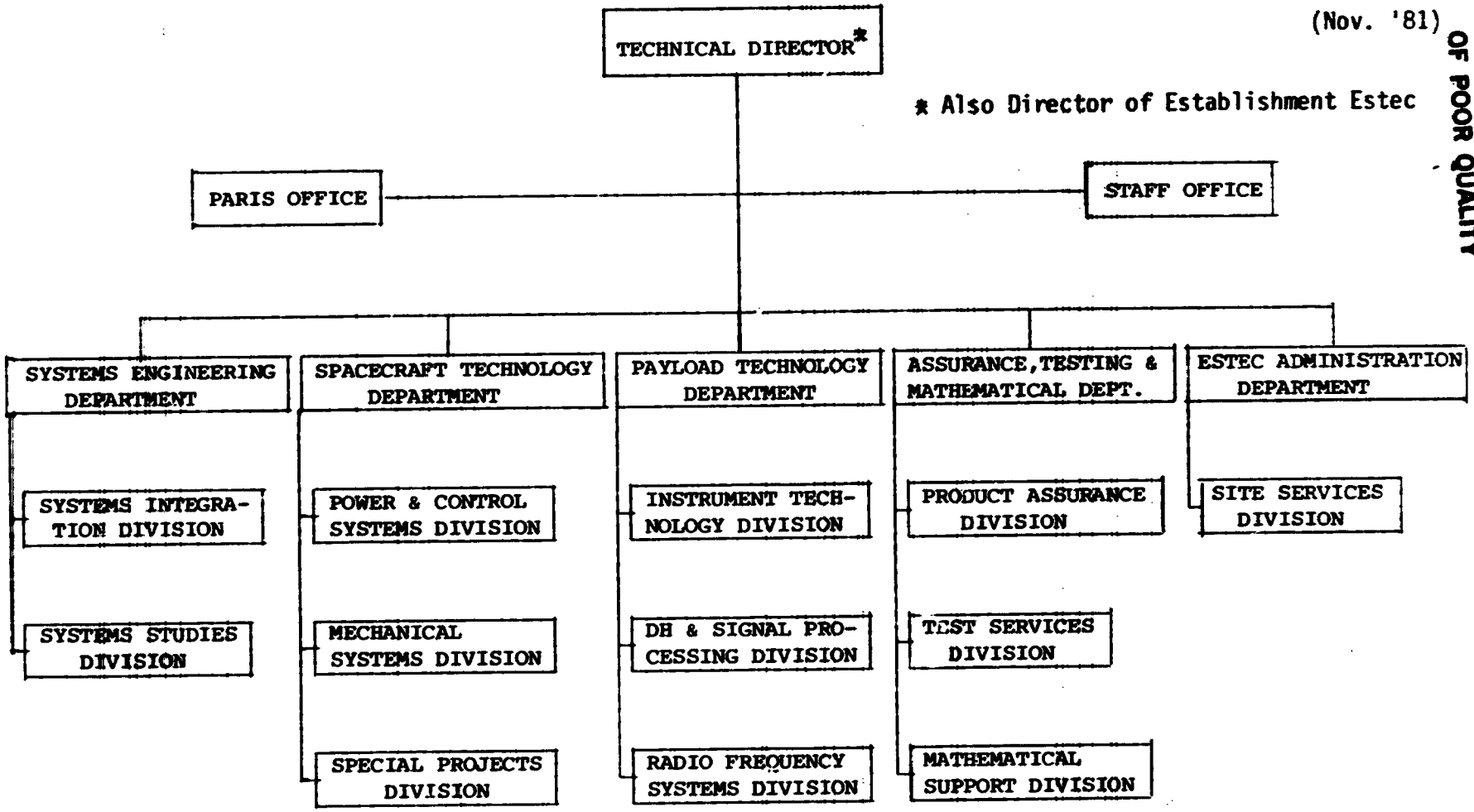

Fig. 2 Organigramme of the Technical Directorate at ESTEC

ORIGINAL PAGE
BLACK AND WHITE PHOTOGRAPH

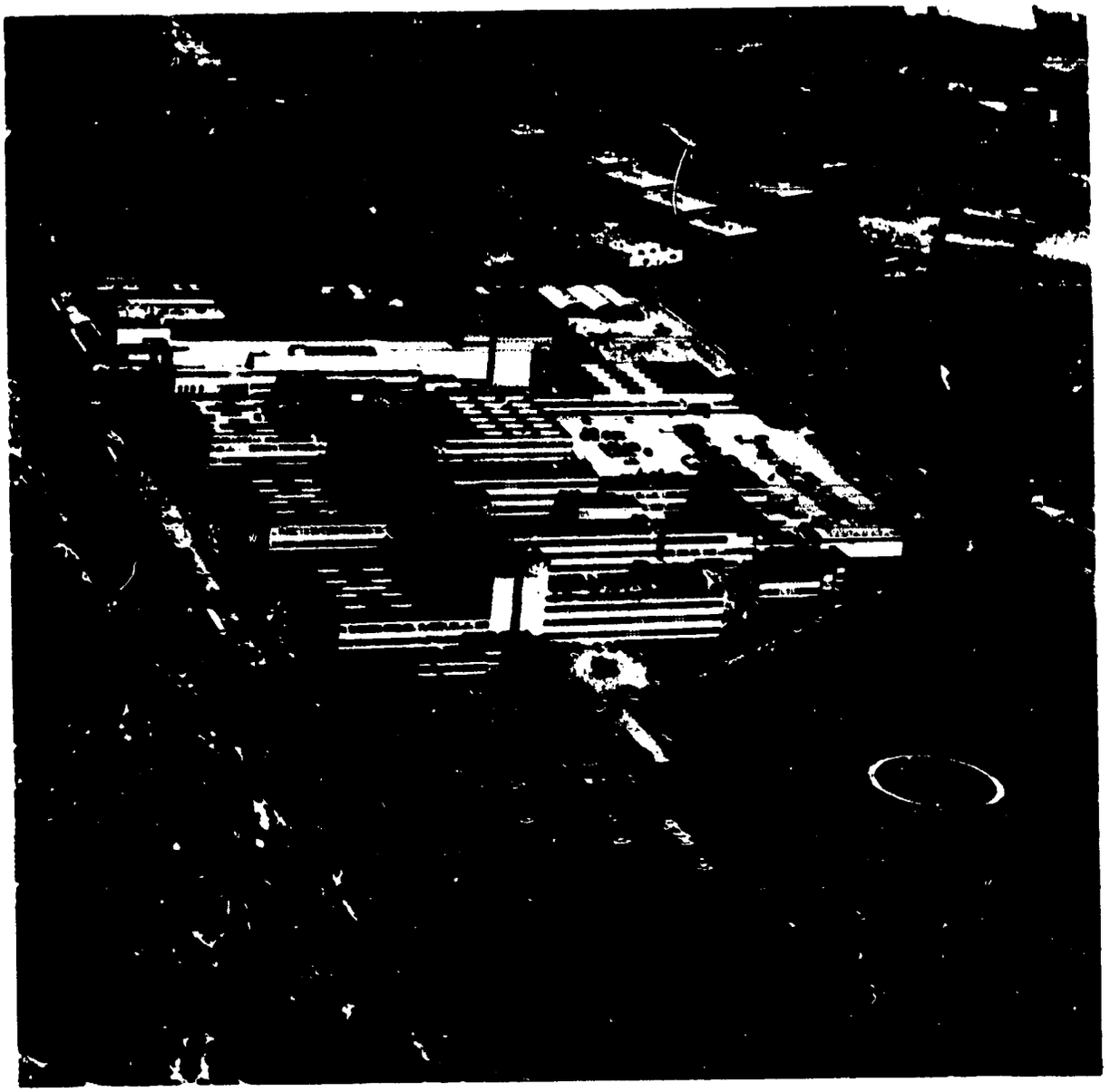

Fig. 3 View of the ESTEC Site at Noordwijk, the Netherlands

ORIGINAL PAGE
BLACK AND WHITE PHOTOGRAPH

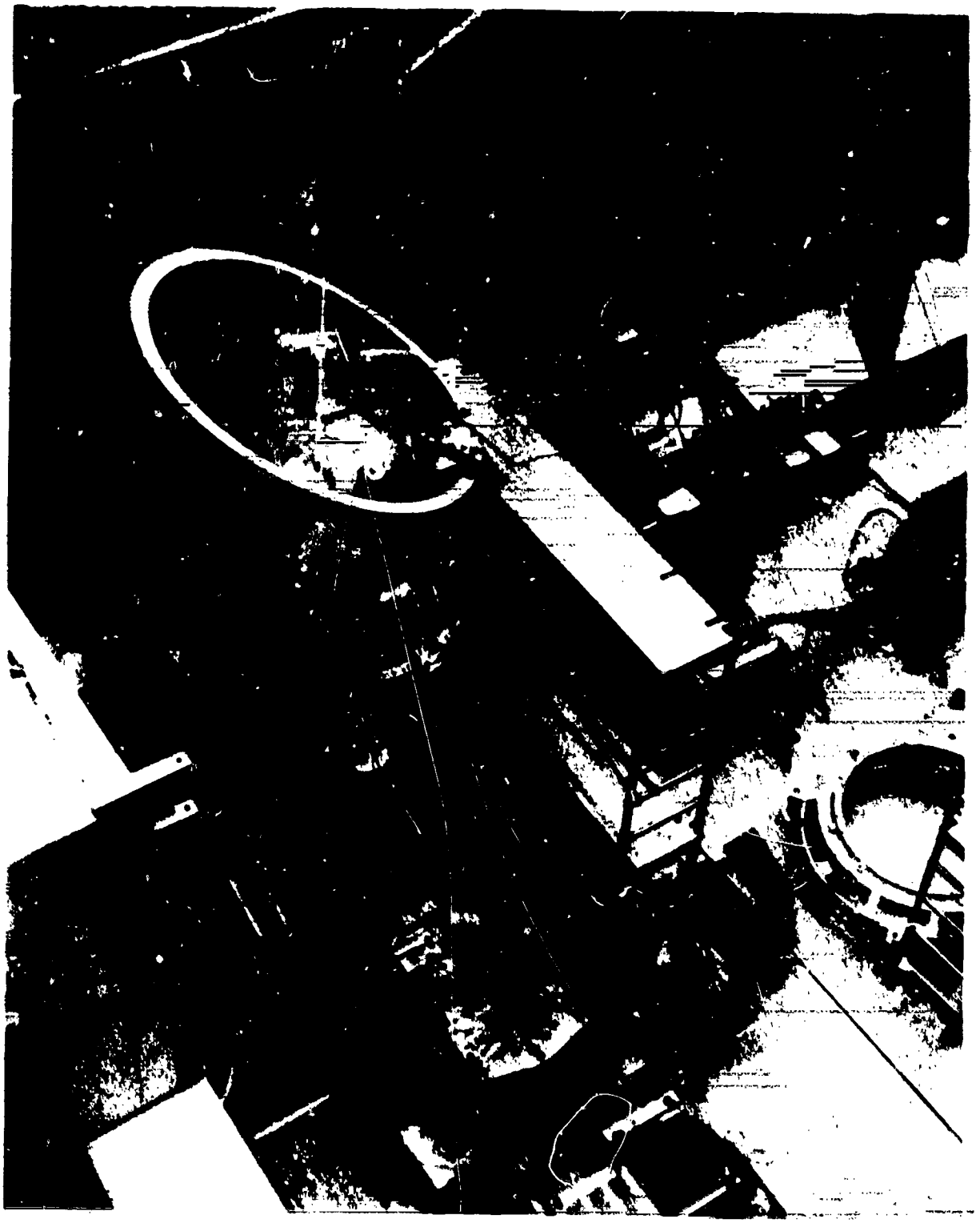

Fig. 4 The Infrared Astronomy Satellite (IRAS) on the ESTEC 140 KN Vibrator

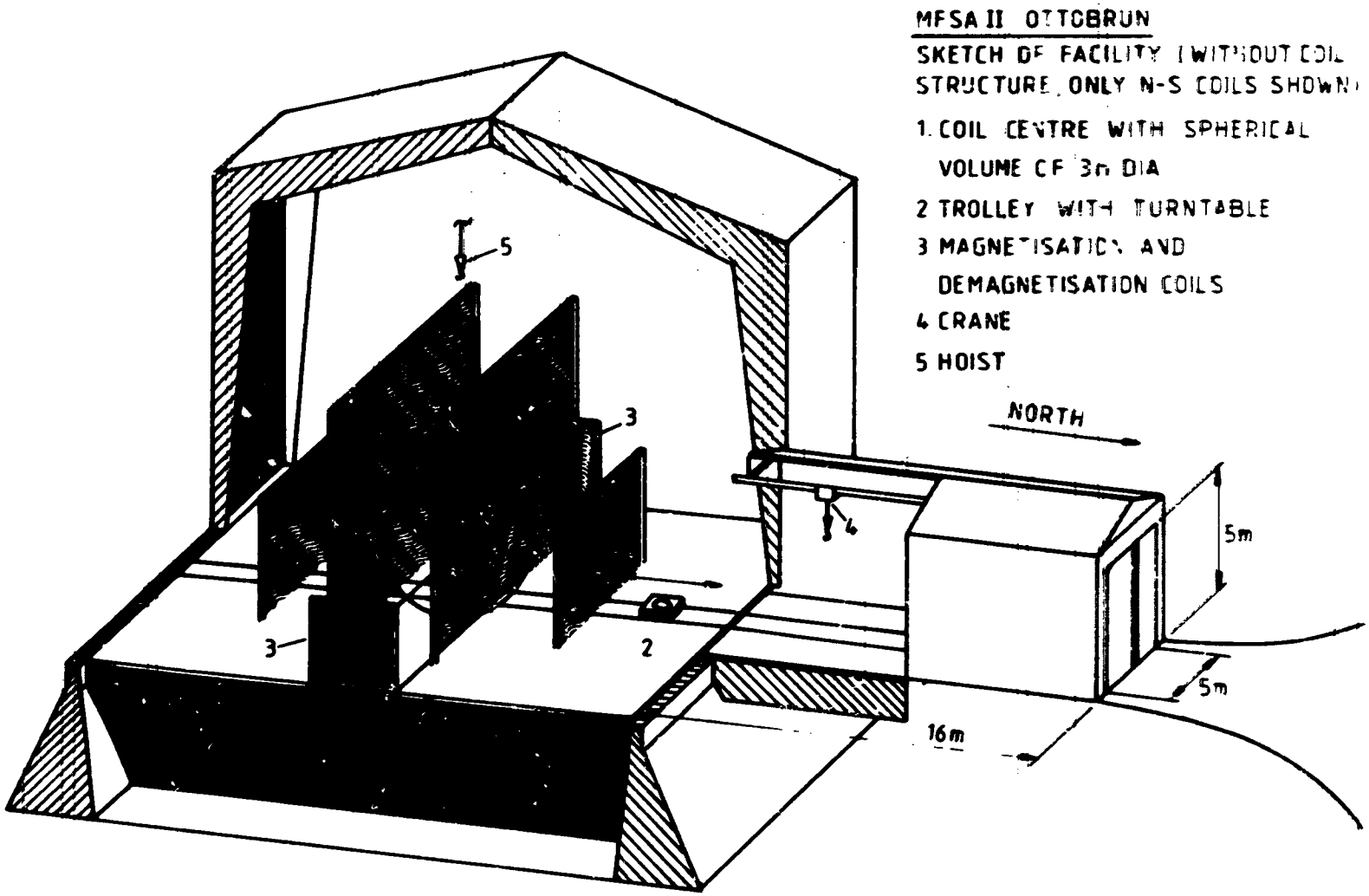

Fig. 5 Sketch of the Magnetic Test Facility at IABG

ORIGINAL PAGE
BLACK AND WHITE PHOTOGRAPH

ORIGINAL PAGE
BLACK AND WHITE PHOTOGRAPH

Fig. 6 Scientific Satellite (GEOS) in the Magnetic Test Facility at IABG

ORIGINAL PAGE IS
OF POOR QUALITY

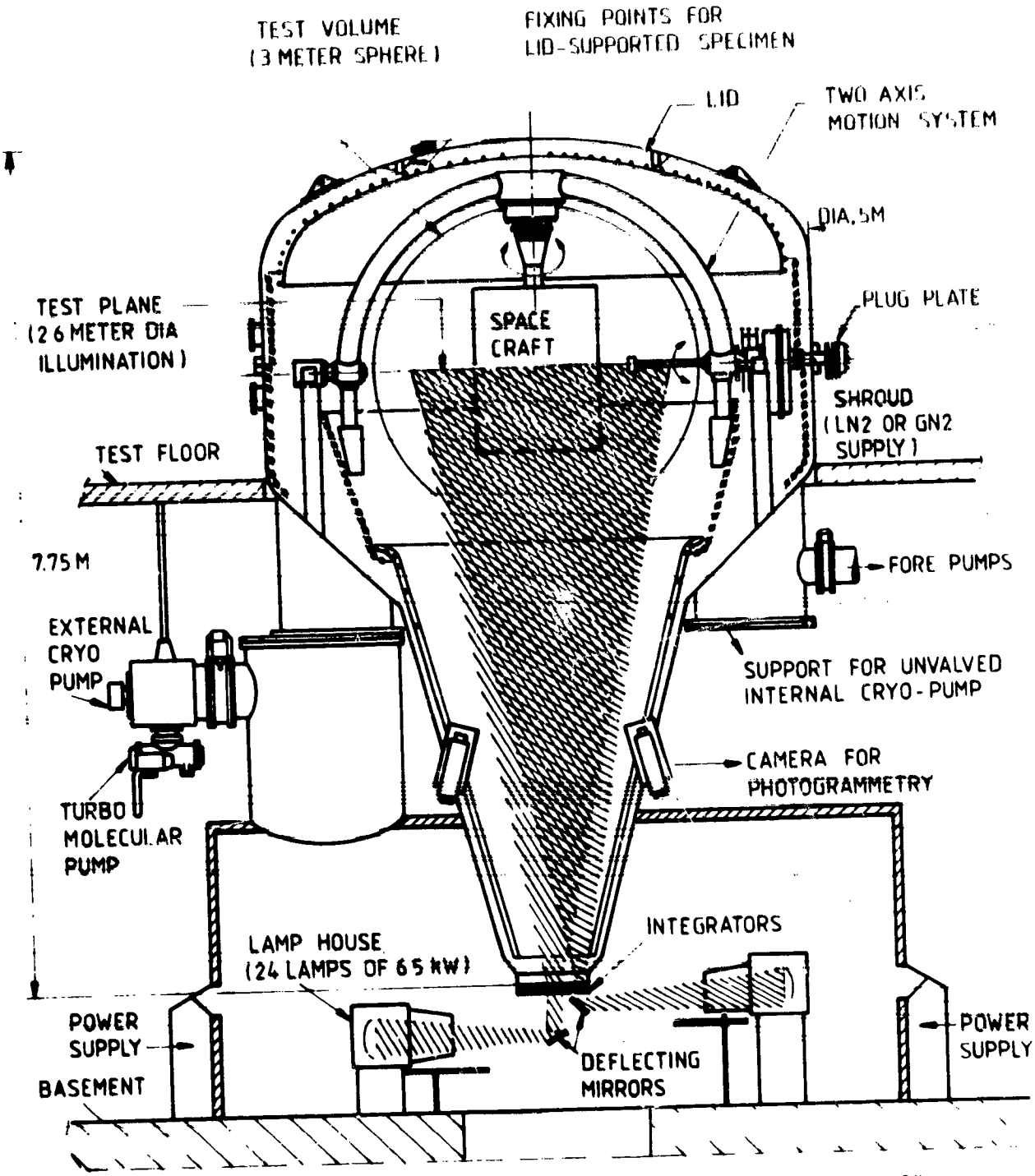

Fig. 7 Lay-out of the ESTEC Heat Balance Facility "HBF-3"

ORIGINAL PAGE IS
OF POOR QUALITY

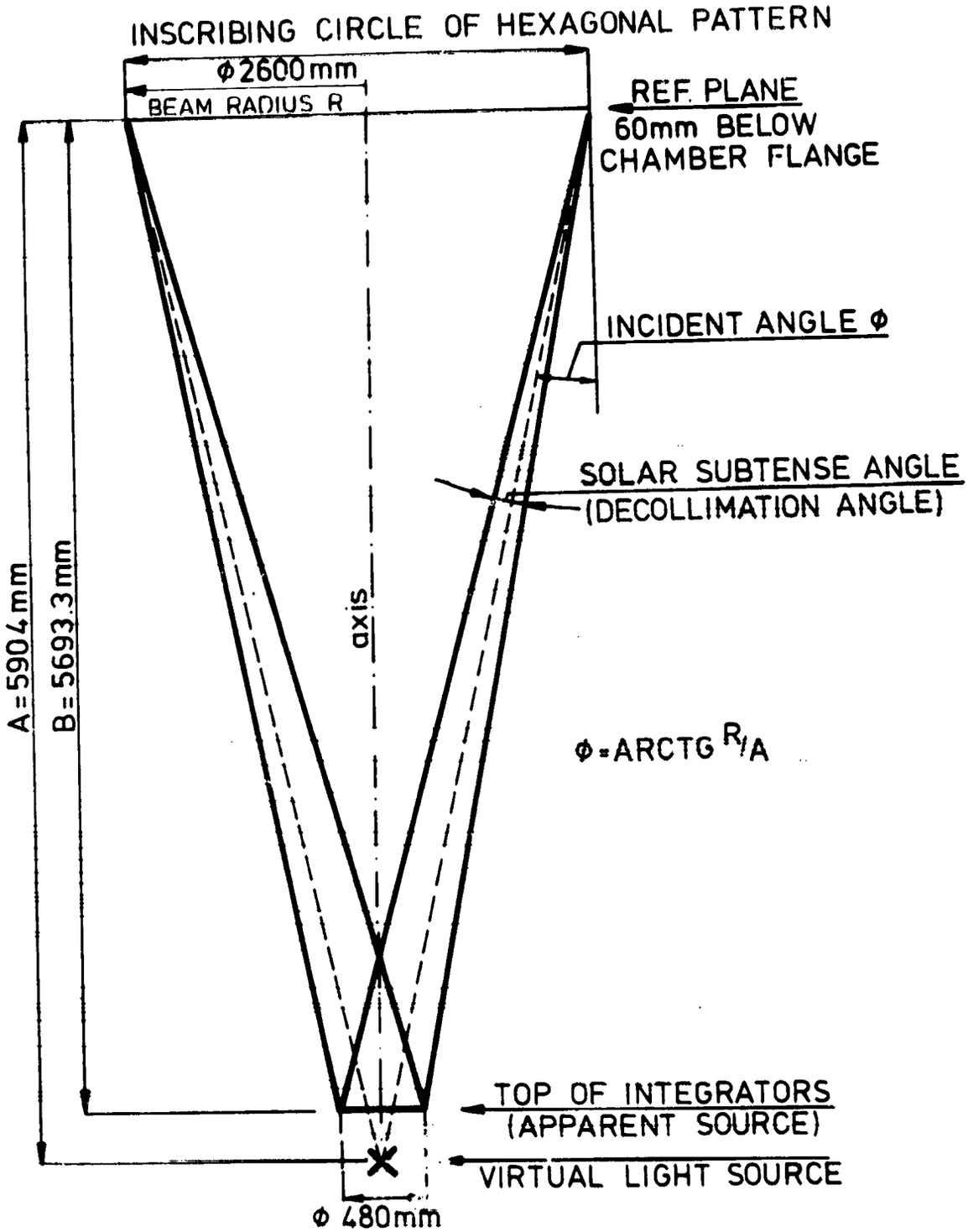

Fig. 8 Main Solar Beam Parameters of ESTEC HBF-3

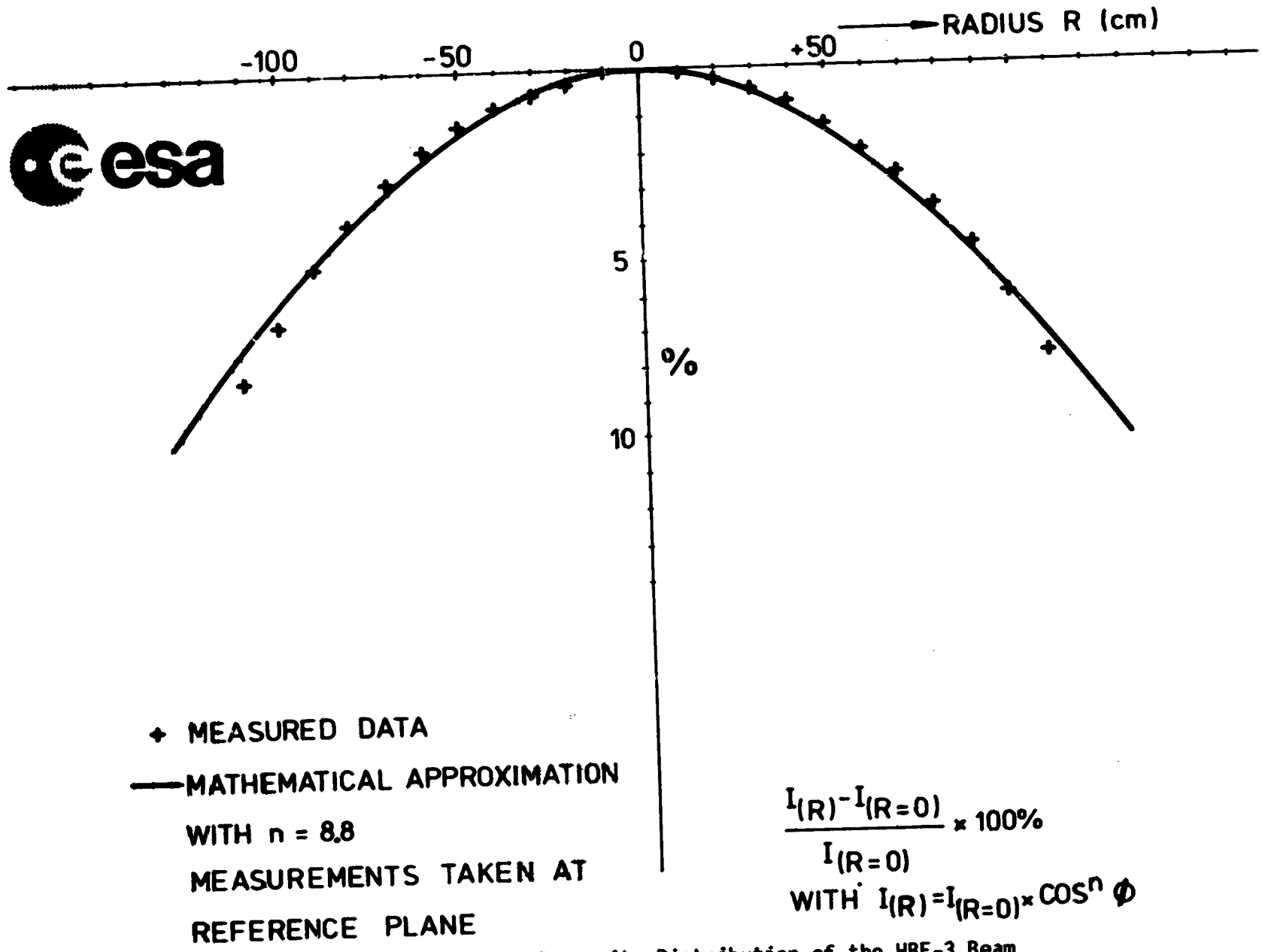

Fig. 9 Relative Intensity Distribution of the HBF-3 Beam

ORIGINAL PAGE IS
OF POOR QUALITY

ORIGINAL PAGE
BLACK AND WHITE PHOTOGRAPH

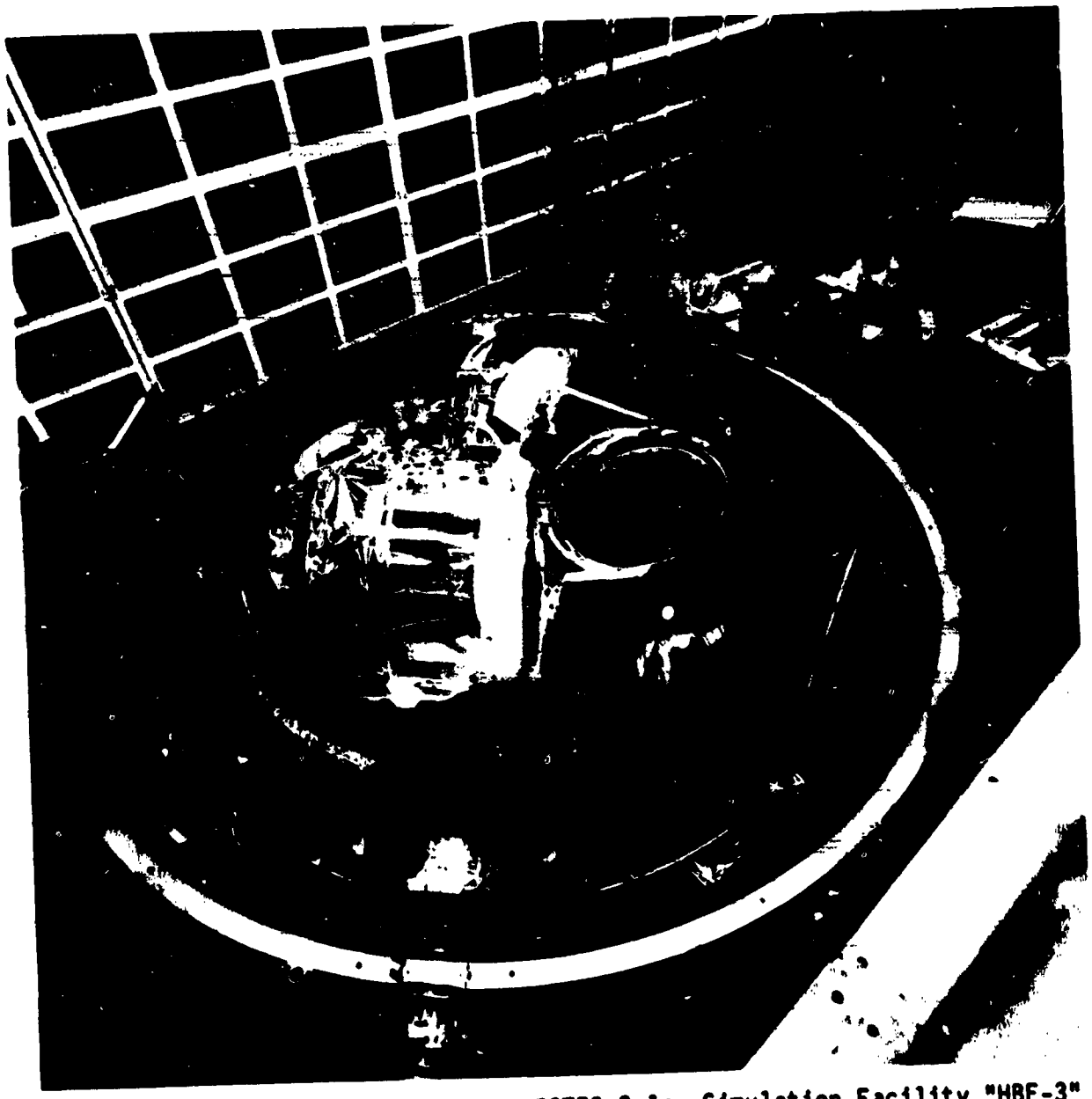

Fig. 10 Spacelab Airlock in the ESTEC Solar Simulation Facility "HBF-3"

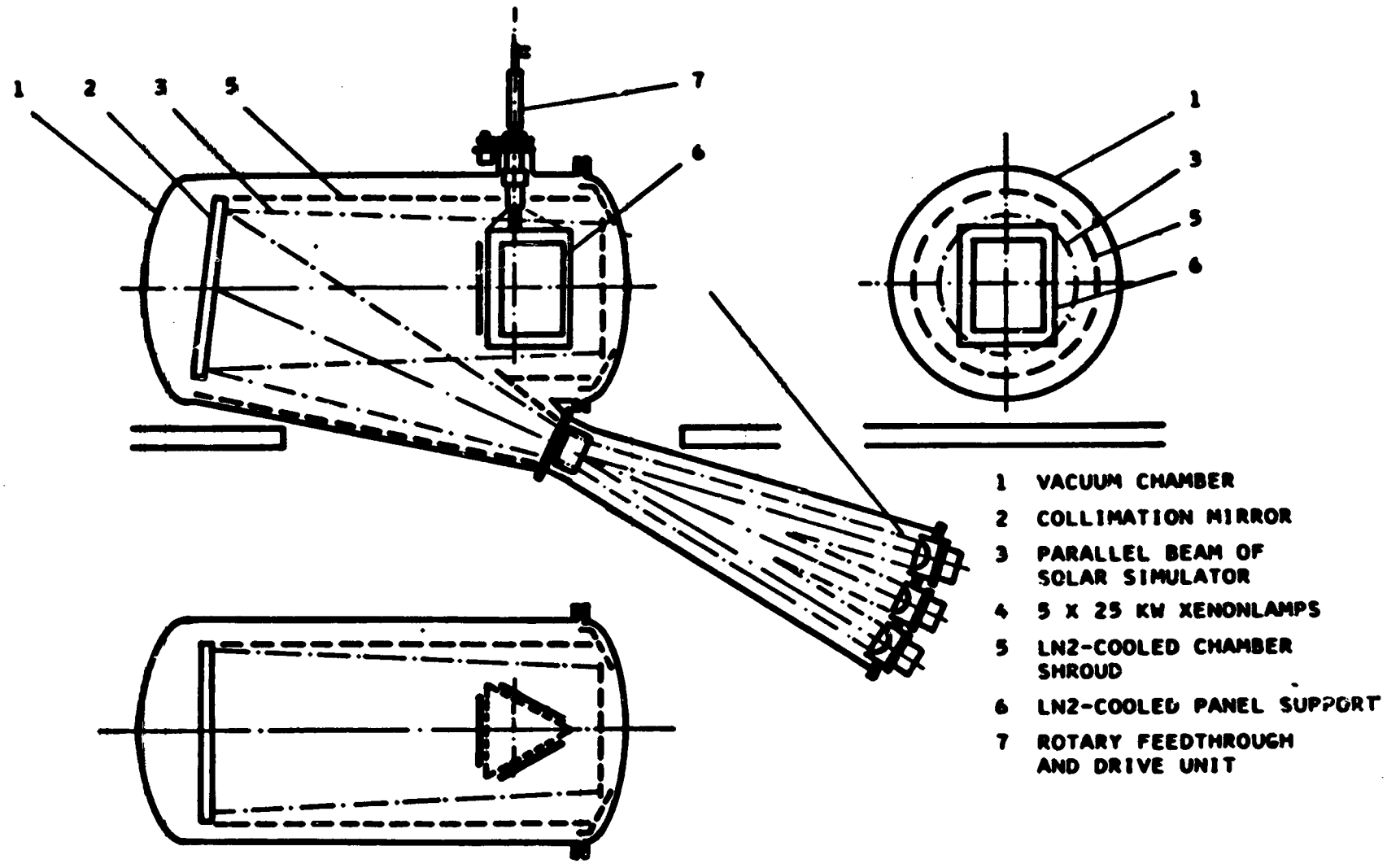

Fig. 11 Multi-Panel Test Rig in the IABG Solar Simulation Facility "3mWSA"

ORIGINAL PAGE IS
OF POOR QUALITY

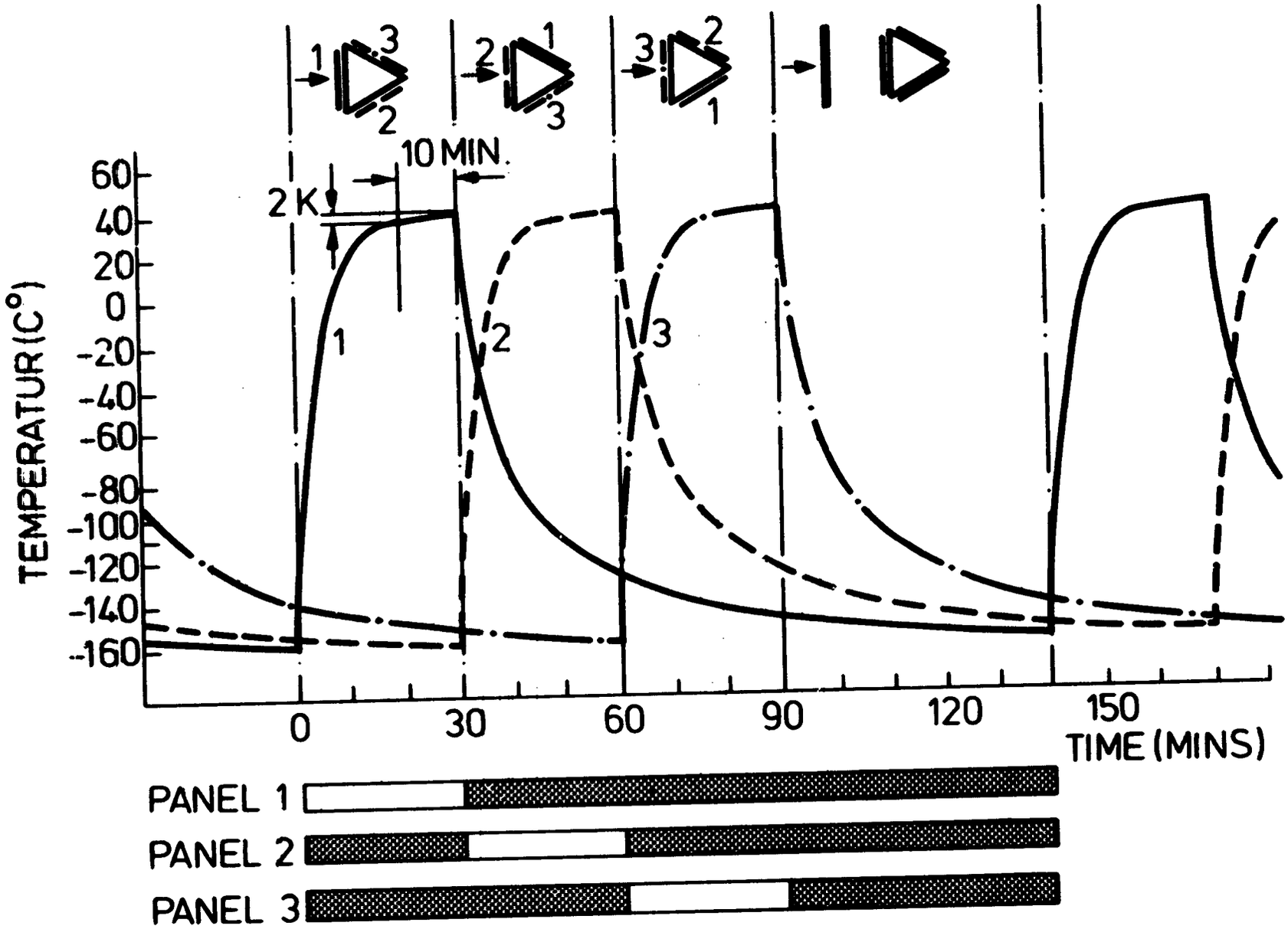

Fig. 12 Temperature Profile achieved with Multi-Panel-Test-Rig

ORIGINAL PAGE IS
OF POOR QUALITY

ORIGINAL PAGE IS
OF POOR QUALITY

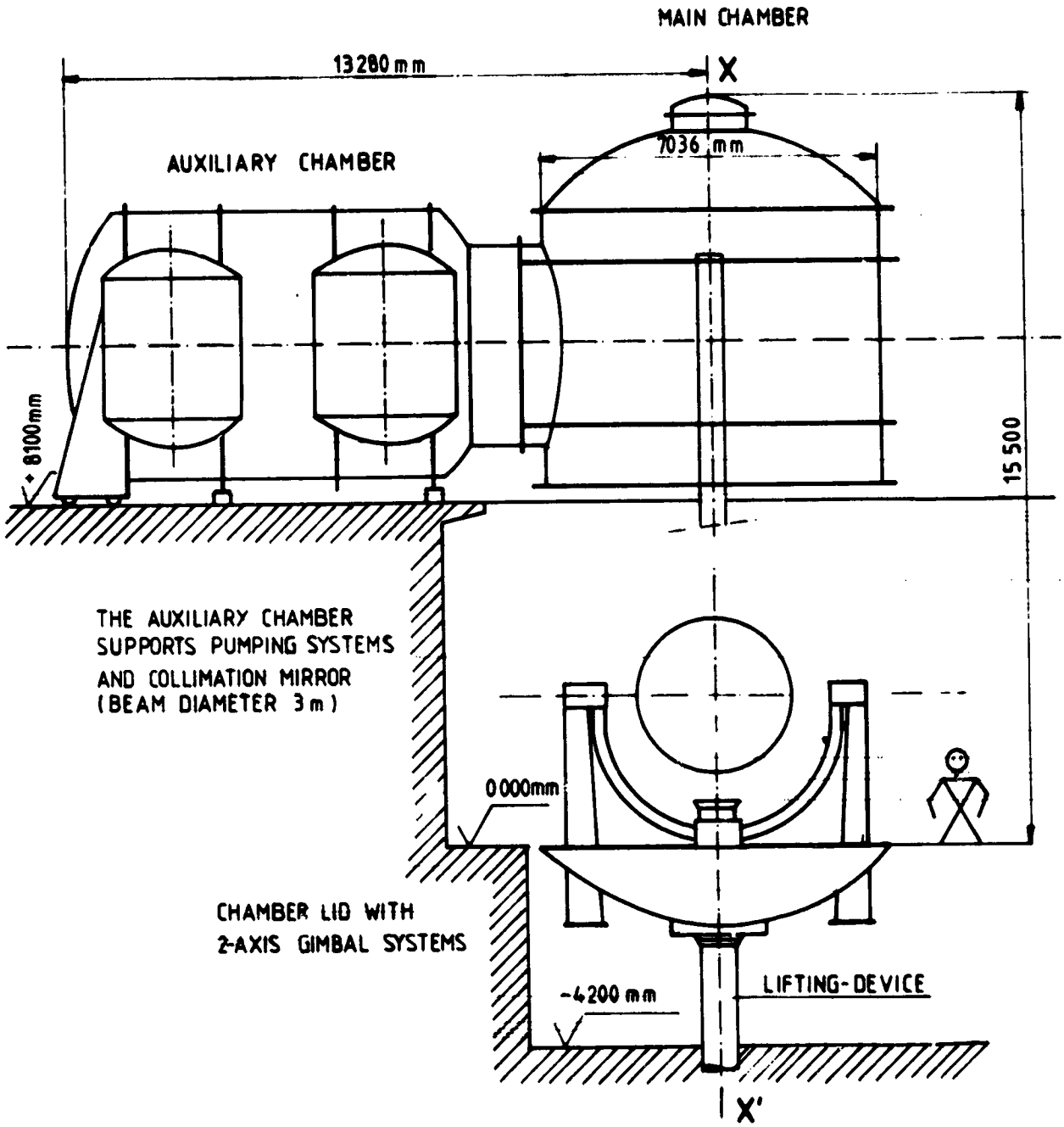

Fig. 13 Sketch of the CNES Solar Simulation Facility "SIMLES"

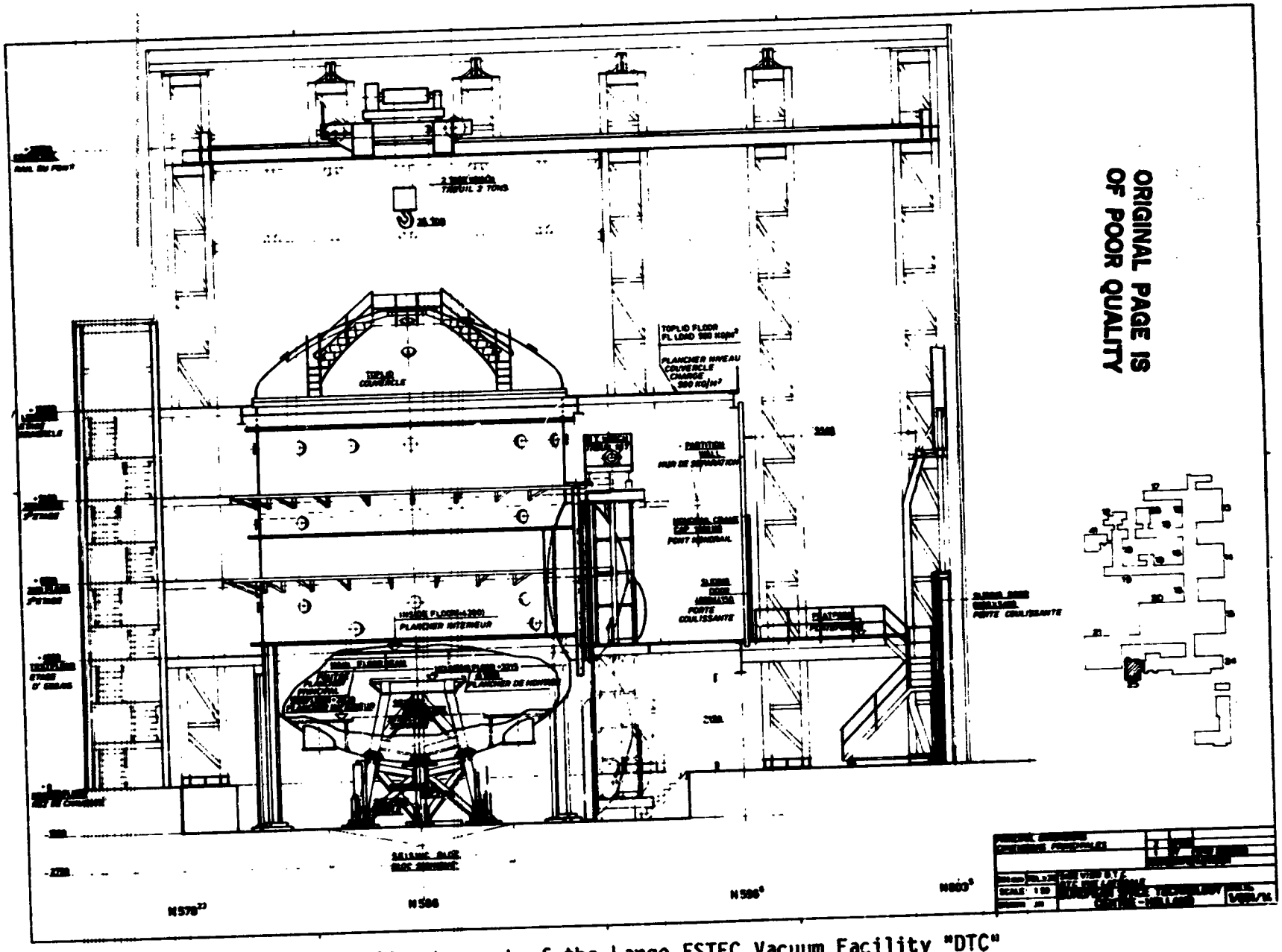

Fig. 14 Lay-out of the Large ESTEC Vacuum Facility "DTC"

ORIGINAL PAGE IS
OF POOR QUALITY

ORIGINAL PAGE IS
OF POOR QUALITY

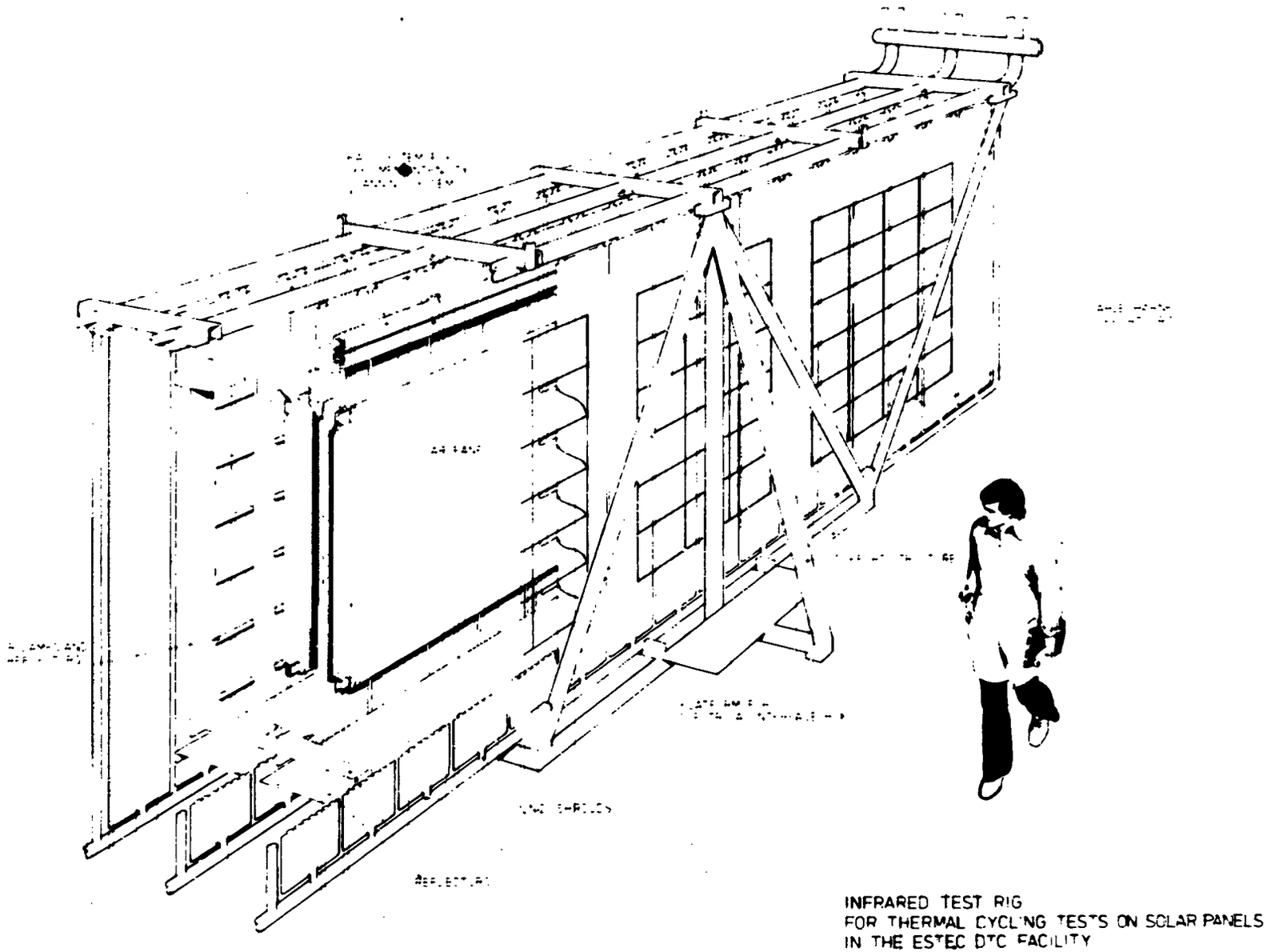

Fig. 15 Large Infrared Test Rig for the ESTEC "DTC"

ORIGINAL PAGE
BLACK AND WHITE PHOTOGRAPH

Fig. 16 INTELSAT V Solar Array Test Preparation in ESTEC Large Vacuum Chamber

ORIGINAL PAGE IS
OF POOR QUALITY

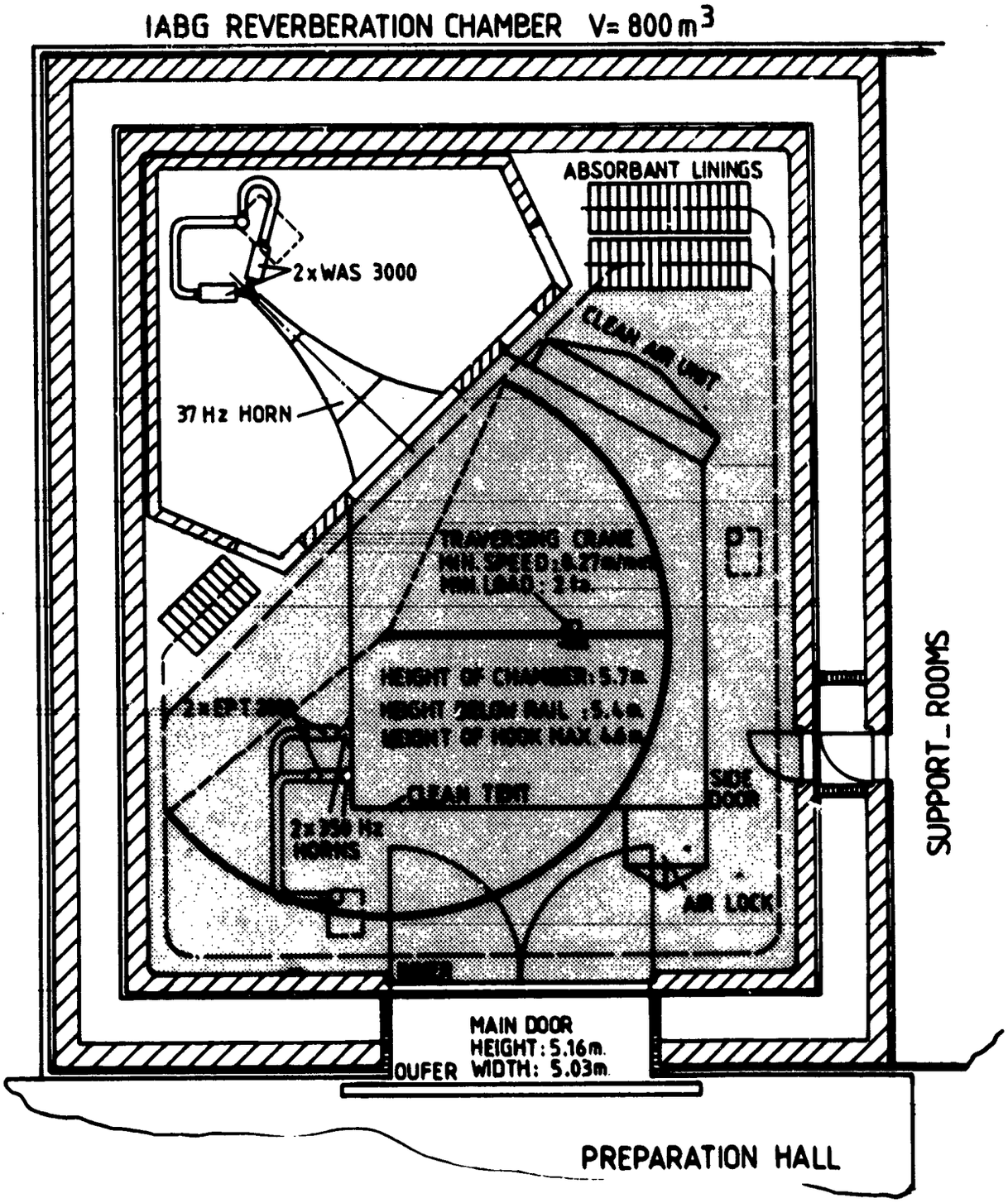

Fig. 17 Acoustic Test Facility at IABG

SESSION VI

DYNAMICS, TESTING AND ASSESSMENT

Session Organizers: Ernest T. Oddo, McDonnell Douglas Astronautics Company

R. A. Colonna, NASA Johnson Space Center

PRECEDING PAGE BLANK NOT FILMED

CORRELATION OF MODEL AND FULL SCALE ACOUSTICAL NOISE GENERATED DURING STS LAUNCH

R. Trudell
McDonnell Douglas Astronautics Company

ABSTRACT

A study task was initiated in 1978 to analyze the similarity aspects of model and full scale Shuttle engine-generated acoustics as part of a check on existing STS acoustic requirements. Theoretical analyses were performed and available model and full scale static firing data were utilized for correlation with and substantiation of theoretical conclusions. The theoretical analyses indicated that the SRB acoustic spectra from model and full scale tests should correlate quite well with geometric scaling, whereas the SSME spectra might not, depending on the scaling parameters used. Analysis of model and full scale static firings corroborated these expectations in the far field, and a scaling parameter hypothesis was developed to account for departures from geometric scaling rules. This paper summarizes the results of this work.

PRECEDING PAGE BLANK NOT FILMED

DATE - THE SHUTTLE PAYLOAD ENVIRONMENTAL MEASUREMENT PROGRAM

W. F. Bangs and E. J. Kirchman
NASA/Goddard Space Flight Center

ABSTRACT

In 1976 NASA originated a program for determining, through measurements, the actual structural dynamic and thermal environments that would be experienced by payloads flying on the Shuttle. The program, entitled DATE, an acronym for Dynamic, Acoustic and Thermal Environments, is divided into two phases: Phase I for gathering data during the 4 test flights, and Phase II for gathering data during operational flights. This paper addresses the results of the early part of Phase I and is restricted to structural responses, vibration and acoustic data.

Instrumentation used by DATE to gather the data consists of 16 transducers mounted in the payload bay, which is a part of the STS Project's Development Flight Instrument (DFI) package, and 38 DATE transducers mounted on payloads for flights 2, 3, and 4. In addition, 8 low-frequency accelerometers were available on flight 3 as part of the OSS-1 flight experiment.

The data from the flights are reported to the NASA and Air Force payload communities in 30-day reports. As of this writing three 30-day reports have been issued: Report 001, Flight Readiness Firing; Report 002, STS-1; and Report 003, STS-2 (OSTA payload flight). During the first two events (reports 001 and 002), only data from the 16 DFI channels were available and the events were used principally for gearing up the program for the 30-day reporting effort, selecting events to be reported, establishing formats, etc. However, the data acquired is considered of value.

STS-2 (report 003) had 54 data collecting instruments. The work of analyzing the data was divided between the Goddard Space Flight Center (GSFC) for the data from 29 high-frequency accelerometers and microphones, and the Jet Propulsion Laboratory for the data from 25 low-frequency accelerometers. Report 003, dated January 1982, is a fully mature report containing more than a thousand data plots. The report contains transducer complement, location, range, and frequency as well as acoustic analyses for SSME rough burn, SRB ignition, maximum exhaust effects, transonic, and maximum q effects. Also reported are instantaneous time histories for selected microphones and one-third octave spectral plots and overall SPL plots for all microphones. The report provides low-frequency acceleration responses (G rms, G peak, PSD, shock spectra and three-dimensional PSD-time-frequency analyses) for selected events. Significant events and anomalies in the data are pointed out. Because the OEX tape recorder failed after launch, no reentry data was acquired.

STS-3 will have the same complement of transducers as Flight STS-2. In addition, 8 low-frequency accelerometers will be recorded in PCM on the payload recorder during launch.

The mission of DATE, Phase I, is being accomplished. Although DATE personnel have not yet fully assessed the significance of the data, comparison of responses in flight 1 and 2 are being made with current flight acceptance levels for expendable launch vehicles. Acoustic levels are also being compared with the preflight predictions and design criteria. Overall, the measured environment appears relatively mild, except for some local conditions, and it is within the Johnson Space Center guidelines. The Phase II instrumentation system is being prepared by the Johnson Space Flight Center for measuring responses of payloads during operational flights.

N82 25301

ORIGINAL PAGE IS
OF POOR QUALITY

DYNAMIC ENVIRONMENTS FOR SPACE SHUTTLE PAYLOADS*

Dennis L. Kern and Michael R. O'Connell
Jet Propulsion Laboratory
California Institute of Technology
Pasadena, California

ABSTRACT

Flights one and two of the Space Shuttle provided the initial data on payload bay dynamic environments. The second flight, in particular, had a considerable amount of dynamic instrumentation installed by the NASA sponsored Dynamic, Acoustic and Thermal Environments (DATE) Program. Payload bay dynamic data from these flights are summarized and evaluated. Development of dynamic environment design and test criteria for Shuttle payloads from measured flight data is discussed. Factors that must be considered are flight to flight variations, spatial variations, temporal variations, measurement bias errors and the degree of confidence desired that a predicted environment will not be exceeded in flight. Summary and conclusions reports will be published after STS-4 and at appropriate intervals thereafter. The nature of these future reports and their impact on the user community is discussed.

INTRODUCTION

The second flight of the Shuttle provides the first significant amount of flight data available for evaluation of the payload bay dynamic environment. This data was acquired and reduced as part of the NASA DATE (Dynamic, Acoustic and Thermal Environments) activity, managed by Goddard Space Flight Center (GSFC). DATE instrumentation on STS-2 consisted of 14 microphones, 8 high frequency accelerometers, and 16 low frequency accelerometers inside the payload bay. Additional payload bay data was provided by the STS Development Flight Instrumentation (DFI) system, which was operational for the STS Flight Readiness Firing (FRF) and STS-1 as well as STS-2. DFI transducers applicable to payloads consisted of 4 microphones and 9 low frequency accelerometers inside the payload bay and 3 microphones externally on the bay doors. DATE has disseminated this environmental data to the payload community through 30-day reports (References 1, 2, and 3). However, in order to be of benefit to Shuttle users for development of payload dynamic environment design and test criteria, engineering interpretation must be applied to the data. The Jet Propulsion Laboratory (JPL) is performing this task for NASA Headquarters, Office of the Chief Engineer, to provide an engineering analysis of the data for the Shuttle payload community. This paper presents a general overview of the "DATE Data Engineering Analysis" task and discusses the expected contents of the summary and conclusions reports to be published as part of this task. It also provides a preliminary evaluation of the acoustics portion of the payload bay dynamic data for STS-1 and -2.

* This study program was carried out at the Jet Propulsion Laboratory, California Institute of Technology, under NASA Contract NAS 7-100.

ORIGINAL PAGE IS
OF POOR QUALITY

OVERVIEW OF DATE DATA ENGINEERING ANALYSIS TASK

The DATE dynamic data engineering analysis task will provide the STS payload community with a basis for derivation of dynamic environment design and test criteria for STS launched payloads. The task includes the engineering analysis of both the low frequency loads and the higher frequency vibroacoustics environments. The analysis information will be disseminated to the payload community through periodic "Summary and Conclusions" reports. JPL is the coordinator of the task, with responsibility for preparing and publishing the reports. JPL will be supported by other NASA centers and the Air Force Space Division through the DATE Working Group chaired by GFSC. The DATE Working Group will review and comment on the draft reports. Working Group members will be requested to contribute specific sections to these reports. The reports will summarize the data from several flights, provide engineering interpretation of the data, and make comparisions with predictions. The first report will cover Shuttle flights STS-1 through STS-4. Additional reports will follow at appropriate intervals.

SUMMARY AND CONCLUSIONS REPORTS

The summary and conclusions reports will summarize the STS payload bay flight dynamic data gathered and analyzed as part of the NASA DATE activity. These summaries will encompass several flights. A statistical approach will be taken to summarize the data wherever feasible.

The reports will provide engineering analysis of the flight data. Flight events, instrumentation characteristics, and data reduction procedures will be evaluated to assist in the interpretation of the measured data. Data uncertainties and errors will be identified and discussed. These uncertainties or errors will be quantified where possible. Data uncertainties include flight to flight variations, spatial variations and bias errors, payload effects, data acquisition and reduction errors or variances, and changes to the STS or the launch pad. Causes of flight to flight variations include, but are not limited to, launch vehicle lateral thrust induced drift, wind, water injection flow rate variances, engine ignition and burn parameter variances, separation device variances, and landing impact variances. Angle of attack and turbulence are sources of flight to flight variations for transonic and supersonic flight. Spatial variations refer to location to location variations in the acoustic environment and spatial bias errors arise from the limited number and the non-uniform distribution of microphones in the bay. Payload bay low frequency dynamic data is dramatically affected by the payload, and is almost meaningless to discuss without relating the measured data to the specific payload. Payload effects will also influence the acoustic environment. Data acquisition and reduction errors or variances can be quite significant. These errors must be understood to properly interpret the measured data. Finally, STS and launch pad changes can greatly affect the payload bay dynamic environment. Relatively minor changes in the launch pad between STS-1 and STS-2 reduced the overpressure experienced by the Orbiter tenfold on the second flight. Changes to the Shuttle structure or the engines for future flights may also drastically affect the payload dynamic environment.

ORIGINAL PAGE IS
OF POOR QUALITY

The report will also contain comparisions of the measured flight data with predictions. For the low frequencies the measured data will generally be compared to payload coupled loads analyses. The acoustic measurements can be compared to model data and to analyses. Measured data may also be compared to payload test data. For instance, higher frequency flight vibration responses can be compared to payload ground acoustic test responses or low and mid frequency flight transient payload responses can be compared to payload ground sine vibration test responses.

Finally, the report will identify and discuss any deficiencies in present Shuttle payload dynamic test and analysis methods uncovered during the preparation of the report. A number of these deficiencies are already commonly recognized. One example is the lack of a final payload coupled loads verification until the payload is nearly complete. Another deficiency is the need for a revised loads analysis for all payloads when a payload mix change occurs for multiple payload flights. A third recognized deficiency is the apparent conservatism in the current methods for combining payload low frequency transient loads and vibroacoustic loads.

PRELIMINARY ACOUSTICS EVALUATION

Low frequency Shuttle payload bay vibration loads are highly influenced by the payload. Detailed structural information and extensive analysis are necessary to use low frequency response measurements to make loads predictions for future payloads. The payload bay acoustic environment is less sensitive to payload effects. These payload influences are generally more readily predicted. A summary of the measured flight acoustic data and uncertainties in their interpretation are presented herein. Taking these uncertainties into account, environmental estimates can be derived with a high confidence that they will not be exceeded in flight. An example of how an acoustic environment estimate might be developed for payloads is presented.

ACOUSTIC INSTRUMENTATION

Shuttle acoustic instrumentation consists of the DFI and DATE transducers. The STS-2 payload consisted of the OSTA pallet in the center third of the bay and the DFI pallet in the aft third of the bay. The full complement of DATE and DFI transducers were installed on STS-2. The STS-1 payload consisted only of the DFI pallet and DFI transducers. All DATE channels were recorded on the Orbiter Experiments (OEX) wide band FM recorder. DFI acoustic channels were recorded on the Ascent Recorder and the Mission Recorder.

Seven DFI payload bay microphones were present on STS-1 and STS-2. There were 4 interior microphones on the bay bulkheads and sidewalls and 3 external microphones on the payload bay doors. External transducer V08Y9401A was noted as a suspect channel in DATE Report 003. Data from this microphone are not presented herein. Orbiter location, frequency response and model number for DFI microphones are listed in Table 1. Installation and calibration of these microphones was the responsibility of Johnson Space Center.

ORIGINAL PAGE IS
OF POOR QUALITY

DATE instrumentation was installed on STS-2 only. DATE microphones were omnidirectional and were isolation mounted. Seven microphones were installed on the OSTA-1 pallet and eight were installed on the DFI pallet. DATE microphone type, location and frequency responses are listed in Table 2. Selection, installation and calibration of DATE transducers was the responsibility of Goddard Space Flight Center (GSFC).

DATA REDUCTION

Data used in this paper are taken from DATE reports 002 and 003, References 2 and 3. This data was reduced by GSFC as 1/3 octave band time histories. A .5 second time constant was used during data reduction. The maximum 1/3 octave band levels for the five most significant events were tabulated by the authors. The mission times for these events, namely, main engine start (rough burn at 20% thrust), main engines only, liftoff exhaust deflection, transonic flight and supersonic flight, are listed on Figures 1 and 2. The low frequency acoustics induced by the overpressure at SRB ignition, evident on STS-1, was almost non-existent on STS-2. Thus, data for this event is not included. The spatial mean and standard deviation were calculated for each 1/3 octave band. Spectra for each event were then plotted by hand.

Noise floor affected the levels of many transducers above 1000 Hz. The data obscured by the noise floor was eliminated from the spectral plots during the tabulation process. According to Rockwell International, the channel noise was generated by the recorder multiplexer.

ACOUSTIC DATA EVALUATION

The first approach to evaluating the STS-2 data was a systematic overlaying of spectral plots from different microphones. Comparing the data for each event in this way indicated that, for a given event, there was little variation in the data recorded by the microphones on the pallets. (An exception to this was certain microphones near vents, which exhibited discrete tones at 315 Hz for transonic and supersonic flight.) Acoustic levels at the Shuttle bulkheads and side walls appeared to be consistently higher than pallet levels below 250 Hz. For subsequent analysis, the payload bay was zoned into a small payload region and a bulkhead/sidewall region. The small payload region is characterized by a reasonably diffuse sound field; that is, the acoustic levels are not affected by local payload bay wall effects. This is predicted by Reference 4 for payloads that occupy less than 60% of the diameter of the payload bay. The validity of grouping all pallet microphones is confirmed by the small 2 sigma values for the 1/3 octave band mean level calculations. Figure 3 compares the mean levels at the OSTA pallet and at the DFI for liftoff exhaust deflection. This plot also indicates small differences in the acoustic levels between the center and the aft regions of the payload bay for the STS-2 payload. Comparision of the mean acoustic levels at the OSTA pallet and at the DFI for the other significant events give similar results. It should be noted that no payload microphones were in the forward third of the bay. Forward bay acoustic levels may not necessarily be inferred from STS-2 measurements.

ORIGINAL PAGE IS
OF POOR QUALITY

The mean and mean plus 2 sigma levels for the five STS-2 launch events are summarized on Figures 1 and 2. Figure 1 shows the means of each of the five most significant events. Mean plus 2 sigma levels are shown on Figure 2. Also shown for reference is the liftoff acoustic spectrum specified in the Space Shuttle System Payload Accommodation document, Volume 14 (Reference 5). Liftoff has the most severe mean levels at 132 dB overall. Main engine ignition mean levels were 126.3 dB overall. Mean plus 2 sigma levels are 136 dB overall at liftoff and 130 dB during main engine start. But, variations in the data during SSME start are greater than during liftoff for several frequency bands. The 2 sigma levels during main engine start are higher than at liftoff below 125 Hz (see Figure 2). Transonic mean values were 125.5 dB overall compared to 123.8 dB during supersonic flight (at 63 seconds after liftoff). A similar difference is seen in the mean plus 2 sigma data with 133 dB overall at transonic and 128 dB during supersonic. Supersonic levels may be slightly higher than 128 dB overall at different flight times.

Figure 4 compares STS-1 and STS-2 payload bay mean acoustic levels for liftoff from the four internal DFI microphones. Level variations, generally within ±1 dB for each 1/3 octave band, are typical for other flight events. STS-1 and STS-2 exterior levels are compared for payload bay door DFI microphone 9402 on Figure 5. The variation in exterior acoustic level, also generally within ±1 dB, is typical for other exterior microphones on the doors.

The mean sidewall/bulkhead STS-2 acoustic levels for liftoff are compared to the OSTA/DFI pallet levels on Figure 6. Sidewall/bulkhead levels were significantly greater than STS-2 pallet levels below 250 Hz. This effect is evident for all flight events, but is most pronounced at liftoff. Liftoff pallet acoustic levels were 5-6dB below sidewall/bulkhead levels below 80 Hz. During transonic flight sidewall/bulkhead acoustic levels were 3-5dB higher than pallet levels between 80 Hz and 315 Hz. Data at supersonic exhibited a similar characteristic.

Figures 1 and 2 compare the mean and mean plus 2 sigma payload acoustic levels for all significant events to the liftoff Volume 14 levels, Reference 5. STS-2 mean plus 2 sigma overall acoustic levels were 9 dB below Volume 14. There are, however, a number of uncertainties in the environment that must be considered in deriving payload acoustic environments from Shuttle data. These uncertainties are discussed in the following section.

ENVIRONMENTAL UNCERTAINTIES

There are a number of uncertainties that must be considered before one can derive a meaningful environment for a payload. Uncertainties in the acoustic environment that must be taken into consideration include payload influences on the dynamic environment, spatial variations, bias errors, flight to flight variations, and data reduction uncertainties.

Large diameter payloads (greater than 60% of the payload bay diameter) can have a significant effect on Shuttle payload bay vibroacoustic levels. The optional thermal radiator in the payload bay will also influence the bay acoustic environment. PACES, a computer program developed by Bolt, Beranek

and Newman for GSFC, is designed to predict the influence of large payloads and sound absorbing areas on the acoustic environment inside the bay (Reference 4). Local variations of 7-10 dB are possible with some payload configurations. Presently, PACES is being verified with the early flight data.

It is expected that small payloads will not have a large influence on payload bay levels. The small variations of mean sidewall/bulkhead levels for STS-1 and STS-2 seem to bear this out. More data is needed to make this observation a firm conclusion.

Spatial bias errors arise from non-representative positioning or small numbers of microphones. Bias error magnitudes from the spatial mean have been calculated for STS-1 through STS-3 by Bolt, Beranek and Newman, Reference 6. However, there are no published bias error values for flights after STS-3 at this time. For STS-2, Reference 6 concludes that bias errors are negligible. This is so because of the large number of transducers and their positions. Thus, an energy average of all the acoustic data is a good representation of the spatial average.

The spatial mean environment can be exceeded at 50% or more of the locations in the payload bay for any time segment. For this reason the mean alone is rarely enough to adequately define an environment. Most organizations developing payload acoustic criteria will add some factor to the mean level. This increases the confidence that a payload's predicted environment will not be exceeded because of deviation from the mean. However, payload structural responses will tend to average the acoustic spatial distribution. This is another factor that should be considered when accounting for acoustic spatial variability.

Flight to flight variations are another category of uncertainty. There is no significant data yet on Shuttle flight to flight acoustic environment variations. This variation may also be different for each flight event. Model tests indicate that launch vehicle drift can cause increases of 3 dB or more in liftoff exhaust reflection acoustic levels. Launch vehicle drift is caused by the combination of lateral thrust vectors and wind. Increased reflected noise results when the exhaust impinges on the launch pad rather than flowing through the SRB and SSME pad exhaust holes. Some heavy lift configurations of the Shuttle will leave the pad at slower rates. This will result in more drift for the same height obtained and thus greater reflected noise. Variation in the flow rates of launch pad water injection can also affect noise levels from flight to flight. Static firings of the main engines have shown several dB variation in acoustic levels during the rough burn at 20% thrust. During transonic and supersonic flight the angle of attack and dynamic pressure changes will influence payload bay levels.

Exterior noise levels offer a sampling of flight to flight variation unaffected by payloads. But, there are so few external microphones in the vicinity of the payload bay that precision of results is questionable. Standard deviations and other statistical properties of the data can not be determined for only 2 or 3 microphones. A large number of flights would be necessary for the data to be statistically meaningful. Finally, there are

ORIGINAL PAGE IS
OF POOR QUALITY

uncertainties associated with data reduction. This is especially true for transient events like those measured during Shuttle launch. The Goddard data used in this report was reduced in 1/3 octave band time histories with a .5 second averaging time. Higher transient levels are obtained if shorter time averages are used. Small calibration reading errors are one type of random error in a data analysis. Data reduction equipment and technique of reduction can introduce large bias errors into data. Tanner, Reference 7, has found that the magnitude of Shuttle acoustic data reduced at different facilities can vary ±5 dB or more below 100 Hz. This indicates that the analysis method for data reduction must be carefully chosen.

Our method of tabulating maximum event levels was to pick the maximum acoustic level at or near the event time of interest. Given the small size of the DATE report figures, this process often requires some personal judgement in picking the level. A careful transcriber can tabulate event levels with an accuracy of ±.25 dB at best. Presumably, this type of reading error will cancel out for a large number of readings (they will cancel unless the transcriber has a "bias" toward estimating up or down).

EXAMPLE ACOUSTIC PREDICTION

A hypothetical example will be used to illustrate how the inclusion of uncertainties and variables in the environment might be accomplished.

Mean payload bay acoustic levels for smaller payloads (not influenced by sidewall effects) are given in Figure 1 for STS-2. To develop acoustic design or test criteria for future payloads, errors or uncertainities must be taken into account for each flight event. Bias errors, which are average values, are added directly to the mean levels. Statistically independent random errors are incorporated by suming the square of each error and adding the square root of the sum to the mean levels. The acoustic levels for the various flight events, with uncertainities or errors included, are then enveloped to obtain a single maximum predicted acoustic spectrum for a payload. However, for this example only, it is assumed that the errors or uncertainities are independent of flight event, thus the mean payload acoustic level for each event may be enveloped first. This envelope mean is shown in Figure 7.

For this example the following formula is used to predict maximum acoustic levels for a Shuttle payload:

$$P_{max} = P_n + P_e + P_b + P_p + [\Delta P_s^2 + \Delta P_f^2]^{1/2}$$

where P_{max} = Maximum acoustic environment
P_n = Mean acoustic environment for small payloads from STS-2 flight data
P_e = Data reduction bias errors
P_b = Spatial bias errors arising from non-representative positioning of small number of microphones on STS-2
P_p = Payload diameter effect
P_s = Spatial variation uncertainity within the payload bay
P_f = Flight to flight uncertainty

ORIGINAL PAGE IS
OF POOR QUALITY

The mean payload bay acoustic environment, P_m, in this example was obtained by enveloping the STS-2 flight data of Figure 1. This is a conservative approach because maximum levels will never occur in all one third octave bands at one time. The data reduction bias error, P_ϵ, is arbitarily taken as 1 dB for this example for all frequencies and events. The data reduction error could also include a separate statistically independent random variable. The spatial bias error, P_b, is negligible for STS-2 (Reference 6). The payload diameter effect, P_D is negligible for STS-2 for small payloads. For expediency, in this example the spatial variation uncertainity, P_s, is approximated by subtracting the STS-2 mean envelope derived from Figure 1 from the mean plus two sigma envelope derived from Figure 2. The flight to fight uncertainity, P_f, is assumed to be ±3 dB for all flight events and frequencies for this example.

The maximum predicted acoustic environment spectrum for this example is shown in Figure 7 above the mean spectrum. Maximum predicted acoustic levels for this hypothetical example are 137.2dB overall compared to 130.7dB overall for the envelope of the mean levels for each flight event. Also shown for reference is the payload bay maximum acoustic spectrum from the Space Shuttle System Payload Accomodations document (Reference 4), which has an overall level of 145 dB.

SUMMARY

The second flight of the Shuttle provides the first significant amount of flight data available for evaluation of the payload bay dynamic environment. Engineering interpretation of this data is necessary in order to be of benefit to Shuttle users for development of payload dynamic environment design and test criteria. The Jet Propulsion Laboratory will provide this engineering analysis to the payload community through periodic "Summary and Conclusions" reports. This effort will be supported by various NASA centers and the Air Force through the DATE Working Group.

A preliminary evaluation of the Shuttle payload bay acoustic environment, based on STS-1 and STS-2 flight data, has been presented. There are a number of uncertainties in the flight environment which must be considered when deriving payload acoustic criteria. An example of how these uncertainties could be accounted for was presented.

ORIGINAL PAGE IS
OF POOR QUALITY

REFERENCES

1) DATE REPORT 001, Dynamic, Acoustic, Thermal Environments; Payload Bay Acoustic and Vibration Data from the Flight Readiness Firings, April '81, NASA.

2) DATE REPORT 002, Dynamics, Acoustic, Thermal Environments; Payload Bay Acoustic and Vibration Data from STS-1 Flight, June '81, NASA.

3) DATE REPORT 003, Dynamics, Acoustic, Thermal Environments; Payload Bay Acoustic and Vibration Data from STS-2 Flight, January '82, NASA.

4) SPACE SHUTTLE PAYLOAD BAY ACOUSTICS PREDICTION STUDY, Volumes 1 through 5; Piersol, Rentz, Wilby, Bolt, Beranek and Newman Inc., March '80.

5) SPACE SHUTTLE PROGRAM, Level II Program Definition and Requirements, Space Shuttle System Payload Accommodations; September 26, '80, JSC 07700, Volume XIV, Revision G.

6) BIAS ERROR CORRECTIONS FOR ACOUSTIC DATA FROM SPACE SHUTTLE FRF AND STS-1 THROUGH STS-3; Piersol; Bolt, Beranek and Newman Inc., December '81.

7) ERRORS ASSOCIATED WITH SHUTTLE ACOUSTICAL DATA REDUCTION TECHNIQUES; Tanner, The Aerospace Corporation, March '82.

Table 1, DFI Microphones

Measurement No.	Location Description	Range (dB)	Frequency Response	Orbiter Station Location X	Y	Z
V08Y9219A	Cargo Bay, Internal	110-150	Wide Band 20-8KHz	863	-100	381
V08Y9220A	Cargo Bay, Internal	110-150	Wide Band 20-8KHz	1080	0	427
V08Y9403A	Cargo Bay, Internal	110-150	Wide Band 20-8KHz	1306	12.0	400
V08Y9405A	Cargo Bay, Internal	110-150	Wide Band 20-8KHz	640	4	423
	Internal Microphones, Gulton, Model Number MC 449-0191-003.					
V08Y9402A	Cargo Bay Door, External	130-170	Wide Band 20-8KHz	1281	4.2	500
V08Y9404A	Cargo Bay Bottom, External	130-170	Wide Band 20-80KHz	1296	0	300
	External Microphones, Gulton, Model Number MC 449-0191-002.					

ORIGINAL PAGE IS OF POOR QUALITY

Table 2, DATE Microphones

Measurement No.	Location Description	Range	Frequency Response	Orbiter Station Location X	Y	Z
V08Y9252A	OSTA-1, OCE SHELF FWD INBD COR	± .4101 PSI	5-2KHz	864	-29	410
V08Y9253A	OSTA-1, OCE SHELF AFT INBD COR	± .4101 PSI	5-2KHz	978	-29	410
V08Y9254A	OSTA-1, OCE SHELF MID TRUSS	± .4101 PSI	5-2KHz	951	-45	394
V08Y9255A	OSTA-1, PALLET FLOOR LWR SURF	± .4101 PSI	5-2KHz	951	0	326
V08Y9256A	OSTA-1, PALLET L.H. SIDE	± .4101 PSI	5-2KHz	951	-85	398
V08Y9257A	OSTA-1, FWD SIR-A ANT TRUSS	± .4101 PSI	20-8KHz	832	+29	427
V08Y9258A	OSTA-1, AFT SIR-A ANT TRUSS	± .4101 PSI	20-8KHz	1001	+29	427
V08Y9275A	DFI, No 1 UPR FWD OUTBD COR	± .4101 PSI	5-2KHz	1139	-68	432
V08Y9276A	DFI, No 2 LWR FWD INBD COR	± .4101 PSI	5-2KHz	1139	+20	384
V08Y9277A	DFI, No 3 UPR AFT OUTBD COR	± .4101 PSI	5-2KHz	1219	-68	432
V08Y9278A	DFI, PALLET CONN PL L.H.	± .4101 PSI	5-2KHz	1194	-44	328
V08Y9279A	DFI, PALLET COOL PUMP BRACE	± .4101 PSI	5-2KHz	1192	+15	384
V08Y9280A	DFI, No 2 UPR FWD OUTBD COR	± .4101 PSI	20-8KHz	1139	+68	432
V08Y9281A	DFI, No 3 LWR AFT	± .4101 PSI	20-8KHz	1219	-68	384

Internal Microphones, Endevco, Model Number 2510

ORIGINAL PAGE IS OF POOR QUALITY

ORIGINAL PAGE IS
OF POOR QUALITY

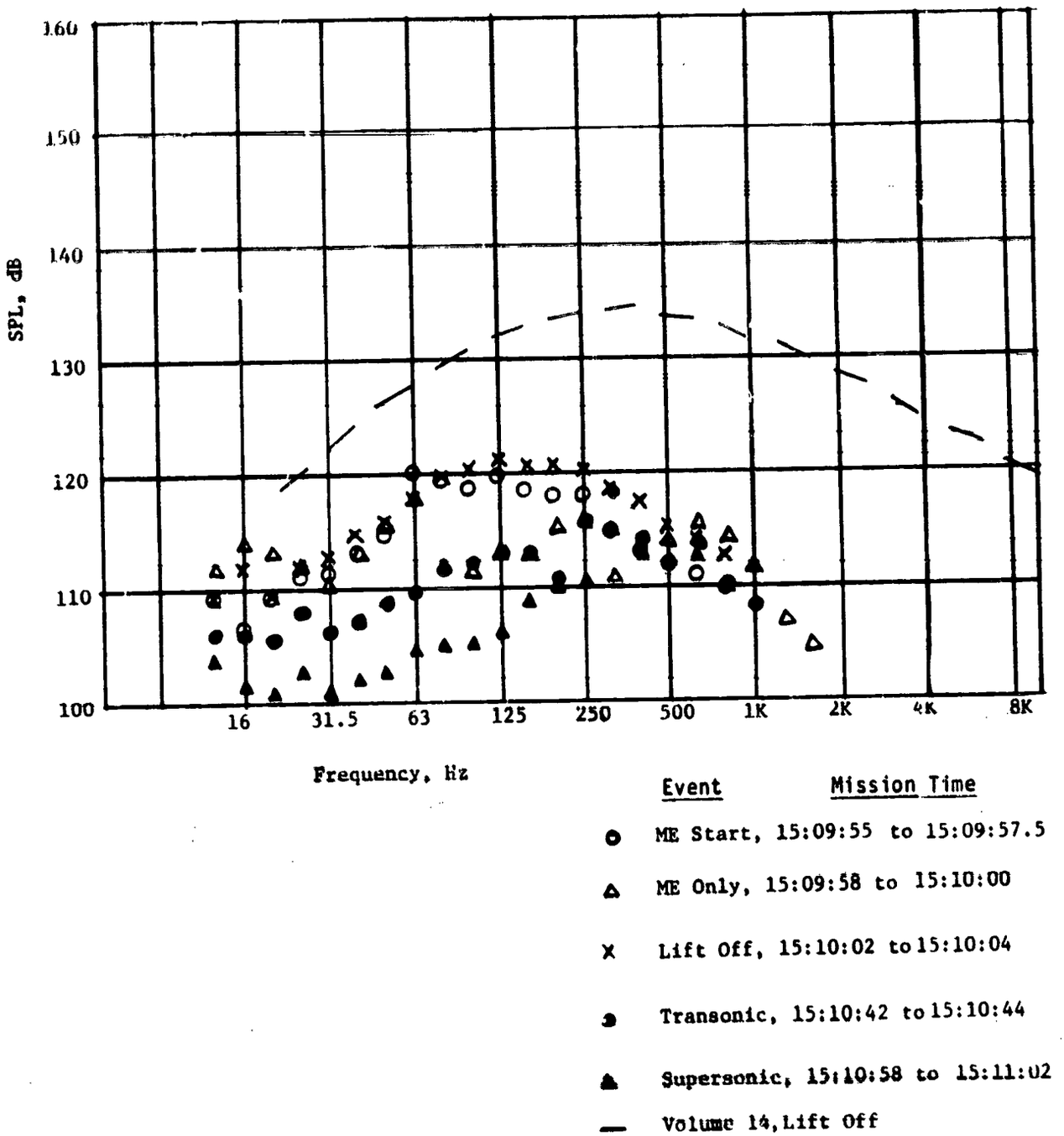

Figure 1, STS-2, Summary, OSTA/DFI, Pallet Levels, Mean Payload Level

ORIGINAL PAGE IS
OF POOR QUALITY

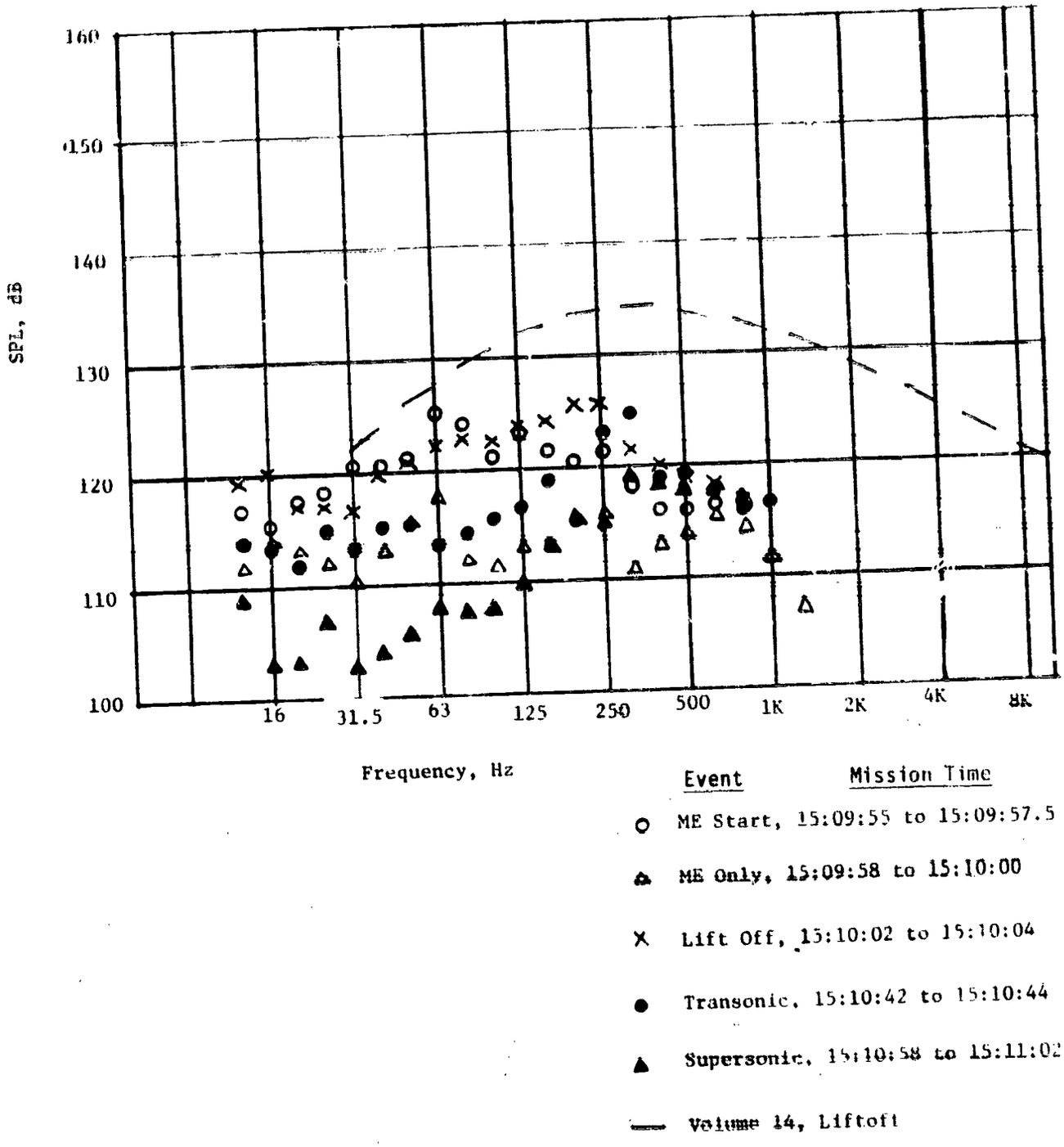

Figure 2, STS-2, Summary, OSTA/DFI, Pallet Levels, Mean Plus 2 Sigma Payload Level

ORIGINAL PAGE IS
OF POOR QUALITY

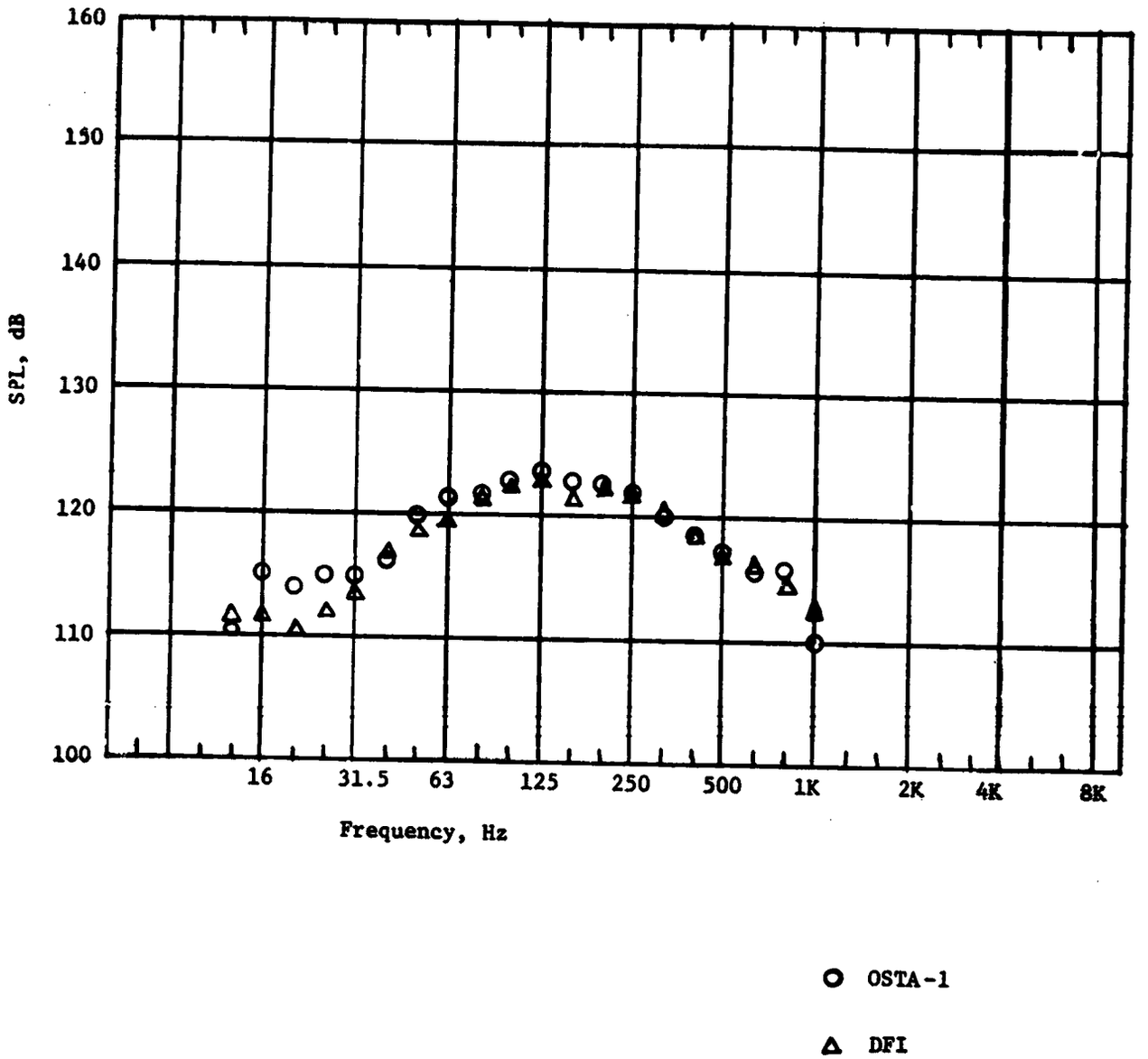

Figure 3, STS-2, OSTA vs DFI Mean Level, Liftoff DATE Data

C-3

ORIGINAL PAGE IS
OF POOR QUALITY

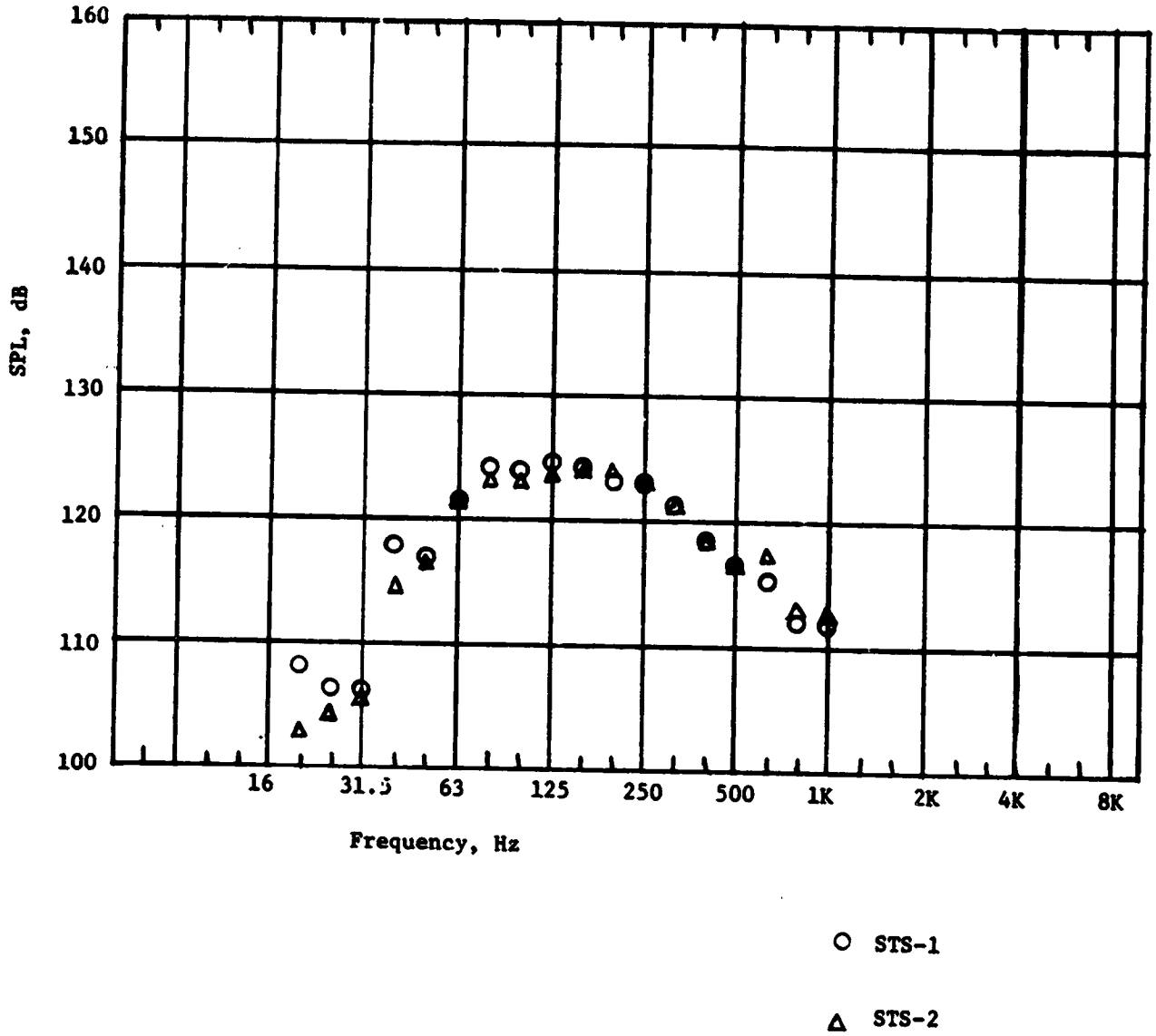

Figure 4, STS-1 vs STS-2 Lift Off, Interior Mean DFI Data

ORIGINAL PAGE IS
OF POOR QUALITY

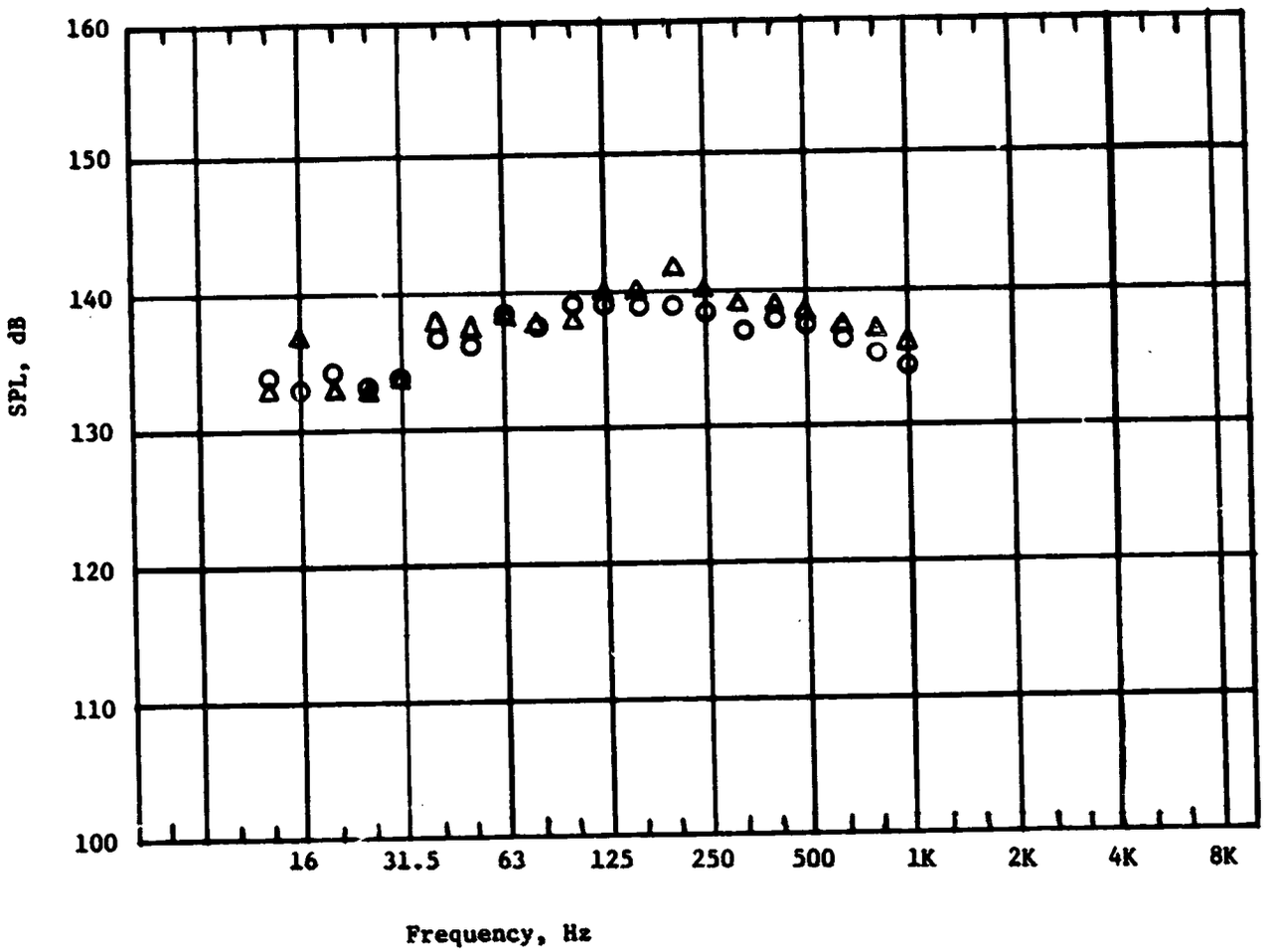

○ STS-1

△ STS-2

Figure 5, External Acoustic Levels, STS-1 vs STS-2, DFI Mic 9402, Liftoff

ORIGINAL PAGE IS
OF POOR QUALITY

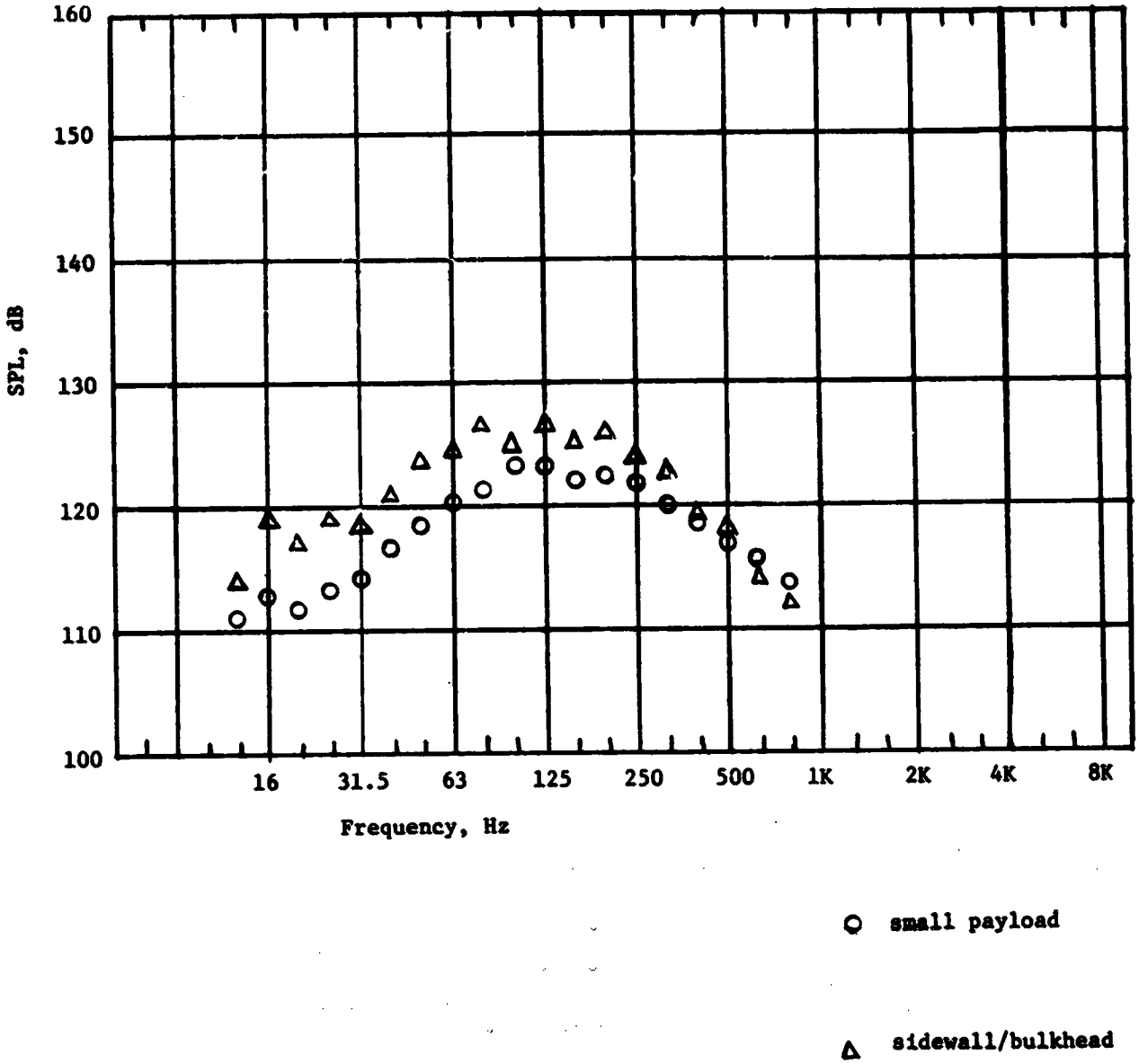

Figure 6, STS-2, Sidewall /Bulkhead vs Pallet Mean Levels, DATE Data, Liftoff

ORIGINAL PAGE IS
OF POOR QUALITY

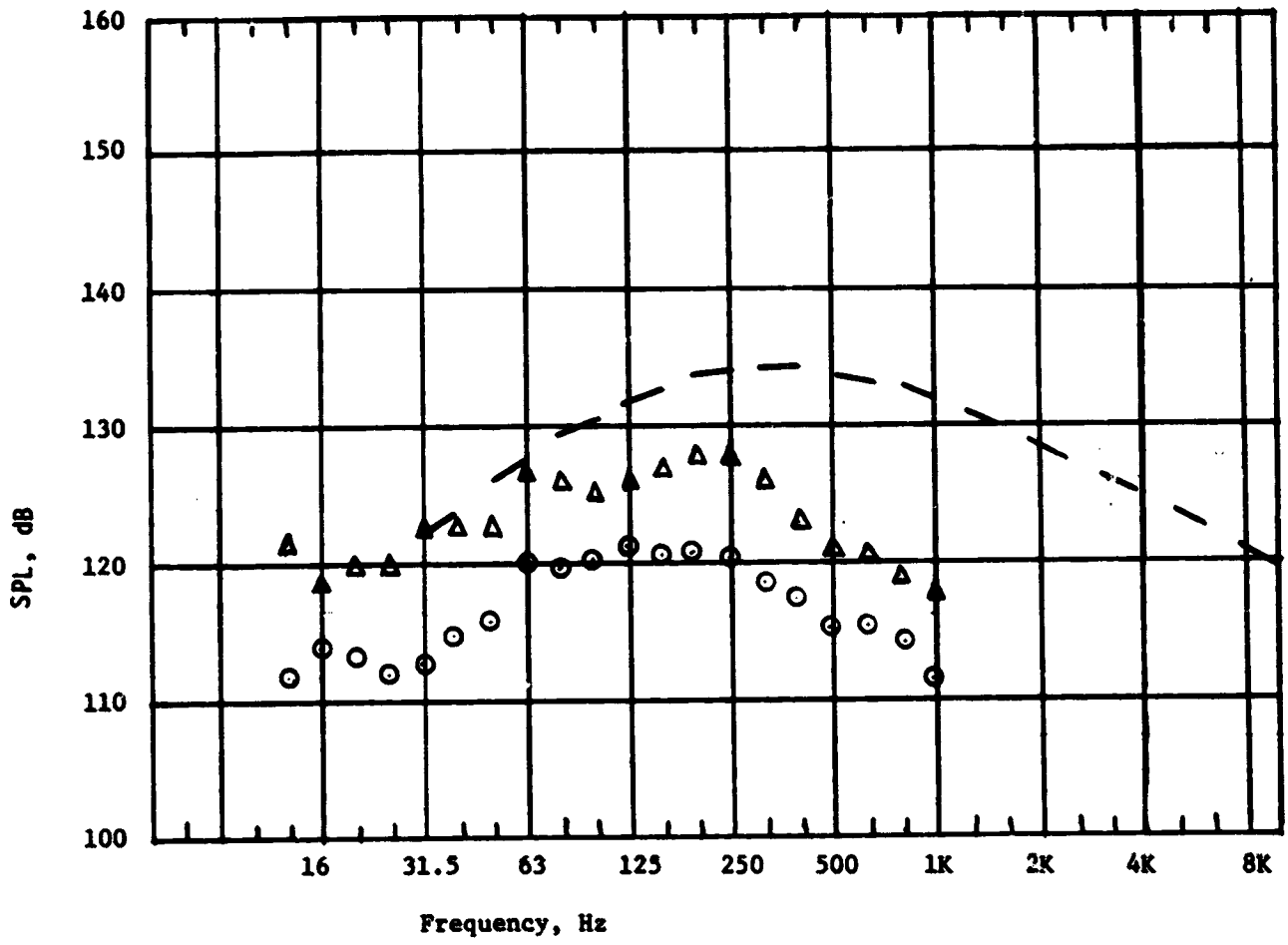

△ example prediction

○ envelope of mean

— Volume 14, liftoff

Figure 7, Example Prediction (with hypothetical uncertainity values) and Envelope of STS-2 Mean Pallet Data

N82 25302

ENVIRONMENTAL NOISE ASSESSMENT
S.T.S.-1 COLUMBIA LAUNCH (U)*

George J. Putnicki
The University of Texas at Dallas
Graduate Program in Environmental Sciences
Richardson, Texas

ABSTRACT

An environmental noise assessment of the initial launch of the Space Transportation System, STS-1 Columbia was conducted on April 12, 1981 by The University of Texas at Dallas, Graduate Program in Environmental Sciences. The assessment was requested by Dr. Albert M. Koller, Jr., Chief, Environmental Management Staff, John F. Kennedy Space Center and was conducted in cooperation with the American Institute of Biological Sciences.

The John F. Kennedy Space Center is the principal site for launch of space systems by the National Aeronautics and Space Administration. The environmental effects of the STS launch activities at the Kennedy Space Center were reported in the March, 1979, Environmental Impact Statement for the John F. Kennedy Space center. Information obtained for expendable launch vehicles, Titan, Saturn and Atlas was used to predict the noise levels that would be generated by the simultaneous firing of the two solid rocket boosters and the three Space Shuttle main engines.

The principal objective of the environmental noise assessment conducted on April 12 was to measure the noise generated during the initial launch of the Space Shuttle to ascertain the validity of the levels predicted in the 1979 E

Fifteen monitoring sites were established in accessable areas located from 4,953 to 23,640 meters from the launch pad. American National Standards Institute ANSI S1.4-1971 Type 1 and Type 2 Sound Level Meters were deployed at four to seven hours prior to the scheduled launch. The monitoring equipment has a sampling rate of 4 per second and a storage capacity of 8-hours data. The noise descriptors recorded were the energy equivalent average sound levels, $L_{eq}(60s)$ and $L_{eq}(H)$. All measurements were A-weighted. The $L_{eq}(60s)$ were converted to Sound Exposure Levels, SEL or L_{ax} to obtain the single event levels. At two sites, Type 1, Precision Sound Level Meters were used to capture the peak level during the launch.

Data obtained was compared to the predicted levels reported in the March 1979 EIS and were also compared to the identified levels, standards and criteria established by the federal agencies with noise abatement and control responsibilities.

The levels predicted in the March 1979 EIS were 95 dB(A) at a distance of 6 kilometers from the launch pad and 80 dB(A) at a distance of 17 kilometers from the launch pad. The measured SEL's obtained at 6 and 17 kilometers from the launch pad were 106 and 89 dB(A) respectively or 11 to 9 dB(A) higher than predicted levels. It was noted that the levels from other sources of noise, namely helicopters and private jet aircraft, exceeded the level measured during the STS-1 Columbia launch at some of the monitoring sites.

The levels at all of the sites exceeded the level identified by the U.S. Environmental Protection Agency as requisite to protect against outdoor activity interference but were within the margin of safety of the levels identified by EPA as requisite to protect against hearing loss consideration.

None of the sites exceeded the U.S. Department of Housing and Urban Development unacceptable site acceptability standard. Most of the sites were in the HUD discretionary range where special approvals would be required for HUD approved residential financing.

The levels at three of the sites exceeded the U.S. Federal Highway Administration Noise Standard.

The levels measured at all of the sites were less than the U.S. Department of Labor, Occupational Safety and Health Administration, Safety and Health Standards.

The acoustical data used in the comparison of the levels measured during the STS-1 Columbia launch with the identified levels, standards and criteria established by the federal agencies represents a "worse case" condition since the levels were influenced by vehicular traffic and spectators, an estimated 35,000 vehicles and over 100,000 persons.

INTRODUCTION

An environmental noise assessment of the initial launch of the Space Transportation System, STS-1, Space Shuttle Columbia was conducted on April 12, 1981, by The University of Texas at Dallas, Graduate Program in Environmental Sciences. The assessment was requested by Dr. Albert M. Koller, Jr., Chief, Environmental Management Staff, John F. Kennedy Space Center and was conducted in cooperation with the American Institute of Biological Sciences. Field monitoring was conducted on April 12, 1981, by personnel from the National Aeronautics and Space Administration, John F. Kennedy Space Center, Patrick Air Force Base, Edwards Air Force Base, Vandenburg Air Force Base and the Marshall Space Center.

The John F. Kennedy Space Center is the principal site for launch of space systems by the National Aeronautics and Space Administration. The environmental effects of the STS launch activities at the Kennedy Space Center have been subjected to a series of evaluations and are reported in the March, 1979, Environmental Impact Statement for the John F. Kennedy Space Center[1]. The 1979 EIS describes the ongoing operation of KSC for expendable launch vehicles and automated spacecraft, continued development of facility

capabilities and the follow-up operations of the Space Transportation System and associated payloads.

Information on peak sound pressure levels obtained for expendable launch vehicles, Titan, Saturn and Atlas were used in the EIS for comparison with predicted Space Shuttle levels. The acoustic level at STS liftoff was predicted to produce about the same levels as a Saturn V launch. It was predicted that the noise generated by the simultaneous firing of the two solid rocket boosters and the three Space Shuttle main engines will build to a peak of 95 dB(A) at a distance of 6 kilometers, 3.7 miles, from the launch site and dwindle to inaudibility over a period of approximately 120 seconds. At 6 kilometers from the launch site, the absolute sound pressure level was predicted to be 123 dB. The predicted sound pressure levels at the nearest mainland area, 17 kilometers, 11 miles, was 110 dB or 80 dB(A)[1].

OBJECTIVES

The objectives of the environmental noise assessment of the initial launch of the Space Transportation System, STS-1, Space Shuttle Columbia conducted on April 12, 1981 were:

1. To provide the National Aeronautics and Space Administration with sufficient acoustical data obtained during the launch of STS-1 to ascertain the validity of the predictions made in the March 1979, Environmental Impact Statement.

2. To compare the measured and computed environmental noise levels obtained at various distances from the launch pad to the identified levels, standards and criteria established by the federal agencies with noise abatement and control responsibilities.

METHODOLOGY

The methodology developed for this environmental noise assessment was tailored to provide acoustical data with sufficient accuracy for use in determining the validity of the predictions made in the March 1979, Environmental Impact Statement for the Kennedy Space Center. In brief, the methodology can be characterized as follows:

1. Acquire and compile suitable maps and predicted sound level information.
2. Select monitoring sites on concentric circles at distances of approximately 5,000 to 24,000 meters from the launch pad.
3. Acquire the necessary monitoring equipment and prepare a monitoring schedule.
4. Assign and train monitoring personnel in the use of the monitoring equipment.
5. Brief key NASA management personnel.
6. Conduct field monitoring.

7. Reduce and evaluate acoustical data.
8. Draft report summarizing results.
9. Edit draft report and prepare final report.
10. Present final report to appropriate NASA and AIBS officials.

Personnel from the NASA Environmental Management Staff provided the necessary maps and a copy of the March 1979 EIS showing the predicted launch noise contours.

Fifteen sites were selected in accessable areas located from 4,953 meters, 3.08 miles, to 23,640 meters, 14.69 miles, from launch Pad A. Table I shows the site designations, range in meters and miles and azimuths of the fifteen sites selected for this assessment. A map of the KSC area showing the location of Pad A and the fifteen monitoring sites are shown in Figure 1.

All sound level meters used in this noise assessment conformed to the American National Standards Institute, ANSI, S1.4-1971 Type 1 and Type 2, Sound Level Meter Specifications and field calibration was traceable to the National Bureau of Standards[2]. A complete listing of the monitoring equipment used in this assessment is shown in Table II.

The Type 2 sound level meters were deployed and activated from four to seven hours prior to the STS-1 scheduled launch. The Type 2 sound level meters had a sampling rate of 4 per second and could store up to 8 hours of acoustical data. At the four monitoring sites nearest to Pad A, the equipment had a baseline of 60 dB(A) and a dynamic range of 64 dB(A). At all other sites the equipment baseline was 40 dB(A) and the dynamic range was 64 dB(A).

ANSI Type 1 precision sound level meters were also used at two of the manned sites, A-4 and A-13. The Type 1 equipment had a "peak hold" feature, whereby the peak level during the launch was captured and displayed.

The temperature, wind velocity and direction, relative humidity and barametric pressure measurements made during the launch are shown in Table III.

DISCUSSION OF RESULTS

Upon completion of the field monitoring, the data obtained was analyzed. The Sound Exposure Levels, SEL(L_{AX}), were computed and graphical presentations of the hourly energy equivalent average sound levels, L_{eq}(H), the day-night average sound levels, L_{dn} and the 60-second energy equivalent average sound levels, L_{eq} were prepared for each site.

The day-night average sound levels, L_{dn}, were compared to the levels identified by the U.S. Environmental Protection Agency, EPA, requisite to protect against outdoor activity interference and hearing loss consideration[3] and the U.S. Department of Housing and Urban Development, HUD, Site Acceptability Standards[4]. The cumulative energy equivalent average sound levels, Leq, were compared to the criteria established by the U.S. Federal Highway

Administration, FHWA, for picnic, recreational and active sports areas, motels, residences, public meeting places, schools, churches, libraries and hospitals[5] and the U.S. Department of Labor, Occupational Safety and Health Administration, OSHA Safety and Health Standards[6].

MEASURED SOUND EXPOSURE LEVELS, SEL(L_{ax})

Acoustical data was obtained at thirteen of the fifteen monitoring sites. Due to either human error or equipment failure, no acoustical data was obtained at sites A-10 and P-3. L_{eq}(60s) were converted to SEL(L_{ax}) by using the formula:

$$SEL(L_{AX}) = (L_{eq}(60s)) + (10 \log_{10} 60)^{7}$$

The site designations, range in meters and miles, azimuths, L_{eq}(60s)'s and SEL(L_{AX}) are shown in Table IV.

A computerized contour map was prepared showing the L_{eq}(60s) acoustical data and is presented in Figure 2. The contours appear to be slightly skewed possibly the result of the lack of monitoring sites near the launch pad and because of some unusually high unidentified sources that may have influenced the data obtained during the launch at some of the sites.

REGRESSION ANALYSIS

Using data obtained at thirteen monitoring sites a regression analysis was conducted to determine the relationship of the sound exposure levels, SEL(L_{AX}) to the distance from the launch pad. Using a Hewlett-Packard, Model 9805A Statistics Calculator and Plotter, the coefficient of determination, r^2 was computed for both linear and parabolic regression analyses. The coefficient of determination, r^2, is the square of the correlation coefficient and is a value between zero and one. When r^2 equals one, the curve fit is perfect and when r^2 equal zero there is no correlation between the two variables, sound exposure level and distance from launch pad.

The linear coefficient of determination was 0.78 and the parabolic coefficient of determination was 0.88, indicating that the data best fits the parabolic curve.

A plot of the parabolic regression is shown in Figure 3.

COMPARISON OF PREDICTED AND MEASURED SOUND EXPOSURE LEVELS

The predicted noise level generated by the simultaneous firing of the two solid state boosters and the three Space Shuttle main engines was 95 dB(A) at a distance of 6 kilometers or 3.7 miles and 80 dB(A) at a distance of 17 kilometers or 11 miles. The measured sound exposure levels obtained

at distances of 6 and 17 kilometers from the launch pad were 106 and 89 dB(A) respectively or 11 to 9 dB(A) higher than the predicted single event levels.

COMPARISON OF MEASURED STS-1 LAUNCH LEVELS TO OTHER SOURCES

At monitoring sites A-15, A-20, P-6, L.H., P-4 and P-5, the L_{eq}(60s) levels of other identified and unidentified sources exceeded the STS Columbia launch level. At manned site P-4, helicopter and private jet aircraft L_{eq} (60s) levels of 74 to 80 dB(A) were recorded as compared to the STS Columbia launch level of 73 dB(A).

COMPARISON OF MEASURED LEVELS WITH EPA IDENTIFIED LEVELS

The day-night average sound levels, L_{dn}, based on 8-hours or less acoustical data for each site were compared to the levels identified by the U.S. Environmental Protection Agency as requisite to protect against outdoor activity and hearing loss consideration.

The levels at all fourteen sites monitored exceeded the level identified by EPA as requisite to protect against outdoor activity interference but were within the margin of safety level identified by EPA as requisite to protect against hearing loss consideration. It must be recognized, however, that the acoustical data used in this comparison represents a "worse case" condition. It was obtained prior to and following the STS Columbia launch and was influenced by vehicular traffic and spectator noise.

A graphical presentation of the comparison of the L_{dn}'s for each site to the EPA identified levels is shown in Figure 4.

COMPARISON OF MEASURED LEVELS WITH HUD SITE ACCEPTABILITY STANDARDS

The L_{dn}'s obtained at five of the fourteen sites were less than 65 dB(A) and would meet the U.S. Department of Housing and Urban Development, Site Acceptability Standards. The remaining nine sites had levels between 65 and 75 dB(A) and would require special approvals for HUD approved residential financing.

A graphical presentation of the comparison of the L_{dn}'s for each site to the HUD Site Acceptability Standards is shown in Figure 5.

COMPARISON OF MEASURED LEVELS WITH THE FHWA NOISE STANDARDS

The cumulative L_{eq}'s obtained for monitoring periods of four to eight hours were used to compare the measured levels at fourteen sites with the U.S. Federal Highway Administration Noise Standards. Three of the fourteen sites, A-4, A-8 and A-15, exceeded the 67 dB(A) FHWA Standard. Site A-15 was influenced by vehicular traffic prior to and following the launch.

A graphical presentation of the comparison of the cumulative L_{eq}'s for each site to the FHWA Noise Standards is shown in Figure 6.

COMPARISON OF MEASURED LEVELS WITH THE OSHA SAFETY AND HEALTH STANDARDS

The cumulative L_{eq}'s obtained for monitoring periods of four to eight hours were used to compare the measured levels at fourteen sites with the U.S. Department of Labor, Occupational Safety and Health Administration, Safety and Health Standards. The levels measured at all fourteen sites were less than 90 dB(A) permissible noise exposure limit established by OSHA for eight hours of occupational exposure.

CONCLUSIONS

The following conclusions can be made as a result of an extensive analysis of the data obtained at the environmental noise assessment conducted on the STS-1 Space Shuttle Columbia launch launch on April 12, 1981

1. The predicted noise levels as presented in the March 1979 EIS were 95 dB(A) at a distance of 6 kilometers from the [illegible] pad and 80 dB(A) at a distance of 17 kilometers from the launch pad as compared to measures of 106 dB(A) at 6 kilometers from the pad and 89 db(A) measured at a distance of 17 kilometers from the launch pad. The predicted levels were 9 to 11 dB(A) less than the measured levels.

2. Other sources of noise exceeded the L_{eq}(60s) levels measured during the STS-1 Columbia launch. The identified sources at site P-4 were helicopters and private jet aircraft.

3. The day-night average sound levels at all fourteen of the sites where acoustical data was obtained exceeded the level identified by the U.S. Environmental Protection Agency as requisite to protect against outdoor activity interference but were within the margin of safety identified by EPA as requisite to protect against hearing loss consideration.

4. The day-night average sound levels at five of fourteen sites were less than the 65 dB(A) U.S. Department of Housing and Urban Development, Site Acceptability Standards. The remaining nine sites had levels between 65 and 75 dB(A) and would require special approvals to qualify for HUD residential financing. None of the sites exceeded the HUD 75 dB(A) unacceptable level.

5. The cumulative L_{eq}'s obtained for monitoring periods of four to eight hours at all fourteen sites were less than the 90 dB(A) permissible noise exposure limit established by the U.S. Department of Labor, Occupational Safety and Health Administration's Safety and Health Standards for eight hours of occupational exposure.

6. The cumulative L_{eq}'s obtained for monitoring periods of four to eight hours at three of the fourteen sites exceeded the U.S. Federal Highway Administration Noise Standards.

7. The acoustical data used in the comparison of the levels measured during the STS-1 Columbia launch with identified levels, standards and criteria of the federal agencies with noise abatement and control responsibilities represent a "worse case" condition since the levels were influenced by vehicular traffic and spectators, an estimated 35,000 vehicles and over 100,000 persons.

REFERENCES

1. "Environmental Impact Statement for the Kennedy Space Center", (March 1979) National Aeronautics and Space Administration, John F. Kennedy Space Center, Washington, D.C. 20546.

2. "Specifications for Sound Level Meters", (April 1971) American National Standards Institute, ANSI S1.4-1971, New York, N.Y. 10010.

3. "Information of Levels of Environmental Noise Requisite to Protect Public Health and Welfare with an Adequate Margin of Safety", (1974) U.S. Environmental Protection Agency Report Number 55/9-74-004, Washington, D.C.

4. "Site Acceptability and Procedures", (February 1973) U.S. Department of Transportation, Federal Highway Administration, RRM 90-2, Washington, D.C.

5. "Noise Standards and Procedures", (February 1973) U.S. Department of Transportation, Federal Highway Administration, RRM 90-2, Washington, D.C.

6. "OSHA Safety and Health Standards", (29CFR 1910. revised November 7, 1978) U.S Department of Labor, Occupational Safety and Health Administration, Washington, D.C. 20402.

7. "Handbook of Noise Control", (Second Edition 1979). McGraw-Hill Company, New York, N.Y.

TABLE I

SITE DESIGNATIONS, RANGES AND AZIMUTHS OF SELECTED MONITORING SITES

SITE DESIGNATION	RANGE METERS	RANGE MILES	AZIMUTH DEGREES
A-4	4,953	3.08	233°
A-8	5,130	3.19	317°
A-2	5,334	3.31	186°
A-9	7,360	4.57	331°
A-10	7,360	4.57	262°
A-15	10,482	6.51	201°
A-20	11,151	6.93	288°
A-19	11,374	7.07	237°
A-13	13,047	8.10	170°
P-8	14,943	9.28	310°
P-3	16,058	9.98	207°
P-6	17,396	10.81	280°
L.H.	17,526	10.89	160°
P-4	21,187	13.16	240°
P-5	23,640	14.69	275°

TABLE II

MONITORING EQUIPMENT AND APPURTENANCES

No.	Description
2	A.N.S.1. S1.4-1971 Type 1 Sound Level Meters, complete with preamplifiers, microphones, windscreens, extension cables, tripods and calibrating screw drivers, Model: GR-1982.
4	A.N.S.I. S1.4-1971 Type 2 Sound Level Meters, complete with microphones, windscreens, tripods and calibrating screw drivers. Model: db-652/301/16
11	A.N.S.I. S1.4-1971 Type 2 Sound Level Meters, complete with microphones, windscreens, tripods and calibrating screw drivers. Model: db-652/301/14
3	Sound Level Calibrators, Calibration traceable to the National Brueau of Standards. 1 Model: B&K 4230 and 2 Model: CL-302

TABLE III

CLIMATOLOGICAL CONDITIONS DURING STS-1 LAUNCH

Temperature: ..... 58°F

Wind, Direction & Velocity: ..... SE-2 MPH

Relative Humidity: 93%

Barametric Pressure: 30.22

TABLE IV

SITE DESIGNATIONS, RANGE, AZIMUTH, L_{eq}(60s) AND SEL(L_{ax})

SITE DESIGNATION	RANGE METERS	RANGE MILES	AZIMUTH DEGREES	L_{eq}(60s) dB(A)	SEL(L_{AX}) dB(A)
A-4	4,953	3.08	233°	93	111
A-8	5,130	3.19	317°	94	112
A-2	5,334	3.31	186°	84	102
A-9	7,360	4.57	331°	87	105
A-10	7,360	4.57	262°	(No Acoustical Data)	
A-15	10,482	6.51	201°	82	100
A-20	11,151	6.93	288°	76	94
A-19	11,374	7.07	237°	75	93
A-13	13,047	8.10	170°	77	95
P-8	14,943	9.28	310°	73	91
P-3	16,058	9.98	207°	(No Acoustical Data)	
P-6	17,396	10.81	280°	73	91
L.H.	17,526	10.89	160°	68	86
P-4	21,187	13.16	240°	73	91
P-5	23,640	14.69	275°	69	87

ORIGINAL PAGE
BLACK AND WHITE PHOTOGRAPH

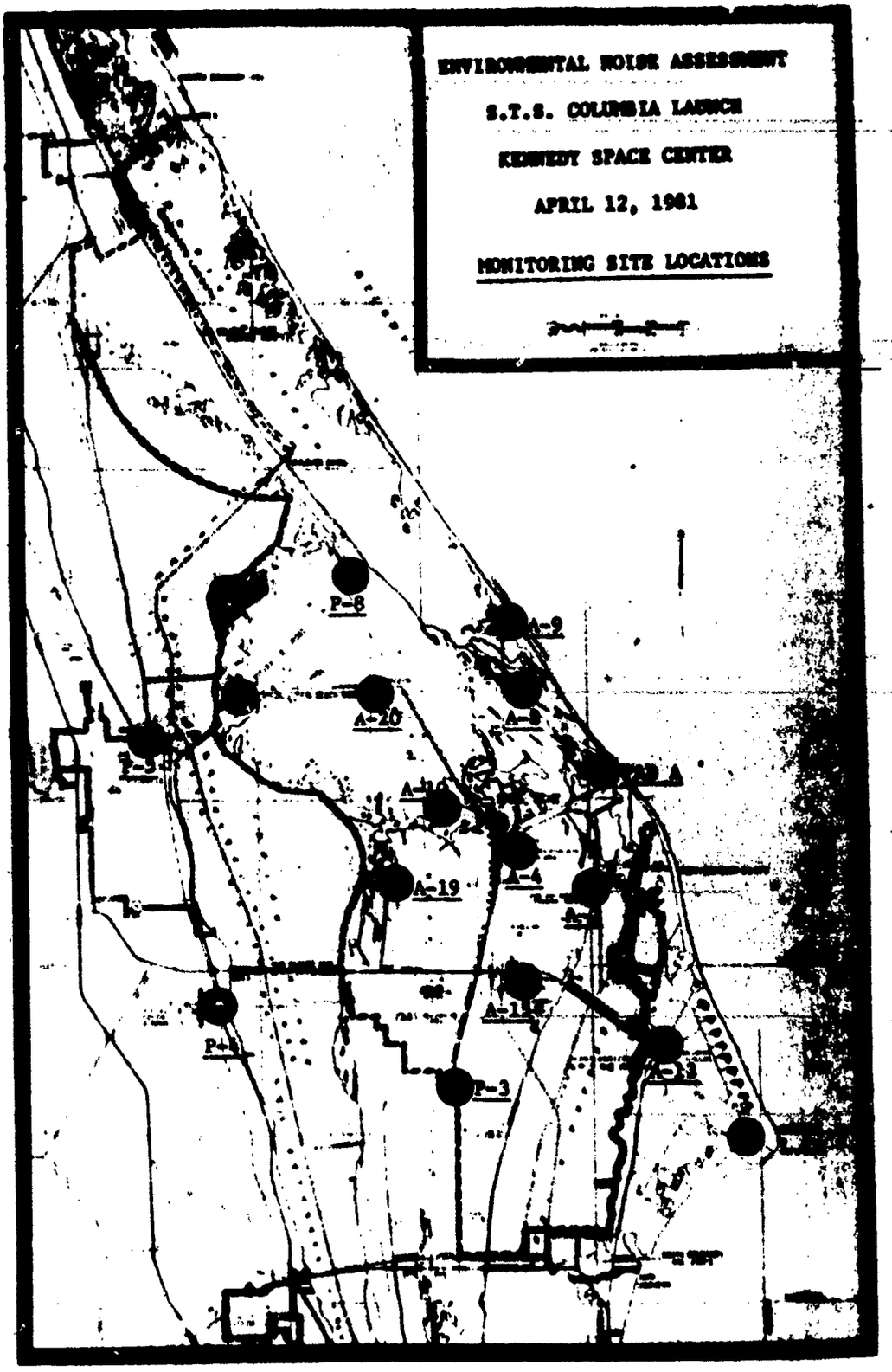

FIGURE 1

ORIGINAL PAGE
BLACK AND WHITE PHOTOGRAPH

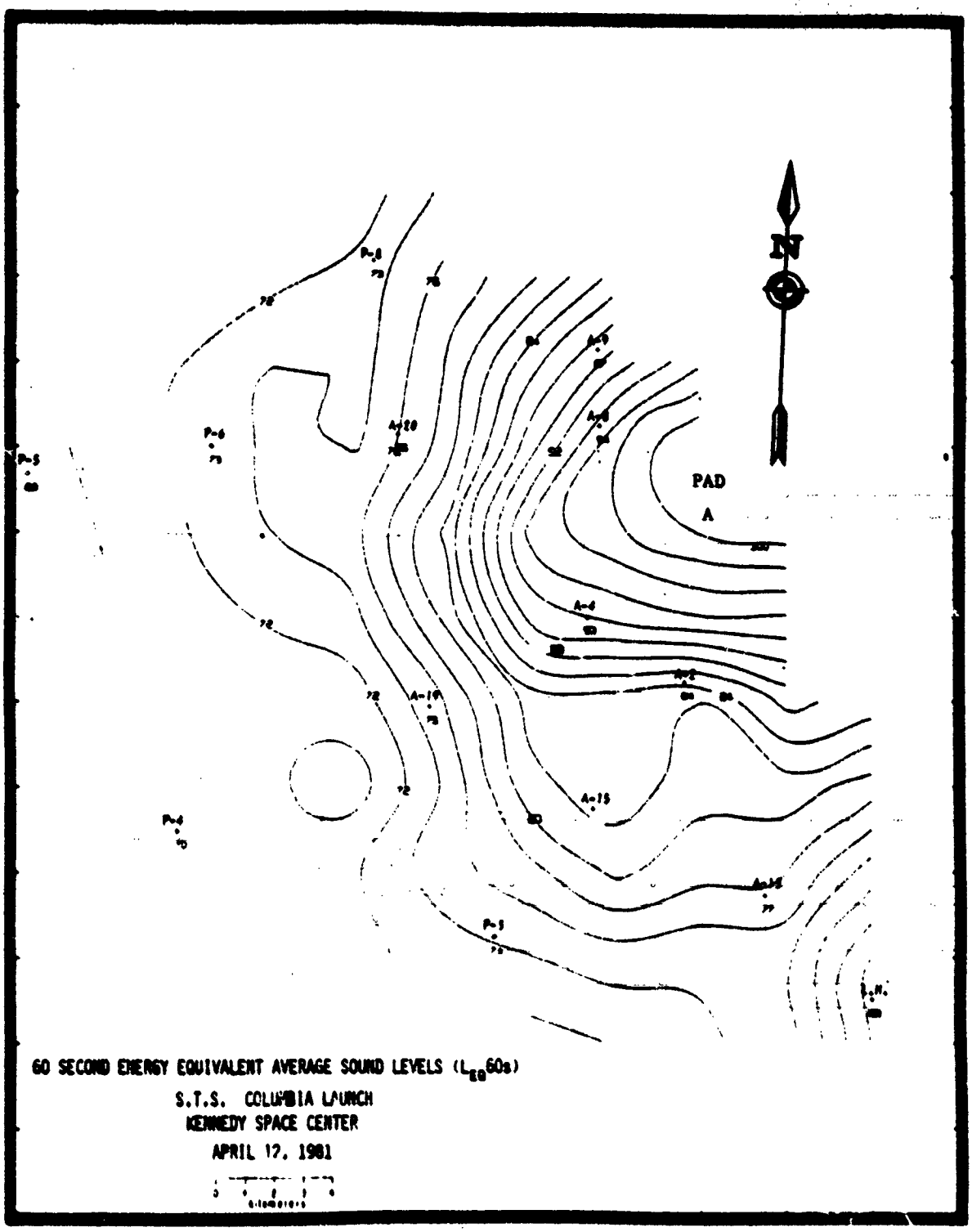

FIGURE 2

ORIGINAL PAGE
BLACK AND WHITE PHOTOGRAPH

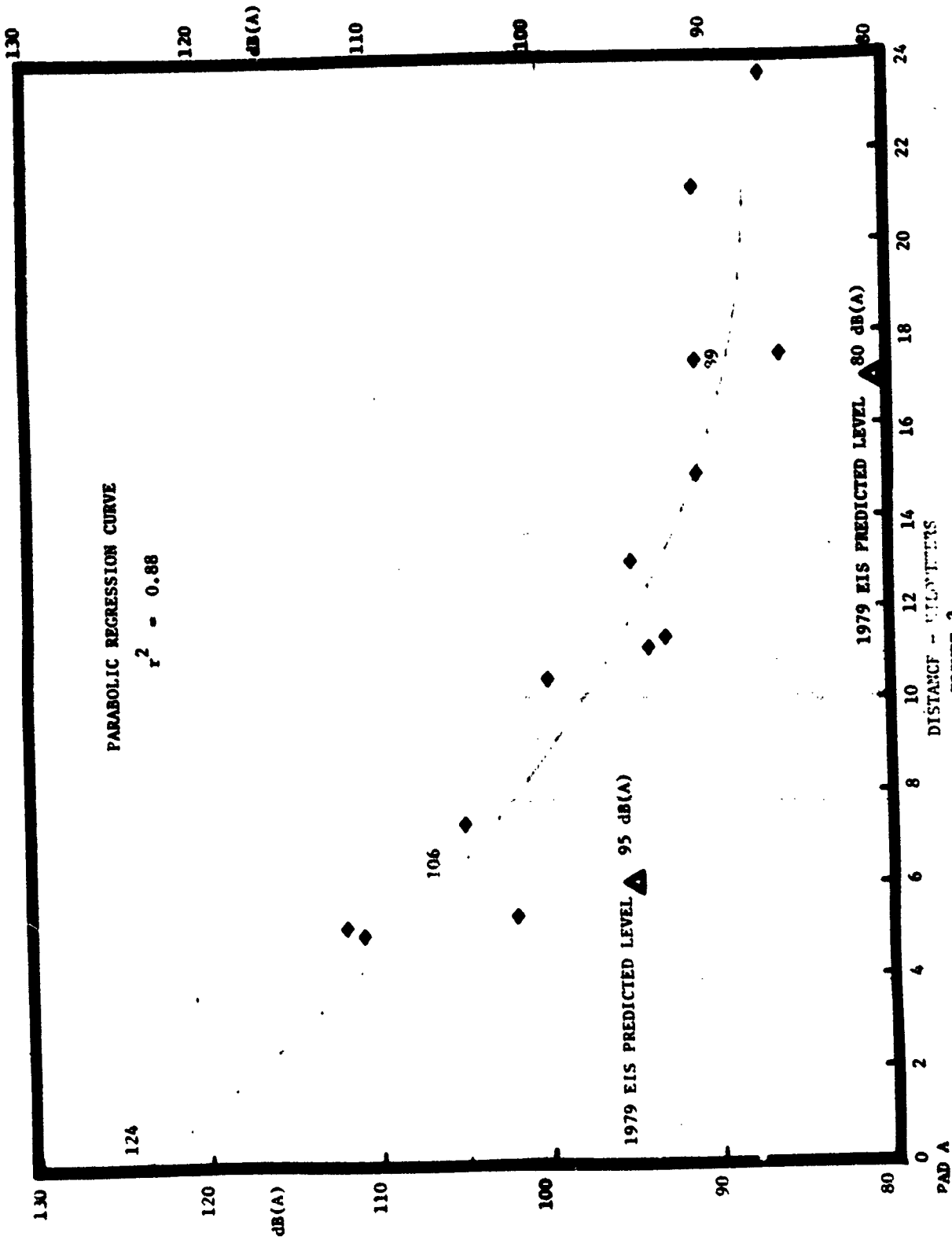

DISTANCE - [illegible]
FIGURE 3

ORIGINAL PAGE
BLACK AND WHITE PHOTOGRAPH

ENVIRONMENTAL NOISE ASSESSMENT

KENNEDY SPACE CENTER

S.T.S. COLUMBIA LAUNCH

APRIL 12, 1981

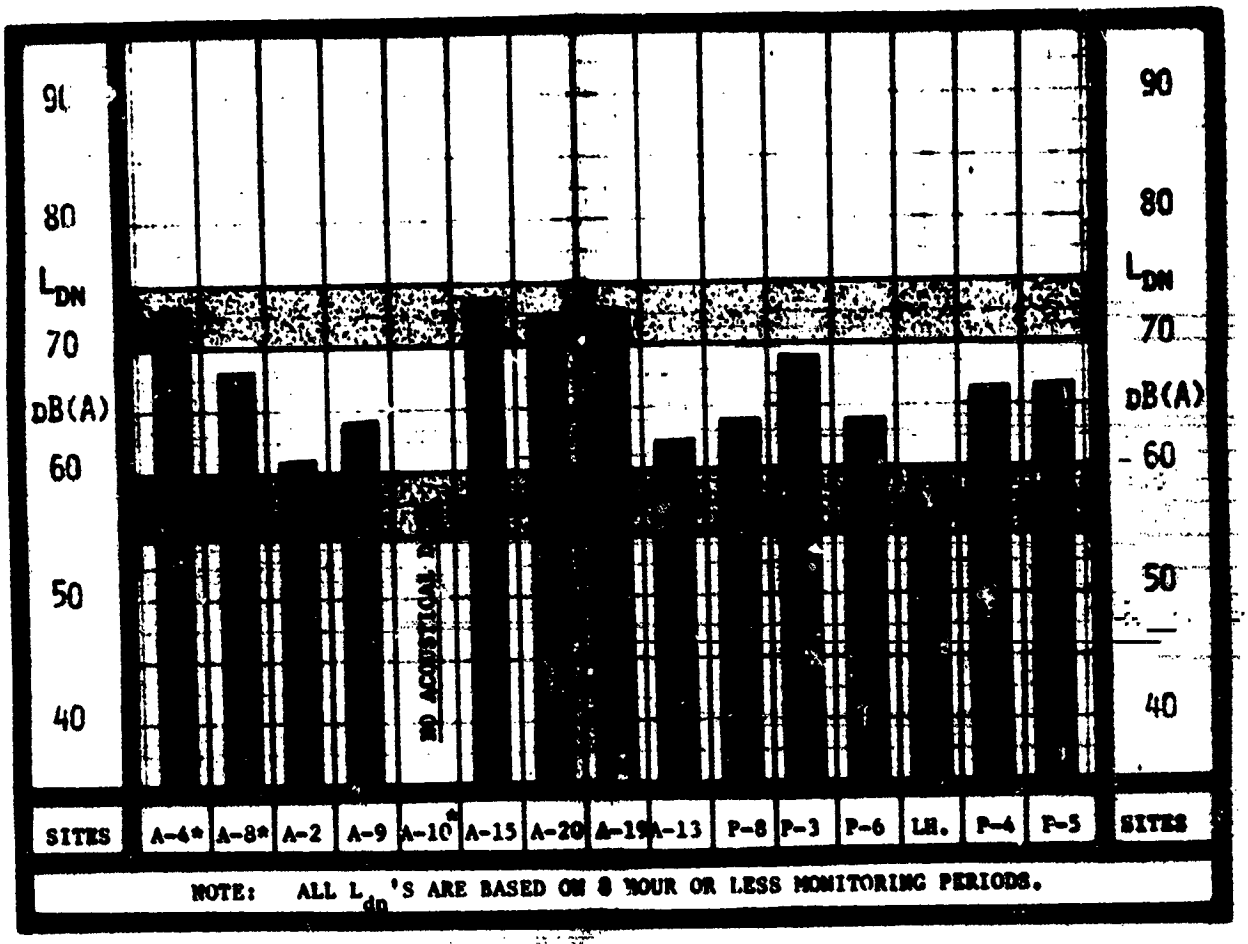

U.S. ENVIRONMENTAL PROTECTION AGENCY IDENTIFIED LEVELS

REQUISITE TO PROTECT AGAINST HEARING LOSS CONSIDERATION:

ACCEPTABLE IF L_{dn} IS LESS THAN 70 dB(A)

REQUISITE TO PROTECT AGAINST OUTDOOR ACTIVITY INTERFERENCE:

ACCEPTABLE IF L_{dn} IS LESS THAN 55 dB(A)

NOTE: BOTH IDENTIFIED LEVELS CONTAIN A 5 dB(A) MARGIN OF SAFETY

* MONITORING EQUIPMENT BASELINE = 60 dB(A) - DYNAMIC RANGE = 64 dB(A)

ALL OTHER SITES: MONITORING EQUIPMENT BASELINE = 40 dB(A) - DYNAMIC RANGE = 64 dB(A)

FIGURE 4

ORIGINAL PAGE
BLACK AND WHITE PHOTOGRAPH

ENVIRONMENTAL NOISE ASSESSMENT

KENNEDY SPACE LAUNCH

S.T.S. COLUMBIA OPERATION

APRIL 12, 1981

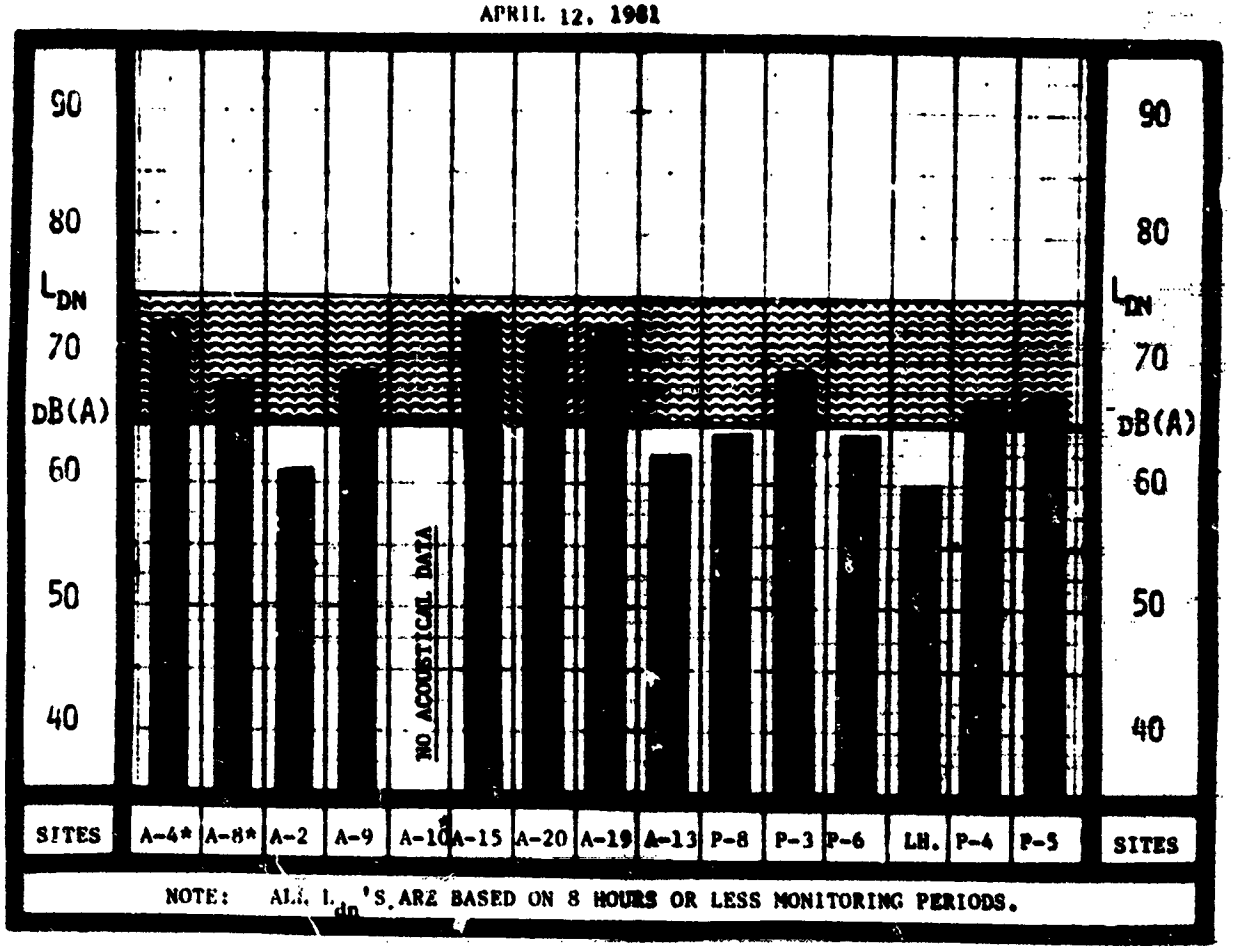

U.S. DEPARTMENT OF HOUSING AND URBAN DEVELOPMENT - SITE ACCEPTABILITY STANDARDS (7/12/79)

ACCEPTABLE: IF L_{dn} DOES NOT EXCEED 65 dB(A)

NORMALLY UNACCEPTABLE: IF L_{dn} IS BETWEEN 65 AND 75 dB(A)- SPECIAL APPROVALS REQUIRED

UNACCEPTABLE: IF L_{dn} EXCEEDS 75 dB(A)

* - - - MONITORING EQUIPMENT BASELINE = 60 dB(A) - DYNAMIC RANGE = 64 dB(A)

ALL OTHER SITES: MONITORING EQUIPMENT BASELINE = 40 dB(A) - DYNAMIC RANGE = 64 dB(A)

FIGURE 5

ORIGINAL PAGE
BLACK AND WHITE PHOTOGRAPH

ENVIRONMENTAL NOISE ASSESSMENT

KENNEDY SPACE CENTER

S.T.S. COLUMBIA LAUNCH

APRIL 12, 1981

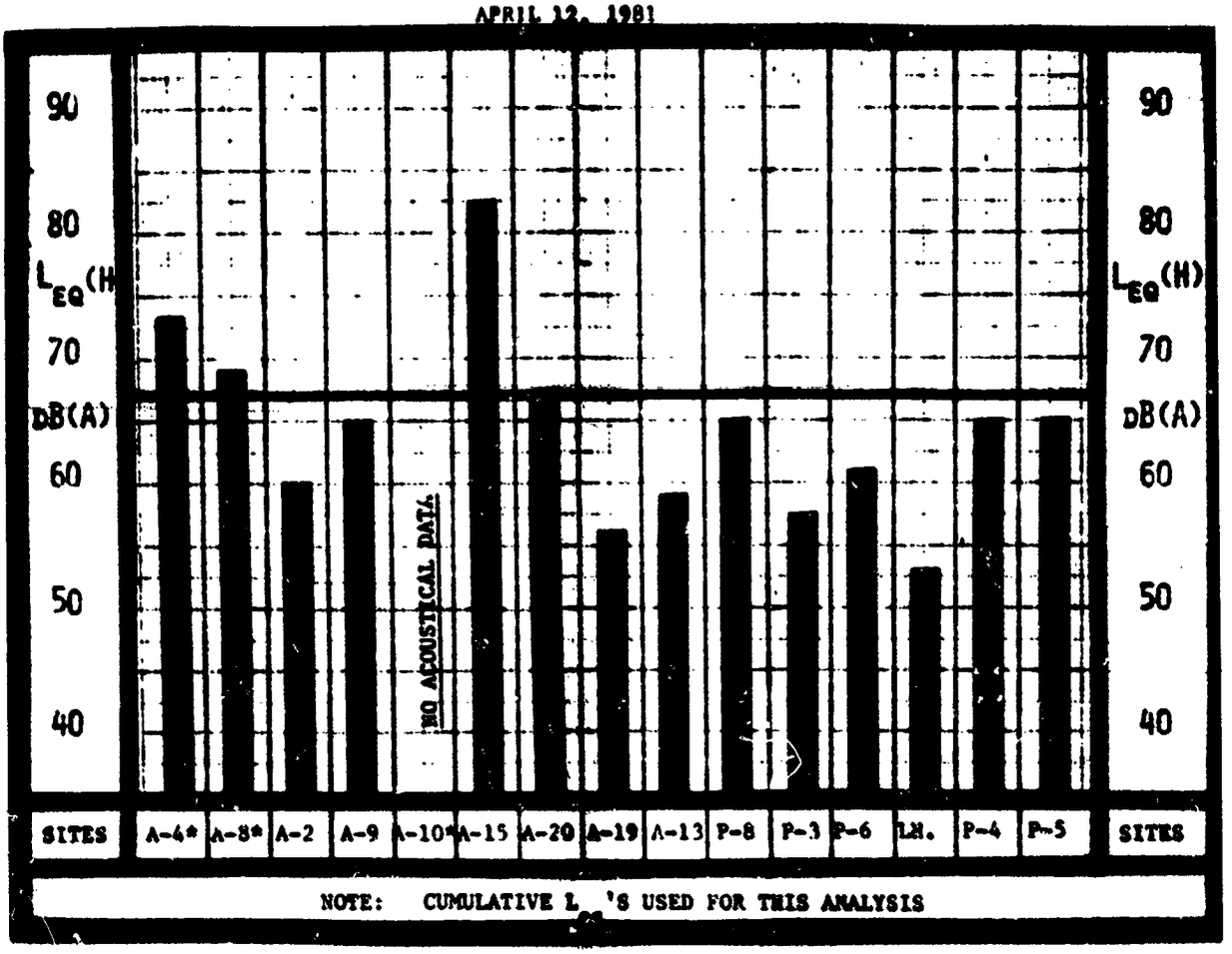

U.S. FEDERAL HIGHWAY ADMINISTRATION NOISE STANDARDS

TRANSMITTAL 192 - HEV-21

MAY 14, 1979

ACCEPTABLE: WHEN L_{eq}(H) EQUALS OR IS LESS THAN 67 dB(A)

* - - - MONITORING EQUIPMENT BASELINE = 60 dB(A) - DYNAMIC RANGE = 64 dB(A)

ALL OTHER SITES: MONITORING EQUIPMENT BASELINE = 40 dB(A) - DYNAMIC RANGE = 64 dB(A)

FIGURE 6

N82 25303

OUTGASSING; ITS EFFECT ON SPACECRAFT VIBRATION DAMPING MATERIALS*

Michael L. Drake, Matthew F. Kluesener and William R. Goddard
University of Dayton Research Institute

ABSTRACT

The future trend of increased size and corresponding structural complexity in orbital spacecraft leads directly to more vibration-prone structures. Concurrently, the increased utilization of steerable appendages provides additional force inputs to excite structural vibrations. Combining these facts with the ever-increasing mission requirements of maintaining dimensional stability and pointing and tracking accuracy, it becomes apparent that the advanced development of spacecraft vibration control is necessary.(ref. 1)

A promising method for obtaining required vibration control is the incorporation of active vibration control systems and passive damping designs into the spacecraft structure.(ref. 2,3,4)

One major concern for any passive damping system is the environmental effect on the damping properties of the material. The system must survive the environment. To date, little information is available about the effects of the space environment upon damping material properties. The following paper presents the results of an experimental test series conducted to evaluate the effects of high vacuum exposure on a group of commercially available damping materials.

INTRODUCTION

The use of spacecraft is increasing in the areas of earth navigation, weather forecasting and communications.(ref. 5) Larger systems for the future are imminent, many evolving from new civilian missions.(ref. 6) The points common to most future systems will be a larger size, with the corresponding increased flexibility, and performance objectives, requiring fast settling times and precise geometric control. Dimensional tolerances for high energy and surveillance electro-optical and electromagnetic systems approach 1/50 of a wavelength. Such tolerances must be maintained not only during orbital operation, but also must be rapidly regained after any required orbital maneuvers. A successful vibration control approach must combine the best isolation of vibration excitation sources, shaped control force inputs, and active modal control systems with passive damping.(ref. 2,7)

*This paper is based on work performed under the sponsorship and technical direction of the International Telecommunication Satellite Organization (INTELSAT). Any views expressed are not necessarily those of INTELSAT.

PASSIVE DAMPING DESIGN REVIEW

To date, most vibration control development for spacecraft systems has been in the area of active control.(ref. 8) There has been little effort in development of passive damping techniques for spacecraft structures.(ref. 9)

The validity of the passive damping approach to the solution of a vibration problem has been well established on numerous aircraft and jet engine projects.(ref. 10,11,12,13)

Passive damping designs are like any other successful designs in that they are developed through a logical progression of data collection and analytical procedures. A haphazard approach will lead directly to an unsuccessful design.

The design methodology successfully used by UDRI consists of the following steps.(ref. 14)

The first step is verifying that the vibration problem is caused by resonant vibration in the structure. In the initial design stages, this means analytically determining the resonant frequencies of the structure and relating these frequencies to the anticipated force versus frequency inputs for the structure. This data directly leads to the location of those resonant modes requiring damping. If the particular structure has reached the proto-type state before problems arise, similar data is collectable from experimental tests.

If the results of step one indicate that increased damping is required, a complete dynamic analysis of the problem resonant frequencies must be done. Knowledge of the mode shapes and inherent structural damping of the modes is necessary. Once again, this data can be obtained from either a reliable analytical model for initial design phases, or from experimental tests conducted on a proto-type structure.

The next step is the definition of the environment in which the damping design must operate. A primary design concern is the temperature environment. Damping properties are very sensitive to temperature. Improper definition of the operational temperature range will eliminate any chance of a successful damping design. There are three basic temperatures needed. Knowledge of the upper and the lower temperature extremes which the damping design must survive is necessary. Also needed is the temperature, or temperature range, over which high damping is desired.

The other major environmental concern for spacecraft passive damping design is the effect of the space environment on the damping material. Little or no data is available about the effects of the space environment on material damping properties.

With the completion of the first steps, the problem has been completely defined. The structural dynamics causing the problem are known and the environment the damping design must survive is also established. At this point, the designer can choose the proper damping configuration and material

to begin the procedure for an optimum damped design. Considerations such as the size, weight dimensional fit, and other factors must also be reviewed in the final decision.

The designer must have total confidence in his choice of damping system. The damping system must remain functional in the space environment for the entirety of the spacecraft's expected life. Current life expenctency of communication spacecraft is seven to ten years. The lack of data relating damping material property stability to time exposure of spacecraft in high vacuum space environments prompted this study. This paper presents the results of a high vacuum exposure test series on eight commercially available damping materials and suggests further programs which will develop the required data to enable confident use of passive damping designs in large space structures.

TEST SERIES CRITERIA

The characteristics of space environment include ultrahigh vacuum and various types of radiation. In many spacecrafts with optical and precision instruments, there are stringent outgassing requirements for all construction materials. This combined with the fact that polymeric materials generally do outgas , led this research effort to study only the effects of ultrahigh vacuum exposure on various polymeric material damping properties. (ref. 15)

Outgassing is directly proportional to the exposed surface area of a material. Any outgassing component must diffuse through the material to the surface, where the difference between the material vapor pressure and environmental pressure can allow an atom or molecule to overcome surface tension and escape. (ref. 16) Outgassing and thermogravimetric analysis data are available for many materials, but no correlation to the stability of damping properties has previously been attemped.(ref. 17)

Currently, commercially available polymeric damping materials are not specifically formulated with spacecraft applications in mind. This test series was devised to obtain basic information from off-the-shelf damping materials. The test results could be considered as a guideline toward the application of these materials.

Eight materials were selected to form a representative cross section of those polymers having both ready availability as commercial damping materials and desirable properties. The materials evaluated are listed in Table 1. This table indicates the temperatures at which peak damping occurs at 1 Hz and the type of beam specimen used in the vacuum exposure tests. These materials as a group cover the temperature range of -85°C to 38°C.

EXPERIMENTAL APPARATUS AND TECHNIQUE

The material evaluation was conducted using the recommended fixture, equipment, and procedures outlined in proposed ASTM standard E-33 "Test

Method for Measuring Vibration Damping Properties of Materials". Depending upon the modulus of the material evaluated, either an Oberst, modified Oberst, or symmetric sandwich cantilever beam is used in the test. The three types of test beams are illustrated in Figure 1.

A block diagram of the evaluation system is shown in Figure 2. The material test beam is excited at its natural frequencies by use of a non-contacting magnetic drive system which is controlled by a precision frequency synthesizer. The beam response is measured with an accelerometer. Half-power bandwidth measurements are made for each resonant mode. The temperature of the beam and fixture are changed at discrete increments until the useful temperature range of the material is covered. A complete description of this test procedure is given in Reference 18.

The experimental test data are the modal damping factors and resonant frequencies of the composite test beam. While exact material properties are not readily apparent in this form, the general trend of the material behavior is evident. It is therefore common practice to plot the composite structural loss factor (ηs) versus temperature for any material being evaluated.

Exact material damping properties can be determined from the experimental data through the use of 4th order beam theory equations. The data reduction employed at the UDRI results in material properties on a reduced temperature nomogram which is illustrated in Figure 3. This format shows the material data as a function of both temperature and frequency, and is useful when incorporating the material into a damping design. A file of nomograms for commercially available damping materials permits one to choose the material best suited for a given application.

TEST SERIES PROCEDURE AND RESULTS

From the outset, it was decided to collect experimental test data for each material as a function of vacuum exposure time. A typical set of experiment data is shown in Figure 4. A quick comparison with the initial baseline results would indicate any trend developing in the material behavior. Then, if the change was determined to be significant, the experimental data would be reduced to obtain the outgassed material damping properties. This information would help to determine possible improvements in the composition of the material, as well as other related factors.

Each beam was individually installed in the standard test fixture, and baseline experimental data (frequencies and modal loss factors) were acquired under normal atmospheric conditions. The beam was then placed in an ultrahigh vacuum chamber and exposed at room temperature to a pressure of 5×10^{-6} Torr or less (ref. 19), for a measured period of time. Then the beam was removed from the chamber, reinstalled in the test fixture, and experimental data again taken. The beam was again placed in the chamber, and the process repeated. This process continued until each beam had received at least 450 hours of exposure time. The minimum exposure period was 12 hours duration.

The rate of vacuum pump down for a typical test run is shown in Figure 5 and the vacuum system is shown in Figure 6.

Test results for a given material at each exposure interval were compared to the baseline data to determine if any significant change in damping properties was developing.

The first three materials (3M Company's ISD 112, ISD 110, and The Soundcoat Company's Dyad 601) were evaluated to test for trends in damping properties versus vacuum exposure time.

A significant change was noted in the loss factor values after the initial vacuum exposure period for each material. However, the loss factor values tended to return to the baseline values as total exposure time increased. Variability was noted in the temperatures at which peak loss factor occurred, and in the resonant frequency for each mode as well. Each of the three materials was placed in the vacuum chamber for a final exposure of 240 hours. The material properties then showed a tendency to stabilize. Table 2 contains the complete set of test data for material ISD 112. Figures 7, 8, and 9 show the structural loss factor versus vacuum exposure time for ISD 112, ISD 110, and Dyad 601 respectfully.

The initial practice was to remove one beam from the chamber and install another. This would permit the damping properties of one beam to be evaluated while the other was exposed to vacuum. The material evaluation test was of a short duration relative to vacuum exposure time, so it was common for the evaluated beam to remain in a normal atmosphere while another beam finished its time interval in the chamber.

After completing the first three material tests, it appeared that the scatter in the data may have been caused by changing atmospheric conditions when the materials were removed from the ultrahigh vacuum to be re-evaluated. Specifically, varying room humidity levels between tests, or different lengths of exposure to normal atmospheric conditions between vacuum exposures, may have contributed to the variability in the data.

To reduce the effect of changing humidity on further tests, a new procedure was incorporated. When the test beam was removed from the ultrahigh vacuum chamber, it was placed in a bell-jar vacuum chamber, which was then evacuated to a pressure of approximately 10^{-3} Torr. The specimen was removed only long enough for damping tests and was then returned to the bell-jar. The level of the vacuum in the bell-jar was not considered significant, therefore the time in the bell-jar was not added to total exposure time.

The new procedure was used to evaluate the second set of five damping materials. For comparison purposes, it was decided to place the material test beams together in the ultrahigh vacuum chamber to receive identical exposure times. Although it was expected that the combined effect of outgassing from all five beams would slightly raise the pressure, this was not considered to be of great importance.

As in the first three materials, a significant change in the loss factor values for all five materials was noted after initial exposure. These values tended to move toward the baseline rapidly as exposure time accumulated. There tended to be variability in both frequency and temperature of peak loss factor from mode to mode, but it was not as significant as with the first three materials. It was decided that this difference must have been a result of the reduced exposure to atmosphere during evaluation. For all five materials, the frequency and temperature of peak loss factor for each mode after 1000 total hours of vacuum exposure was not dramatically changed from the baseline. Figures 10, 11, 12, 13, and 14 illustrate the results from all 5 materials in this second test series.

There were trends in all eight materials after their total exposure which leads to the belief that the materials will be stable in the vacuum environment of space. Much longer exposure times would be required for any generalization of the data. The materials as a group tended to remain more or less stable, but there were exceptions. It is felt that each damping material should therefore be appraised individually, as any difference in behavior is directly connected to the composition. Any material which may be utilized in a contrained layer damping treatment should be significantly isolated from the space environment, thereby minimizing long term reliability problems.

RECOMMENDATIONS FOR FURTHER STUDIES

Based upon the results of this test series, various recommendations may be made for further studies.

It would be desirable to design a test fixture which would permit a given material test beam to remain in an ultrahigh vacuum chamber for the duration of exposure time. That is, all testing would be conducted without removing the test specimen from the vacuum chamber. A means for accurately and uniformly controlling the temperature of the beam during each test interval would be needed. Incorporation of a drive transducer and response accelerometer would be relatively straightforward. This set-up would eliminate any variables resulting from atmospheric exposure, such as absorbtion of moisture.

Determination of outgassing components by addition of a Quadrapole Type Residual Gas Analyzer to the ultrahigh vacuum chamber would be helpful. A correlation between outgassing components and material damping property changes would assist in devising new or improved materials.

It would not be difficult to include an ultraviolet source in the test chamber. Previous extensive studies have indicated that this is an important type of exposure affecting material properties. As with outgassing, correlation studies of ultraviolet exposure and damping properties would be beneficial.

A test series to provide long-term exposure data in a simulated space environment for commercially available damping materials is needed. This

would provide definite conclusions about the practical application of each material in spacecraft design. This data would also be useful when devising new damping material compositions specifically for spacecraft use.

A goal of any future studies should be to establish both a standardized set of environmental conditions and a practical test apparatus for the purpose.

REFERENCES

1. Degener, M., "Effect of Structural Damping on the Dynamic Response of Spacecraft", AGARD Conference Proceedings No. 277, April 1979.

2. Trudell, R. W., Curley, R. C., Rogers, L. C., "Passive Damping In Large Precision Space Structures", 21st Structures, Structural Dynamics, and Materials Conference, Seattle, Washington, May 12-14, 1980.

3. Hughes, P. C., "Passive Damper Analysis for Reducing Attitude Controller/ Flexibility Interaction", Journal of Spacecraft and Rockets, Vol. 13, No. 5, May 1976, pp. 271-274.

4. Hughes, P. C., "Passive Dissipation of Energy in Large Space Structures", Journal of Guidance and Control, Vol. 3, No. 4, July/August 1980, p.380.

5. Henry, R. C., "Benefits of the Military Use of Space", Astronautics & Aeronautics, July/August 1979, pp. 32-33,39.

6. A Collection of 7 Articles on Large Space Structures, Astronautics & Aeronautics, Vol. 16, No. 10, October 1978.

7. Soosar, K., et al., "Passive and Active Suppression of Vibration Response in Precision Structures", State-of-the-Art Assessment, Vol. 2, Technical Analysis.

8. ACOSS Five (Active Control of Space Structures) Phase 1A, Final Technical Report, Lockheed Missiles & Space Company, Inc., November 1981.

9. Otth, D., "Shear DAmpers for Deflections of Micro-inch Magnitudes", Proceedings - Institute of Environmental Sciences, Circa 1975.

10. Drake, M. L., Sharp, J. D., "Ellimination of A Resonant Fatigue Problem for Major Maintenance Benefits", ASME publication 77-DET-135, September 1977.

11. Cannon, C. M., "Examples of the Use of Additive Elastomeric Damping Treatments to Control Vibration Problems in Air Force Systems", Viscoelastic Damping 1980 Conference, AFFDL-TM-78-78-FBA.

12. Drake, M. L., Sharp, J. D., "An Example of Additive Damping As A Cost Savings Alternative to Redesign", Winter Annual Meeting, Atlanta, Georgia, ASME paper No. 77-WA/GT-2, November 1977.

13. Jones, D. I. G., Cannon, C. M., Parin, M. L., "Controlling the Dynamic Response of Jet Engine Components", Shock and Vibration Bulletin 45, June 1975.

14. Drake, M. L., Whitford, D. H., editors, Vibration Damping Short Course Notes, 1981, University of Dayton Research Institute.

15. Landel, Robert F., Rembaum, Alan, editors, Chemistry in Space Research, pp. 321-360, American Elsevier Publishing Company, Inc., 1972.

16. Simkin, Donald J., editor, Chemical Engineering Techniques in Aerospace, Vol. 60, pp 68-79, 1964.

17. Cambell, Jr., William A., Marriott, Richard S., Park, John J., "Outgassing Data for Spacecraft Materials", NASA Reference Publication 1061, August 1980.

18. Drake, M. L., Terborg, G. E., "Polmeric Material Testing Procedures to Determine Damping Properties and the Results of Selected Commercial Material", Technical Report AFWAL-TR-80-4093, July 1980.

19. Van Vliet, R. M., Passive Temperature Control in the Space Environment, pp. 186-237, The Macmillan Company, NY, 1965.

TABLE 1
MATERIALS EXPOSED TO ULTRAHIGH VACUUM

Test Beam No.	Manufacturer	Damping Material	Temperature (°C) of Maximum Loss Factor at 1 Hz	Test Beam Type
I-01	3M Company	ISD 112	-25	Sandwich
I-02	3M Company	ISD 110	10	Sandwich
I-03	Soundcoat Co.	Dyad 601	-23	Sandwich
I-04	3M Company	NPE-9046	55	Sandwich
I-05	E-A-R Div Cabot Corp.	ISODAMP C-1002	27	Oberst
I-06	E-A-R Div. Cabot Corp.	EXODAMP C-2003	24	Oberst
I-07	Soundcoat Co.	D	38	Sandwich
I-08	3M Company	ISD 830	-85	Sandwich

TABLE 2
DAMPING PROPERTIES VERSUS VACUUM EXPOSURE TIME

MATERIAL ISD 112 **MANUFACTURER** 3M Company

TYPE OF TEST SPECIMEN Sandwich TEST BEAM NO. I-01

TOTAL EXPOSURE (HOURS)				12		24		90		234		474	
				12 hrs. @ 1×10^{-5} torr @ 25 °C		12 hrs. @ 1×10^{-7} torr @ 25 °C		66 hrs. @ 1×10^{-7} torr @ 25 °C		144 hrs. @ 1×10^{-8} torr @ 25 °C		240 hrs. @ 6×10^{-8} torr @ 25 °C	
T (°C)	Mode	Prior to Outgassing η	Prior to Outgassing f_c	η	f_c	η	f_c	η	f_c	η	f_c	η	f_c
-3.8	1	0.0604	102.58	0.0537	104.904	0.0288	106.516	0.0228	106.929	0.0386	104.734	0.0513	104.931
	2	0.0761	595.91	0.1289	610.776	0.0860	633.271	0.0747	645.221	0.1111	625.616	0.1193	617.415
	3	0.1645	1582.51	0.1509	1632.6	0.1030	1696.49	0.0802	1731.45	0.1242	1676.51	0.1602	1677.46
	4	0.2332	2797.61	0.2162	2861.62	0.1337	3076.09	0.2199	3177.53	0.1634	3003.87	0.2383	2943.50
10	1	0.2064	95.33	0.1991	96.0641	0.1440	99.2081	0.1828	95.4011	0.1331	98.3901	0.1337	98.6260
	2	0.3125	501.37	0.2871	494.207	0.2653	533.556	0.2982	489.481	0.2474	522.411	0.2733	528.395
	3	0.3341	1397.31	0.3333	1301.34	0.2820	1379.34	0.2915	1309.35	0.2691	1403.46	0.3864	1302.03
	4	0.3917	2192.17	0.2822	2209.55	0.3493	2381.53	0.3282	2247.75	0.3466	2373.14	--	2328.14
23.8	1	0.4795	79.50	0.3973	84.6551	0.3140	89.1161	0.3280	89.0601	0.3461	85.2072	0.5734	71.2500
	2	0.2848	399.81	0.2991	416.677	0.3034	443.168	0.3548	458.631	0.2670	426.161	0.3700	468.080
	3	0.2697	1048.27	0.3093	1093.74	0.3083	1135.83	0.3071	1151.70	0.2870	1102.41	--	1169.23
	4	0.1707	1378.34	0.2343	1962.55	0.2725	2030.23	0.2925	2037.31	0.2314	1969.23	0.4258	1998.74
37.7	1	0.3322	64.48	0.0352	64.7411	--	--	0.4695	78.1441	0.3795	69.9836	0.3262	66.9420
	2	0.1717	351.87	0.1685	353.181	0.2067	365.361	0.3052	410.417	0.2055	368.704	0.1837	363.760
	3	0.1482	949.08	0.1418	954.261	0.1630	962.241	0.1976	998.331	0.1795	978.001	0.1629	966.190
	4	0.0572	1359.01	0.0854	1814.77	0.0978	1830.35	0.1654	1910.14	0.1094	1835.57	0.1149	1345.75

ORIGINAL PAGE IS OF POOR QUALITY

ORIGINAL PAGE IS
OF POOR QUALITY

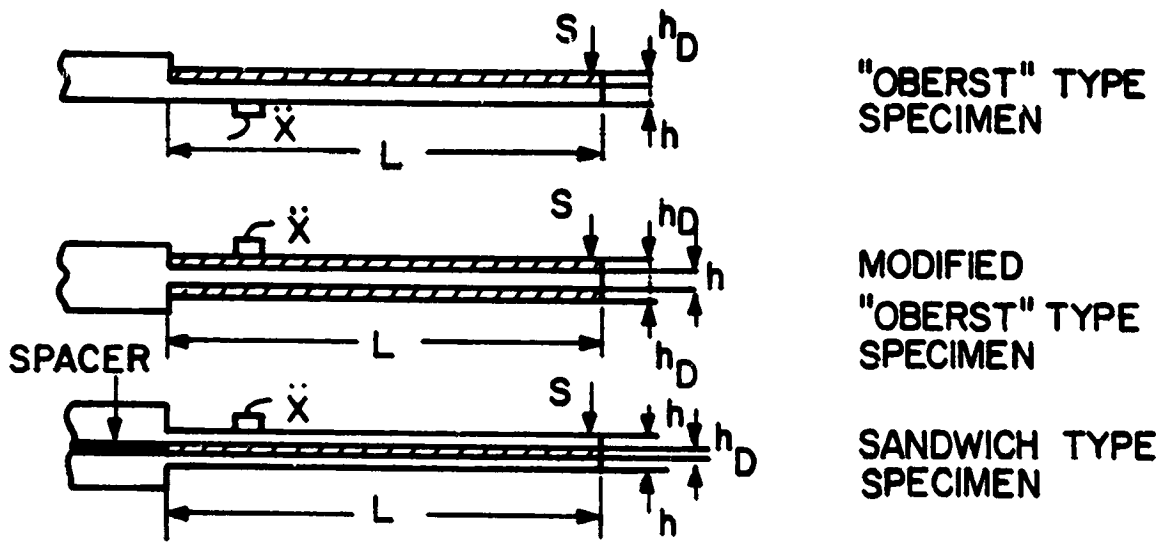

Figure 1. Vibrating Beam Test Specimens

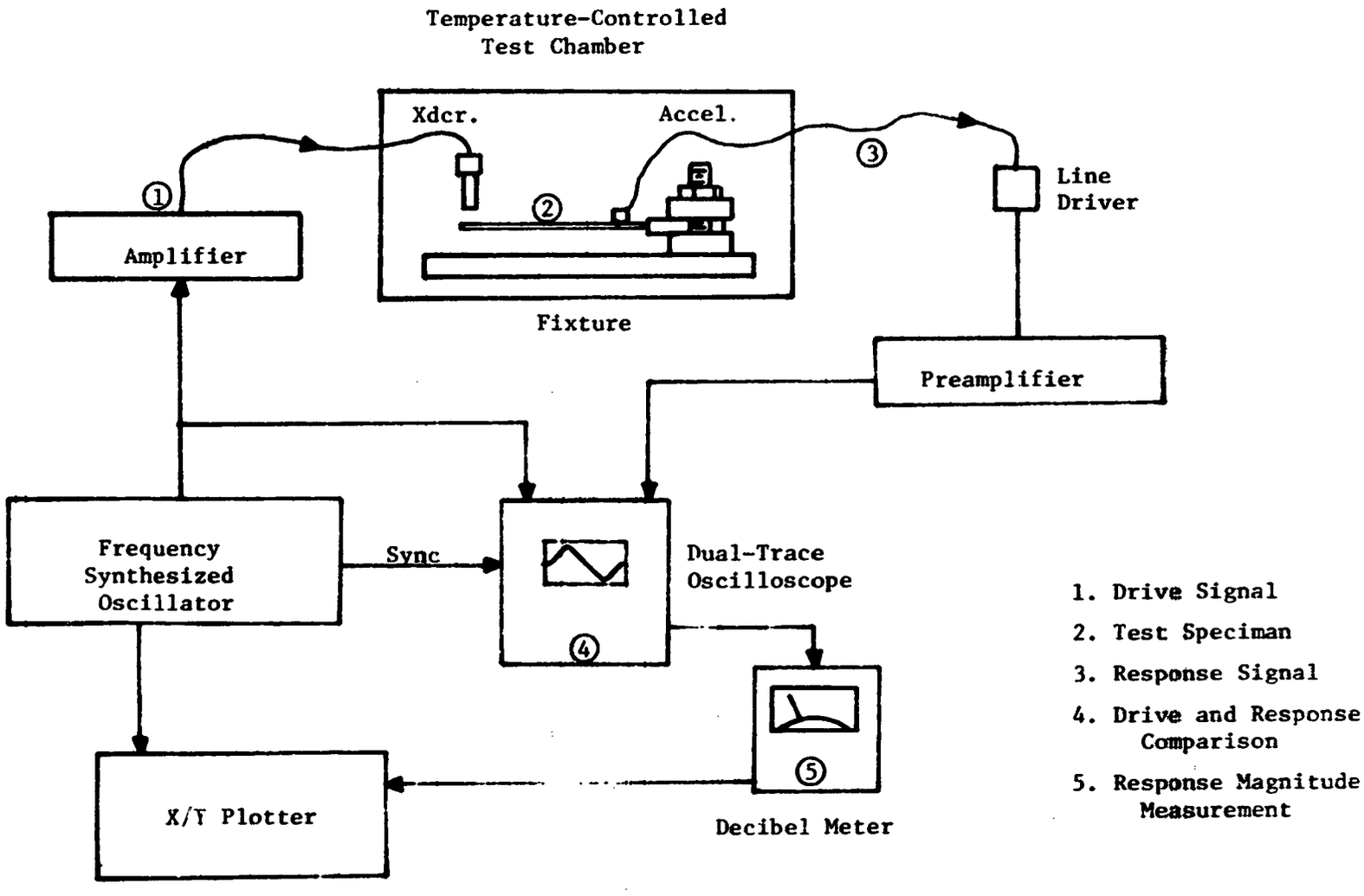

Figure 2. Block Diagram of Material Property Evaluation System

ORIGINAL PAGE IS
OF POOR QUALITY

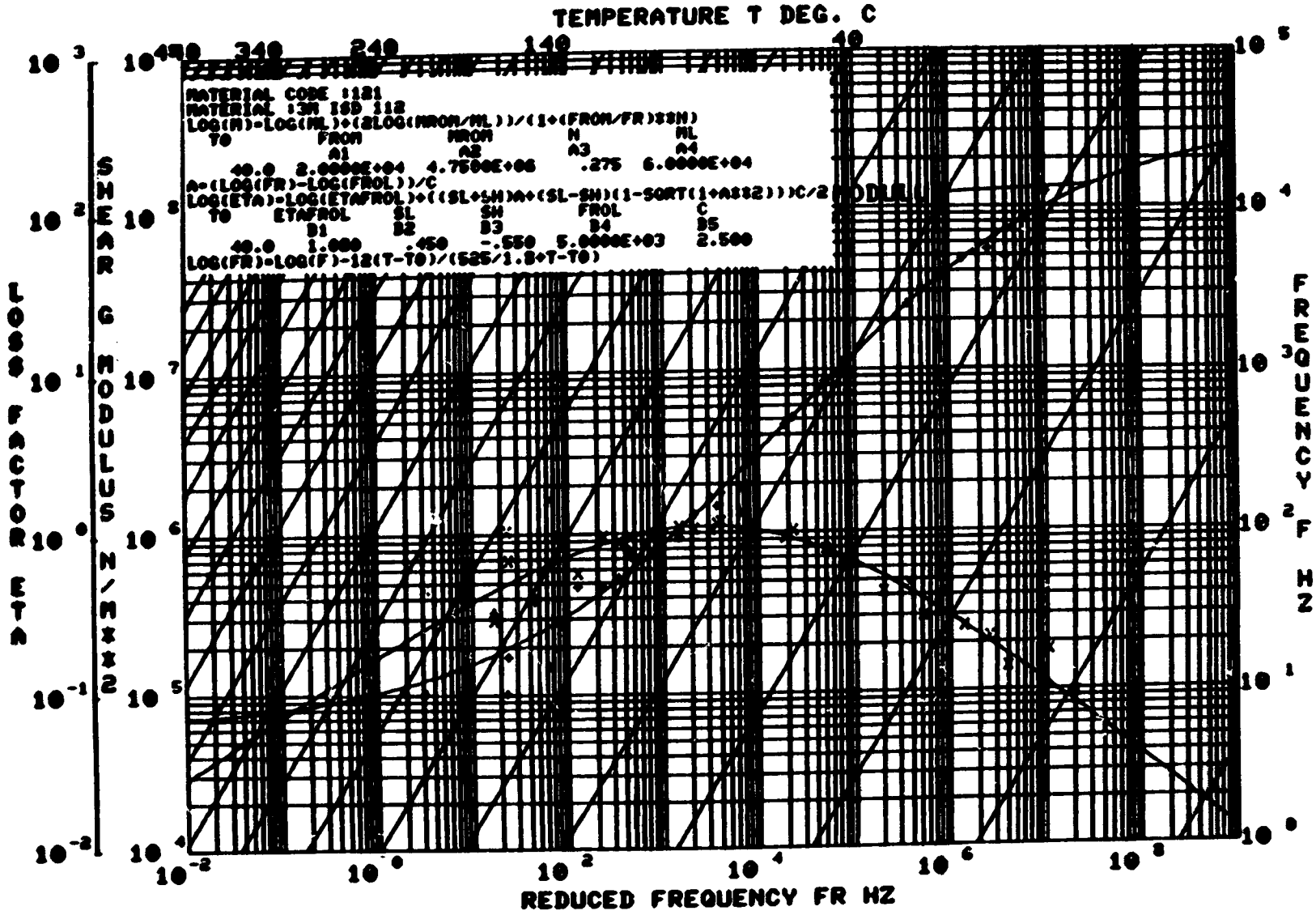

Figure 3. Typical Nomogram for a Damping Material

ORIGINAL PAGE IS OF POOR QUALITY

ORIGINAL PAGE IS
OF POOR QUALITY

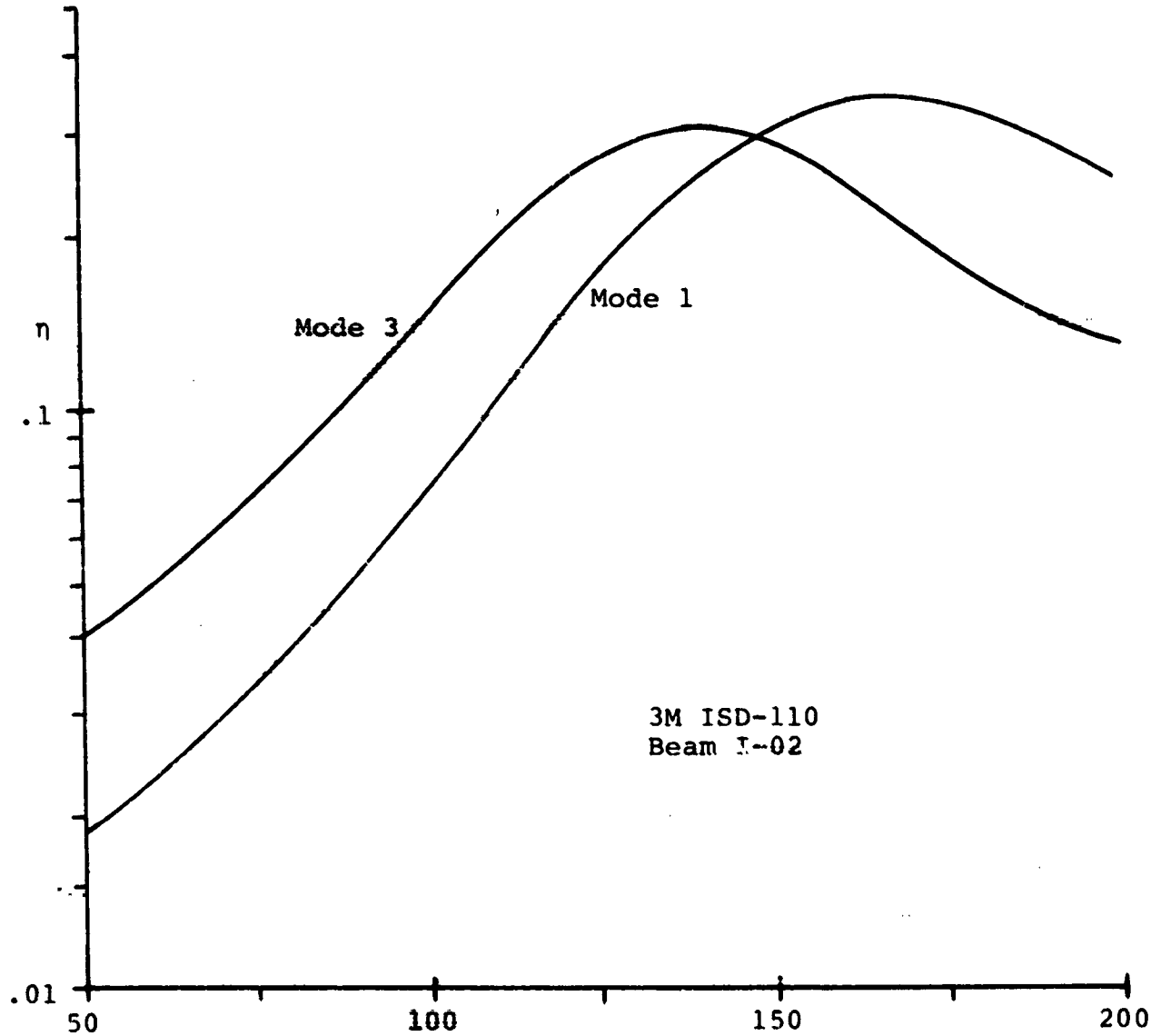

Figure 4. Loss Factor vs Temperature for ISD-110 at Zero Hours Exposure

ORIGINAL PAGE IS
OF POOR QUALITY

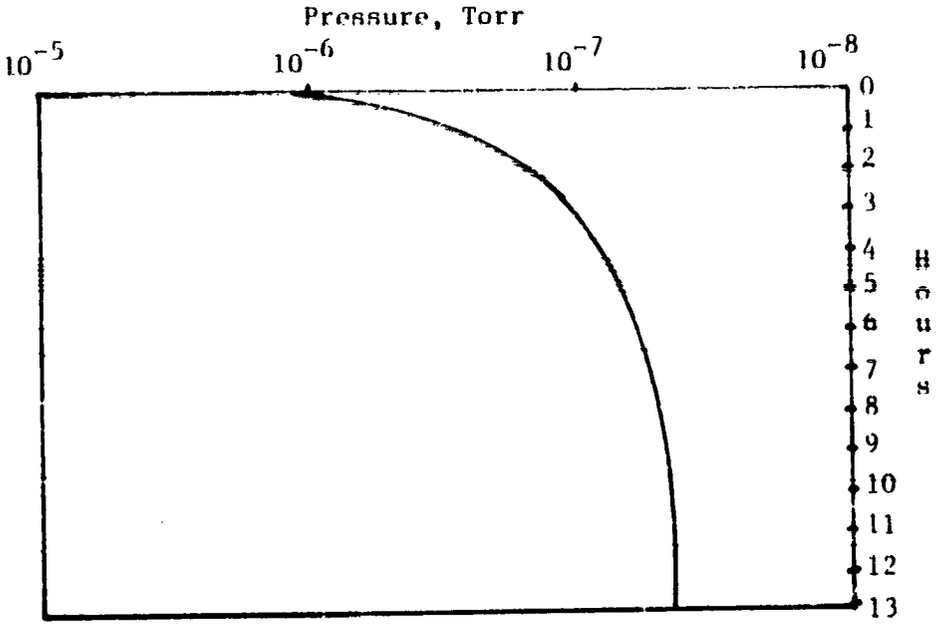

t (hrs)	Press	Avg.
0	2.5×10^{-6}	7.5×10^{-7}
1	2.5×10^{-7}	2×10^{-7}
2	1.5×10^{-7}	1.2×10^{-7}
3	1×10^{-7}	8.9×10^{-8}
4	7.8×10^{-8}	7.3×10^{-8}
5	6.8×10^{-8}	6.4×10^{-8}
6	6×10^{-8}	5.8×10^{-8}
7	5.5×10^{-8}	5.5×10^{-8}
8	5.5×10^{-8}	5.2×10^{-8}
9	5×10^{-8}	5×10^{-8}
10	5×10^{-8}	4.9×10^{-8}
11	4.8×10^{-8}	4.8×10^{-8}
12	4.8×10^{-8}	4.6×10^{-8}
13	4.5×10^{-8}	
13		16.54 Total area Press-hrs.

Time avg. press = 1.27×10^{-7} Torr for 13 hours

Figure 5. Typical Chamber Pressure During Initial Vacuum Exposure

ORIGINAL PAGE IS
OF POOR QUALITY

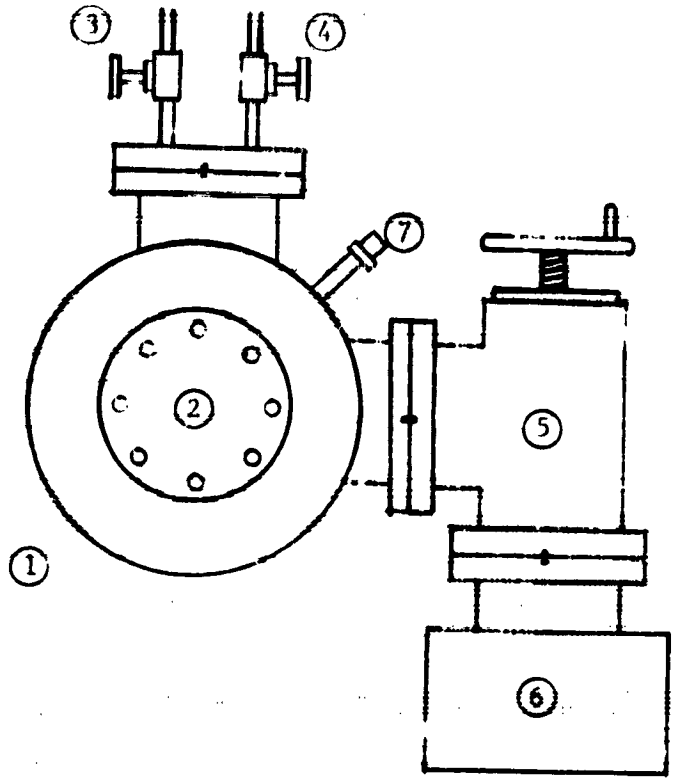

1. Cylindrical stainless steel vacuum exposure chamber, $\approx$ 1.5 ft^3
2. Access port for test beam placement/removal
3. Nitrogen gas inlet for purging system
4. To roughing out pump (down to $\approx$ ($x10^{-4}$ Torr.)
5. Access valve to Ion pump
6. Ion pump (below $\approx 1x10^{-4}$ Torr.)
7. Ion Vacuum gage

Figure 6. Ultrahigh Vacuum Chamber and System as used for Exposure Test Series

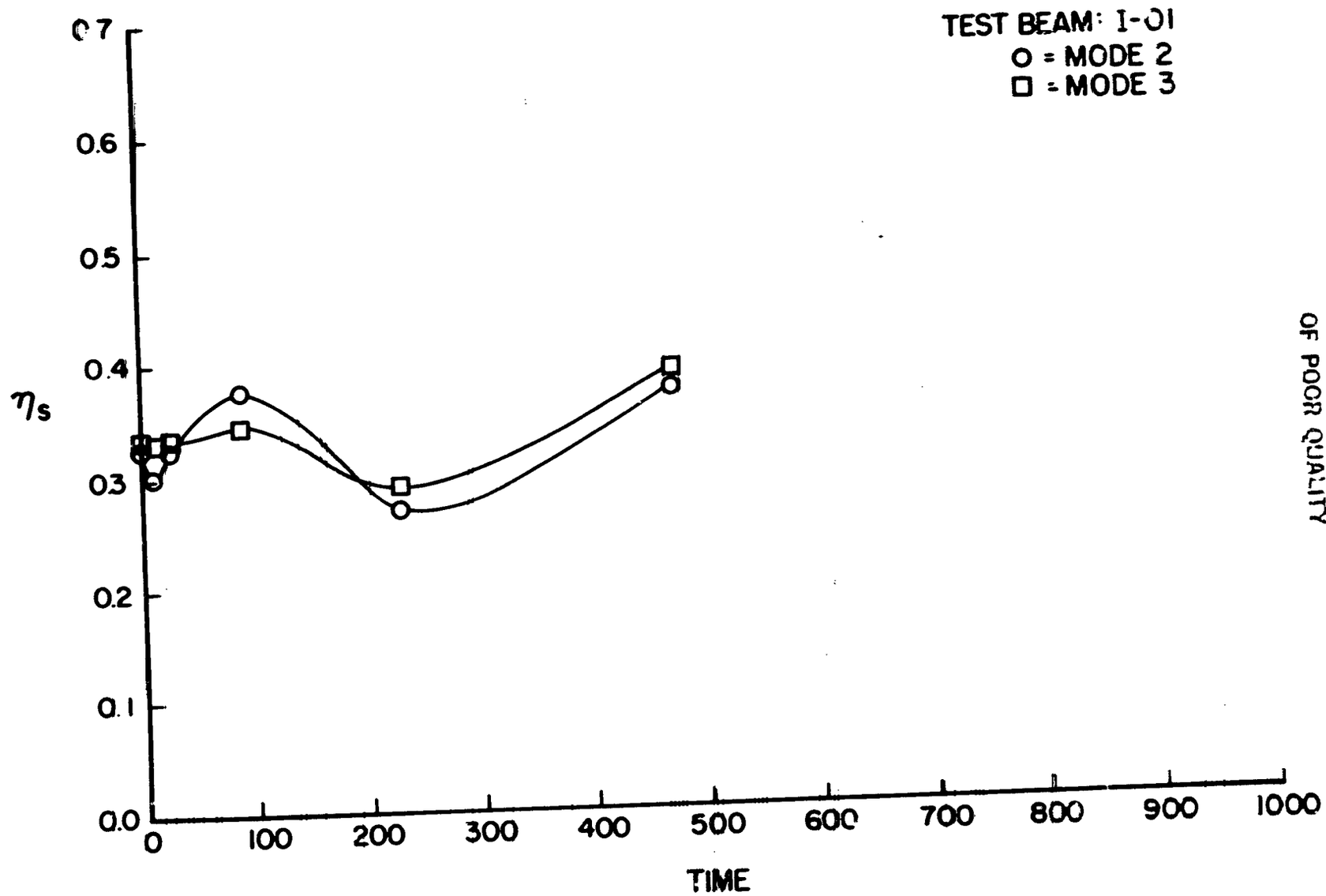

Figure 7. Composite Loss Factor Versus Hours for 3M Company's ISD 112

ORIGINAL PAGE IS
OF POOR QUALITY

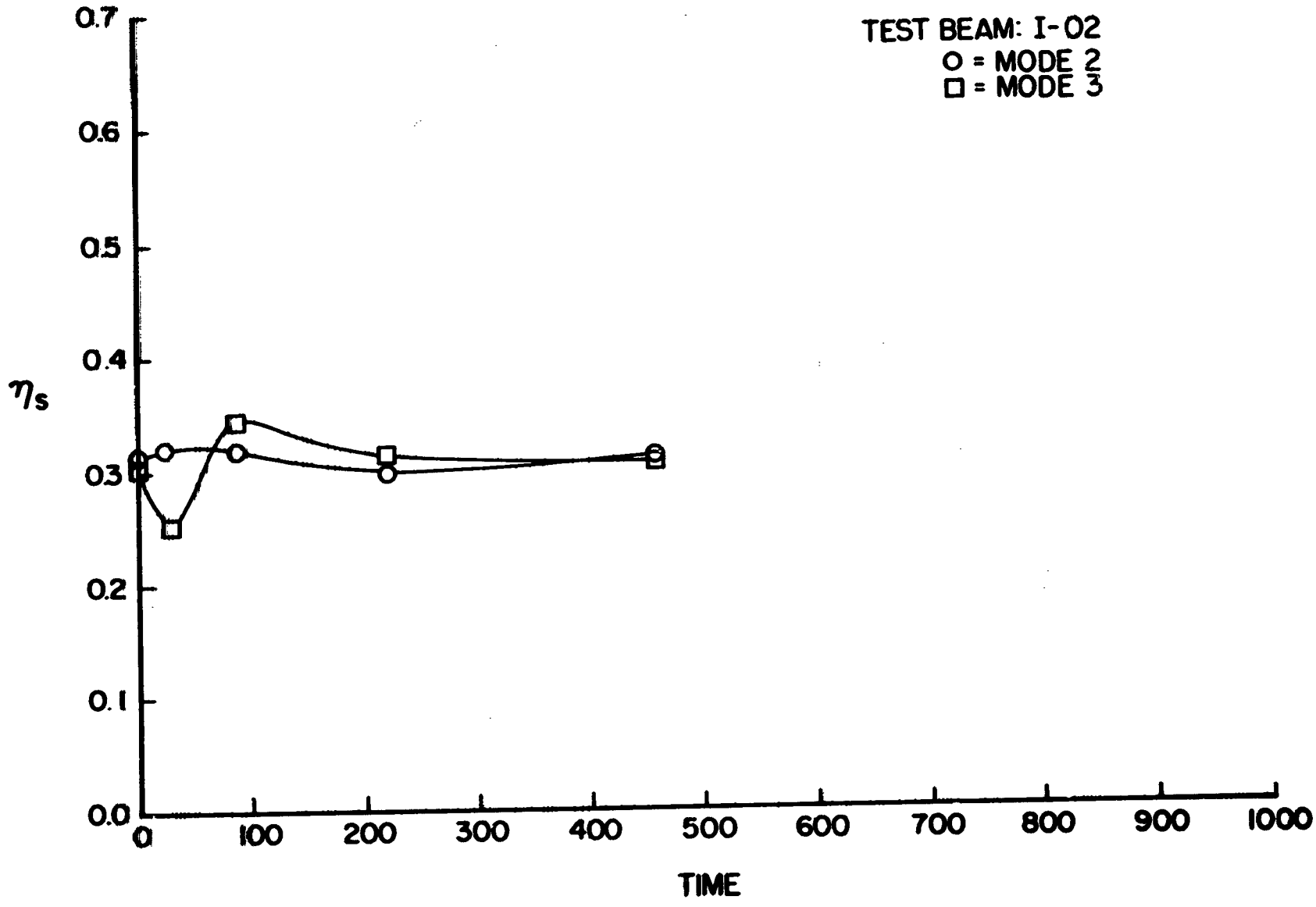

Figure 8. Composite Loss Factor Versus Hours for 3M Company's ISD 110

ORIGINAL PAGE IS
OF POOR QUALITY

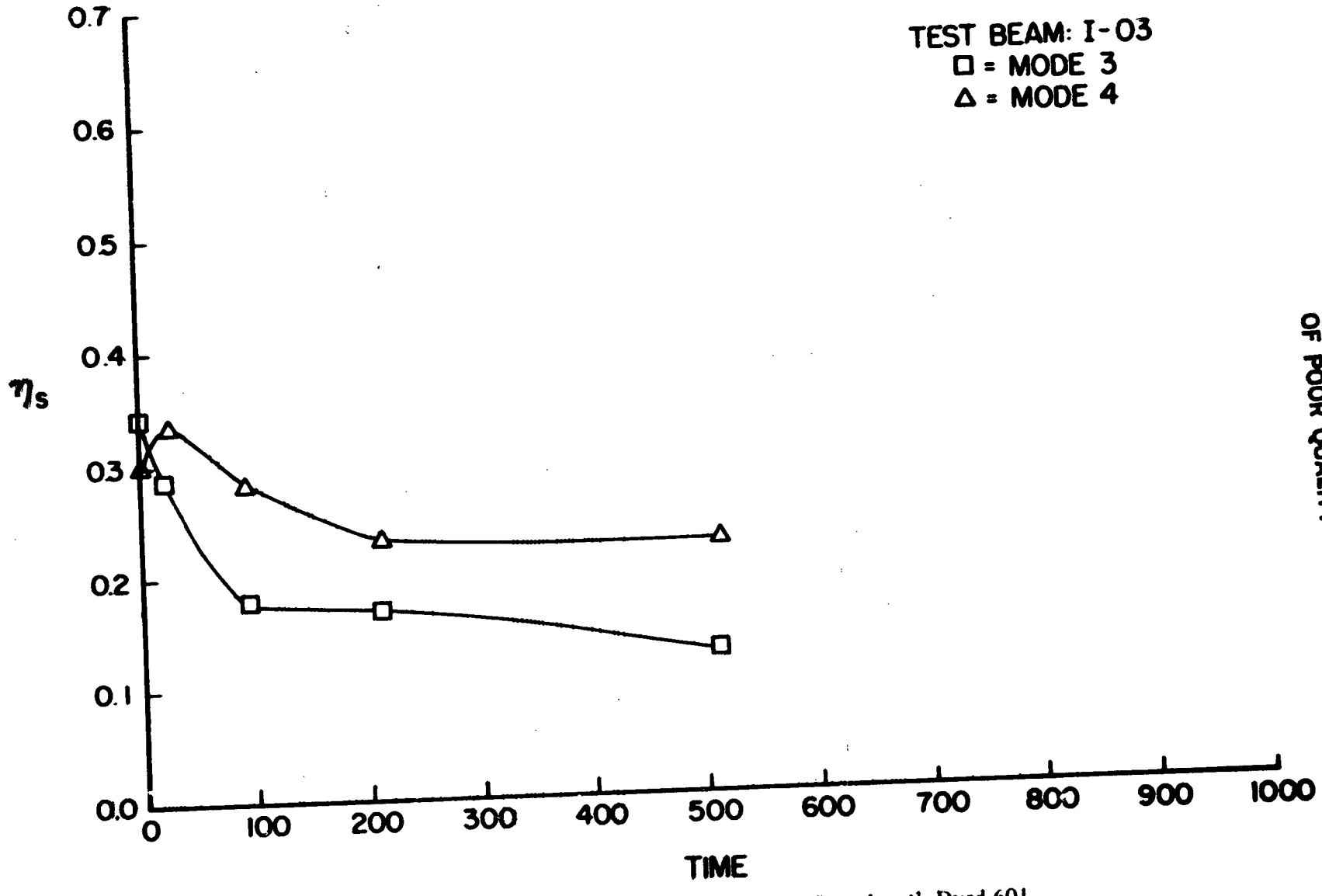

Figure 9. Composite Loss Factor Versus Hours for Soundcoat's Dyad 601.

ORIGINAL PAGE IS
OF POOR QUALITY

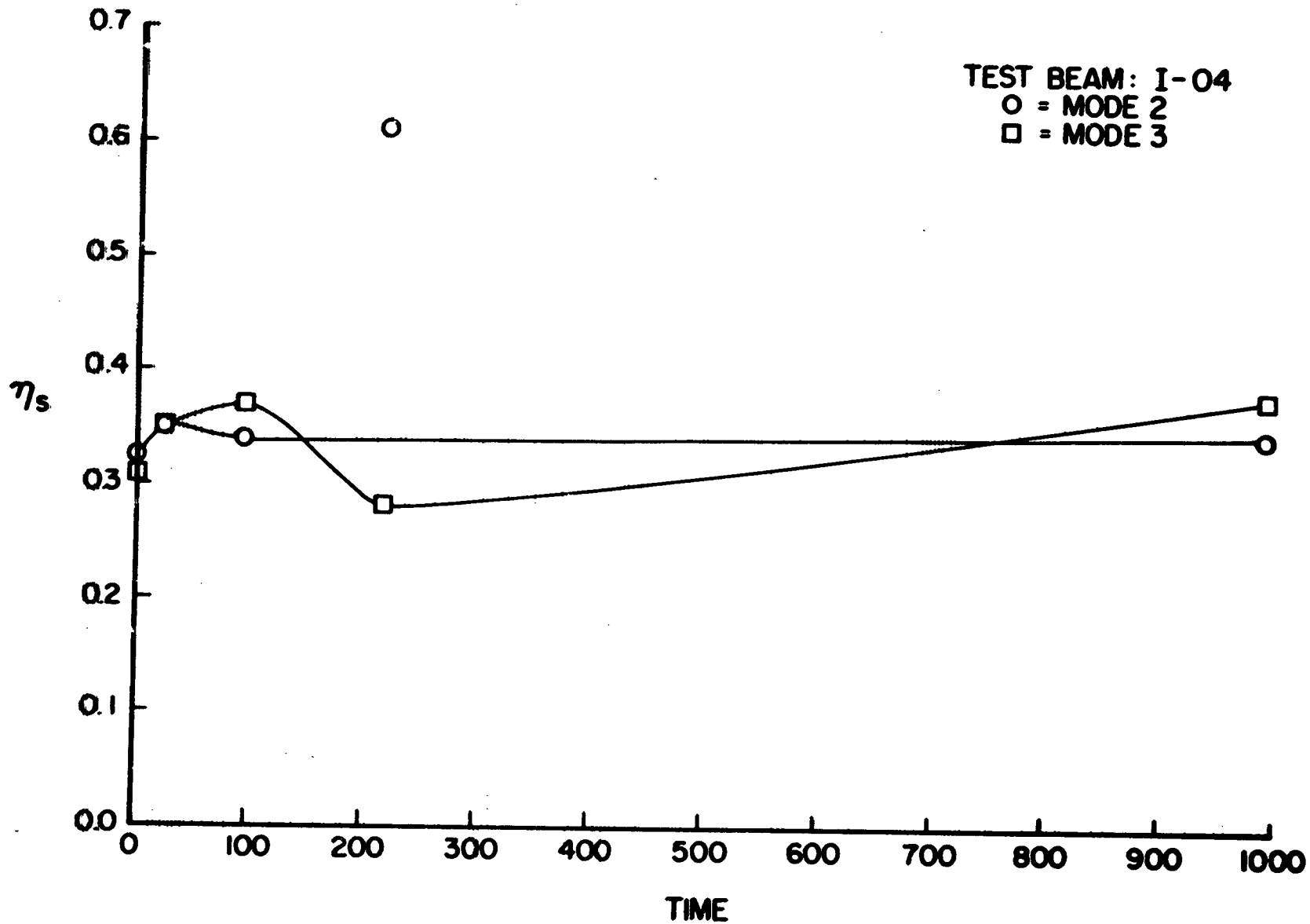

Figure 10. Composite Loss Factor Versus Hours for 3M Company's NPE-9046

ORIGINAL PAGE IS
OF POOR QUALITY

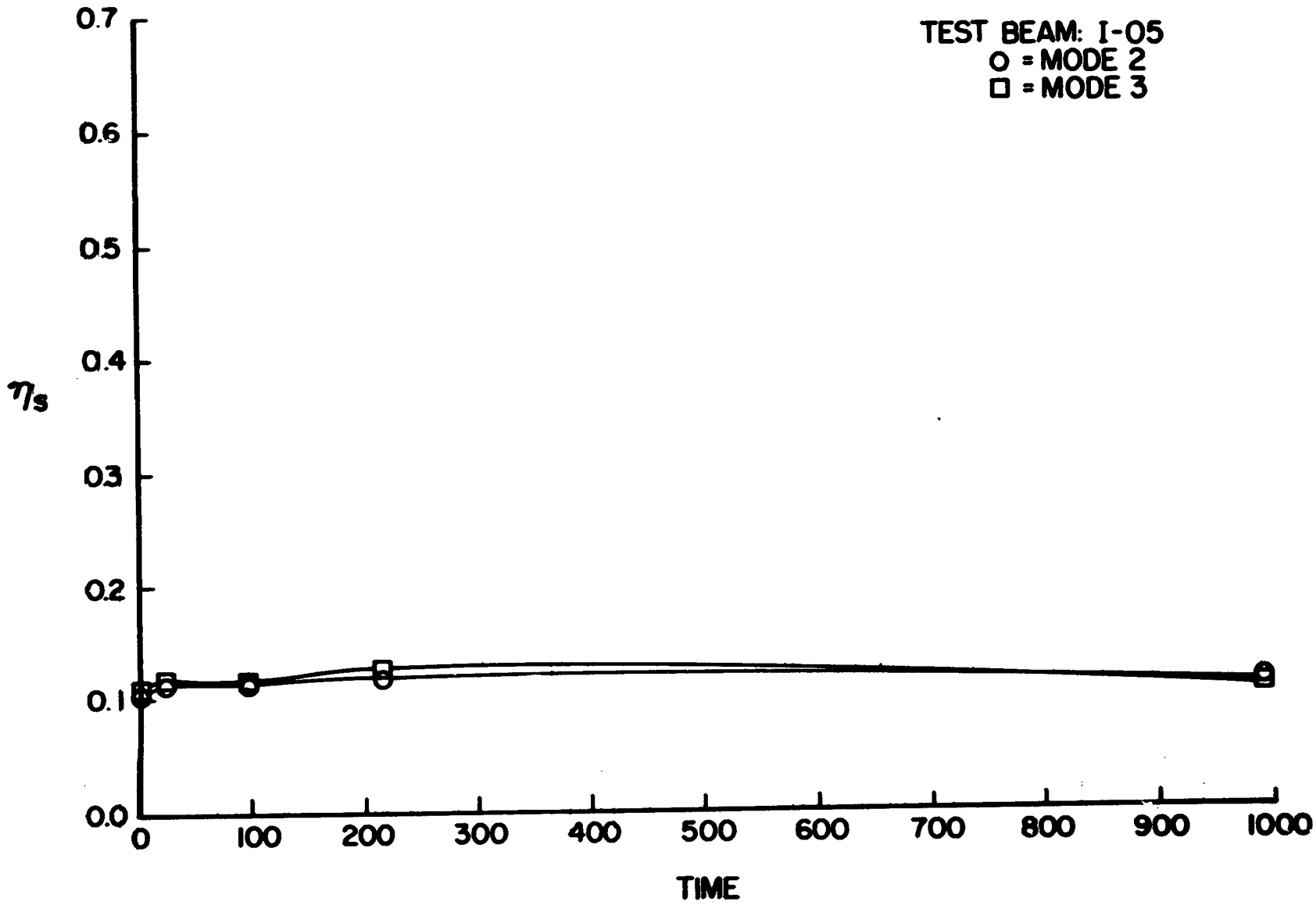

Figure 11. Composite Loss Factor Versus Hours for E-A-R's C-1002

ORIGINAL PAGE IS
OF POOR QUALITY

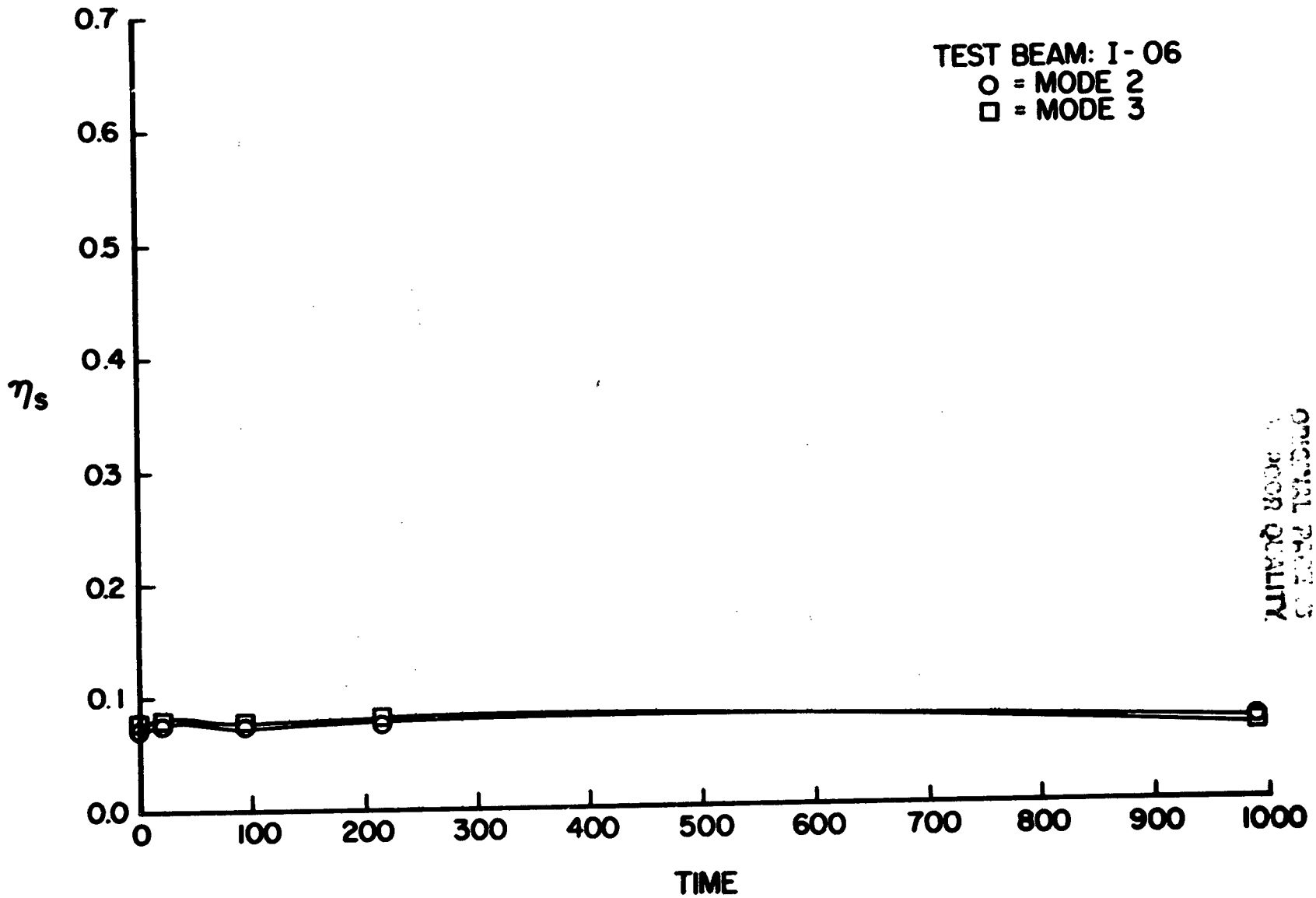

Figure 12. Composite Loss Factor Versus Hours for E-A-R's C-2003

ORIGINAL PAGE IS
OF POOR QUALITY

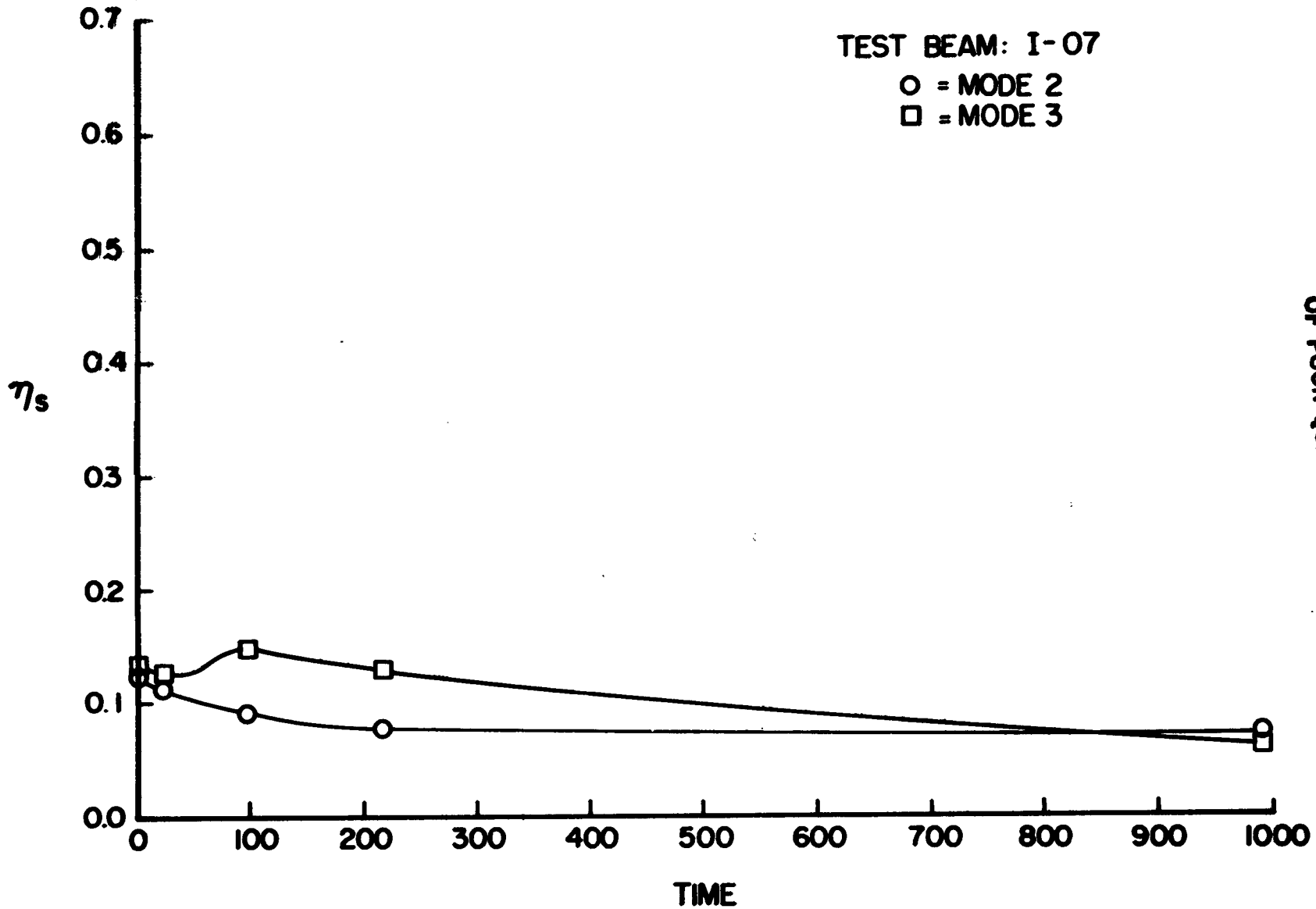

Figure 13. Composite Loss Factor Versus Hours for Soundcoat D

ORIGINAL PAGE IS
OF POOR QUALITY

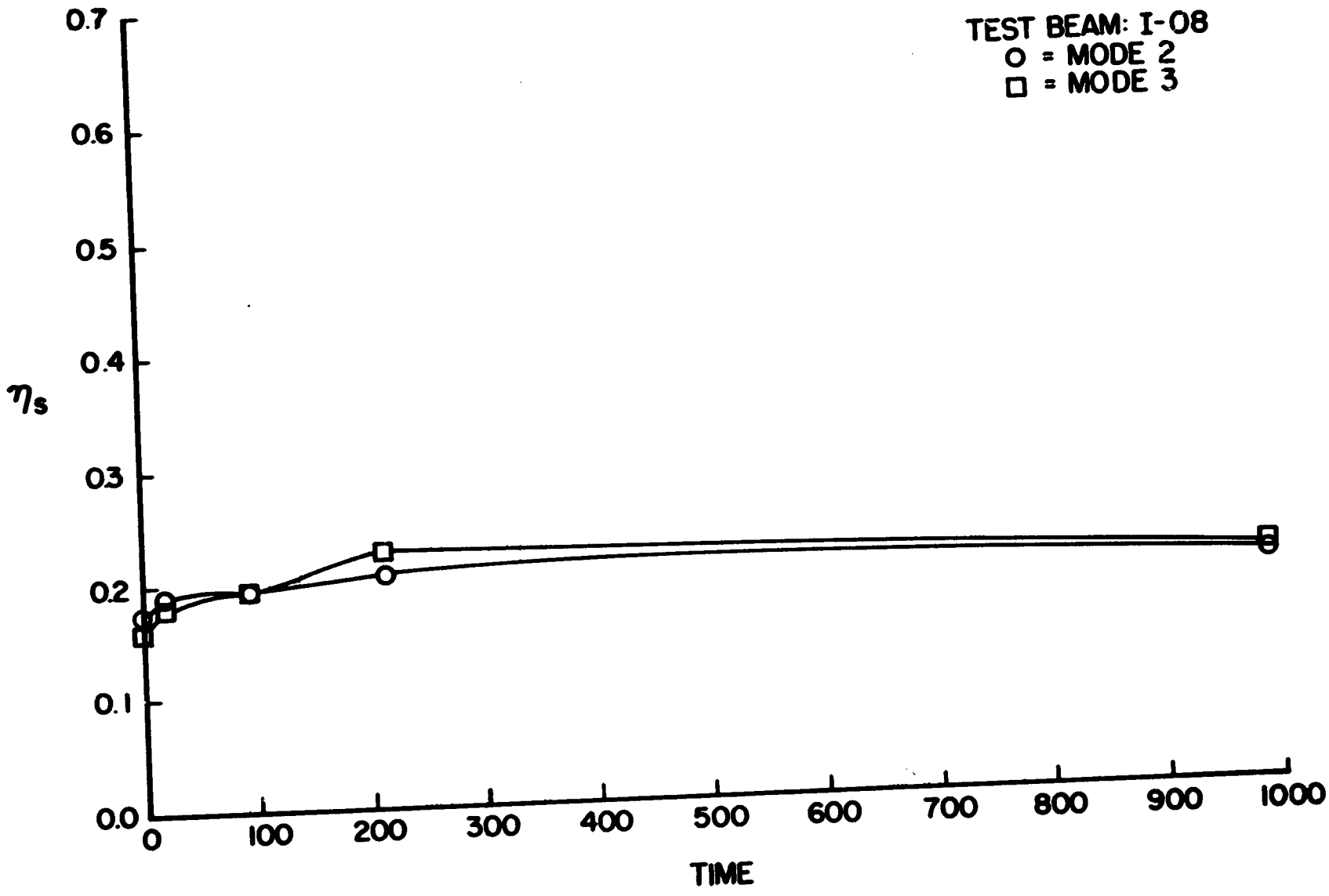

Figure 14. Composite Loss Factor Versus Hours for 3M Company's ISD 830

ORIGINAL PAGE IS
OF POOR QUALITY

ERRORS ASSOCIATED WITH SHUTTLE ACOUSTICAL DATA REDUCTION TECHNIQUES

C. S. Tanner
The Aerospace Corporation

ABSTRACT

Comparison of acoustic data early in the Shuttle test program resulted in a concern about data variations attributed to data processing, instrumentation, and methods. As a result, an acoustic calibration tape was generated and copies circulated to various agencies and companies for processing. Results of the requested one-third octave band processing are presented and illustrated the magnitude of variations which may occur when a variety of data processing equipment are used.

PRECEDING PAGE BLANK NOT FILMED

PRECEDING PAGE BLANK NOT FILMED

SESSION VII

REMOTE SENSING

Session Organizers: Emile S. J. Wang, McDonnell Douglas Corporation

Richard Hartenbaum, RCA Corporation

PRECEDING PAGE BLANK NOT FILMED

THUNDERSTORM OVERFLIGHT PROGRAM

O. H. Vaughan, Jr.
NASA/Marshall Space Flight Center
Huntsville, Alabama 35812

B. Vonnegut
State University of New York at Albany
Albany, New York 12222

M. Brook
New Mexico Tech
Socorro, New Mexico 87801

R. E. Orville
State University of New York at Albany
Albany, New York 12222

ABSTRACT

Photo-optical measurements were made during the spring and summer of 1980 from an instrumented NASA U-2 aircraft flying above thunderstorms. The airborne instrumentation showed excellent correlation between the optical signatures and the ground based signatures of cloud-to-ground lightning discharges. Optical signatures of the cloud-to-ground lightning discharges could be clearly detected from above thru the intervening thunderstorm cloud.

For the spring program the U-2 aircraft was modified to include a slow antenna field measuring device, a spectrometer made by placing a grating in front of a NASA CCD line scan camera and photographic system of three Vinten cameras employing 70 mm film. This camera system is arranged so that it could be operated in the open-shutter mode at night to provide photographs of lightning cannels and cloud structures illuminated by lightning.

Over 100 lightning flashes were recorded by the photoelectric optical recorder, the slow antenna, and the spectrometer. Data and analyses are presented.

PRECEDING PAGE BLANK NOT FILMED

N82 25304

DESIGN AND DEVELOPMENT OF THE ERBE DATA MANAGEMENT SYSTEM

James F. Kibler
NASA Langley Research Center

ORIGINAL PAGE IS
OF POOR QUALITY

ABSTRACT

Earth Radiation Budget Experiment (ERBE) instruments will be launched on Shuttle and two NOAA satellites in the 1984-1985 time frame. The data from these instruments will be processed at the NASA Langley Research Center using algorithms specified by an international ERBE Science Team. The ERBE Data Management Team is developing the processing software using an iterative approach of three releases, each of increasing levels of complexity and solidity. Results from Release 1 development indicate that problem areas can be identified at an early stage of the development process. A Release 2 status report is presented to identify the major steps in the design and implementation of the software system.

INTRODUCTION

An Earth Radiation Budget Experiment (ERBE) payload is currently scheduled for a Shuttle launch in mid-1984 (refs. 1-3). Two other nearly identical instrument packages will be launched on NOAA operational satellites (TIROS F and G) in 1984 and 1985. The instruments will sense longwave and shortwave radiation from the Earth as well as total radiation from the Sun to monitor the long-term energy balance of the Earth at various spatial scales ranging from 2.5° regions to global averages. Table I summarizes several pertinent instrument measurement parameters.

All of the ERBE data will be processed at the Langley Research Center (LaRC) into usable scientific output products. An international ERBE Science Team (ref. 3) has been assembled to provide guidance to the development of the science algorithms (see, for example, refs. 4-6) and to interpret the resulting data products. Using Science Team specifications, the ERBE Data Management Team (Table II) is designing and developing the computer software which will process the ERBE data. An iterative development approach has been adopted which provides for three releases or versions of the processing system, each of increasing levels of complexity and solidity. The final release of the system will be used to process the flight data. The goal of this development approach is to be ready for flight data processing at the launch of the first satellite.

This paper describes the ERBE software development approach. The major phases for each iterative release consist of specifications developed in concert with the Science Team, preliminary design, subsystem reviews, coding, subsystem code walkthroughs, system testing, system documentation, and project status review. Release 1 of the ERBE Data Management System has been completed and a status report of Release 2 activities is presented.

ORIGINAL PAGE IS
OF POOR QUALITY

ACRONYMS

CDC	Control Data Corporation
ERBE	Earth Radiation Budget Experiment
ERBS	Earth Radiation Budget Satellite
GSFC	Goddard Space Flight Center
LaRC	Langley Research Center
MAT	Master Archival Tape
NESS	National Environmental Satellite Service
NOAA	National Oceanic and Atmospheric Administration
NSSDC	National Space Science Data Center
TDRSS	Tracking and Data Relay Satellite System

DATA MANAGEMENT SYSTEM REQUIREMENTS

The ERBE data processing system at LaRC must perform several major functions. An overview of the processing flow is presented in figure 1. The diagram identifies interagency sources of data and indicates the major processing steps required to produce final output products. As indicated in the figure, Science Team validation is an iterative process which may involve changes to algorithms or model coefficients at any stage in the processing flow.

EXTERNAL DATA INTERFACES

Several sources of data are shown in figure 1. Correlative measurements are received from NOAA and must be reformatted and edited before being used by the Science Team to validate the ERBE data.

Spacecraft telemetry data for the TIROS satellites are received and initially processed at NOAA's National Environmental Satellite Service (NESS) in Suitland, Maryland. Goddard Space Flight Center (GSFC) will receive telemetry data for the Earth Radiation Budget Satellite (ERBS) which is launched on Shuttle. These telemetry data contain the ERBE radiometric data as well as key instrument and spacecraft housekeeping parameters, and are shipped from the receiving agency to LaRC using magnetic tape for each 24-hour period of data.

Spacecraft orbit data for all three satellites are processed at GSFC. Air Force tracking data are used to provide position information for the TIROS satellites, and TDRSS data are used to calculate definitive position

information for the ERBS spacecraft. A weekly set of orbit information is transmitted to LaRC on a magnetic tape for each satellite.

GSFC is also responsible for calculating definitive attitude parameters for the ERBE spacecraft. These calculations are based upon measurements included in the telemetry stream from the onboard attitude control system. If the onboard system is not sufficiently accurate, ground-processed attitude data will be appended to the magnetic tapes which contain the ERBS telemetry data.

Figure 1 also indicates data interfaces for products generated by the ERBE Data Management system. These data products are initially reviewed by the Science Team to assure that they are accurate. After validation, the data products are released for initial science investigations and for archival at the National Space Science Data Center (NSSDC) at GSFC.

TELEMETRY DATA PROCESSING

The first steo in processing the telemetry data received from NOAA and GSFC is to make these data compatible with the ERBE processing system and to ensure efficient operation on the LaRC central computer complex. During this processing phase, the data remain in a 16-second logical record format provided by NOAA or GSFC. Individual records, however, must be reformatted, and all decommutations are performed. All housekeeping data are converted to engineering units, and editing checks are applied to instrument and spacecraft housekeeping data outputs and to the rates at which these change. Statistical computations include means and standard deviations of housekeeping attitude data. Checks are also applied for time consistency and redundancy, and data editing flags are inserted into the primary data streams for use at other processing stages. A quality control report summarizes the editing and statistical computations to indicate the volume and type of errors encountered. The principal data set resulting from this preprocessing phase is the edited instrument and spacecraft housekeeping measurements to be passed to the merge phase.

ORBIT DATA PROCESSING

Spacecraft orbit data and ephemeris data require some reformatting to ensure compatibility with the LaRC computer complex and with the other input data. Initial editing of the satellite and solar position data is performed at this stage to assure that valid position information is used in later processing. An editing summary is produced for data quality analysis and an orbit groundtrack plot is produced to be used in field-of-view location validation. The principal data set produced at this phase is the edited orbit and ephemeris data which will be input to the merge phase.

ATTITUDE DATA PROCESSING

The definitive ERBS attitude data are provided as a separate data stream by GSFC and require some reformatting and editing. Criteria for initial spacecraft attitude checks include pitch, roll, and yaw within acceptable

ORIGINAL PAGE IS
OF POOR QUALITY

limits and acceptable rates of change. An editing summary provides a measure of the data quality. The principal data produced at this phase are the edited ERBS attitude data which will be merged with the other telemetry and position data.

MERGE DATA STREAMS AND COMPUTE FIELD-OF-VIEW LOCATIONS

In this processing step, all telemetry, orbit, and attitude data relevant to a specific instrument measurement are combined to produce a record for each 16-second cycle of radiation measurements. The input instrument and spacecraft housekeeping, orbit and ephemeris, and attitude data sets are combined on the basis of spacecraft time. Ephemeris and attitude data are interpolated to obtain precise position coincident with instrument measurements. The location at the reference altitude on the Earth of each instrument's field-of-view is computed for each radiometric measurement, and a procedure using selected radiometric data verifies field-of-view location accuracy.

RADIOMETRIC COUNT CONVERSION

The conversion and calibration of all radiometric measurements are performed at this processing stage. Other information required includes the calibration coefficients from ERBE instrument performance models and algorithms for converting raw counts to engineering units. Editing checks are applied to the converted radiometric values. A summary of the onboard calibration measurements from the ERBE instruments is produced for use by the Science Team to verify and, if needed, update the calibration coefficients. The principal product of this subsystem is a Master Archival Tape (MAT) of data at satellite altitude.

INVERSION TO REFERENCE ALTITUDE

The satellite altitude data set from the merge phase is further processed to produce the values representing the measurements at the reference altitude. This data inversion is dependent on several factors, including the characteristics of the Earth's surface, the zenith angle of the Sun, and the viewing angle at the field-of-view location. Bidirectional models and scene identification algorithms provided by the Science Team are used in this process. Based on scene identification, the appropriate functions are selected to convert the radiation measurements to the reference altitude. The output of the inversion phase includes a validation summary for use in instrument intercomparisons and a set of data items required for further processing in the next phase.

TIME/SPACE AVERAGING

At the time/space averaging phase, individual radiation parameter estimates are available along with their time and location (latitude, longitude). On a daily basis, these estimates are assembled into a data base which is organized into various spatial scales ranging from 2.5° by 2.5° regions to 10° by 10° regions. After a full month of data are collected in

ORIGINAL PAGE IS
OF POOR QUALITY

the data base, a monthly averaging process is used to obtain a working data base from which all subsequent output products can be generated. Determination of daily and monthly averages requires the use of diurnal models which are an input to the process. Refined data editing is performed during this phase as appropriate, and a validation summary is produced.

OUTPUT PRODUCTS

The working data base containing the hourly, daily, and monthly averages serves as the input for generation of the final output products. The basic structure of 2-1/2° geographic regions allows averaging to larger regions, latitudinal zones, and finally global resolution. Final output products consist of a variety of printed reports, plots, summaries, and data tapes to be used in subsequent investigations. Key output products are archived at NSSDC after validation by the Science Team.

LaRC CENTRAL COMPUTER COMPLEX

The operational ERBE data processing system will run on the central computer complex at LaRC. Figure 2 is a schematic diagram of the major hardware elements of the complex. Most of the equipment is Control Data Corporation (CDC) computers and peripherals. Each of the seven main frame computers works with 60 bit words, and the central memory capacity of each is listed in the figure. A large permanent file system (disk) is accessible from any of the computers, and a tape library of 30,000 reel capacity is available for storing intermediate and archival results. A "front-end" switching system is used to allow remote interactive and batch terminals access to most of the main frames at speeds ranging from 300 to 9600 bits per second. The CDC standard Network Operating System controls the main frames, and a wide variety of supporting software, such as math packages and plotting routines, is available for use by applications programs.

SOFTWARE DEVELOPMENT PROCEDURE

Based on requirements outlined above, the ERBE Data Management Team is developing a software system to operationally process the instrument data using the LaRC central computers. The overall development procedure is illustrated in figure 3 and each step is described below. The Team has adopted an iterative software development approach with three releases of the Data Management System. Each release proceeds through all steps in the development cycle with increasing levels of complexity and solidity at each release. The intent is to eliminate many possible error sources at an early development stage such that the final system will require relatively few modifications to process the flight data.

The first release was completed in May 1981 and included the basic structure of the processing steps as well as some prototype algorithms. The second release is scheduled for completion in June 1982 and includes refined algorithms for every processing step. Simulated data runs will enable the Team to verify the accuracy and completeness of the system and to estimate computer resource usage. The third system release is scheduled for mid-1983 and will represent a fully implemented system. It will use the most accurate

algorithms available based on Science Team evaluation of Release 2. At this point, the system will enter formal configuration control procedures wherein changes must be carefully evaluated and approved prior to implementation.

After Release 3 is completed, the period prior to the first satellite launch will be used to optimize the computer code. In this way, the operational processing system will use fewer computer resources. Further, this step isolates the tradeoff of "correct" computing versus "efficient" computing.

SPECIFICATIONS

The software development cycle begins with a set of specifications for the computer programs. The Science Team outlines the functions which the software must perform and the data products which must be generated. These software requirements are then iterated with the Data Management Team to assure their feasibility and completeness.

PRELIMINARY DESIGN

The overall processing system is separated into major subsystems with a design team assigned to each subsystem. This team develops a preliminary design document which meets the specifications established by the Science Team. The document includes a narrative which describes the function of the subsystem, module structure and data flow charts to outline all processing steps, and detailed specification sheets which list the inputs, outputs, and processing method for each module in the subsystem.

SUBSYSTEM DESIGN REVIEW

As the preliminary design for each subsystem is completed, a panel of Science and Data Management Team members reviews the document. System interfaces are examined to assure compatibility and the overall design is reviewed to assure that it meets specifications. After review comments are incorporated, the design is published as a Preliminary Design Document.

PROGRAM CODING

A programming team is assigned to each subsystem and uses the design document as the guide for coding each module in the subsystem. A set of coding standards has been developed around FORTRAN V to insure a measure of uniformity in coding practices, internal code documentation, and portability. These standards are followed by every member of the programming team. The lead programmer on each team tracks progress using milestone charts for all modules versus a preliminary schedule established when the subsystem coding begins. Unit testing is performed on each module using a minimal amount of test data.

SUBSYSTEM CODE WALKTHROUGH

As the coding for each subsystem is completed, the design document is updated to reflect any necessary changes. The code is then reviewed by the

same panel which reviewed the subsystem design. During the review, several items are emphasized: accurate implementation of the design, adherence to standards, understandable program structure, and clarity and readability of the code. Any necessary corrections as a result of the code walkthrough are incorporated into the source version of the subsystem.

SYSTEM TESTING

After all subsystems have been completed, a comprehensive testing phase begins. A test data base has been developed which simulates all external data sources. Various error conditions are introduced into the test data by a data set team which is independent of the programming team. The full system is then exercised using realistic amounts of the test data as inputs to the preprocessing subsystems. The output of each subsystem in turn serves as the input to the next subsystem in the processing stream. This technique assures that all subsystem interfaces are carefully tested. Any errors detected during this testing phase are corrected in the final version of the system release.

SYSTEM DOCUMENTATION

The Preliminary Design Document is updated at each development step to reflect changes made in coding or testing. User documentation which describes job control procedures and operator instructions mark the final step in the software development cycle.

PROJECT STATUS REVIEW

At the completion of each release, a detailed status report is presented to Project Management and members of the Science Team. The results of each release then serve as the baseline for modifications and enhancements in the next release.

RELEASE 2 STATUS REVIEW

Using the software development procedures outlined above, the Data Management Team has completed Release 1 of the ERBE Processing System and is in the coding phase for Release 2. Several major milestones for the Release 2 development activity are given in Table III.

The specification phase has isolated several problem areas from Release 1. For example, the radiometric count conversion is now recognized to be a function of the scene which the sensors are viewing. In Release 1, this count conversion was performed in the preprocessing and editing part of the system. It has been moved for Release 2 to the merge part of the system which allows the scene to be located on the Earth prior to the conversion from counts to engineering units.

Another Release 2 change identified a large data base management function which has to be performed on a daily basis. This function was

included in the monthly averaging subsystem in Release 1, but it is now highlighted as a separate subsystem for daily processing.

The preliminary design phase has overlapped the specifications phase as shown in Table III. This period represents a large amount of interaction between the Science and Data Management Teams as the specifications are iterated to produce a feasible design. This phase has culminated in design reviews and a set of design documents in six volumes which describe the entire system.

At this writing in January 1982, the Data Management Team is actively coding the Release 2 system. Over 450 subroutines have been identified for programming. This estimate is somewhat larger than original estimates, so a larger team of engineers and programmers has been assembled to assist in the coding phase. This team was drawn from research divisions at LaRC and existing contractor organizations.

One of nine subsystems has been completed with a code walkthrough in January. The design document is being updated to reflect coding changes and walkthrough comments. After final code revisions, the subsystem will be ready for full system testing. Substantial progress is being made in the remainder of the subsystems as each programming team becomes familiar with the design requirements and coding standards.

CONCLUDING REMARKS

The software development approach adopted for the ERBE Data Management System appears to be a sound one. With multiple releases of the software leading to a flight-ready system, serious design deficiencies can be identified at an early stage. The step-by-step development procedure in each release cycle provides good interaction with the ERBE Science Team which will use the data produced by the system. With this approach, the goal of a processing system ready at the launch of the first ERBE instruments may indeed be met.

REFERENCES

1. Woerner, C. V.; Cooper, J. E.; and Harrison, E. F.: The Earth Radiation Budget Satellite System for Climate Research. Remote Sounding of the Atmosphere from Space, H. J. Bolle, ed., Pergamon Press, Inc., 1979, pp. 201-215.

2. Young, G. R.; and Kibler, J. F.: Earth Radiation Budget and Smart Sensors. Progress in Astronautics and Aeronautics, Vol. 67, 1979, pp. 74-85.

3. Barkstrom, B. R.; and Hall, J. B.: Earth Radiation Budget Experiment (ERBE): An Overview. Journal of Energy, 1982, paper E 796 in press.

4. Spiers, Jr., R. B.; Huck, F. O.; Park, S. K.; Staylor, W. F.; and Halyo, N.: ERBE: Assessment of Measurement Accuracy. Proceedings of AIAA Conference: Sensor Systems for the 80's, Colorado Springs, CO, Dec. 2-4, 1980, paper no. 1952.

5. Smith, G. L.; and Green, R. N.: Deconvolution of Wide Field-of-View Radiometer Measurements of Earth-Emitted Radiation. Part I: Theory. J. Atmos. Sci., Vol. 38, no. 3, 1981, pp. 171-176.

6. Weaver, W. L.; and Green, R. N.: Simulation Study of a Geometric Shape Factor Technique for Estimating Earth-Emitted Radiant Flux Densities from Wide-Field-of-View Radiation Measurements. NASA TP-1629, 1980.

ORIGINAL PAGE IS
OF POOR QUALITY

TABLE I. ERBE Instrument Parameters

Instrument Package	Weight, Kg	Average Power, W	Data Rate, bps	Channel	Spectral Interval (μm)	Filter	Field-of-View
Non-Scanner	30	15	240	1. Total	0.2-50+	None	Limb-to-Limb
				2. Shortwave	0.2-5	Suprasil-W Dome	Limb-to-Limb
				3. Total	0.2-50+	None	10° Earth Central Angle
				4. Shortwave	0.2-5	Suprasil-W Dome	10° Earth Central Angle
				5. Solar	0.2-50+	None	Solar Disk
Scanner	25	35	880	6. Shortwave	0.2-5	Suprasil-W	3° x 4.5°
				7. Longwave	5-50+	Diamond + SW Cutoff	3° x 4.5°
				8. Total	0.2-50+	None	3° x 4.5°

TABLE II. ERBE Data Management Team

Name	Affiliation	Areas of Responsibility
J. F. Kibler	NASA LaRC	Team Leader, Budgets, Schedules, Project and Science Team Coordination
W. L. Weaver	NASA LaRC	External Data Interfaces, Ephemeris, Telemetry and Attitude Subsystems
M. A. Woerner	NASA LaRC	Data Archival, Output Products Subsystem
R. C. Dunkum, Jr.	NASA LaRC	Computer Complex Coordination, Test Data Base Generation
P. G. Renfroe	LTV Corporation	Merge, FOV Calculation and Inversion Subsystems
J. E. Satran	SDC	Time and Space Averaging Subsystem
E. T. Taylor	OAO Corporation	System Design, Software Development Planning and Coordination
P. A. Chaffee	OAO Corporation	Documentation Support
O. L. Crawford	OAO Corporation	Daily Data Base Subsystem and System Utilities
D. M. Kennedy	OAO Corporation	Documentation Support
M. O. Self	OAO Corporation	Telemetry and Ephemeris Subsystems
S. N. Shah	OAO Corporation	Count Conversion Subsystem

ORIGINAL PAGE IS
OF POOR QUALITY

TABLE III.- Release 2 Milestones

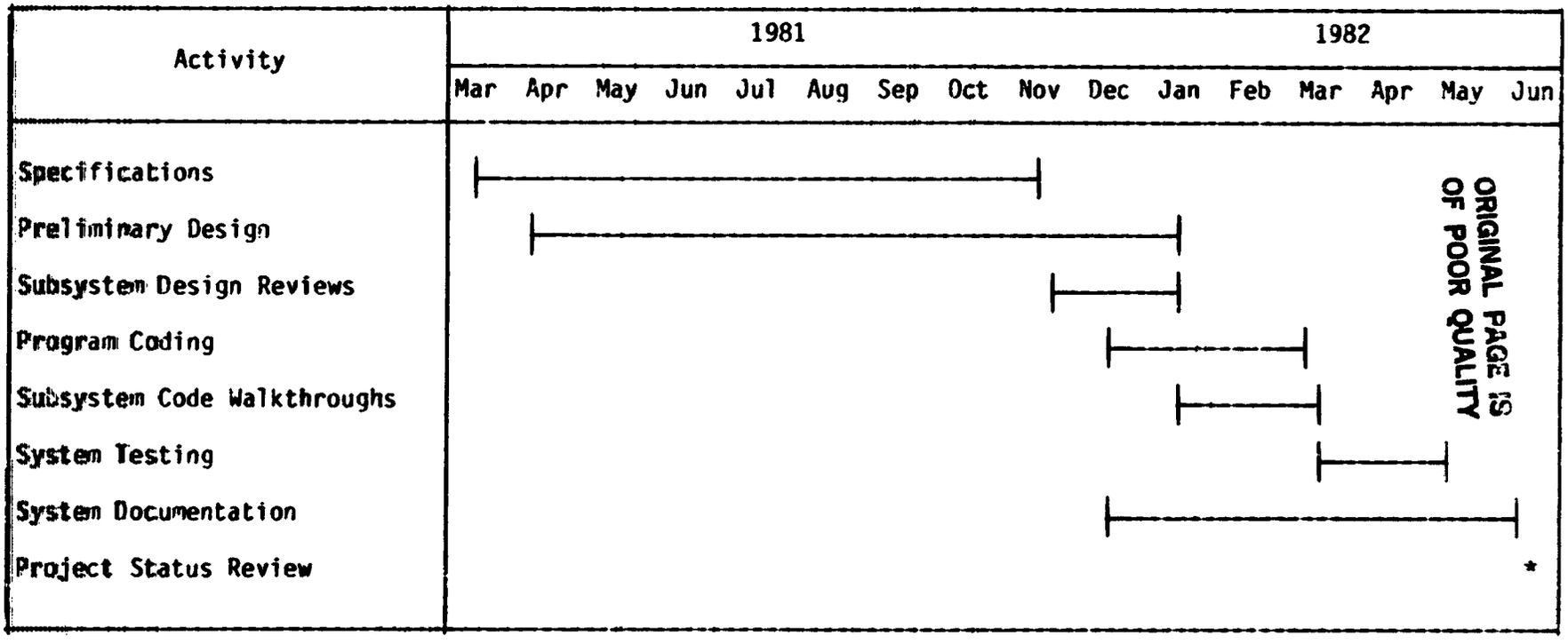

ORIGINAL PAGE IS
OF POOR QUALITY

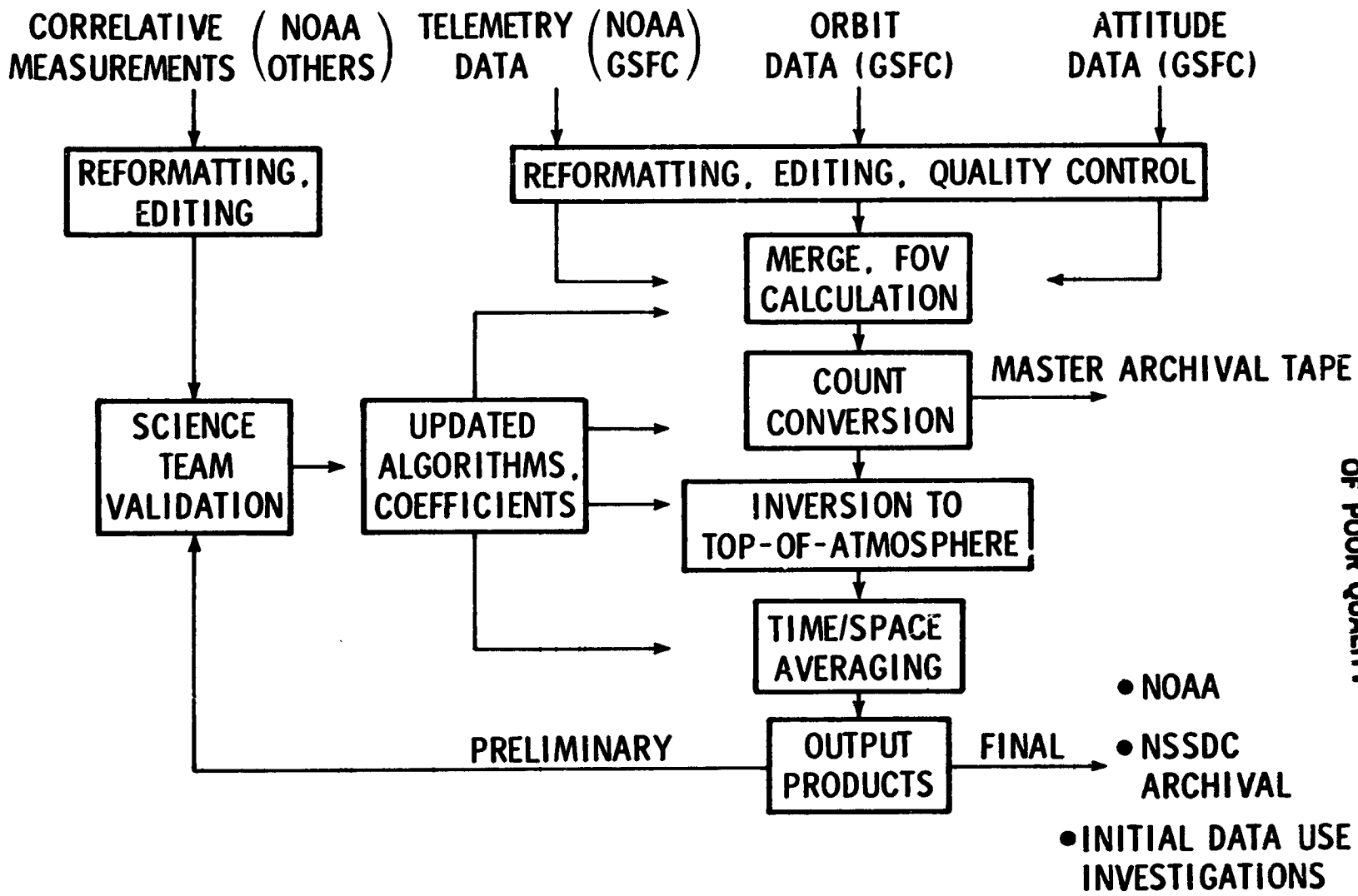

Figure 1. - ERBE Data Processing at LaRC

ORIGINAL PAGE IS OF POOR QUALITY

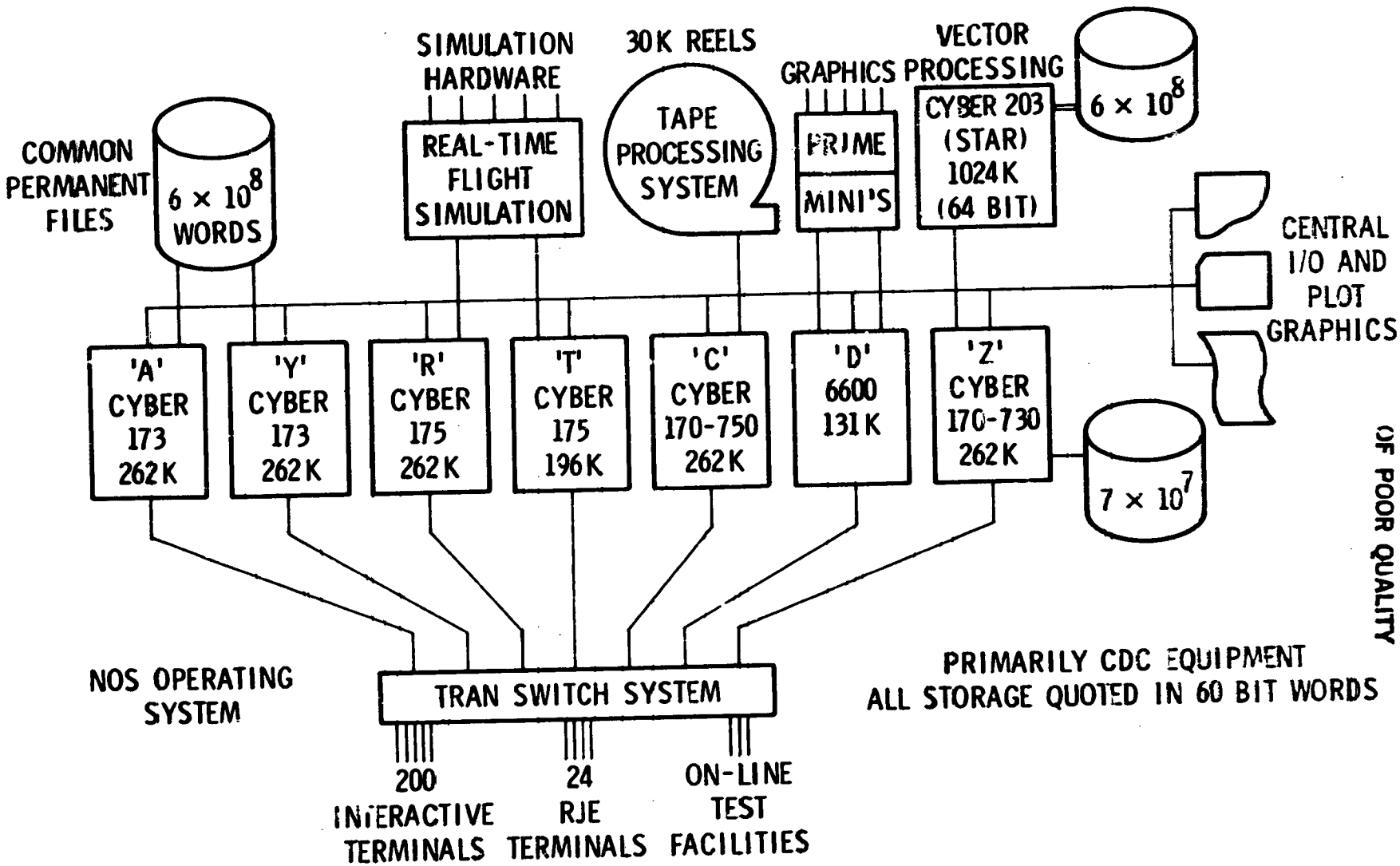

Figure 2. - LaRC Central Computer Complex

ORIGINAL PAGE IS OF POOR QUALITY

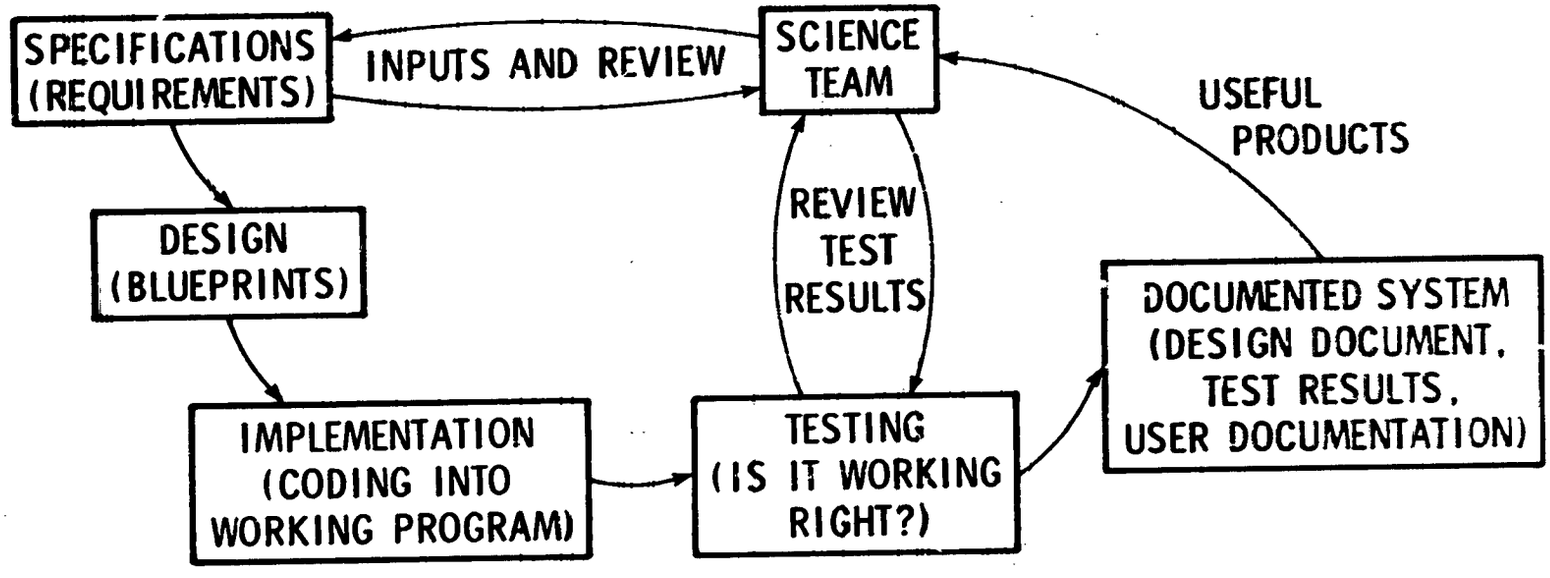

THIS PROCESS IS REPEATED FOR EACH SYSTEM RELEASE
TO SUCCESSIVELY REFINE THE PROCESSING SYSTEM

Figure 3. - Software Development Procedure

ORIGINAL PAGE IS
OF POOR QUALITY

PRECEDING PAGE BLANK NOT FILMED

PROVIDING RADIO FREQUENCY SPACE-LINKS BETWEEN EARTH STATION AND SATELLITE FOR MEASURING SATELLITE ELECTRICAL PERFORMANCE WITHIN SIMULATED SPACE ENVIRONMENT

Kenneth R. Rauhala

General Electric Company
Philadelphia, Pennsylvania 19101

ABSTRACT

This paper will describe the design features of an antenna coupling unit, or antenna "hat," developed by General Electric to simulate RF communication paths or space-links and measure RF performances of an orbiting satellite communicating with an Earth Station. The Defense Satellite Communications System (DSCS) III Qualification and Flight Models have been successfully demonstrated, with this special test equipment, to meet electrical performance characteristics within a simulated space environment. The test equipments feature computer-aided testing, high test equipment reliability, accurate positioning, high repeatability from test-to-test, satellite safety, and extremely high quality of test path signals to enhance satellite performance analysis. Significant savings in manpower and reductions in test schedules have resulted using this test equipment; more savings will accrue for all subsequent satellite testing, for DSCS and other satellite or spacecraft test programs.

32

530

NCI

PRECEDING PAGE BLANK NOT FILMED

N82 25305

REMOTE SENSING OF TORNADIC STORMS FROM SPACE

R. J. Hung
The University of Alabama in Huntsville

R. E. Smith
NASA/Marshall Space Flight Center

ABSTRACT

The life span of a severe storm is on the order of a few hours. Rapid scan infrared and visible observations from geosynchronous satellites can be useful for studying the life cycle of a severe convective storm. By using infrared images obtained from GOES satellite, the digital count values of pixels representing blackbody temperatures of the cloud top, convective storms can be observed throughout their life cycles. In this article, clouds associated with a tornadic storm are compared with those without a tornadic storm to illustrate how the infrared and visible observations from a geosynchronous satellite can be used to study the differences in their life cycles.

INTRODUCTION

Geosynchronous satellite visible and infrared observations provide a powerful tool for studying severe convective storms, such as thunderstorms, tornadoes, hail storms, hurricanes, etc. (refs. 1 to 5). The infrared image provides an indication of the equivalent blackbody temperature of the observed cloud tops. In the Geosynchronous Operational Environmental Satellite (GOES) infrared sensor, 256 different digital count values are assigned to represent specific ranges of blackbody temperatures. By referencing the temperature-height profiles from conventional rawinsonde observations to the satellite infrared data sets at different time periods, the development of convective clouds can be studied in detail from the formation of the cloud, the initiation of the updraft motion, to the development of the tornadic cloud.

Association of gravity waves and severe convective storms have been studied extensively in the laboratory and in the field during the past decade (refs. 6, 7, 8). Recently, gravity waves associated with tornado activity (refs. 9, 10) and hurricanes (ref. 11) have been observed. These observations were made with a high-frequency CW Doppler array system in which radio wave receivers located at a central site, NASA/Marshall Space Flight Center, monitored signals transmitted from three independent remote sites on three sets of frequencies and reflected off the ionosphere approximately halfway between the transmitter and receiver sites. By using a ray tracing technique, Hung et al. (refs. 12, 13) have shown that the enhanced convection-initiated gravity waves associated with tornadoes were

ORIGINAL PAGE IS
OF POOR QUALITY

generated by thunderheads embedded in a squall line and/or an isolated cloud with intense convection. A comparison of the location of the computed wave sources and the time of wave excitation with published tornado touchdown data showed that the computed wave sources were near the locations where tornadoes touched down more than one hour after the waves were excited (refs. 9, 14).

Recently, Hung et al. (ref. 2) investigated the change of cloud top temperature with respect to time for the clouds associated with the source of gravity waves compared to the clouds which were not associated with gravity wave generation. The study of GOES infrared data during the time period between when the gravity waves were being excited and the touchdown of the tornado indicated that clouds associated with tornado activity are characterized by both a very low temperature at the cloud top, which is equivalent to a higher penetration above the cirrus canopy, and a very high growth rate of the cold region of the cloud top, the signature of enhanced convection in the cloud.

In this article the life cycles of two isolated cloud systems, one in Olkahoma on May 28-29, 1977, and the other in Arkansas on April 11, 1976, are used to illustrate how the visible and infrared images observed from geosynchronous satellite can be utilized to study severe storm development. A comparison of the life cycles of the cloud systems associated with tornadic storms and non-tornadic storms are made. There are some special features of the cloud associated with the tornado. These special features are the very low cloud top temperature of the overshooting turret; a much higher growth rate of cloud top above the tropopause; and also a much larger area above the tropopause.

SATELLITE IMAGE PROCESSING AND DATA ANALYSIS

An Image Data Processing Systems (IDAPS) was developed by NASA/Marshall Space Flight Center to be used for the image processing requirements of the Skylab experiments. IDAPS can be used to process high resolution photographs, both visible and infrared, from satellites to study cloud top height variability, temperature distribution, and growth and collapse rates of clouds. GOES digital infrared (IR) during the time period between three hours before the touchdown of tornadoes and the tornado touchdown time for two severe convective storms on May 29, 1977, and April 11, 1976, and the other non-tornado-associated clouds in the entire United States were used in this study. The period between satellite observations was 15 minutes for the case of May 29, 1977, and was 30 minutes for the case of April 11, 1976.

In this study, a cumulative histogram is compiled starting from the cold end of the temperature distribution. The number of pixels (picture elements), N_i, with blackbody temperature equal to or less than temperature T_i, is obtained. Physically the number of pixels, N_i, is proportional to the area of the cold cloud top with temperature $\leq T_i$. This also provides data about the horizontal area of the cloud penetrating above certain altitudes.

Growth rate or penetrative overshooting cloud top is a significant characteristic for the evolution of thunder clouds to tornadic clouds. The following equation was used to calculate the growth and expansion rate of the cloud:

$$\gamma_i = \frac{dN_i}{dt} \quad (\text{Pixels} - \text{sec}^{-1})$$

where γ_i denotes the growth rate of the cloud area with temperature $\leq T_i$; N_i, the number of pixels with temperature $\leq T_i$; and t, the nominal time period between observations.

(A) Study of Severe Convective Clouds on May 29, 1977

GOES digital IR data for the entire United States during the period from 2333 GMT, May 28, 1977, to 0203 GMT, May 29, 1977, were analyzed in this study. It was found that the isolated cloud in north central Oklahoma was the only cloud with a cloud top temperature $\leq -70.2^{\circ}C$ during this time period.

The area expansion of the cold elements of the cloud top was studied. Comparison between IR digital data of cloud top located at north central Oklahoma and rawinsonde data from Oklahoma City, Oklahoma, shows that the cloud top started to penetrate above the tropopause at the time about 0004 GMT, May 29, 1977. Figure 1 shows the changes in the areas of the cloud top at different temperatures during the 0004-0203 GMT time period. Cloud top started to grow to the altitude with equivalent blackbody temperature, $T_{BB} \leq -65.2^{\circ}C$ at 0004 GMT. The cloud top temperature had fallen to $\leq -67.2^{\circ}C$ by 0033 GMT; to $\leq -70.2^{\circ}C$ by 0103 GMT; to $\leq -74.2^{\circ}C$ by 0148 GMT, which indicates the highest altitude reached by cloud top. The area of the cloud top with temperature $\leq -72.2^{\circ}C$ had its maximum size at 0133 GMT, gradually decreased until 0148 GMT, and then sharply decreased. The tornado finally touched down at 0205 GMT, apparently as the cloud top was rapidly collapsing. This result is in good agreement with the aircraft observations made by Fujita and his associates (refs. 15, 16).

For the purpose of relating the temperature of the penetrating turret to an altitude, the rawinsonde data from Oklahoma City, Oklahoma, were analyzed. Based on the rawinsonde data of 2300 GMT, May 28, 1977, and 1100 GMT, May 29, 1977, the temperature of the tropopause was around $-64^{\circ}C$ and the altitude of the tropopause was around 13 km, while the lowest cloud top temperature observed on the satellite IR imagery was $-74.2^{\circ}C$ about 15 to 30 minutes before the touchdown of the tornado. It can be seen from Figure 1 that cloud top started to penetrate above the tropopause approximately two hours before touchdown of the tornado. The coldest overshooting cloud top temperature was more than $10^{\circ}C$ below the temperature of the tropopause. The area of the cloud top which had penetrated above the tropopause just before the touchdown of the tornado, for this particular case, was 650 pixels.

The relationship of the heights of overshooting tops of clouds above the tropopause and some physical parameters have been investigated by a group of scientists at NASA Goddard Space Flight Center. By using a

ORIGINAL PAGE IS
OF POOR QUALITY

downward pointing lidar on a high-altitude aircraft and by using sideviews of the thunderclouds photographed every 30 seconds from a second aircraft, Simpson and her associates determined the heights of clouds (ref. 17). A detailed examination of the values of infrared equivalent blackbody temperature of the cloud tops obtained from the satellite and the lidar-determined heights for overshooting tops above the tropopause shows a high correlation between the heights and temperatures, with the slope of the relation indicating an approximate adiabatic lapse rate (ref. 17).

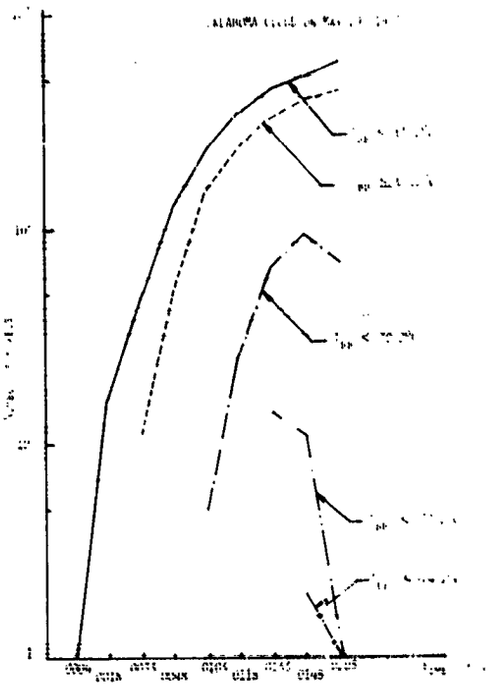

Figure 1. Cold area expansion and vertical growth of the cloud top in terms of time change of number of pixels with temperatures $\leq -65.2^{o}C$, $\leq -67.2^{o}C$, $\leq -70.2^{o}C$, $\leq -72.2^{o}C$, and $\leq -74.2^{o}C$ during 0004-0203 GMT, May 29, 1977, for an isolated tornado located in north central Oklahoma.

Figure 2 shows the growth of cloud top height in comparison with the height of tropopause during the 0004-0203 GMT time period based on the relationship suggested by Simpson and her associates. It is shown in this figure that the highest altitude of the turret top of the Oklahoma cloud was more than 4.2 km higher than the tropopause altitude approximately 15 to 30 minutes before the touchdown of the tornado. Since the overshooting top temperature was more than $10C^{o}$ below the temperature of the surrounding air, the density of the overshooting turret is much higher than the density of the surrounding air. The overshooting turret can only exist as long as it is dynamically supported by intensive vertical convection. As the intensive vertical convection conditions disappeared, the overshooting turrets collapsed. This occurred about 15 to 30 minutes before the touchdown of the tornado.

ORIGINAL PAGE IS
OF POOR QUALITY

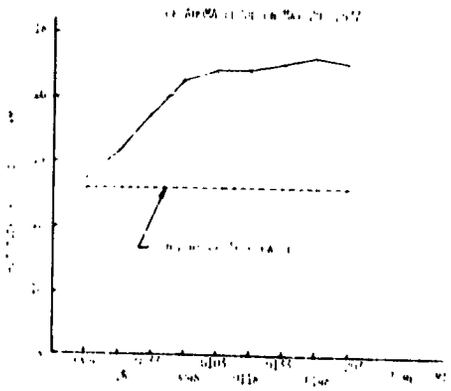

Figure 2. Change of the altitudes for overshooting turret of Oklahoma cloud during 0004-0203 GMT, May 29, 1977 and the height of tropopause.

Figure 3 shows the growth rate of cloud top areas penetrated above the tropopause. The maximum growth rate of the area with temperature $\leq -65.2^{o}C$ (0.5 km or more above the tropopause) with the value of 12.2 x 10^{-2} pixels-sec^{-1} occurred about 45 minutes before the tornado touchdown. In other words, the maximum growth rate of the penetrative overshooting turret above the tropopause (essential for formation of tornadic storms) occurs approximately one hour or less before the tornado touchdown. On the other hand, the growth rate of the high-altitude cloud with temperatures $\leq -70.2^{o}C$, $\leq -72.2^{o}C$ and $\leq -74.2^{o}C$ became negative, implying that the higher altitude cloud began collapsing approximately 15 to 30 minutes before the tornado touchdown.

During the period 0200-0245 GMT, May 29, 1977, three gravity wave trains, detected by the Doppler sounder array located at Huntsville, Alabama, were analyzed (ref. 2). Ray tracing computation shows that the computed probable sources of waves were located at north central Oklahoma, and the wave traveling times from the computed probable sources to the observation point were 138-162 minutes. Thus, the gravity waves were excited while the overshooting turret penetrated above the tropopause.

(B) Study of Severe Convective Clouds on April 11, 1976

GOES digital IR data for the entire United States during 2031-2231 GMT, April 11, 1976, were analyzed in this study. For the large cloud of the squall line extending from Oklahoma through Arkansas, Tennessee and North Carolina, only a small portion of this cloud located in central and eastern Arkansas had a cloud with a cloud temperature $\leq -60.2^{o}C$.

The area expansion of the cloud elements of this cloud top was studied. Comparison of the IR digital data of this cloud top located in Arkansas and the rawinsonde data from Nashville, Tennessee, shows that the cloud top started to penetrate above the tropopause around 2031 GMT, April 11, 1976. Figure 4 shows the changes in the areas of the cloud top at different

ORIGINAL PAGE IS
OF POOR QUALITY

temperatures during the 2031-2231 GMT time period. The cloud top started to grow to the altitude with equivalent blackbody temperature, $T_{BB} \leq -59.2^{o}C$ at 2031 GMT. At 2101 GMT, the cloud top reached the altitude with a temperature $\leq -64.2^{o}C$; and at 2201 GMT, the cloud finally reached the highest altitude with the lowest temperature at $-66.2^{o}C$.

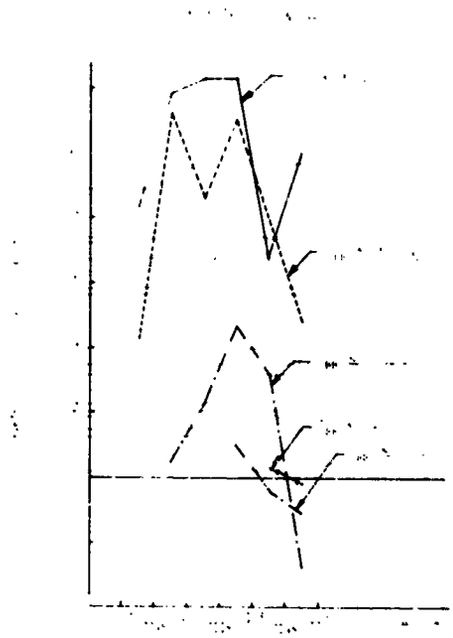

Figure 3. Growth/collapse rate of penetrative overshooting cloud top with temperatures $\leq -65.2^{o}C$, $\leq -67.2^{o}C$, $\leq -70.2^{o}C$, $\leq -72.2^{o}C$, and $\leq -74.2^{o}C$ during the time period 0004-0203 GMT, May 29, 1977 for cloud at north central Oklahoma.

The rawinsonde data from Nashville, Tennessee were used to relate the temperature of the penetrating turret to an altitude. Based on the rawinsonde data of 2300 GMT the same day, the temperature of the tropopause was around $-59^{o}C$ and the altitude of the tropopause was around 11.2 km, while the lowest cloud top temperature observed on the satellite IR imagery was $-66.2^{o}C$ about 30 minutes before the touchdown of the tornadoes. Our earlier case studies of March 24, 1976 and May 29, 1977 using the 15 minute interval IR data show that the lowest cloud top temperature is observed about 15 minutes before the touchdown of the tornado, just before the overshooting turret collapsed. In the present case, the lowest cloud top temperature could be even lower than $-66.2^{o}C$ because there was no 15 minute interval data available and thus there is no way to determine what the cloud top temperature was 15 minutes before the touchdown of the tornado. For the very same reason, the time of the collapse of the overshooting turret could not be determined precisely since it occurred about 15 minutes before the touchdown of the tornado (refs. 15, 16). However, it can be seen from Figure 4 that (1) the cloud top started to penetrate above the tropopause approximately two and

ORIGINAL PAGE IS
OF POOR QUALITY

one-half hours before the touchdown of the tornado, (2) the coldest overshooting top temperature was more than 7C° below the temperature of the tropopause, and (3) the area of the cloud top above tropopause before the touchdown of the tornadoes covered 213 pixels.

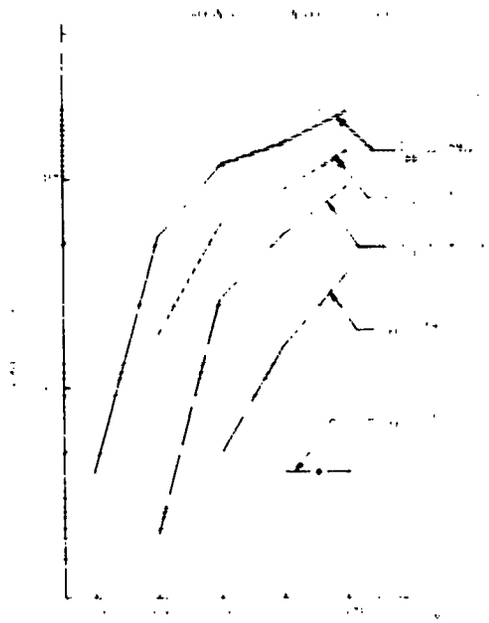

Figure 4. Cold area expansion and vertical growth of the cloud top in terms of time change of number of pixels with temperatures $\leq$ -59.2°C, $\leq$ -61.2°C, $\leq$ -62.2°C, $\leq$ -64.2°C, and $\leq$ -66.2°C during 2031-2231 GMT, April 11, 1976, for cloud located in Arkansas.

Figure 5 shows the growth of the cloud top height above the tropopause during the 2031-2231 GMT time period based on the relationship suggested by Simpson and her associates. This figure shows that the highest altitude of the turret top of the Arkansas cloud was more than 5.3 km higher than the tropopause altitude approximately 30 minutes before the touchdown of the tornado. Since the overshooting top temperature was more than 7C° below the temperature of the surrounding air, the density of the overshooting turret is much higher than the density of the surrounding air. The overshooting turret can only exist as long as it is dynamically supported by intensive vertical convection; therefore, as the intense vertical convection dissappears, the overshooting turret should collapse. In this case, the exact time that the overshooting turret collapsed could not be determined due to use of 30 minute interval satellite data.

Figure 6 shows the growth rate of the cloud top areas above the tropopause. The maximum growth rate of the area with temperature $\leq$ -59.2°C (with an altitude just above the tropopause) with the value of 4.74×10^{-2}

ORIGINAL PAGE IS
OF POOR QUALITY

pixels - sec^{-1} occurred about 45 minutes before the tornado touchdown. In other words, the maximum growth rate of this overshooting turret above the tropopause (apparently essential for the formation of tornadic storms occurred approximately one hour or less before the tornado touchdown.

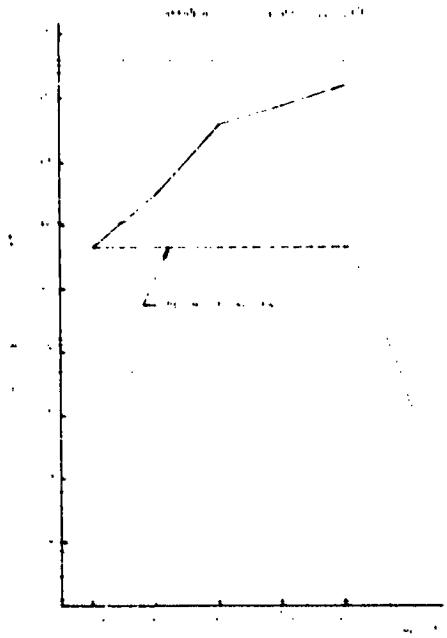

Figure 5. Change of the altitudes for overshooting turret of Arkansas cloud during 2031-2231 GMT, April 11, 1976, and the height of tropopause.

Similar analyses of both areal expansion rates and growth of cloud top heights during the same time period were accomplished throughout the United States. It was found that the Arkansas cloud was the only cloud with a temperature lower than -60.2°C combined with a high growth rate of the cloud top above the tropopause.

DISCUSSIONS AND CONCLUSIONS

From the present analysis, the results obtained from the combination of the cloud top temperature changes from the satellite infrared imagery, the rawinsonde data, and the Doppler sounder gravity wave observations lead to the following :

(1) Tornado-associated clouds have overshooting turrets penetrating above the tropopause.

(2) The difference between the overshooting cloud top temperature and

ORIGINAL PAGE IS
OF POOR QUALITY

the tropopause temperature, a measure of how much the cloud has penetrated above the tropopause, rather than either the absolute temperature of the penetrative cloud or the height of the top of overshooting turret is important in the development of severe storms.

(3) The growth rate of the overshooting turret above the tropopause for severe storm-associated clouds is much greater than that for non-severe storm-associated clouds.

(4) The high density penetrative overshooting turret (temperature of the overshooting turret is much colder than the surrounding air temperature) above the tropopause collapses about 15 to 30 minutes before the tornado touchdown based on our previous analysis. However, the collapsing of overshooting turret was missing in this analysis because the satellite observations was at 30 minute intervals.

(5) The life of a tornado-associated cloud, from the moment the overshooting turret penetrates above the tropopause to the touchdown of the tornado, is no more than 3 hours.

(6) Gravity waves are observed when there are severe convective storms. Ray tracing results show that the source of these gravity waves is located at the cloud with intensive convection at the time the overshooting turret of the cloud is penetrating above the tropopause.

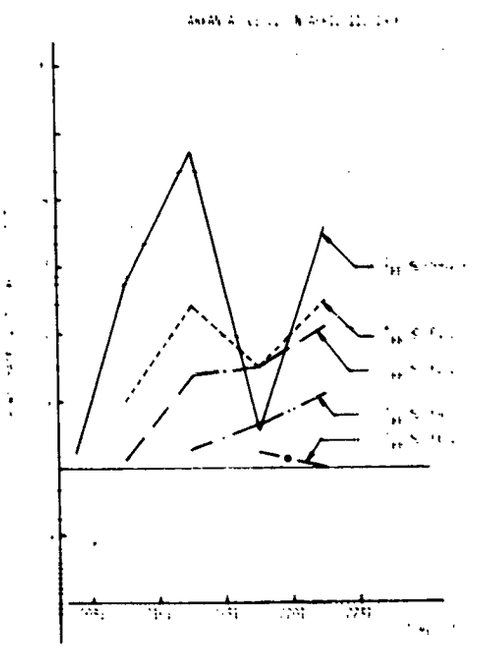

Figure 6. Growth rate of penetrative overshooting cloud top with temperatures $\leq -59.2^{\circ}C$, $\leq -61.2^{\circ}C$, $\leq -62.2^{\circ}C$, $\leq -64.2^{\circ}C$, and $\leq -66.2^{\circ}C$ during the time period 2031-2231 GMT, April 11, 1976 for cloud at Arkansas.

This research suggests that the combination of satellite imagery, rawinsonde and gravity wave observations, and radar summaries is useful for studying the evolution of tornadic clouds from thunderclouds. However, rapid scan, ≤ 15 minute intervals, satellite observation is necessary for the study of short-life mesoscale phenomena. Otherwise, important phenomena such as the time of the collapse of the overshooting turret before the tornado touchdown can be missed.

REFERENCES

1. Purdom, J. F. W: Some Uses of High Resolution GOES Imagery in the Mesoscale Froecasting of Convection and its Behavior. Mon. Wea. Rev., vol. 105, pp. 1474-1483, 1976.

2. Hung, R. J.; Phan, T.; Lin, D. C.; Smith, R. E.; Jayroe, R. R.; and West, G. S.: Gravity Waves and GOES IR Data Study of an Isolated Tornadic Storm on 29 May 1977. Mon. Wea. Rev., vol. 108, pp. 456-464, 1980.

3. Adler, A. F.; and Fenn, D. D.: Satellite-Based Thunderstorm Intensity Parameters, NASA Tech. Memo 78094, NASA/Goddard Space Flight Center, pp. 42, 1978.

4. Gentry. R. C.; Rodgers, E.; Steranka, J.; and Shenk, W. E.: Predicting Tropical Cyclone Intensity Using Satellite-Measured Equipment Black-body Temperatures of Cloud Tops. Mon, Wea. Rev., vol. 108, pp. 445-455, 1980.

5. Sikdar, D. N.; Suomi, V. E.; and Anderson, C. E: Convective Transport of Mass and Energy in Severe Storms Over the United States-An Estimate from Geostationary Altitude. Tellus, vol. 22, pp. 521-532, 1970.

6. Gossard, E.; and Sweezy, W. B.: Dispersion and Spectra of Gravity Waves in the Atmosphere. J. Atmos. Sci., vol. 31, pp. 1540-1548, 1974.

7. Hung, R. J.; and Smith, R. E.: Dynamics of Severe Storms Through the Study of Thermospheric-Tropospheric Coupling. J. Geomag. Geoelect., vol. 31, pp. 183-194, 1979.

8. Baker, D. M.; and Davies, K.: F2-Region Acoustic Waves from Severe Weather. J. Atmos. Terr. Phys., vol. 31, pp. 1345-1352, 1969.

9. Hung R. J.; Phan, T.; and Smith, R. E.: Observation of Gravity Waves During the Extreme Tornado Outbreak of April 3, 1974. J. Atmos. Terr. Phys., vol. 40, pp. 831-843, 1978.

10. Hung, R. J.; and Smith, R. E.: Ray Tracing of Gravity Waves as a Possible Warning System for Tornadic Storms and Hurricanes. J. Appl. Meteor., vol. 17, pp. 3-11, 1978.

11. Hung, R. J.; and Kuo, J. P.: Ionospheric Observation of Gravity Waves Associated with Hurricane Eloise. J. Geophys., vol. 45, pp. 67-80, 1978.

12. Hung, R. J.; Phan, T.; and Smith, R. E.: Case Studies of Gravity Waves Associated with Isolated Tornadic Storms on January 13, 1976. J. Appl. Meteor., vol. 18, pp. 460-466, 1979.

13. Hung, R. J.; Phan, T.; and Smith, R. E.: Coupling of Ionosphere and Troposphere During the Occurrence of Isolated Tornadoes on November 20, 1973. J. Geophys. Res., vol. 84, pp. 1261-1268, 1979.

14. Hung, R. J.; Phan, T.; and Smith, R. E.: Ionosphere Doppler Sounder for Detection and Prediction of Severe Storms. AIAA J., vol. 16, pp. 763-766, 1978.

15. Fujita, T. T.; and Byers, H. R.: Spearhead Echo and Downburst in the Crash of an Airliner. Mon. Wea. Rev., vol. 105, pp. 129-146, 1977.

16. Fujita, T. T.; and Caracena, F.: An Analysis of Three Weather-Related Aircraft Accidents. Bull. Amer. Meteor. Soc., vol. 58, pp. 1164-1181, 1977.

17. Simpson, J: Progress Report for the Period October 1, 1979 to Octoberl, 1980, NASA/GSFC, Greenbelt, Md., pp. 88, 1980.

N82 25306

PRECEDING PAGE BLANK NOT FILMED

MEASUREMENTS BY THE PLASMA DIAGNOSTICS PACKAGE ON STS-3

Stanley D. Shawhan
Gerald B. Murphy

University of Iowa

ABSTRACT

The Plasma Diagnostics Package provides a comprehensive set of measurements about the Orbiter environment by providing information about ion and electron particle densities, energies, and spatial distribution functions; about ion mass for identification of particular molecular ion species; and about magnetic fields, electric fields and electromagnetic waves over a broad frequency range. Shuttle environmental measurements will be made both on the pallet and, by use of the Remote Manipulator System (RMS), the PDP will be maneuvered in and external to the bay area to continue environmental measurements and to carry on a joint plasma experiment with the Utah State University Fast-Pulsed Electron Generator (FPEG).

Results of Orbiter environment EMI measurements and S-band field strengths as well as preliminary results from wake search operations indicating wake boundary identifiers will be reported. An evaluation of the use of the RMS and PDP latch down and grapple mechanism will be discussed.

Comparisons of results with the FPEG experiments conducted on this flight will be made with results from a similar electron beam experiment conducted during March 1981 in the large vacuum chamber at Johnson Space Center.

THE PDP INSTRUMENT

On the OSS-1 payload, the Plasma Diagnostics Package (PDP) is a first generation set of instruments to assess the plasma environment and the plasma wake created by the Orbiter, to test the capabilities of the Remote Manipulator System (RMS) and to carry out an active beam-plasma experiment in conjunction with the Fast Pulse Electron Generator (FPEG) of the Vehicle Charging and Potential Experiment. These objectives are illustrated in Figure 1. The PDP instrumentation and measurement ranges are listed in Table 1. These measurements include electric and magnetic fields, plasma waves, energetic ions and electrons and plasma parameters--density, composition, temperature and directed velocity.

INDUCED ENVIRONMENT MEASUREMENTS

The PDP is operated both latched onto the OSS-1 pallet and attached to the RMS. On the RMS, the PDP is positioned and rotated through sets of

preplanned "automode" trajectories. As the PDP is moved in and around the Orbiter bay, measurements are made of the ambient pressure and of the spectrum of electromagnetic interference (EMI) generated by the Orbiter subsystems. These pressure profiles in time and in distance from the Orbiter are of interest for instruments sensitive to gaseous contamination and for instruments with high voltage power supplies. Upper limits to the levels of EMI expected from the Orbiter are shown in Figure 2 in comparison to the PDP receiver ranges and to the OSS-1 pallet noise. The sensitivity of wave receivers and of plasma sounders to be flown on future Spacelabs will be determined by these Orbiter EMI levels.

ORBITER WAKE

In the ionosphere, the Orbiter moves at supersonic velocity compared to the characteristic plasma (ion acoustic) sound speed. The Mach number is about 6 (2). Consequently, the Orbiter creates a plasma wake which may be identified by plasma depletion, energization of particles and the creation of Alfven waves behind the Orbiter. These processes are thought to be important as bodies move through plasmas. Evidence exists that Alfven waves behind the Jovian moon Io accelerate particles which cause the decametric radio noise bursts (3). RMS trajectories have been designed to move the PDP through the wake boundary at preferred points in the orbit. The Ion Mass Spectrometer, Retarding Potential Analyzer and AC/DC electric field probes aboard the PDP will be used to help identify characteristics of the wake depletion region, wake boundary and the shock. When the PDP flies again on the Spacelab-2 mission as a subsatellite, the wake will be examined out to 20 km behind the Orbiter (4).

PDP/VCAP JOINT ELECTRON BEAM EXPERIMENT

The active experiment of firing an electron beam into a plasma has been carried out in a number of laboratory and sounding rocket experiments (5). These experiments have made use of the electron beam to create artificial aurora, to excite plasma waves, to sound magnetic field lines for electric fields and to examine the charging, light emission and other plasma properties in the vicinity of the electron source. In planetary and astrophysical situations, it is thought that energetic particle streams lead to a variety of radio, light and x-ray emissions which is our only source of information about these distant entities. With OSS-1, the Fast Pulse Electron Generator (FPEG) of the VCAP experiment provides the electron beam; effects in the plasma are measured with the Plasma Diagnostics Package (PDP).

A perspective view of the OSS-1 beam-plasma experiment is shown in Figure 3. The FPEG fires a beam of electrons at an angle to the Earth's magnetic field line determined by the Orbiter position and attitude. Attached to the RMS, the PDP is moved back and forth through the beam region to measure fields, waves, energetic particles and plasma characteristics in the beam and remote from it.

Similar experiments have been conducted in laboratory space simulation chambers (5). Under certain conditions a phenomenon called the beam-plasma discharge (BPD) occurs in which the electron beam is destroyed and the plasma column is energized to emit intense light and radio waves.

The BPD condition is a plasma instability which, when studied in vacuum chambers, is found to depend on the value of beam current and energy, ambient pressure, magnetic field strength and injection angle of the electron beam with respect to the magnetic field. BPD is characterized by a diffuse beam, with orders of magnitude higher light intensity than the electron beam in a pre-BPD configuration, as well as certain electric field and electrostatic wave modes. Particle distribution functions show electrons with a significant suprathermal tail which are believed to be the prime source of ionization.

Considerable controversy exists over whether BPD can take place in this Orbiter beam experiment and whether BPD can be significant factor in neutralizing the vehicle as it emits electrons. Since the PDP has been used in ground-based vacuum chamber studies it will be able to help answer these and other questions which are of interest to plasma studies done on the Orbiter in the future (6).

The OSS-1 PDP/VCAP experiments will investigate other interactions as well. The charge condition of the Orbiter is to be assessed through electric field and particle measurements with the PDP. Wave stimulation over a wide frequency range will be studied by pulsing the electron beam and measuring the emitted wave spectra with the PDP. The PDP will also be used as an in situ probe for natural plasma processes occurring at the Orbiter's attitude.

REFERENCES

1. Active Experiments Working Group, Solar-Terrestrial Science in Earthspace: A Strategy for Shuttle-Spacelab Missions, Essex Corporation, 1981.

2. Samir, P. and Stone, N. H., "Shuttle-Era Experiments in the Area of Plasma Flow Interactions with Bodies in Space," Acta Astronautica, 1, 1041-1141, 1980.

3. Gurnett, D. A. and Goertz, C. K., "Multiple Alfven Wave Reflections Excited by Io: Origin of the Jovian Decametric Arcs," J. Geophys. Res., 86, A1, 717, 1981.

4. Shawhan, S. D., Burch, J. L. and Fredricks, R. W., "Subsatellite Studies of Wave, Plasma and Chemical Injections from Spacelab," AIAA Paper 82-0085, Orlando, Florida, January 1982.

5. Grandal, B. (ed.), Artificial Particle Beams Utilized in Space Plasma Physics, Plenum Press, 1982.

6. Raitt, W. J., P. M. Banks, Burch, J. L., Williamson, P. R., Baker, K. D. and Obayashi, T., "Early Experiments in Charged Particle Beams from the Space Shuttle," AIAA Paper 82-0083, Orlando, Florida, January 1982.

TABLE 1: OSS-1 PDP INSTRUMENTATION AND MEASUREMENTS

- LOW ENERGY PROTON AND ELECTRON DIFFERENTIAL ENERGY ANALYZER
  - Nonthermal electron and ion energy spectra and pitch angle distributions for particle energies between 2 eV and 50 keV
- AC MAGNETIC WAVE SEARCH COIL SENSOR
  - Magnetic fields with a frequency range of 10 Hz to 30 kHz
- TOTAL ENERGETIC ELECTRON FLUXMETER
  - Electron flux 10^9 - 10^{14} electrons/cm^2sec
- AC ELECTRIC AND ELECTROSTATIC WAVE ANALYZERS
  - Electric fields with a frequency range of 10 Hz to 1 GHz
  - S-band field strength meter
- DC ELECTROSTATIC DOUBLE PROBE WITH SPHERICAL SENSORS
  - Electric fields in one axis from 2 mV/m to 2 V/m
- DC TRIAXIAL FLUXGATE MAGNETOMETER
  - Magnetic fields from 12 milligauss to 1.5 gauss
- LANGMUIR PROBE
  - Thermal electron densities between 10^4 and 10^7 cm^{-3}
  - Density irregularities with 10 m to 10 km scale size
- RETARDING POTENTIAL ANALYZER/DIFFERENTIAL VELOCITY PROBE
  - Ion number density from 10^2 to 10^7 cm^{-3}
  - Energy distribution finction below 16 eV
  - Directed ion velocities up to 15 km/sec
- ION MASS SPECTROMETER
  - Mass ranges of 1 to 64 atomic mass units
  - Ion densities from 20 to 2 x 10^7 ions cm^{-3}
- PRESSURE GAUGE
  - Ambient pressure from 10^{-3} to 10^{-7} torr

ORIGINAL PAGE IS
OF POOR QUALITY

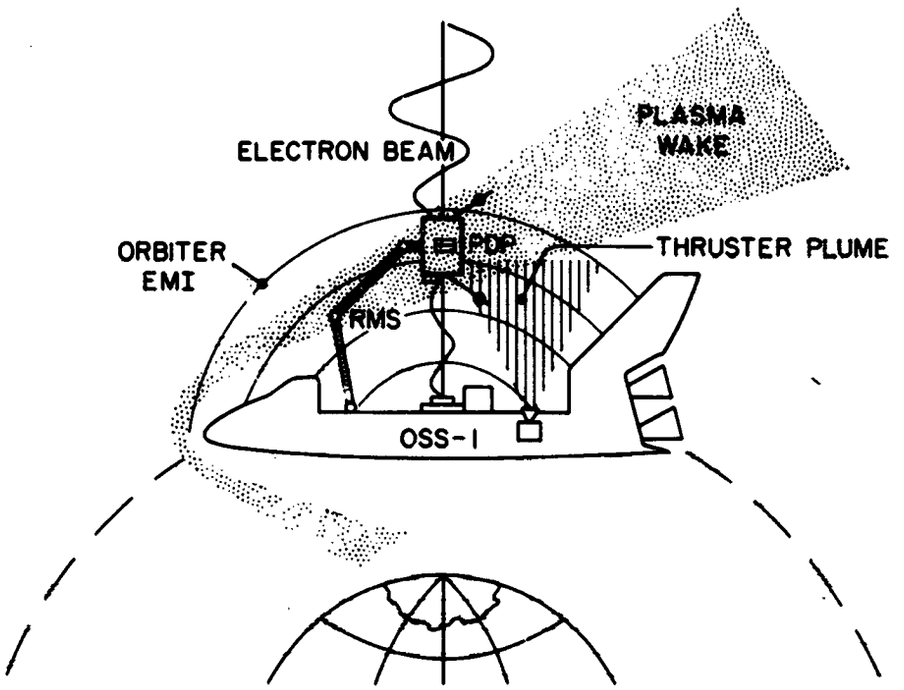

Figure 1. Illustration indicating the principal science objectives for the Plasma Diagnostics Package (PDP). The PDP contains instruments for measuring plasma fields, waves, composition, temperature and distribution functions. The Remote Manipulator System (RMS) moves the PDP about the Orbiter in pre-planned trajectories to measure electromagnetic interference (EMI) levels, the pressure profile, properties of the plasma wake formed behind the Orbiter and effects due to firing an electron beam into the plasma.

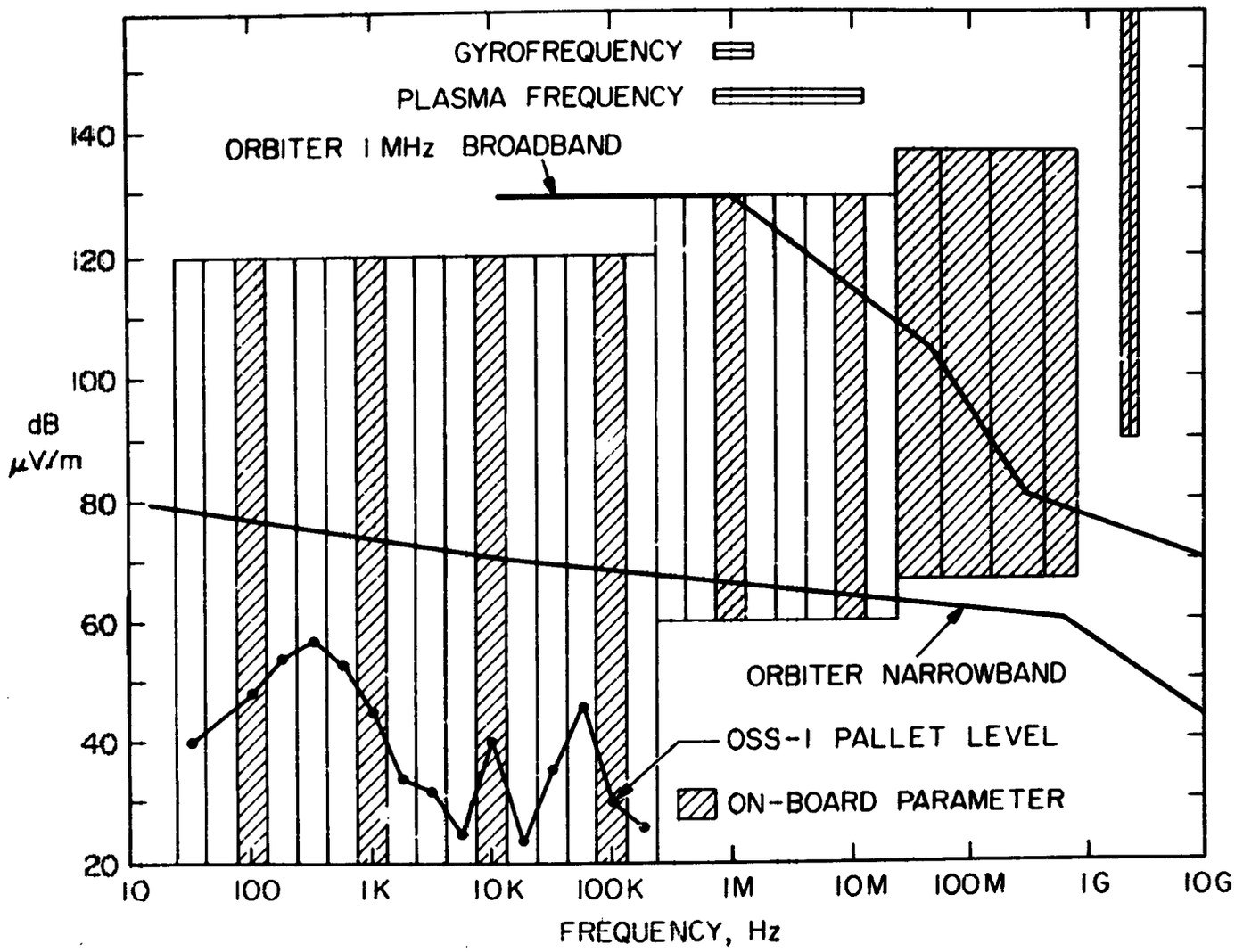

Figure 2. Plot of the expected upper limits of Orbiter electromagnetic wave emissions (EMI), the PDP wave receiver ranges and the EMI emission levels measured from the OSS-1 pallet itself. Natural and stimulated wave emissions occur at the lower levels.

ORIGINAL PAGE IS
OF POOR QUALITY

ORIGINAL PAGE IS
OF POOR QUALITY

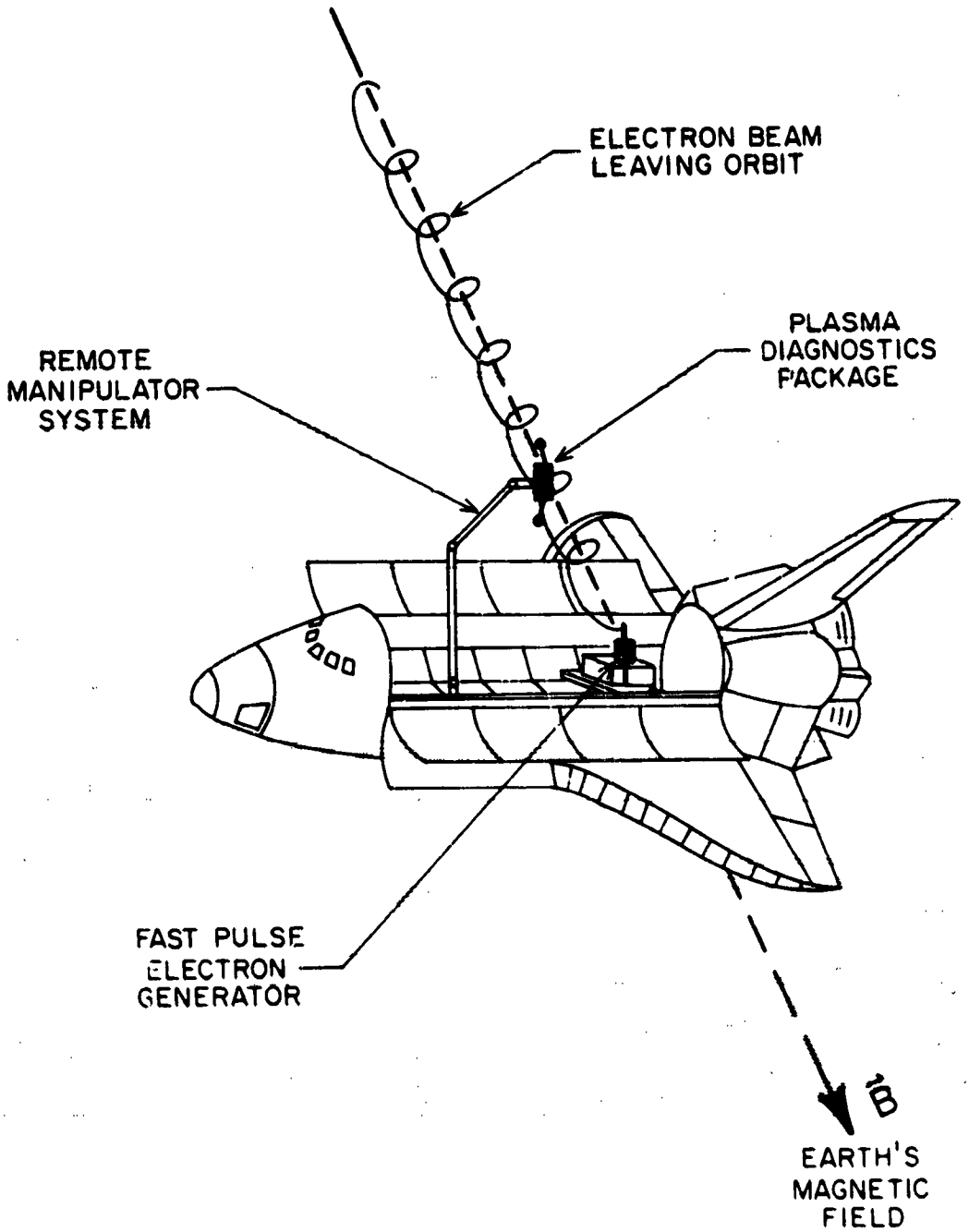

Figure 3

Scheme for the joint PDP and FPEG operations. As the electron beam is fired along some angle to the earth's magnetic field, the RMS sweeps the PDP back and forth across the beam region to make measurements of plasma fields and waves and of the energy distributions for electrons and ions.

SESSION VIII

CONTAMINATION

Session Organizers: Raymond Kruger, NASA Goddard Space Flight Center

Eugene Borson, The Aerospace Corporation

N82 25307

PRECEDING PAGE BLANK NOT FILMED

SPACE SHUTTLE PRELIMINARY

CONTAMINATION ASSESSMENT FROM STS-1 AND STS-2

L. J. Leger, H. K. F. Ehlers, and S. Jacobs
NASA Lyndon B. Johnson Space Center

E. Miller
NASA George C. Marshall Space Flight Center

ABSTRACT

A preliminary assessment of the Space Shuttle contamination environment has been made using data from the first two Orbital Flight Tests, STS-1 and STS-2. Data sources consisted of crew observations during flight, postflight vehicle inspection, and the induced environment contamination monitor which was used on STS-2 and consists of 10 instruments. These instruments are used to measure gas phase contaminants, particle population, humidity, and molecular deposition in the Orbiter payload bay during ascent and descent and particle population, molecular deposition, and gas cloud during orbital flight.

Results of the measurements described are presented in summary form and indicate low molecular deposition rates for both pressurized and orbital flight. Particle migration did occur for ascent and descent. Overall assessment of particle density representative of operational flight will be made after further data are obtained on STS-3 and STS-4. Preliminary molecular cloud calculations based on mass spectrometer data indicate water column densities in the range of 10^{13} molecules/cm^2 during the initial mission phase followed by a gradual decay. Analysis of gas densities for other species is not complete. Particle production during orbital flight occurred predominantly during the early mission phase (<12 hr mission elapsed time) and immediately before vehicle reentry. Significant periods of the STS-2 mission seem to be free of particles.

INTRODUCTION

The Space Shuttle, which has been under development for the last 10 yr, has been designed to provide a versatile Earth-orbital payload delivery system and experimentation base. This development is coming to fruition in the Orbital Flight Tests (OFT's), which provide for a complete assessment of system performance and verification of the system requirements (ref. 1). Data from the first two OFT's, Space Transportation System 1 (STS-1) and STS-2, provide the basis for a preliminary definition of the Shuttle contaminant environment during flight. A summary of preliminary results obtained is provided in this report.

Several sources of data have been used for definition of the Shuttle environment. The induced environment contamination monitor (IECM) (ref. 2) provides the bulk of the data as derived from STS-2 (ref. 3) for quantitative definition. Other sources, such as in-flight crew observations and postflight vehicle examination, are also used as necessary (only data available from STS-1) to provide a qualitative evaluation or support of IECM measurements.

Since most of the contamination data, as obtained from measurements or preflight predictions (refs. 4 to 7), are point source dependent, a description of general mission events/time line is included in the discussion. A summary of measurement plans for STS-3 and STS-4 is also included.

A large group of people participated in the IECM design, development, and mission measurements. The prime participants of the program were as follows: quartz crystal monitors (QCM's), James A. Fountain; air sampler, Palmer N. Peters; cascade impactor, Billy J. Duncan; optical effects module (OEM) and passive sample array (PSA), Roger C. Linton; camera/photometer, Jerry K. Owens and Stuart K. Clifton; humidity monitor and dewpointer, Henry W. Parker; electrets, Michael Susko; data reduction, Fred Wills; and system lead engineer, Larry Russell. The effort of these people, as well as members of the Particles and Gases Contamination Panel and the Contamination Requirements Working Group, is gratefully acknowledged.

MISSION DESCRIPTION

A general description of major mission events is given for correlation with contamination measurements. Since detailed contamination data were not available from STS-1, only a brief description is given for this mission.

STS-1

The primary Orbiter vehicle attitude used in the STS-1 mission consisted of the payload bay facing the Earth (-ZLV, Y-POP) and was used for 54 hr, or almost 37 orbits. Water dumps occurred three times, and the flash evaporator operated during the orbital phase of flight. Both main reaction control system (RCS) engines and vernier RCS (VRCS) engines were used extensively for vehicle attitude control.

STS-2

The STS-2 mission was originally scheduled for 5 days but was shortened to 54 hr because of loss of one of the three Orbiter fuel cells. Like STS-1, vehicle orientation with the payload bay facing the Earth was the primary attitude used for the STS-2 mission. Major mission events used for contamination assessment are shown in figure 1. The payload bay doors were opened at 2.53 hr mission elapsed time (MET), and the mass spectrometer (MS) was initiated shortly thereafter, at 3.33 hr MET.

A gas release of neon (Ne^{22}) and water vapor (H_2O^{18}) occurred at 33 hr MET. The gas release was to occur in conjunction with a vehicle roll of 180°; however, because of the shortened mission, the vehicle remained in -ZLV attitude.

A planned power outage caused the IECM to be turned off for 3.0 hr at 33.58 hr MET. Two major water dumps occurred at 11.81 hr MET and 36.16 hr MET and a minor one at 23 hr MET.

Steady-state flash evaporator operations lasting 40 min or more each occurred seven times during on-orbit operations. In addition, shorter duration flash evaporator operations occurred 11 times. Operation of both VRCS and discrete primary RCS was prevalent throughout the mission. Remote manipulator system (RMS) continuous operation took place from 23.25 hr MET to 28.50 hr MET.

IN-FLIGHT OBSERVATIONS

In-flight observations by the Shuttle crews provide a qualitative assessment of certain contamination source characteristics. For example, it was apparent from STS-1 crew observations that a significant number of large particles (debris) were released during payload bay door opening operations. The particles were described as pieces of films, fibers, and even washers, generally what appeared to be manufacturing residue. A few particles were also noticed on STS-2 during door operation, however, at a considerably reduced level, which is consistent with vehicle cleanup from STS-1, since considerable debris was removed from the lower midfuselage and wing areas after the STS-1 flight.

Particles were observed during liquid waste and water dumps. These dumps seemed to cut off cleanly. No particles were observed as being associated with RCS firings or water flash evaporator operation, although RCS engine plumes were visible during night portions of flight.

POSTFLIGHT ORBITER INSPECTION

The Orbiter payload bay surfaces were inspected after flight for evidence of contamination for both STS-1 and STS-2. In general, the surfaces were free of condensable films with the following exceptions: inside surfaces of thermal control blankets on development flight instrumentation (DFI) unit and inside surfaces of optics on the television cameras. The exterior surface of the television camera blankets, consisting of Kapton, a high-temperature polyimide film manufactured by E. I. du Pont de Nemours & Co., Inc., was affected from both the STS-1 and the STS-2 flights.

Contamination found on the television camera lens originated inside the lens assembly because of the use of an unacceptable lubricant. These camera lenses have been vacuum baked and reinstalled.

Light contamination deposits were found on internal surfaces of the DFI package thermal blankets and brackets. These deposits are being analyzed.

The affected Kapton on the television camera blankets of STS-1 and STS-2 has so far been somewhat puzzling. Cursory examination of the affected surface indicated that the film had been contaminated; however, subsequent scanning electron microscope examinations showed that the surface had lost material (lower than surrounding unaffected area). In addition, the surface had a "foamy" appearance, as shown in figure 2, not inconsistent with material removal from the surface. Strong shadow effects evident on some surfaces of the blanket suggested a solar radiation effect. To date, radiation simulations in vacuum have failed to reproduce the flight results.

Wipe samples were taken from the payload bay door surfaces to measure contaminant film thickness. Trichloroethane/ethanol was the solvent used for the wipes, and approximately 0.1 m^2 (1 ft^2) of surface was sampled. The wipes were extracted with additional solvent, and the solvent was filtered and evaporated to obtain the nonvolatile residue. Results from both flights are shown in table I. Surfaces sampled for STS-1 served as control areas for STS-2 measurements.

Since the IECM was not carried on STS-1, a portion of the IECM passive sample assembly was flown on the DFI. This assembly consisted of samples of aluminum overcoated with magnesium fluoride, gold mirror, 181.0-nm (1810 Å) filter, calcium fluoride window, and several electrets developed for particle collection. Published results of optical property measurements made before and after flight on these samples (ref. 8) indicated minor changes in optical properties. All of the changes can be attributed to particles collected during the long exposure to the Orbiter Processing Facility (OPF). In general, no molecular film was detected except for the back surfaces of some of the samples which had a large view of painted DFI structure.

IECM SUBSYSTEM PERFORMANCE

During the STS-2 mission, the IECM subsystems performed as planned with only one known anomaly, that being a low battery voltage condition occurring during the descent phase of flight. The data acquisition system, which is programable and microprocessor-based, sequenced instrumentation, operated properly and collected approximately 6 million bits, which were stored on the IECM recorder. These data were recovered when the IECM was returned to the NASA George C. Marshall Space Flight Center (MSFC).

The IECM battery consists of four 64 800-C (18 A-hr) lithium carbon monofluoride primary cells connected in parallel. This battery powers the IECM for ascent, descent, and postlanding operations. It appears that the battery system did not deliver the full 259 200 C (72 A-hr) of energy as expected.

Thermal control is accomplished with a system that is designed for active heating and passive cooling. The top and sides, which are coated with S13G-LO paint, manufactured by Illinois Institute of Technology Research Institute, are thermally isolated from the internal structure. Active heating is provided in the baseplate, on which most of the instruments are mounted. Flight measurements showed that the IECM internal temperatures were all within acceptable limits (284 to 308 K (11° to 35° C)).

IECM MEASUREMENTS

IECM instrument descriptions and measurements made on STS-2 are discussed in this section. Comparison of measured values to prediction and/or requirements are made, if appropriate.

GAS SAMPLER

Gas samples are collected during pressurized phases of flight for ground-based chemical analysis and in-flight humidity measurements. This system consists of five gas collection vessels and a dewpoint and humidity sensor. Vessels 2, 3, and 4 are used during ascent, and vessels 1 and 5 are used during descent. Vessel 2 contains absorbent material for the determination of trace gases and consensable material. Desorbed constituents from the absorbents are analyzed by gas chromatography/mass spectroscopy. Vessel 4 contains silver-oxide-coated platelets, which react with any hydrogen chloride (HCl) in the vehicle environment. These platelets are analyzed using electron spectroscopy for chemical analysis (ESCA) and dispersive X-ray energy analysis for traces of chlorine subsequent to flight. Vessel 3 also contains silver oxide and is used for sampling at high altitude for HCl. Void volume gas is also analyzed after flight for trace contaminants.

Vessel 1 is used during descent and contains the same absorbents as vessel 2. Nitrogen base compounds such as ammonia (NH_3) and hydrazine (N_2H_4) are absorbed in vessel 5 on ruthenium-chloride-coated platelets, which are analyzed using ESCA and X-ray energy analysis. As with the other three vessels, void volume gases are also analyzed for trace components using mass spectroscopy.

Results from the gas sampler are available for the humidity monitors, reactive surface analyses, and void volume gas analyses. Ascent humidity was below the 266.5-K (20° F) dewpoint limitation of the dewpointer, and relative humidity was <1 percent. These results are expected since the payload bay was purged with dry nitrogen gas before flight for both STS-1 and STS-2. Descent humidity increased beginning at 3 km and rapidly leveled off as shown in figure 3. This humidity buildup is lower than that expected from the entry environment payload bay temperatures.

Analysis of the reactive surfaces has been completed. No evidence could be found for chlorine on the silver-oxide-coated platelets indicating an HCl concentration of <2 ppm. The ESCA on the ruthenium-coated platelets

indicates very little, if any, reaction with nitrogen compounds. A minor indication after long counting times was noticed. Analysis of residual gas in several of the vessels did not reveal any significant amount of contaminant gas.

CAMERA/PHOTOMETER

Two 16-mm photographic cameras, using Kodak Double X film, type 7222, manufactured by Eastman Kodak Co., made stereoscopic observations of contaminant particles and background. Each was housed within a pressurized canister and operated automatically throughout the mission, making simultaneous exposures on a continuous basis every 150 sec. The cameras were equipped with 18-mm, f/0.9 lenses and subtended overlapping 20° fields of view. An integrating photometer was used to inhibit the exposure sequences during periods of excessive illumination and to terminate the exposures at preset light levels. During the exposures, a camera shutter operated in a chopping mode to isolate the movement of particles for velocity determinations. Calculations based on the preflight film calibration indicate that particles as small as 25 μm can be detected under ideal observing conditions.

More than 1075 exposures were obtained by each camera during the time that the Orbiter payload bay doors were open. Of these, more than 500 frames had exposure times of between 1 and 80 sec, with the length of the exposure dependent on the background illumination recorded by the photometer. Preliminary analysis of the data indicates that as many as 45 exposures from each camera show potential contamination due to particulates. The low percentage of data frames indicating particulates is partly because contamination can only be detected during periods in which the Orbiter environment is sunlit and the background is dark enough not to mask the illuminated particle tracks. The occurrences of these conditions were severely limited on STS-2 but will be considerably more frequent on STS-3 and STS-4. However, preliminary analysis indicates that a majority of data frames obtained during these conditions do not show contaminant particles.

The contamination recorded by the cameras sometimes took the form of "snowstorm" events, with sometimes better than 30 individual particle tracks visible in a single frame. Many of these events have been temporally correlated with water dumps, engine firings, and payload bay door activities. A number of frames show single tracks which must be discriminated from background (e.g., lights of cities) by further analysis.

The photometer section of the system is capable, in the configuration used on this flight, of measuring brightness levels B between $B/B_{\odot} = 2.9 \times 10^{-15}$ and $B/B_{\odot} = 5.5 \times 10^{-12}$, where $B_{\odot}$ is the solar brightness. The primary sources of error in the measurement are high voltage to the photomultiplier tube (PMT) and integration time, which were measured during the mission. It is estimated that the error in PMT gain due to the uncertainty of the high-voltage value is approximately 10 percent, and the integration time is known to ±1 sec. Therefore, the error in the background brightness measurement is $\Delta(B/B_{\odot}) = \pm 1.04 \times 10^{-14}$. For the longest exposure recorded (i.e., t = 80 sec), $B/B_{\odot} = 6.9 \pm 1 \times 10^{-14}$.

Efforts continuing in the correlation of these data with Orbiter events include terminator and umbra crossings throughout the mission, Sun angle, Moon angle, and latitude and longitude toward which the -Z axis is pointed. Decay times for "snowstorm" events will be studied, and measurements of angular velocities and of particle distances from the camera will be made. Spatial and velocity distributions will be determined, as will the size of individual particles.

CASCADE IMPACTOR

Volumetric concentrations of suspended particulates were measured by the cascade impactor during ascent and descent phases of the STS-2 mission. The resultant instantaneous concentrations are plotted as a function of mission time in figure 4. Mass concentrations were much higher for the smaller particulates, with the 5-μm and larger particles showing concentrations of approximately 30 $\mu g/m^3$ or less. Making assumptions for density and mean size of $\rho = 2\ g/cm^3$ and $d = 10\ \mu m$, respectively, this mass concentration measurement translates to approximately 3×10^4 particles/m^3. Within the accuracies involved, this meets the Space Shuttle goal of an equivalent 100 K cleanroom environment.

The smaller particles showed significantly higher mass concentrations, peaking in the 1- to 5-μm range at approximately 1350 $\mu g/m^3$ during ascent and approximately 700 $\mu g/m^3$ during descent. Somewhat lower concentrations are indicated for particles less than 1 μm in size, 700 $\mu g/m^3$ and 180 $\mu g/m^3$, respectively, during ascent and descent. However, the concentration measurements for these smallest particles should be considered only as a lower limit because the stage was operating near saturation, with reduced collection efficiency.

In addition to ascent and descent particulate measurements, the cascade impactor was operated during the prelaunch phase in the Operations and Checkout area, the Orbiter Processing Facility area, and during the approximately 11-hr hold on the pad at the NASA John F. Kennedy Space Center (KSC). Microscopic examination indicates good particle size discrimination between the three measuring stages and, qualitatively, sparsely populated particles of 5 μm diameter and larger when compared with the 1- to 5-μm stage. Saturation of the 0.3- to 1-μm stage is also indicated in this examination. Most of these particles were, of course, collected during prelaunch operations, principally during the hold, because of the relatively longer operating times. These samples will be analyzed for particle size distribution and elemental content of particulates collected during operation in prelaunch and mission environments.

Nonvolatile residue at ambient temperature was measured throughout the mission and is still being analyzed.

C-4

OPTICAL EFFECTS MODULE AND PASSIVE SAMPLE ARRAY

Optical Effects Module

The OEM is an active monitor of monochromatic (253.7 nm (2537 Å)) ultraviolet transmittance and scatter, and operates during the orbital phase of the mission. Five optical samples are mounted at equal intervals on the circumference of a carousel that rotates in the Shuttle X-Y plane. A sixth, empty, sample mount is included to provide for self-calibration of the transmission measurements during each operational sequence. Three of the five optical samples accumulated, as programed, more than 90 percent of the direct exposure to the cargo bay environment.

A materials listing of the five OEM samples and a summary of total mission results are shown in figure 5. The level of uncertainty for OEM transmittance measurements, established by laboratory investigation, is approximately ±1 percent.

Most of the in-flight optical change noted for OEM samples occurred within the first 4 hr of the mission. Throughout the remainder of the flight, continued gradual degradation at a lowered rate was generally evident. The levels of change indicated during time intervals less than 1 hr are generally within the range of measurement uncertainty.

The OEM scatter data provided some indication of increased diffuse reflectance from the samples; particulate contamination would cause such an increase. The magnitude of scatter change, however, was in all cases less than or nearly equal to the uncertainty level of these measurements.

Passive Sample Array

The PSA included 42 optical samples of various materials plus 2 KRS-5 crystals and 8 electrets for enhanced chemical identification. Orbital mission results indicate an average specular degradation of 0 to 2 percent in the spectral region 120 to 300 nm. Generally, no significant change was evident for diffuse measurements over the range 250 to 2500 nm. These results are generally compatible with the results of the passive optical sample array (POSA) unit flown on STS-1.

For a measure of contamination due to the ground operating environment, measured particle counts from samples removed from the OPF at KSC indicate particle distributions of $10^5/cm^2$ for the preflight exposed samples, as compared to $10^3/cm^2$ for the flight and ferry-flight samples. In all cases, the distribution of particle sizes is heavily concentrated in the size range <10 μm diameter (similar to STS-1 POSA results). Optical measurements on the samples removed before flight of STS-1 and STS-2 indicate some degradation (0 to 5 percent). No significant (measurable) change was measured for these samples at wavelengths in the range 250 to 2500 nm.

Passive sample array electrets, investigated before and after the flight with an X-ray microprobe, indicated accumulations of quantities

of chlorine, silicon, potassium, calcium, aluminum, copper, phosphorus, sulfur, and chromium. Chlorine, phosphorus, and silicon were most clearly of flight origins, as distinguished from the ferry flight.

An electret removed from the OPF at KSC before flight indicated the presence of all elements seen on the flight electrets plus sodium, magnesium, iron, and nickel, and greater relative abundance of all elements detected.

Several of the optical samples were investigated using the technique of Auger spectroscopy. There is not convincing evidence of even a monolayer-thick contaminant film. Trace quantities of carbon and oxygen were detected on all samples, including controls and samples of the ferry flight.

QUARTZ CRYSTAL MONITOR

THERMALLY CONTROLLED QCM

The IECM carries five thermally controlled QCM's (TQCM's), one on each side and one on the top surface. Each unit contains two 15-MHz quartz crystals; one of these is the sensor crystal coated with magnesium fluoride and the other is the reference crystal. The frequency difference, called beat frequency, changes proportionally to the sensor crystal mass change.

The mass deposition rate is a function of impinging mass flux and sensor crystal temperature. To differentiate between material species, the sensor crystal cycles through certain temperature levels during the mission. The levels chosen for STS-2 are 303 K (+30° C), 273 K (0° C), 243 K (-30° C), and 213 K (-60° C), lasting 2 hr each, with a level of 353 K (+80° C) of 30 min duration in between for crystal cleanup and a stepwise temperature increase at the end of each full cycle for desorption analysis. The STS-2 mission allowed four full 11.5-hr cycles on orbit, as described previously. In addition, the TQCM's were operating during ascent and descent without temperature control.

During the STS-2 mission, the side TQCM's measured mainly direct in-bay surface-to-surface flux, whereas the top TQCM measured essentially return flux. In addition, the forward TQCM collected some return flux and the top TQCM a fraction of direct flux. Each of the instruments functioned throughout the mission and provided frequency and temperature data.

Analysis of the beat frequencies recorded at 1-min intervals for the five units during the mission is complex because these frequencies depend not only on mass adsorption/desorption rates but also on sensor crystal temperature, which unfortunately cannot be kept as stable as desirable. Therefore, only a summary of the overall contamination effects will be presented here. The results from a detailed analysis will be published later.

For this discussion, only maximum deposition rates during stable temperature conditions will be used. Among the five sensors, the one pointing forward appears to indicate the highest mass deposition rates. This is understandable since it is exposed to most of the payload bay and its cargo, in this case the Office of Space and Terrestrial Applications 1 (OSTA-1) package. It also received by far the largest share of the return flux. There does not seem to be a significant trend (beyond measurement uncertainty) of its output with respect to mission elapsed time, as well as sensor temperature. Its equivalent mass deposition rate averages approximately 1×10^{-11} g/cm^2-sec for all temperatures, a value that is very close to the one predicted by the SPACE II/STS-2 mathematical model after thorough outgassing. There is no obvious rate reduction with time indicated by this sensor.

The TQCM located on the +Y side of the IECM collected only a fraction of the rate measured by the forward TQCM. As can be expected, its rate decreases with time and increases with lower sensor temperature. A deposition rate of approximately 2×10^{-12} g/cm^2-sec at 273 K (0° C) is indicated near the end of the mission. The TQCM's placed on the -Y side and aft side of the IECM showed even lower output.

The top TQCM presents a very complex or erratic frequency output pattern. At least part-time instrument malfunction is indicated. No attempt to interpret its output has been made.

In summary of the TQCM data, it appears that deposition rates either are already near the goal or at least are in reach (forward sensor) of the goal of 3×10^{-12} g/cm^2-sec despite the direct flux input from STS-2 payloads.

CRYOGENIC QCM

A pair of cryogenic QCM's (CQCM's) is mounted on top of the IECM. They are insulated from the structure (to a different degree) and cooled by way of passive radiative coupling. Sensor temperature, therefore, varies with the radiation environment. If exposed long enough to "cold space," sensor temperature may get as low as necessary to permit deposition of water for return flux measurement. However, it may take 12 hr to lower the sensor temperature from 293 K (20° C) to 140 K (-133° C) under optimum conditions.

The STS-2 mission did not provide for these conditions, and it is fair to assume that return flux of water was not detected. Since the sensor temperature varied throughout the mission, data analysis is time consuming and not completed. However, CQCM deposition rates are consistent with TQCM deposition rates.

MASS SPECTROMETER

The IECM is equipped with one mass spectrometer of the quadrupole type. Located at the top surface of the IECM, the MS points in the Orbiter +Z direction with a field of view of 0.1 sr. The spectral range extends from 1 to 150 AMU's, and the sensitivity ranges from 10^8 to 10^{17} molecules/cm^2-sec flux. Normally, it takes 2 sec to scan each AMU resulting in an integrated flux converted to "counts" per AMU. A complete scan cycle includes the full mass range and a time period of equal duration to scan the mass 18 peak repeatedly.

During the STS-2 mission, the MS performed only return flux measurements. The results may be analytically converted into column density data and further related to the special characteristics of individual mass sources.

This task is complicated by an interference of a number of known and little-known parameters, such as ambient gas density, Orbiter orientation, differential scattering cross section, angular mass flow distribution, and MS characteristics, namely instrument background. As is well known, the latter poses evaluation problems, particularly for water, but also for gases like hydrogen and methane. To aid in this data analysis, a special gas release maneuver was executed during the STS-2 mission. Both Ne^{22} and H_2O^{18} were released to serve as marked reference gas sources.

The MS functioned excellently throughout the mission and was operated from 3.33 hr MET to 49.16 hr MET with the exception of a 3.0-hr loss of data due to IECM shutdown, beginning at about 33.58 hr MET.

Instrument output, above background, is indicated up to about AMU 100 with the dominant output limited to maximum AMU 44. Atomic mass units 2, 14, 15, 16, 18, and 28 make up the major contributions. These peaks point at the presence of water, nitrogen/carbon monoxide, hydrogen, and methane.

The discussion of the results here will be limited to parts of the AMU 18 behavior because of the major interest in this area. The AMU 18 output in unit counts is plotted as a function of STS-2 MET in figure 6. Discounting for the moment specific peaks, a general downward trend of the output from a high of approximately 27 000 counts at 5.0 hr MET to about 2700 counts at 46.0 hr MET is indicated. This slowly changing output represents the combined vehicle and MS background. These two contributions need to be separated, a task which is incomplete at this time. A number of characteristic changes of the general background appear, however, at certain times during the mission, correlating well with specific mission events. Some of these are also noted in figure 6.

Among specific events that affect data output are Orbiter attitude changes, particularly ram and wake attitudes. Their occurrence may assist data analysis. During wake attitude, few molecules enter the MS, whereas during ram attitude, the flux into the MS is at its maximum. In the case of the STS-2 mission for instance, maximum wake attitude was established at about 7.58 hr MET, as well as at about 8.33 hr MET; ram attitude occurred at

approximately 9.0 hr MET. Evaluation of the instrument output during the time period including these times leads to an upper limit for column density on the order of some 10^{13} molecules/cm^2. A better estimate of column density will be derived when MS background definition is available. The question of an additional water source besides normal desorption still remains. There is some evidence that the thermal protection system absorbed more water on STS-2 than for normal missions.

Water dumps are also expected to contribute significantly to the environment. Such an event occurred, for example, during the time period between 11.81 hr MET and 12.41 hr MET, and is reflected in a considerable instrument output increase. These measurements agree quantitatively well with SPACE II model predictions.

Another important source of water is the flash evaporator system (FES). During the STS-2 mission, the FES was intermittently in operation, for instance, from 21.66 until 32.38 hr MET as well as after 46.36 hr MET. The MS response clearly followed the intensity variations of the source (fig. 6). The results also agree quantitatively with the SPACE II model predictions. The measured column densities are on the order of 10^{13} molecules/cm^2.

The output peaking at about 27.45 hr MET has not yet definitely been related to any specific event. It is known, though, that RMS/RCS tests were performed at that particular time with several of the engines firing for 1-sec periods each.

The gas release was performed for about 30 min during a -ZLV vehicle attitude. The resulting Ne^{22} peak height falls within the order of magnitude predicted by the SPACE II model, but the MS reaction to the H_2O^{18} release requires more analysis before any definite result is known.

FUTURE PLANS

The IECM has been programed for the same measurements for STS-3 as STS-2 (IECM in the payload bay at $X_c = 1179$ and mass spectrometer gas release), but an option has been included to conduct a contamination mapping sequence by using the RMS to place the IECM into 25 locations in the payload bay vicinity. The direct flux from specific sources will be measured at each of these locations. The mapping option will be used if mission conditions permit.

Plans for the STS-4 mission also call for an IECM flight. In addition to the normal operations, as previously described, as well as the contamination mapping, if required, a survey of the RCS plumes will be made using the RMS to maneuver the IECM into the RCS plume flowfield. These measurements will verify the RCS plume impingement analytical models used in analyzing payload rendezvous and capture conditions, as well as giving additional contamination information.

CONCLUSIONS

A considerable amount of high-quality data regarding the Shuttle contamination environment has been obtained on STS-1 and STS-2. The bulk of these data has been derived from the 10 instruments in the IECM, which worked well during the STS-2 mission. Successful performance on the other two planned IECM flights will provide a thorough definition of the Shuttle environment.

Preliminary assessment of the STS-1 and STS-2 data has been completed. In general, mass deposition during any of the mission phases is within the Shuttle requirements and goals. It is not possible at this time to unambiguously establish whether the water molecular column density, as derived from general instrument background, is in compliance with requirements. Upper limits, which have been established from STS-2, are slightly higher than expected for water. Determination of concentrations of other gases must await further analysis.

Particulate contamination during preflight exposures has resulted in particle migration during ascent and entry. Since the Orbiter payload bay had not been finally cleaned before the STS-1 and STS-2 flights, this result is not unexpected. Cleaning of the bay before STS-3 should reduce the particle population considerably.

It is not possible to completely define particle production during the mission because of limited data analysis to date, but it does appear that significant portions of the STS-2 mission had low light levels ($<1 \times 10^{-13}$ $B_{\odot}$), which is encouraging considering the full Moon conditions that existed for the flight. Particle emission rates for sources, as well as quiescent portions of flight, will be established in the near term.

REFERENCES

1. Space Shuttle Flight and Ground System Specification. JSC-07700, Vol. X, NASA Lyndon B. Johnson Space Center, Apr. 27, 1978.

2. Miller, E. R.; and Decker, R.: An Induced Environment Contamination Monitor for the Space Shuttle. NASA TM-78193, Aug. 1978.

3. Miller, E. R.: STS-2 Induced Environment Contamination Monitor - Quick Look Report. NASA TM-82457, Jan. 1982.

4. Jacobs, S.; Ehlers, H. K.; and Miller, E. R.: STS-1 Mission Contamination Evaluation Approach. 11th Space Simulation Conference, NASA CP-2150, 1980, pp. 201-215.

5. Leger, L.; Jacobs, S.; and Ehlers, H. K. F.: Space Shuttle Contamination Overview. J. Environ. Sci., vol. 21, no. 5, Sept./Oct. 1978, pp. 28-33.

6. Jarossy, F. J.; Bareiss, L. E.; Pizzicaroli, J. C.; and Owen, N. L.: Shuttle/Payload Contamination Evaluation Program - Final Report. MCR-81-510, Martin Marietta Corp., Denver Aerospace (Contract NAS9-15826), Mar. 1981.

7. Scialdone, J. J.: Assessment of Shuttle Payloads Gaseous Environment. NASA TM-80286, May 1979.

8. Linton, R. C.; Miller, E. R.; and Susko, M.: Passive Optical Sample Assembly (POSA): Final Report. NASA TM-82446, Aug. 1981.

TABLE 1.- FILM CONDENSATE COLLECTED ON PAYLOAD BAY RADIATORS

Surface sampled	Surface density, g/cm^2	
	STS-1[a]	STS-2[b]
Forward right radiator	1.2×10^{-6}	3.1×10^{-7}
Mid right radiator	8.6×10^{-7}	(c)
Aft right radiator	3.6×10^{-7}	3.1×10^{-7}
Aft left radiator	2.7×10^{-7}	1.4×10^{-7}
Mid left radiator	(d)	(c)
Forward left radiator	(d)	5.7×10^{-7}

[a]STS-1 blank contained 6.9×10^{-7} g/cm^2.
[b]STS-2 blank contained 1.9×10^{-6} g/cm^2.
[c]Less than blank.
[d]No measurement made.

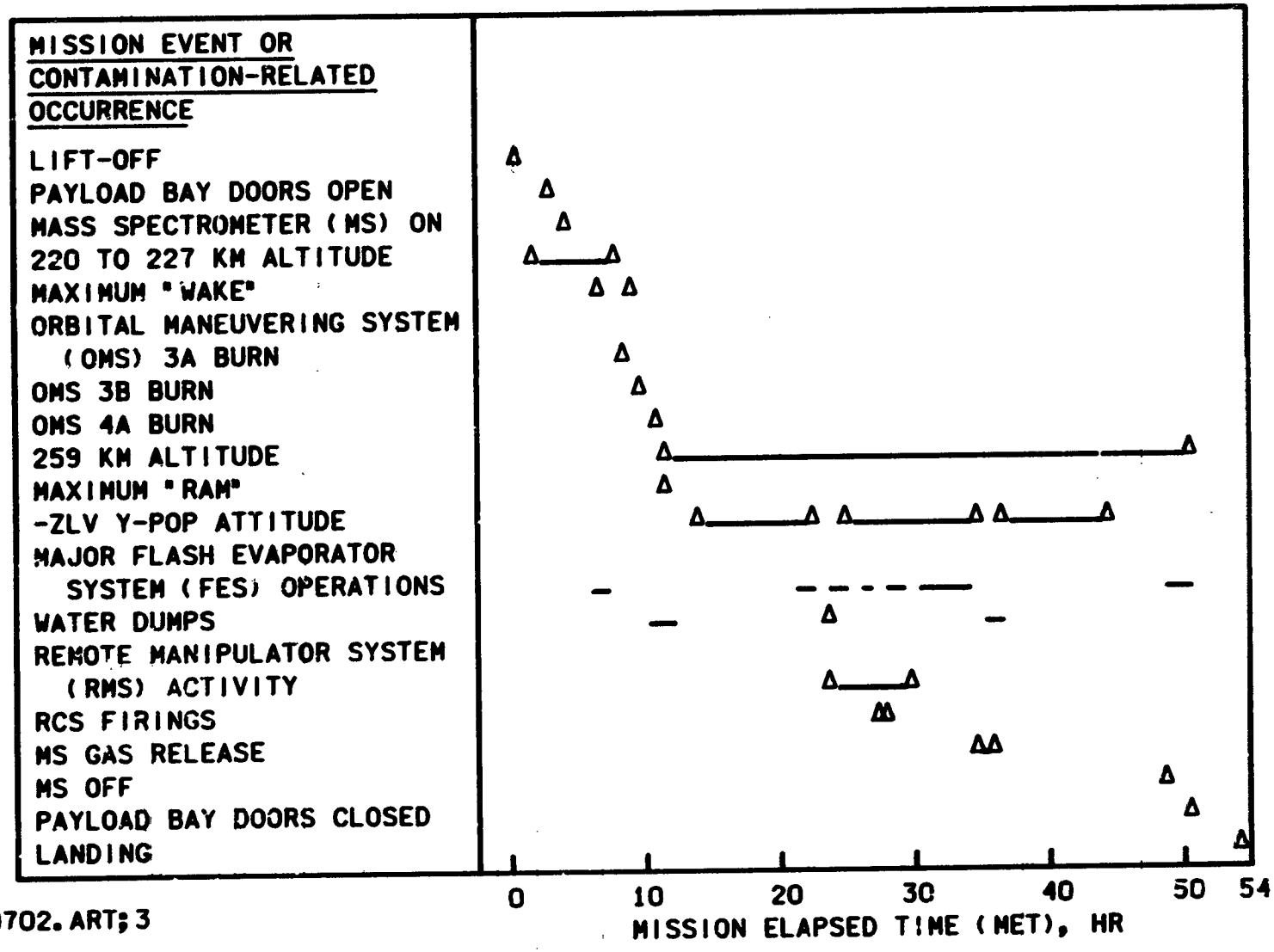

0702.ART;3

Figure 1.- Major STS-2 mission events used for contamination assessment.

ORIGINAL PAGE IS OF POOR QUALITY

ORIGINAL PAGE
BLACK AND WHITE PHOTOGRAPH

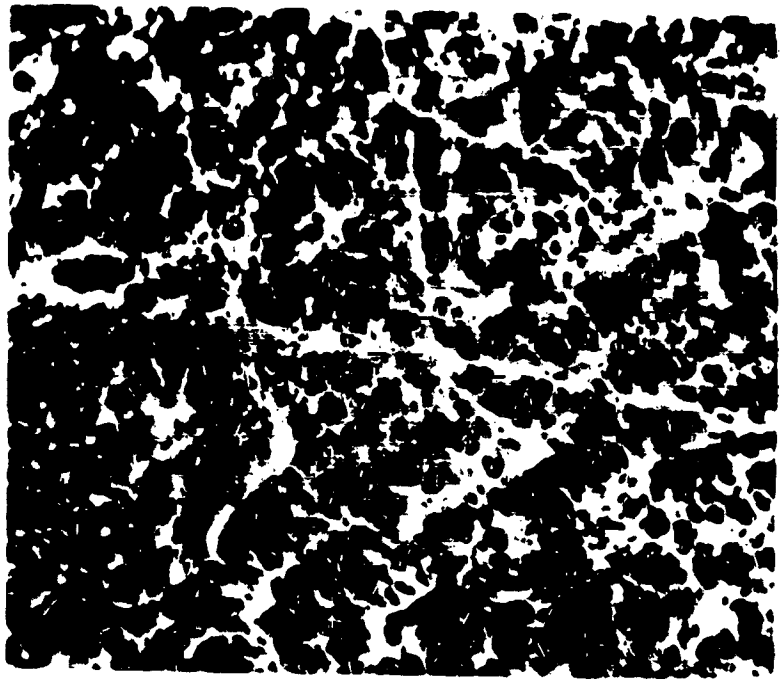

(b) Affected region.

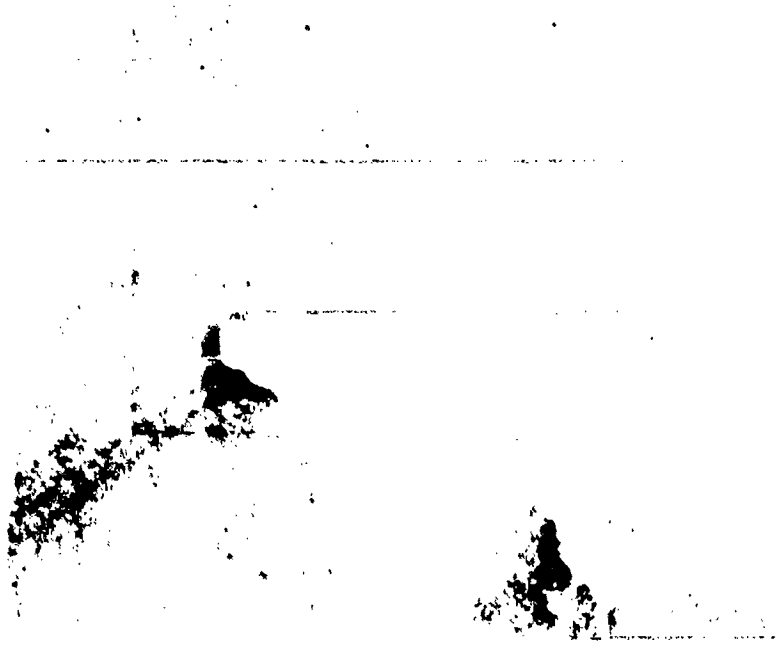

(a) Unaffected region.

Figure 2.- Surface of Kapton film at 10 000x magnification.

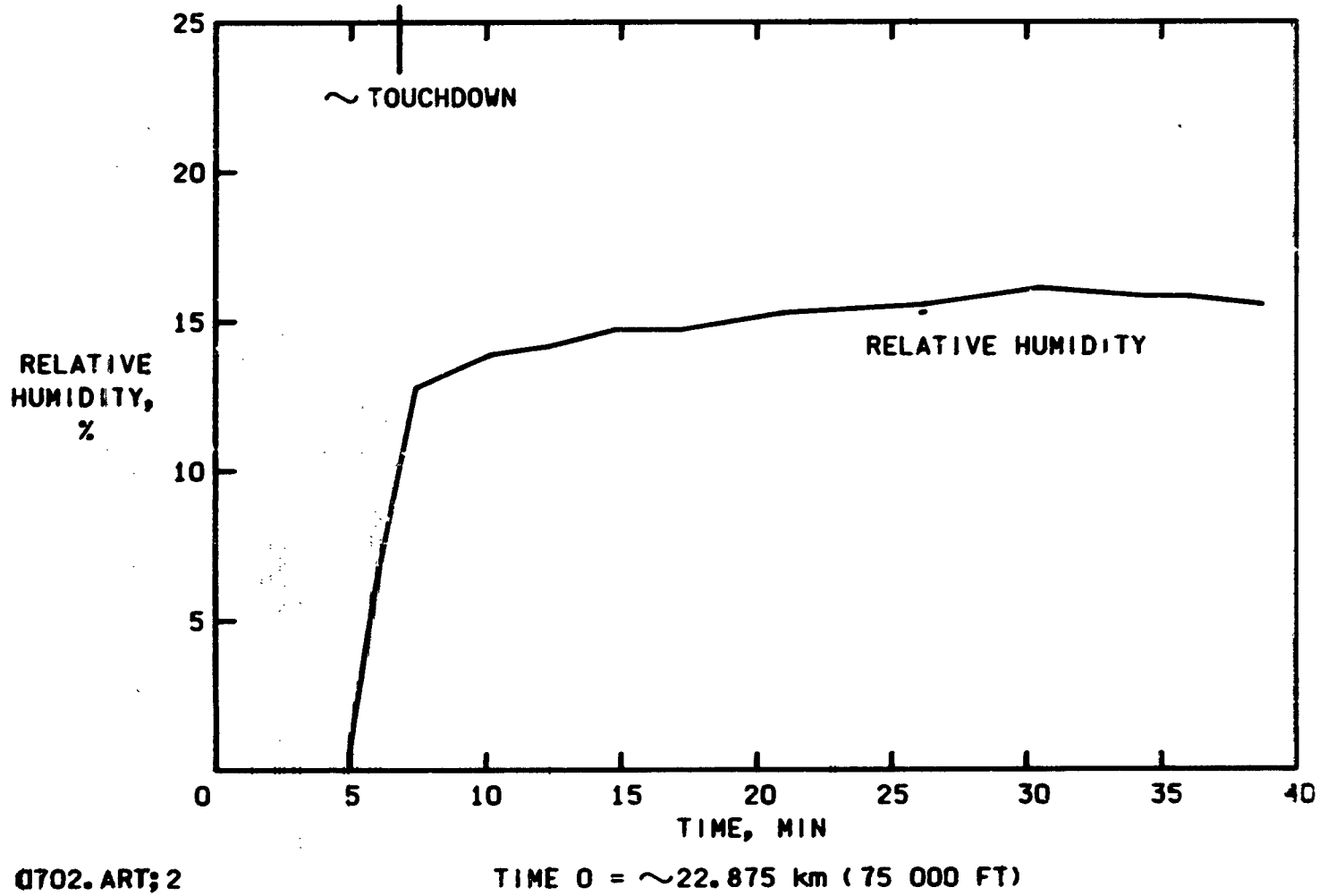

0702.ART;2

Figure 3.- Orbiter payload bay humidity buildup during STS-2 entry.

ORIGINAL PAGE IS
OF POOR QUALITY

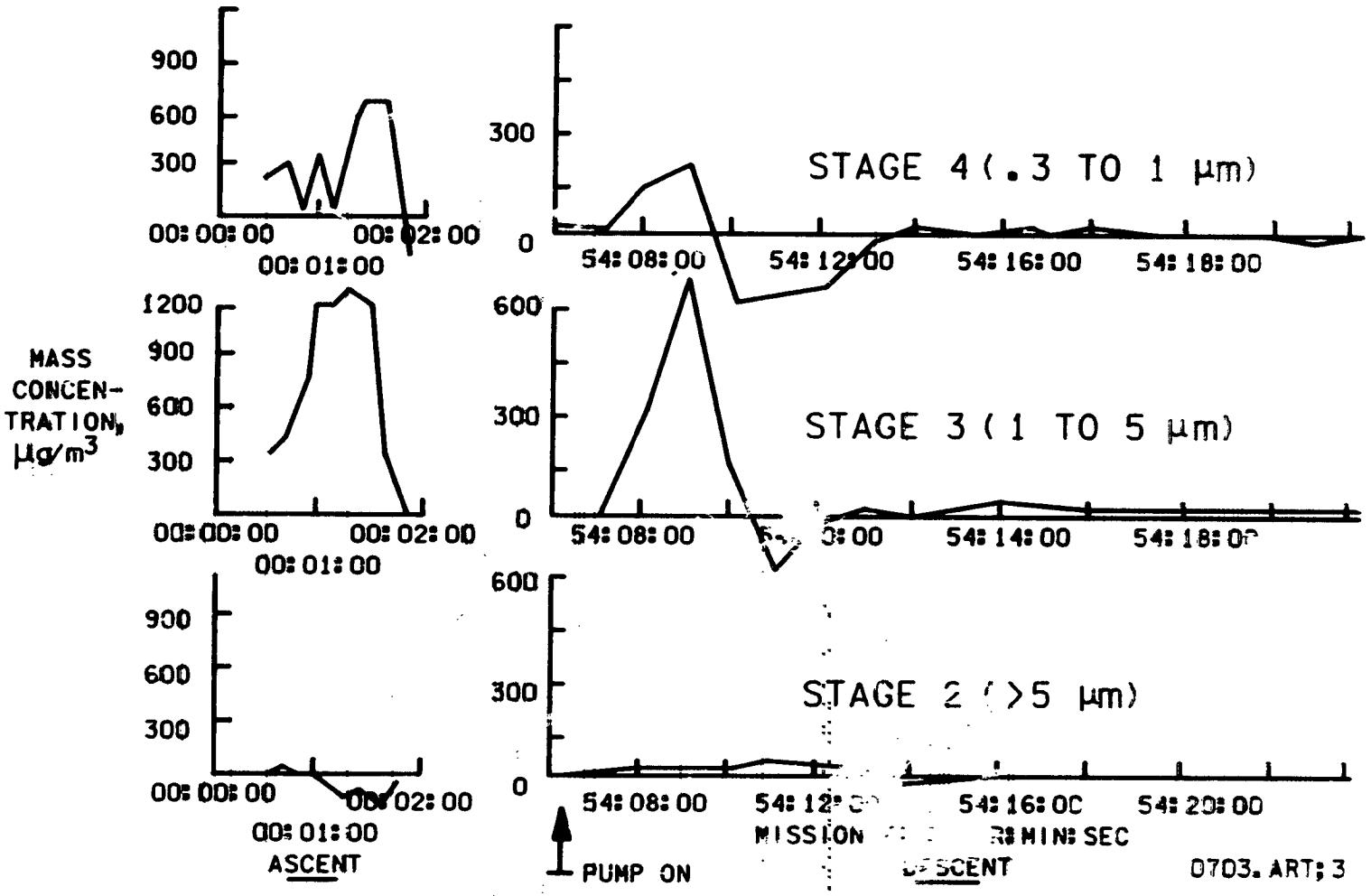

Figure 4.- Mass concentrations as a function of STS-4 mission time.

SAMPLE LISTING:

POSITION	MATERIAL
I_0	OPEN APERTURE
I_1	SAPPHIRE
I_2	LITHIUM FLUORIDE
I_3	CALCIUM FLUORIDE
I_4	MAGNESIUM FLUORIDE
I_5	QUARTZ

EVENT/LOCATION	TRANSMITTANCE I_1	I_2	I_3	I_4	I_5
ORIGINAL VALUES/MSFC	0.73	0.86	0.91	0.89	0.87
IECM/OEM FUNCTIONAL TEST/OPF/KSC	.72	.85	.91	.88	.87
* INITIAL ORBITAL VALUES	.72	.84	.91	.87	.87
FINAL ON-ORBIT VALUES	.70	.83	.91	.86	.86
FINAL VALUES/MSFC	.69	.80	.89	.86	.85
TOTAL CHANGE	-5.5%	-7.0%	-2.2%	-3.4%	-2.3%
CHANGE IN-FLIGHT	-2.8%	-1.2%	0	-1.2%	-1.2%
PREFLIGHT CHANGE (GROUND OPS)	-1.4%	-1.2%	0	-1.1%	0
ORIGINAL TO INITIAL ON-ORBIT CHANGE	-1.4%	-2.3%	0	-2.3%	0
FINAL ON-ORBIT TO FINAL LAB VALUES CHANGE	-1.4%	-3.6%	-2.2%	0	-1.2%

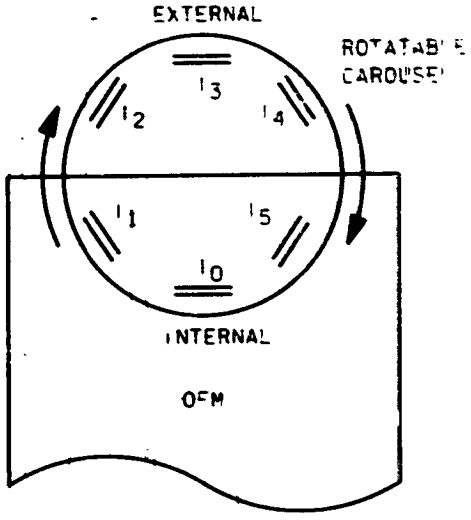

* CORRECTED VALUES, SUBJECT TO POSSIBLE REVISION PENDING SYSTEMATIC ANALYSIS OF INSTRUMENT FLIGHT PERFORMANCE. IN-FLIGHT PERCENTAGE CHANGE NOT SUBJECT TO REVISION.

0704.ART# 2

Figure 5.- Optical effects module: STS-2 results summary.

ORIGINAL PAGE IS OF POOR QUALITY

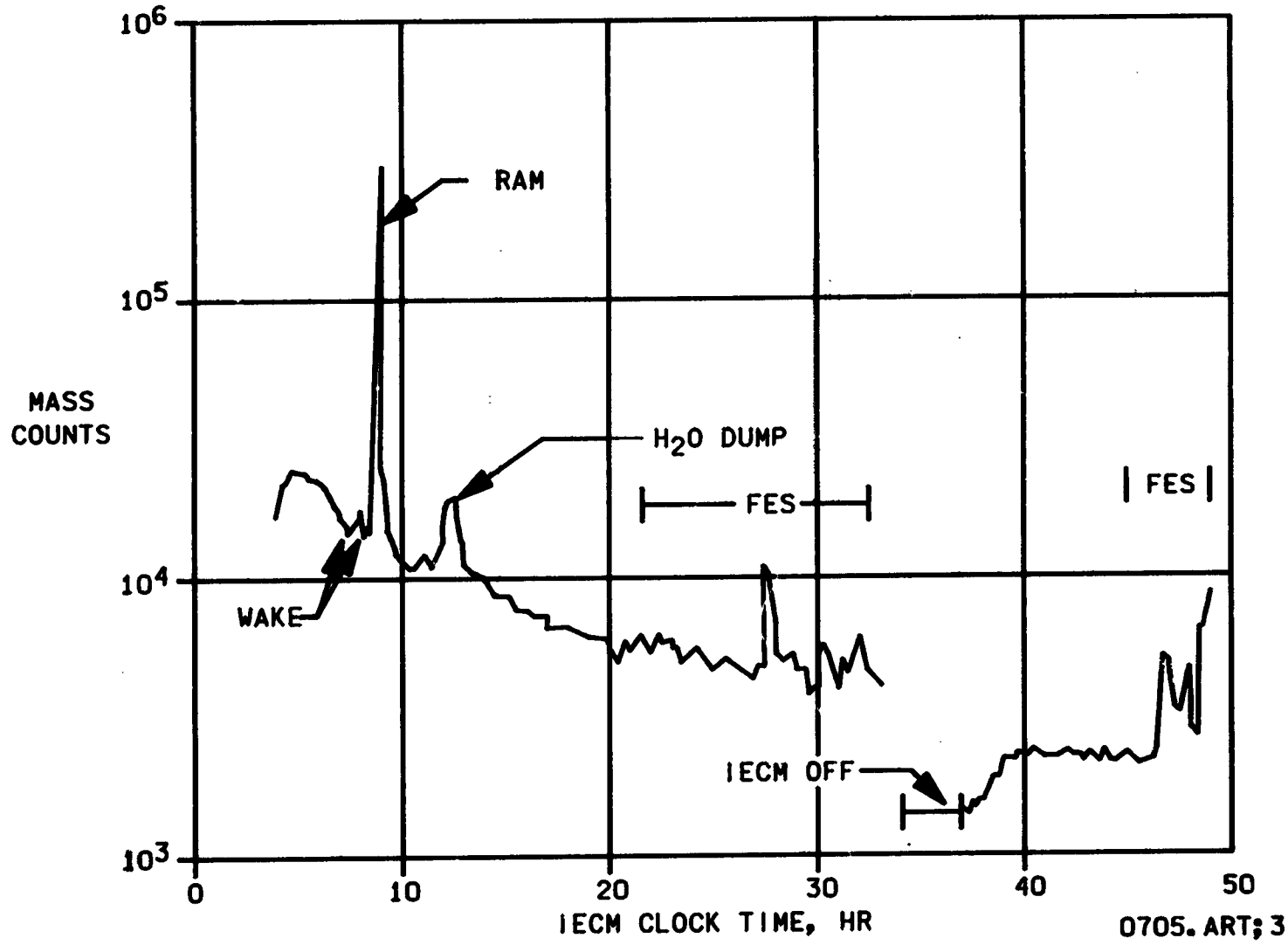

Figure 6.- IECM mass spectrometer output for water (AMU 18) during STS-2 flight.

ORIGINAL PAGE IS OF POOR QUALITY

PRECEDING PAGE BLANK NOT FILMED

N82 25308

A FACILITY FOR THE SIMULATION OF LOW ORBIT ATMOSPHERIC OXYGEN BOMBARDMENT

G. S. Arnold, R. R. Herm, and D. R. Peplinski

The Aerospace Corporation
Los Angeles, California 90009

ABSTRACT

As a vehicle travels through space in relatively low orbit, it experiences bombardment by fast (~8 km/sec) Oxygen atoms by virtue of its orbital velocity. A vessel in orbit at 200 nmi, e.g. a Shuttle Sortie, with an assumed velocity, 8 km sec^{-1} is subjected to an O atom flux of about 10^{14} cm^{-2} sec^{-1}. At 425 nmi, e.g. the Defense Meteorological Satellite Program (DMSP), the flux is about 10^{11} cm^{-2} sec^{-1}. This readily reveals the potential importance of the chemistry of oxygen atoms. Although the ambient atmospheric temperature is not extremely high, ~1000 K, the orbital velocity of the spacecraft causes the oxygen atom collisions to occur at high energy (~5 eV).

In order to investigate the consequences of atmospheric bombardment upon the performance of satellite components in low orbit, we have designed a molecular beam facility to simulate the space environment of a spacecraft at low orbit, with the intent of studying the effect on the properties of optical elements of oxygen atoms impacting at orbital velocity. The current knowledge of high energy O atom surface chemistry and physics is severely limited. One of the reasons for this is the difficulty of producing a fast oxygen atom beam in the laboratory. Production of fast O atoms beams of high intensity, needed in these studies, requires state-of-the-art beam source technology. The four-stage differentially pumped molecular beam facility that we have designed includes a variety of oxygen atom beam sources which cover a wide range of velocities (1 km/sec to $\gtrsim$8 km/sec), in addition to the ultra-clean experimental environment of an ultra-high vacuum (UHV) chamber and an optical diagnostic set-up.

The primary oxygen atom beam source used to obtain the 8 km/sec O atoms is an arc heated source. It consists of a modified commercially available plasma torch. The modifications include attachments which provide for a nozzle which is used to expand the atomic beam into the vacuum system, and exhaust channels to dispose of excess torch gas. The torch operates in the "non-transferred" mode of operation, that is the electric arc is confined within the torch. A plasma is formed in helium by a dc arc. A small amount of O_2 is injected downstream from the arc where it is thermally dissociated by the hot He into oxygen atoms. The high temperature and isentropic expansion give the oxygen atoms their velocity.

Two other beam sources are also used to product oxygen atoms in this facility – a resistively heated source and a microwave discharge source. Using seeded beam techniques, oxygen atom beams of ~3.5 and ~1.5 km/sec, respectively, are obtained.

The UHV chamber provides for the ultra-clean environment needed for proper performance of surface chemistry measurements.

The optical diagnostics set up provides for measuring the effect of O atom bombardment on the transmission of optical materials and on the reflectivity of mirrors. Changes in optical properties are measured as a function of total O atom flux and of incident velocity. An in situ volatile condensible material (VCM) deposition apparatus will also be described. It permits the investigation of the effect of O atoms on satellite outgassing impurities which can be deposited upon optical surfaces.

This molecular beam space simulation facility provides for a unique testing apparatus of the effects of the ambient atmosphere on low orbit vehicles.

N82 25309 D8

PRECEDING PAGE BLANK NOT FILMED

AUTOMATING A RESIDUAL GAS ANALYZER

Ward F. Petrie/Alvin H. Westfall
The Optical Technology Division of the Perkin-Elmer Corporation

INTRODUCTION

A residual gas analyzer (RGA) as "a device for measuring the amounts and species of various gases present in a vacuum system" (ref. 1) can provide information needed to properly evaluate an outgassing test, to troubleshoot an improperly operating vacuum system, or to monitor a vacuum process. To satisfy any of these requirements, it is necessary to obtain and interpret an RGA mass spectrum to determine the gases present in the vacuum system. The gases can be identified by their unique fragmentation patterns which may consist of several peaks at different mass-to-charge ratios (m/e). Depending upon the condition of the vacuum system and the RGA being used, the mass spectrum may be very complex with many peaks - some overlapping and additive - being present. Obtaining a clear readable spectrum may be very cumbersome.

A recent update of the RGA at Perkin-Elmer's Optical Technology Division found that microprocessor technology had revolutionized this important diagnostic tool. This revolution is exemplified by the Inficon IQ200 RGA which was selected to meet the needs of this update. Since its purchase nearly one year ago, experience with its operation has shown it to be a vast improvement over the more cumbersome and hard-to-operate equipment which it replaced. However, even with these improvements, we found that the operator interactions required to obtain data from the instrument are still extensive and require that the operator have an intimate knowledge of the instrument and its operation. Training of the operators would overcome this shortcoming, but lack of a computer-compatible data format still presents a very significant shortcoming (this problem has been addressed by the manufacturer, but details are still lacking on the extent to which this problem has been solved).

Early on, these limitations in the Inficon IQ200 were recognized. In order to circumvent them, we ordered the IQ200 with a digital output module. This option outputs the values of digital data from the table display previously programmed by the operator for mass number, gain and dwell. At that time, a Zilog Z80 16K microcomputer was also purchased. Our intention was to interface the microcomputer to the RGA in order to both command it and to receive and format the digital data from the RGA.

This paper describes our approach to meeting this objective using the Inficon RGA and the Zilog microcomputer.

DESCRIPTION OF APPROACH

In interfacing the microcomputer to the RGA, it was possible to use the paper tape command interface that is provided as a standard feature on the RGA and the digital data module described in the introduction. The basic design of this interface is intended to allow the microcomputer to command the RGA in order to set the proper mass and gain values for the table mode of operation. Figure 1 shows the cathode ray tube (CRT) output provided on the RGA for this mode of operation. The peak values that are given in the table, once the gain, multiplier voltage, and dwell are set, are provided through the digital output option that was purchased with the RGA.

The actual interfacing is accomplished by adding switchable gates to control the data direction and using a parallel data input/output (PIO) chip to transmit and receive the data and to control the gates. Figure 2 shows a simple schematic of the approach. Note that the PIO chip has two ports: one of these ports is used to handle the data while the other port is used for control purposes, providing necessary "handshakes" for the RGA and to switch the gates. Simply by writing the appropriate command characters (eight-bit ASCII characters) into the data port, and then by appropriate writes or reads into the other port, the various handshakes can be generated or read as appropriate. The microcomputer board is configured in such a way that the necessary gates and wiring can be easily added directly on the board. Once the hardware is properly modified, the only remaining effort is to program the microcomputer.

The control program was written in stages. First, a program was written that would perform the basics of commanding the RGA and allow for the testing of the command and read interfaces between the RGA and the microcomputer. Once this capability was demonstrated, a program was written that would command the RGA to scan all 200 masses in groups of ten (this approach is dictated by the limit of ten channels on the digital data output option of the RGA). The data is stored in the microcomputer random access memory (RAM) space as it is acquired. The scanning starts with masses 1 through 10 and the lowest gain value. The data obtained from the first scan at the lowest gain value is then tested for validity, i.e., it is tested to see if it is non-zero. If it is zero, the gain value for that particular mass is incremented by one. This process is repeated with the gain values being incremented as necessary, until either all ten masses have valid data, or until data is obtained at the maximum gain value. This data is now sent out to be recorded on a computer-compatible medium. In our approach, the medium most useful to us is magnetic tape. The microcomputer also provides proper formatting of the data, organizing it into proper records for recording (80 character records) with appropriate characters to signify the end of each record.

Troubleshooting or debugging the program showed up some idiosyncrasies of the RGA that required changes in the command sequences. Since the program is structured for convenience, valid data is not immediately loaded into the RAM space when it is first identified. Rather, a flag is set in memory, and no further changes are made in gain. Only when all ten channels

ORIGINAL PAGE
BLACK AND WHITE PHOTOGRAPH

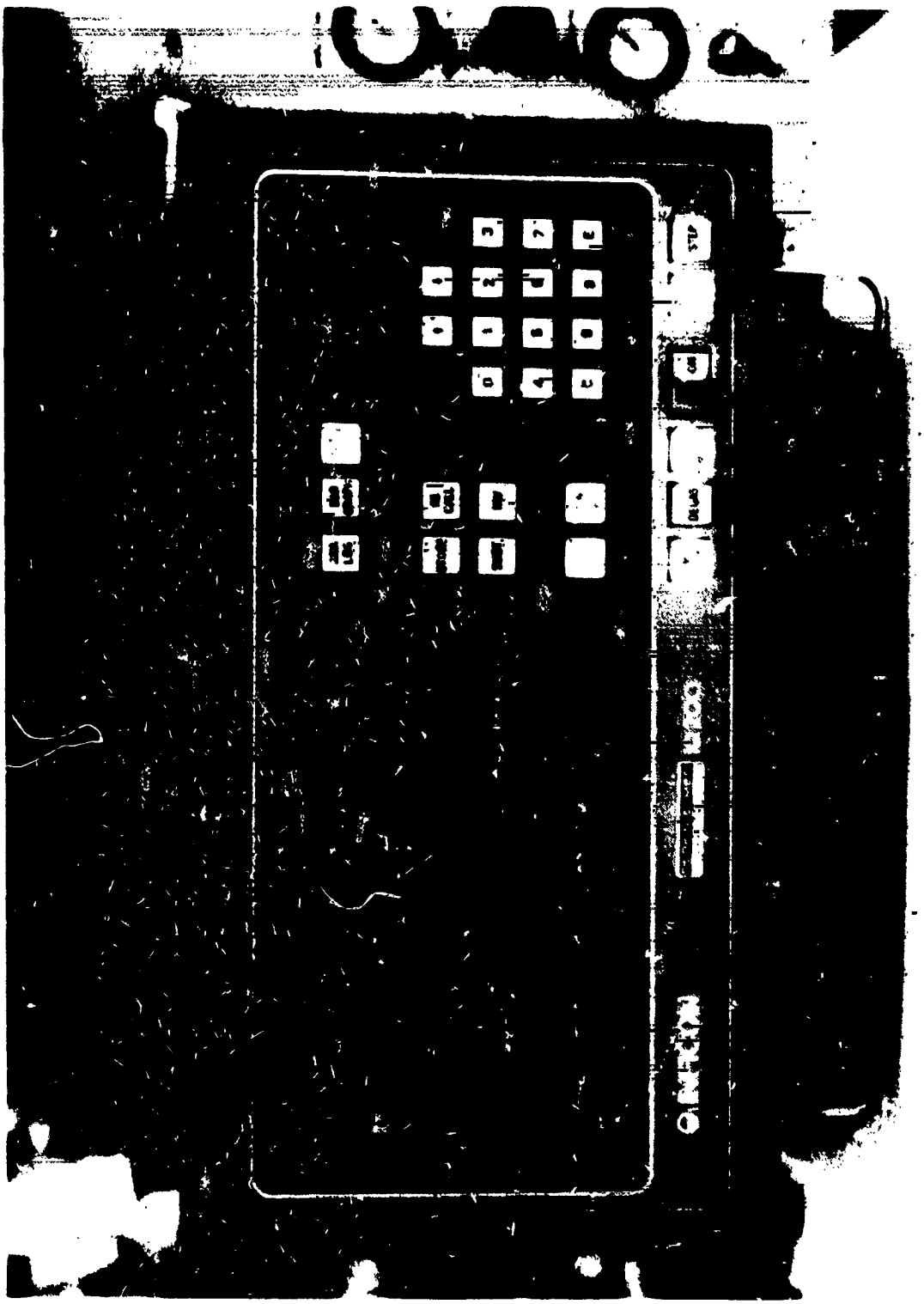

Figure 1. RCA Table Mode Display

ORIGINAL PAGE IS
OF POOR QUALITY

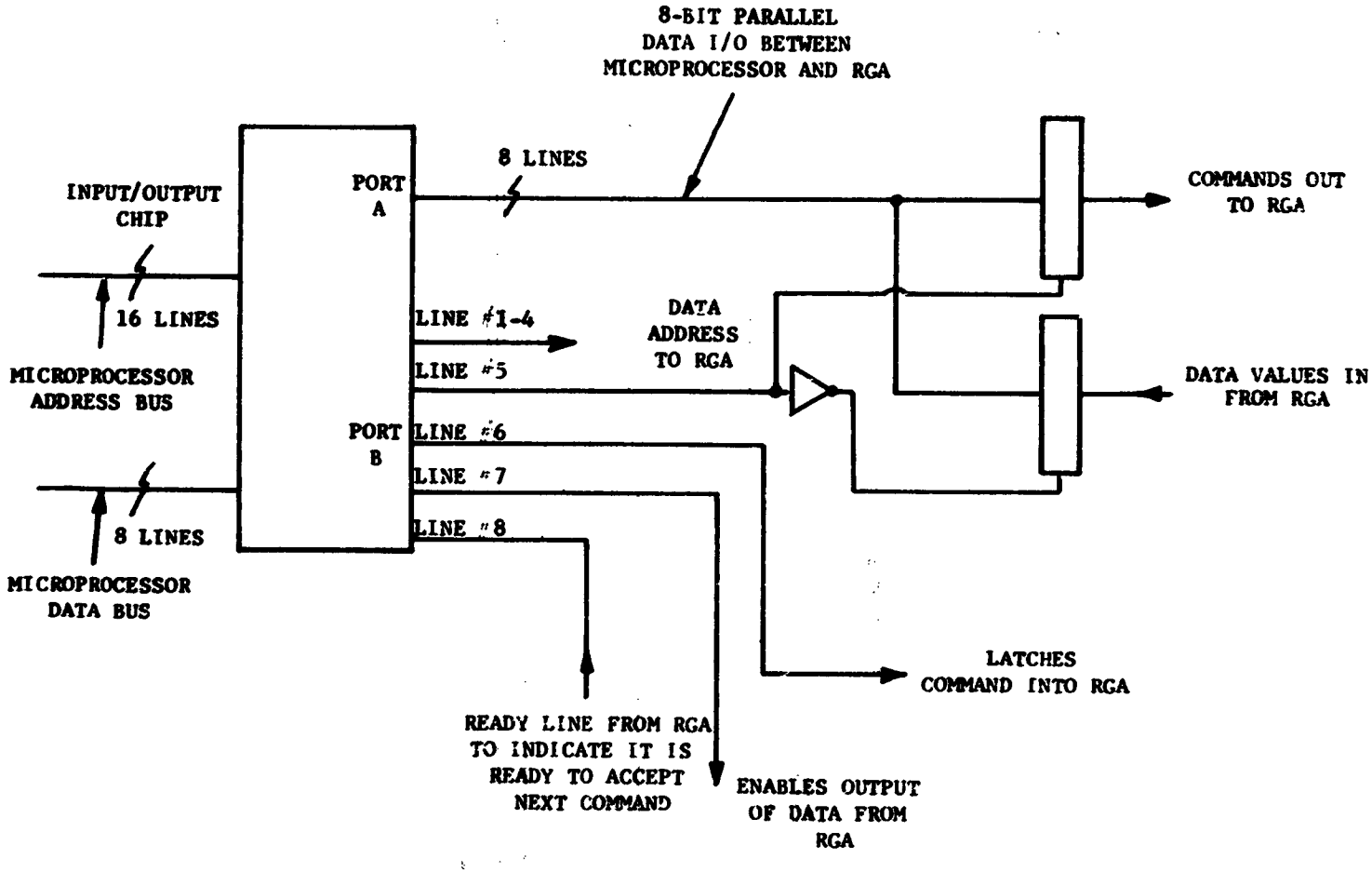

Figure 2. Microprocessor - RGA Interface Schematic

are showing valid data or when the maximum gain value is achieved, is data sent out. This means that the values from the last scan are the ones that are used. Consequently, some masses that attain valid data on earlier scans can be found to have saturated values. A compromise had to be incorporated both in the selection process for valid data, i.e., in the minimum value for valid data, and in adjusting data, when the final scan indicated that a value had saturated. For the latter case, it was found that adjusting to a value just below the saturated value was as valid an approach as either redoing the scan or trying other more complicated programming maneuvers to correct the problem, such as decrementing the gain value to the next lower value and repeating the scan.

Once debugging of the basic control program was completed, the program was expanded to query the operator for input of additional information that is important to the completeness of the RGA data. This so-called header information included date, time, pressure of the chamber, pressure of the RGA head, status of the valving connecting the RGA head to the chamber (since the valve can be either in closed mode isolated from the chamber, communicating with the chamber by means of an orifice controlled bypass for use when the chamber pressure is high (as high as 1.5×10^{-2} torr), or directly communicating with the chamber), the multiplier voltage, and the dwell. Changes were also made giving the operator the option of scanning only a limited number of masses rather than all 200 masses. The only restriction on the mass channels scanned was that they be in multiples of ten, e.g., masses 11 through 40, 101 through 120. By making this restriction, the programming was kept simple, yet gave the operator sufficient flexibility to allow him to look at a small group of peaks of interest more quickly than if he had to scan all 200 masses to look at these same peaks. Figure 3 shows a flow diagram for the final program.

With the completion of the changes to the control program, the entire program was put into UVEPROM (ultraviolet erasable programmable read only memory) which puts the program into the microcomputer as part of the hardware. As long as UVEPROM is left in place in the microcomputer, no write-over or accidental erasure of the program is possible even if the power is shut off. Additionally, it is relatively simple to remove UVEPROM, erase it, and rewrite a new program into it. This feature makes the program always resident for the operator, thus not requiring any software loading into the microcomputer which would be the case if the program were loaded and operated from RAM space.

RESULTS AND CONCLUSION

The basic program has been used as a means of obtaining data for outgassing evaluations of parts to determine their cleanliness. These tests gave us a first hand opportunity to see how useful this automated operation and data collection from the RGA really is. The RGA settings which the operator is required to carry out is the setting of an appropriate multiplier voltage and ensuring that the dwell is set at the correct value for all ten channels. With the simple first command of "J 1000", the operator just enters the appropriate responses to the queries presented by the microcomputer. Figure 4 shows the basic data collection process as seen by the

ORIGINAL PAGE IS
OF POOR QUALITY

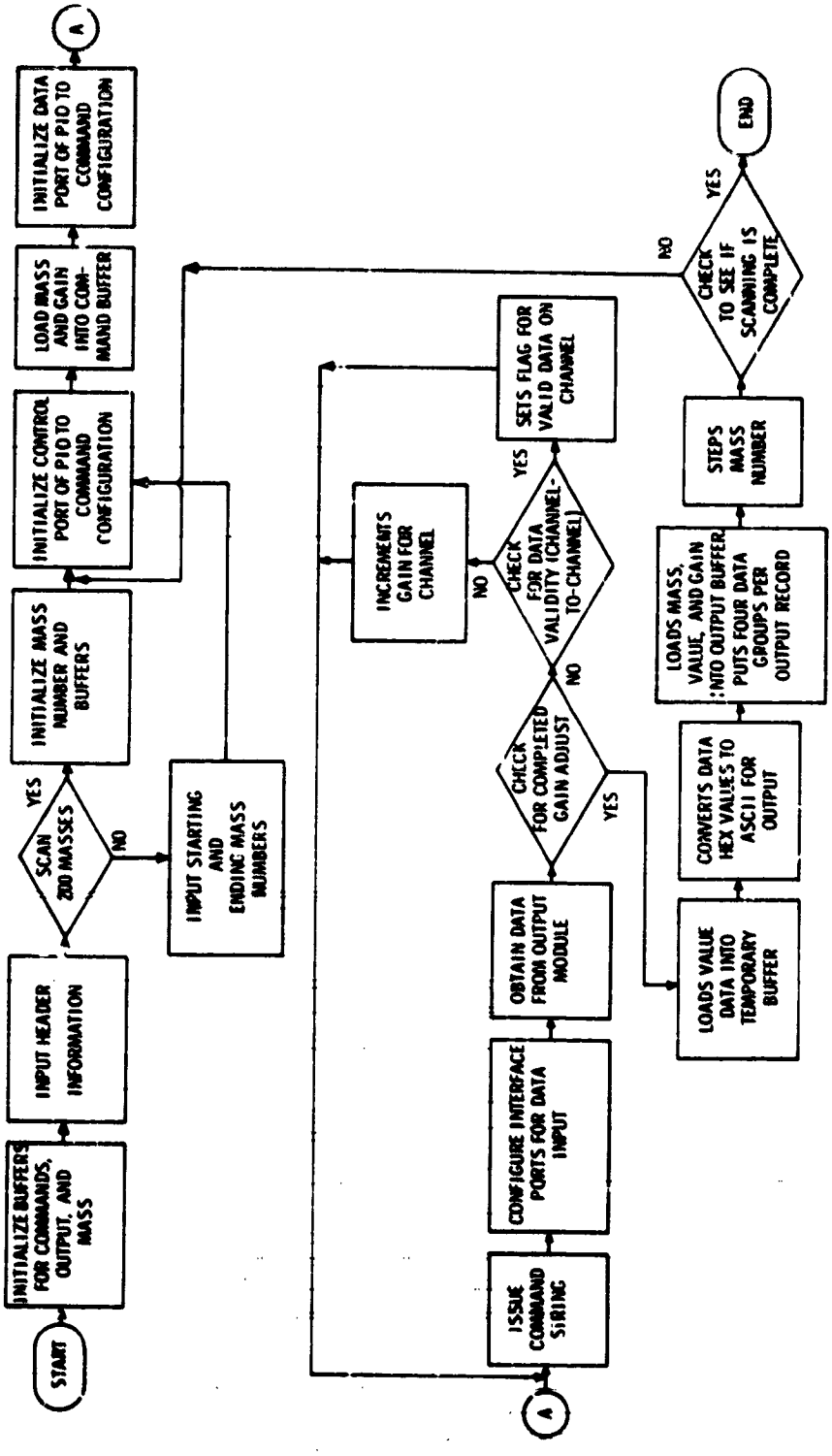

Figure 3. RGA Control Program Flow Diagram

```
? J 1000
 TYPE IN DATE AS MM/DD/YY

01/5/82

 THE INPUT IS INCORRECT; TRY AGAIN, PLEASE!

 TYPE IN DATE AS MM/DD/YY

01/05/82

 TYPE IN TIME AS HH:MM

08:45

 TYPE IN CHAMBER PRESSURE AS 0.0XE-00

3XE-07

 THE INPUT IS INCORRECT; TRY AGAIN, PLEASE!

 TYPE IN CHAMBER PRESSURE AS 0.0XE-00

3.0XE-07

 TYPE IN VOLTAGE AS 0000

3000

 TYPE IN VALVE STATUS AS; M(MAIN), B(BYPASS), OR C(CLOSED)

C

 TYPE IN RGA HEAD PRESSURE AS 0.0XE-00

1.0XE-07

 DO YOU WISH TO SCAN ALL 200 AMU VALUES?(Y/N)

N

 ENTER STARTING ADDRESS AS XX1

001

 ENTER ENDING ADDRESS AS XX0

020

DATE: 01/05/82
TIME: 08:45
CHAMBER PRESS 3.0XE-07
VOLTAGE 3000
VALVE STATUS C
RGA HEAD PRESS 1.0XE-07
DWELL 32
001 AMU 03.5 G09  002 AMU 05.0 G10  003 AMU 01.4 G10  004 AMU 00.7 G10
005 AMU 06.2 G11  006 AMU 03.0 G11  007 AMU 07.1 G11  008 AMU 08.5 G1
```

Figure 4. Operator Input Format for Partial Scan

ORIGINAL PAGE IS
OF POOR QUALITY

```
?>J 1000
 TYPE IN DATE AS MM/DD/YY

01/05/82

 TYPE IN TIME AS HH:MM

08:45

 TYPE IN CHAMBER PRESSURE AS #.#XE-##

3.0XE-07

 TYPE IN VOLTAGE AS ####

3000

 TYPE IN VALVE STATUS AS: M(MAIN), B(BYPASS), OR C(CLOSED)

C

 TYPE IN RGA HEAD PRESSURE AS #.#XE-##

1.0XE-07

 DO YOU WISH TO SCAN ALL 200 AMU VALUES?(Y/N)

Y

DATE: 01/05/82
TIME: 08:45
CHAMBER PRESS 3.0XE-07
VOLTAGE 3000
VALVE STATUS C
RGA HEAD PRESS 1.0XE-07
DWELL 32
001 AMU 07.5 G09  002 AMU 10.0 G10  003 AMU 01.8 G10  004 AMU 00.9 G10
005 AMU 03.8 G11  006 AMU 03.4 G11  007 AMU 02.8 G11  008 AMU 10.0 G12
009 AMU 06.5 G11  010 AMU 02.2 G11  011 AMU 01.2 G10  012 AMU 06.8 G11
013 AMU 01.6 G10  014 AMU 03.1 G10  015 AMU 01.1 G09  016 AMU 01.3 G09
017 AMU 03.1 G10  018 AMU 02.5 G10  019 AMU 00.9 G11  020 AMU 00.1 G11
```

Figure 5. Operator Input Format for Full Scan

ORIGINAL PAGE IS
OF POOR QUALITY

DATE: 01/05/82
TIME: 08:45
CHAMBER PRESS 3.0XE-07
VOLTAGE 3000
VALVE STATUS C
RGA HEAD PRESS 1.0XE-07
DWELL 32

001	AMU	05.9	G09	002	AMU	11.8	G10	003	AMU	01.8	G10
005	AMU	06.7	G11	006	AMU	02.6	G11	007	AMU	04.0	G11
009	AMU	02.6	G11	010	AMU	07.4	G11	011	AMU	06.9	G11
013	AMU	01.8	G10	014	AMU	03.9	G10	015	AMU	01.1	G09
017	AMU	02.7	G10	018	AMU	02.8	G10	019	AMU	09.4	G11
021	AMU	00.0	G12	022	AMU	00.0	G12	023	AMU	08.0	G12
025	AMU	03.5	G11	026	AMU	09.9	G11	027	AMU	01.5	G10
029	AMU	03.5	G11	030	AMU	04.3	G11	031	AMU	08.5	G11
033	AMU	00.0	G12	034	AMU	02.5	G12	035	AMU	00.1	G11
037	AMU	00.0	G12	038	AMU	01.4	G11	039	AMU	00.2	G11
041	AMU	06.0	G11	042	AMU	01.6	G10	043	AMU	03.2	G10
045	AMU	02.0	G11	046	AMU	02.6	G12	047	AMU	00.0	G12
049	AMU	04.0	G12	050	AMU	00.0	G12	051	AMU	00.0	G12
053	AMU	00.0	G12	054	AMU	00.0	G12	055	AMU	00.0	G12
057	AMU	01.7	G11	058	AMU	00.0	G12	059	AMU	01.3	G12
061	AMU	00.0	G12	062	AMU	00.0	G12	063	AMU	00.0	G12
065	AMU	00.0	G12	066	AMU	00.0	G12	067	AMU	00.0	G12
069	AMU	00.0	G12	070	AMU	00.0	G12	071	AMU	00.0	G12
073	AMU	01.9	G12	074	AMU	00.0	G12	075	AMU	00.0	G12
077	AMU	01.8	G12	078	AMU	07.3	G12	079	AMU	00.0	G12
081	AMU	00.0	G12	082	AMU	01.0	G11	083	AMU	00.0	G12
085	AMU	00.6	G12	086	AMU	01.1	G12	087	AMU	00.6	G12
089	AMU	00.0	G12	090	AMU	01.8	G12	091	AMU	00.0	G12
093	AMU	00.0	G12	094	AMU	00.0	G12	095	AMU	02.1	G12
097	AMU	03.6	G12	098	AMU	00.0	G12	099	AMU	00.0	G12
101	AMU	00.5	G12	102	AMU	01.3	G12	103	AMU	00.0	G12
105	AMU	00.0	G12	106	AMU	00.0	G12	107	AMU	00.3	G12
109	AMU	00.0	G12	110	AMU	00.0	G12	111	AMU	02.2	G12
113	AMU	00.0	G12	114	AMU	00.0	G12	115	AMU	00.0	G12
117	AMU	00.0	G12	118	AMU	00.0	G12	119	AMU	00.0	G12
121	AMU	00.0	G12	122	AMU	00.0	G12	123	AMU	03.8	G12
125	AMU	00.0	G12	126	AMU	00.0	G12	127	AMU	00.4	G12
129	AMU	00.0	G12	130	AMU	00.0	G12	131	AMU	00.0	G12
133	AMU	03.6	G12	134	AMU	01.8	G12	135	AMU	02.2	G11
137	AMU	00.0	G12	138	AMU	00.0	G12	139	AMU	00.0	G12
141	AMU	00.0	G12	142	AMU	00.0	G12	143	AMU	01.0	G12
145	AMU	00.6	G12	146	AMU	00.0	G12	147	AMU	00.0	G12
149	AMU	00.0	G12	150	AMU	00.0	G12	151	AMU	00.0	G12
153	AMU	00.0	G12	154	AMU	01.2	G12	155	AMU	03.0	G12
157	AMU	00.0	G12	158	AMU	00.0	G12	159	AMU	00.0	G12
161	AMU	00.0	G12	162	AMU	00.0	G12	163	AMU	01.9	G12
165	AMU	00.0	G12	166	AMU	00.0	G12	167	AMU	00.4	G12
169	AMU	01.1	G12	170	AMU	00.0	G12	171	AMU	05.1	G12
173	AMU	00.0	G12	174	AMU	00.0	G12	175	AMU	02.6	G12
177	AMU	00.0	G12	178	AMU	00.0	G12	179	AMU	00.7	G12
181	AMU	02.4	G12	182	AMU	01.6	G11	183	AMU	01.8	G12
185	AMU	03.2	G12	186	AMU	00.5	G12	187	AMU	06.6	G12
189	AMU	00.0	G12	190	AMU	00.0	G12	191	AMU	04.8	G12
193	AMU	04.8	G12	194	AMU	00.0	G12	195	AMU	00.8	G12
197	AMU	04.6	G12	198	AMU	02.0	G12	199	AMU	03.5	G12

BREAK AT 1437

Figure 6. Header and Data for Complete Scan

ORIGINAL PAGE IS
OF POOR QUALITY

ORIGINAL PAGE IS
OF POOR QUALITY

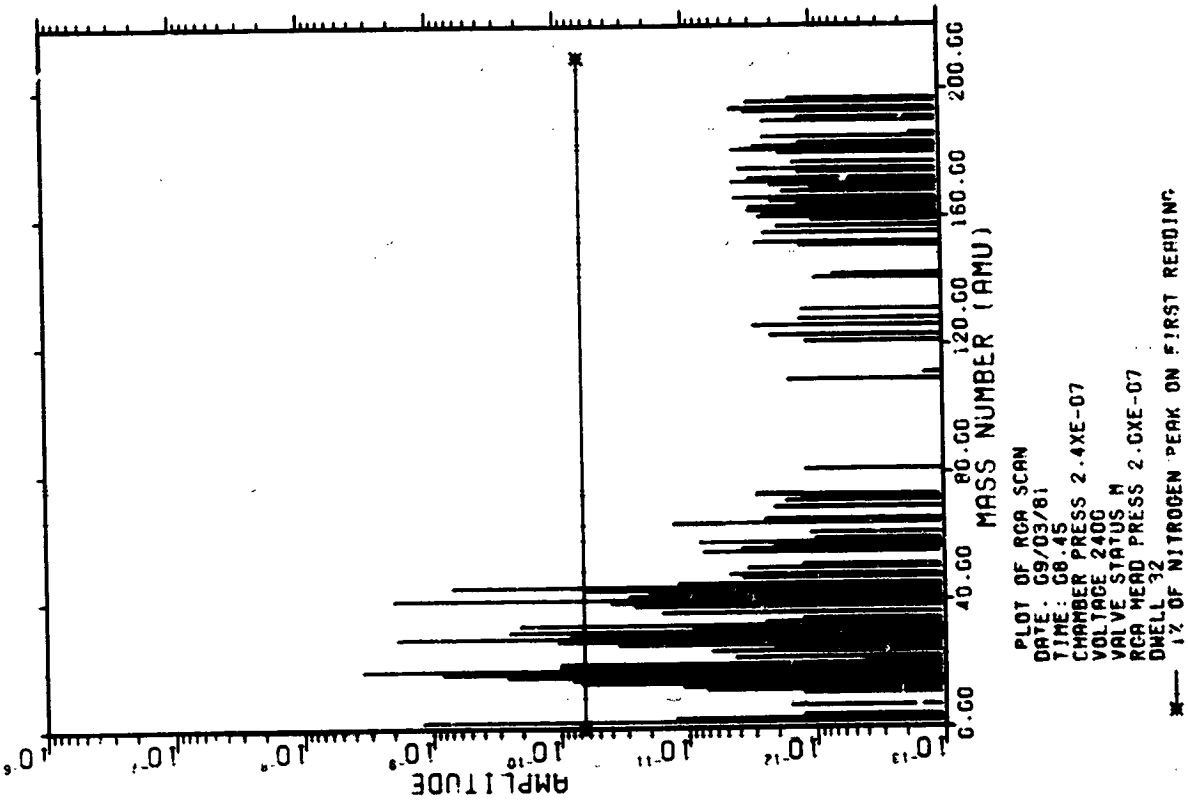

Figure 7. Plot of Complete Scan

ORIGINAL PAGE IS
OF POOR QUALITY

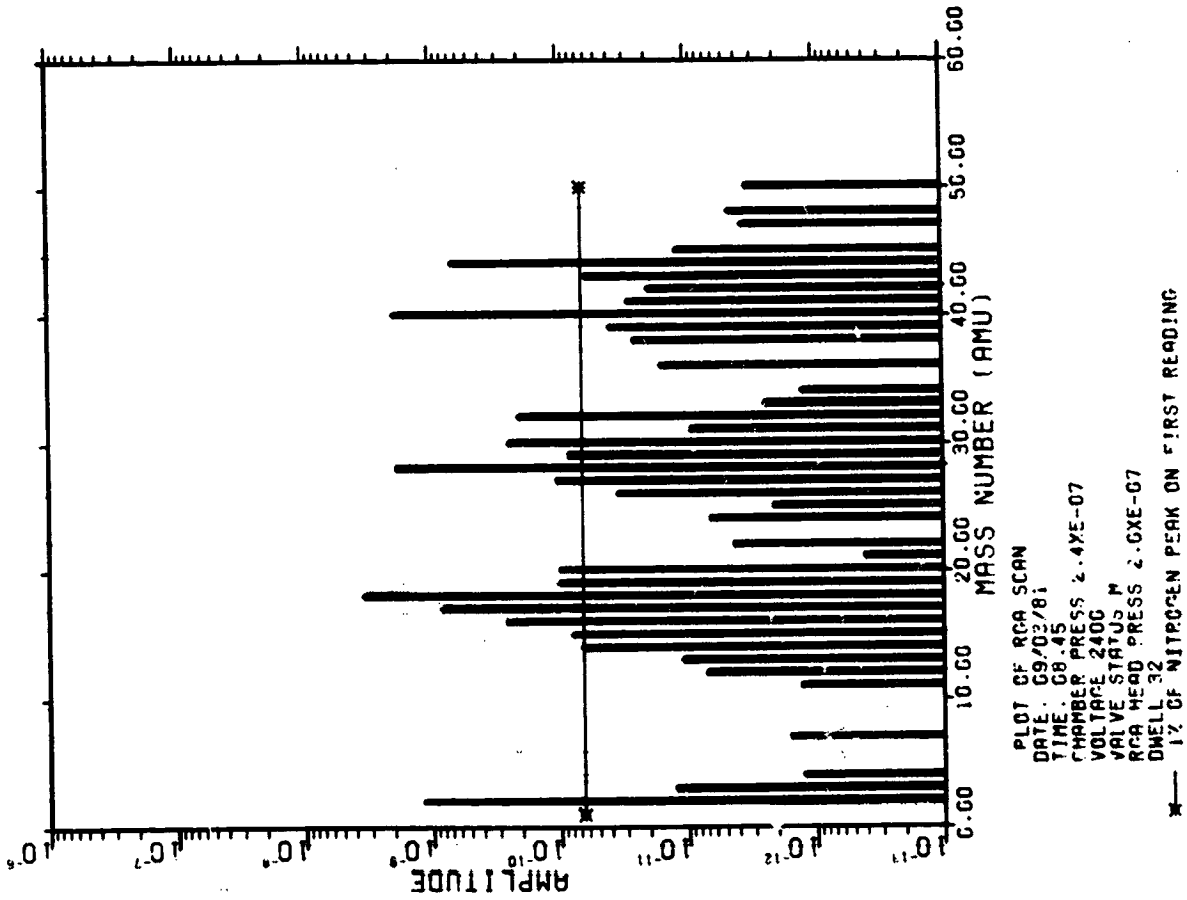

Figure 8. Expanded Plot of Figure 7 Data

ORIGINAL PAGE IS
OF POOR QUALITY

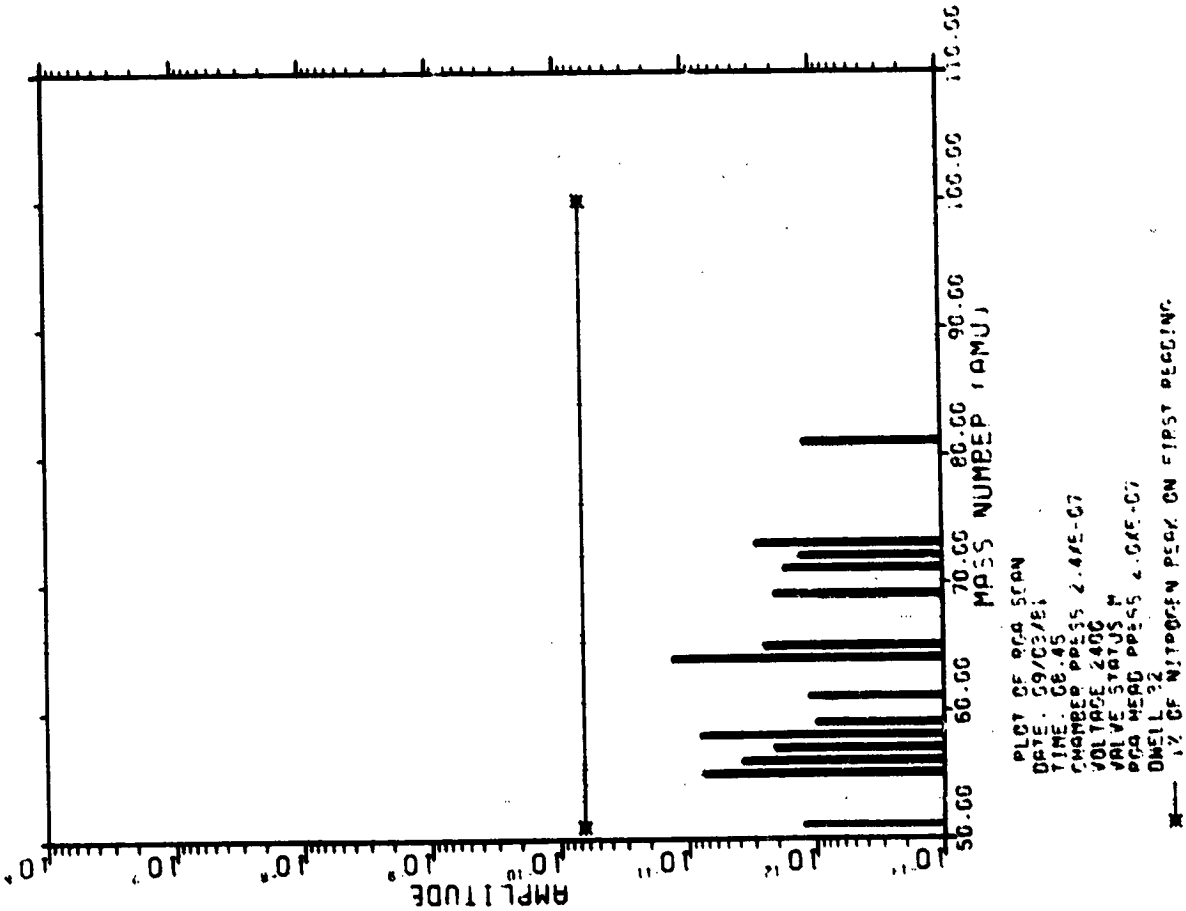

Figure 9. Expanded Plot of Figure 7 Data

ORIGINAL PAGE IS
OF POOR QUALITY

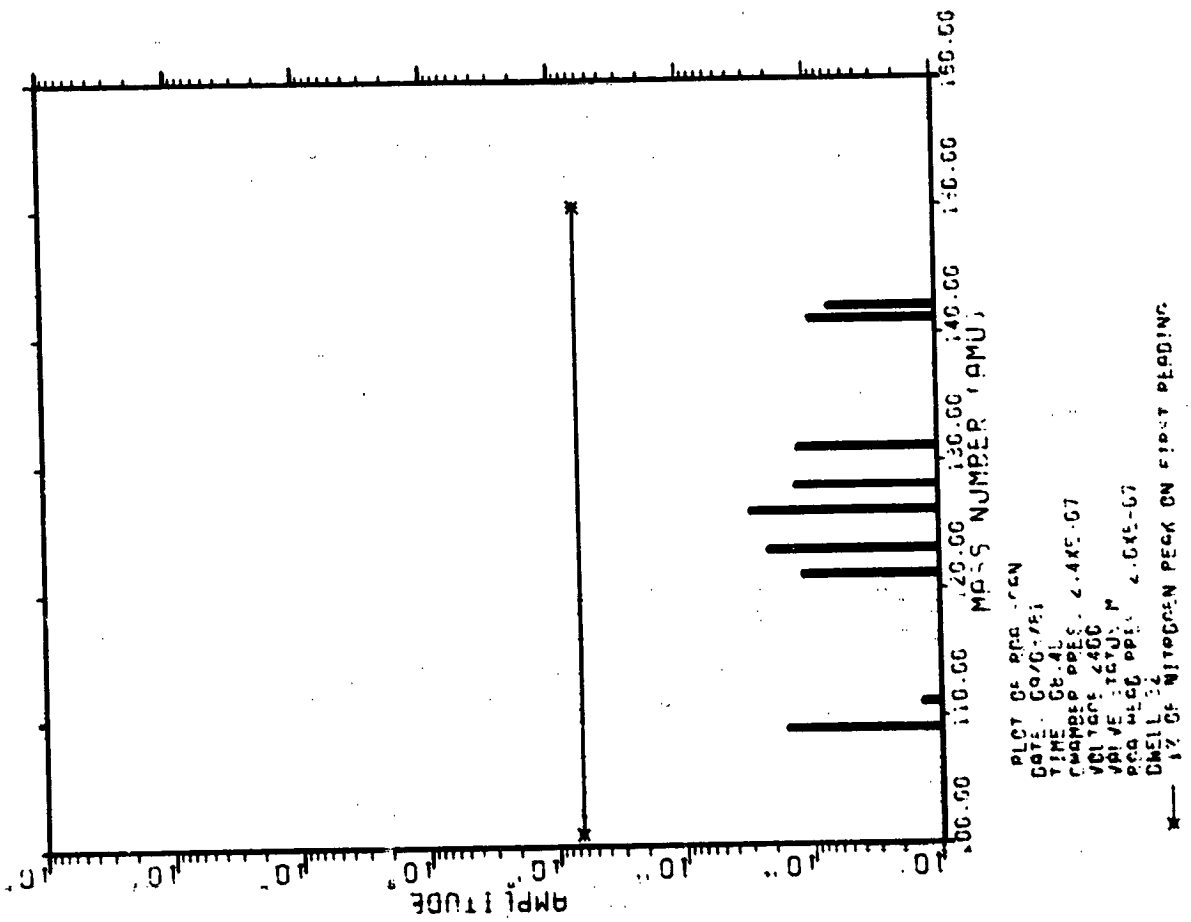

Figure 10. Expanded Plot of Figure 7 Data

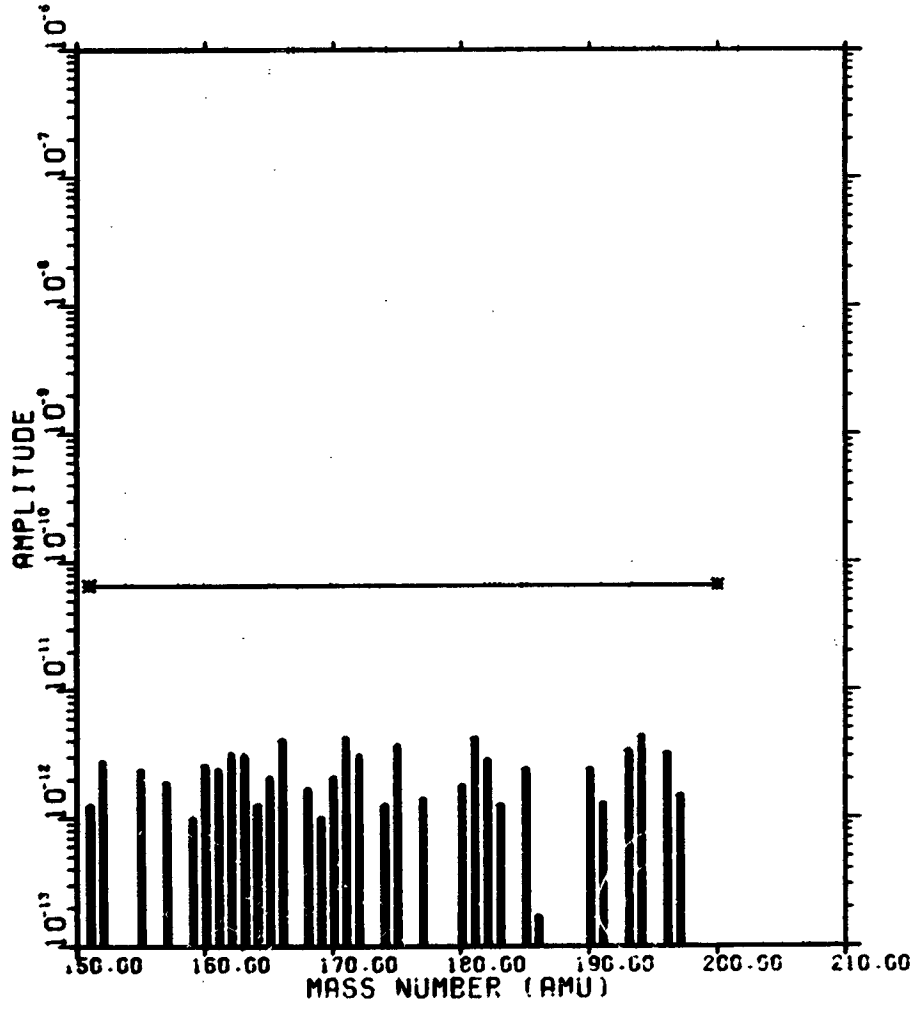

PLOT OF RGA SCAN
DATE. 09/03/81
TIME: 08.45
CHAMBER PRESS 2.4XE-07
VOLTAGE 2400
VALVE STATUS M
RGA HEAD PRESS 2.0XE-07
DWELL 32
1% OF NITROGEN PEAK ON FIRST READING

Figure 11. Expanded Plot of Figure 7 Data

ORIGINAL PAGE IS
OF POOR QUALITY

operator, indicating a partial scan; figure 5 shows the beginning of a complete scan of 200 masses. Figure 6 shows the data output for the 200 masses; this output is recorded by the operator on magnetic tape cartridges. The data can now be loaded into a larger computer for further processing.

Figures 6 through 10 show a sample of computer-generated plots prepared on an IBM 370 computer. The plots are a semi-log plot of amplitude versus mass number (mass-to-charge ratio (m/e)). Gain is an exponential factor and is related to amplitude according to the following relationships:

$$\text{output value} = \text{true peak height} \times 10^{\text{gain}} \quad (1)$$

$$\text{true peak height} = \text{amplitude} \quad (2)$$

$$\text{output value} = \text{amplitude} \times 10^{\text{gain}} \quad (3)$$

$$\text{amplitude} = \text{output value} \times 10^{-\text{gain}} \quad (4)$$

Amplitude plotted logarithmically allows all peak heights to be visible on one graph as shown in figures 7 through 11. This was a significant advantage to us compared to the original bar graph of the IQ200 since the low peak values were not visible unless the high peaks were displayed as saturated values. Figure 7 is a plot of the entire scan from 0 to 200 mass for a quick overall look; figures 8 through 11 are expanded plots of the same data in increments of 50 mass numbers for more detailed study. The horizontal line on the plot is a reference value of amplitude which is 0.1% of the amplitude of the 28 peak from the first reading at the beginning of the test from which this data was obtained.

Based on this experience, we found that even minimally trained operators were able to obtain proper data with little or no difficulty. Also, the desired plots could be generated with relative ease for inclusion in the final report on the test.

As noted earlier, the manufacturer of the IQ200 has advertised an option which would do much of what is currently done by the microcomputer which we have added to our system. However, not enough information is available at this time to judge how versatile this option might be when compared with our own approach. Nevertheless, we can state that experience with other types of equipment has shown the need for costly modifications in order to receive a properly formatted output that is compatible with IBM 370's input requirements.

The adaptability of our approach to automating other available RGA systems will depend on several factors. Some of the RGAs available have automated options which may have the desired output and data manipulations, and do not require any further modifications. These options must be assessed and compared with the advantages of automating an RGA. If automation is a more practical approach, then several requirements must be met. The RGA must have a capability of being remotely commanded for the mass (m/e) ratio and gain, or as a minimum must have a port to allow access to the switches which control these parameters. Also, data output must be

available in a form which will allow it to be digitized. Usually, any analog output of the peak values will permit the data to be digitized. The input format required by the computer to be used to analyze the collected spectral data must be known, along with the means of data transfer that is available or desired between the RGA and the computer. With this information available, the economics of automating should be considered in relation to the RGA output as there may not be sufficient range or sensitivity available to justify the conversion. The Inficon RGA's flexibility aided our automation because, being microprocessor-controlled, it could be commanded with simple ASCII standard characters through a readily accessible port available as a standard part of the unit.

The freedom that our own particular approach offers will enable us to respond to any changes that future requirements may dictate. Moreover, only a small portion of the capability of the microcomputer has been tapped at this time. It may be possible to make use of this capability to perform other more advanced types of data reduction in addition to its basic data logging capability. The automated approach to data acquisition actually gives the output considerably more information than could be obtained from the basic system without significant front panel programming. This is clearly illustrated by the plots generated from the data. Note in particular that using the gain values that have been automatically obtained, it is possible to have all peaks plotted on the same scale to give a better overall view than the RGA's own graphical outputs can provide. Therefore, we feel that the addition of the microcomputer has provided a significant improvement in the capability of the RGA and is well worth the investment in time and money to produce it. It should also be pointed out that the particular microcomputer used is more sophisticated than required and that simpler single board microcomputers should also be able to provide the same capability at a lower cost.

REFERENCES

1. Drinkwine, M.J. and Lichtman, D.: Partial Pressure Analyzers and Analysis. American Vacuum Society Monograph Series; editors N. Rey Whetten and Robert Long, Jr. 335E 45th St., N.Y., N.Y., 1979.

SESSION IX

CONTAMINATION

Session Organizers: Raymond Kruger, NASA Goddard Space Flight Center

Eugene Borson, The Aerospace Corporation

PRECEDING PAGE BLANK NOT FILMED

THE EXPERIMENTAL DETERMINATION OF THE EXTENT OF OFFGASSING FROM THE EUROPEAN EXPERIMENTS FOR SPACELAB

M. Debeir
European Space Agency

ABSTRACT

The offgassing test is one of the many tests to which Experiments to be flown in Spacelab must be subjected prior to their acceptance. This test is performed in order to assess the nature and the quantity of potentially toxic volatile contaminants which could be released within the Spacelab module.

This paper will describe the method adopted by ESTEC and applied to the European part of the First Spacelab Payload (FSLP) and will give examples of the data obtained on selected European Experiments. In addition a description will be given of how this approach was utilised in the performance of the offgassing test on the Spacelab Flight Module.

PRECEDING PAGE BLANK NOT FILMED

N82 25310 D19

CONTAMINANT CHARACTERIZATION OF FIVE SATELLITE MATERIALS

J. A. Muscari, Martin Marietta Denver Aerospace, Denver, Colorado

ABSTRACT

An extensive laboratory test program was performed to characterize outgassing of five satellite materials. The materials were Chemglaze Z-306 over 9922 primer, M-773 adhesive, multilayer insulation, polyurethane foam, and silverized Teflon. The sources were prepared to the specifications of a typical satellite program.
Dynamic thermogravimetric mass loss characteristics of these five materials were obtained in vacuum with a beam microbalance. The temperature of the material was linearly raised from 25°C to over 650°C while monitoring the mass loss, rate of mass loss, temperature, and the composition of the outgassed material by residual gas analysis. Isothermal source emission/capture coefficients/reemission parameters were obtained with an array of quartz crystal microbalances (QCM). A detailed test matrix in which the temperatures of the QCMs (-160°C, -100°C, -40°C, and +10°C) and the source material (125°C, and 90°C, and 50°C) were varied was performed. The array of QCMs was also used to measure the spatial distribution of the source emission. The effects of vacuum ultraviolet radiation on the deposition and reemission parameters was determined.

INTRODUCTION

Spacecraft contamination has been widely recognized as a serious problem on many operational satellite systems. Contamination, whether naturally generated as a result of spacecraft design or operational activities must be better understood and effectively controlled so that the operational lifetime of costly spacecraft sensors and systems may be protected and extended. This paper addresses this problem by obtaining laboratory source outgassing characteristics, transport data, and reemission parameters required by modeling equations used to assess contamination problems.

SOURCE MATERIALS

The decision was made to simulate as close as possible the materials as they are used on typical spacecraft. The selected materials were Chemglaze Z-306 over 9922 primer, M-773 adhesive, multilayer insulation (MLI), polyurethane foam, and silverized Teflon.

Chemglaze Z-306 is a flexible flat black polyurethane based thermal control paint. Chemglaze 9922 A/B is a two part epoxy primer for metal and epoxy-glass surfaces. Bondmaster M-773 is a two part epoxy adhesive which is mixed one to one by weight. MLI blanket material consists of 23 layers. The outer surface (exposed vacuum) is a Kapton film with vapor deposited gold on the inside layer reinforced with Beta-Marquisett glass cloth. The next 21 layers are alternately nylon net and mylar film aluminized both sides. The last layer is the same as the first, except the Kapton is coated with aluminum. A narrow doughnut shaped strip of aluminized Teflon tape (adhesive on aluminum side, 3M-Y955 Sheldahl adhesive) was used to hold the MLI onto the aluminum substrate discs. Silver Teflon is a thermal control coating

consisting of fluorinate dethylene-propylene film (FEP teflon-type A) with vacuum deposited silver on one surface. The silver is overcoated with a protective layer of nickel-chrominum-iron alloy (inconel 600). The FEP Teflon surface is covered by a removable protective overlay . The overlay has a thin layer of Mystic PD-570 to adhere loosely to the FEP Teflon. The Inconel surface has a thin layer of 3M-Y966 pressure sensitive adhesive to adhere to the cleaned aluminum substrates. Open cell flexible polyurethane foam is sandwiched between sheets of aluminized Kapton. The Kapton is bonded to the foam by M-773 adhesive.

SOURCE EMISSION BY DYNAMIC THERMOGRAVIMETRY

When classical rate theory is applied to source emission, it can be shown that (Ref. 1)

$$m_s = W_s a_o (1 - e^{-Ae^{\frac{-B}{RT}}}) \qquad (1)$$

where
- m_s = source mass lose, g,
- W_s = total mass of source, g,
- a_o = initial mass fraction available for outgassing,
- A = empirical constant, min^{-1},
- B = empirical constant, $cal \cdot mole^{-1}$,
- R = molar gas constant, 1.986 $cal \cdot mole^{-1} \cdot K^{-1}$, and
- T = absolute temperature of source, K.

Dynamic thermogravimetry (DTG) obtains values for a_o, A, and B. The test facility has been described in an early paper (Ref. 1). DTG samples were prepared using aluminum foil as a substrate for the paint and adhesive materials. The foil was first conditioned by washing with acetone and vacuum baking at 300°C for six hours. The foil was used to provide a barrier similar to its flight use.

Table 1 lists the results of the DTG analysis. Chemglaze Z-306 thermal control black paint over 9922 primer has four different outgassing components (each component may be a composite of many molecular species) whose outgassing rate peaks at successively higher temperatures. The first component completely outgasses with the first hour for source temperatures greater than 90 C; yielding about 2.1% of the initial material mass. The second component is not as volatile as it requires more than 10 days to outgas its 2.7%. Both the third and fourth components only contribute significant outgassing rates at elevated temperatures greater than 300°C.

ISOTHERMAL SOURCE EMISSION TRANSPORT REEMISSION PARAMETER VCM

SOURCE OUTGASSING THEORY

An indirect method for determining source kinetic properties is to use QCMs which are maintained at LN_2 temperatures so that the volatile condensable material (VCM) reemission is negligible. The source temperature is maintained at a constant value so that this method is designated isothermal QCM TG (QTG). Its principle shortcoming is that the outgassing mass loss distribution of the source must be known. This distribution can be estimated by an array of QCMs.

To rigorously obtain the kinetic parameters of the source materials, it was necessary to model the test configuration. Complete details can be found in Reference 1. For a source with two first order components

$$m_Q = F_{SQ} W_s (a_o^{(1)} + a_o^{(2)} - a_o^{(1)} e^{-k_s^{(1)} t} - a_o^{(2)} e^{-k_s^{(2)} t}) \qquad (2)$$

where m_Q = deposition on QCM, g,

F_{SQ} = diffuse viewfactor from source to QCM,

W_s = mass of source, g,

$a_o^{(1)}$ = initial source mass fraction available for emission, first component

$k_s^{(1)}$ = source rate constant, first component, min^{-1},

$a_o^{(2)}$ = initial source mass fraction available for emission, second component,

$k_s^{(2)}$ = source rate constant, second component, min^{-1},

t = time, min.

Dynamic TG exhausts the volatile component of a source because it raises the source temperature to decomposition, thus the values of $a_o^{(1)}$ and $a_o^{(2)}$ are obtained. Thus, any arbitrary time during the isothermal QCM test, the equations could be iteratively solved to obtain the two unknown rate constants. Allowing the tests to run long enough for the high volatile component to be completely depleted leaves only the lower volatile material. This procedure requires that the two active components have large differences in their rate constants so that equations together with the values of $a_o^{(2)}$ from DTG will uniquely determine $k_s^{(2)}$. Once the two properties of the low volatile component have been determined, earlier data where both species are active can be used to compute the values of $a_o^{(1)}$ and $k_s^{(1)}$. This procedure can be used to analyze sources with more than two components provided that the rate constants of the components are significantly different. The method simply starts at the end of the test and works backwards to the beginning solving for the components of each successive active component.

CVCM REEMISSION THEORY

Reemission kinetics can range from a first order rate process, exponential in character, to a constant mass loss reemission rate (zero order). The test for the collected volatile condensable material (CVCM) reemission kinetics are to be evaluated. Then, the source is raised to a high temperature (about 125°C), and the VCM allowed to deposit until a peak is reached, at which time the source is quenched with LN_2. The basic governing equation, assuming first order VCM reemission kinetics is

$$m_Q(t) = \sum_{i=1,2} \left[m_a^{(i)} + (m_{Q0}^{(i)} - m_a^{(i)}) e^{-k_e^{(i)} t} \right] \qquad (3)$$

where

$m_Q(t)$ = total mass on the QCM at time, g,

ORIGINAL PAGE IS
OF POOR QUALITY

$m_a^{(i)}$ = mass of ith component which is permanently absorbed onto the QCM, g,

$m_{QO}^{(i)}$ = mass of the ith component initially on the QCM immediately after quenching the source, g,

$k_e^{(i)}$ = first order rate reemission rate constant for the ith component, min^{-1}.

As typical deposition test data show, the high volatile component (HVC) is rapidly reemitted so that after eight hours only the low volatile component (LVC) is still actively being reemitted. By plotting ln m_Q versus time in this domain, the rate constant $k_e^{(2)}$ and the mass differential $m_{QO}^{(2)} - m_a^{(2)}$ can be obtained from the slope and intercept respectively.

Using the data from the ln-linear plot of m_Q versus t, it is possible to evaluate the HVC rate constant

$$k_e^{(1)} = \frac{\dot{m}_Q(0) - k_e^{(2)}(m_{QO}^{(2)} - m_a^{(2)})}{m_Q(0) - m_Q(\infty) - (m_{QO}^{(2)} - m_a^{(2)})} \tag{4}$$

TRANSPORT THEORY

The testing is primarily aimed at measuring the capture coefficients for VCM molecules emitting from the source at the source temperature, T_s, and impinging on the QCM receptor at T_Q. The basic Q/TG transfer equation assuming first order kinetics and the two components is

$$m_Q = \sum_{i=1,2}\left[m_a^{(i)} + F_{SQ}W_s\left(\frac{\sigma_{SQ}^{(i)}a_o^{(i)}k_s^{(i)}}{k_e^{(i)}-k_s^{(i)}}\right)(e^{-k_s^{(i)}t} - e^{-k_e^{(i)}t})\right] \tag{5}$$

where F_{SQ} = diffuse angle factor from the source to the QCM crystals,
W_S = total source weight, g,
σ_{SQ} = condensation coefficient of the ith component arriving at the QCM from the source,
$k_s^{(i)}$ = first order source rate constant for the ith component, min^{-1} and
$a_o^{(i)}$ = weight fraction of the ith component in the source.

The QCM mass rate equation is obtained by differentiating to give

$$\dot{m}_Q = \sum_{i=1,2} F_{SQ}W_s\left[\frac{\sigma_{SQ}^{(i)}a_o^{(i)}k_s^{(i)}}{k_e^{(i)} - k_s^{(i)}}\left[k_e^{(i)}e^{-k_e^{(i)}t} - k_s^{(i)}e^{-k_s^{(i)}t}\right]\right] \tag{6}$$

Allowing sufficient time (>eight hours) to deplete the source of the high volatile component (HVC), eq. 4, which is now an expression involving only the low volatile component (LVC), can be rearranged to determine the corresponding capture coefficient as follows:

$$\sigma_{SQ}^{(2)} = \frac{(k_e^{(2)} - k_s^{(2)})\dot{m}_Q}{F_{SQ}a_o^{(2)}W_s k_s^{(2)}(k_e^{(2)}e^{-k_e^{(2)}t} - k_s^{(2)}e^{-k_s^{(2)}t})} \tag{7}$$

at any value of t >eight hours.

All the parameters on the right hand side of eq. 7 are known from the source kinetics test and the reemission test. For good results, considering the typical difficulties with data reduction in analyzing "tail" data, several values of σ_{SQ} at different times in the "tail" domain are calculated and the results averaged. Finally, the capture coefficient for the HVC can now be calculated using eq. 6 at any time during the initial hours of the transport test. The simplest result is the initial deposition rate $\dot{m}_Q(0)$, which gives the following expression for the desired coefficient,

$$\sigma_{SQ}^{(1)} = \frac{\dot{m}_Q(0) - F_{SQ}W_s \sigma_{SQ}^{(2)} a_o^{(2)} k_s^{(2)}}{F_{SQ}W_s a_o^{(1)} k_s^{(1)}} \qquad (8)$$

TEST MATRIX AND FACILITY

The source isothermal outgassing kinetics were determined by monitoring the deposition onto a QCM at -173°C at three source isothermal temperatures 125°C, 90°C and 50°C for a duration of 24 hours. Knowing the configuration of the source/QCM systems and assuming that all the VCM flux striking the crystal will condense and remain on the surface, allows the source outgassing parameters to be obtained. The CVCM reemission tests consist of elevating the source to temperature for about one hour then quenching the outgassing by using LN_2 to quickly lower the source temperature. Three symetrically configured QCM's, one at -100°C, another at -40°C and the last at +10°C, monitor the reemission mass loss for 24 hours. Source temperature of 125°C, 90°C and 50°C are used. Similar tests were performed using the laser radiation to heat the source. The reemission tests were repeated using vacuum ultraviolet to irradiate the CVCM. The transport parameters were determined during the source outgassing tests by having another QCM (at -173°C) at a different angle to the source normal to determine the spatial distribution of the outgassing material. The capture coefficients were determined by monitoring the three symmetrically configured QCM's (-100°C), -40°C and +10°C) while the source temperature remained constant during a 24 hour period.

The facility allows simultaneous measurements of the VCM outgassing kinetics at discrete receptor temperatures and verification of the assumed VCM Lambertian emission. This was accomplished by positioning three coplanar sensing QCM units clustered symmetrically about the source normal 3.18 cm from QCM centers to the normal, each with a separate independent temperature control capibility. A fourth, redundant QCM was also instrumented but was located off-set at a further distance 6.35 cm from the source normal in the same plane as the basic triad. A detailed description of the facility is in Reference 1. The closely spaced cluster also allowed simultaneous and uniform irradiation of the three QCMs with a microwave excited low pressure krypton resonance lamp operating at 1236 A.

ISOTHERMAL QCM TEST RESULTS

Z-306/9922 RESULTS

The Chemglaze Z-306/9922 black paint was the first source material tested. The data for the QCM at +10°C shows the reemission rate was greater than the incoming flux after the first 10 min. since the QCM frequency slowly decreases

from its peak value. Tests indicate that the ultraviolet radiation increases the reemission rate for the QCM at -40°C, since the frequency decreases after the first hour of deposition. The CVCM reemission from the QMCs at -100°C and -40°C show a very high reemission for only a fraction (about 15%) of the deposited VCM within the first 80 minutes of reemission. The QCM at +10°C emits all of the CVCM at a lower rate in about 830 min. Again, the tests indicate that ultraviolet radiation increases the reemission of CVCM from Z-306/9922.

The parameters in the following tables were developed using the equations from the theory section. The second component available mass, $a_o^{(2)}$ = 2.00%, was taken from the DTG data since the isothermal test only last 24 hours and does not completely deplete the medium volatile component. The parenthesis in Table 3 indicate questionable data. Using the data from Table 2 to plot the ln k versus T_s^{-1}, the generalized source parameters for Z-306/9922 are determined; namely,

A_1	= 6.29×10^4 min^{-1}	A_2	= 6.04 min^{-1}
B_1	= 10700 cal.mole^{-1}	B_2	= 7070 cal.mole^{-1}
$a_o^{(1)}$	= 2.10%	$a_o^{(2)}$	= 2.00%

The data shown in Table 3 is not easily understood. One would expect k_e to increase at T_Q increases. However, in all three cases, the rate constant is smaller for the QCM at 10°C than either of the other two colder QCMs. In all of the tests, the CVCM reemitted linearly and did not show exponential decrease. This indicates a zero order rate. However, the data is complicated by the fact that reemission is occurring during the time the source is still at T_s. Thus, the resulting frequency combines the exponential source emission with the reemission kinetics. No scheme is available now to unfold the data. Another explanation of Table 3 is that the rate constant for T_Q = -100°C and -40°C is for the first CVCM components and the rate constant for T_Q = +10°C is the second CVCM component. The low values of a_e are not accurate since it is difficult to determine the amount of the first active component lost during the relatively long disposition period (one hour). The relatively permanent absorbed VCM for the QCMs at -100°C and -40°C could be the very low reemission of the second component at that low temperature. Assuming first order kinetics we have for emission,

A_{e1} = 2.39×10^{-2} min^{-1}	$k_e^{(2)}$ (T_Q=+10°C)	= 1.99×10^{-3} min^{-1}
B_{e1} = 611 cal·mole^{-1}	$k_e^{(2)}$ (T_Q=-40°C)	= 0
	$k_e^{(2)}$ (T_Q=-100°C)	= 0.

The deposition for reemission with vacuum ultraviolet and T_s = 94°C was too small to determine any parameters.

The capture coefficients are shown in Table 4. The wide variation in values seems to indicate difficulty in matching the rates from the source and reemission tests to another set of deposition tests.

Table 5 shows the higher temperature laser tests. Complete details on the tests and the results can be found in the classified Reference 2. The first column shows the maximum temperature the source reached. The laser was incident on th source for only a short period. The second and third columns show the maximum increase in the frequency of the two TQCMs. TQCM #1 was temperature ranged from its starting temperature 10 +100°C and the

reemission parameters are determined from the data. Tables 6 and 7 summarizes the results of this analysis. The first five tests were all performed with the TQCM starting at about -160°C, thus it can be expected that the high volatile component is strongly represented in the data. The last test (T_s = 288°C) had the TQCM at +2.9°C and should represent only the second component. Thus, it is assumed that a generalized expression for the CVCM reemission parameters of Z-306/9922 is as follows:

A_{e1}	= 1.96×10^9 min^{-1}	A_{e2}	= 4.80×10^3 min^{-1}
B_{e1}	= 9630 $cal \cdot mole^{-1}$	B_{e2}	= 7830 $cal \cdot mole^{-1}$
$a_e^{(1)}$	= 90%	$a_e^{(2)}$	= 1.5%

Table 7 shows the derived parameters for the isothermal reemission. The first test (T_s = 202°C) only shows a rate constant for the CVCM which was exposed to vacuum ultraviolet. The reemission was exponential in character and thus has a two component rate constant. These results differ from the linear reemission seen in the Molekit tests. The test of T_s = 228°C shows a very small amount of CVCM reemission during the 26 hour isothermal test at 2.9°C. Table 8 shows the capture coefficients calculated by using the parameters derived from TQCM D/TG reemisson after the reemission laser tests.

SOURCE OUTGASSING SPATIAL DISTRIBUTION

Taking the ratio of the deposition on the near QCM (A) to that of the far QCM (B) during the four source tests (including the laser test) provides a check on the diffuse character of VCM emission. At least eight different times were used to determine an average value for each test. The results are listed; as follows,

T_s (°C)	$\frac{f_A}{f_B}$
125	3.1
93	3.2
50	2.0
125L	1.8

If the spatial distribution of the VCM were cosine then the ratio should be 2.0. The spatial distribution of the VCM for the laser tests with both QCM at -160°C varied from 1.7 to 2.2 (except for the first test, 4.0) with an average value of 2.0. The expected ratio for a cosine emission is 1.1 for configuration. Thus, the high temperature laser source emission is more forward directed.

M-773 RESULTS

The M-773 adhesive showed far less source outgassing than the Z-306/9922 black paint. The laser test results showed faborable agreement with its thermal counterpart except that the far QCM in the laser test had more mass deposit. Again, a higher reemission for the +10°C QCM than the incoming source flux was seen. At T_s = 90°C no resultant deposition was seen for the QCM at +10°C. At T_s = 50°C the deposition is too low for any parameters to be determined.

None of the reemission data was usable since the deposition was too small, less than 20 Hz (about 11A).

Table 9 shows the source parameters for M-773 determined from the isothermal tests. Using this data to plit the ln k versus T_s^{-1}, the generalized source parameters for M-773 are determined; namely,

A_1	$= 39.5\ min^{-1}$	A_2	$= 2.44\ min^{-1}$
B_1	$= 4270\ cal\ mole^{-1}$	B_2	$= 5095\ cal\ mole^{-1}$
$a_0^{(1)}$	= 6.3%	$a_0^{(2)}$	= 1.9%

The value for $a_0^{(2)}$ was derived from the value for the amount of active material for M-773 shown in Table 1, namely, $a^{(1)}$= 8.2%. It was assumed that the DTG did not separate the high volatile component into the two components seen in the isothermal QCM tests.

Taking the ratio of the two QCMs frequency gave the following results; (T_s = 126°C) 1.9 and (T_s = 90°C) 2.1. Thus, the measure distribution agrees with a cosine prediction of 2.0.

MLI RESULTS

The MLI samples did not outgas significantly. This was in part the result of its sealed edge and low outgassing outer layer (aluminized Kapton), but also because of the large temperature gradient existed across the sample thickness. When heated from the back, as in all the thermally induced cases, the front surface temperature was much lower than the rear thermocouple indicated. Another source of temperature uncertainty resulted from the aluminized Teflon tape used to seal the edge of the sample, which provided a relatively large thermal conductance between the back and the front. This conductance generated a spatial temperature nonuniformity on the front surface but also reduced some of the transverse temperature gradient. On the other hand, in the laser beam, the temperature gradient was in the reversed direction. But for this type of testing, the thermocouple was inside the sample and close to the outer layer. Therefore, the front surface temperature was higher than the thermocouple reading. The effect of this temperature disparity between the two kind of source emission tests is amply illustrated by their test result, where the laser induced is seen to deposit three times as much. It should be noted that with this source material and the polyurethane foam to be discussed later, it is very difficult to produce in a cryogenic environment a front surface temperature of 125° by applying heat to the back of the samples.

Table 10 shows the source parameters derived from the data. The scatter in the data does not allow any generalized source parameters to be derived. Likewise, the very low reemission data precludes deriving reemission parameters and capture coefficients. The spatial distribution of the VCM varies from the cosine prediction of 2.0, as follows,

T_s (°C)	$\frac{f_A}{f_B}$
125	2.8
90	1.8
50	1.5
127L	1.8

FEP/Ag RESULTS

The silvered Teflon was expectedly the weakest outgassing material tested in this program. In fact, the source outgassing was so low that only tests at higher temperatures yielded usable data. It is difficult to assess the emission flux spatial distribution because of the extremely small deposits (hence large uncertainty involved). The laser testing resulted in mass deposit which was 200% higher than the corresponding thermal testing.

Table 11 shows the source parameters derived from the data. There are too few points to derive generalized parameters. The ratio of the change in frequency of the near QCM to that of the far approximates the expected cosine value of 2.0; namely,

T_s (°C)	$\frac{f_A}{f_B}$
127	1.4
90	1.7
125L	1.9

SANDWICH FOAM RESULTS

Aside from the temperature gradient problem as encountered in MLI samples, the interpretation of the polyurethane foam test results are complicated by at least two more factors. First, the samples were a crumpled, pillow-like shape. As a result, the view factors from the source to the QCMs will differ by some unknown amounts from the assumed flat surface. Secondly, unlike the other source samples, the edges of the sandwiched foam samples were quite thick (as much as 6mm) and were left unsealed. Thus, additional, view factors existed. In fact, it is believed that the somewhat strong source outgassing observed was attributable to the exposed foam. This belief was enhanced by the laser tests. The rapid increase in the QCM beat frequencies shortly after the exposure of the sample to incident laser beam was not anticipated and it became necessary to change the bias constants to bring the curves back on scale. What happened was, as found out later at the end of the test, that approximately 90% of the sample foam content had vaporized, as a result of excessive heating. The sample temperature went up from 83°C at time 37 minutes to 280°C in just 3 minutes. The aluminised Kapton film front surface was not damaged. It remained attached to the residual foam content at the bottom edge but its upper portion tilted away from the sample disc, forming a V shaped opening. This geometry readily explained why the "far" QCM response was greater than the "near" QCM for then the far unit was exposed more the decomposed foam flux emanating from the edge than the near unit.

The reemission tests showed that the QCMs at -100°C and -40°C instead of losing mass showed a slight gain. The +10°C QCM had a rate constant of 9.42×10^{-4} min $^{-1}$ over the full 23 hr of reemission. The reemission during the deposition period was greater than the incoming source flux. All of the CVCM was reemitted. The effect of the vacuum ultraviolet radiation on the CVCM was to increase the reemission such that within the first 30 minutes of reemission all of the CVCM was removed.

Table 12 shows the source parameters for the sandwich foam. The generalized expression for the first component is as follows:

A_1 = 2.69×10^4 min^{-1}
B_1 = 10300 $cal \cdot mole^{-1}$
$a_0^{(1)}$ = 0.47%

The data for the second component does not indicate any usable trend.

The spatial distribution for the foam VCM was as follows:

T_s (°C)	$\frac{f_A}{f_B}$
126	2.1
91	2.2
53	1.3
126L	0.1

CONCLUSIONS AND RECOMMENDATIONS

This test program has provided a wealth of test data that can be used to assess and predict space contamination. Although choosing to use qualified space materials and configurations made the testing and acquiring of the contamination paramaters difficult, the data can be applied directly to many space systems. The dynamic thermogravimetric test provided the source emission parameters for five typical space materials. The accompanying residual gas analysis data clearly shows that the major portion of outgassing consists of light gases that will not deposit on surfaces except at cryogenic temperatures.

All five selected materials for the complete test matrix are low outgassing materials. Except for the Z-306/9922 material, the other sources were at the sensitivity of the test facility, resulting in fewer generalized source parameters. Future tests should include larger areas of source materials and shorter distances between the source and QCM for low outgassing materials. The complex configuration of the MLI and sandwich foam sources made it difficult to affirm the diffuse natural of VCM. Characterizing the source temperature of these insulators was also difficult. It is expected that there were large temperature gradients both across the sample thickness and in the plane of its front surface. As a result of the transverse gradient, the source front surface temperatures differed significantly when heated from behind as in the thermally induced cases and when heated from the front (laser tests). In the future more consideration should be given to developing a source heater to overcome these difficulties. While a heated cavity would remove the gradients, it introduces an artificial source geometry (dicing the material).

For a simple source configuration (single layer), the data does indicate (not conclusive) that VCM emission is diffuse. Energetic laser irradiation indicates the need for a higher power than the first for the cosine relation. The VCM spatial distribution is more forward directed than pure thermal emission.

Isothermal thermogravimetry at temperatures below 125°C does not within a reasonable time period allow an accurate measurement of the active mass for any but the first component. The dynamic thermogravimetry is necessary to obtain the percent of active mass for each component.

Vacuum ultraviolet radiation seems to increase the CVCM reemission for these four materials. This result is in contradiction to current belief that vacuum uv may cause photopolymerization of the CVCM, resulting in permanent deposition.

Application of modeling equations to the test data is anything but routine. The unexpected linear reemission observed in the Z-306/9922 isothermal tests in contrast to the exponential reemission of dynamic TG using QCMs does underline the need for scientific judgement in interpretating the data. The calculations are long and complex and should be programmed to a calculator in order to allow variatons in the data processing.

Energetic laser irradiation by elevating the temperature of the source material beyond its usual curing and operating range produces large amounts of VCM. Dynamic TG can provide the source emission parameters to allow assessment and prediction of deposition levels.

ACKNOWLEDGEMENTS

The research work leading to this paper was performed under Contract 33615-78-C-5168 for AFWAL, WPAFB. The laboratory work for the isothermal QCM source emission/transport/reemission tests was performed by Aerojet ElectroSystems Company (AESC). Principal AESC contributors were E. Zeiner, Y. Chen and R. Fisher. All other tests and the entire data analysis was performed by the principal Martin Marietta Denver Aerospace contributors, namely, J.A. Muscari and G. Beverlin.

REFERENCES

1. J.A. Muscari, D. Mah, and R. Somers, Satellite Contamination - II, Volume I, Analytical Equations, Laboratory Tests, and Space Application, AFWAL-TR-81-4059, Wright Patterson Air Force Base, Ohio, August 1981.

2. J.A. Muscari and J. Pizzicarolli, Satellite Contamination - II, Volume II, Contaminants Produced By Laser Irradiation, AFWAL-TR-81-4059, Wright Patterson Air Force Base, Ohio, August 1981.

ORIGINAL PAGE IS
OF POOR QUALITY

TABLE 1. DYNAMIC THERMOGRAVIMETRIC DERIVED SOURCE EMISSION PARAMETERS

MATERIAL	a_{oi} (%)	a_{oi} ($g \cdot cm^{-2}$)	B_i ($cal \cdot mole^{-1}$)	A_i (s^{-1})
Chemglaze Z-306 Plus 9922 Adhesive Volatile Component				
i=1	2.1	4.58×10^{-4}	13000	4.7×10^{4}
i=2	2.0	3.83×10^{-3}	25200	1.4×10^{8}
i=3	27.0	4.99×10^{-3}	82900	1.8×10^{26}
i=4	6.2	1.21×10^{-3}	41300	4.7×10^{9}
M-773 Adhesive				
i=1	8.2	9.94×10^{-5}	16800	1.1×10^{7}
i=2	76.1	9.19×10^{-4}	57000	3.3×10^{16}
MLI				
i=1	0.17	5.33×10^{-5}	10200	4.7×10^{3}
i=2	79.5	3.17×10^{-2}	73500	1.9×10^{20}
FEP/AG/3M-Y966				
i=1	0.028	-	8000	6.4
i=2	26.1	-	71400	1.2×10^{17}
i=3	70.2	-	92100	3.3×10^{20}
Sandwich Foam				
i=1	0.22	6.77×10^{-5}	16200	7.6×10^{6}
i=2	19.6	6.03×10^{-5}	28400	3.6×10^{9}
i=3	54.4	1.66×10^{-2}	38900	9.5×10^{9}
Aluminized Tape Plus Adhesive				
i=1	32.9	5.50×10^{-3}	89600	5.1×10^{29}
i=2	24.1	4.03×10^{-3}	67100	3.0×10^{19}
i=3	38.3	6.40×10^{-3}	85700	4.7×10^{22}

TABLE 2. SOURCE PARAMETERS FOR CHEMGLAZE Z-306/9922

T_s (°C)	$k_s^{(1)}$ (min^{-1})	$a^{(1)}$ (%)	$k_s^{(2)}$ (min^{-1})
125	9.76×10^{-2}	6.87	2.31×10^{-4}
93	1.81×10^{-2}	2.06	3.60×10^{-4}
50	3.88×10^{-3}	0.755	9.85×10^{-5}
125L	5.42×10^{-2}	7.60	4.29×10^{-4}

ORIGINAL PAGE IS
OF POOR QUALITY

TABLE 3. REEMISSION PARAMETERS FOR CHEMGLAZE Z-306/9922

T_s (°C)	T_Q (°C)	k_e (min^{-1})	a'_e (%)
125	-100	4.04×10^{-3}	16.9
	-40	6.39×10^{-3}	12.6
	+10	1.09×10^{-3}	100
90	-100	(1.14×10^{-2})	22.3
	-40	(2.58×10^{-2})	13.3
	+10	2.25×10^{-3}	100
125	-100/UV	2.56×10^{-2}	44.7
	-40/UV	3.23×10^{-2}	13.2
	+10/UV	1.62×10^{-3}	100

TABLE 4. CAPTURE COEFFICIENTS FOR CVCM FROM CHEMGLAZE Z-306/9922

T_Q (°C)	-100		-40		+10	
T_s (°C)	$\sigma^{(1)}$	$\sigma^{(2)}$	$\sigma^{(1)}$	$\sigma^{(2)}$	$\sigma^{(1)}$	$\sigma^{(2)}$
125	0.50	0.25	0.40	0.11	--	--
90	0.05	0.10	0.04	0.07	0.06	0.32

ORIGINAL PAGE IS
OF POOR QUALITY

TABLE 5. LASER TESTS ON CHEMGLAZE Z-306/9922

T_s (°C)	Δf #1 (Hz)	Δf #2 (Hz)	T_{Q1} (°C)	T_{Q2} (°C)	UV #1 (Hr)	Isothermal /TG	Dynamic /TG
363	116568	29119	-158	-158	No	No	Yes
255	11885	6258	-164	-164	No	No	Yes
160	2534	1454	-165	-165	No	No	Yes
187	6408	2878	-160	-176	No	No	Yes
249	11216	5306	-160	-163	48	Yes	Yes
202	1228	526	-40	-38	48	Yes	Yes
228	0	1579	+10	+2.9	No	Yes	Yes
133	178	94	+10	+2.9	48	Yes	No

TABLE 6. CVCM REEMISSION PARAMETERS FOR CHEMGLAZE Z-306/9922 LASER TESTS

T_s (°C)	A_{e1} (min^{-1})	B_{e1} (cal $mole^{-1}$)	a'_{e1} (%)	A_{e2} (min^{-1})	B_{e2} (cal $mole^{-1}$)	a'_{e2} (%)	UV
363	9.72×10^{10}	10100	19.3	1.91×10^{7}	6930	17.3	No
255	4.84×10^{13}	8960	85.6				No
160	1.96×10^{9}	9630	99.7				No
187	5.02×10^{11}	10700	100				No
249	1.21×10^{21}	18300	34.2	3.91×10^{9}	19500	43.7	Yes
228	4.80×10^{3}	7830	14.9				No

TABLE 7. CVCM ISOTHERMAL REEMISSION PARAMETERS FOR CHEMGLAZE Z-306/9922 LASER TESTS

T_s (°C)	T_Q (°C)	$k_e^{(1)}$ (min^{-1})	a'_{e1} (%)	$k_e^{(2)}$ (min^{-1})	a'_{e2} (%)
202	-38	0	0	-	-
202	-40/UV	1.32×10^{-3}	55	3.95×10^{-4}	45
228	2.9	4.63×10^{-2}	2.0	4.78×10^{-4}	0.5
133	2.9	2.82×10^{-3}	36	3.86×10^{-3}	64
133	10.0/UV	2.86×10^{-3}	48	2.84×10^{-4}	27

ORIGINAL PAGE IS
OF POOR QUALITY

TABLE 8. CAPTURE COEFFICIENTS FOR CVCM FROM CHEMGLAZE Z-306/9922 USING DYNAMIC TG REEMISSION PARAMETERS

T_0 (°C) / T_s (°C)	-100		-40		+10	
	$\sigma^{(1)}$	$\sigma^{(2)}$	$\sigma^{(1)}$	$\sigma^{(2)}$	$\sigma^{(1)}$	$\sigma^{(2)}$
125	0.50	0.25	0.40	0.16	--	--
90	0.05	3×10^{-5}	0.04	3×10^{-5}	0.07	1×10^{-3}

TABLE 9. SOURCE PARAMETERS FOR M-773 ADHESIVE

T_s (°C)	$k_s^{(1)}$ (min^{-1})	$a_o^{(1)}$ (%)	$k_s^{(2)}$ (min^{-1})
126	0.181	6.32	3.94×10^{-3}
90	0.106	3.49	2.08×10^{-3}
125L	4.69×10^{-2}	6.79	4.19×10^{-3}

TABLE 10. SOURCE PARAMETERS FOR MLI

SOURCE REAR TEMPERATURE (°C)	$k_s^{(1)}$ (min^{-1})	$a_o^{(1)}$ (%)	$k_s^{(2)}$ (min^{-1})
125	5.92×10^{-2}	0.227	3.68×10^{-4}
90	9.36×10^{-2}	0.183	7.21×10^{-4}
51	3.06×10^{-2}	0.048	6.26×10^{-4}
127L	7.25×10^{-3}	1.09	1.49×10^{-3}

ORIGINAL PAGE IS
OF POOR QUALITY

TABLE 11. SOURCE PARAMETERS FOR FEP/AG

T_s (^oC)	$k_s^{(1)}$ (min^{-1})	$a_o^{(1)}$ (%)	$k_s^{(2)}$ (min^{-1})
127	5.00×10^{-2}	1.31	2.31×10^{-3}
90	9.74×10^{-3}	0.20	4.30×10^{-4}
125L	2.98×10^{-2}	0.92	1.77×10^{-3}

TABLE 12. SOURCE PARAMETERS FOR SANDWICH FOAM

T_s (^oC)	$k_s^{(1)}$ (min^{-1})	$a_o^{(1)}$ (%)	$k_s^{(2)}$ (min^{-1})
126	5.83×10^{-2}	0.47	3.68×10^{-6}
92	1.75×10^{-2}	0.41	5.41×10^{-6}
53	3.17×10^{-3}	0.24	5.92×10^{-6}
125L	0.238	--	2.82×10^{-6}

N82 25311

IUS MATERIALS OUTGASSING CONDENSATION EFFECTS ON SENSITIVE SPACECRAFT SURFACES*

C. R. Mullen, C. G. Shaw, and E. R. Crutcher
Boeing Aerospace Company

ABSTRACT

Four materials used on the Inertial Upper Stage (IUS) were subjected to vacuum conditions and heated to near-operational temperatures (93 to 316°C), releasing volatile materials. A fraction of the volatile materials were collected on 25°C solar cells, optical solar reflectors (OSR's) or aluminized Mylar. The contaminated surfaces were exposed to 26 equivalent sun hours of simulated solar ultraviolet (UV) radiation. Measurements of contamination deposit mass, structure, reflectance and effects on solar cell power output were made before and after UV irradiation. Standard Total Mass Loss - Volatile Condensible Materials (TML - VCM) tests were also performed.

A 2500 Å thick contaminant layer produced by EPDM rubber motor-case insulation outgassing increased the solar absorptance of the OSR's from 0.07 to 0.14, and to 0.18 after UV exposure. An 83,000 Å layer caused an increase from 0.07 to 0.21, and then to 0.46 after UV exposure. The Kevlar-epoxy motor-case material outgassing condensation raised the absorptance from 0.07 to 0.13, but UV had no effect. Outgassing from multi-layer insulation and carbon-carbon nozzle materials did not affect the solar absorptance of the OSR's. Photomicroscopic examination revealed complex patterns of liquid droplets and crystalline forms which varied with the type and temperature of the outgassing materials.

Solar cell power output losses varied from less than 1% to 23% with contamination and UV exposure.

INTRODUCTION

The Inertial Upper Stage (IUS) is the prime Air Force earth orbit transfer and interplanetary spacecraft booster and is an integral part of the space transportation system which includes the space shuttle orbiter. During launch and ascent into low earth orbit by the space shuttle or Titan T34D and during IUS transfer orbits, the materials of the IUS are subjected to the vacuum conditions of space and are heated in some cases to high temperatures. Both conditions will cause IUS materials to outgas, creating a potential contamination environment for the spacecraft.

This paper describes limited laboratory tests conducted on four IUS materials to measure outgassing rates and effects of outgassed, condensed material on three different spacecraft surfaces. The IUS materials tested

*This work was accomplished under Air Force contract F04701-78-C-0053.

ORIGINAL PAGE IS
OF POOR QUALITY

were: the Ethylene Propylene Diene Monomer (EPDM) rubber insulation inside the motor cases of the IUS; the multi-layer insulation (MLI) used on the outside of the motor cases; the carbon-carbon material of the nozzle exit cones; and Kevlar epoxy, which is the main material used in the motor cases. The spacecraft surfaces used were solar cells, optical solar reflectors (OSR's) and aluminized Mylar.

The IUS materials were heated to temperatures in the range of 93°C (200°F) to 316°C (600°F) for times of 1 to 24 hours in a vacuum (10^{-6} torr) and deposited on the spacecraft surfaces at 25°C. The contaminated surfaces were measured for reflectance, photomicroscopically examined, exposed to ultraviolet (UV) radiation, measured again for reflectance, and photomicroscopically examined after UV exposure. Solar cell outputs were measured before and after contamination and following UV exposure. Infrared characteristic identifications were conducted on the material deposits. A quartz crystal microbalance (QCM) at 25°C was used in the vacuum chamber to record the rate of material being outgassed and collected from the four IUS materials. All of the measurements except the outgassing rates were made in room air.

Standard VCM outgassing tests at 125°C with collectors at 25°C were conducted for comparison to the shorter high temperature VCM's. Complete thermogravimetric analysis (TGA), differential thermogravimetric analysis (DTGA) and differential thermal analysis (DTA) were conducted on all four IUS materials.

In this paper, we will concentrate primarily on the contamination effects measurements. Additional data can be obtained from Boeing document D290-10590-1, dated 15 March 1980.

TEST DESCRIPTION

FACILITIES

A standard Micro-Volatile-Condensible-Materials (VCM) system was used for producing contamination from the four materials. Reflectance measurements were made with a Beckman DK-2A ratio recording spectrophotometer, using an integrating sphere to catch both diffuse and specular reflection. To simulate the effects of ultraviolet radiation, a 2500 watt high-pressure xenon lamp was used as a source in a special irradiation facility. Three contaminated samples at a time were mounted near the source on arms cooled to keep the samples at 15°C during irradiation. Flowing dry nitrogen was passed through open cylinders around each sample, to maintain an inert environment. At the sample positions, the source provided about 2.9 equivalent ultraviolet solar constants, for wavelengths down to about 1850 Å.

Other equipment used in the testing included a Spectrolab X-25 solar simulator for testing solar-cell output, a Mettler recording vacuum thermoanalyzer, a Faraday quartz-crystal microbalance, and microscope optics and photographic equipment for sample examination, and an infrared spectrometer.

OUTGASSING IUS MATERIALS

Descriptions of the four IUS materials and their preparation for testing are contained in the following paragraphs.

Carbon-Carbon—The carbon-carbon exit cone material is manufactured by Kaiser-Aerotech, using phenolic graphite prepregnated cloth laid up in an involute exit cone configuration. The material undergoes a debulking, curing, post-cure, carbonization, graphitization and densification process which exposes the material to over 2500°C for long periods of time.

Multi-Layer Insulation—The MLI used in the test covers both the forward equipment support section and the sides of the motor cases of both Solid Rocket Motor (SRM) 1 and 2. The MLI consists of ten layers; the outer layer is aluminized Kapton with Kapton side out. The inner eight layers are crinkled aluminized Mylar which are perforated. The innermost layer of the blanket is aluminized Kapton, also perforated. Velcro tape is used to fasten the blanket to the IUS interstage and forward rings.

Kevlar Epoxy—The solid rocket motors of the IUS are made by filament winding, using a high modulus aramid fiber (Kevlar) and heat setting epoxy resin system. The motors are then cured at various temperatures and periods of time. Specifications for the motor cases and their curing cycles can be found in Specification No. SE0852A of the Chemical Systems Division of United Technologies.

EPDM—Ethylene Propylene Diene Monomer (EPDM) is the designation for the rubber insulation used to insulate the Kevlar epoxy motor case from the hot exhaust gasses of the combustion chamber. The rubber insulation contains a large number of ingredients, of which the major ones are EPDM (Nordel 1040), Neoprene FB, 1/4" carbon fibers and Phenolic (BKR 2620). This material also goes through a curing process as specified in Specification No. SE0875.

Approximately 200 milligrams of material were prepared for each pot in the VCM facility. The carbon-carbon material was crushed into a powder form. The multi-layer blanket was cut into very small pieces. A percentage of each type of material from the multi-layer blanket was a part of the sample including a piece of the Velcro fastener. The Kevlar case and EPDM rubber were shaved with a knife to obtain the desired samples.

SPACECRAFT SURFACE MATERIALS (COLLECTORS)

The collectors which were used as substrates for contaminant deposits are described in the following paragraphs.

Optical Solar Reflectors—The optical solar reflector (OSR) or second surface thermal control mirror is built by Optical Coatings Laboratory, Inc. It consists of 0.2 mm thick fused silica with a vapor deposit of silver on one side with an Inconel protective overcoating. The uncoated fused silica side of the 2.5 x 2.5 cm square OSR is exposed to contamination.

Aluminized Mylar—The aluminized Mylar consists of 0.5 mil Mylar with vacuum deposited aluminum on both sides. The nominal solar absorptance of the aluminized Mylar is 0.14 and infrared emittance is 0.05.

Solar Cells—The solar cells are rectangular wafers of dimensions 4 x 2 x 0.1 cm, consisting of a ceramic base, an 0.02 cm-thick silicon photovoltaic cell with tantalum oxide anti-reflection coating and the necessary electrical contacts, and a protective fused-silica cover glass with magnesium fluoride anti-reflection coating and a .35 micron cutoff filter. The outermost surface, upon which contaminant materials are deposited in this test, thus consists of magnesium fluoride. The outer electrical contact is a grid of silver lines reaching out 1 centimeter to either side of a 4 centimeter central bus of 0.1 centimeter width. There are 30 lines on either side of the bus, each of approximately 0.01 centimeter width. Thus, approximately 10% of the front surface is highly reflective. Four leads are attached to the cell contacts (two apiece) to provide accurate current and voltage measurement. In addition, a thermocouple is available to monitor cell temperature during testing.

The OSR's, solar cells and aluminized Mylar are attached to a 3.8 cm diameter aluminum disk using BMS 529 epoxy, which has very low outgassing characteristics. The aluminum disks could be easily mounted in the micro-VCM facility. All spacecraft material surfaces were thoroughly cleaned by gently wiping the surfaces with cotton gauze dipped in high grade acetone until the cotton gauze came clean after wiping.

TEST PROCEDURE

Pots containing approximately 200 milligrams of outgassing material were weighed on a microbalance accurate to ± 10 micrograms, then inserted into the copper heating bar in the VCM apparatus, facing the spacecraft surfaces to be contaminated. Cooling water was circulated through the copper bar to which the collector surfaces were attached, the chamber was evacuated to 10^{-6} torr, and then the heater turned on. The heater bar was held at a predetermined temperature for a fixed period of time after the initial heat-up. Then the heater was switched off; near room temperature, the system was back-filled with dry N_2. The collector surfaces (all of which were previously weighed, except for the bulky solar cells) and pots were removed and weighed to determine total mass loss (from the pots) and total collected mass.

From this point, some collector samples were measured for reflectance change and some were installed in the UV apparatus for 9 hours of exposure to about 2.9 suns, giving about one solar day of ultraviolet irradiation. (Studies by Martin-Marietta Aerospace have indicated that most of the degradation of contamination by UV radiation occurs within the first 20 sun hours of exposure.) Following irradiation, these samples were measured for reflectance. Selected samples were then subjected to microscopic examination. All solar cells were then sent to the solar simulator for output measurements. When all tests had been finished for one material at a given exposure time and temperature, the spacecraft surfaces were cleaned by gently wiping with acetone. At this point, the sample surfaces were ready for the next dose of contamination.

ORIGINAL PAGE IS
OF POOR QUALITY

TEST MEASUREMENTS

The object of the test program was to deposit outgassed materials of different quantities from four IUS materials on various spacecraft materials and measure the optical effects. The following paragraphs describe the measurements made.

Total Mass Loss and Volatile Condensible Materials

The Total Mass Loss (TML) of material was measured by first measuring the weight of IUS material which was put into a small pot prior to insertion into the vacuum facility. (The pot and material had been equilibrated for 24 hours in a 50% humidity desiccator.) After the specimen was exposed to vacuum and temperature conditions for a designated time, the pot is removed, equilibrated and then re-weighed. The difference in weight before and after exposure is the TML usually quoted as a percent of the initial total mass of material.

The percentage of volatile condensible materials (VCM) was measured by weighing a small disk after a 24-hour equilibration, then installing the disk in the vacuum, maintaining a disk temperature of 25°C, exposing the disk to materials being outgassed from the IUS materials, removing the disk, equilibrating for 24 hours and re-weighing the disk. The change in weight divided by the total weight of the sample before vacuum exposure is the percent VCM of the material.

Surface Reflectance

With the reflectance of a sample denoted by $R(\lambda)$, the solar absorptance of a sample is calculated by

$$\alpha_s = 1-\left(\int_{.25\mu}^{2.5\mu} R(\lambda)\, I_s(\lambda)d\lambda\right)/\left(\int_{.25\mu}^{2.5\mu} I_s(\lambda)d\lambda\right)$$

where $I_s(\lambda)$ is the solar spectral irradiance. The range of integration covers approximately 96% of the solar spectrum. The actual integration was performed by digitizing all reflectance curves in intervals of 21, 91 and 35 points for the wavelength ranges from .25 to .35, .35 to .8 and .8 to 2.5 microns respectively. Linear interpolation was used to input the solar spectrum function in the same intervals. The random error in solar absorptivity was approximately ± 0.01.

Solar Cell Output

Voltage-current characteristics of the solar cells used in this study were obtained under illumination of the cells by a Spectrolab X25 solar simulator. The xenon lamp source is constructed to give a spectral output very similar to one zero-air-mass sun. Lamp intensity is calibrated by a standard cell and fine-tuned before each solar-cell measurement.

ORIGINAL PAGE IS
OF POOR QUALITY

Cells being tested were always mounted in the same place, with temperature maintained at 28°C, as verified by the thermocouple attached to each cell. One set of leads was connected to a digital voltmeter and the other to an electronic load in series with a digital milliammeter. Voltage output was recorded on the Y-axis and cell current on the X-axis of an X-Y recorder, as the load was varied from 0 to∞. Digital values of the open-circuit voltage and the short-circuit current were noted for each sample.

Photomicroscopic Examination

Examination of the contaminated samples was carried out with various microscopic and photographic equipment, with background illumination selected to enhance the most important features of the contaminant. Most of the materials tested formed transparent films on brass and copper disks. However, on the spacecraft surfaces, the outgassed materials formed strongly-scattering layers of liquid droplets and solid crystals, requiring detailed microscopic examination in order to understand the effects on surface absorptance.

TEST RESULTS

TML AND VCM

These measurements were made both under standard conditions (125°C source temperature for 24 hours) and for higher temperatures, more characteristic of the operational IUS. Table 1 lists the TML and the VCM from copper and brass collector disks.

General conclusions from the weight changes are:

1) EPDM is the most volatile of the outgassing materials, followed in descending order by Kevlar, multi-layer blanket, and carbon-carbon.

2) Heating the test materials to 316°C produced 4-10 times more VCM than the standard test (125°C) produced.

3) At a temperature of 205°C, changing exposure time from 2 to 6 hours does not change the VCM, indicating that the majority of the material is outgassed within the first two hours.

CONTAMINATION MEAN THICKNESS

Mean thicknesses of the contamination layer were estimated using the VCM data, estimating the deposit area and assuming a deposit density of one gram per cubic centimeter. The mean thicknesses are listed in Table 2.

SURFACE REFLECTANCE

The results of the reflectance measurements are listed in Table 3 as solar absorptance of the clean surfaces and with the presence of contamination, both before and after UV irradiation. Aluminized Mylar is by far the most susceptible of the three spacecraft surfaces to changes in solar absorptance. OSR's are more susceptible than the solar cells. EPDM is the only material to cause

large increases in solar absorptance after UV exposure. The increase in solar absorptance caused by outgassing of the MLI, Kevlar epoxy or carbon-carbon was partially reversed by exposure to UV in most cases. The outgassing products of Kevlar epoxy (205°C) are resistant to any UV-induced changes in solar absorptance.

SOLAR-CELL POWER LOSS

To obtain the contamination-induced solar-cell power loss, a curve of voltage versus current was generated for each of six clean cells. Following each contaminant deposition, three contaminated cells were tested under the solar simulator. Then, they were wiped with acetone and tested again, to generate a "clean" solar-cell curve for the next run.

Table 4 lists the percentage changes in output power of the solar cells at 0.45V, (the typical operating point). For each contamination run, two cells were tested without UV exposure and one cell after 26 equivalent solar hours of UV exposure. Solar cell power output losses at or near operating voltage (.45 volts) varied from fractions of 1 percent to 23 percent.

PHOTOMICROSCOPIC EXAMINATION

Examples of the widely varied types of crystalline and droplet formations on the contaminated spacecraft surfaces are given for each material in Figures 1 through 12. All the photographs were taken at a magnification of 50X. The verticle side of each picture is .4 millimeters actual size. The photographs in Figure 1 through 6 show the contaminant films collected on OSR's at one outgassing temperature before and after UV exposure for the EPDM, MLI, and Kevlar epoxy materials. Figures 7 through 10 are before-and after-UV photographs of the carbon-carbon deposits at two different exposure times. The carbon-carbon outgassing deposit on a solar cell is depicted in Figures 11 and 12, to show the effect of different substrates (compare Figures 9 and 10 with 11 and 12). It is evident that the deposit structure is dependent on the type of surface being deposited on.

The effects of exposure to 26 equivalent sun-hours of UV radiation also varied widely. Except for EPDM, crystal structures were almost entirely removed, leaving behind only the liquid droplets, whose volume was often reduced. In the case of the multi-layer blanket, UV exposure always removed almost the entire deposit. EPDM crystallites seemed relatively impervious to UV.

CONCLUSIONS

We can summarize the results of this work as follows:

(a) Volatile condensible materials and total mass loss data have been obtained at standard conditions and also at high temperature and short time periods on four IUS materials.

(b) Mean contaminant film thickness varied from 2000 Angstroms to 83,000 Angstroms. Microscopic observations showed crystals between 5000 to

ORIGINAL PAGE IS
OF POOR QUALITY

500,000 Angstroms with liquid droplets from 5000 to 50,000 Angstroms in height. In some cases, only part of the surface area is covered with crystals and liquid. This illustrates the wide variation which exists between a contaminant film of uniform "mean" thickness and the real surface deposits.

(c) The optical solar reflectors were greatly affected by the VCM from the EPDM rubber. The solar absorptance changed from 0.07 to 0.14 with a mean 2500 Angstrom layer of contamination. When exposed to UV, it increased to 0.18. With a mean 83,000 Angstrom layer, the absorptance went to .24 and with solar radiation exposure, it degraded to 0.46. 1900 Angstroms of Kevlar epoxy VCM (from 121°C, 1 hour exposure) on the OSR's had no effect on the absorptance with or without solar radiation. When the Kevlar Epoxy was heated to 205°C and a deposit of 3200 Angstroms of material was made on an OSR, the absorptance changed from .07 to .13 with no effect from solar irradiation. No effect of VCM from the multi-layer insulation or from the carbon-carbon nozzle material was evident on the solar absorptance of the OSR's.

(d) Solar cell power output losses at or near operating voltage (.45 volts) varied from fractions of 1 percent to 23 percent. The solar cell data trends generally correlated with OSR reflectance changes, but there seemed to be significant scatter in the data.

ORIGINAL PAGE IS
OF POOR QUALITY

Table 1: IUS Materials TML and VCM

TEMP °C	TEMP °F	TIME HR	MATERIAL: EPDM TWL %	EPDM VCM %	MULTI-LAYER TWL %	MULTI-LAYER VCM %	KEVLAR TWL %	KEVLAR VCM[a] %	CARBON-CARBON TWL %	CARBON-CARBON VCM %
125	256	24	3.65	0.88	.095	0.045	0.72	0.018	0.019	0.013
205	400	2	4.85	1.60	.800	0.050	1.06	0.055	0.040	0.010
205	400	6		1.70		0.030		0.030		0
316	600	2		3.54		0.550		1.400		

Table 2: Mean Thickness of Collected Material

IUS MATERIAL	TEMPERATURE °C	EXPOSURE TIME HR	THICKNESS Å
EP DM	107	1	2500
	205	1	83,000
MULTI-LAYER INSULATION	135	1	3800
	205	1	6400
KEVLAR EPOXY	121	1	1900
	205	1	600 - 3200
CARBON-CARBON	316	1	600 - 3800
	316	2	3800

Thickness defined by:

a. Weights from VCM deposits
b. Area of deposit on collector from photographs
c. A unit density of 1 gm/cm^3 is assumed

ORIGINAL PAGE IS
OF POOR QUALITY

Table 3: Solar Absorptance Measurements

IUS Material	Temp °C	Optical Solar Reflector			Solar Cell			Aluminized Mylar		
		Clean	No UV	UV	Clean	No UV	UV	Clean	No UV	UV
EP DM	107	.07	.14	.18	.85	.87	.86	.09	.17	.25
	205	.07	.21	.46	.85	.90	.99	.09	.30	.36
Multi-Layer Insulation	135	.07	.08	.07	.80	.84	.87	.09	.16	.11
	205	.07	.07	.06	.80	.88	.87	.09	.21	.17
Kevlar	121	.07	.07	.07	.85	.88	.85	.09	.14	.12
	205	.07	.13	.13	.85	.88	.88	.09	.26	.26
Carbon-Carbon	316	.07	.08	.07	.80	.88	.82	.09	.21	.24
	316*	.07	.07	.09	.80	.87	.84	.09	.19	.17

* Exposure time at constant temperature was 2 hours. All others were exposed for 1 hour.

Table 4: Solar Cell Power Output Change at 0.45V Percentage Change

IUS MATERIAL	TEMP (°C)	NO UV	UV
EP DM	107	-2.1	-7.1
	205	-12.0	-22.4
MULTI-LAYER INSULATION	135	-23.1	-10.4
	205	-3.1	-4.6
KEVLAR	121	-3.1	-0.4
	205	-4.5	-4.9
CARBON-CARBON	316(1)	-2.3	-6.6
	316(2)	-4.0	-5.8

- "No UV" percentage changes are averages of results from two solar cells.
- Exposure times at constant temperature were 1 hour except for second carbon-carbon which was for 2 hours.

ORIGINAL PAGE
BLACK AND WHITE PHOTOGRAPH

Figure 1. EPDM Contaminant on OSR before UV (1 hour at 205°C)

ORIGINAL PAGE
BLACK AND WHITE PHOTOGRAPH

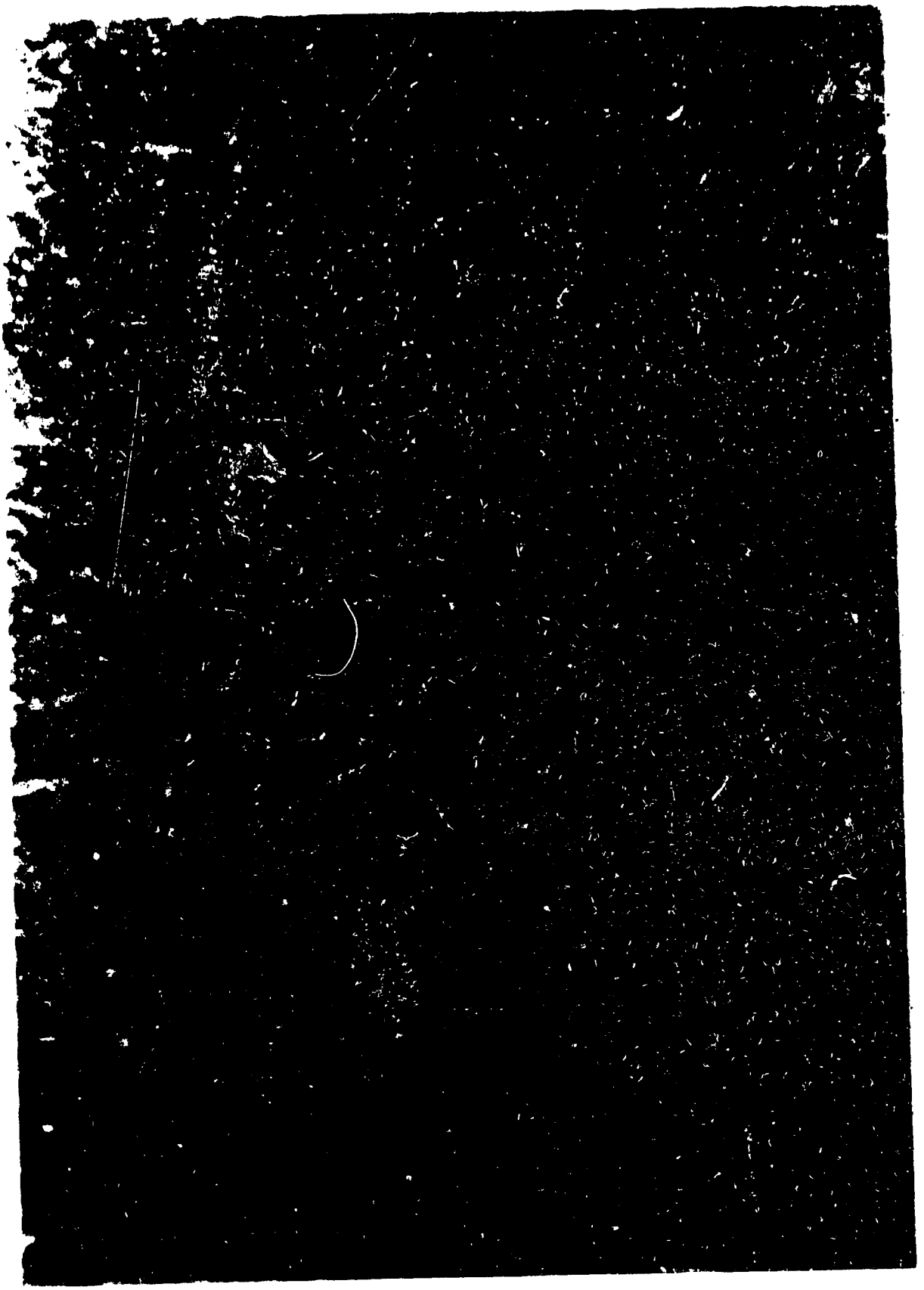

Figure 2. EPDM Contaminant on OSR after UV (1 hour at 205°C)

ORIGINAL PAGE
BLACK AND WHITE PHOTOGRAPH

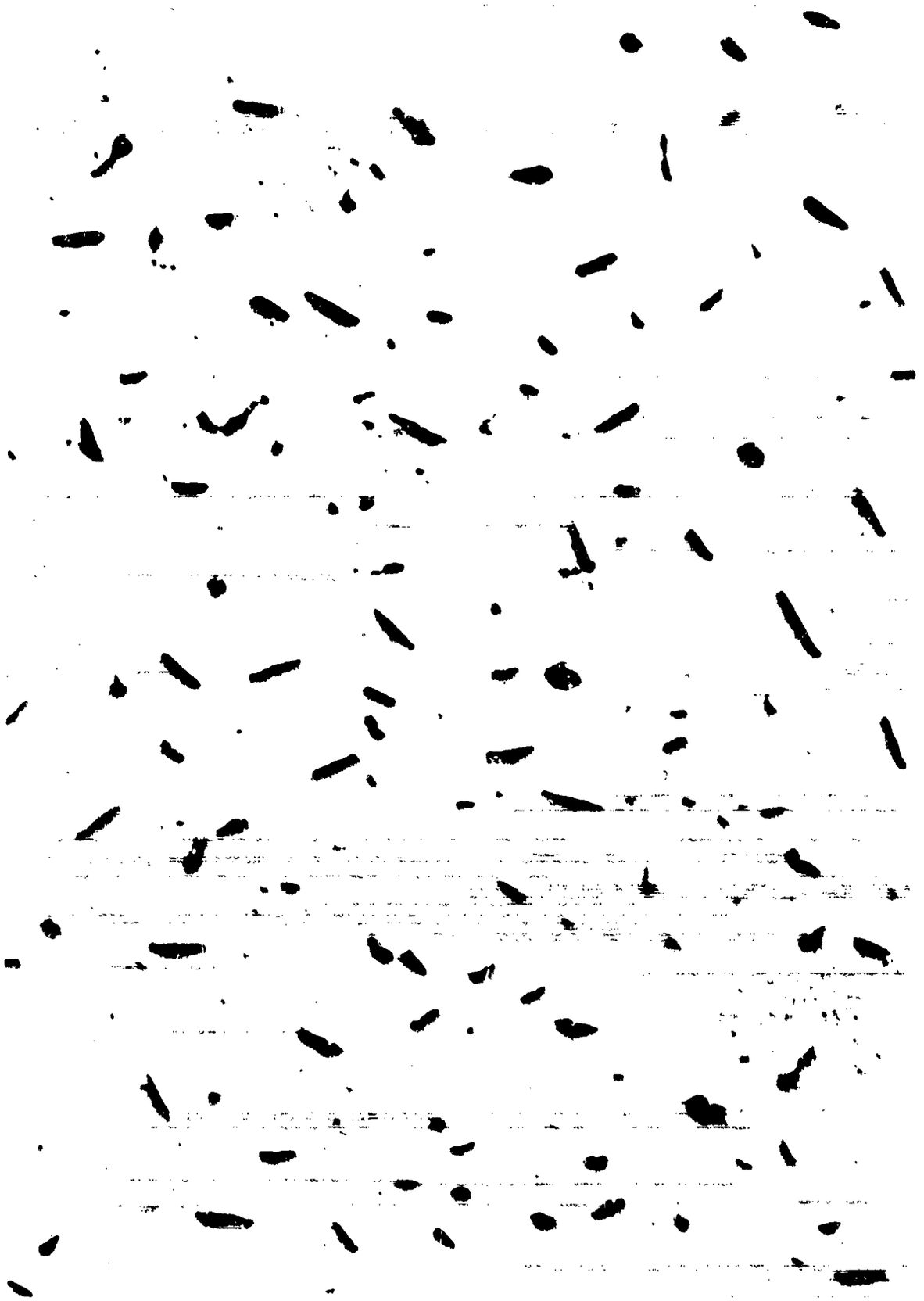

Figure 3. Multilayer Insulation Contaminant on OSR before UV (1 hour at 205°C)

ORIGINAL PAGE
BLACK AND WHITE PHOTOGRAPH

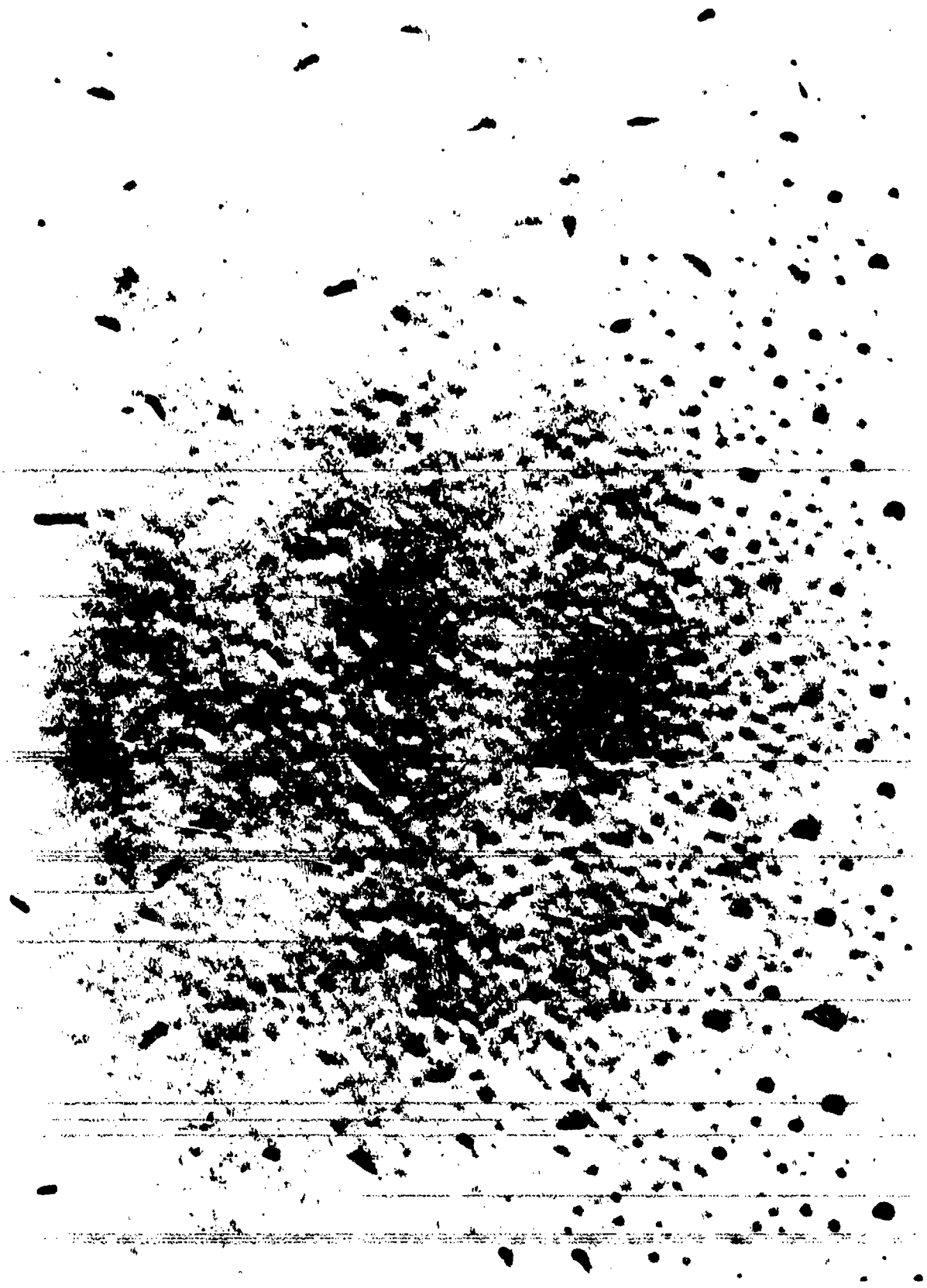

Figure 4. Multilayer Insulation Contaminant on OSR after UV (1 hour at 205°C)

ORIGINAL PAGE
BLACK AND WHITE PHOTOGRAPH

Figure 5. Kevlar-Epoxy Contaminant on OSR before UV (1 hour at 121°C)

ORIGINAL PAGE
BLACK AND WHITE PHOTOGRAPH

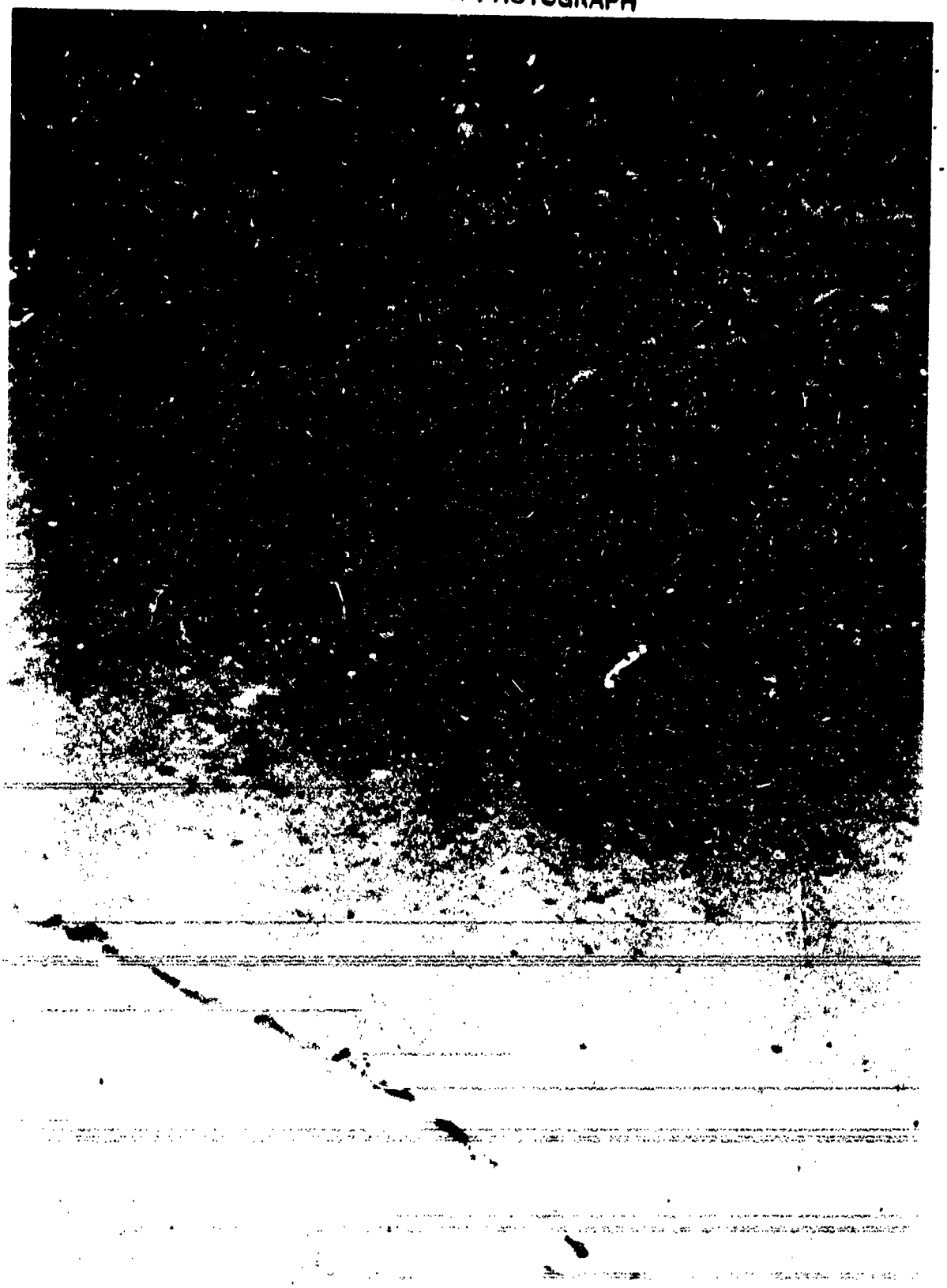

Figure 6. Kevlar-Epoxy Contaminant on OSR after UV (1 hour at 121°C)

ORIGINAL PAGE
BLACK AND WHITE PHOTOGRAPH

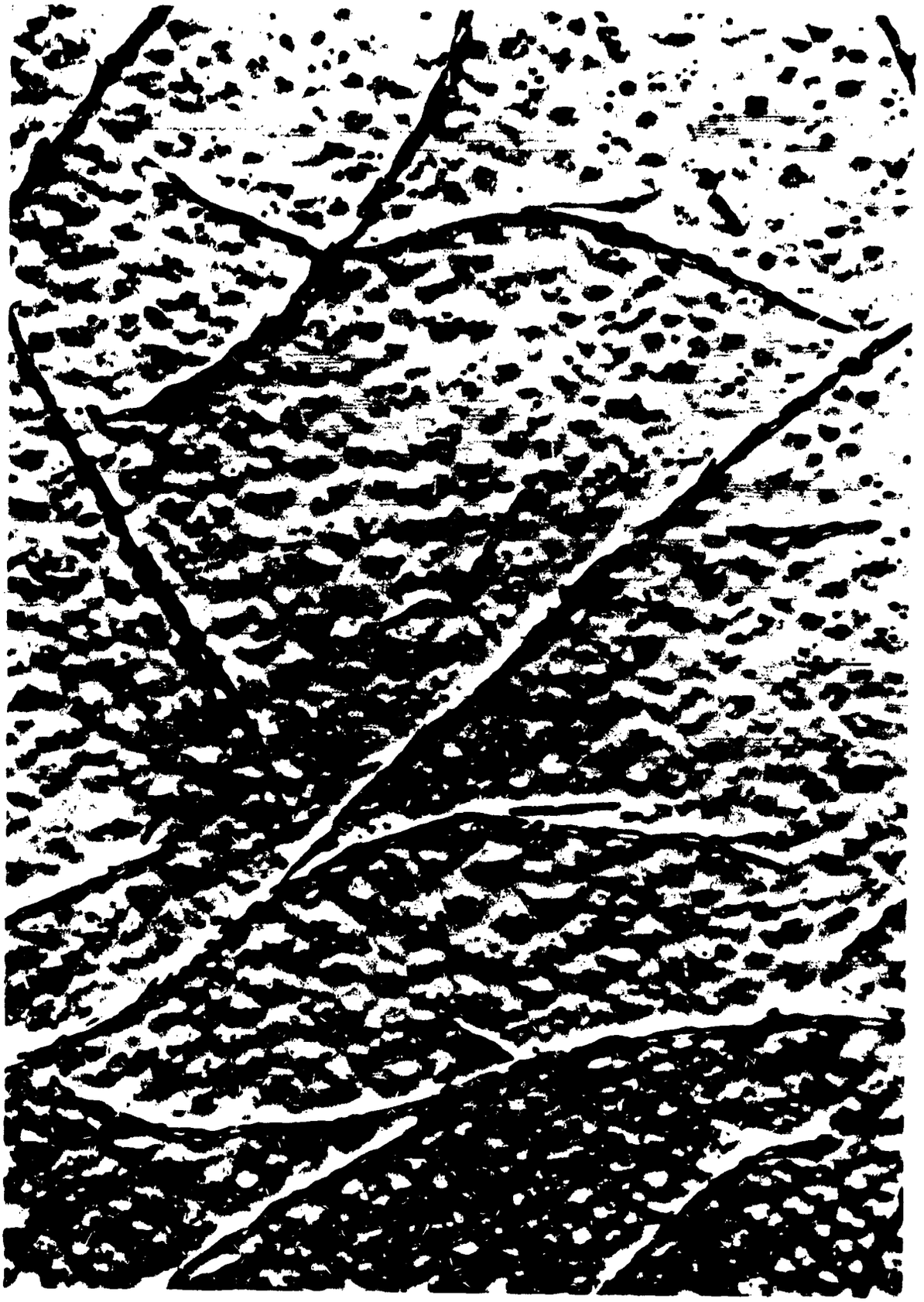

Figure 7. Carbon-Carbon Contaminant on OSR before UV (1 hour at 316°C)

ORIGINAL PAGE
BLACK AND WHITE PHOTOGRAPH

Figure 8. Carbon-Carbon Contaminant on OSR after UV (1 hour at 316°C)

ORIGINAL PAGE
BLACK AND WHITE PHOTOGRAPH

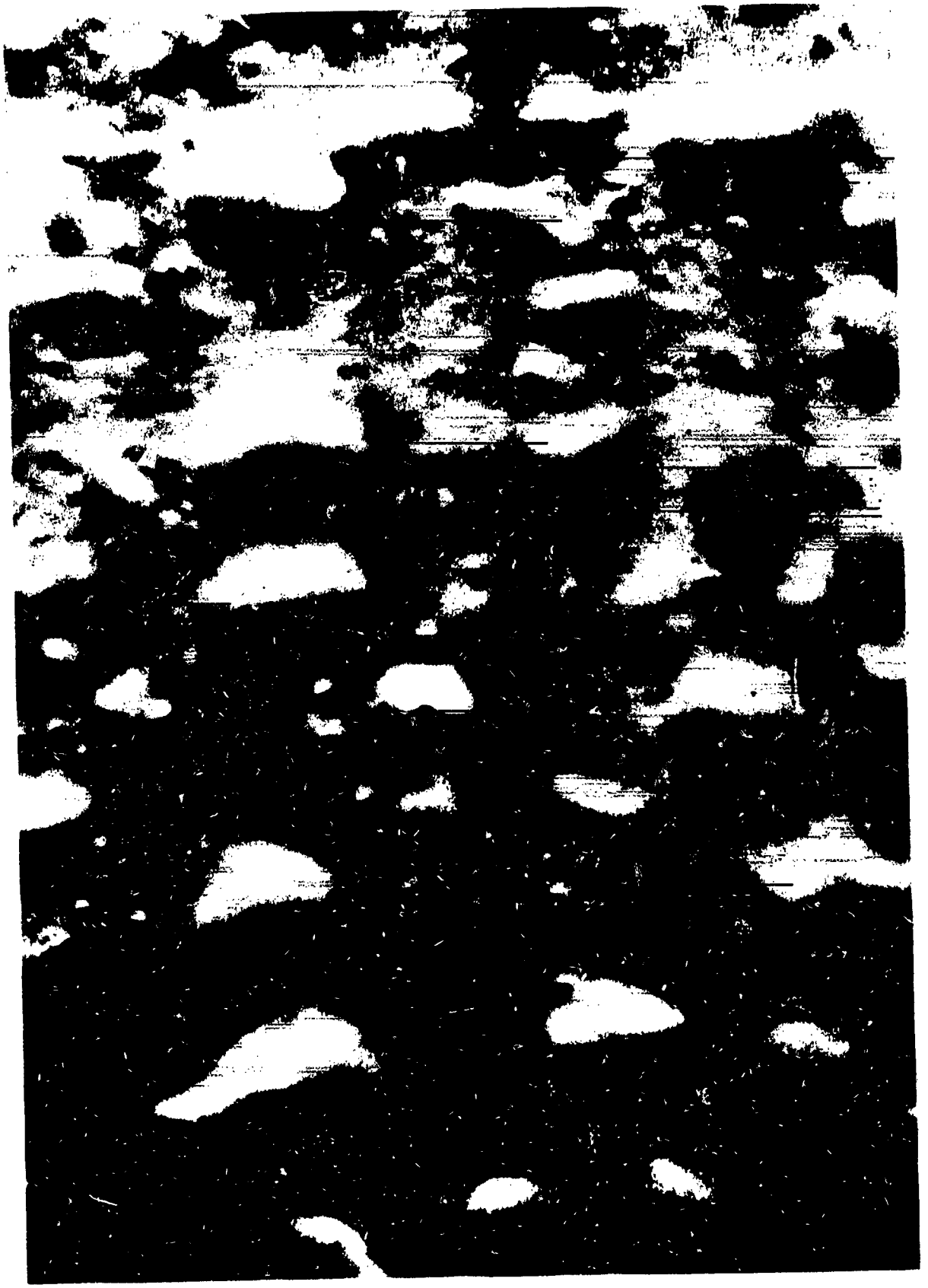

Figure 9. Carbon-Carbon Contaminant on OSR before UV (2 hours at 316°C)

ORIGINAL PAGE
BLACK AND WHITE PHOTOGRAPH

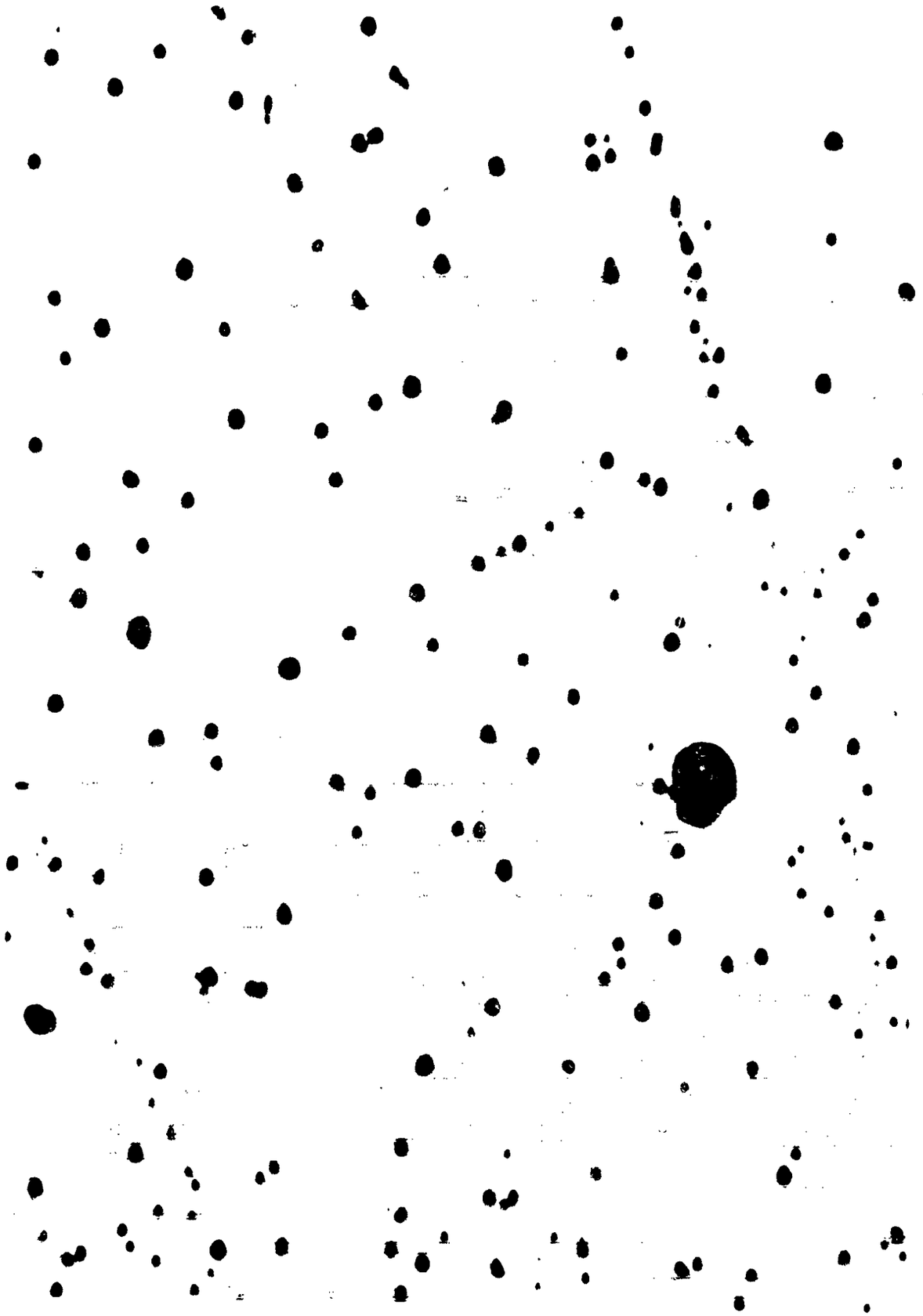

Figure 10. Carbon-Carbon Contaminant on OSR after UV (2 hours at 316°C)

ORIGINAL PAGE
BLACK AND WHITE PHOTOGRAPH

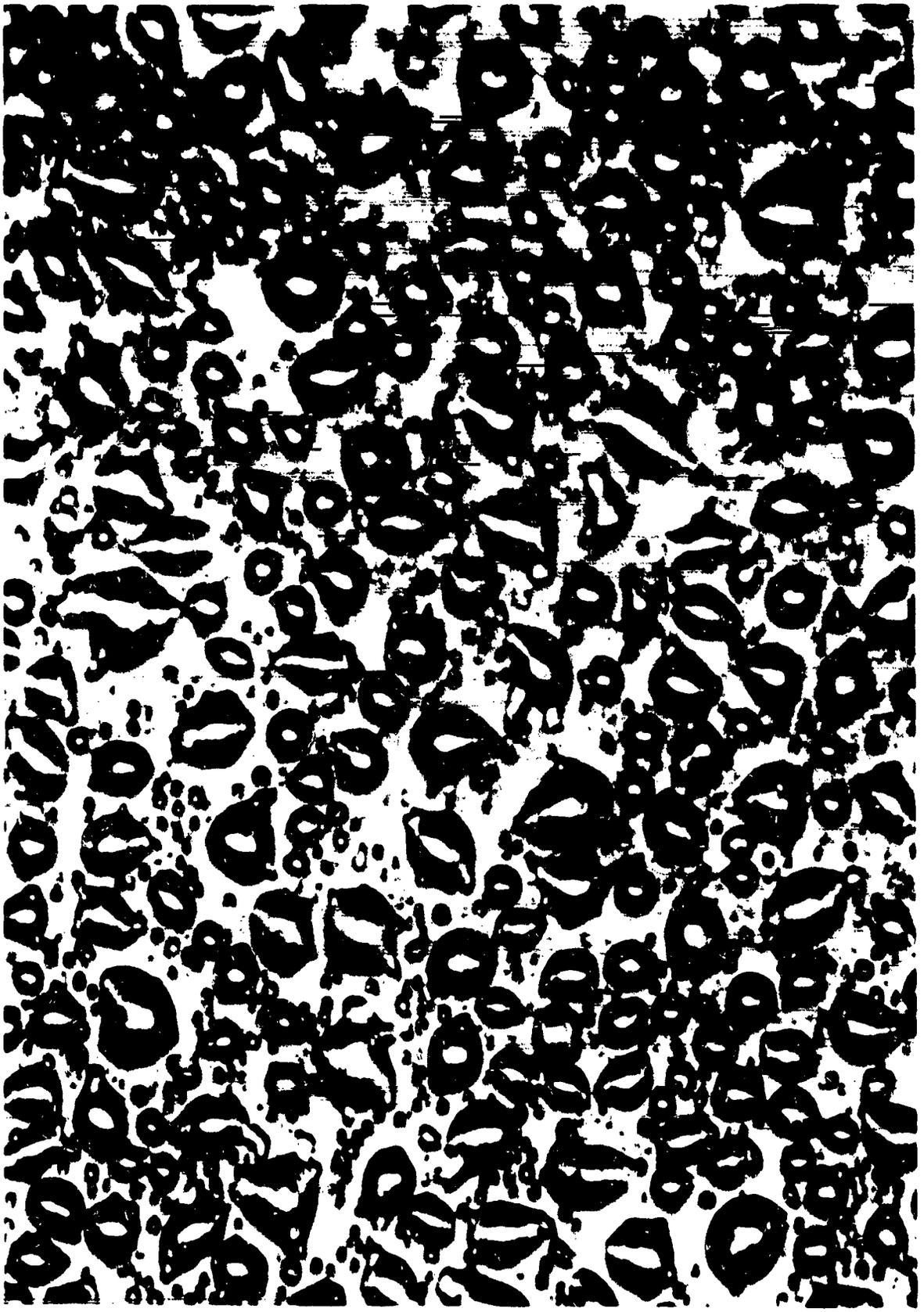

Figure 11. Carbon-Carbon Contaminant on Solar Cell before UV (2 hours at 316°C)

ORIGINAL PAGE
BLACK AND WHITE PHOTOGRAPH

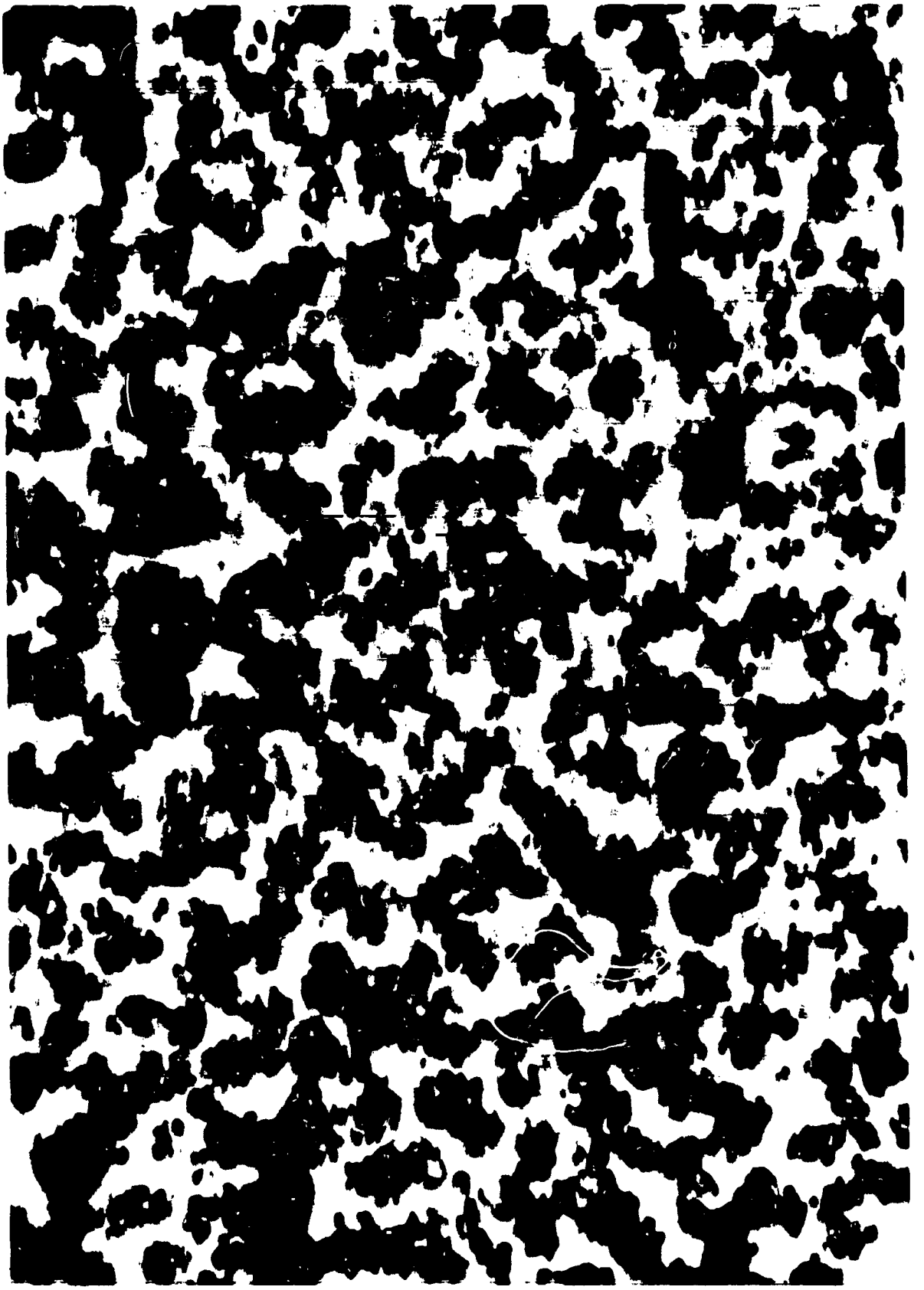

Figure 12. Carbon-Carbon Contaminant on Solar Cell after UV (2 hours at 316°C)